

FOREWORD

This report presents the results of a laboratory and field study of composite piles for use as foundation elements for bridges. Two types of composite piles were studied, a fiber-reinforced polymer (FRP) concrete-filled shell, and a plastic pile reinforced with a welded steel cage. Both axial and lateral short-term load displacement behavior was studied, as well as interfaced mechanical properties. Axial and lateral load-displacement behavior was similar for the concrete control pile and the FRP pile, and the plastic pile was significantly less stiff in both loading modes.

Gary Henderson
Director, Office of Infrastructure Research
and Development

NOTICE

This document is disseminated under the sponsorship of the U.S. Department of Transportation in the interest of information exchange. The U.S. Government assumes no liability for the contents or the use thereof. The contents of this report reflect the views of the contractor, who is responsible for the accuracy of the data presented herein. The contents do not necessarily reflect the official policy of the U.S. Department of Transportation. The report does not constitute a standard, specification, or regulation.

The U.S. Government does not endorse products or manufacturers. Trademarks and manufacturers' names appear in this report only because they are considered essential to the object of this document.

QUALITY ASSURANCE STATEMENT

The Federal Highway Administration (FHWA) provides high-quality information to serve Government, industry, and the public in a manner that promotes public understanding. Standards and policies are used to ensure and maximize the quality, objectivity, utility, and integrity of its information. FHWA periodically reviews quality issues and adjusts its programs and processes to ensure continuous quality improvement.

1. Report No FHWA-HRT-04-043	2. Government Accession No. N/A	3. Recipient's Catalog No. N/A	
4. Title and Subtitle A Laboratory and Field Study of Composite Piles for Bridge Substructures		5. Report Date March 2006	
		6. Performing Organization Code N/A	
7. Authors(s) Miguel A. Pando, Carl D. Ealy, George M. Filz, J.J. Lesko, and E.J. Hoppe		8. Performing Organization Report No. N/A	
9. Performing Organization Name and Address Virginia Transportation Research Council 530 Edgemont Road Charlottesville, VA 22903		10. Work Unit No. (TRAIS) N/A	
		11. Contract or Grant No. DTFH61-99-X-00023	
		13. Type of Report and Period Covered Final Report July 1999–May 2003	
12. Sponsoring Agency Name and Address Office of Infrastructure R&D Federal Highway Administration 6300 Georgetown Pike McLean, VA 22101-2296		14. Sponsoring Agency Code	
15. Supplementary Notes Contracting Officer's Technical Representative: Carl Ealy, HRDI-06			
16. Abstract <p>The most commonly used pile materials are steel, concrete, and wood. These materials can degrade, and the degradation rate can be relatively rapid in harsh marine environments. It has been estimated that the U.S. spends over \$1 billion annually for repair and replacement of waterfront piling systems. This high cost has spurred interest in alternative composite pile materials such as fiber-reinforced polymers (FRPs), recycled plastics, and hybrid materials. Because only minimal performance data have been collected for composite piles, a research project was undertaken to investigate (1) soil-pile interface behavior of composite piles, (2) the long-term durability of concrete-filled FRP shell composite piles, and (3) the driveability and axial and lateral load response of concrete-filled FRP composite piles and steel-reinforced recycled plastic piles by means of field tests and analyses. In addition, a long-term monitoring program was implemented at a bridge over the Hampton River in Virginia.</p> <p>According to laboratory test results, values of residual interface friction angle between three pile surfaces and a subrounded to rounded sand were 27, 25, and 28 degrees for a FRP composite pile, the recycled plastic pile, and the prestressed concrete pile respectively, while the values of residual interface friction angle between these piles and a subangular to angular sand were 29, 29, and 28 degrees for the FRP composite pile, the recycled plastic pile, and the prestressed concrete pile, respectively. Regarding durability of FRP composite piles, it was found that moisture absorption caused degradation of strength and stiffness of the FRP shells, but that freeze-thaw cycles had little effect. Analyses indicate that FRP degradation due to moisture absorption should have minimal impact on axial capacity of the FRP composite piles because most of the axial capacity is provided by the concrete infill; however, FRP degradation has a larger effect on lateral capacity because the FRP shell provides the capacity on the tension side of the pile. The field tests demonstrated that there were not major differences in driveability of the FRP composite pile, the recycled pile, and the prestressed concrete pile. In static load tests, the FRP composite pile and prestressed concrete pile exhibited similar axial and lateral stiffness, and the plastic pile was significantly less stiff. Conventional static analyses of axial load capacity, axial load versus settlement, and lateral load versus deflection provided reasonable predictions for the composite piles, at least to the levels of accuracy that can be achieved for more common pile materials. The long-term monitoring program has been implemented for an FRP composite pile and a prestressed concrete pile so that their load-transfer performance can be compared over time. The long-term monitoring is being done by Virginia DOT.</p>			
17. Key Words Composite piles, driven piles, dynamic analysis of piles, FRP piles, recycled plastic piles, CAPWAP		18. Distribution Statement No restrictions. This document is available to the Public through the National Technical Information Service; Springfield, VA 22161	
19. Security Classif. (of this report) Unclassified	20. Security Classif. (of this page) Unclassified	21. No. of Pages 384	22. Price N/A

SI* (MODERN METRIC) CONVERSION FACTORS

APPROXIMATE CONVERSIONS TO SI UNITS

Symbol	When You Know	Multiply By	To Find	Symbol
LENGTH				
in	inches	25.4	millimeters	mm
ft	feet	0.305	meters	m
yd	yards	0.914	meters	m
mi	miles	1.61	kilometers	km
AREA				
in ²	square inches	645.2	square millimeters	mm ²
ft ²	square feet	0.093	square meters	m ²
yd ²	square yard	0.836	square meters	m ²
ac	acres	0.405	hectares	ha
mi ²	square miles	2.59	square kilometers	km ²
VOLUME				
fl oz	fluid ounces	29.57	milliliters	mL
gal	gallons	3.785	liters	L
ft ³	cubic feet	0.028	cubic meters	m ³
yd ³	cubic yards	0.765	cubic meters	m ³
NOTE: volumes greater than 1000 L shall be shown in m ³				
MASS				
oz	ounces	28.35	grams	g
lb	pounds	0.454	kilograms	kg
T	short tons (2000 lb)	0.907	megagrams (or "metric ton")	Mg (or "t")
TEMPERATURE (exact degrees)				
°F	Fahrenheit	5 (F-32)/9 or (F-32)/1.8	Celsius	°C
ILLUMINATION				
fc	foot-candles	10.76	lux	lx
fl	foot-Lamberts	3.426	candela/m ²	cd/m ²
FORCE and PRESSURE or STRESS				
lbf	poundforce	4.45	newtons	N
lbf/in ²	poundforce per square inch	6.89	kilopascals	kPa

APPROXIMATE CONVERSIONS FROM SI UNITS

Symbol	When You Know	Multiply By	To Find	Symbol
LENGTH				
mm	millimeters	0.039	inches	in
m	meters	3.28	feet	ft
m	meters	1.09	yards	yd
km	kilometers	0.621	miles	mi
AREA				
mm ²	square millimeters	0.0016	square inches	in ²
m ²	square meters	10.764	square feet	ft ²
m ²	square meters	1.195	square yards	yd ²
ha	hectares	2.47	acres	ac
km ²	square kilometers	0.386	square miles	mi ²
VOLUME				
mL	milliliters	0.034	fluid ounces	fl oz
L	liters	0.264	gallons	gal
m ³	cubic meters	35.314	cubic feet	ft ³
m ³	cubic meters	1.307	cubic yards	yd ³
MASS				
g	grams	0.035	ounces	oz
kg	kilograms	2.202	pounds	lb
Mg (or "t")	megagrams (or "metric ton")	1.103	short tons (2000 lb)	T
TEMPERATURE (exact degrees)				
°C	Celsius	1.8C+32	Fahrenheit	°F
ILLUMINATION				
lx	lux	0.0929	foot-candles	fc
cd/m ²	candela/m ²	0.2919	foot-Lamberts	fl
FORCE and PRESSURE or STRESS				
N	newtons	0.225	poundforce	lbf
kPa	kilopascals	0.145	poundforce per square inch	lbf/in ²

*SI is the symbol for the International System of Units. Appropriate rounding should be made to comply with Section 4 of ASTM E380. (Revised March 2003)

TABLE OF CONTENTS

CHAPTER 1. INTRODUCTION	1
1.1 GENERAL INTRODUCTION	1
1.2 OBJECTIVES.....	2
1.3 ORGANIZATION OF REPORT.....	2
CHAPTER 2. BACKGROUND AND LITERATURE REVIEW.....	5
2.1 INTRODUCTION	5
2.2 COMPOSITE PILE BACKGROUND.....	5
2.2.1 Types of Composite Piles.....	5
2.3 LITERATURE REVIEW FOR THE COMPOSITE PILES SELECTED.....	9
2.3.1 Structural Behavior	9
2.3.2 Long-Term Durability Behavior.....	17
2.3.3 Geotechnical Behavior	19
2.4 SUMMARY.....	23
CHAPTER 3. EXPERIMENTAL STUDY OF INTERFACE BEHAVIOR BETWEEN COMPOSITE PILES AND TWO SANDS	25
3.1 INTRODUCTION	25
3.2 SOIL MATERIALS	28
3.2.1 Index Properties	28
3.2.2 Direct Shear Tests of Sands.....	30
3.3 PILE SURFACES.....	34
3.3.1 Introduction.....	34
3.3.2 Surface Topography Characterization	35
3.3.3 Interface Hardness.....	40
3.4 INTERFACE SHEAR TESTS	41
3.5 DISCUSSION OF RESULTS.....	51
3.5.1 Multiple Linear Regression for Density Sand $\tan \delta_{peak}$ Values.....	52
3.5.2 Multiple Linear Regression for Density Sand $\tan \delta_{cv}$ Values.....	53
3.5.3 Multiple Linear Regression for Model Sand $\tan \delta_{peak}$ Values.....	54
3.5.4 Multiple Linear Regression for Model Sand $\tan \delta_{cv}$ Values.....	55
3.5.5 Observations from the Linear Regression Analyses Results	56
3.5.6 Influence of Angularity of Sand.....	56
3.6 SUMMARY.....	57
CHAPTER 4. EXPERIMENTAL DURABILITY STUDY OF FRP COMPOSITE PILES	59
4.1 INTRODUCTION	59
4.2 BACKGROUND ON DEGRADATION OF GLASS FRP COMPOSITES	59
4.3 LABORATORY STUDY OF DURABILITY	60
4.3.1 Description of Test Specimens	61
4.3.2 Test Equipment and Procedures	65

4.3.3	Baseline Mechanical Properties.....	70
4.3.4	Properties as a Function of Submergence Time and Moisture.....	72
4.3.5	Freeze-Thaw Degradation of Saturated FRP Samples.....	93
4.3.6	SEM Imaging.....	95
4.4	LONG-TERM STRUCTURAL CAPACITY OF FRP COMPOSITE PILES.....	97
4.4.1	Long-Term Structural Capacity of Composite Pile.....	97
4.4.2	Comments Related to the Axial Strain Levels in Piles	99
4.5	SUMMARY.....	100
CHAPTER 5. FIELD LOAD TESTS AT THE ROUTE 40 BRIDGE		103
5.1	INTRODUCTION	103
5.2	DESCRIPTION OF THE BRIDGE	103
5.2.1	The Former Bridge	103
5.2.2	The New Bridge.....	105
5.3	DESCRIPTION OF TEST PILES.....	107
5.3.1	Composite Test Pile.....	107
5.3.2	Prestressed Concrete Test Pile.....	109
5.4	SOIL CONDITIONS AT THE TEST SITE	110
5.5	PILE FABRICATION AND INSTALLATION	111
5.5.1	Fabrication of the Piles	111
5.5.2	Pile Installation.....	114
5.5.2	Pile Installation.....	114
5.6	STATNAMIC FIELD TESTING OF TEST PILES	117
5.6.1	Instrumentation.....	118
5.6.2	Axial Load Tests.....	119
5.6.3	Lateral Load Tests	122
5.7	COMPOSITE PILES IN THE NEW ROUTE 40 BRIDGE.....	130
5.7.1	Connection of Piles with Pile Cap Beam.....	130
5.8	SUMMARY AND CONCLUSIONS.....	133
CHAPTER 6. FIELD LOAD TESTS AT THE ROUTE 351 BRIDGE		135
6.1	INTRODUCTION	135
6.2	DESCRIPTION OF THE BRIDGE	135
6.2.1	The Original Bridge	135
6.2.2	The New Bridge.....	138
6.3	DESCRIPTION OF TEST PILES.....	140
6.3.1	Prestressed Concrete Test Pile.....	140
6.3.2	FRP Composite Test Pile.....	140
6.3.3	Polyethylene Composite Test Pile.....	143
6.4	SOIL CONDITIONS AT THE TEST SITE	146
6.4.1	Geology.....	146
6.4.2	Subsurface Conditions.....	147
6.4.3	Hampton River	148
6.5	TEST PILE INSTRUMENTATION AND FABRICATION	150
6.5.1	Test Pile Instrumentation.....	150
6.5.2	Fabrication of Prestressed Concrete Test Pile	155

6.5.3	Fabrication of FRP Composite Test Pile.....	156
6.5.3	Fabrication of FRP Composite Test Pile.....	156
6.5.4	Fabrication of Plastic Composite Test Pile.....	160
6.6	PILE INSTALLATION AND DYNAMIC TESTING.....	162
6.6.1	Pile Driving.....	162
6.6.2	Dynamic Testing.....	166
6.7	PILE INTEGRITY TESTING OF TEST PILES.....	169
6.8	FIELD TESTING OF TEST PILES.....	174
6.8.1	Axial Load Tests.....	174
6.8.2	Lateral Load Tests.....	182
6.9	SUMMARY AND CONCLUSIONS.....	183
CHAPTER 7. ANALYSES OF THE AXIAL LOAD TESTS AT THE ROUTE 351 BRIDGE		185
7.1	INTRODUCTION.....	185
7.2	AXIAL PILE CAPACITY.....	185
7.2.1	Methods to Estimate Axial Load Capacity of Driven Piles in Sand.....	185
7.2.2	Predicted Axial Capacities.....	195
7.2.3	Summary of Axial Pile Capacity Predictions.....	202
7.3	LOAD-SETTLEMENT BEHAVIOR, AXIALLY LOADED SINGLE PILES..	204
7.3.1	Introduction.....	204
7.3.2	Background, Load-Transfer Method for Pile Settlement Predictions.....	205
7.3.3	Predictions Using Empirical Load-Transfer Curves.....	206
7.3.4	Predictions Using Theoretical Load-Transfer Curves.....	217
7.3.5	Residual Stresses.....	235
7.3.5	Residual Stresses.....	235
7.4	CONCLUSIONS.....	235
CHAPTER 8. ANALYSES OF THE LATERAL LOAD TESTS AT THE ROUTE 351 BRIDGE		237
8.1	INTRODUCTION.....	237
8.2	GOVERNING DIFFERENTIAL EQUATION FOR THE LATERALLY LOADED PILE PROBLEM.....	237
8.2.1	Assumptions and Limitations of the Governing Differential Equation.....	241
8.3	METHODOLOGY USED TO ANALYZE THE LATERALLY LOADED TEST PILES.....	242
8.3.1	P-y Curves.....	242
8.3.2	P-y Method of Analysis.....	247
8.4	NUMERICAL ANALYSES RESULTS.....	248
8.4.1	General Input Information.....	249
8.4.2	P-y Analyses Results.....	252
8.4.2	P-y Analyses Results.....	252
8.4.3	Comparison of the Initial p-y Modulus Curves for the Three Test Piles.....	266
8.5	LIMITATIONS OF P-Y ANALYSES.....	266
8.6	SUMMARY.....	267

CHAPTER 9. LONG-TERM MONITORING AT THE ROUTE 351 BRIDGE.....	269
9.1 INTRODUCTION	269
9.2 INSTRUMENTED PRODUCTION PILES	269
9.2.1 Prestressed Concrete Production Pile	270
9.2.2 FRP Composite Production Pile	272
9.3 SOIL CONDITIONS AT THE INSTRUMENTED PRODUCTION PILES	275
9.4 PILE INSTALLATION AND DYNAMIC TESTING.....	278
9.4 PILE INSTALLATION AND DYNAMIC TESTING.....	278
9.4.1 Pile Driving	278
9.4.2 Dynamic Testing.....	279
9.5 PILE INTEGRITY TESTING OF TEST PILES.....	281
9.6 MONITORING DATA GATHERED TO DATE	284
9.7 SUMMARY.....	287
CHAPTER 10. COST INFORMATION FOR COMPOSITE PILES	289
10.1 INTRODUCTION	289
10.2 COST INFORMATION FOR THE ROUTE 40 BRIDGE PROJECT.....	289
10.3 COST INFORMATION FOR THE ROUTE 351 BRIDGE PROJECT.....	289
10.3.1 Hardcore FRP Composite Pile.....	290
10.3.2 Plastic Pile.....	290
10.3.3 Prestressed Concrete Pile	290
10.3.4 Summary of the Route 351 Bridge Cost Information.....	290
10.4 SUMMARY.....	290
CHAPTER 11. SUMMARY AND CONCLUSIONS	293
11.1 INTRODUCTION	293
11.2 SUMMARY OF ACTIVITIES AND CONCLUSIONS.....	294
11.2.1 Literature Review	295
11.2.2 Interface Study	295
11.2.3 Durability Study	296
11.2.4 Field Tests at the Route 40 Bridge.....	297
11.2.5 Field Tests at the Route 351 Bridge.....	298
11.2.6 Axial Analyses	299
11.2.7 Lateral Analyses.....	300
11.2.8 Long-Term Monitoring	301
11.2.9 Cost Information for Composite Piles.....	302
11.3 RECOMMENDATIONS FOR FUTURE WORK	302
11.3.1 Geotechnical Studies	302
11.3.2 Durability Studies	303
11.3.3 Structural Tests	303
11.3.4 Cost Analyses.....	304
APPENDIX A. INTERFACE TEST RESULTS.....	305

APPENDIX B. MOISTURE DIFFUSION INTO A CYLINDRICAL FRP COMPOSITE	321
APPENDIX C. STRUCTURAL TESTS RESULTS FROM COMPOSITE PILE CUTOFF SECTIONS FROM THE ROUTE 40 BRIDGE PROJECT.....	325
C.1 PUSHOUT TEST RESULTS	326
C.2 CREEP BENDING TEST.....	328
APPENDIX D. GEOTECHNICAL FIELD INVESTIGATIONS AT THE ROUTE 351 BRIDGE TEST SITE.....	331
REFERENCES.....	347

LIST OF FIGURES

Figure 1. Photos. Degradation of conventional piles (Iskander and Hassan 1998).	5
Figure 2. Illustration. Common types of composite piles.	6
Figure 3. Graph and Photos. Confinement effect of FRB tube on concrete (Fam and Rizkalla 2001a, b).	11
Figure 4. Graph. Experimental versus predicted load-strain behavior using Fam and Rizkalla's model.	13
Figure 5. Illustration. Strip elements for sectional analysis (Mirmiran and Shahawy 1996).	14
Figure 6. Graphs. Experimental versus analytical moment-curvature response (adapted from Fam and Rizkalla 2002).	15
Figure 7. Graph. Interaction diagrams, concrete-filled FRP tubes (Mirmiran 1999).	16
Figure 8. Graphs. Moisture absorption-related durability model.	18
Figure 9. Images. SEM images showing FRP damage (McBagonluri, et al., 2000).	19
Figure 10. Illustration. Influence of soil-pile friction on pile capacity.	26
Figure 11. Graph. Grain size curves to test sands.	29
Figure 12. Photos. Microscopic views of the test sands.	29
Figure 13. Graphs. Direct shear test results for Density sand (average $D_r = 70\%$).	31
Figure 14. Graphs. Direct shear test results for Density sand (average $D_r = 100\%$).	32
Figure 15. Graphs. Direct shear test results for Model sand (average $D_r = 75\%$).	33
Figure 16. Illustration. Stylus profilometer sketch (Johnson 2000).	35
Figure 17. Chart. Graphical representation of roughness parameters R_t , S_m , and R_a .	36
Figure 18. Photo and Graph. Surface characteristics of Lancaster FRP composite pile.	37
Figure 19. Photo and Graph. Surface characteristics of Hardcore FRP composite pile.	37
Figure 20. Photo and Graph. Surface characteristics of Hardcore FRP plate.	38
Figure 21. Photo and Graph. Surface characteristics of Hardcore surface-treated FRP plate.	38
Figure 22. Photo and Graph. Surface characteristics of Plastic Piling plastic composite pile.	39
Figure 23. Photo and Graph. Surface characteristics of prestressed concrete pile.	39
Figure 24. Photo and Graph. Surface characteristics of steel sheet pile.	40
Figure 25. Illustration. Sketch of modified interface shear test setup.	42
Figure 26. Graphs. Typical interface shear test results for Density sand ($\sigma'_n \approx 100$ kPa).	45
Figure 27. Graphs. Typical interface shear test results for Model sand ($\sigma'_n \approx 100$ kPa).	46
Figure 28. Graph. Interface shear strength envelopes for Lancaster Composite FRP shell.	47
Figure 29. Graph. Interface shear strength envelopes for Hardcore Composites FRP shell.	47
Figure 30. Graph. Interface shear strength envelopes for untreated Hardcore FRP plate.	48
Figure 31. Graph. Interface shear strength envelopes for treated Hardcore FRP plate.	48
Figure 32. Graph. Interface shear strength envelopes for PPI plastic.	49
Figure 33. Graph. Interface shear strength envelopes for concrete.	49
Figure 34. Graph. Interface shear strength envelopes for steel.	50
Figure 35. Graph. Multiple linear regression on Density sand $\tan \delta_{peak}$ values.	52
Figure 36. Graph. Multiple linear regression on Density sand $\tan \delta_{cv}$ values.	53
Figure 37. Graph. Multiple linear regression on Model sand $\tan \delta_{peak}$ values.	54
Figure 38. Graph. Multiple linear regression on Model sand $\tan \delta_{cv}$ values.	55
Figure 39. Photos. Burnoff testing.	66
Figure 40. Photo. Typical tension test setup.	67

Figure 41. Photos. Typical split disk test setup.	68
Figure 42. Photo. Freeze-thaw chamber.	68
Figure 43. Photo and Illustration. Freeze-thaw fixture.	69
Figure 44. Graph. Average freeze-thaw cycle undergone by FRP samples.	69
Figure 45. Graph. Representative baseline longitudinal tension stress-strain curves.	70
Figure 46. Graph. Representative baseline hoop tension stress-strain curves.	71
Figure 47. Graph. Absorption curves for Lancaster 12-inch FRP tube.	72
Figure 48. Graph. Absorption curves for Lancaster 24-inch FRP tube.	73
Figure 49. Graph. Absorption curves for Hardcore 12-inch FRP tube.	73
Figure 50. Graph. Absorption curves for Hardcore 24-inch FRP tube.	74
Figure 51. Graphs. Selected diffusion analyses for Lancaster 12-inch FRP samples.	76
Figure 52. Graphs. Selected diffusion analyses for Lancaster 24-inch FRP samples.	77
Figure 53. Graphs. Selected diffusion analyses for Hardcore 12-inch FRP samples.	78
Figure 54. Graphs. Selected diffusion analyses for Hardcore 24-inch FRP samples.	79
Figure 55. Graph. Longitudinal tensile properties versus submergence time for Lancaster 24-inch FRP tube.	82
Figure 56. Graph. Hoop tensile properties versus submergence time for Lancaster 24-inch FRP tube.	82
Figure 57. Graph. Longitudinal tensile properties versus submergence time for Lancaster 12-inch FRP tube.	83
Figure 58. Graph. Hoop tensile properties versus submergence time for Lancaster 12-inch FRP tube.	84
Figure 59. Charts. Longitudinal tensile properties versus moisture content for Lancaster 12-inch tube.	85
Figure 60. Charts. Hoop tensile properties versus moisture content for Lancaster 12-inch FRP tube.	86
Figure 61. Graph. Longitudinal tensile properties versus submergence time for Hardcore 24-inch FRP tube.	87
Figure 62. Charts. Longitudinal tensile properties versus moisture content for Hardcore 24-inch FRP tube.	88
Figure 63. Graph. Longitudinal tensile properties versus submergence time for Hardcore 12-inch FRP tube.	89
Figure 64. Graph. Hoop tensile properties versus submergence time for Hardcore 12-inch FRP tube.	90
Figure 65. Charts. Longitudinal tensile properties versus moisture content for Hardcore 12-inch FRP tube.	91
Figure 66. Charts. Hoop tensile properties versus moisture content for Hardcore 12-inch FRP tube.	92
Figure 67. Graph. Influence of freeze-thaw cycling on the longitudinal tensile properties for the Lancaster 24-inch FRP tube.	93
Figure 68. Graph. Influence of freeze-thaw cycling on the longitudinal tensile properties for the Lancaster 12-inch FRP tube.	94
Figure 69. Graph. Influence of freeze-thaw cycling on the longitudinal tensile properties for the Hardcore 24-inch FRP tube.	94
Figure 70. Graph. Influence of freeze-thaw cycling on the longitudinal tensile properties for the Hardcore 12-inch FRP tube.	95

Figure 71. Photo. SEM images of Lancaster 24-inch FRP tube.	96
Figure 72. Photo. SEM images of Lancaster 12-inch FRP tube.	96
Figure 73. Photo. SEM images of Hardcore 24-inch FRP tube.	96
Figure 74. Photo. SEM images of Hardcore 12-inch FRP tube.	97
Figure 75. Graph. Estimated long-term axial capacity of the 12-inch Lancaster pile.	98
Figure 76. Graph. Estimated long-term flexural capacity of the 12-inch Lancaster pile.	99
Figure 77. Map. Location map of the Route 40 Bridge project in Sussex County, VA (Fam, et al., 2003).	104
Figure 78. Photo. Former Route 40 Bridge.	104
Figure 79. Photos. Signs of deterioration of the former Route 40 Bridge (Fam, et al., 2003). ..	105
Figure 80. Illustration. Schematic of the new Route 40 Bridge.	106
Figure 81. Photo and Illustration. Concrete-filled tubular piles.	108
Figure 82. Graph. Stress-strain response of concrete used in the composite pile.	109
Figure 83. Illustration. Reinforcement details of prestressed concrete pile.	110
Figure 84. Illustration. Simplified soil stratigraphy near test pile area.	111
Figure 85. Photo. Fabrication of prestressed concrete pile.	112
Figure 86. Photos. Fabrication of concrete-filled FRP Piles.	113
Figure 87. Photos. Driving of test piles.	114
Figure 88. Graph. Driving records for test piles.	115
Figure 89. Graphs. End-of-driving PDA recordings.	116
Figure 90. Illustration. Test Pile Instrumentation.	119
Figure 91. Photo. Axial load test using the Statnamic device.	120
Figure 92. Graph. Pile head displacement versus equivalent axial static load.	121
Figure 93. Graph. Axial load—axial strain behavior of test piles.	121
Figure 94. Illustration and Graph. Variation of axial strain along pile length for three Statnamic loads.	122
Figure 95. Photos. Lateral Statnamic setup at the Route 40 project.	123
Figure 96. Graphs. Displacement time histories at the loading point for both piles (Pando, et al., 2004).	124
Figure 97. Graphs. Peak lateral displacement profiles for both test piles at different cycles of Statnamic load.	124
Figure 98. Graph. Calculated static and dynamic (static + damping) resistances for both test piles.	127
Figure 99. Graph. Moment-curvature responses for composite and pretressed concrete piles.	129
Figure 100. Graph. Computed and measured lateral load-displacement response for both test piles (Pando, et al., 2004).	130
Figure 101. Illustration. Details of pile head showing the bars used to connect the pile to cap beam.	131
Figure 102. Illustration. Connection of composite piles to cap beam at Pier No. 2.	132
Figure 103. Photos. Pier No. 2 including the composite piles and reinforced concrete cap beam.	132
Figure 104. Photo. The new Route 40 Bridge over the Nottoway River in Virginia.	133
Figure 105. Map. Location map of the Route 351 Bridge in Hampton, VA.	136
Figure 106. Photo. Aerial view of the Route 351 Bridge in Hampton, VA.	136
Figure 107. Photos. Wide-angle views of the original Route 351 Bridge.	137

Figure 108. Photo. Signs of deterioration of the original Route 351 Bridge.....	138
Figure 109. Illustration. Schematic of the new Route 351 Bridge.....	139
Figure 110. Illustration. Test pile cross section details.....	140
Figure 111. Graphs. Test pile material properties.....	142
Figure 112. Graph. Axial load-axial strain behavior of test piles.....	143
Figure 113. Graphs. Flexural characteristics for the three test piles.....	145
Figure 114. Map. Location of test pile site at the Route 351 Bridge.....	146
Figure 115. Charts. Simplified soil stratigraphy near test pile area.....	148
Figure 116. Illustration. Pile load test layout.....	149
Figure 117. Illustration. Instrumentation layout for prestressed concrete test pile.....	151
Figure 118. Illustration. Instrumentation layout for FRP composite test pile.....	153
Figure 119. Illustration. Instrumentation layout for plastic composite test pile.....	154
Figure 120. Photos. Fabrication of prestressed concrete test pile.....	155
Figure 121. Photos. Fabrication of concrete-filled FRP piles.....	157
Figure 122. Photos. Setup used for concrete filling of FRP composite piles.....	158
Figure 123. Photos. Concrete filling of FRP composite piles.....	159
Figure 124. Photos. Rebar cage of the plastic composite test pile.....	160
Figure 125. Photos. Manufacturing process for the plastic composite test pile.....	161
Figure 126. Graph. Driving records for test piles.....	162
Figure 127. Photos. Installation of prestressed concrete test pile.....	163
Figure 128. Photos. Installation of FRP composite test pile.....	164
Figure 129. Photos. Installation of plastic composite test pile.....	165
Figure 130. Graphs. PDA recordings during restrike.....	167
Figure 131. Photos. PIT tests on test piles.....	170
Figure 132. Graph. PIT sounding on the prestressed concrete test pile before installation.....	171
Figure 133. Graph. PIT sounding on the prestressed concrete test pile after installation.....	171
Figure 134. Graph. PIT sounding on the FRP composite test pile before installation.....	172
Figure 135. Graph. PIT sounding on the FRP composite test pile after installation.....	172
Figure 136. Graph. PIT sounding on the plastic composite test pile before installation.....	173
Figure 137. Graph. PIT sounding on the plastic composite test pile after installation.....	173
Figure 138. Photos. Axial load test of prestressed concrete pile.....	175
Figure 139. Graph. Axial load test results.....	176
Figure 140. Graph. Distribution of residual loads.....	178
Figure 141. Graph. Distribution of residual stresses.....	178
Figure 142. Graph. Load distribution for the three test piles at the Davisson failure loads.....	179
Figure 143. Graph. Mobilized average unit shaft resistance—toe resistance relationships for the three test piles.....	181
Figure 144. Graph. Apparent strength gain with time in the three test piles.....	181
Figure 145. Graphs. Deformed shapes of piles at different lateral loads.....	182
Figure 146. Graph. Measured lateral deflections at ground surface for the three test piles.....	183
Figure 147. Illustration. Load transfer in an axially loaded pile.....	186
Figure 148. Graphs. Interpreted average CPT and SPT design profiles for Route 351 test site.....	195
Figure 149. Graph. Accuracy of Nordlund’s method predictions using δ values from Nordlund’s charts.....	196

Figure 150. Graph. Accuracy of Nordlund’s method predictions using δ values from interface shear tests.	197
Figure 151. Graph. Accuracy of API method predictions using δ values from table 36.	198
Figure 152. Graph. Accuracy of API method predictions using δ values from interface shear tests.	199
Figure 153. Graph. Accuracy of LCPC method predictions using steel pile assumption.	200
Figure 154. Graph. Accuracy of LCPC method predictions using concrete pile assumption. ..	201
Figure 155. Graph. Accuracy of IC method predictions using δ values from interface shear tests.	202
Figure 156. Illustration. Idealized model used in T-Z load-transfer analyses.	205
Figure 157. Graph. Pile tip load—pile tip displacement curve (Q-Z) (API 1993).	206
Figure 158. Graph. Maximum shear stress distribution along pile shaft, according to API (1993).	207
Figure 159. Graph. Settlement predictions for the prestressed concrete pile using API (1993).	208
Figure 160. Graph. Settlement predictions for the FRP pile using API (1993).	209
Figure 161. Graph. Settlement predictions for the plastic pile using API (1993).	210
Figure 162. Graph. Normalized T-Z curves according to API (1993) and Vijayvergiya (1977).	211
Figure 163. Graph. Normalized Q-Z curves according to Vijayvergiya (1977) and API (1993).	212
Figure 164. Graph. Maximum shear stress distributions used in predictions using Vijayvergiya (1977).	213
Figure 165. Graph. Settlement predictions for the concrete pile using Vijayvergiya (1977). ...	214
Figure 166. Graph. Settlement predictions for the FRP pile using Vijayvergiya (1977).	215
Figure 167. Graph. Settlement predictions for the plastic pile using Vijayvergiya (1977).	216
Figure 168. Illustrations. Concentric cylinder model for settlement analysis of axially loaded piles (adapted from Randolph and Wroth 1978).	218
Figure 169. Graph. Linear T-Z curve obtained using Randolph and Wroth (1978).	221
Figure 170. Graph. Linear Q_b -Z curve obtained using Boussinesq’s theory.	222
Figure 171. Graph. Hyperbolic T-Z curve.	226
Figure 172. Graph. Variation of secant shear modulus for different hyperbolic-type models.	227
Figure 173. Graph. Theoretically derived T-Z curve using concentric cylinders and the modified hyperbola from Fahey and Carter (1993).	228
Figure 174. Graph. Theoretically derived Q-Z curve using Boussinesq’s theory and the modified hyperbola from Fahey and Carter (1993).	229
Figure 175. Graph. Route 351 initial shear modulus profile from CPT correlations.	230
Figure 176. Graph. Settlement predictions for the concrete pile using theoretically derived transfer curves.	232
Figure 177. Graph. Settlement prediction for the FRP pile using theoretically derived transfer curves.	233
Figure 178. Graph. Settlement predictions for the plastic pile using theoretically derived transfer curves.	234
Figure 179. Illustration. Laterally loaded pile problem.	239

Figure 180. Illustration. Distribution of stresses against a pile before and after lateral loading (adapted from Reese and Van Impe 2001).	243
Figure 181. Graphs. Typical p-y curve and resulting p-y modulus (Reese and Van Impe 2001).	244
Figure 182. Illustration. Schematic showing the influence of shape of cross section of pile on the soil reaction p (adapted from Reese and Van Impe 2001).	245
Figure 183. Graph. Elements of a characteristic p-y curve for sand based on recommendations by Reese, et al. (1974).	246
Figure 184. Illustration. Schematic showing p-y model used for analysis of laterally loaded piles.	248
Figure 185. Graphs. In situ test data for the upper soils at the northern end of the test pile site.	250
Figure 186. Graphs. In situ test data for the upper soils at the southern end of the test pile site.	251
Figure 187. Graph. Initial p-y modulus profile used to define p-y default curves for LPILE analyses on the prestressed concrete pile.	253
Figure 188. Graphs. Predicted versus measured lateral displacement profile for prestressed concrete pile (low lateral loads).	254
Figure 189. Graphs. Predicted versus measured lateral displacement profile for prestressed concrete pile (medium lateral loads).	254
Figure 190. Graphs. Predicted versus measured lateral displacement profile for prestressed concrete pile (high lateral loads).	255
Figure 191. Graph. Calculated load-deflection curve for the prestressed concrete pile.	256
Figure 192. Graph. Calculated load-slope curve for the prestressed concrete pile.	256
Figure 193. Graph. Initial p-y modulus profile used to define default p-y curves for LPILE analyses on the FRP pile.	258
Figure 194. Graphs. Predicted versus measured lateral displacement profile for FRP pile (low lateral loads).	258
Figure 195. Graphs. Predicted versus measured lateral displacement profile for FRP pile (medium lateral loads).	259
Figure 196. Graphs. Predicted versus measured lateral displacement profile for FRP pile (high lateral loads).	259
Figure 197. Graph. Calculated load-deflection curve for the FRP pile.	260
Figure 198. Graph. Calculated load-slope curve for the FRP pile.	261
Figure 199. Graph. Initial p-y modulus profile used to define default p-y curves for LPILE analyses on the plastic pile.	262
Figure 200. Graphs. Predicted versus measured lateral displacement profile for plastic pile (low lateral loads).	263
Figure 201. Graphs. Predicted versus measured lateral displacement profile for plastic pile (medium lateral loads).	263
Figure 202. Graphs. Predicted versus measured lateral displacement profile for plastic pile (high lateral loads).	264
Figure 203. Graph. Calculated load-deflection curve for the plastic pile.	265
Figure 204. Graph. Calculated load-slope curve for the plastic pile.	265
Figure 205. Illustration. Location of instrumented production piles at the Route 351 Bridge.	270

Figure 206. Illustration. Load transfer instrumentation layout for prestressed concrete production pile.	271
Figure 207. Illustration. Instrumentation layout for FRP composite production pile.	273
Figure 208. Illustration. Layout of external durability instrumentation used in the FRP composite production pile.	274
Figure 209. Graph. Simplified stratigraphy along the Route 351 Bridge alignment.	275
Figure 210. Graph. Simplified stratigraphy in the vicinity of the instrumented prestressed concrete pile installed at Pier 10.	276
Figure 211. Graph. Simplified stratigraphy in the vicinity of the instrumented FRP composite pile installed at Pier 11.	277
Figure 212. Graph. Driving records for instrumented production piles.	278
Figure 213. Graph. PDA recordings during restrike (Spiro and Pais 2002b).	280
Figure 214. Graph. PIT sounding on the prestressed concrete production pile before installation.	282
Figure 215. Graph. PIT sounding on the prestressed concrete production pile after installation and restrike.	282
Figure 216. Graph. PIT sounding on the FRP composite production pile before installation.	283
Figure 217. Graph. PIT sounding on the FRP composite production pile before installation.	283
Figure 218. Photo. Route 351 Bridge under construction on December 30, 2002.	285
Figure 219. Graph. Load distributions on November 7, 2002, and December 30, 2002, for the prestressed concrete production pile at Pier 10.	286
Figure 220. Graph. Load distributions on November 7, 2002, and December 30, 2002, for the FRP composite production pile at Pier 11.	287
Figure 221. Graphs. Interface shear test results, Density sand-to-Lancaster FRP shell interface.	306
Figure 222. Graphs. Interface shear test results, Density sand-to-Hardcore FRP shell interface.	307
Figure 223. Graphs. Interface shear test results, Density sand-to-Hardcore FRP plate (untreated) interface.	308
Figure 224. Graphs. Interface shear test results, Density sand-to-treated Hardcore FRP plate interface.	309
Figure 225. Graphs. Interface shear test results, Density sand-to-plastic interface.	310
Figure 226. Graphs. Interface shear test results, Density sand-to-concrete interface.	311
Figure 227. Graphs. Interface shear test results, Density sand-to-steel interface.	312
Figure 228. Graphs. Interface shear test results, Model sand-to-Lancaster FRP shell interface.	313
Figure 229. Graphs. Interface shear test results, Model sand-to-Hardcore FRP shell interface.	314
Figure 230. Graphs. Interface shear test results, Model sand-to-Hardcore FRP plate (untreated) interface.	315
Figure 231. Graphs. Interface shear test results, Model sand-to-treated Hardcore FRP plate interface.	316
Figure 232. Graphs. Interface shear test results, Model sand-to-plastic interface.	317
Figure 233. Graphs. Interface shear test results, Model sand-to-concrete interface.	318

Figure 234. Graphs. Interface shear test results, Model sand-to-steel interface	319
Figure 235. Graph. FRP moisture concentration profile, inner radius dry, outer radius saturated.	324
Figure 236. Graph. FRP moisture concentration profile, inner and outer radii saturated.....	324
Figure 237. Photo. VTRC pushout test setup.	326
Figure 238. Photo. VT pushout test setup.....	327
Figure 239. Photo. Creep bending test setup.	329
Figure 240. Graph. Creep deflection test results.....	329
Figure 241. Map. Location of field tests.....	332
Figure 242. Chart. Boring B-1 (SPT-1).	333
Figure 243. Chart. Boring B-2 (SPT-2).	335
Figure 244. Chart. CPT-1.....	337
Figure 245. Chart. CPT-2.....	338
Figure 246. Chart. CPT033.....	339
Figure 247. Chart. CPT034.....	343
Figure 248. Chart. DMT.	346

LIST OF TABLES

Table 1. Selected projects involving installation of composite piles.....	7
Table 2. Expressions for the strength of confined concrete and maximum axial strain (adapted from Shehata, et al., 2002).	10
Table 3. Available structural information for steel-reinforced plastic composite piles.....	17
Table 4. Comparison of pile impedance.	21
Table 5. Interface behavior test matrix.	27
Table 6. Index parameter values of the sands used in this study.	28
Table 7. Internal friction angles obtained from direct shear tests. ⁽¹⁾	30
Table 8. Summary of surface roughness measurements.	40
Table 9. Surface hardness.	41
Table 10. Summary of interface shear test results on Density sand.	43
Table 11. Summary of interface shear test results on Model sand.	44
Table 12. Summary of interface friction angles.....	50
Table 13. Multiple linear regression results for $\tan \delta_{\text{peak}}$ of Density sand.	52
Table 14. Multiple linear regression results for $\tan \delta_{\text{cv}}$ of Density sand.	53
Table 15. Multiple linear regression results for $\tan \delta_{\text{peak}}$ of Model sand.	54
Table 16. Multiple linear regression results for $\tan \delta_{\text{cv}}$ of Model sand.	55
Table 17. Characterization data for Lancaster Composite 12-inch FRP tube.....	62
Table 18. Characterization data for Lancaster Composite 24-inch FRP tube.....	62
Table 19. Characterization data for Hardcore Composites 12-inch FRP tube.....	64
Table 20. Characterization data for Hardcore Composites 24-inch FRP tube.....	64
Table 21. As-received longitudinal tensile properties.	70
Table 22. As-received hoop tensile properties.....	71
Table 23. Fickian diffusion parameters for the Lancaster 12-inch FRP.	80
Table 24. Fickian diffusion parameters for the Lancaster 24-inch FRP.	80
Table 25. Fickian diffusion parameters for the Hardcore 12-inch FRP.....	81
Table 26. Fickian diffusion parameters for the Hardcore 24-inch FRP.....	81
Table 27. Mechanical properties of FRP shell of composite pile.	108
Table 28. Pile-driving measurements for the prestressed and composite piles.	117
Table 29. Summary of signal-matching analyses at end of driving (from Muchard, et al., 1999).	117
Table 30. Summary of pile-driving measurements for the prestressed and composite piles (after Spiro and Pais 2002a and b).	168
Table 31. Summary of CASE and CAPWAP analyses results (Spiro and Pais 2002a and b)....	169
Table 32. Test dates for the test pile program at the Route 351 Bridge project.	174
Table 33. Comparison of failure loads for the three test piles.	177
Table 34. Load distributions from static load tests at the Davisson failure loads.	180
Table 35. Unit shaft and toe resistances from static axial load tests.....	180
Table 36. API recommendations for side friction in siliceous soil (API 1993).....	189
Table 37. API recommendations for tip resistance in siliceous soil (API 1993).....	190
Table 38. LCPC friction coefficient α_{LCPC} for driven piles in sands (Bustamante and Gianeselli 1982).	191

Table 39. LCPC bearing capacity factors for driven piles in sands (Bustamante and Gianceselli 1982).....	191
Table 40. Predicted axial capacities for the test piles at Route 351.....	203
Table 41. Relationships commonly used for elastic piles in flexion.	238
Table 42. Recommended criteria for p-y curves in different soils (adapted from Reese, et al., 1997).	244
Table 43. Properties of test piles.....	249
Table 44. Parameters used to define default p-y curves in LPILE for the prestressed concrete pile.....	253
Table 45. Parameters used to define default p-y curves in LPILE for the FRP pile.....	257
Table 46. Parameters used to define default p-y curves in LPILE for the plastic pile.	262
Table 47. Summary of pile-driving measurements for the prestressed and FRP production piles (after Spiro and Pais 2002b).....	280
Table 48. Summary of CASE and CAPWAP analyses results (Spiro and Pais 2002b).	281
Table 49. Test dates for the instrumented production pile program at the Route 351 Bridge....	284
Table 50. Monitoring dates for prestressed concrete pile at the Route 351 Bridge.....	284
Table 51. Monitoring dates for FRP composite pile at the Route 351 Bridge.....	284
Table 52. Detailed project objectives.....	294
Table 53. Organization of the figures in appendix A.....	305
Table 54. Summary of pushout test results.....	327

CHAPTER 1. INTRODUCTION

1.1 GENERAL INTRODUCTION

This research project was undertaken to investigate the potential of using composite piles for load-bearing applications, specifically bridge substructures. Composite piles refer to alternative pile foundations composed of fiber reinforced polymers (FRPs), recycled plastics, or hybrid materials that are placed in the ground to support axial and/or lateral loads. Traditionally, piles are made of materials such as steel, concrete, and timber. These pile materials have limited service life and high maintenance costs when used in harsh marine environments (Lampo, et al., 1998). Degradation problems of conventional piles include chloride attack on concrete, steel corrosion, and marine borer attack on timber piles. It has been estimated that repair and replacement of piling systems costs the United States more than \$1 billion annually (Lampo, et al., 1997). High repair and replacement costs drive the need to investigate the feasibility of using FRP composite materials for pile foundations (Lampo, et al., 1998, Iskander and Hassan 1998). FRP composite materials are considered an attractive alternative for marine and other harsh environments because they are resistant to the degradation mechanisms mentioned above.

Composite piles have been available in the North American market since the late 1980s, but to date their use has been limited mainly to marine fender piles, load-bearing piles for light structures, and experimental test piles (Iskander, et al., 2001). Composite piles have not yet gained wide acceptance in the civil engineering industry, primarily due to the lack of a long track record of performance, and the scarcity of well-documented field load tests. However, FRP composite piles may exhibit longer life cycle and improved durability in harsh marine environments, thereby presenting the potential for substantially reduced costs. Potential disadvantages of using composite piles are related to cost and performance. At present, composite piles are generally more expensive than traditional piles (Hoy 1995, Iskander and Hassan 1998). Driveability may be less efficient with these piles. Structural properties, including low bending and axial stiffness, could result in large deformations. Piles with composite exteriors may have low surface friction. The scope and extent of potential problems with composite piles are uncertain due to the lack of a long-term track record of their use.

Some of these potential disadvantages may be relative. The apparent higher cost is expected to decrease as composite pilings gain wider penetration in the civil engineering industry (Iskander and Hassan 1998). Ballinger (1994) pointed out that, although the cost of FRP composite materials may be higher, the cost of labor and use of equipment necessary for construction work may be lower due to their lighter weight. Furthermore, the author suggested that not only should costs be compared on a total installed first-cost basis but also on a reasonable total life cycle cost basis. Most composite piling manufacturers believe their products may be competitive when compared to the life cycle cost of traditional piles in some applications (Ballinger 1994). Some manufacturers claim their composite piles may last twice as long as treated wooden piles (Iskander and Hassan

1998). However, to confidently design facilities using composite piles, engineers need more information about composite piles.

1.2 OBJECTIVES

The main focus of this research project is to determine the potential of composite piles for use in load-bearing applications such as bridge substructures. To confidently establish the feasibility of using composite piles for load-bearing structures, more information and performance data were gathered in critical areas, such as long-term durability, geotechnical behavior (including driveability), and soil-pile load transfer interactions.

The overall objective of this research project is to establish the feasibility of using composite piles in bridge substructures. More specific objectives are to:

1. Evaluate the long-term durability of concrete-filled FRP composite pipe piles.
2. Perform laboratory tests to evaluate the soil-pile interface behavior of concrete-filled FRP composite pipe piles and compare them with tests carried out on conventional prestressed concrete piles.
3. Design and perform a field test pile program to evaluate the driveability and axial and lateral behavior and capacity of a concrete-filled FRP composite pile, and a steel-reinforced recycled plastic composite pile, and to compare them to a conventional prestressed concrete pile.
4. Design and perform a production pile testing and monitoring program in a real bridge project to compare long-term performance, load transfer, and durability of concrete-filled FRP composite piles and conventional prestressed concrete piles.

1.3 ORGANIZATION OF REPORT

This report is organized into 11 chapters and 4 appendices. Chapter 2 presents background information on composite piles in general, and a literature review with specific focus on the two composite piles investigated in this research (i.e., concrete-filled FRP composite piles and steel-reinforced recycled plastic composite piles).

Chapter 3 presents the results of the experimental study on interface behavior between composite piles and two sands. A summary of the interface shear test results is given for seven pile material types (five composite pile materials and two conventional pile materials) against two types of sands. The soil materials, pile materials, and test procedures employed are also described in chapter 3.

Chapter 4 presents the methods and results of the experimental durability study of FRP composite piles. Overview and background information related to durability of FRP composite materials also is presented in this chapter.

Chapters 5 and 6 present the findings from the field load tests at the Route 40 and Route 351 Bridges, respectively. For each field load test program, information is provided pertaining to the description of the bridges, the description of the test piles, the soil conditions at the test sites, pile fabrication, instrumentation, and installation. The results of axial and lateral load tests are presented and discussed for each field load test program. Chapter 5 also presents details of the finished Route 40 Bridge, including a description of Pier No. 2 of the bridge, which is solely supported by concrete-filled FRP composite piles.

The results from axial and lateral analyses for the field load tests carried out at the Route 351 Bridge are presented in chapters 7 and 8, respectively.

In chapter 9, the long-term monitoring program implemented for two production piles at the Route 351 Bridge is described. Only preliminary load transfer instrumentation data are presented because the bridge is still under construction. The long-term monitoring will be carried out by the Virginia Department of Transportation.

Chapter 10 provides cost information for the composite piles and prestressed concrete piles used in this research project.

Summary, conclusions, and recommendations for future work are presented in chapter 11.

The results of the laboratory tests performed for the interface behavior study are presented in appendix A. The solution for the moisture diffusion into a cylindrical FRP composite is presented in appendix B. The results of the structural tests carried out on pile cutoff pieces from the Route 40 project are presented in appendix C. These tests included a creep bending test and pushout tests to investigate the bond strength between the concrete core and FRP shell of the composite piles. Appendix D includes the results of geotechnical field investigations carried out at the test site at the Route 351 Bridge project.

CHAPTER 2. BACKGROUND AND LITERATURE REVIEW

2.1 INTRODUCTION

This chapter presents the general background of composite piles and a literature review, with specific focus on the two types of composite piles selected for this research: concrete-filled FRP composite piles and steel-reinforced recycled plastic composite piles.

2.2 COMPOSITE PILE BACKGROUND

Composite piles refer to alternative pile foundations which make use of FRPs, recycled plastics, and other materials to replace and/or protect steel or concrete, with the intent to produce piles that have lower maintenance costs and longer service lives than conventional piles, especially when used in marine applications and other corrosive environments. Examples of deteriorated conventional piles are shown in figure 1.

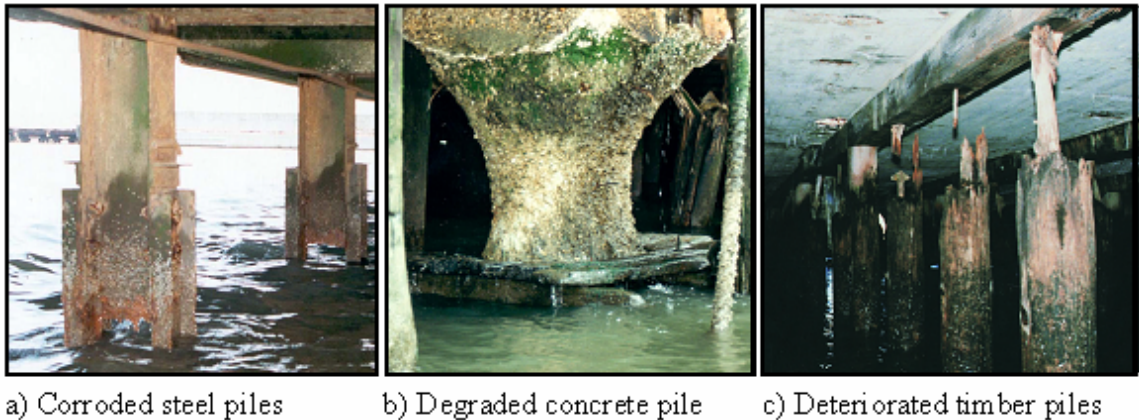


Figure 1. Photos. Degradation of conventional piles (Iskander and Hassan 1998).

Composite piles were first used in the United States in the late 1980s as replacements for timber fender piles at the Port of Los Angeles (Heinz 1993). The first composite pile prototype was driven in 1987 and consisted of a composite steel pipe encased by recycled plastic (Horeczko 1995). Since the first composite pile application in 1987, several other projects have used composite piles. A list of selected projects where composite piles have been used is presented in table 1. As shown in the table, and reported by Iskander, et al., (2001), composite piles have been primarily used as marine fender piles, as load-bearing piles for light structures, and as experimental test piles.

2.2.1 Types of Composite Piles

Several composite pile products are available in the market today, such as steel pipe core piles, structurally reinforced plastic matrix piles, concrete-filled FRP pipe piles, fiberglass pultruded piles, and plastic lumber piles. Of these five pile types, the first three

are considered to be better suited for load-bearing applications (Lampo, et al., 1998). These three pile types are shown in figure 2.

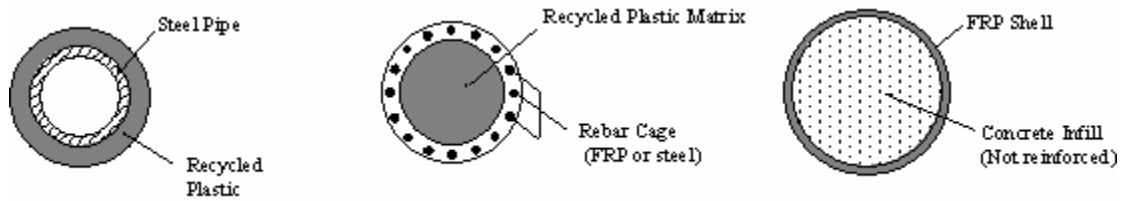


Figure 2. Illustration. Common types of composite piles.

The following subsections describe these three load-bearing composite pile candidates in more detail.

2.2.1.1 Steel pipe core pile

This pile consists of a recycled plastic shell with a steel pipe core interior, as shown in figure 2a. This pile may be obtained in diameters ranging from 8 to 24 inches (20.3 to 61.0 cm) and up to 75 feet (22.9 m) in length (Plastic Pilings 2001). The steel pipe core ranges from 4 to 16 inches (10.2 to 40.6 cm) outer diameter, with pipe wall thicknesses between 6 to 40 millimeters (0.236 to 1.57 inches) (Plastic Pilings 2001).

Table 1. Selected projects involving installation of composite piles.

Site	Year	Application	Pile Manufacturer	Pile Type	Source
Port of Los Angeles, CA	1987	Fender piles	Plastic Pilings, Inc.	Steel pipe with thick plastic shell	Heinz (1993), Hoy (1995)
	1991–5	Fender piles	Plastic Pilings, Inc.; Seaward International, Inc.; Hammer’s Plastic Recycling	Plastic piling with steel core	
Port of NJ, Newark, NJ	1991	Fender piles	Plastic Pilings, Inc.	Steel pipe with thick plastic shell	Hoy (1995)
Naval Station Roosevelt Roads, Puerto Rico	1991	Trial fender piles	Plastic Pilings, Inc.	Steel pipe with thick plastic shell	Hoy (1995)
Port of Grays Harbor, Aberdeen, WA	1992–3	Fender piles	Plastic Pilings, Inc.	Steel pipe with thick plastic shell	Hoy (1995) www.plasticpilings.com
Port of Seattle, WA	1993	Fender piles	Plastic Pilings, Inc.	Steel pipe with thick plastic shell	Hoy (1995) www.plasticpilings.com
Port of Oakland, CA	1993	Fender piles	Plastic Pilings, Inc.	Steel pipe with thick plastic shell	Hoy (1995) www.plasticpilings.com
Pearl Harbor, HI	1994	Fender piles	Plastic Pilings, Inc.	Steel pipe with thick plastic shell	Hoy (1995) www.plasticpilings.com
Port of NY/NJ	1994	Fender piles	Seaward International, Inc.	Recycled plastic with fiberglass reinforcing	Hoy (1995)
			Creative Pultrusions, Inc.	Ultra high molecular weight polyethylene	
Pier Bravo, NAS North Island, San Diego, CA	1995	Fender piles	Plastic Pilings, Inc.	Recycled plastic reinforced with welded steel rebar cage	Tetra Tech EM, Inc. (1999)
Delaware Bay, DE	1996	Fender piles	Hardcore Composites	Fiberglass shell filled with concrete	Phair (1997) www.hardcorecomposite.com
Port of New Orleans, LA	1996	Fender piles	Seaward International, Inc.	Recycled plastic with fiberglass reinforcing	Eustis Engineering Co, Inc. (1996)
Pier 16—Naval Amphibious Base Coronado, San Diego, CA	1996	Fender piles	Plastic Pilings, Inc.	Recycled plastic reinforced with welded steel rebar cage	Tetra Tech EM, Inc. (1999)
US Navy EMR Facility Pier Ingleside, TX	1997	Pier piles	Lancaster Composites	FRP shell with concrete core	Stapleman (1997)
Pier 23, Norfolk, VA	1997	Fender piles	Lancaster Composites	FRP shell with concrete core	Lancaster (2000) www.lancastercomposite.com

The steel core provides the structural strength while the plastic shell protects the pile from degradation. The plastic shell can be omitted below the portion of the pile exposed to water (Plastic Pilings 2001). If the plastic shell is used only in the upper portion of the pile that is exposed to water, the design procedure for this pile would be essentially the same as for a conventional steel pipe pile. The plastic shell does not come into play structurally, since its only function is to protect the steel pipe along the exposed portion of the pile. Since the design procedure of steel pipe piles is well established, it was decided that there was relatively little need for further research on this kind of pile.

2.2.1.2 Structurally reinforced plastic matrix pile

This composite pile consists of a recycled plastic matrix structurally reinforced with FRP rods or a welded steel rebar cage. The typical configuration of this type of pile is shown in figure 2b. An attractive feature of this pile is that when reinforced with FRP rods, the pile is nonmagnetic and 100 percent recyclable (Lindsay 1996). This environmentally friendly composite pile type uses approximately 240 recycled 1-gallon (3.79-L) milk jugs per linear foot (0.305 m) of a 12-inch (0.305-m) nominal diameter pile (Taylor 1995). The piles are commercially available in diameters ranging from 8 to 24 inches (0.203 to 0.610 m), and are reinforced with 6 to 24 FRP or steel reinforcing rods, which range between 0.75 to 1.41 inches (1.91 to 3.58 cm) in diameter (Plastic Pilings 2001, Seaward International 2001).

These piles are produced by a continuous extrusion process that enables the production of continuous pile of virtually any length (Lindsay 1996, Taylor 1995). This continuous length precludes design problems inherent in segmented piles (Horeczko 1995). To enhance durability, the plastic matrix is chemically treated with antioxidants and ultraviolet (UV) inhibitors that retard the effects of UV light on plastic (Taylor 1995, Iskander and Hassan 1998).

To date, these piles have been used primarily as fender piles in several naval facilities (Hoy 1995). Lindsay (1996) reported preliminary tests on 12-inch (0.305 m) diameter, 60-ft (18.3 m) long piles. The results indicated the piles could carry axial working loads of up to 10 tons (89 kN) and 20 tons (178 kN) per pile when reinforced with FRP and steel rods, respectively. Some potential problems associated with these piles include the possibility of debonding of the reinforcing FRP rods and the potential for high creep rates associated with the high polymeric content of these piles. One version of this pile is structurally reinforced with a reinforcement cage with the rebars welded to a continuous steel spiral. This version of the pile is reported not to have the aforementioned problems (Plastic Pilings 2001).

Although this type of composite pile is considered to have potential for load-bearing applications, it was not initially selected for the second phase of the project due to budget limitations. The late withdrawal of one of the pile manufacturers allowed inclusion of this pile at the last minute.

2.2.1.3 Concrete-filled FRP tube pile

In a concrete-filled FRP composite pile there are two main structural components: an FRP shell or tube, and a concrete infill without steel reinforcement. The FRP shell provides, among other things, a stay-in-place concrete form, confinement to the concrete, tensile reinforcement, and corrosion protection (Fam and Rizkalla 2001a, b). The concrete infill provides compressive load capacity. The two main manufacturers of this type of pile in the United States are Hardcore Composites and Lancaster Composite (Iskander, et al., 2001).

Hardcore piles can be installed by driving the empty FRP shell and then filling it with concrete, although they are also installed by filling with concrete and then driving after the concrete has cured (Hardcore Composites 2001). Lancaster Composite's piles are sold under the commercial name CP40, and are filled with concrete and allowed to cure prior to driving (Stapleman 1997, Lancaster Composite 2000).

The FRP shells used by Hardcore Composites are fabricated using a vacuum-assisted resin transfer molding process (VARTM), while Lancaster Composite's FRP shells are made using a filament winding technique. Typically, both piles are available in diameters ranging from 8 to 24 inches (0.203 to 0.610 m), with wall thicknesses ranging between 0.18 to 0.36 inches (0.46 to 0.91 cm). Both manufacturers have the flexibility to modify the FRP composite shell laminate architecture (including number of layers, fiber orientation, and resin and fiber types) to better suit the load demands of a specific project. These piles can be produced in virtually any length (Lancaster Composite 2000, Hardcore Composites 2001).

This type of composite pile was considered to have good potential for load-bearing applications, hence it was selected for the second phase of the research project.

2.3 LITERATURE REVIEW FOR THE COMPOSITE PILES SELECTED

The initial research plan entailed focusing the study on concrete-filled composite piles, which were selected after the initial pile screening phase. The piles were to be manufactured by Lancaster Composite, Inc., and Hardcore Composites. The late withdrawal of Lancaster Composite, Inc. allowed the inclusion of a recycled plastic composite pile manufactured by Plastic Pilings, Inc. Information available for concrete-filled FRP composite piles and steel-reinforced recycled plastic composite piles is presented in the following subsections.

2.3.1 Structural Behavior

2.3.1.1 Concrete-filled FRP composite piles

Considerable effort has been expended to research the structural behavior of concrete-filled FRP composite tube piles (e.g., Lampo, et al., 1998, Samaan, et al., 1998, Mirmiran, et al., 1999, Fam 2000, Fam and Rizkalla 2001a, b, Mirmiran, et al., 2001,

Moran and Pantelides 2002a, Becque, et al., 2003). Relevant findings from selected research studies are described in the following subsections.

2.3.1.1.1 Behavior under axial loading

The structural behavior of concrete-filled FRP composite tubes under axial compression has been studied extensively and several analytical models have been proposed to predict their response. Table 2 lists these models.

Table 2. Expressions for the strength of confined concrete and maximum axial strain (adapted from Shehata, et al., 2002).

Author	Type of Confinement	Ultimate Strength f_{cc}	Ultimate Axial Strain ε_{cc}
Fardis and Khalili (1981)	GFRP-encased concrete	$f_{co} \left[1 + 2.05 \left(\frac{f_l}{f_{co}} \right) \right]$	$0.002 \left[1 + 0.5 \left(\frac{E_f t_f}{D f_{co}} \right) \right]$
Karbahari and Eckel (1993)	FRP-encased concrete	$f_{co} \left[1 + 2.1 \left(\frac{f_l}{f_{co}} \right)^{0.87} \right]$	$0.002 \left[1 + 5 \left(\frac{2t_f f_f}{D f_{co}} \right) \right]$
Mirmiran and Shahawy (1997)*	GFRP-encased concrete	$f_{co} + 4.269 f_l^{0.587}$	—
Miyauchi, et al. (1997)**	CFRP-wrapped concrete	$f_{co} \left[1 + 3.5 \left(\frac{f_l}{f_{co}} \right) \right]$	$0.002 \left[1 + 10.6 \left(\frac{2t_f f_f}{D f_{co}} \right)^{0.373} \right]$
Samaan, et al. (1998)*	GFRP-encased concrete	$f_{co} + 6.0 f_l^{0.7}$	$\frac{f_{cc} - 0.872 f_{co} - 0.371 f_l - 6.258}{245.61 f_{co}^{0.2} + 1.3456 \left(\frac{E_f t_f}{D} \right)}$
Saafi, et al. (1999)	CFRP and CFRP encased concrete	$f_{co} \left[1 + 2.2 \left(\frac{f_l}{f_{co}} \right)^{0.84} \right]$	$\varepsilon_{co} \left[1 + (537 \varepsilon_f + 2.6) \left(\frac{f_{cc} - 1}{f_{co}} \right) \right]$
Toutanji (1999)	CFRP and GFRP wrapped concrete	$f_{co} \left[1 + 3.5 \left(\frac{f_l}{f_{co}} \right)^{0.85} \right]$	$\varepsilon_{co} \left[1 + (310.57 \varepsilon_f + 1.9) \left(\frac{f_{cc} - 1}{f_{co}} \right) \right]$
Spoelstra and Monti (1999)	CFRP and GFRP-wrapped and encased concrete	$f_{co} \left[0.2 + 3 \left(\frac{f_l}{f_{co}} \right)^{0.5} \right]$	$\varepsilon_{co} \left[2 + 1.25 \left(\frac{E_c}{f_{co}} \right) \varepsilon_f \sqrt{\frac{f_l}{f_{co}}} \right]$

Notes: * units are in MPa, ** Equation for ε_{cc} is valid for $f_{co} = 30$ MPa

CFRP = Carbon fiber-reinforced polymer, GFRP = Glass fiber-reinforced polymer,

f_{co} = compressive strength of unconfined concrete, ε_{co} = ultimate strain of unconfined concrete,

E_f = Hoop modulus of elasticity of FRP tube, f_f = Hoop tensile strength of FRP tube,

f_l = lateral confining stress, t_f = thickness of FRP tube, D = diameter of concrete core.

Recently, other models have been proposed by Fam (2000), Fam and Rizkalla (2001a, b), Moran and Pantelides (2002b), Shehata, et al. (2002), and Becque, et al. (2003). Most of these models build upon the simple observation that the typical stress-strain curve of concrete-filled FRP composite columns has an approximately bilinear shape, as shown in figure 3.

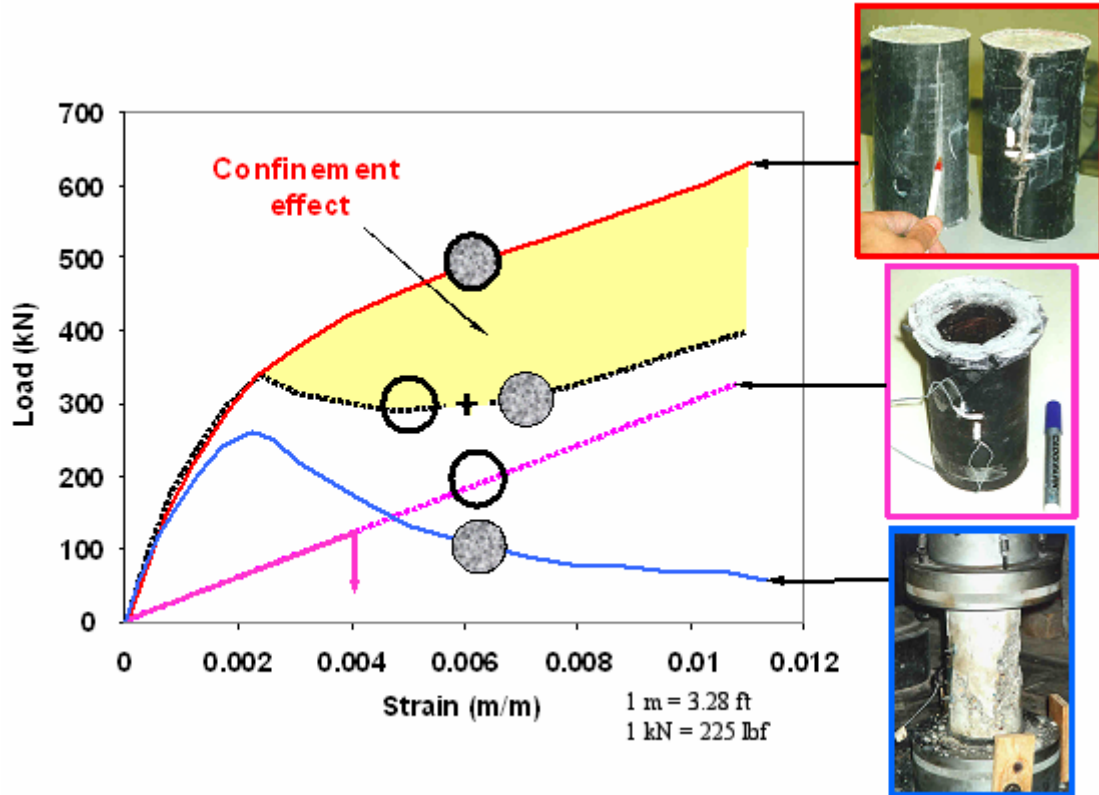


Figure 3. Graph and Photos. Confinement effect of FRB tube on concrete (Fam and Rizkalla 2001a, b).

As shown in figure 3, the FRP tube of a composite pile contributes structurally to the pile by resisting some of the axial load, and by providing confinement to the concrete core. The beneficial effect of confinement on the total load-carrying capacity of a short, concrete-filled FRP tubular element was studied by Fam and Rizkalla (2001a). As illustrated in figure 3, the capacity of the composite stub significantly exceeds the load-sharing capacity of the two individual materials (Fam and Rizkalla 2001a). The load-strain curve starts to depart from the unconfined concrete curve in the vicinity of the unconfined concrete strength. As this stress level is approached, the concrete core starts to experience significant microcracking as well as increased lateral expansion. In response to the lateral expansion of the concrete, the FRP shell applies a radial confining pressure, which continuously increases due to its linear elastic properties (Fam 2000). The second slope of the load-strain curve is a function of the hoop tensile stiffness of the FRP shell, and the ultimate peak strength is governed by the hoop tensile strength of the FRP shell. A more detailed description of the behavior of concrete-filled FRP tubes under axial compression loading can be found in Fam and Rizkalla (2001a, b).

The short-term axial capacity of a concrete-filled FRP tube can be predicted using a confinement model such as the one proposed by Fam and Rizkalla (2001b). This model is an incremental variable confinement model that satisfies equilibrium and radial displacement compatibility between the concrete core and the FRP tube, and it makes use of the constant confinement model of Mander, et al. (1988).

The radial confinement pressure applied by the FRP shell can be obtained from equilibrium and by imposing radial displacement compatibility between the concrete core and the FRP shell. When both the concrete core and FRP shell are axially loaded with the same strain level (ε_{cc}), the radial confinement pressure (σ_R) can be estimated as follows (Fam 2000):

$$\sigma_R = \frac{(v_c - v_{FRP})}{\frac{R_{FRP}}{E_{FRP-Hoop} \cdot t_{FRP}} + \frac{1 - v_c}{E_c}} \cdot \varepsilon_{cc} \quad (1)$$

where

- v_c is the Poisson ratio of concrete (can be varied by using the secant Poisson's ratio)
- v_{FRP} is the Poisson ratio of the FRP shell (-hoop strain /axial strain under axial loading)
- R_{FRP} and t_{FRP} are the radius and wall thickness of the FRP tube, respectively
- $E_{FRP-Hoop}$ is the elastic modulus of the FRP shell in the hoop direction (hoop tension)
- E_c is the elastic modulus of the concrete core (can be varied by using the secant modulus)
- ε_{cc} is the axial strain of the concrete-filled FRP tube stub

The variable radial confining pressure is obtained from equation 1 by using the secant elastic modulus and the secant Poisson's ratio of the concrete as a function of axial strain level.

The model relates the axial stress of the confined concrete core (f_{cc}), at any given axial strain level (ε_{cc}), to the peak confined strength of the concrete (f'_{cc}) as follows:

$$f_{cc} = \frac{f'_{cc} \cdot x^r}{r - 1 + x^r} \quad (2)$$

where

$$x = \frac{\varepsilon_{cc}}{\varepsilon'_{cc}} \quad (3)$$

and where

- ε'_{cc} is the strain at peak strength f'_{cc}
- $r = E_{co} \div (E_{co} - E_{sec})$

- E_{co} is the initial tangent elastic modulus of unconfined concrete, and can be estimated as $E_{co}(\text{MPa}) \approx 5000 \cdot (\text{square root of } f'_c)$, where f'_c is the strength of the unconfined concrete in MPa
- E_{sec} is the secant elastic modulus of confined concrete ($\approx f'_{cc} / \varepsilon'_{cc}$)

The peak confined strength (f'_{cc}) can be estimated using the following expression proposed by Mander, et al. (1988):

$$f'_{cc} = f'_c \left(2.254 \sqrt{1 + \frac{7.94 \sigma_R}{f'_c}} - 2 \frac{\sigma_R}{f'_c} - 1.254 \right) \quad (4)$$

The load-strain response, predicted using the model shown above, and the experimental load-strain behavior obtained for Test Stub No. 1 (from Fam and Rizkalla 2001a), are shown in figure 4. The figure shows good agreement between the model and the experimental results.

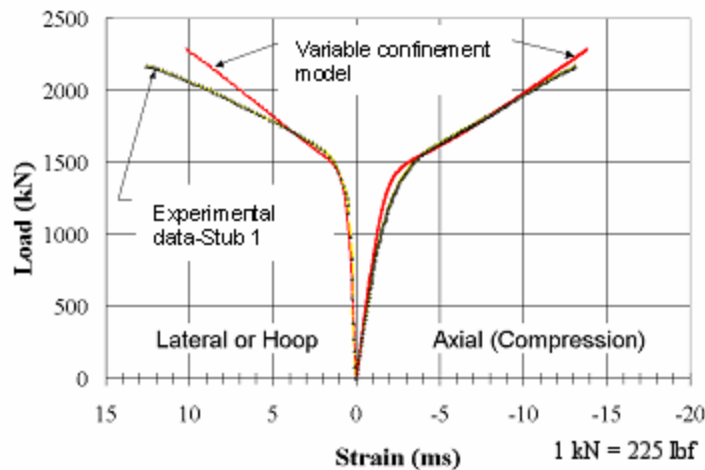


Figure 4. Graph. Experimental versus predicted load-strain behavior using Fam and Rizkalla's model.

This model will be used later in chapter 4 to illustrate the influence that the degradation of the hoop properties (stiffness and strength) of FRP tube has on the long-term axial capacity of concrete-filled tubular FRP piles.

2.3.1.1.2 Flexural behavior

Research on the flexural behavior of concrete-filled FRP circular tubes includes studies by Mirmiran (1999), Fam (2000), Mirmiran, et al. (2000), Fam and Rizkalla (2000), Mirmiran, et al. (2001), and Fam and Rizkalla (2002). These structural elements can be used to resist bending moments, but the benefits of concrete confinement are less in bending than the purely axial loading case (Fam 2000). In flexure, the FRP tube acts as a noncorrosive reinforcement, while the concrete provides the internal resistance force in

the compression zone and increases the stiffness of the member (Fam and Rizkalla 2002). The concrete core also prevents local buckling of the FRP tube.

A comprehensive experimental program to study the short-term flexural behavior and failure modes of concrete-filled FRP tubes was recently completed by Fam and Rizkalla (2002). Their study showed that the flexural behavior is highly dependent on the stiffness and diameter-to-thickness ratio of the FRP tube, and to a lesser extent on the concrete strength. The study also showed that, in general, the cracking moment resistance is relatively small compared to the ultimate moment capacity

The short-term flexural capacity of a concrete-filled FRP tube can be predicted using a strain compatibility/equilibrium model such as the one proposed by Mirmiran and Shahawy (1996) or Fam (2000). The methodology assumes that sections normal to the neutral axis remain plane after bending, and that the FRP shell is perfectly bonded to the concrete interior (i.e., a linear strain distribution through the cross section). The method consists in discretizing the pile cross section into a series of strip elements for integrating the normal stresses over the cross-sectional area. The discretization results in both FRP and concrete strip elements, as shown in figure 5. The stress integration is done by assigning the appropriate constitutive model for each material. Details of the development of the model and its validation through experimental results can be found in Fam (2000) and Fam and Rizkalla (2002).

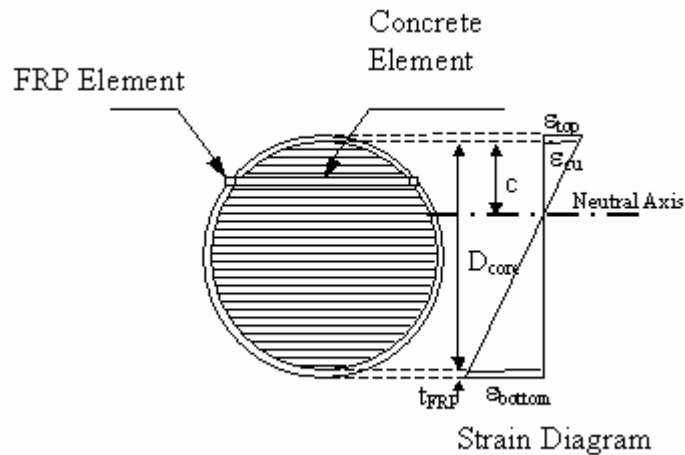


Figure 5. Illustration. Strip elements for sectional analysis (Mirmiran and Shahawy 1996).

The load-curvature response, predicted using the model just described, and the experimental load-strain behavior for Beams 4 and 13 from Fam and Rizkalla (2002), are shown in figure 6. The figure shows good agreement between the model and the experimental results, especially when accounting for tension stiffening.

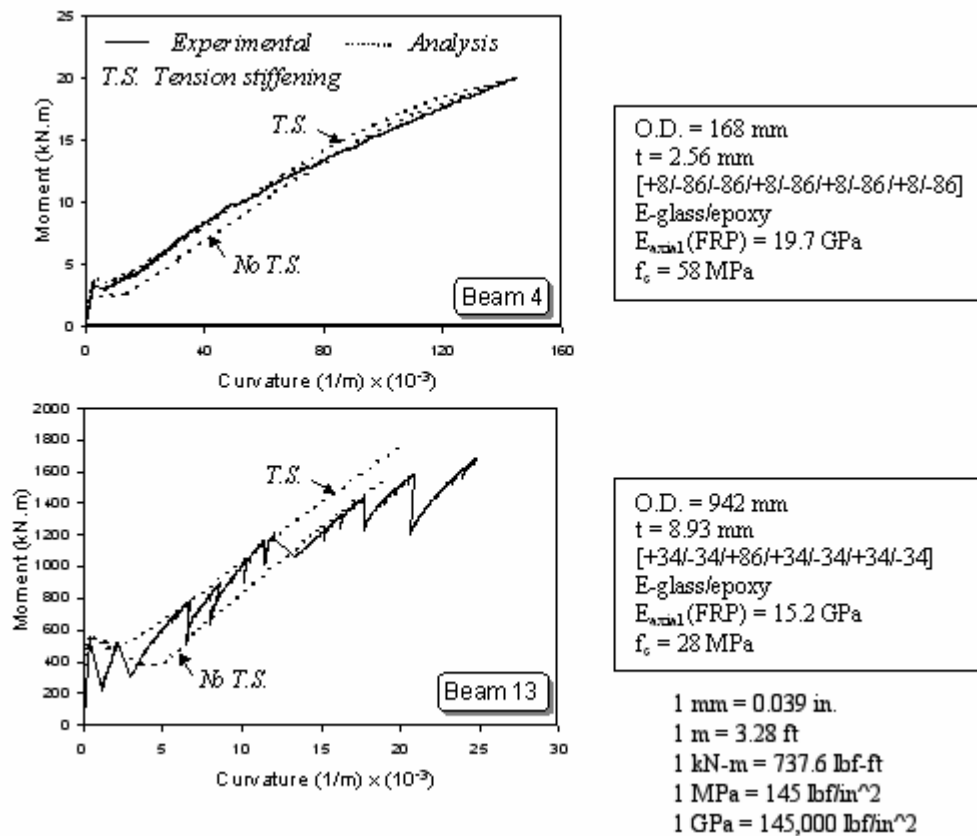


Figure 6. Graphs. Experimental versus analytical moment-curvature response (adapted from Fam and Rizkalla 2002).

This model will be used later in chapter 4 to illustrate the influence that the degradation of the FRP tube properties (stiffness and strength) has on the long-term axial capacity of concrete-filled tubular FRP piles.

2.3.1.1.3 Behavior under combined bending and axial loading

Mirmiran and Shahawy (1999) performed a detailed study on concrete-filled FRP tubes under various combinations of axial and flexural loads. Two types of FRP tubes were used to simulate the conditions of overreinforcement (where compression failure governs) and underreinforcement (where tension failure governs). The overreinforced specimens were prepared using tubes 348 mm (13.7 inches) in diameter with a wall thickness of 14 mm (0.551 inches), while the underreinforced specimens used 369-mm (14.5-inch) tubes with a 6-mm (0.236-inch) wall thickness. The reinforcement ratios (ratio of area of FRP shell to area of concrete core) for the over- and underreinforced concrete-filled tubes were 18.27 and 7.56 percent, respectively. Since the strength of the FRP tubes differed in these specimens, the authors proposed the use of a reinforcement index, defined as the reinforcement ratio multiplied by the ratio of the axial tensile strength of the FRP tube to the concrete compressive strength. The reinforcement indices of the over- and underreinforced sections were 3.39 and 0.19, respectively. The interaction diagrams for the two types of specimens are shown in figure 7.

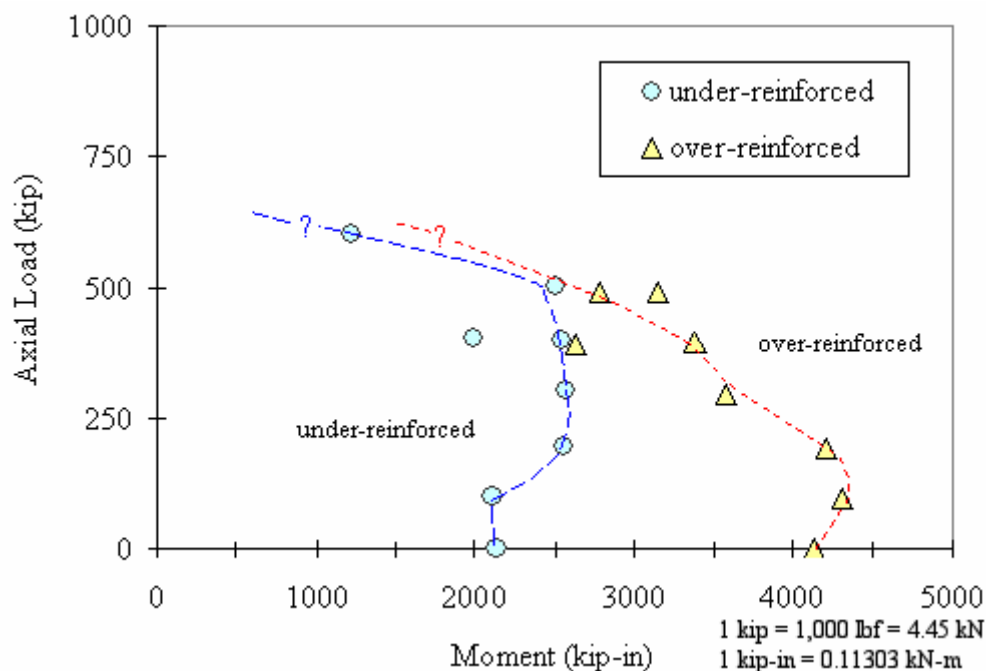


Figure 7. Graph. Interaction diagrams, concrete-filled FRP tubes (Mirmiran 1999).

The overreinforced specimens were found to behave better as beam columns. They deflected to a lesser extent (ultimate deflections of the overreinforced specimens were about 25 to 50 percent lower than the underreinforced specimens), and failed at much higher bending moments. Failure of the overreinforced specimens while in compression was considered to be gradual or ductile. The underreinforced failure mode was brittle and sudden. Based on this study, the authors concluded that concrete-filled FRP tubes could be used for beam-column applications, and recommended the use of overreinforced specimens. Test observations also indicated that bond failure or slippage in beam columns is not as significant as in beam specimens (pure flexure), as long as the end connections are designed properly. For beam specimens, shear transfer mechanisms such as internal ribs or treatments of the inner surface of the tubes were recommended to enhance the composite action between the FRP shell and the concrete core.

Design of concrete-filled FRP tubes for this type of loading can be done using the same sectional analysis as described in section 2.3.1.1.2 for pure flexure. This analysis methodology can be easily programmed and used to generate moment-curvature and interaction diagrams. A more detailed description of the methodology can be found in Mirmiran and Shahawy (1996), Mirmiran (1999), and Fam (2000).

2.3.1.2 Steel-reinforced recycled plastic composite piles

Research on the structural behavior of steel-reinforced recycled plastic piles is notably absent in published literature. Information about the performance of these piles is limited to reports commissioned by pile manufacturers. Table 3 lists the available structural

information from the manufacturer. This information consists of test results, and it does not include design methods.

Table 3. Available structural information for steel-reinforced plastic composite piles.

Type of test	Source
Three-point bend test	Asaro (2000)
Limited flexural tests	Warren (1996)
Axial compression test	Stokes (2002)

Iskander, et al. (2003), studied the compressive strength of the plastic material used for these kinds of piles. The results showed a marked nonlinear behavior and significant spatial distribution of strength and density within the specimens. However, the results from tests shown in table 3 indicate that the majority of the structural capacity and stiffness comes from the welded steel rebar cage.

2.3.2 Long-Term Durability Behavior

The lack of long-term performance and durability data on composite piles is a concern (Lampo, et al., 1998, Iskander and Hassan 1998, Iskander, et al., 2001). There is an urgent need for research in this area.

2.3.2.1 Concrete-filled FRP composite piles

The principal mechanisms for degradation of the FRP composites used in piles are moisture absorption over time and freeze-thaw cycles. Chemical degradation and UV radiation also affect long-term durability, but to a lesser extent. Furthermore, UV degradation resistance of most composites is improved by applying protective coats and additives during the manufacturing process. The degradation mechanisms related to moisture absorption and freeze-thaw cycles are discussed below.

Degradation due to moisture absorption may significantly reduce the life of FRP composites (Garcia, et al., 1998). Absorbed moisture can cause pronounced changes in modulus, strength, and strain to failure (Springer, et al., 1980). The moisture content of submerged FRP composites increases through diffusion. The absorbed moisture can act as a plasticizer of the composite resin, and can cause matrix cracking, fiber-matrix debonding, and corrosion of glass fibers (stress corrosion) (Garcia, et al., 1998). These effects result in a reduction of strength and stiffness of the FRP composite. For example, Schulheisz, et al. (1997), recorded strength and stiffness reductions on the order of 20 percent and 5 percent, respectively, for E-glass/vinyl ester composites submerged in

25 °C (77 °F) water for a period of 200 days. The implications of such strength and stiffness reductions on the design of composite piles can be significant.

In addition to submergence time, temperature and stress level also influence the amount of moisture that FRP will absorb while submerged. An FRP composite subject to tensile stresses is expected to have a faster rate of moisture absorption. Figure 8 shows schematically how time and temperature influence moisture absorption, how moisture absorption degrades property values, and how exposure time thus produces a reduction in property values. Evidence of the existence of damage to FRP composites after submergence in water is illustrated in the scanning electron microscope (SEM) images shown in figure 9. The SEM image of the submerged sample shows fiber damage and crack formation at the fiber-matrix interface (McBagonluri, et al., 2000).

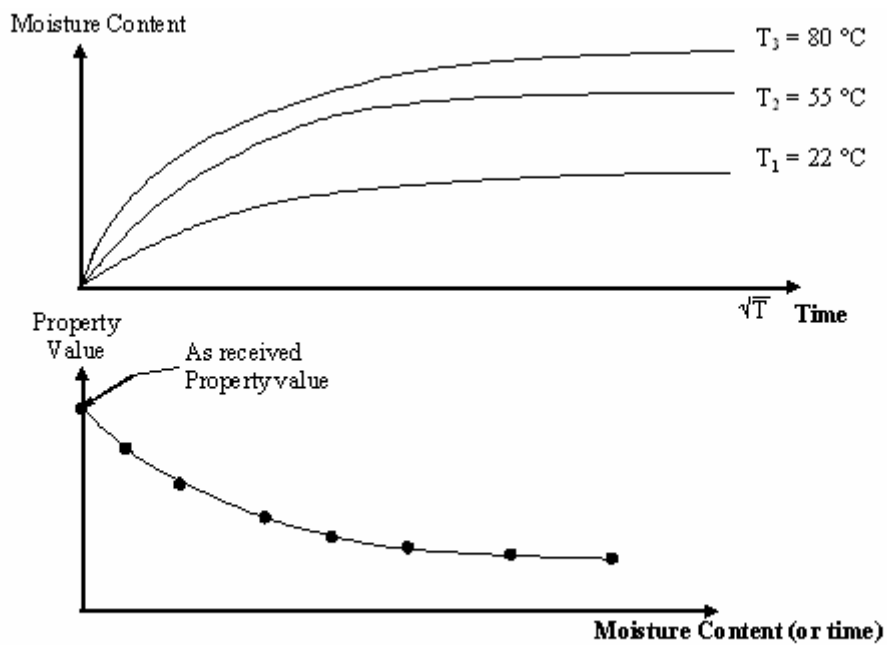


Figure 8. Graphs. Moisture absorption-related durability model.

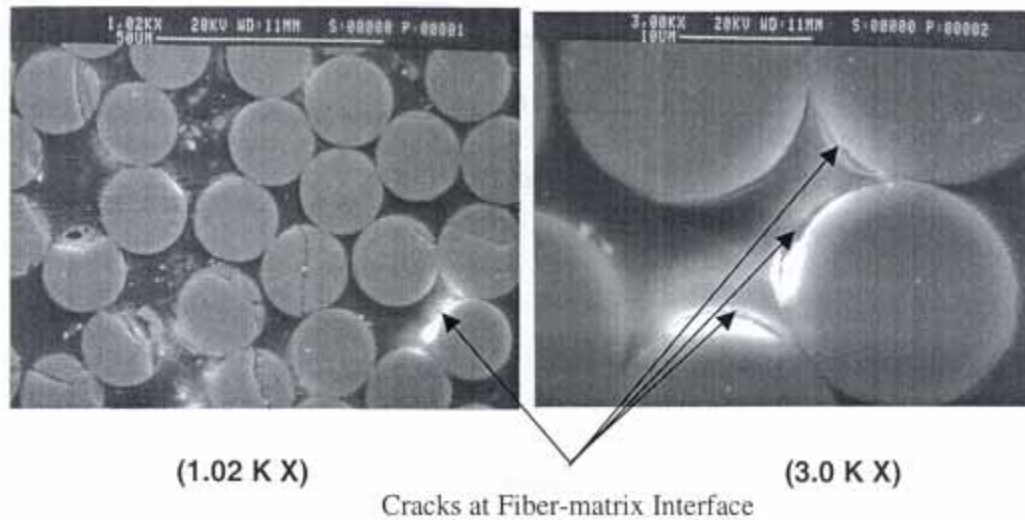


Figure 9. Images. SEM images showing FRP damage (McBagonluri, et al., 2000).

Freeze-thaw cycles can also degrade FRP composites. Freeze-thaw cycles cause the volume of absorbed water to increase. Such volume changes lead to crack propagation and damage to FRP (Verghese, et al., 1999).

2.3.2.2 Steel-reinforced recycled plastic composite piles

Iskander and Hassan (2001) carried out an accelerated degradation study on the recycled plastic material used in the plastic piling manufactured by Seaward International. Their study involved compression tests on coupon samples submerged in aqueous solutions with pH ranging between 2 and 12. A 25 percent loss in compressive resistance was predicted to take place after a 21-year exposure to the types of aqueous solutions used.

The durability of steel-reinforced plastic piles installed at Pier Bravo in NAS North Island, San Diego, CA was evaluated in 1999. The piles were manufactured by Plastic Pilings, Inc. and were installed in December 1995. Inspections carried out 3.5 years after installation showed no significant degradation.

2.3.3 Geotechnical Behavior

There has been little research to date on geotechnical issues related to either concrete-filled FRP composite or steel-reinforced recycled plastic piles. Some important issues are pile driveability, lateral load capacity, and axial load capacity. These issues are discussed in the following subsections.

2.3.3.1 Pile driveability

To date, very few case histories are available with monitored driving information of composite piles. Parametric or analytical driveability studies have been recently performed (e.g., Ashford and Jakrapiyanun 2001, Iskander, et al., 2001, Iskander and Stachula 2002) using wave equation analysis (e.g., computer code GRLWEAP™ (GRL Wave Equation Analysis Program)) to investigate the feasibility of driving FRP composite piles efficiently and without damage, and to compare their performance to conventional steel and concrete piles. These analytical studies found that composite piles can attain equivalent design capacity of conventional piles, but the low impedance of some composite piles may limit their driveability and pile capacity. These studies did not involve any field testing. The sparse field information available has been mostly generated by pile manufacturers.

A recent study involving field data not generated by pile manufacturers was carried out by Mirmiran, et al. (2002). This study involved driving four FRP composite piles and one prestressed concrete pile. The FRP tubes used for the piles had an outside diameter of 0.348 m (1.14 ft) and a wall thickness of 14 mm (0.546 inches). Two of the composite piles were driven with concrete infill and the other two were driven empty with a steel cone tip. The total length of the FRP piles was between 7.9 and 9.1 m (25.9 and 29.8 ft). The prestressed concrete pile was 0.356 m (1.17 ft) square and 9.1 m (29.8 ft) long. The filled FRP piles and the prestressed concrete pile were driven to depths of about 7.3 m (23.9 ft). The authors found that driving stresses in filled tubes were comparable to those for the prestressed concrete pile. The empty tubes were found to be susceptible to buckling and damage during driving, unless driven to shallow depths in soft soils or with a steel mandrel. No geotechnical information was provided about the site where the field tests were carried out.

It is clear that a significant amount of research is needed in this area. Particularly, there is an urgent need for more field tests carried out in a controlled fashion at well-characterized sites to carefully assess and verify the driveability of these new piles.

In general, pile driveability depends on the energy delivered to the pile by the pile-driving hammer, the resistance to driving offered by the soil, the ability of the pile to transfer driving stresses to the pile tip, and the strength of the pile to resist driving stresses. Good driving occurs when the hammer effectively transmits energy to the pile and the induced stress wave develops a force in the pile sufficient to overcome the soil resistance. Poor driving occurs when the transmitted energy is too low to develop a force capable of overcoming the soil resistance. If the stresses induced during driving are higher than the strength of the pile, the pile will be damaged.

The ability of the pile to transfer the energy imparted by the driving hammer into a force in the pile is related to the pile impedance (or dynamic stiffness). Impedance is defined as $Z = EA/c$, where E is the elastic modulus of the pile, A is the pile cross-sectional area, and c is the wave propagation speed in the pile. The greater the impedance of the pile, the greater is the force that will be transmitted by the pile into the ground. Table 4 compares

typical impedance values of four selected composite piles with impedances of three conventional piles of similar cross sections.

Table 4. Comparison of pile impedance.

Pile Description	Impedance $\frac{E \cdot A}{c} \left(\frac{\text{MN} \cdot \text{s}}{\text{m}} \right)$	Impedance Ratio ¹	Source
12 inch square prestressed concrete	750	8	Iskander and Stachula 2002, Ashford and Jakrapiyanun 2001
12.8 inch diameter concrete-filled FRP	691	7.4	Ashford and Jakrapiyanun 2001
10.6 inch diameter plastic encased steel pipe	412	4.4	Iskander and Stachula 2002
13.4 inch diameter steel pipe pile (0.374 inch wall thickness)	391	4.2	Ashford and Jakrapiyanun 2001
12.4 inch diameter timber pile	266	2.8	Iskander and Stachula 2002
15.7 inch diameter recycled plastic pile (reinforced with FRP tendons)	215	2.3	Iskander and Stachula 2002
14 inch diameter hollow FRP shell (0.51 inch wall thickness)	93.7	1	Ashford and Jakrapiyanun 2001

Note: (1) Impedance ratio = Pile impedance/Impedance of hollow FRP pile.
1 inch = 25.4 mm.

Table 4 shows the impedance ratio of each pile compared to the pile of lowest impedance (the empty FRP shell). It can be seen that the prestressed concrete pile and the concrete-filled FRP pile have similar impedance values, and they have the highest values. The plastic-encased steel pipe pile and the FRP-reinforced recycled plastic pile impedance values are about 55 percent and 29 percent of the impedance of the prestressed concrete pile, respectively. The lowest impedance corresponds to the empty FRP shell with a value equal to about 12.5 percent of the prestressed concrete pile.

2.3.3.2 Lateral load capacity

The design of piles for use against lateral loads is usually governed by the maximum tolerable deflection (Poulos and Davis 1990). Lateral deflections of single piles depend on the lateral load, the bending stiffness (EI) of the pile, and the soil resistance to lateral movement (characterized by soil strength and stiffness). Based on the available structural studies of concrete-filled FRP composite pipe piles mentioned earlier, it is expected that these composite piles will generally have lower bending stiffness than the conventional prestressed concrete piles commonly used for bridge substructures. Therefore, lateral deflections of composite piles are expected to be greater than for conventional piles subjected to the same lateral loads. The higher flexibility of these composite piles could prove to be very important in cases where lateral deflections control design. The reduced bending stiffness will also have an important impact on the load transfer mechanism and the depth to which lateral soil resistance is mobilized.

For laterally loaded “conventional” piles, it is common practice to analyze the load-deflection response by using analytical methods such as the Winkler Method (subgrade reaction method), elastic continuum theory, p-y method, and finite element-based methods. Detailed descriptions of these methods can be found elsewhere (e.g., Reese 1984, Poulos and Davis 1990). All of these methods tend to model the pile as an elastic beam. However, for composite piles, this assumption may no longer be acceptable. Han (1997) and Han and Frost (1997) pointed out that to reasonably predict the load-deflection response of a laterally loaded composite pile, the shear deformation effects should be taken into account. This issue arises due to the fact that composite materials have considerably lower shear modulus (G) than conventional materials (Scott, et al., 1998). Therefore, strictly speaking, the classical Bernoulli-Euler beam theory, which ignores shear deformation, is not applicable (Bank 1989, Han and Frost 1997). For example, a study by dos Reis and Goldman (1987) on FRP composite tubular shells indicated that deflections predicted using classical beam theory yielded deflections about 30 percent lower than predictions using finite element analysis that incorporated the effect of shear deformations. Han and Frost (1997) did a theoretical study that extended the existing elastic continuum solution to include shear deformation effects and pile-soil slip. Their solution, from the theoretical point of view, offers a reasonable design approach for composite piles. However, their model is quite complex and requires considerable computational effort. Also, their model has not yet been confirmed by model or full-scale tests of composite piles. Certainly more research is required in this area. Further research should aim not only to improve understanding of the load-deflection response of composite piles, but also to develop reliable and easy-to-use design procedures that can be readily implemented by practitioners.

2.3.3.3 Axial load capacity

The behavior of piles during axial loading depends on the axial stiffness (AE) of the pile, residual stresses left in the pile and the soil after pile installation, and the resistance of the soil to pile downward movement.

The axial stiffness of concrete-filled FRP composite pipe piles is expected to be comparable to that of conventional prestressed concrete piles, since the composite axial stiffness of these piles is largely determined by the stiffness of the concrete infill.

An important potential difference between composite piles and conventional piles is that the shear strength at the interface between the pile and the soil may be different due to unique interface properties such as lower surface hardness and different surface roughness. Such differences could have a significant influence on the applicability of standard procedures for estimating pile skin friction. To date, most laboratory studies published in this area involve interface shear tests on traditional pile materials. Relatively few studies are available on interface shear behavior between FRP composite pile materials and soils.

Han (1997) carried out an experimental study that compared the interface friction between an E-glass/polyester composite sheet pile and sand with the interface friction

between mild steel (A36) and sand. In general, Han found that the FRP specimen was relatively rougher than the steel specimen, which resulted in higher peak interface friction angles for the FRP composite than for the steel. However, issues like surface roughness degradation were not explored. Interface creep deformations were not studied either.

Interface shear test data for other types of composite piles are not currently available. Clearly, this area requires a considerable amount of study.

2.4 SUMMARY

This chapter provides background information on composite piles and reviewed literature related to the two pile types used in the research project: concrete-filled FRP piles and steel-reinforced recycled plastic piles. Research on structural behavior, long-term durability behavior, and geotechnical behavior for each pile type was reviewed. The literature review indicates that the following knowledge gaps exist.

1. While research on the structural behavior of concrete-filled FRP piles has received a fair amount of attention, similar research on steel-reinforced recycled plastic piles is restricted to reports commissioned by pile manufacturers.
2. Long-term durability research for both pile types is limited, and further study is needed to understand the effects of moisture absorption and freeze-thaw cycles.
3. There is only a small body of research on geotechnical behavior of composite piles. There is a need for more controlled field tests at well-characterized sites to carefully assess and verify pile driveability. Future research should aim to improve understanding of the load-deflection response for composite piles, and also to develop reliable and easy-to-use design procedures for practitioners.

CHAPTER 3. EXPERIMENTAL STUDY OF INTERFACE BEHAVIOR BETWEEN COMPOSITE PILES AND TWO SANDS

3.1 INTRODUCTION

The properties of materials used in composite piles can differ significantly from those of conventional pile materials (e.g., steel and concrete), including differences in anisotropy, stiffness, surface hardness, and surface roughness. These differences may produce differences in the behavior of interfaces between the piles and the surrounding soil. Interface behavior plays an important role in the ultimate capacity and load transfer characteristics of the pile, as shown schematically in figure 10. For example, the axial pile capacities of a composite pile and a conventional pile, with identical dimensions and soil conditions, may be quite different due to differences in the developed shaft capacity. To date, most laboratory studies published in this area involve interface shear tests on traditional pile materials. Relatively few studies are available on interface shear behavior between composite pile materials and soils. The principal focus of this chapter is on the soil-pile interface behavior characteristics of composite piles against sand. This chapter summarizes interface shear tests results for seven pile material types (five composite pile materials and two conventional pile materials) against two types of sands. The interface behavior of the different piles is studied within the geotribology framework proposed by Dove and Jarrett (2002).

This chapter is divided into five sections:

1. Soil materials. Describes the gradation and strength properties of each of the soils used for interface testing.
2. Pile surfaces. Describes the surface texture and hardness of the different interface materials tested.
3. Interface shear tests. Describes the equipment and procedures used for interface shear testing, and summarizes the results obtained.
4. Discussion of results.
5. Summary.

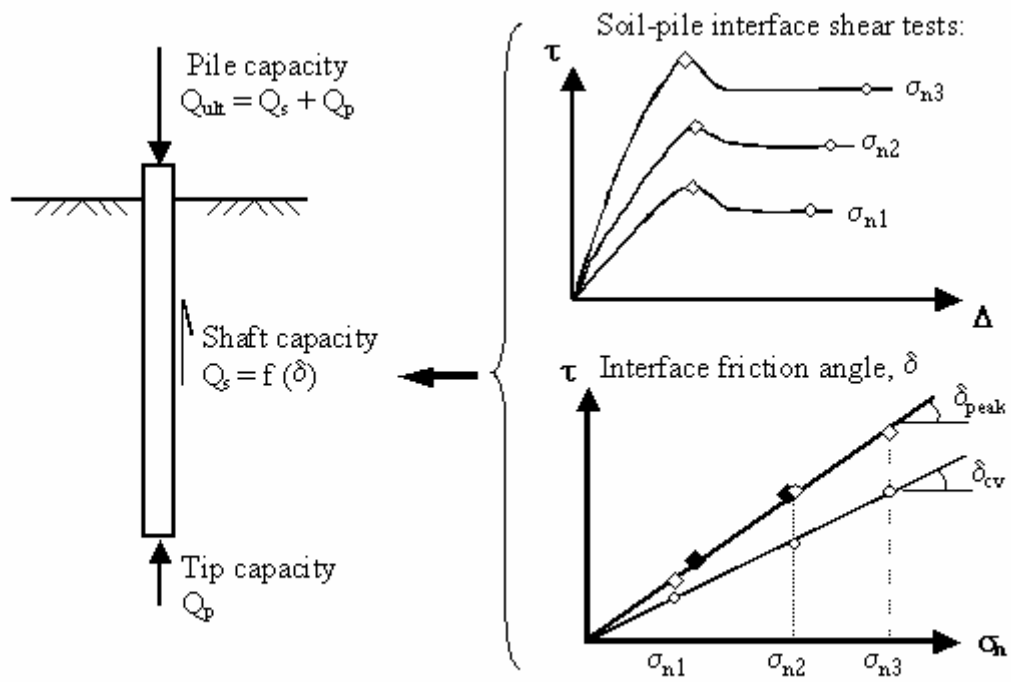


Figure 10. Illustration. Influence of soil-pile friction on pile capacity.

A matrix summarizing the tests carried out for the interface behavior study is provided in table 5.

Table 5. Interface behavior test matrix.

Type of Test	Type of Soil	Type of Pile Surface	Comments
Direct shear test	Density sand	Not applicable	Average $D_r = 70\%$
Direct shear test	Density sand	Not applicable	Average $D_r = 100\%$
Direct shear test	Model sand	Not applicable	Average $D_r = 75\%$
Interface shear test	Density sand	Lancaster CP40	Curved specimen, 24-inch nominal diameter
Interface shear test	Model sand	Lancaster CP40	Curved specimen, 24-inch nominal diameter
Interface shear test	Density sand	Hardcore 24-4	Curved specimen, 24-inch nominal diameter
Interface shear test	Model sand	Hardcore 24-4	Curved specimen, 24-inch nominal diameter
Interface shear test	Density sand	Hardcore FRP, no bonded sand	Flat plate, surface untreated with no acrylic coating
Interface shear test	Model sand	Hardcore FRP, no bonded sand	Flat plate, surface untreated with no acrylic coating
Interface shear test	Density sand	Hardcore FRP, with bonded sand	Flat plate, textured surface with bonded sand
Interface shear test	Model sand	Hardcore FRP, with bonded sand	Flat plate, textured surface with bonded sand
Interface shear test	Density sand	Plastic Piling recycled plastic	Flat coupons from prismatic rectangular beams
Interface shear test	Model sand	Plastic Piling recycled plastic	Flat coupons from prismatic rectangular beams
Interface shear test	Density sand	Concrete	Coupon from prestressed concrete pile
Interface shear test	Model sand	Concrete	Coupon from prestressed concrete pile
Interface shear test	Density sand	Steel	Coupon from sheet pile
Interface shear test	Model sand	Steel	Coupon from sheet pile

1 inch = 25.4 mm.

3.2 SOIL MATERIALS

Two sands were used in this study: Density sand and a Model sand. The Density sand is a fine- to medium-grained, silica sand with subrounded to rounded grains, and the Model sand consists of a blend of Light Castle sand with Bedding sand. The Model sand consists predominantly of fine-grained sand with subangular to angular grains. The Density sand was used in a previous study by Gómez, et al. (2000). The Model sand was prepared to mimic the foundation soils of the pile test site at the Route 351 Bridge.

3.2.1 Index Properties

Index parameter values for both sands used in this study are listed in table 6. Grain size distribution curves for these sands are shown in figure 11. The Density sand has grain sizes ranging from 0.2 to 0.9 mm (0.0078 to 0.035 inches) with no fines. The Model sand has grain sizes ranging from 0.1 to 2 mm (0.0039 to 0.078 inches) with about 5 percent fines. Microscopic views of the sands are shown in figure 12.

Table 6. Index parameter values of the sands used in this study.

Parameter	Density Sand ⁽¹⁾	Model Sand	ASTM Standard
D ₁₀ (mm)	0.3	0.08	D2487
D ₅₀ (mm)	0.5	0.18	
C _u	1.8	2.6	
C _c	1.1	0.8	
γ _{max} (kN/m ³)	17.5	17.0	D4253
γ _{min} (kN/m ³)	15.1	14.1	D4254
G _s	2.65	2.65	D854

Note: (1) After Gómez, et al. (2000); 1 mm = 0.039 inches; 1 kN/m³ = 6.36 lbf/ft³.

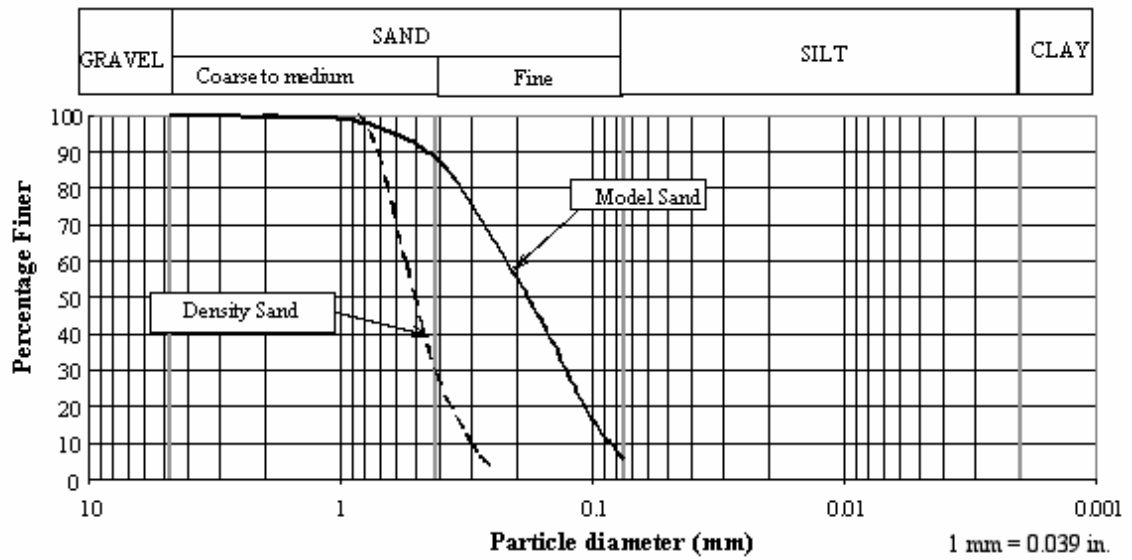


Figure 11. Graph. Grain size curves to test sands.

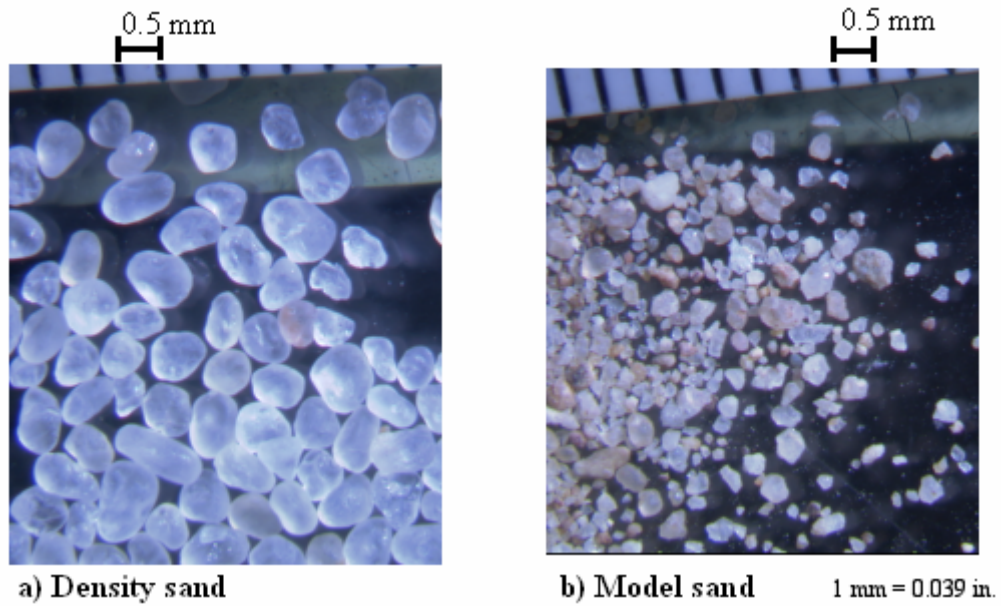


Figure 12. Photos. Microscopic views of the test sands.

3.2.2 Direct Shear Tests of Sands

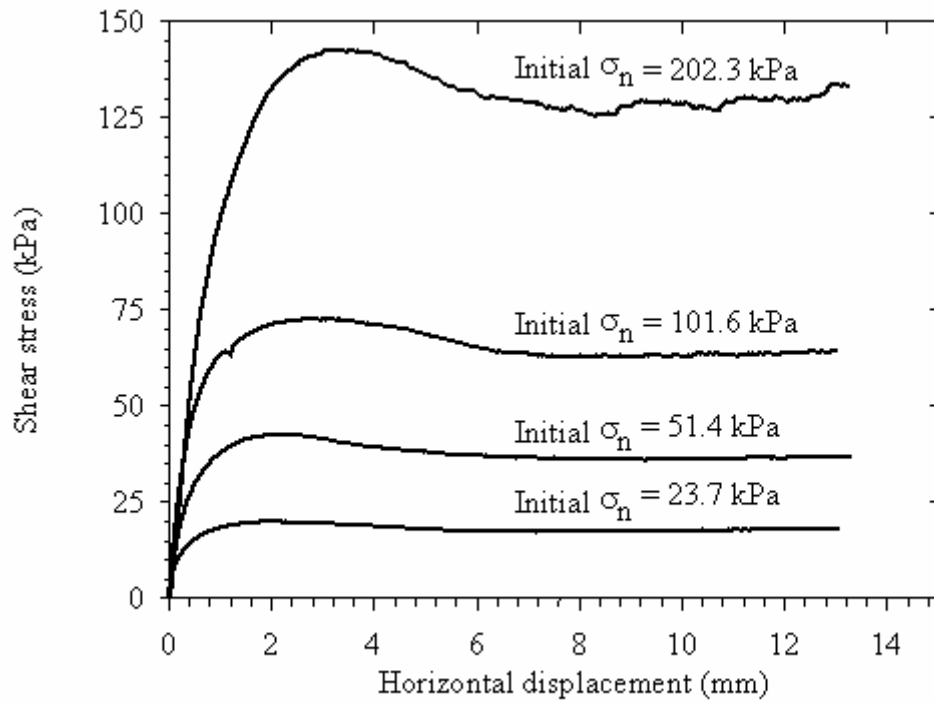
Direct shear tests were performed to determine the internal friction angles of the Density and Model sands. Displacement controlled direct shear tests with a 101.6 mm (4-inch) square shear box were performed. All tests were carried out at a horizontal displacement rate of 0.9 mm/minute (min) (0.036 inch/min). The direct shear tests were performed in accordance with American Society for Testing and Materials (ASTM) Standard D3080-98 (ASTM 1998). Samples were prepared by means of air pluviation and tamping. Dry sand was poured through a 6.5 mm (0.254 inch) funnel positioned at 10 mm (0.39 inch) above the top of the sand surface. Increased density was achieved by means of a small tamping device. To minimize the friction between the sand and the soil box, the inside of the walls was coated with a thin film of vacuum grease.

Direct shear test results, in terms of shear stress versus horizontal displacement curves, are presented in figures 13 through 15 for the medium-dense to dense Density and Model sands, respectively. For the entire range of relative densities and normal pressures tested, all of the direct shear tests exhibited a peak shear stress followed by a stress reduction toward a residual shear stress with a nearly constant volume state. The peak and residual (nearly constant volume state) friction angles obtained from the direct shear tests are summarized in table 7.

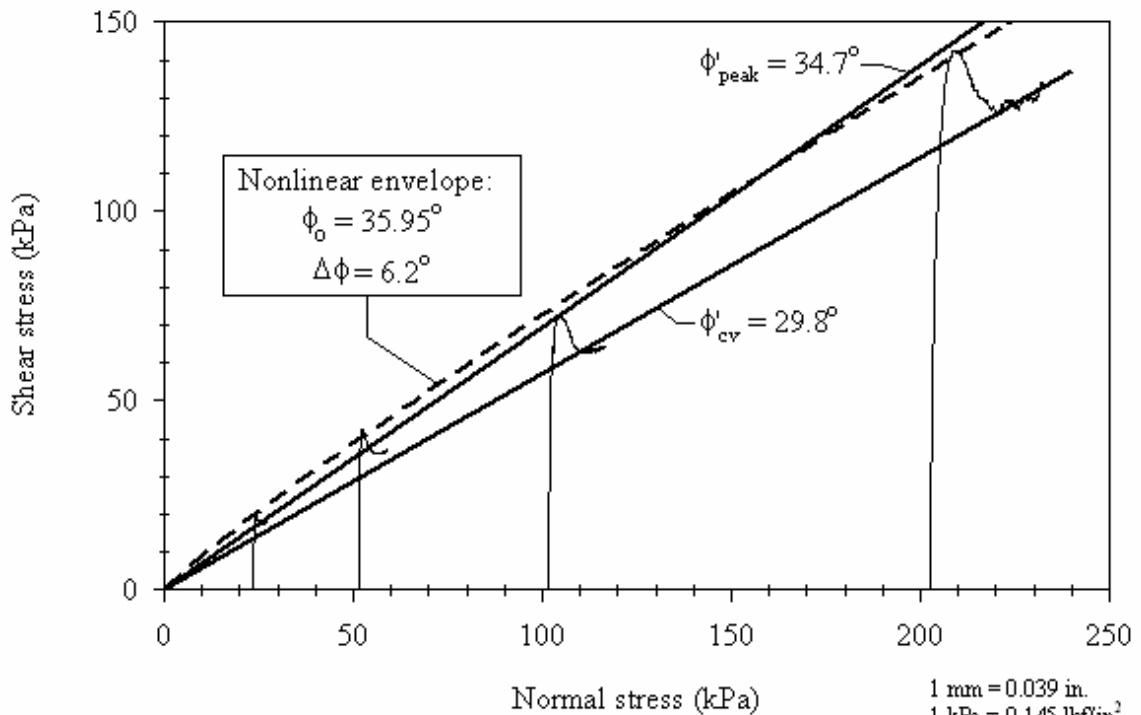
Table 7. Internal friction angles obtained from direct shear tests.⁽¹⁾

Parameter	Density Sand (Average $D_r = 70\%$)	Density Sand (Average $D_r = 10\%$)	Model Sand (Average $D_r = 75\%$)
Peak ϕ'_p	34.7 °	39.3 °	43.4 °
Residual ϕ'_{cv}	29.8 °	29 °	36.2 °

Notes: (1) Four normal stresses were used: 25, 50, 100, and 200 kPa (3.63, 7.25, 14.5, and 29 lbf/inch²).

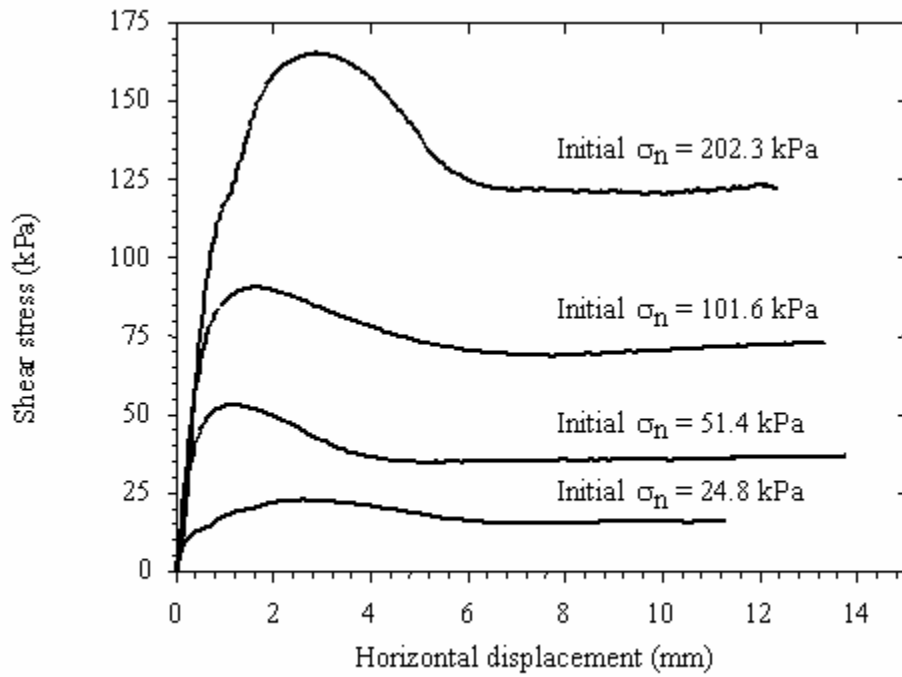


a) Shear stress—displacement curves

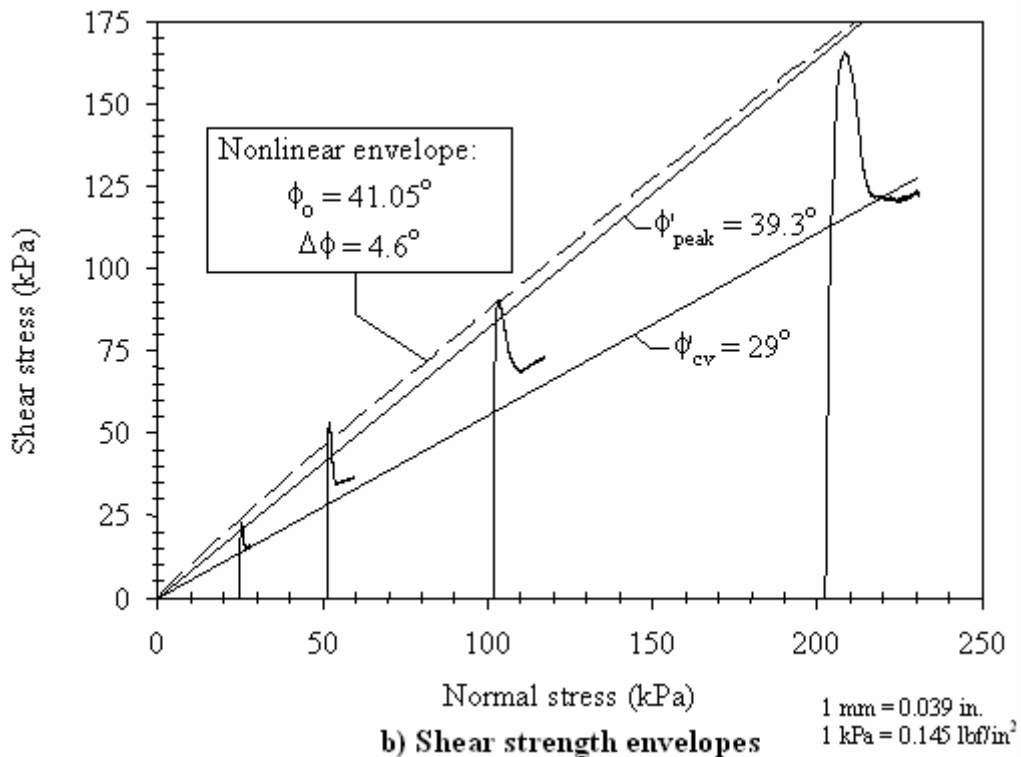


b) Shear strength envelopes

Figure 13. Graphs. Direct shear test results for Density sand (average $D_r = 70\%$).

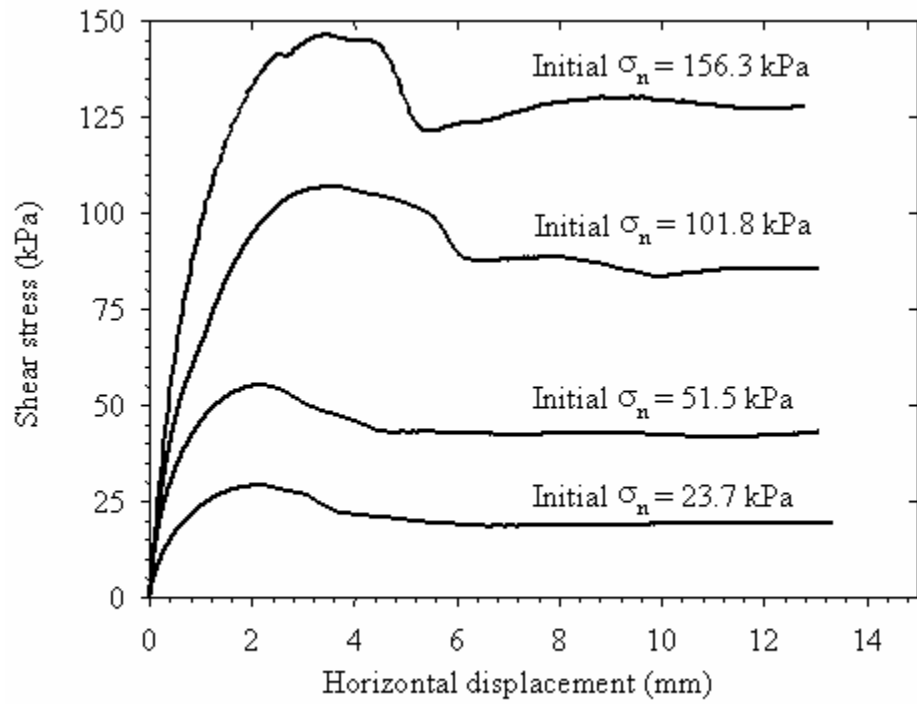


a) Shear stress—displacement curves

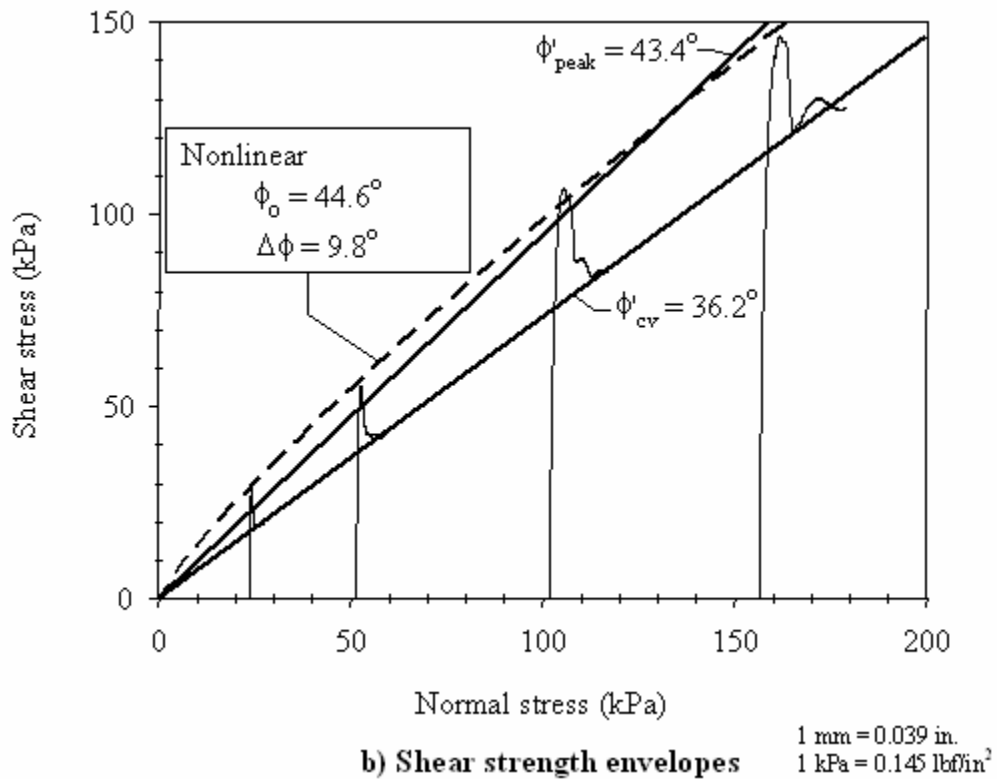


b) Shear strength envelopes

Figure 14. Graphs. Direct shear test results for Density sand (average $D_r = 100\%$).



a) Shear stress—displacement curves



b) Shear strength envelopes

Figure 15. Graphs. Direct shear test results for Model sand (average $D_r = 75\%$).

In table 7, D_r refers to the sample's relative density, which can be calculated as follows:

$$D_r = \frac{\frac{1}{\gamma_{min}} - \frac{1}{\gamma_{dry}}}{\frac{1}{\gamma_{min}} - \frac{1}{\gamma_{max}}} \times 100\% \quad (5)$$

where

- γ_{max} and γ_{min} = are the maximum and minimum dry unit weights for each sand (values given in table 6)
- γ_{dry} = dry unit weight of the samples in the direct shear tests

Both linear and curved-peak shear strength envelopes are shown in figures 13 through 15. The nonlinear shear strength envelopes were obtained using the following expression proposed by Duncan, et al. (1980):

$$\phi = \phi_0 - \Delta\phi \cdot \log_{10} \left(\frac{\sigma'_n}{P_a} \right) \quad (6)$$

where

- ϕ_0 = peak secant friction angle at a normal stress equal to the atmospheric pressure ($P_a = 101.4$ kPa)
- $\Delta\phi$ = reduction in peak secant friction angle for a tenfold increase in normal stress, σ'_n

The values of ϕ_0 and $\Delta\phi$ for both sands are shown in figures 13 through 15.

The shearing area of the soil specimens decreases during direct shear testing. The direct shear test stress paths, shown in figures 13 through 15 in τ - σ space, have been corrected for this effect.

3.3 PILE SURFACES

3.3.1 Introduction

The interface testing program included determining interface friction angles between the two sands described above and the following seven pile surfaces: Lancaster FRP shell (curved), Hardcore™ FRP shell (curved), Hardcore FRP plate without bonded sand (flat), Hardcore FRP plate with bonded sand (flat), Plastic Piling recycled plastic (flat), steel sheet pile (flat), and prestressed concrete (flat). The following subsections describe these pile surfaces within a geotribology framework.

3.3.2 Surface Topography Characterization

The importance of surface topography, and the degree of surface roughness in interface behavior and soil-structure interaction response, have been noted by many investigators (e.g., Yoshimi and Kishidi 1982, Kishida and Uesugi 1987, Lehane, et al., 1993, Dove, et al., 1997, Han 1997, Dove and Frost 1999, Dove and Jarrett 2002).

The surface roughness of each pile material investigated was measured with a Taylor-Hobson Talysurf stylus profilometer. A schematic of the profilometer used in this study is shown in figure 16. As the figure illustrates, the profilometer comes equipped with a diamond stylus tip that traverses the surface to be characterized. Transducers in the profilometer help record the vertical and horizontal coordinates of the stylus tip. Therefore, the raw surface profile data consists of a series of discrete coordinate pairs (x, z) that can be postprocessed and analyzed to obtain the surface topography characterization of the material investigated (Dove and Jarrett 2002).

Surface topography was quantified by three commonly used roughness parameters: the maximum peak-to-valley height (R_t), the average mean line spacing (S_m), and the arithmetic average roughness (R_a). S_m is twice the mean distance between locations at which the profiles cross the centerline drawn through the centroid of the profile. R_a is the arithmetic average value of the profile departure from the mean line along the profile length. These three roughness parameters are illustrated in figure 17. More detailed discussion of these parameters is given in International Organization for Standardization (ISO) Standard 4287 (ISO 1997).

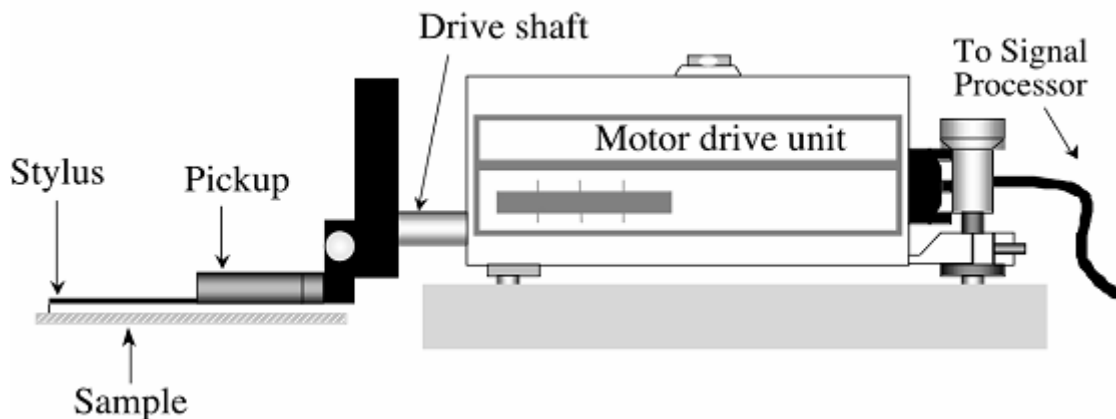


Figure 16. Illustration. Stylus profilometer sketch (Johnson 2000).

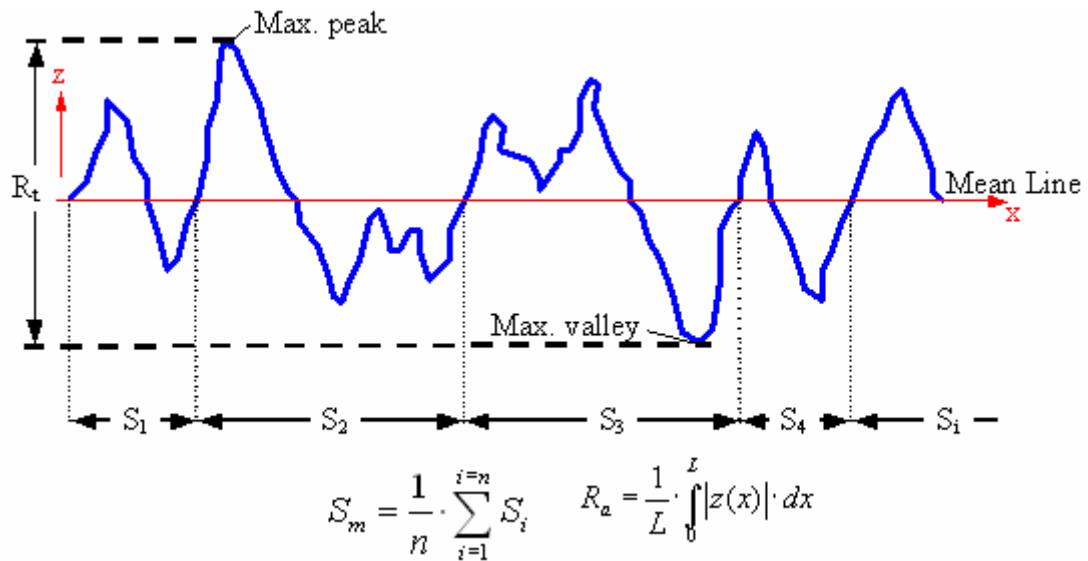


Figure 17. Chart. Graphical representation of roughness parameters R_t , S_m , and R_a .

Coupons approximately 25 mm (0.975 inch) by 200 mm (7.8 inches) were cut from each pile material. A series of six profiles, each 49 mm (1.91 inches) in length, were made on the surface of each coupon. All profiles were made in the longitudinal direction of the piles. Photos of the 7 pile surfaces and corresponding representative surface profiles are shown in figures 18 to 24.

The roughness parameters for the seven interface materials are summarized in table 8. The parameter values reported and subsequently used are averages of the six individual values obtained for each coupon.

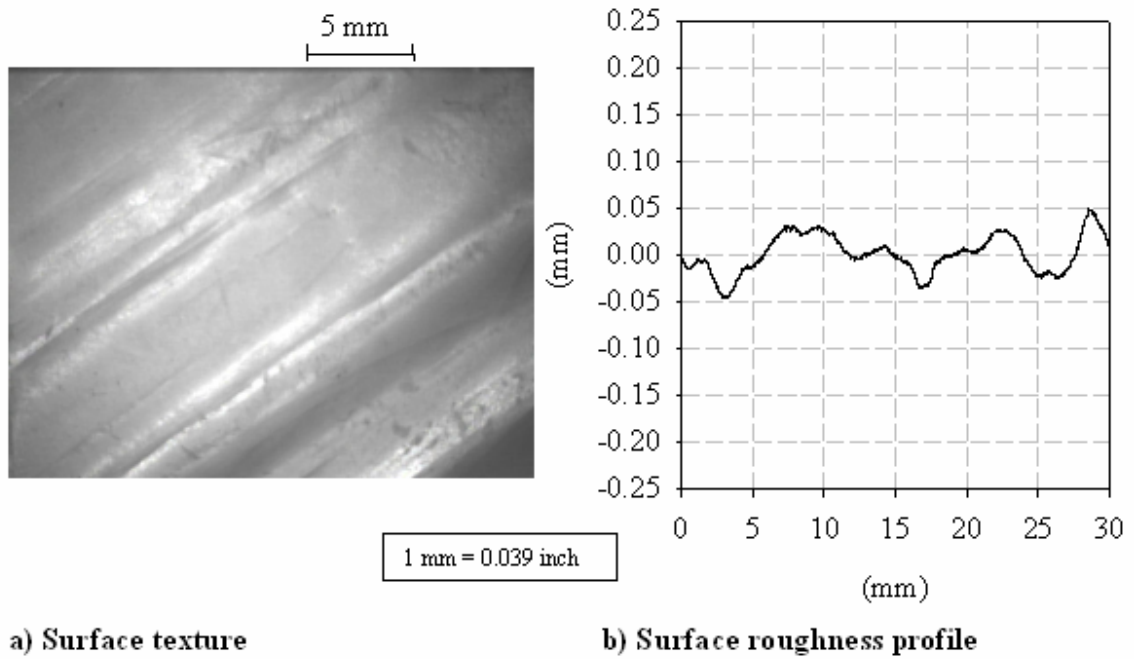


Figure 18. Photo and Graph. Surface characteristics of Lancaster FRP composite pile.

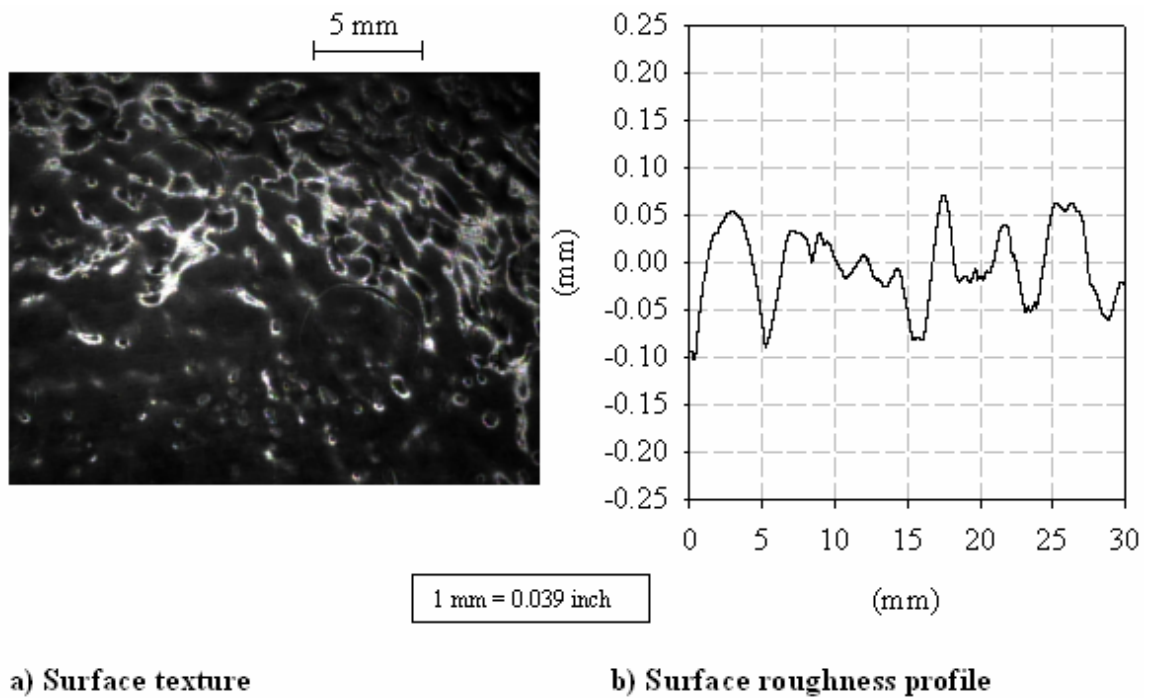
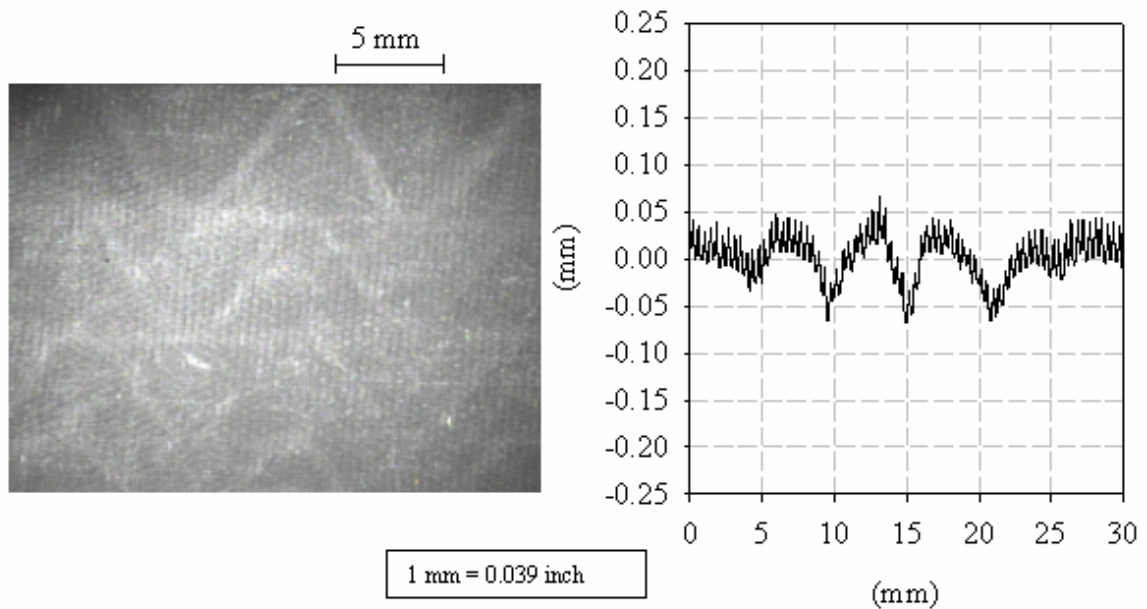


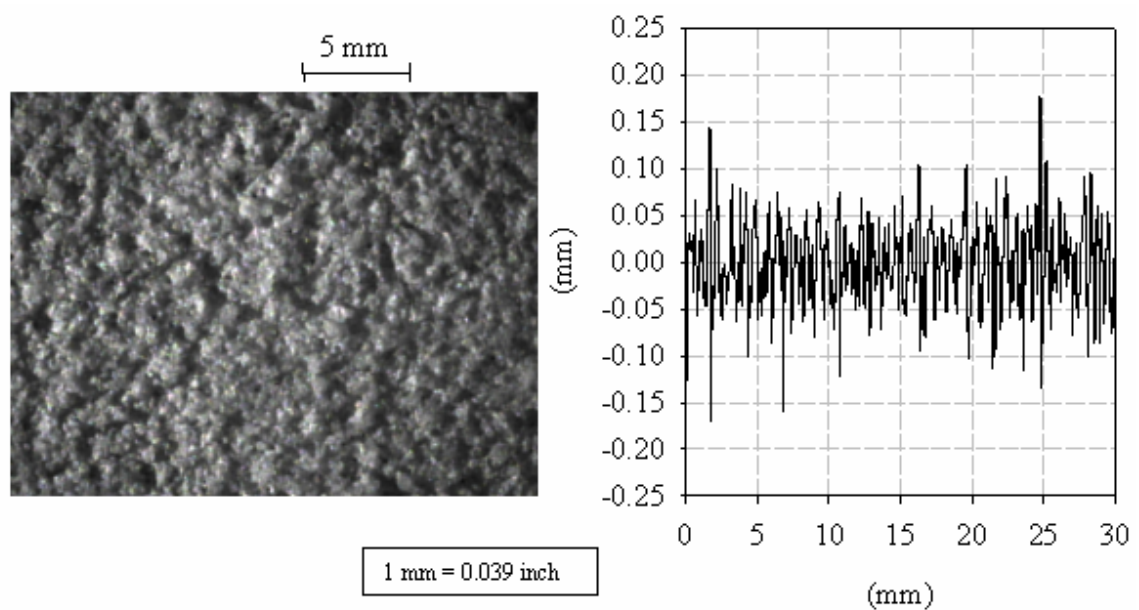
Figure 19. Photo and Graph. Surface characteristics of Hardcore FRP composite pile.



a) Surface texture

b) Surface roughness profile

Figure 20. Photo and Graph. Surface characteristics of Hardcore FRP plate.



a) Surface texture

b) Surface roughness profile

Figure 21. Photo and Graph. Surface characteristics of Hardcore surface-treated FRP plate.

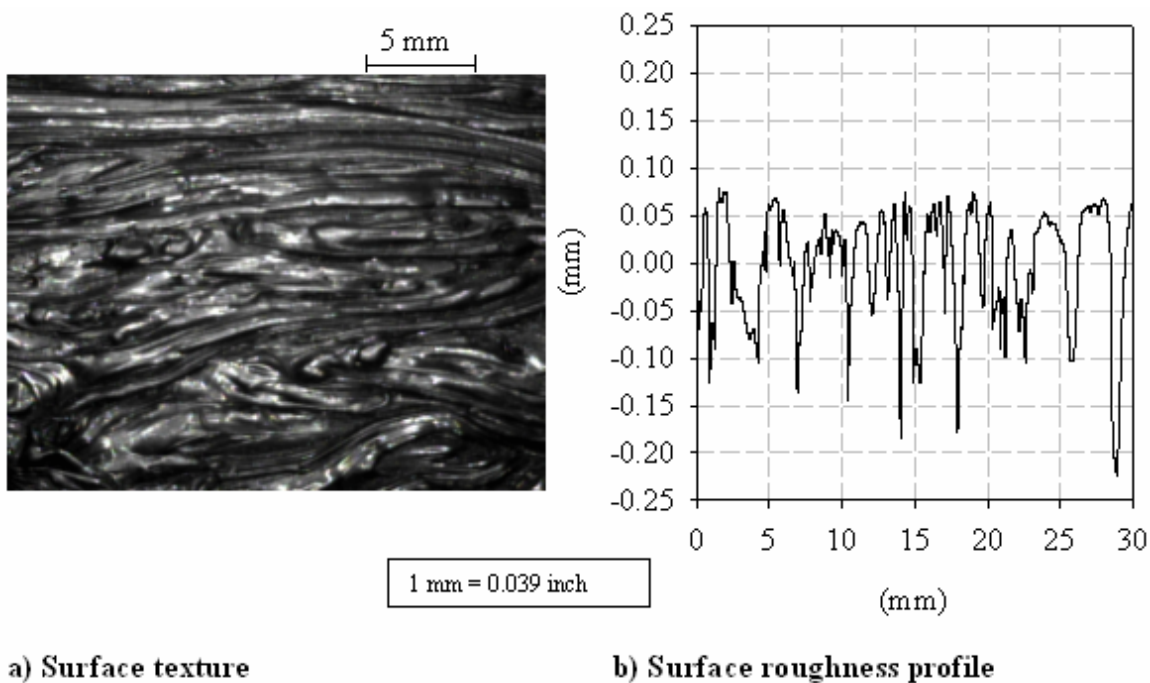


Figure 22. Photo and Graph. Surface characteristics of Plastic Piling plastic composite pile.

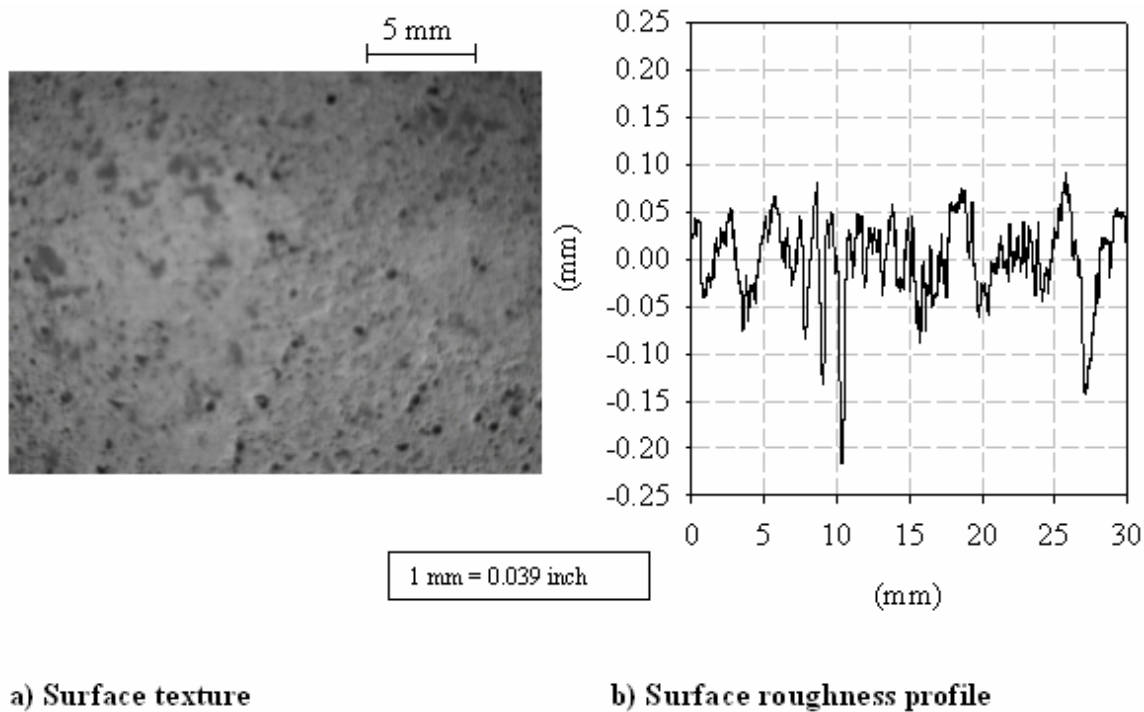


Figure 23. Photo and Graph. Surface characteristics of prestressed concrete pile.

found that relatively hard and smooth polymer surfaces did not show significant dilatancy, and the sand grains tended to slide along the polymer interface; whereas the particle movement on relatively soft and smooth polymer surfaces involved predominantly rolling and temporary grain indentations that resulted in higher interface friction values. The findings by O'Rourke, et al. (1990), are mainly applicable to smooth polymeric materials since, as the authors pointed out, surface roughness of rough polymers will promote dilation and result in increased shear resistance.

The surface hardness of the different pile/interface materials was investigated by means of the Vickers hardness test. The Vickers hardness test has the flexibility to allow application of small loads, which is convenient for testing softer materials such as recycled plastic and FRP composites, and consists of pressing a standard diamond pyramid into the sample. The Vickers hardness number (HV) is related to the load applied and the area of the diamond pyramid indentation. Vickers hardness tests were performed in accordance with ASTM Standard E384-99 (ASTM 1999). The results of the hardness tests are summarized in table 9.

Table 9. Surface hardness.

Interface Material	Vickers Hardness (HV)		
	Mean	SD	N
LC—CP40	24.0	1.83	20
HC—24-4	17.7	2.14	20
HC untreated FRP flat plate	35.7	10.38	20
HC treated FRP flat plate	Not measurable ⁽¹⁾		
PPI plastic	8.5	5.05	20
Concrete	63.7	36	36
Steel	184.2	10.28	20

Notes: (1): Not measurable because it is difficult to clearly measure the diamond indentation mark due to presence of the bonded sand particles.

HV = Vickers hardness number (ASTM Standard E384-99) (carried out at room temperature).

LC = Lancaster Composite, Inc., HC = Hardcore Composites.

PPI = Plastic Pilings, Inc. SD = standard deviation, n = number of tests performed.

3.4 INTERFACE SHEAR TESTS

Representative coupons were obtained from each of the seven different pile materials investigated. Careful consideration was given to selecting pile coupons that were representative of the average surface texture of the piles. The coupons from the plastic, concrete, and steel piles, and from the two Hardcore FRP plates, were all flat surfaced. Therefore, it was possible to use a flat shear box for interface shear testing of these materials.

The coupons from the cylindrical FRP shells (i.e., Lancaster CP40 and Hardcore 24-4) were cut with a water-cooled saw to dimensions that fit into the bottom half of the shear box. However, because both composite FRP shells were fabricated with thermoset resins, their curvature could not be removed. To permit testing of these curved-pile specimens,

the top half of the shear box was modified such that it could conform to the outside curvature of the piles, as shown in figure 25. The interface shear tests carried out on the other pile materials involved the use of the unmodified top half of the direct shear box. The interface shear tests were performed in accordance with ASTM Standard D5321-97 (ASTM 1997), and the horizontal displacement rate was 0.9 mm/min (0.35 inch/min).

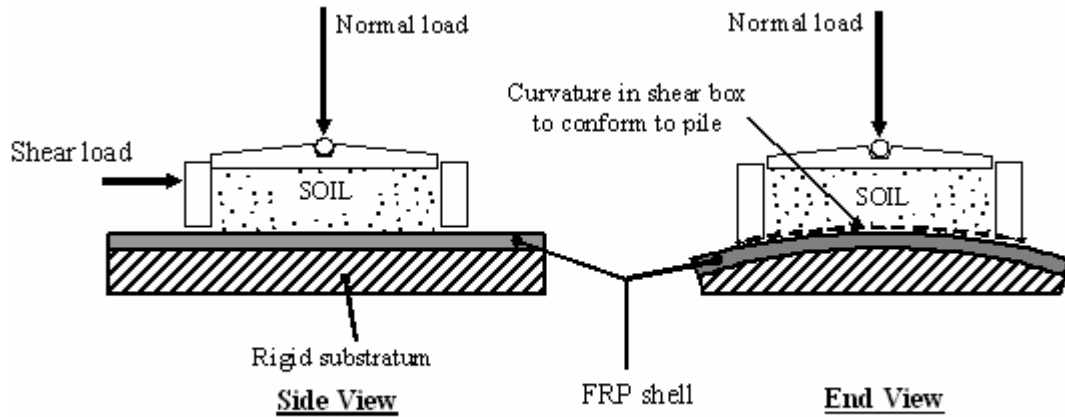


Figure 25. Illustration. Sketch of modified interface shear test setup.

The interface tests performed using the Density and Model sands are summarized in tables 10 and 11, respectively. Interface shear tests were carried out at constant normal stresses ranging from 23 to 200 kPa (3.3 to 29 lbf/inch²) (the contact area of the soil sample remained constant throughout the test). Typical interface shear stress versus interface displacement curves for the seven pile material types are shown in figures 26 and 27 for the Density and Model sands, respectively. Additional details of the interface tests performed for this investigation are presented in appendix A.

Interface strength envelopes for the seven pile materials and for the Density and Model sands are shown in figures 28 through 34. Curvature of the strength envelopes with increasing normal stresses was generally not significant. The interface friction angles obtained from linear fits to the test data are summarized in table 12.

Table 10. Summary of interface shear test results on Density sand.

Pile/Material	D_r (%)	σ'_n (kPa)	S_m (mm)	R_t (μm)	Hardness (HV)	S_m/D_{50}	R_t/D_{50}	τ_p (kPa)	d_p (mm)	τ_{cv} (kPa)	d_{cv} (mm)
Lancaster Composite	57.5	38.2	7.49	93.5	24	14.97	0.19	14.5	0.45	12.1	14
FRP shell (CP40)	64.3	63.2	7.49	93.5	24	14.97	0.19	22.8	0.35	19.2	13.5
	62.4	113.2	7.49	93.5	24	14.97	0.19	40.0	0.42	33.1	8
	65.7	200	7.49	93.5	24	14.97	0.19	70.2	0.60	59.6	3.4
Hardcore Composites	61.4	22.5	5.08	177.5	17.7	10.16	0.36	13.1	2.14	12.8	9.6
FRP shell (24-4)	66.0	50	5.08	177.5	17.7	10.16	0.36	28.7	2.27	27.3	11.5
	66.3	100	5.08	177.5	17.7	10.16	0.36	57	1.77	52.9	10.3
	68.3	200	5.08	177.5	17.7	10.16	0.36	111.1	1.99	102.0	13
Hardcore FRP plate; untreated surface	64.6	26.15	1.55	133.8	35.7	3.10	0.27	15.02	0.96	13.03	2.8
	61.5	50.06	1.55	133.8	35.7	3.10	0.27	29.81	1.17	24.73	6.7
	63.4	107.3	1.55	133.8	35.7	3.10	0.27	57.93	1.61	52.03	11.1
	66.2	199.73	1.55	133.8	35.7	3.10	0.27	107.55	1.59	95.45	10.9
Hardcore FRP plate; treated surface	62.6	26.15	0.49	341.2	See note (1)	0.98	0.68	18.48	1.22	15.54	11.0
	64.7	50.06	0.49	341.2	See note (1)	0.98	0.68	30.97	1.91	27.29	10.7
	63.7	107.17	0.49	341.2	See note (1)	0.98	0.68	63.34	1.74	55.3	10.8
	64.9	183.5	0.49	341.2	See note (1)	0.98	0.68	116.03	2.26	97.15	10.6
PPI plastic	65.9	29.11	1.86	365.9	8.5	3.73	0.73	17.10	1.26	13.19	6.7
	61.1	56.77	1.86	365.9	8.5	3.73	0.73	32.63	1.28	27.96	5.3
	60.8	105.37	1.86	365.9	8.5	3.73	0.73	56.05	2.20	51.83	5.07
	61.9	180.37	1.86	365.9	8.5	3.73	0.73	93.91	1.82	81.94	6.56
	61.1	199.72	1.86	365.9	8.5	3.73	0.73	103.39	1.66	92.67	9.45
Prestressed concrete pile	63.2	23.7	1.94	335.3	63.7	3.88	0.67	18.1	1.71	14.2	12.2
	61.9	51.5	1.94	335.3	63.7	3.88	0.67	35.4	0.93	26.3	12
	63.3	101.9	1.94	335.3	63.7	3.88	0.67	68.5	1.70	50.7	10.6
	64.0	175.4	1.94	335.3	63.7	3.88	0.67	111.5	2.55	93.7	9
Steel from sheet pile	67.0	25.57	0.43	66.7	184.2	0.86	0.13	13.48	0.73	11.07	3.6
	65.9	51.27	0.43	66.7	184.2	0.86	0.13	31.38	1.10	23.61	10.7
	64.1	101.85	0.43	66.7	184.2	0.86	0.13	59.11	0.79	49.11	6.8
	65.4	202.33	0.43	66.7	184.2	0.86	0.13	105.11	1.06	94.36	8.8

Notes: (1) Not measurable because it is difficult to clearly measure the diamond indentation mark due to presence of the bonded sand particles.

D_{50} = 0.5 mm for Density sand, D_r = Relative density after sample consolidation (as per equation 5), σ'_n = Normal pressure, S_m = Average mean line spacing,

R_t = Maximum peak-to-valley height, Hardness (HV) = Average Vickers hardness number,

τ_p = Peak interface shear stress, d_p = Horizontal displacement at peak,

τ_{cv} = Residual interface shear stress, d_{cv} = Horizontal displacement at residual.

1 mm = 0.039 inches; 1 μm = 0.000039 inch; 1 kPa = 0.145 poundforce per square inch.

Table 11. Summary of interface shear test results on Model sand.

Pile/Material	D_r (%)	σ'_n (kPa)	S_m (mm)	R_t (μm)	Hardness (HV)	S_m/D_{50}	R_t/D_{50}	τ_p (kPa)	d_p (mm)	τ_{cv} (kPa)	d_{cv} (mm)
Lancaster Composite	57.8	22.5	7.49	93.5	24	41.59	0.52	10.3	2.48	10	10.7
FRP shell (CP40)	58.7	50	7.49	93.5	24	41.59	0.52	27.5	8.81	27.2	10
	63.2	100	7.49	93.5	24	41.59	0.52	52.3	2.11	50.2	10
	64.9	200	7.49	93.5	24	41.59	0.52	102.4	2.51	96.2	11
Hardcore Composite	56.1	22.5	5.08	177.5	17.7	28.22	0.99	14.5	0.31	14.0	10.4
FRP shell (24-4)	64.4	50	5.08	177.5	17.7	28.22	0.99	28.6	12.3	28.1	10
	60.9	100	5.08	177.5	17.7	28.22	0.99	56.5	9.26	55.8	10.3
	67.9	200	5.08	177.5	17.7	28.22	0.99	113.2	12.36	112.3	13
Hardcore FRP plate; untreated surface	65.4	26.15	1.55	133.8	35.7	8.61	0.74	16.44	0.98	14.24	6.4
	59.1	50.06	1.55	133.8	35.7	8.61	0.74	33.55	1.15	27.49	11.1
	64.7	107.17	1.55	133.8	35.7	8.61	0.74	66.38	1.71	59.20	2.6
	66.4	183.52	1.55	133.8	35.7	8.61	0.74	112.68	1.92	96.12	9.2
Hardcore FRP plate; treated surface	63	26.15	0.49	341.2	See note (1)	2.71	1.90	23.26	0.91	16.51	5.4
	65	50.08	0.49	341.2	See note (1)	2.71	1.90	39.00	1.61	30.17	9.5
	60.1	107.3	0.49	341.2	See note (1)	2.71	1.90	80.45	1.97	69.67	10.2
	62	152.2	0.49	341.2	See note (1)	2.71	1.90	115.75	2.26	97.29	9.8
PPI plastic	64.4	26.15	1.86	365.9	8.5	10.36	2.03	14.42	0.91	10.73	11.3
	58.1	50.06	1.86	365.9	8.5	10.36	2.03	28.63	0.80	23.41	9.7
	65.1	107.25	1.86	365.9	8.5	10.36	2.03	74.64	1.00	57.43	5.2
	66.4	152.2	1.86	365.9	8.5	10.36	2.03	105.69	1.47	81.98	8.2
	62.4	199.7	1.86	365.9	8.5	10.36	2.03	126.73	1.64	113.27	8.3
Prestressed concrete pile	58.9	23.7	1.94	335.3	63.7	10.79	1.86	19.8	1.00	11.9	11.8
	58.7	51.5	1.94	335.3	63.7	10.79	1.86	37.8	1.35	29.9	9.5
	61.9	101.9	1.94	335.3	63.7	10.79	1.86	72.5	1.12	55.5	9.5
	68.2	175.4	1.94	335.3	63.7	10.79	1.86	116.7	1.42	91.7	11.7
Steel from sheet pile	63.5	26.08	0.43	66.7	184.2	2.39	0.37	17.42	0.46	12.00	8.7
	62.5	51.27	0.43	66.7	184.2	2.39	0.37	31.84	0.79	27.57	3.6
	64.3	101.85	0.43	66.7	184.2	2.39	0.37	63.33	0.97	56.69	5.4
	67.0	202.33	0.43	66.7	184.2	2.39	0.37	121.47	1.39	109.85	4.5

Notes: (1) Not measurable because it is difficult to clearly measure the diamond indentation mark due to presence of the bonded sand particles.

D_{50} = 0.18 mm for Model sand, D_r = Relative density after sample consolidation (as per equation 5), σ'_n = Normal pressure, S_m = Average mean line spacing,

R_t = Maximum peak-to-valley height, Hardness (HV) = Average Vickers hardness number, τ_p = Peak interface shear stress, d_p = Horizontal displacement at peak,

τ_{cv} = Residual interface shear stress, d_{cv} = Horizontal displacement at residual.

1 mm = 0.039 inches; 1 μm = 0.000039 inch; 1 kPa = 0.145 poundforce per square inch.

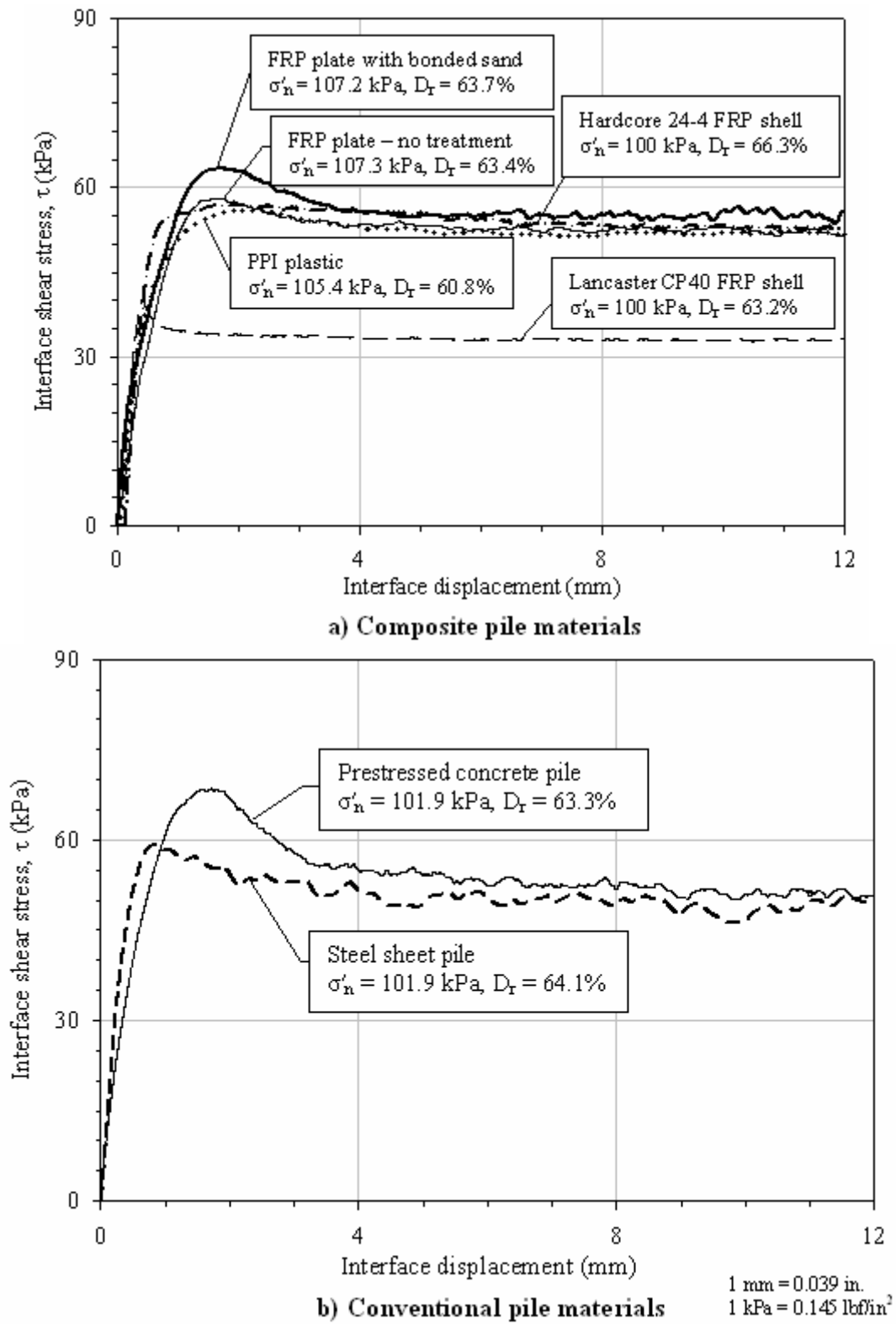
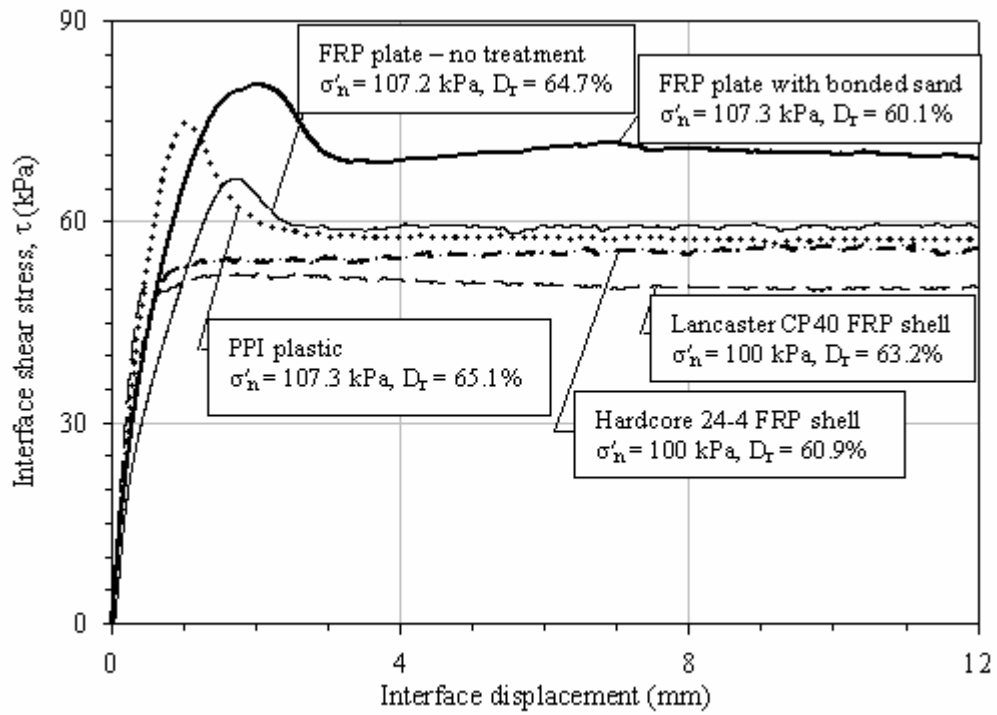
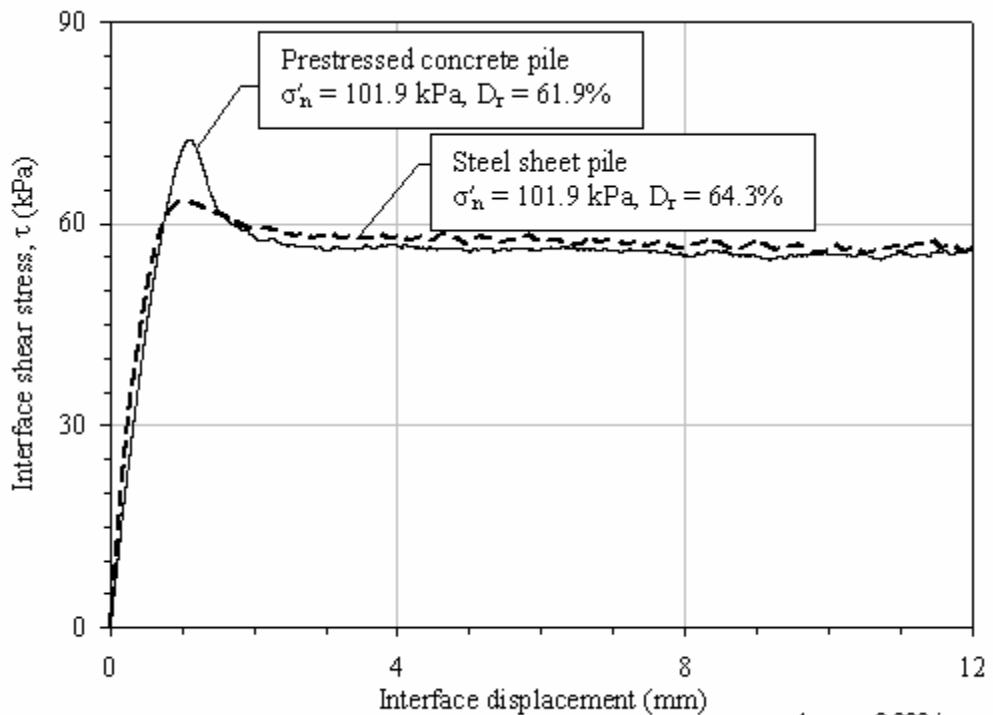


Figure 26. Graphs. Typical interface shear test results for Density sand ($\sigma'_n \approx 100$ kPa).



a) Composite pile materials



b) Conventional pile materials

1 mm = 0.039 in.
1 kPa = 0.145 lbf/in²

Figure 27. Graphs. Typical interface shear test results for Model sand ($\sigma'_n \approx 100$ kPa).

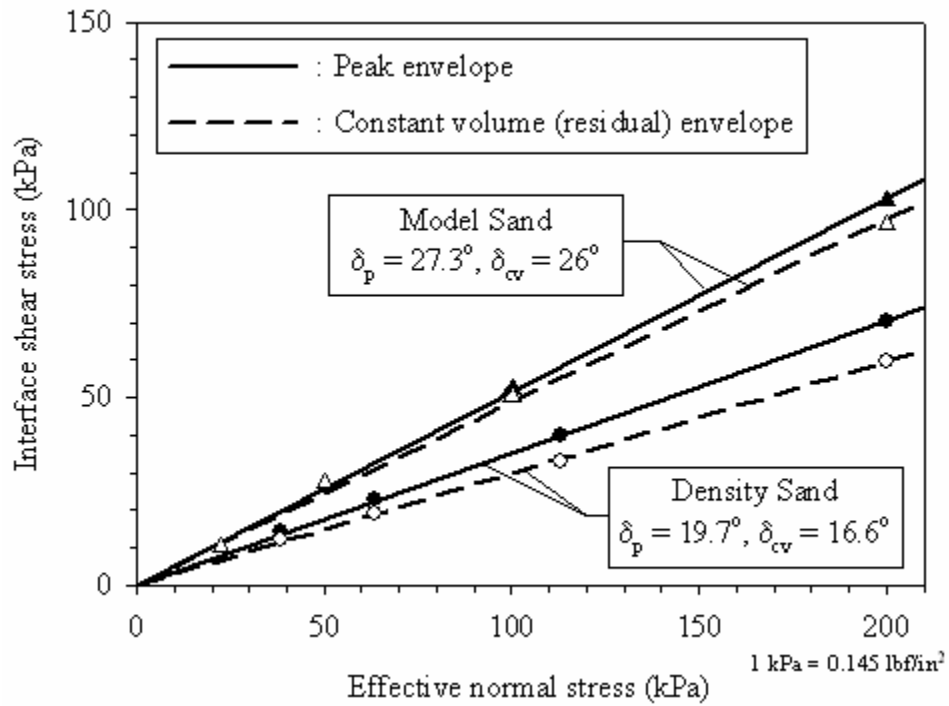


Figure 28. Graph. Interface shear strength envelopes for Lancaster Composite FRP shell.

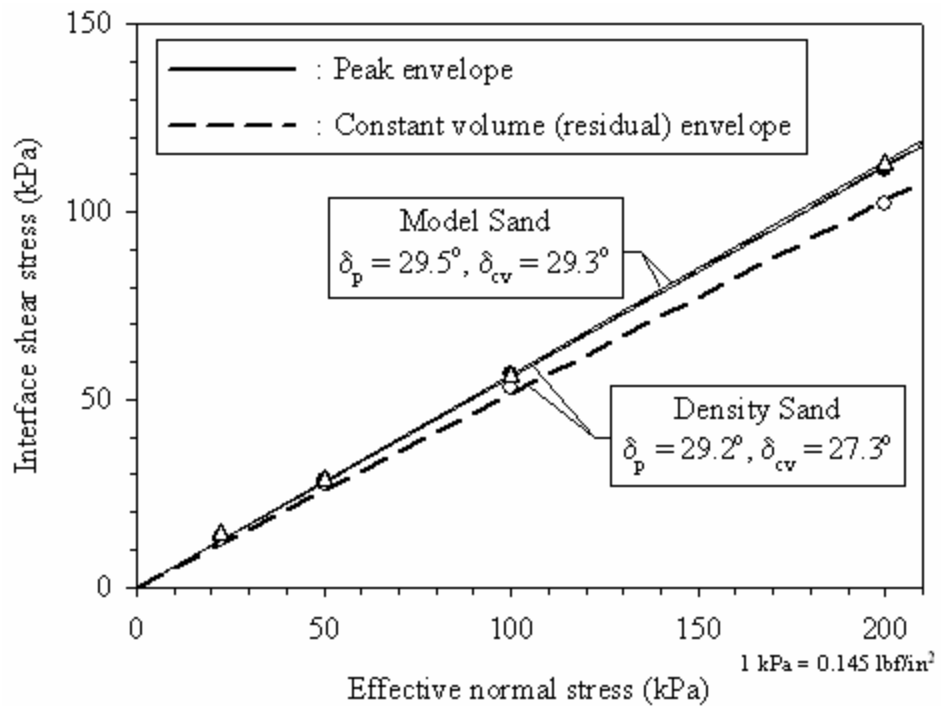


Figure 29. Graph. Interface shear strength envelopes for Hardcore Composites FRP shell.

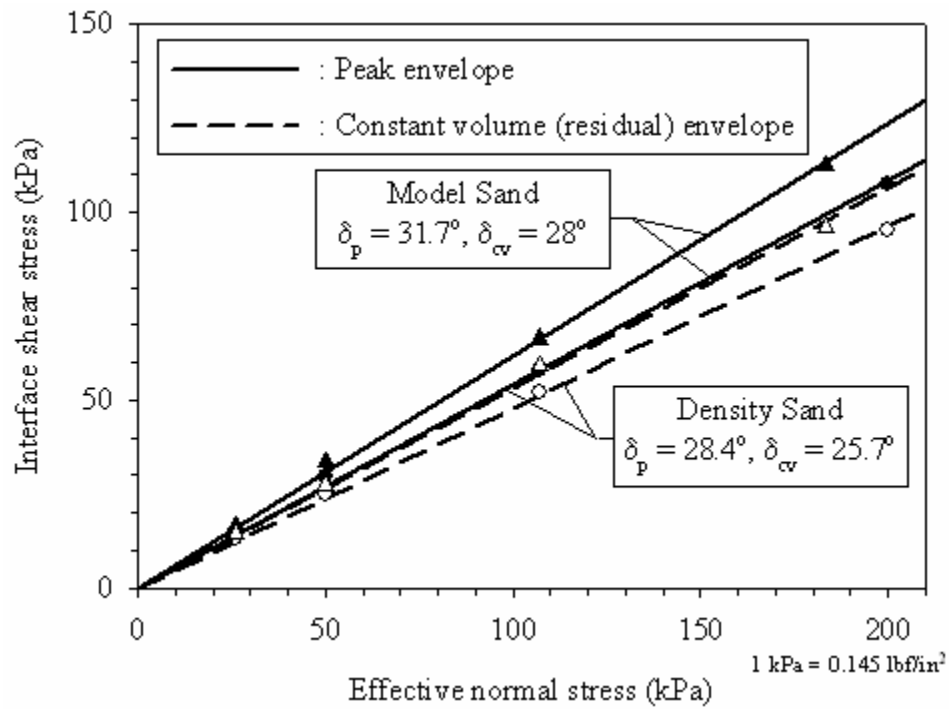


Figure 30. Graph. Interface shear strength envelopes for untreated Hardcore FRP plate.

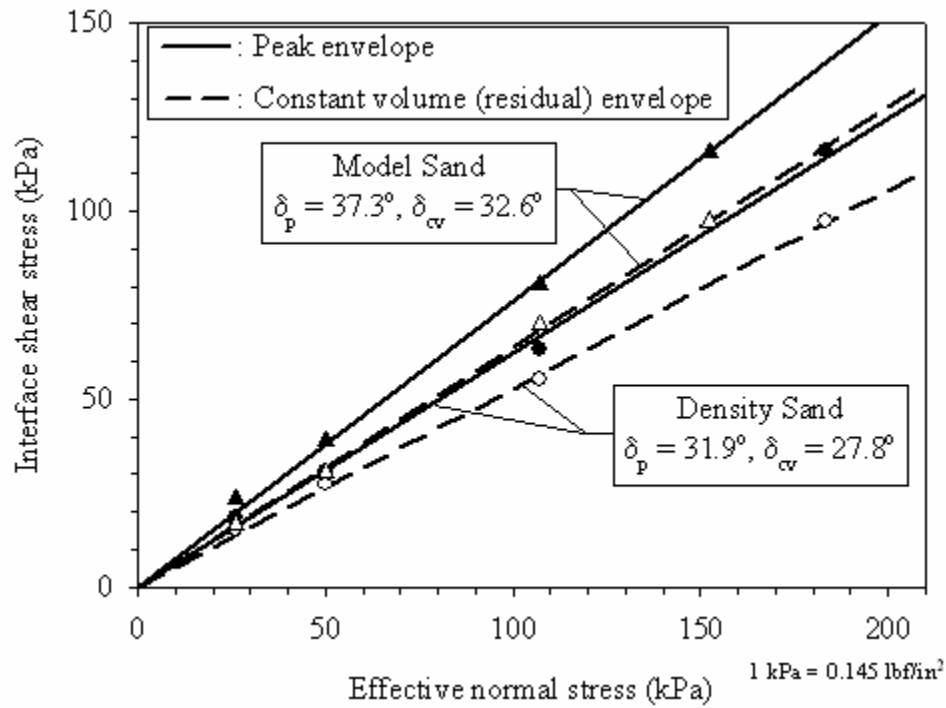


Figure 31. Graph. Interface shear strength envelopes for treated Hardcore FRP plate.

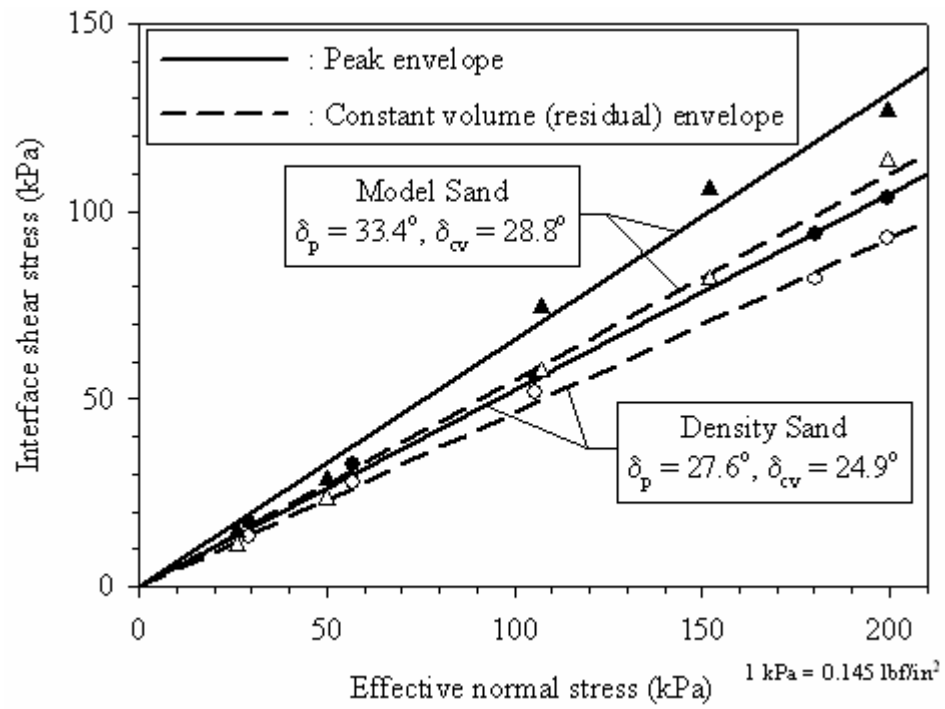


Figure 32. Graph. Interface shear strength envelopes for PPI plastic.

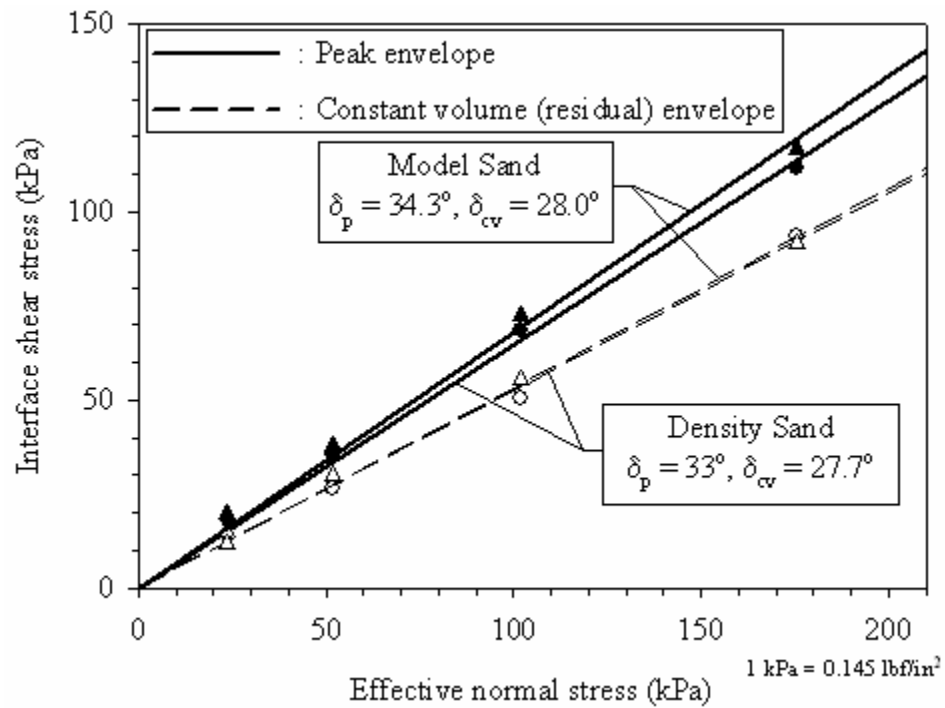


Figure 33. Graph. Interface shear strength envelopes for concrete.

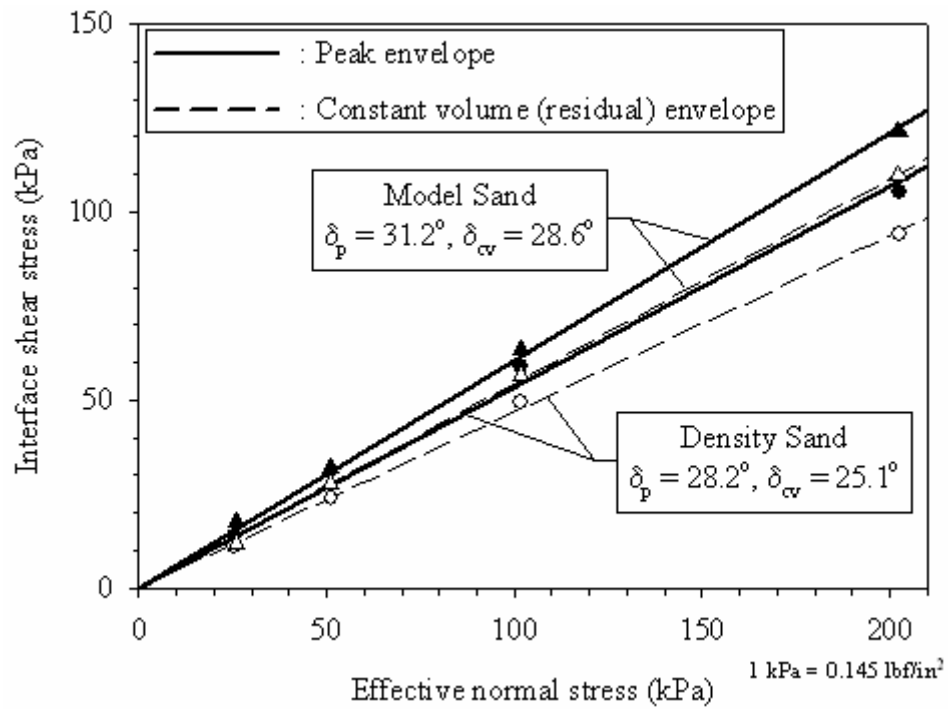


Figure 34. Graph. Interface shear strength envelopes for steel.

Table 12. Summary of interface friction angles.

Soil	Pile	Soil properties		Surface Hardness (HV)	Relative Roughness		Interface Angles	
		Average D_r (%)	D_{50} (mm)		R_t/D_{50}	S_m/D_{50}	δ_p ($^\circ$)	δ_{cv} ($^\circ$)
Density Sand	LC FRP	62.5	0.50	24.0	0.19	14.97	19.7	16.6
	HC FRP	65.5		17.7	0.36	10.16	29.2	27.3
	Untreated FRP plate	63.9		35.7	0.27	3.10	28.4	25.7
	Treated FRP plate	64.0		N/T	0.68	0.98	31.9	27.8
	PPI plastic	62.2		8.5	0.73	3.73	27.6	24.9
	Concrete	63.1		63.7	0.67	3.88	33.0	27.7
	Steel	65.6		184.2	0.13	0.86	28.2	25.1
Model Sand	LC FRP	61.2	0.18	24.0	0.52	41.59	27.3	26.0
	HC FRP	62.3		17.7	0.99	28.22	29.5	29.3
	Untreated FRP plate	63.9		35.7	0.74	8.61	31.7	28.0
	Treated FRP plate	62.5		N/T	1.90	2.71	37.3	32.6
	PPI plastic	63.3		8.5	2.03	10.36	33.4	28.8
	Concrete	61.9		63.7	1.86	10.79	34.3	28.0
	Steel	64.3		184.2	0.37	2.39	31.2	28.6

Note: N/T = not testable.

1 mm = 0.039 inch

3.5 DISCUSSION OF RESULTS

It has been demonstrated previously that the strength and volume change behaviors of an interface system composed of a granular soil and a construction material are largely controlled by three factors: the relative size of the sand grains with respect to the surface asperity height and spacing, the hardness of the materials, and the soil grain shape (Kishida and Uesugi 1987, O'Rourke, et al., 1990, Irsyam and Hryciw 1991, Hryciw and Irsyam 1993, Dove and Harpring 1999, Dove and Frost 1999, Frost and Han 1999, and Dove and Jarrett 2002). The interface shear test program conducted in this study was not designed to systematically investigate the different factors that influence the interface shear behavior of sands and FRP materials. Nevertheless, the interface friction angle values obtained in this study (shown in table 12), were obtained from interface shear tests having important differences in the following basic variables:

1. Mean grain size of sand, D_{50} .
2. Angularity of sand.
3. Maximum peak-to-valley height of pile surface, R_t .
4. Average mean line spacing of pile surface, S_m .
5. Pile surface Vickers hardness, HV.

The first two variables are related to soil characteristics, and the remaining three are related to pile surface characteristics. All of these variables, except angularity, were measured quantitatively. Therefore, the influence of the quantitative variables on the interface friction coefficients (peak and residual $\tan \delta$) can be investigated by performing multiple linear regressions. Linear regression analyses for both sand types and for peak and residual interface friction coefficients are presented in the following subsections. The regressions were carried out with the interface friction coefficient as the dependent variable, and R_t/D_{50} , S_m/D_{50} , and HV as independent variables. Due to small sample size ($N = 7$), statistically significant results (at the 5 percent level) were not expected.

The linear regression analysis results for both sand types and for peak and residual interface friction coefficients are presented in sections 3.5.1 through 3.5.4. The general discussion of the regression results is provided in section 3.5.5.

3.5.1 Multiple Linear Regression for Density Sand $\tan \delta_{\text{peak}}$ Values

Results of the regression analysis for the $\tan \delta_{\text{peak}}$ values from tests using the Density sand are summarized in table 13.

Table 13. Multiple linear regression results for $\tan \delta_{\text{peak}}$ of Density sand.

Regression Equation	$\tan \delta_{\text{peak}} = 0.504 + 0.174 \cdot \left(\frac{R_t}{D_{50}}\right) - 8.93 \cdot 10^{-3} \cdot \left(\frac{S_m}{D_{50}}\right) + 1.919 \cdot 10^{-4} \cdot (\text{HV})$
R^2 (N=7)	0.662
R^2 change due to R_t/D_{50}	0.355
R^2 change due to S_m/D_{50}	0.302
R^2 change due to HV	0.005

The coefficient of determination (R^2) for this fit was 0.66, shown graphically in figure 35. The contributions of R_t/D_{50} , S_m/D_{50} , and HV to R^2 were 53.6 percent, 45.6 percent, and 0.8 percent, respectively. This indicates that hardness (HV) is the least significant predictor of the $\tan \delta_{\text{peak}}$ values compared to R_t/D_{50} and S_m/D_{50} .

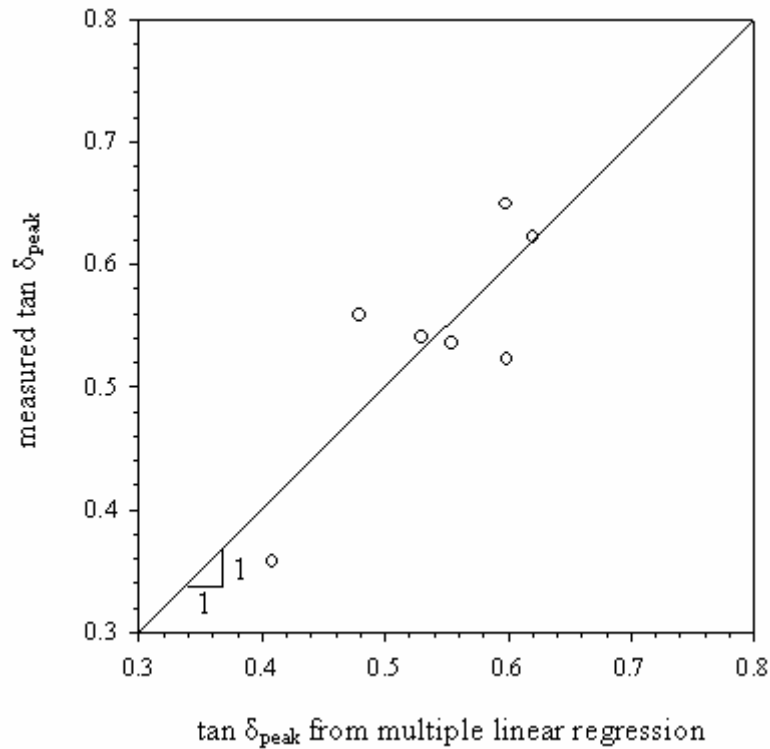


Figure 35. Graph. Multiple linear regression on Density sand $\tan \delta_{\text{peak}}$ values.

3.5.2 Multiple Linear Regression for Density Sand $\tan \delta_{cv}$ Values

Results of the regression analysis for the $\tan \delta_{cv}$ values from tests using the Density sand are summarized in table 14.

Table 14. Multiple linear regression results for $\tan \delta_{cv}$ of Density sand.

Regression Equation	$\tan \delta_{cv} = 0.502 + 6.839 \cdot 10^{-2} \cdot \left(\frac{R_t}{D_{50}}\right) - 1.03 \cdot 10^{-2} \cdot \left(\frac{S_m}{D_{50}}\right) - 1.48 \cdot 10^{-4} \cdot (HV)$
R^2 (N=7)	0.581
R^2 change due to R_t/D_{50}	0.264
R^2 change due to S_m/D_{50}	0.313
R^2 change due to HV	0.004

The coefficient of determination (R^2) for this fit was 0.58, and is shown graphically in figure 36. The contributions of R_t/D_{50} , S_m/D_{50} , and HV to R^2 were 45.4 percent, 53.9 percent, and 0.7 percent, respectively. As in the previous analyses, this indicates that the hardness (HV) has considerably less influence on the $\tan \delta_{cv}$ values than R_t/D_{50} and S_m/D_{50} .

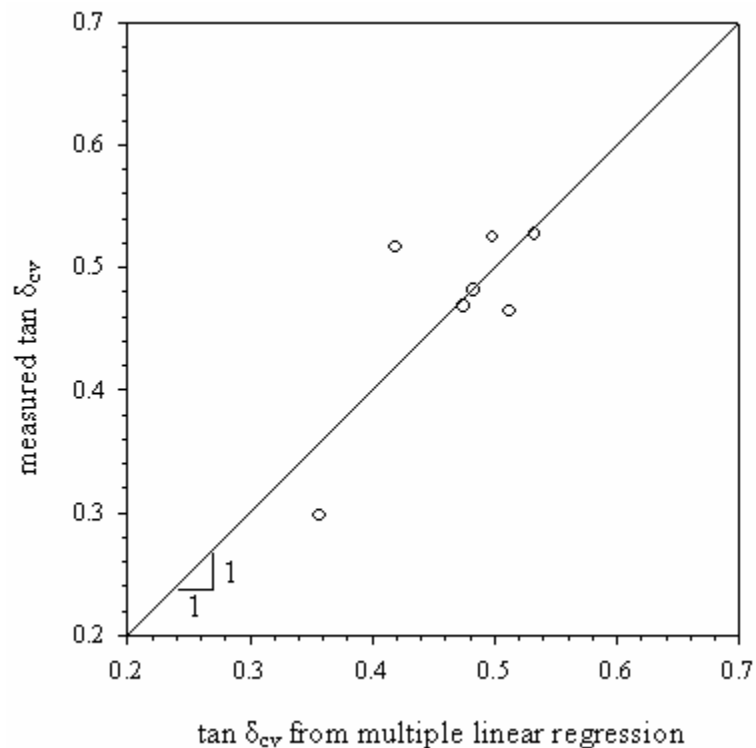


Figure 36. Graph. Multiple linear regression on Density sand $\tan \delta_{cv}$ values.

3.5.3 Multiple Linear Regression for Model Sand $\tan \delta_{\text{peak}}$ Values

Results of the regression analysis for the $\tan \delta_{\text{peak}}$ values from tests using the Model sand are summarized in table 15.

Table 15. Multiple linear regression results for $\tan \delta_{\text{peak}}$ of Model sand.

Regression equation:	$\tan \delta_{\text{peak}} = 0.608 + 6.160 \cdot 10^{-2} \cdot \left(\frac{R_t}{D_{50}}\right) - 3.31 \cdot 10^{-3} \cdot \left(\frac{S_m}{D_{50}}\right) - 5.81 \cdot 10^{-5} \cdot (\text{HV})$
R^2 (N=7)	0.892
R^2 change due to R_t/D_{50}	0.612
R^2 change due to S_m/D_{50}	0.279
R^2 change due to HV	0.001

The coefficient of determination (R^2) for this fit was 0.89, and is shown graphically in figure 37. The contributions of R_t/D_{50} , S_m/D_{50} , and HV to R^2 were 68.6 percent, 31.3 percent, and 0.1 percent, respectively. As in the previous analysis, this indicates that hardness (HV) has considerably less influence on the $\tan \delta_{\text{peak}}$ values than R_t/D_{50} and S_m/D_{50} .

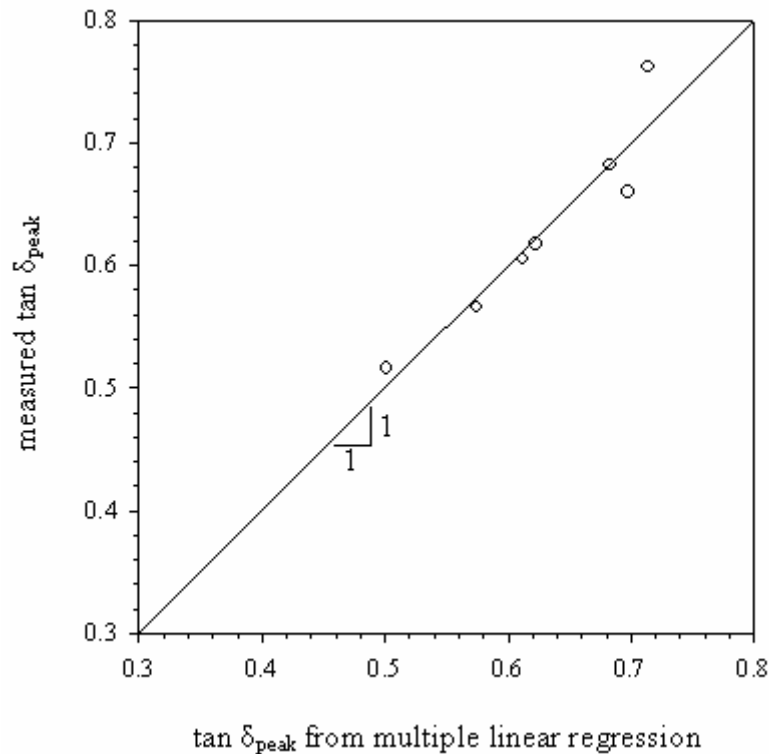


Figure 37. Graph. Multiple linear regression on Model sand $\tan \delta_{\text{peak}}$ values.

3.5.4 Multiple Linear Regression for Model Sand $\tan \delta_{cv}$ Values

Results of the regression analysis for the $\tan \delta_{cv}$ values from tests using the Model sand are summarized in table 16.

Table 16. Multiple linear regression results for $\tan \delta_{cv}$ of Model sand.

Regression equation	$\tan \delta_{cv} = 0.574 + 1.236 \cdot 10^{-2} \cdot \left(\frac{R_t}{D_{50}}\right) - 1.97 \cdot 10^{-3} \cdot \left(\frac{S_m}{D_{50}}\right) + 1.79 \cdot 10^{-4} \cdot (HV)$
R^2 (N=7)	0.474
R^2 change due to R_t/D_{50}	0.275
R^2 change due to S_m/D_{50}	0.179
R^2 change due to HV	0.020

The coefficient of determination (R^2) for this fit was 0.47, and is shown graphically in figure 38. The contributions of R_t/D_{50} , S_m/D_{50} , and HV to R^2 were 58 percent, 37.8 percent, and 4.2 percent, respectively. As in the previous analysis, this indicates that hardness (HV) has considerably less influence on the $\tan \delta_{cv}$ values than R_t/D_{50} and S_m/D_{50} .

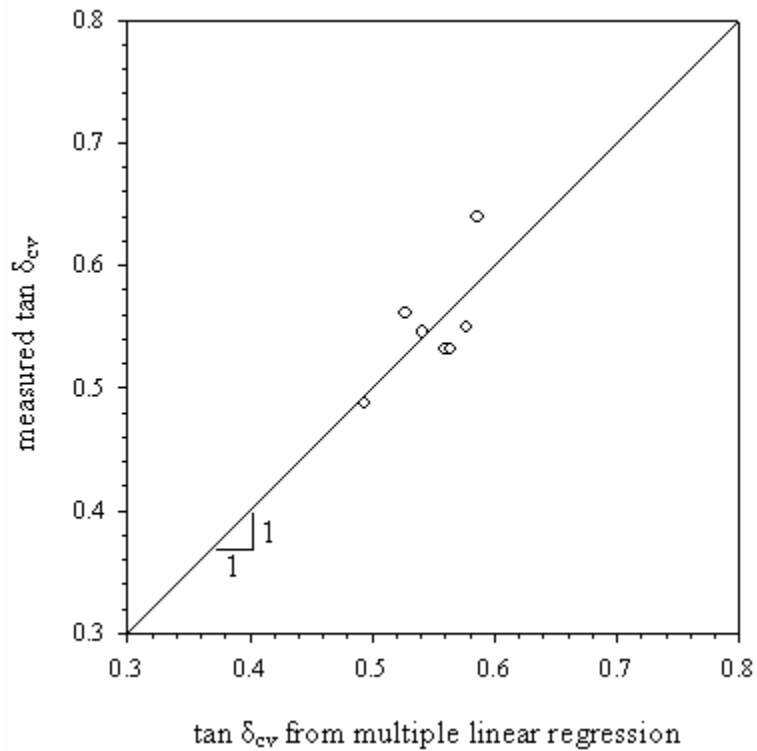


Figure 38. Graph. Multiple linear regression on Model sand $\tan \delta_{cv}$ values.

3.5.5 Observations from the Linear Regression Analyses Results

Based on the four linear regression analyses presented above, the following observations and comments are made.

1. The limited size of the samples used for the regression analyses diminishes the statistical significance of the results of the regression analyses.
2. All four regression equations showed a positive coefficient for the R_t/D_{50} term. This indicates a general trend that the interface friction coefficients (peak and residual) increase with increasing relative asperity height, R_t/D_{50} . This finding concurs with the observations noted by Uesugi (1987) and Frost and Han (1999).
3. All four regression equations showed a negative coefficient for the relative spacing term (S_m/D_{50}), indicating that the interface friction coefficients (peak and residual) decrease with increasing relative spacing, S_m/D_{50} , which is reasonable over the range of S_m/D_{50} values tested.
4. The four regression equations showed both positive and negative coefficients for the Vickers hardness (HV) term. This finding, and the low contribution of this variable to the overall R^2 coefficient of the fit, indicate that hardness (HV) is not a significant predictor of the interface friction coefficients values.
5. The regressions show only moderate fit strengths, with coefficients of determination (R^2) ranging from 0.47 to 0.89. This indicates that other factors besides R_t/D_{50} , S_m/D_{50} , and HV also have important influences on the values of the interface friction coefficient.
6. Although soil angularity could not be included in the regression analyses, it can be seen that inclusion of an angularity variable alone will not be enough to improve the strength of the fits. This can be seen in figure 34, where the goodness of the fit is poor despite the fact that all points correspond to the same sand with the same angularity. Adding an angularity term to the regression equation would not increase the strength of this fit. This indicates that factors other than soil angularity influence the values of the interface friction coefficient.

3.5.6 Influence of Angularity of Sand

The regression analyses presented in the preceding sections did not include the influence of soil angularity. As explained earlier, this was because the angularity of the sands used in this study was only described qualitatively. The sand angularity for the Density sand was described as subrounded to rounded, and for the Model sand as subangular to angular. In general, angular sands have values of higher interface friction angle than rounded sands (Han and Frost 1999). This is consistent with results for the Model and Density sands, as listed in table 12. Due to the higher contact stresses at sharp grain edges, angular soil grains are able to penetrate into the surfaces of some of the pile

materials. For this reason, and because angular particles may interlock better with the pile surface roughness, interface friction angles tend to be larger for angular soil grains than for rounded grains.

3.6 SUMMARY

The following laboratory activities were performed for this investigation:

1. Selection of sand specimens for interface testing.
2. Soil characterization tests to determine grain size distribution, minimum/maximum density, and specific gravity testing.
3. Direct shear tests on Density and Model sands to determine internal friction angles.
4. Selection of pile surface specimens for interface testing.
5. Surface topography characterization and surface hardness determination of seven pile surfaces. The seven pile surfaces included four FRP composites (commercially available from two FRP composite pile manufacturers), one recycled plastic pile, and two conventional pile materials (a prestressed concrete pile and a steel sheet pile).
6. Design and construction of a modified top half shear box to permit testing of curved pile surfaces obtained from the FRP composite tubes.
7. Interface shear tests for the seven piles and two sand types to determine the interface behavior and interface friction angles of these interfaces.

Interface shear tests were performed on 14 types of soil-pile interfaces. Tests were carried out for two types of sands: Density sand ($D_{50} = 0.5$ mm (0.019 inch), subrounded to rounded particle shape) and Model sand ($D_{50} = 0.18$ mm (0.007 inch), subangular to angular particle shape). Seven pile surfaces were tested: Lancaster FRP composite (curved), Hardcore FRP composite (curved), Hardcore FRP composite plate (flat), Hardcore FRP composite plate with bonded sand treatment (flat), PPI recycled plastic coupon (flat), prestressed concrete pile coupon (flat), and a steel sheet pile coupon (flat). The results of these tests are summarized in appendix A.

The peak and residual interface friction angles for the 14 sand-to-pile interfaces tested are summarized in tables 10 through 12. The following points and observations can be made regarding the experimental data.

1. The interface friction angle values obtained for the Density sand tested against the Lancaster FRP composite pile were much lower than the values obtained for the other pile surfaces. The peak and residual interface friction angles obtained for the Lancaster FRP composite pile were 19.7° and 16.6° , respectively. In contrast, the interface friction angle values obtained for the Density sand tested against the other

pile surface types ranged from 27.6° to 33°, and from 24.9° to 27.8°, for the peak and residual conditions, respectively.

2. The Lancaster FRP composite pile was measured to have the largest average mean line spacing (S_m) and the second lowest maximum peak to valley height (R_t) as reported in table 8. These values make this pile surface the smoothest of all seven surfaces tested.
3. In general, the subangular to angular Model sand gives slightly higher interface friction angles than the subrounded to rounded Density sand. However, for the Lancaster FRP composite pile, the interface friction angles obtained with the Model sand are much higher than the Density sand values.
4. In general, the interface friction angles, both peak and residual, were found to increase with increasing relative asperity height, R_t/D_{50} .
5. In general, the interface friction angles, both peak and residual, were found to increase with decreasing relative spacing, S_m/D_{50} , which is reasonable over the range of S_m/D_{50} tested.
6. Linear regression analyses between the interface friction coefficients and the variables R_t/D_{50} , S_m/D_{50} , and HV showed moderate fit strengths. The regression analyses suggest other factors besides R_t/D_{50} , S_m/D_{50} , and HV also have important influences on the values of interface friction coefficient.
7. The bonded sand surface treatment used for the Hardcore FRP plate was successful in increasing the interface friction angle values.

CHAPTER 4. EXPERIMENTAL DURABILITY STUDY OF FRP COMPOSITE PILES

4.1 INTRODUCTION

The lack of long-term performance and durability data of composite piles is an important concern that must be addressed to permit confidence in the use of these piles for long-term load-bearing applications. Consequently, a durability study was undertaken to assess the rate degradation of mechanical properties (strength and stiffness) of commercially available glass FRP (GFRP) tubes used to fabricate concrete-filled FRP composite piles. The study focused on the degradation effects of moisture absorption and exposure to freeze-thaw cycles.

The durability study was carried out on four FRP tubes supplied by two manufacturers of FRP composite piles. The laboratory degradation study included FRP shell characterization, determination of baseline mechanical properties, measurement of moisture absorption as a function of time, measurement of mechanical properties as a function of moisture absorption, and mechanical properties as a function of exposure to freeze-thaw cycles. The methodology and results of this durability study are presented in this chapter. The durability study did not include the steel-reinforced plastic pile because this pile type was initially not included in the scope of this project, and was only included for field testing after the late withdrawal of one of the FRP composite pile manufacturers.

4.2 BACKGROUND ON DEGRADATION OF GLASS FRP COMPOSITES

Some of the factors that contribute to the degradation of the GFRP composites over time include temperature, sunshine (UV rays), moisture absorption, freeze-thaw cycles, and load (Garcia, et al., 1998, Nishizaki and Meiarashi 2002). Among these factors, the influence of moisture absorption and exposure to freeze-thaw cycles are considered to be the most critical factors. Exposure to alkaline environments and UV radiation also affect long-term durability, but to a lesser extent. Furthermore, UV degradation resistance of most composites is being improved by applying protective coats and additives during the manufacturing process. The degradation mechanisms related to moisture absorption and freeze-thaw cycles are discussed below.

Degradation due to moisture absorption may significantly reduce the life of FRP composites. The influence that moisture absorption has on the mechanical properties of GFRP composites is well documented (e.g., Shen and Springer 1976, Garcia, et al., 1998, Prian and Barkatt 1999, Verghese, et al., 1999, Shao and Kouadio 2002, Phifer 2003). Absorbed moisture can cause pronounced changes in modulus, strength, and strain to failure (Springer, et al., 1980). Moisture content of submerged FRP composites increases through diffusion. The absorbed moisture can act as a plasticizer of the composite resin, and can cause matrix cracking, fiber-matrix debonding, and corrosion of glass fibers (stress corrosion) (Garcia, et al., 1998). These effects result in a reduction of strength and stiffness of the FRP composite. For example, Phifer (2003) recorded tensile strength and

stiffness reductions on the order of 60 percent and 10 percent, respectively, for E-glass/vinyl ester composites submerged in fresh water for a period of about 2 years. The author projected FRP tensile strength loss of about 80 percent after 50 years' submergence. The implications of such strength reductions on the design of composite piles can be significant.

In addition to submergence time, temperature and stress level also influence the amount of moisture that FRP will absorb while submerged. The moisture absorption increases with increasing water temperature and stress level. Evidence of the existence of damage to FRP composites after submergence in water has been found in SEM images (e.g., figure 9), where fiber damage and crack formation at the fiber-matrix interface were observed (McBagonluri, et al., 2000).

Freeze-thaw cycles can also degrade FRP composite properties. The degradation due to freeze-thaw cycling is primarily related to microcracking caused by the volume increase of the absorbed water in the composite (Verghese, et al., 1999). The mechanical properties of the composite are also affected by cold temperatures and by the cycling process (Karbhari 2002).

The FRP shell will potentially be exposed to chemical agents as a result of the alkaline pore water from the concrete inside the FRP shell. Karbahari, et al. (2002), studied the effect of concrete-based alkali solutions on the durability of vinylester GFRP composites. The authors found evidence of significant degradation and strength loss due not only to moisture absorption but also to the exposure to the high pH levels and characteristic solution chemistry of concrete pore fluid. The experimental durability program carried out for this study did not include investigation of possible degradation effects due to exposure to concrete pore fluid solutions.

A concrete-filled FRP composite pile installed in tidal and marine environments would be exposed to salt water. However, McBagonluri, et al. (2000), found that the rate of strength loss was not significantly affected by salt content, but rather by absorption of moisture. Therefore, the durability experiments carried out for this study were performed using fresh water.

4.3 LABORATORY STUDY OF DURABILITY

The general approach used in this study was to track moisture diffusion into the material and to evaluate the degradation of the mechanical properties of the different FRP shells as a function of submergence time and moisture absorption. The loss of material strength and stiffness is then related to the long-term structural capacity of the pile using conventional structural models for FRP composite piles available in the literature (e.g. Fam and Rizkalla 2000, Mirmiran 1999), as summarized in chapter 2. The study described herein does not include effects of creep or chemical attack as a result of the presence of the concrete infill in the composite pile. Changes in the concrete properties with time (e.g., possible increases or decreases in strength and/or stiffness) were not included in this study.

4.3.1 Description of Test Specimens

Commercially available FRP tubes from two manufacturers that specialize in concrete-filled FRP composite piles were used for the durability experimental program. Tubes with 0.305-m (12-inch) and 0.610-m (24-inch) nominal diameter were tested. The results presented here are based on tests carried out on their standard FRP tube designs. It should be noted, however, that both pile manufacturers have the flexibility to modify the FRP composite shell laminate architecture (including number of layers, fiber orientation, and resin and fiber types) to better suit the load demands of a specific project.

The following subsections provide detailed descriptions of the tubes from each manufacturer, including dimensions, material, number of layers, laminate structure, fiber volume fraction, and manufacturing technique.

4.3.1.1 Specimens from Lancaster Composites, Inc.

The two sizes of tubes supplied by Lancaster Composites, Inc. were fabricated by Ameron International Corporation. The FRP tubes were manufactured using the filament-winding technique, in which E-Glass continuous fiber rovings are impregnated with resin (epoxy or polyester) and wound over a rotating steel mandrel, following a predetermined winding pattern.

Characterization of the FRP tubes was based on visual inspection, information supplied by the manufacturers, and burnoff tests on coupon samples. The burnoff tests were performed in general accordance with ASTM Standard D2584. The burnoff test results and other characterization information are provided in tables 17 and 18 for the 12- and 24-inch (0.31- and 0.61-m) diameter tubes, respectively.

Table 17. Characterization data for Lancaster Composite 12-inch FRP tube.

Manufacturer pile designation	CP40 12-inch
Nominal diameter	305 mm (12 in)
Measured outside diameter	324.7 ± 1.9 mm ⁽¹⁾
Total wall thickness	6.05 ± 0.14 mm ⁽¹⁾
Liner thickness	0.59 ± 0.05 mm ⁽¹⁾
Liner material	Epoxy resin sandwiched between industrial paper
Unit weight of tube	17.45 kN/m ³
Fiber type	Owen Corning Type 30 113 Yield E-glass
Matrix resin type	Epoxy anhydrite hardener/Dow Der 331 (83/100 ratio)
Fiber layup angles	[-88°/+8° /-88° /+8° /-88°/+8° /-88°/+8° /-88]T ⁽²⁾
Fiber layer average thicknesses	[0.54/0.69/0.54/0.69/0.54/0.69/0.54/0.69/0.54] (mm)
Total resin fraction by weight	38.6%
Total fiber fraction by volume	45.8 ± 1.0% ^{(1), (3)}
Fiber volume fraction 88° layers	38.4 ± 1.0% ⁽¹⁾
Fiber volume fraction 8° layers	55.8 ± 0.3% ⁽¹⁾
Percentage of fiber at 88°	40.1 ± 0.6% ⁽¹⁾ (by weight)
Percentage of fiber at 8°	59.9 ± 0.6% ⁽¹⁾ (by weight)

Notes: (1) Mean ± standard deviation. 1 mm = 0.039 inch
(2) Angles are measured with respect to pile longitudinal axis. Subscript T indicates orientation for the layers of the total laminate are presented within the brackets.
(3) Based on volume of FRP laminate only; liner is excluded from volume.

Table 18. Characterization data for Lancaster Composite 24-inch FRP tube.

Manufacturer pile designation	CP40 24-inch
Nominal diameter	610 mm (24 in)
Measured outside diameter	625 ± 1.8 mm ⁽¹⁾
Total wall thickness	7.35 ± 0.23 mm ⁽¹⁾
Liner thickness	1.68 ± 0.09 mm ⁽¹⁾
Liner material	C-veil, a chopped fiber mat and resin
Unit weight of tube	17.36 kN/m ³
Fiber type	Owen Corning Type 30 113 Yield E-glass
Matrix resin type	Ashland Chemical Apropol 7241 isophthalic acid polyester resin
Fiber layup angles	[+35°/-35° /+85° /+35° /-35°]T ⁽²⁾
Fiber layer average thicknesses	[1.13/1.13/1.13/1.13/1.13] (mm)
Total resin fraction by weight	39.3%
Total fiber fraction by volume	51.2 ± 2.4% ^{(1), (3)}
Fiber volume fraction ± 35° layers	52.7 ± 2.9% ⁽¹⁾
Fiber volume fraction 85° layers	45.5 ± 1.0% ⁽¹⁾

Notes: (1) Mean ± standard deviation. 1 mm = 0.039 inch
(2) Angles are measured with respect to pile longitudinal axis. Subscript T indicates orientation for the layers of the total laminate are presented within the brackets.
(3) Based on volume of FRP laminate only; liner is excluded from volume.

The 0.305-m (12-inch) nominal diameter tube has an outer diameter of 325 mm (12.8 inches) and an average total wall thickness of 6.05 mm (0.238 inches). The tube has a 0.59-mm (0.023-inch) thick liner at the inner surface, which results in a net structural wall thickness of 5.46 mm (0.215 inches). The wall structure of the tube consists of nine layers of fibers oriented at -88 degrees and +8 degrees with respect to the longitudinal axis of the tube. The stacking sequence of the layers is $[-88^{\circ}/+8^{\circ} / -88^{\circ} / +8^{\circ} / -88^{\circ}/+8^{\circ} / -88^{\circ}/+8^{\circ} / -88^{\circ}]_T$ (subscript T indicates the stacking sequence for the total FRP laminate is presented within the brackets). The layers with fibers oriented at -88 degrees with respect to the longitudinal axis are 0.54-mm (0.021-inch) thick, and the layers with fibers oriented at +8 degrees with the respect to the longitudinal axis are 0.69 mm (0.027 inches). The FRP tube liner is composed of overlapped industrial paper impregnated with epoxy resin, and is about 0.59 mm (0.023 inches) thick. The average overall fiber volume fraction of this tube is 45.8 percent. The matrix resin for this FRP tube consisted of Dow D.E.R. 331 epoxy mixed with anhydrite hardener. The fiber type was Owens Corning Type 30 113 Yield E-Glass rovings.

The 0.610-m (24-inch) nominal diameter tube has an outer diameter of 625 mm (24.6 inches) and an average total wall thickness of 7.35 mm (0.289 inches). The tube has a 1.68-mm (0.066-inch) thick liner at the inner surface, which results in a net structural wall thickness of 5.67 mm (0.223 inches). The wall structure of the tube consists of five layers of fibers oriented at $[+35^{\circ}/-35^{\circ}/+85^{\circ}/+35^{\circ}/-35^{\circ}]_T$, measured with respect to the longitudinal axis of the tube. The fiber layers are about 1.13 mm (0.044 inches) thick. The FRP tube liner is composed of C-veil and a mat of chopped fiber impregnated with resin, and is about 1.68 mm (0.066 inches) thick. The average overall fiber volume fraction of this tube is 51.2 percent. The matrix resin for the 0.610-m (24-inch) FRP shell was isophthalic acid polyester resin (Ashland Chemical Apropol 7241). The fiber type was Owens Corning Type 30 113 Yield E-Glass rovings.

4.3.1.2 Specimens from Hardcore Composites

Two FRP tube sizes were supplied by Hardcore Composites. The tubes had 12-inch and 24-inch (0.31-m and 0.61-m) nominal diameters and were fabricated at its manufacturing plant in New Castle, DE. Both FRP tubes sizes were fabricated using a vacuum assisted resin transfer molding (VARTM) process. The matrix resin used in the tubes is Dow vinyl ester Derakane resin, and the fiber reinforcing consists of plies of stitch-bonded multiaxis glass fiber fabric. Each ply includes four layers of fibers oriented at 0, +45, -45, and 90 degrees with respect to the longitudinal axis of the tube.

Characterization of the FRP tubes was based on visual inspection, information supplied from the manufacturer, and burnoff tests performed on coupon samples. The burnoff tests were carried out in general accordance with ASTM Standard D2584. Characterization information, including burnoff test results, are provided in tables 19 and 20 for the 12- and 24-inch (0.31- and 0.61-m) diameter tubes, respectively.

Table 19. Characterization data for Hardcore Composites 12-inch FRP tube.

Manufacturer pile designation	12-3
Nominal diameter	305 mm (12 in)
Measured outside diameter	321.7 ± 3.8 mm ⁽¹⁾
Total wall thickness	5.66 ± 0.28 mm ⁽¹⁾
Liner thickness	0.68 ± 0.11 mm ⁽¹⁾
Liner material	Screen
Unit weight of tube	18.6 kN/m ³
Fiber type	E-glass multiaxis fabric type Quad Q-9100. 4 stitched layers oriented at [0°/+45°/-45°/90°] ⁽²⁾
Matrix resin type	Dow vinyl ester Derakane resin
Number of multiaxis plies	3 x [0°/+45°/-45°/90°] ⁽²⁾
Multi-axis fiber layer thicknesses	1.66 ± 0.11 mm ⁽¹⁾
Total resin fraction by weight	28.2%
Total fiber fraction by volume	52.8 ± 0.1% ^{(1), (3)}
Fiber volume fraction 0° layers	60.6 ± 2.6% ⁽¹⁾
Fiber volume fraction ±45° layers	41.7 ± 6.7% ⁽¹⁾
Fiber volume fraction 90° layers	34.2 ± 8.3% ⁽¹⁾
Percentage of fiber at 0°	56.1 ± 1.4% ⁽¹⁾ (by weight)
Percentage of fiber at ±45°	37.1 ± 1.1 % ⁽¹⁾ (by weight)
Percentage of fiber at 90°	6.8 ± 0.3 % ⁽¹⁾ (by weight)

Notes: (1) Mean ± standard deviation. (2) Angles are measured with respect to pile longitudinal axis.
(3) Based on volume of FRP laminate only; liner is excluded from volume. 1 mm = 0.039 inch

Table 20. Characterization data for Hardcore Composites 24-inch FRP tube.

Manufacturer pile designation	24-4
Nominal diameter	610 mm (24 in) outside
Measured outside diameter	622 ± 1.6 mm ⁽¹⁾
Total wall thickness	8.86 ± 0.68 mm ⁽¹⁾
Liner thickness	0.68 ± 0.15 mm ⁽¹⁾
Liner material	Screen
Unit weight of tube	18.67 kN/m ³
Fiber type	E-glass multiaxis fabric type Quad Q-9100. 4 stitched layers oriented at [0°/+45°/-45°/90°] ⁽²⁾
Matrix resin type	Dow vinyl ester Derakane resin
Number of multi-axis plies	4 x [0°/+45°/-45°/90°] ⁽²⁾
Multiaxis fiber layer thicknesses	2.05 ± 0.14 mm ⁽¹⁾ (mm)
Total resin fraction by weight	28.6%
Total fiber fraction by volume	52.1 ± 0.5% ^{(1), (3)}
Fiber volume fraction 0° layers	61.2 ± 1.4% ⁽¹⁾
Fiber volume fraction ±45° layers	45.2 ± 0.6% ⁽¹⁾
Fiber volume fraction 90° layers	40.7 ± 1.1% ⁽¹⁾
Percentage of fiber at 0°	53.9 ± 0.7% ⁽¹⁾ (by weight)
Percentage of fiber at ±45°	38.9 ± 0.8% ⁽¹⁾ (by weight)
Percentage of fiber at 90°	7.3 ± 0.1% ⁽¹⁾ (by weight)

Notes: (1) Mean ± standard deviation. (2) Angles are measured with respect to pile longitudinal axis.
(3) Based on volume of FRP laminate only; liner is excluded from volume. 1 mm = 0.039 inch

The 305-mm (12-inch) nominal diameter tube has an outer diameter of 322 mm (12.7 inches) and a total wall thickness of 5.66 mm (0.223 inches). The tube has a 0.68-mm (0.027-inch) thick liner at the inner surface, which results in a net structural wall thickness of 4.98 mm (0.196 inches). The wall structure of the tube consists of three layers of multiaxis fabric. Each fabric layer consists of four layers of fibers oriented at $[0^\circ/90^\circ /+45^\circ/-45^\circ]$. The symbol typically used to designate this fiber lay-up is $[0^\circ/90^\circ /+45^\circ/-45^\circ]_{3T}$ (where the subscript 3T indicates the FRP laminate is composed of three plies each with four layers oriented at $0^\circ/90^\circ /+45^\circ/-45^\circ$). The average thickness of the multiaxis fabric layers is 1.66 mm (0.065 inches). The average thicknesses of the layers with fibers oriented at ± 45 , 0, and 90 degrees with respect to the longitudinal axis of the tube are 0.74 mm (0.029 inches), 0.76 mm (0.030 inches), and 0.16 mm (0.006 inches), respectively. The FRP tube liner is composed of a plastic screen material used to facilitate the injection of resin during the manufacturing process. The average overall fiber volume fraction of these tubes was measured to be 52.8 percent.

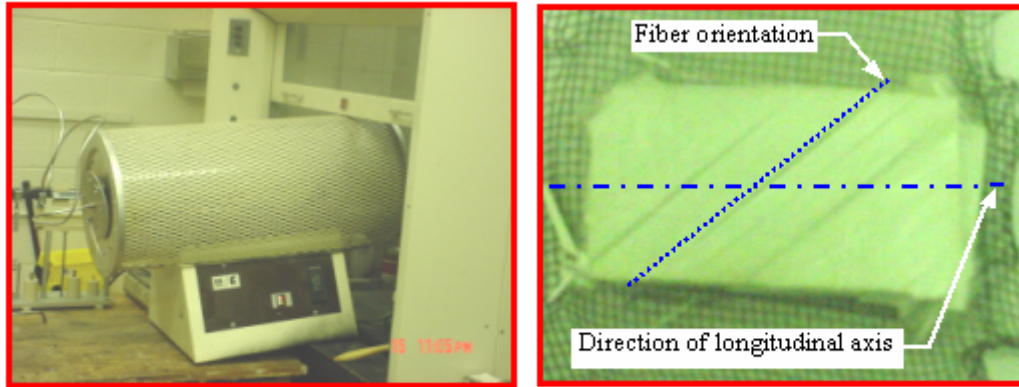
The 610-mm (24-inch) nominal diameter tube has an outer diameter of 622 mm (24.5 inches) and a total wall thickness of 8.86 mm (0.349 inches). The tube has a 0.68-mm (0.027-inch) thick liner at the inner surface, which results in a net structural wall thickness of 8.18 mm (0.322 inches). The wall structure of the tube consists of four layers of multiaxis fabric. Each fabric layer consists of four layers of fibers oriented at $[0^\circ/90^\circ /+45^\circ/-45^\circ]$. The symbol typically used to designate this type of fiber layup is $[0^\circ/90^\circ /+45^\circ/-45^\circ]_{4T}$ (where the subscript 4T indicates the FRP laminate is composed of four plies each with four layers oriented at $0^\circ/90^\circ /+45^\circ/-45^\circ$). The average thickness of the multiaxis fabric layers is 2.05 mm (0.081 inches). The average thicknesses of the layers with fibers oriented at ± 45 , 0, and 90 degrees with respect to the longitudinal axis of the tube are 0.92 mm (0.036 inches), 0.94 mm (0.037 inches), and 0.19 mm (0.007 inches), respectively. The average overall fiber volume fraction of these tubes was measured to be 52.1 percent.

4.3.2 Test Equipment and Procedures

The test procedures and apparatus used in this durability study are described in this subsection.

4.3.2.1 Burnoff tests

As indicated earlier, coupons from the different FRP tubes investigated were subjected to burnoff tests to determine information such as fiber volume content, resin content, the number of fiber layers, and orientations. The tests were carried out in general accordance with ASTM Standard D2584. The tests consist of heating coupon samples from the FRP tubes in a furnace oven to a temperature of about 550 °C (1022 °F). The heat from the oven is used to burn the resin matrix, leaving the fiber layers exposed. The oven used for burnoff testing is shown in figure 39a. An FRP coupon sample after resin burnoff is shown in figure 39b. The number of fiber layers and orientation can be determined from this test, as shown in figure 39b.



a) Oven used for burnoff testing

b) Sample after resin burnoff

Figure 39. Photos. Burnoff testing.

4.3.2.2 Axial tension tests

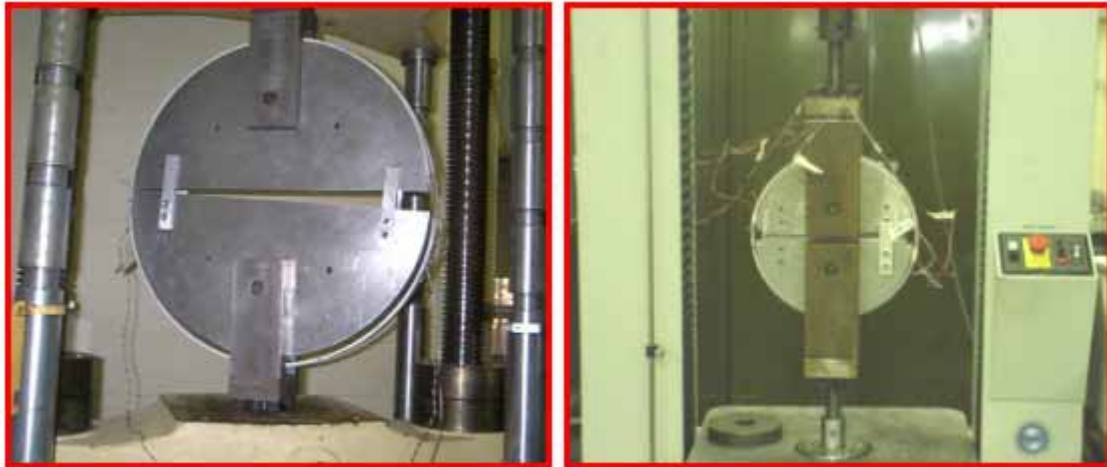
Axial tensile properties were evaluated using tensile tests performed on FRP samples in accordance with ASTM Test Method for Tensile Properties of Polymer Matrix Composite Materials (D3039). Test specimen strips were cut in the longitudinal direction using a water-cooled saw. The average test specimen dimension was 25 mm by 200 mm (0.98 inch by 7.8 inch). The tests were carried out using an INSTRON[®] test frame operated at a constant rate of displacement of 1.27 mm/min (0.05 inches/min). Axial strain was measured primarily with the use of extensometers; however, selected samples were also instrumented with strain gages. A typical tension test setup is shown in figure 40.



Figure 40. Photo. Typical tension test setup.

4.3.2.3 Hoop tension tests

Tensile properties in the hoop direction were evaluated using the split disk test method. The split disk fixtures were custom made to fit the two FRP tube diameter sizes investigated in this study. The split disk tests were performed in accordance with ASTM Test Method for Apparent Hoop Tensile Strength of Plastic or Reinforced Plastic Pipe by Split Disk Method (D2290). Split disk specimens were precision cut from the FRP shells with a nominal width of 40 mm (1.6 inches). The tests were carried out using a 534 kN Tinius-Olsen machine and an INSTRON test frame at a constant rate of displacement of 2.5 mm/min (0.1 inches/min). The typical split disk test setup is shown in figure 41.



a) 24-inch split disk fixture

b) 12-inch split disk fixture

Figure 41. Photos. Typical split disk test setup.

4.3.2.4 Freeze-thaw testing

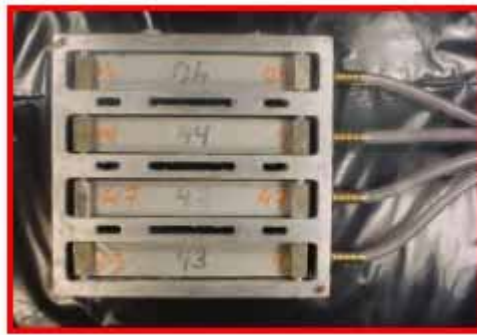
Saturated FRP specimens were subjected to freeze-thaw cycles using a programmable freeze-thaw chamber shown in figure 42.



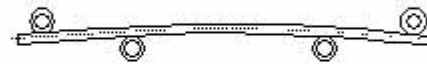
Figure 42. Photo. Freeze-thaw chamber.

The FRP specimens were fitted into special freeze-thaw fixtures that loaded the specimens in four-point bending. This arrangement was chosen to approximate the bending moment present in piles near the pile cap. The fixture used is shown in figure 43. Use of this fixture resulted in tensile strains in the outer extreme fiber of the 24-inch

diameter tube specimens ranging from 2,800 to 5,500 microstrains. The specimens from the 12-inch tubes were subjected to freeze-thaw cycles in an unloaded state, i.e., unstrained. The chamber was programmed to produce approximately 10 freeze-thaw cycles per day. A typical freeze-thaw cycle is shown in figure 44. Specimens were subjected to 100, 300, and 500 freeze-thaw cycles. As a point of interest, Southwest Virginia experiences about 50 freeze-thaw cycles per year (i.e., 500 freeze-thaw cycles in about 10 years).



a) Lancaster 24-inch specimens



b) Loaded sample in 4-point bending

Figure 43. Photo and Illustration. Freeze-thaw fixture.

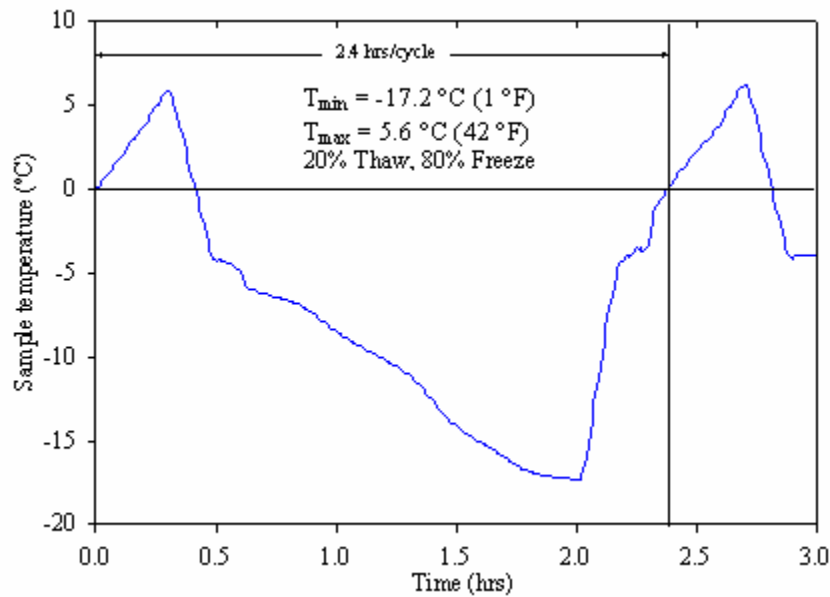


Figure 44. Graph. Average freeze-thaw cycle undergone by FRP samples.

More details on the freeze-thaw study are presented later in this chapter.

4.3.3 Baseline Mechanical Properties

To study the durability and long-term performance of FRP composite piles, it was necessary to first evaluate the baseline mechanical properties of the FRP shell in the longitudinal (axial) and hoop directions.

4.3.3.1 Longitudinal tension

The baseline properties of each pile type were obtained from a series of longitudinal tension tests, and the results are summarized in table 21. Typical stress-strain curves obtained from these tests for each FRP type are shown in figure 45.

Table 21. As-received longitudinal tensile properties.

Property		Lancaster FRP		Hardcore FRP tube	
		24-inch	12-inch	24-inch	12-inch
Tensile strength (MPa) ⁽¹⁾	Mean	113.1	249.3	432.2	494.3
	SD ⁽³⁾	7.3	17.7	46.9	60.6
Peak strain (%)	Mean	1.02	1.70	1.86	1.78
	SD	0.1	0.25	0.27	0.12
Initial modulus (Gpa) ⁽²⁾	Mean	14.8	23.2	27.3	29.6
	SD	1.9	2.1	3.15	0.9
Number of specimens	N	29	9	9	5

- Notes: (1) Strength calculated using total thickness of FRP tube (includes liner).
 (2) Initial modulus calculated between 0 and 4,000 microstrains.
 (3) SD = Standard deviation
 (4) 1 inch = 25.4 mm; 1 MPa = 145 lbf/inch²; 1 GPa = 145,000 lbf/inch²

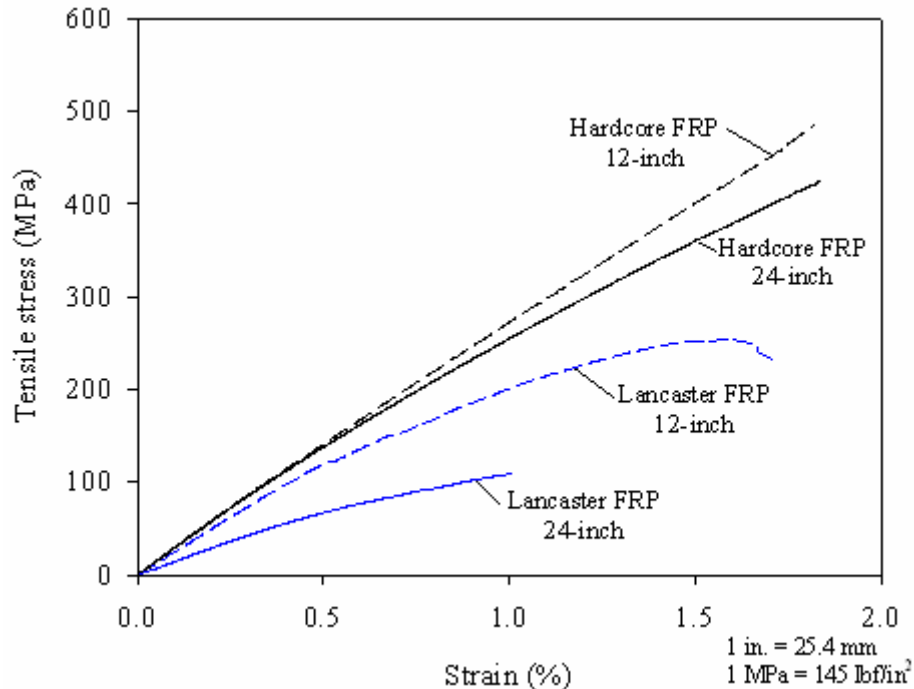


Figure 45. Graph. Representative baseline longitudinal tension stress-strain curves.

4.3.3.2 Hoop tension

The baseline hoop tensile properties for the composite piles are summarized in table 22. Typical stress-strain curves obtained from split disks tests are shown in figure 46.

Table 22. As-received hoop tensile properties.

Property		Lancaster FRP		Hardcore FRP
		24-inch	12-inch	12-inch
Tensile strength (MPa) ⁽¹⁾	Mean	121.4	195.2 ⁽²⁾	93.5
	SD ⁽⁵⁾	5.9	15.9	7.9
Peak strain (%)	Mean	1.26 ⁽³⁾	1.28	1.45
	SD	0.34	0.10	0.40
Initial modulus (Gpa) ⁽⁴⁾	Mean	19.1	16.5	11.9
	SD	2.3	2.2	3.1
Number of specimens	N	5	11	5

- Notes: (1) Strength calculated using total thickness of FRP tube (includes liner).
 (2) The strain and modulus values are based only on the second batch of tests that used inner and outer strain gages (5 tests).
 (3) No inner gages were used for this test batch; hence strain values are from outer gages only.
 (4) Initial modulus calculated between 0 and 4,000 microstrain.
 (5) SD = Standard deviation.
 (6) 1 inch = 25.4 mm; 1 MPa = 145 lbf/inch²; 1 GPa = 145,000 lbf/inch²

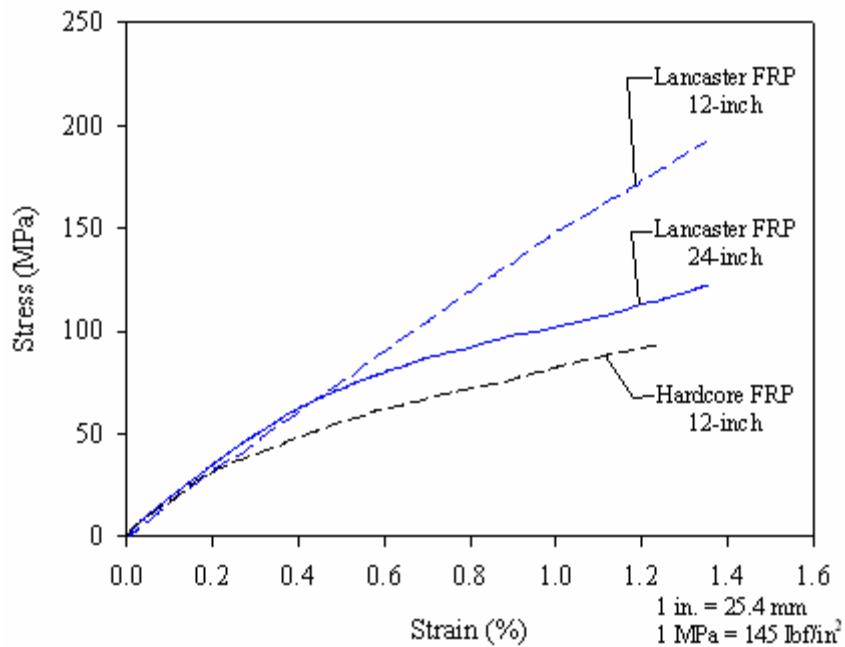


Figure 46. Graph. Representative baseline hoop tension stress-strain curves.

It was not possible to perform split disk tests on the 24-inch (0.61 m) Hardcore FRP shell specimens due to the noncircular shape of the inside of these shell. Hardcore shells have several resin transfer tubes attached to the inner wall (running longitudinally) that are used to inject the resin into the composite during manufacturing of the FRP shell, and at

the end of the process, the tubes are left in place filled with resin. The size and number of these tubes made it impractical to test these specimens, as the internal clearance is not circular.

4.3.4 Properties as a Function of Submergence Time and Moisture

4.3.4.1 Moisture absorption tests

Moisture absorption isothermal curves were obtained by immersing samples in fresh water tanks at the following temperatures: 22 °C (72 °F), 35 °C (95 °F), 45 °C (113 °F), 55 °C (131 °F), 65 °C (149 °F), and 80 °C (176 °F). The submerged FRP coupons were about 100 mm (3.9 inches) long and 25 mm (0.98 inch) wide, with their edges epoxy-coated to promote one-dimension diffusion. Plots of moisture absorption versus time for the 12-inch and 24-inch (0.31-m and 0.61-m) diameter Lancaster FRP shells are shown in figures 47 and 48, respectively. Moisture absorption plots for the 12-inch and 24-inch (0.31-m and 0.61-m) diameter Hardcore FRP shells are shown in figures 49 and 50, respectively. The moisture content shown in these figures corresponds to the percentage of weight gain with respect to the initial weight of the samples before submergence.

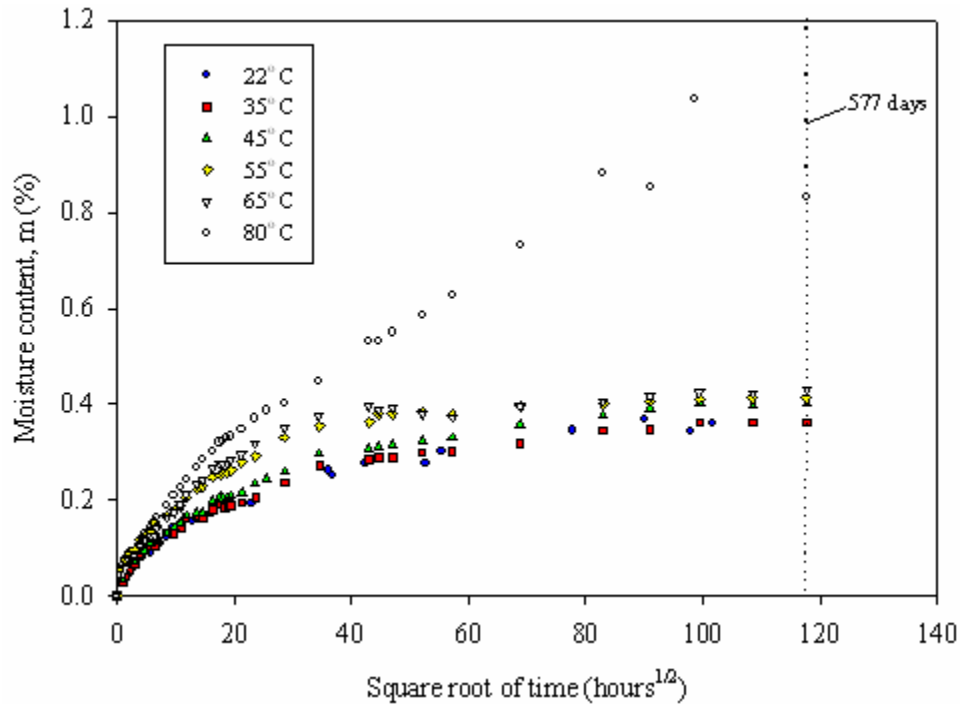


Figure 47. Graph. Absorption curves for Lancaster 12-inch FRP tube.

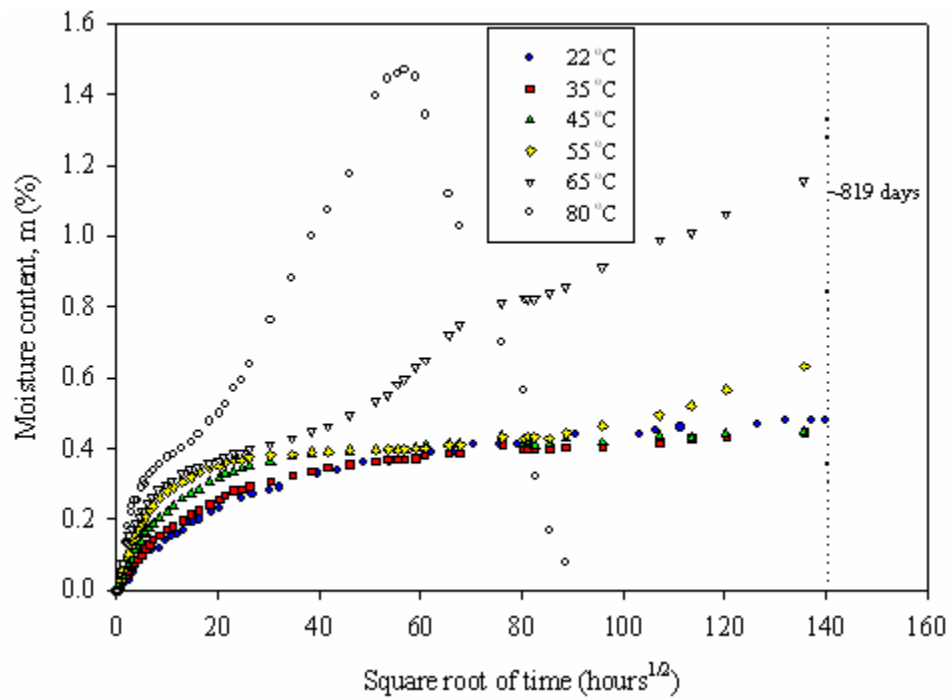


Figure 48. Graph. Absorption curves for Lancaster 24-inch FRP tube.

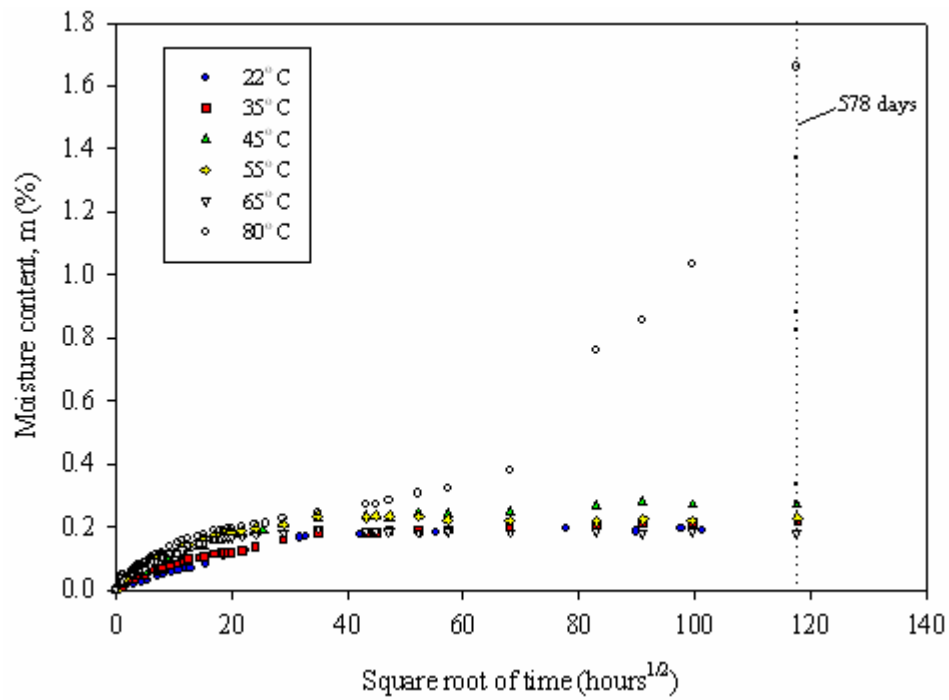


Figure 49. Graph. Absorption curves for Hardcore 12-inch FRP tube.

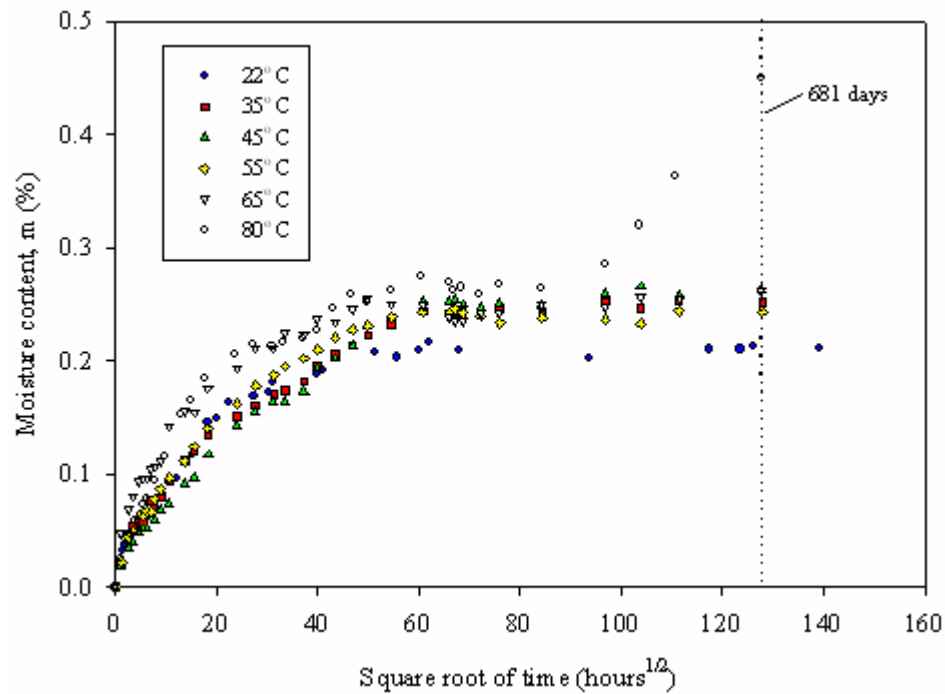


Figure 50. Graph. Absorption curves for Hardcore 24-inch FRP tube.

All moisture absorption tests showed a rapid gain of weight at the start of the experiments, with the rate of increase being the greatest at the highest temperature (80 °C (176 °F)). With time, most of the tests below 65 °C (149 °F) stabilized, reaching a saturation or equilibrium moisture content. For the tests at 80 °C (176 °F), the weights either continued to increase gradually, or in some cases like the Lancaster 24-inch (0.61-m) at 80 °C (176 °F), the samples started to decrease sharply in weight after reaching a peak. Nishizaki and Meiarashi (2002) reported similar decreases in moisture content for samples submerged at high temperatures. The authors attributed this behavior to loss of material from the composite matrix. The Lancaster 24-inch (0.61-m) samples with water temperatures between 55 and 65 °C (131 and 149 °F) seem to have a non-Fickian or two-stage absorption behavior. Phifer (2003) found that, in some cases, Langmuirian diffusion predicts the behavior of E-glass vinyl ester composites better than Fickian diffusion. Diffusion analyses using Fickian and Langmuirian models are presented in the following subsection.

4.3.4.2 Diffusion properties

Two types of diffusion models were used to fit the experimental absorption data: Fickian and Langmuirian. These models are described briefly below.

The Fickian diffusion model is commonly used to predict moisture absorption of composite materials. This model has the convenience of being simple. The model assumes a constant diffusivity, D , and a saturation moisture, M_{∞} , to which the sample

tends to as the submergence time increases. The expression for Fickian diffusion of a thin plate of thickness, h , is given by the following expression (Shen and Springer 1976):

$$M(t) = M_{\infty} \left[1 - \sum_{n=0}^{\infty} \frac{8}{(2n+1)^2 \pi^2} e^{-D(2n+1)^2 \pi^2 t / h^2} \right] \quad (7)$$

where

- $M(t)$ = moisture content of the FRP specimen at submergence time, t
- M_{∞} = moisture content at saturation
- t = time of submergence
- D = diffusivity through the thickness of the FRP specimen
- h = thickness of FRP specimen

Gurtin and Yatomi (1979) proposed using a Langmuirian diffusion model for FRP composites exhibiting non-Fickian absorption behavior. The following expression is given to track the moisture content of specimens following Langmuirian diffusion:

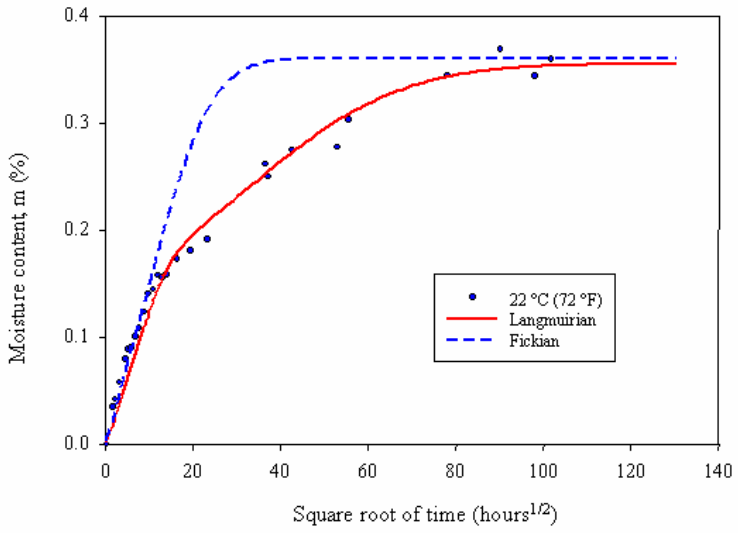
$$M(t) = M_{\infty} \left[1 - \left(\frac{\beta}{\alpha + \beta} \right) e^{-\alpha t} - \frac{\alpha}{\alpha + \beta} \sum_{n=0}^{\infty} \frac{8}{(2n+1)^2 \pi^2} e^{-D(2n+1)^2 \pi^2 t / h^2} \right] \quad (8)$$

where

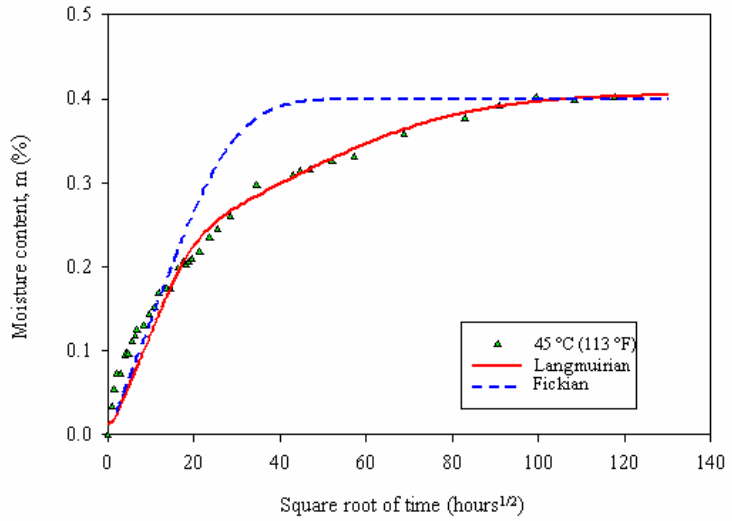
- $M(t)$ = moisture content of the FRP specimen at submergence time, t
- M_{∞} = the Fickian moisture content at saturation
- t = time of submergence
- D = the Fickian diffusivity through the thickness of the FRP specimen
- α and β = constants usually obtained from curve fitting
- h = thickness of the FRP specimen

The similarity of this model to the Fickian is evident from comparing equations 7 and 8. The first non-unity term in equation 8 is indicative of a two-stage diffusion process. More details on the Langmuirian model can be found in Gurtin and Yatomi (1979).

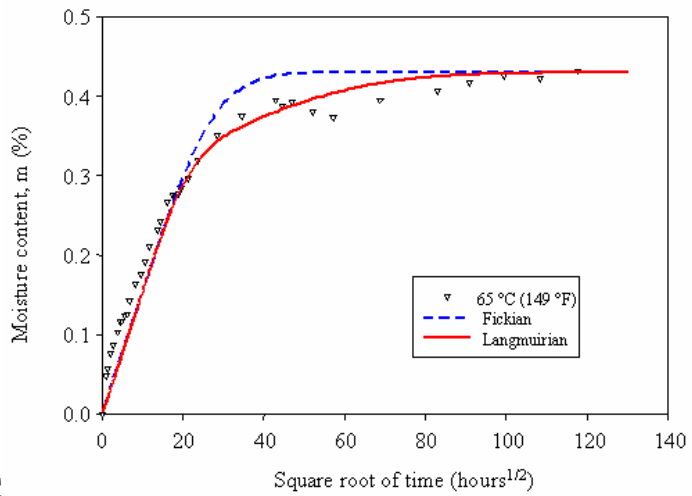
Curve fits using the Fickian and Langmuirian models were performed on the experimental moisture absorption data gathered for the different FRP shells evaluated in this study. The curve fits for water temperatures 22 °C (72 °F), 45 °C (113 °F), and 65 °C (149 °F) are shown in figures 51 and 52 for the 12-inch and 24-inch (0.31-m and 0.61-m) diameter Lancaster FRP shells, respectively. Fits for these same water temperatures for the 12-inch and 24-inch (0.31-m and 0.61-m) diameter Hardcore FRP shells are shown in figures 53 and 54, respectively.



(a) Water at 22 °C

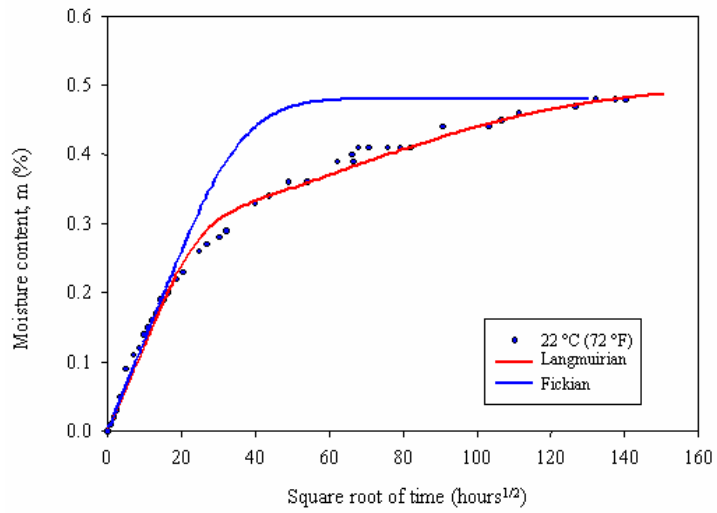


(b) Water at 45 °C

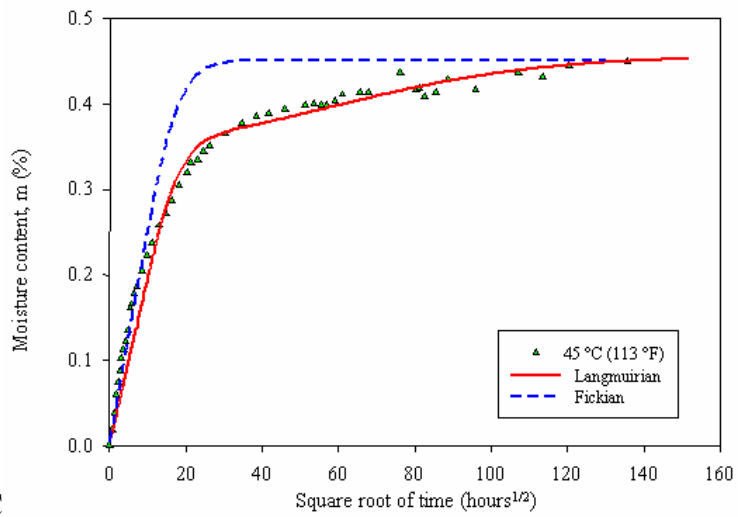


(c) Water at 65 °C

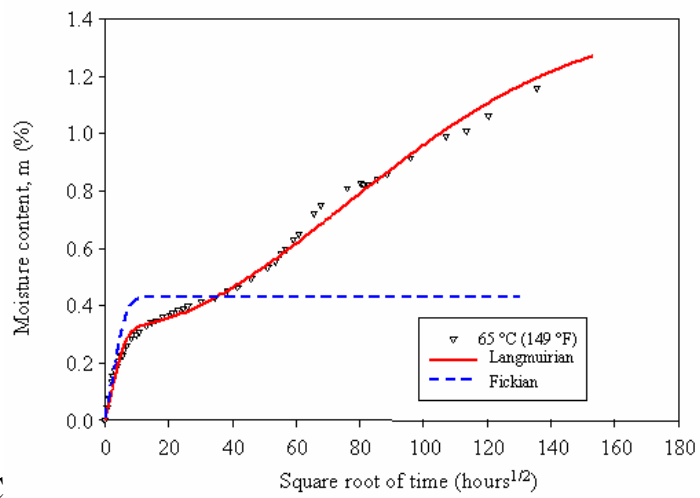
Figure 51. Graphs. Selected diffusion analyses for Lancaster 12-inch FRP samples.



(a) Water at 22 °C

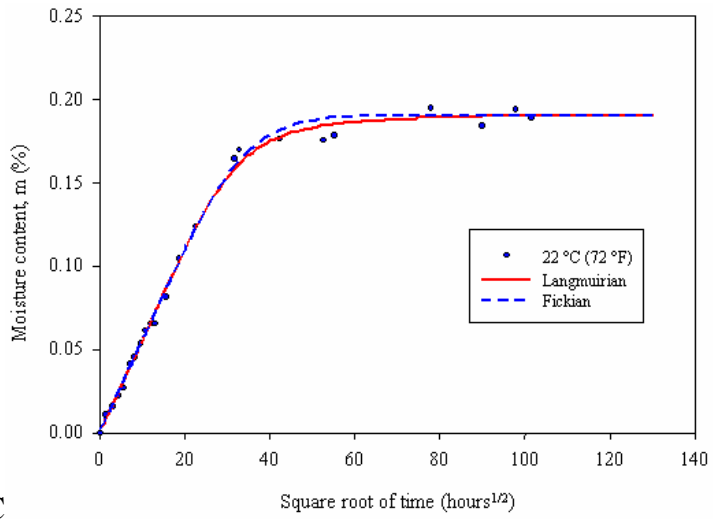


(b) Water at 45 °C

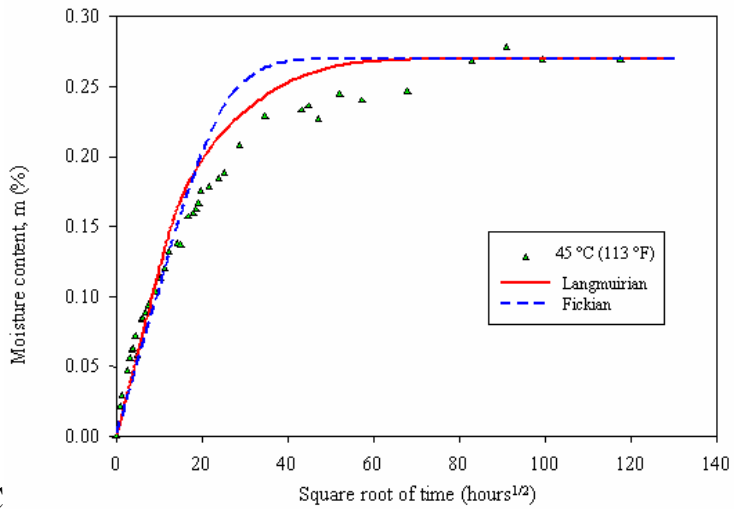


(c) Water at 65 °C

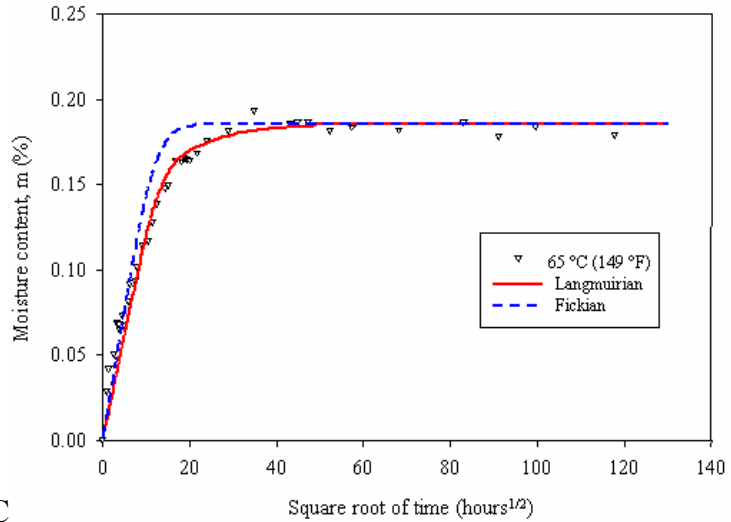
Figure 52. Graphs. Selected diffusion analyses for Lancaster 24-inch FRP samples.



(a) Water at 22 °C

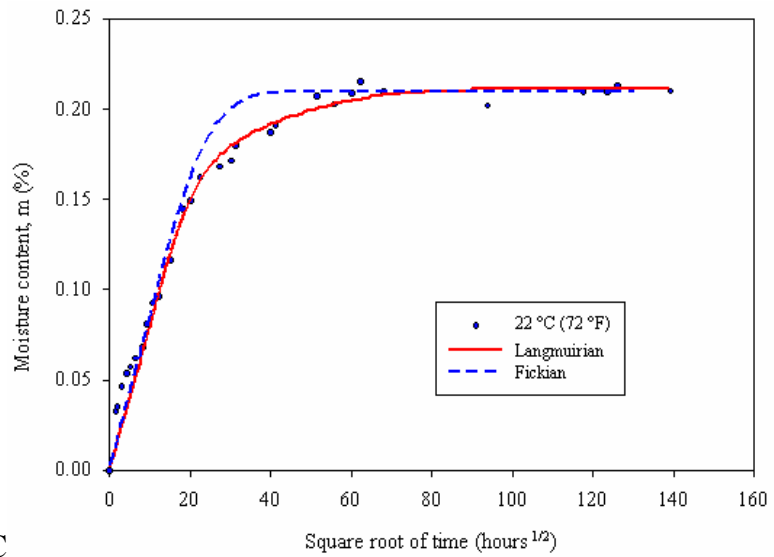


(b) Water at 45 °C

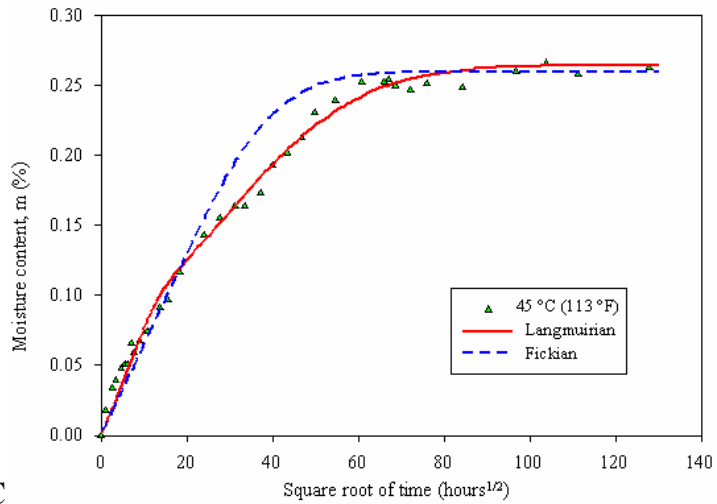


(c) Water at 65 °C

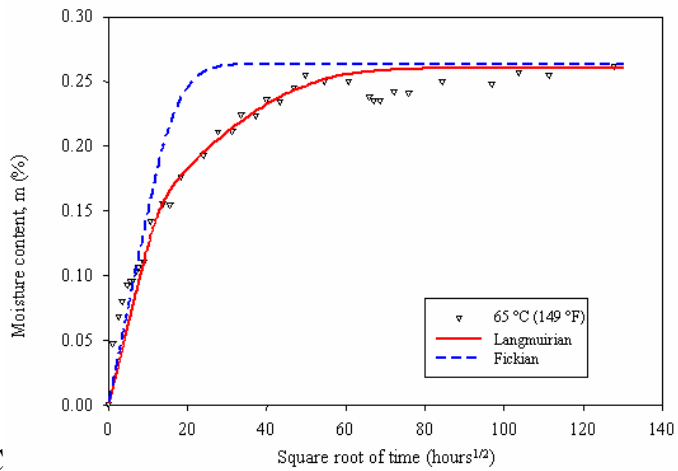
Figure 53. Graphs. Selected diffusion analyses for Hardcore 12-inch FRP samples.



(a) Water at 22 °C



(b) Water at 45 °C



(c) Water at 65 °C

Figure 54. Graphs. Selected diffusion analyses for Hardcore 24-inch FRP samples.

These figures indicate that Langmuirian diffusion, which has four curve-fitting parameters (D , M_{∞} , α , β), is better able to track the measured moisture absorption than the Fickian diffusion, which has two curve-fitting parameters (D , M_{∞}), for samples submerged at temperatures between 55 and 80 °C (131 and 176 °F).

The diffusivity (or diffusion coefficient D) and the saturation moisture content (M_{∞}) obtained from Fickian diffusion analyses are summarized in tables 23 through 26 for the Lancaster 12-inch (0.31-m), Lancaster 24-inch (0.61-m), Hardcore 12-inch (0.31-m), and Hardcore 24-inch (0.61-m) samples, respectively. Although there is much scatter in the values, it can be seen in the tables that the diffusivity and the saturation moisture tend to increase with temperature. Even though Langmuirian diffusion provided a better fit to the data, the Fickian model and parameter values are used for predicting the long-term composite pile strength, as described later in this chapter, because of the simplicity of the Fickian model.

Table 23. Fickian diffusion parameters for the Lancaster 12-inch FRP.

Water Temperature (°C)	Diffusivity, D (cm ² /hr)	Saturation Moisture, M_{∞} (%)
22	1.25 E-4	0.36
35	1.53 E-4	0.36
45	8.57 E-5	0.40
55	1.21 E-4	0.42
65	9.22 E-5	0.43
80	3.38 E-5	0.87 ⁽¹⁾

Note: (1) Did not stabilize at the end of test; value is only used for curve fitting Fickian curves to data.
 (2) 1 cm² = 0.15 inch²

Table 24. Fickian diffusion parameters for the Lancaster 24-inch FRP.

Water Temperature (°C)	Diffusivity, D (cm ² /hr)	Saturation Moisture, M_{∞} (%)
22	1.23 E-5	0.48
35	2.04 E-5	0.45
45	4.89 E-4	0.45
55	1.48 E-4	0.40 ⁽¹⁾
65	3.08 E-4	0.43 ⁽¹⁾
80	4.59 E-4	0.45 ⁽¹⁾

Note: (1) Did not stabilize at the end of test; value is only used for curve fitting Fickian curves to data.
 (2) 1 cm² = 0.15 inch²

Table 25. Fickian diffusion parameters for the Hardcore 12-inch FRP.

Water Temperature (°C)	Diffusivity, D (cm ² /hr)	Saturation Moisture, M _∞ (%)
22	8.17 E-6	0.19
35	1.99 E-5	0.19
45	1.52 E-5	0.27
55	4.81 E-5	0.22
65	6.08 E-5	0.18
80	1.17 E-5	0.50 ⁽¹⁾

Note: (1) Did not stabilize at the end of test; value is only used for curve fitting Fickian curves to data.
(2) 1 cm² = 0.15 inch²

Table 26. Fickian diffusion parameters for the Hardcore 24-inch FRP.

Water Temperature (°C)	Diffusivity, D (cm ² /hr)	Saturation Moisture, M _∞ (%)
22	1.16 E-4	0.21
35	7.85 E-5	0.26
45	4.42 E-5	0.26
55	9.54 E-5	0.24
65	2.30 E-4	0.26
80	1.70 E-4	0.26 ⁽¹⁾

Note: (1) Did not stabilize at the end of test, value is only used for curve fitting Fickian curves to data.
(2) 1 cm² = 0.15 inch²

4.3.4.3 Measured properties as a function of submergence time and moisture

The effect of time of submergence and moisture on the mechanical properties of the FRP tubes was evaluated by performing longitudinal and hoop tension tests on specimens aged in 22 °C (72 °F) water for submergence times ranging between 4 and 787 days. Typically, five or more specimens were tested at each submergence period. The tests were carried out using the same procedure used to determine the baseline properties.

Variations of the mechanical properties of the aged FRP samples are presented in the following subsections. The results presented are normalized with respect to the baseline property values.

4.3.4.3.1 Aged properties for Lancaster 24-inch FRP tube

Variations of the longitudinal and hoop properties versus submergence time for this FRP shell are shown in figures 55 and 56, respectively. The error bars shown in these figures correspond to ± one standard deviation. Longitudinal tensile test results on this particular FRP composite shell showed no evidence of significant degradation of property values. This is likely related in part to the fiber orientation of this composite ($\pm 35^\circ/85^\circ/\pm 35^\circ$)_T, which makes it a matrix-dominated composite in the longitudinal direction, and also possibly due to a gain of ductility of the matrix upon immersion in water. Tensile properties in the hoop direction showed some degradation, but it was not very significant. The hoop tensile strength decreased by about 8 percent. The error bars shown in these figures indicate considerable scatter.

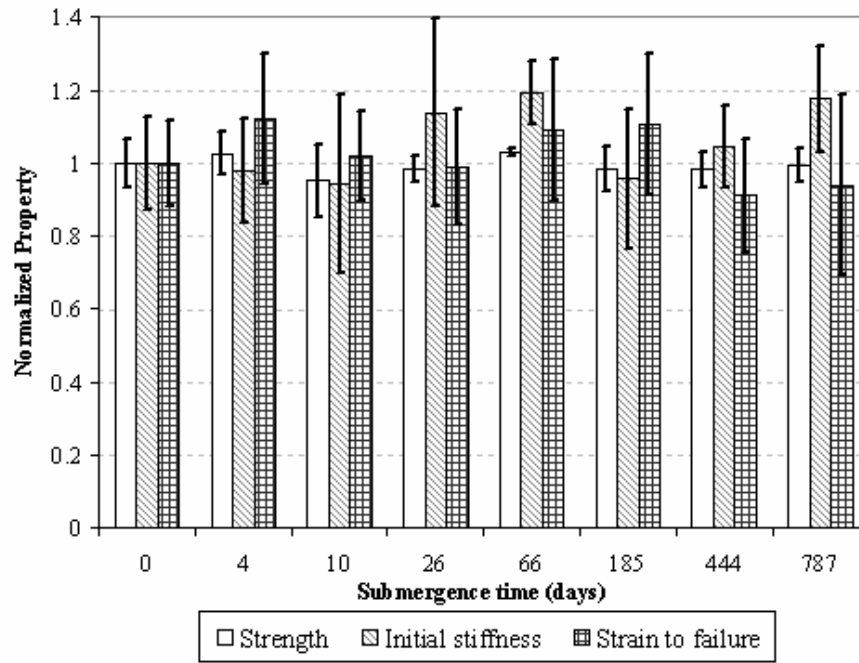


Figure 55. Graph. Longitudinal tensile properties versus submergence time for Lancaster 24-inch FRP tube.

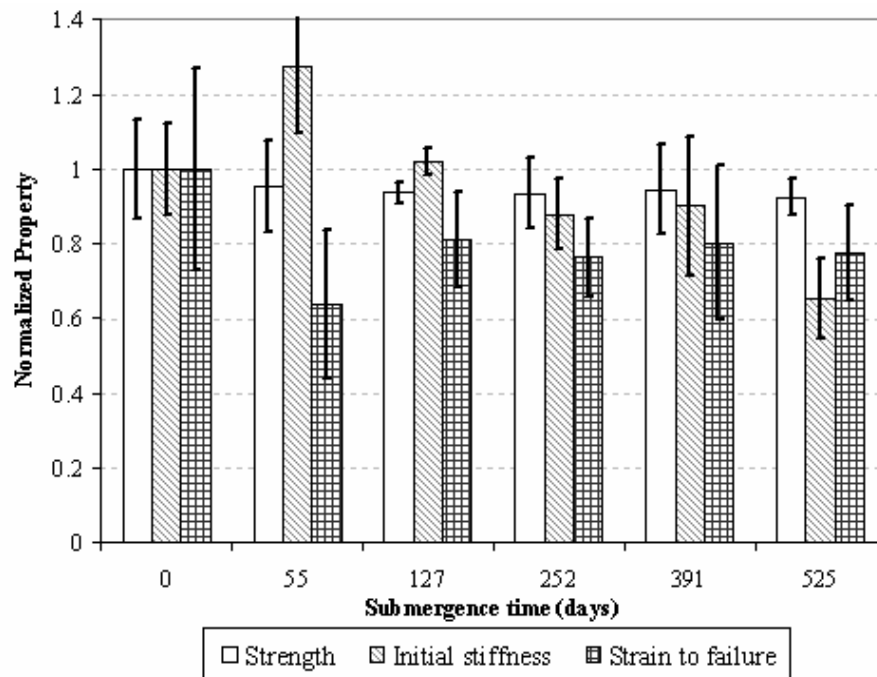


Figure 56. Graph. Hoop tensile properties versus submergence time for Lancaster 24-inch FRP tube.

4.3.4.3.2 Aged properties for Lancaster 12-inch FRP tube

The longitudinal and hoop properties versus submergence time for this FRP shell are shown in figures 57 and 58, respectively.

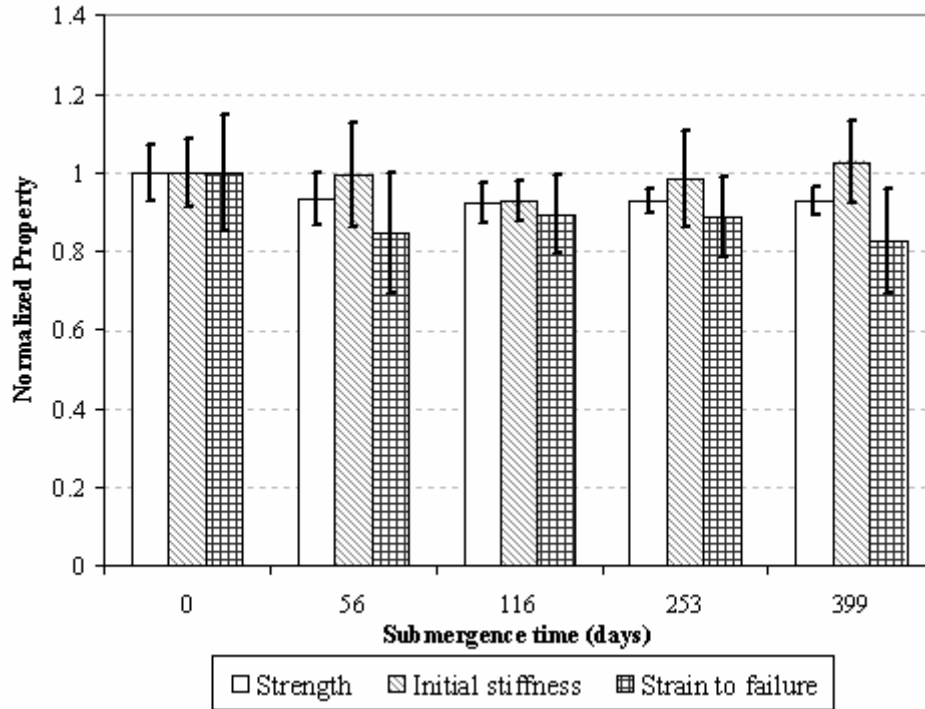


Figure 57. Graph. Longitudinal tensile properties versus submergence time for Lancaster 12-inch FRP tube.

Figure 57 shows that after approximately 400 days of submergence in fresh water at 22 °C (72 °F), the longitudinal tensile strength and strain to failure decreased about 9 and 18 percent, respectively. The initial stiffness (in the 0 to 4,000 microstrains range) remained almost constant.

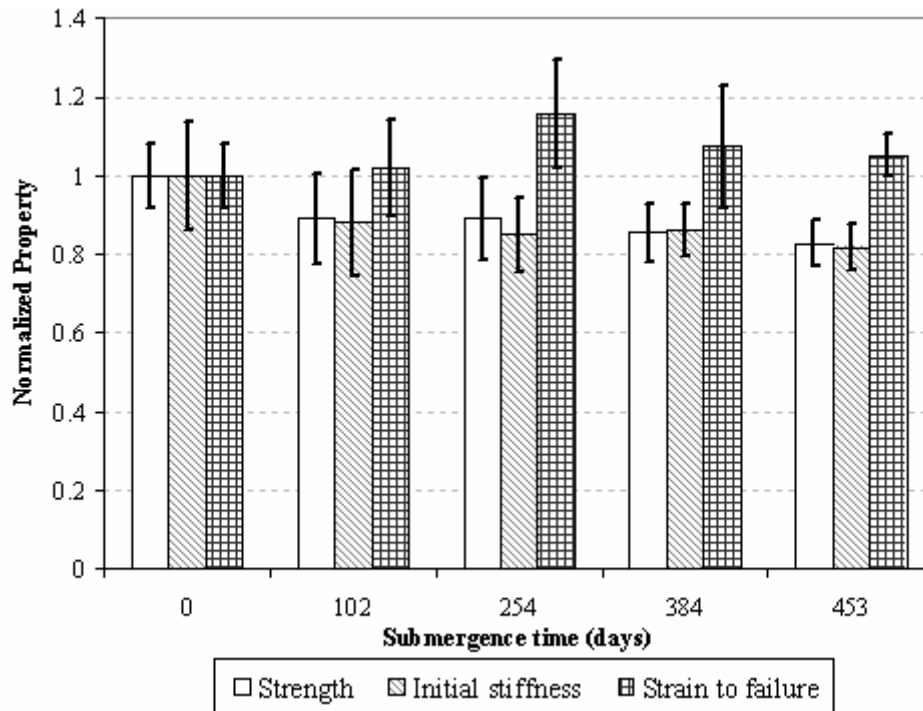
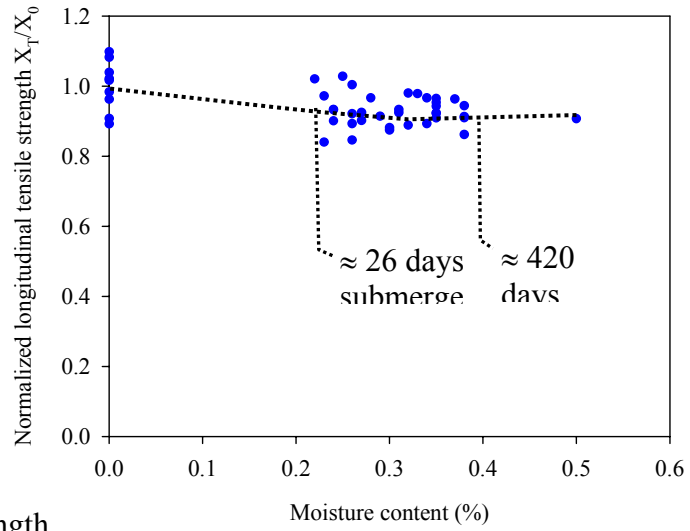


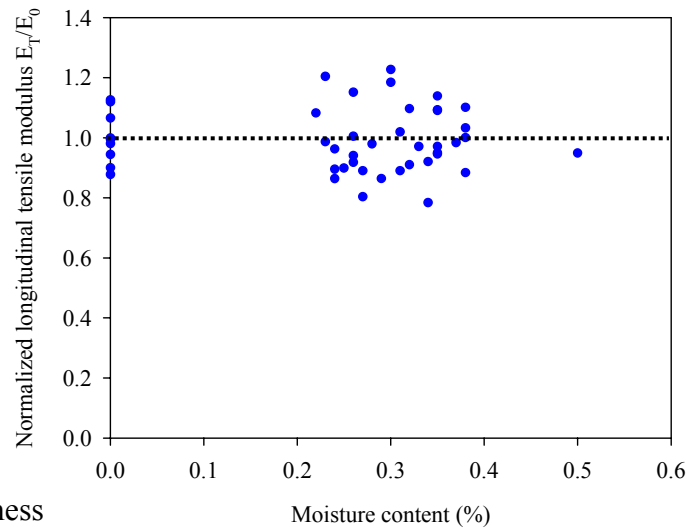
Figure 58. Graph. Hoop tensile properties versus submergence time for Lancaster 12-inch FRP tube.

Figure 58 shows that the hoop tensile strength and initial stiffness decreased about 17 percent and 18 percent, respectively. Degradation levels for strength and stiffness are more significant for the 12-inch (0.31-m) sample compared to the 24-inch (0.61-m) sample, because the fiber layup of the 12-inch (0.31-m) composite is more fiber dominated. However, the strain to failure did not change much.

Strength and stiffness versus percentage of moisture absorption are shown in figures 59 and 60 for the longitudinal and hoop directions, respectively. Both figures show tensile strength decreases with increasing moisture content, but the strength values tend to stabilize at higher moisture contents. The hoop tensile stiffness displayed a similar behavior, as shown in figure 60b. These plots are useful for predicting mechanical properties versus time, as shown later in this chapter.

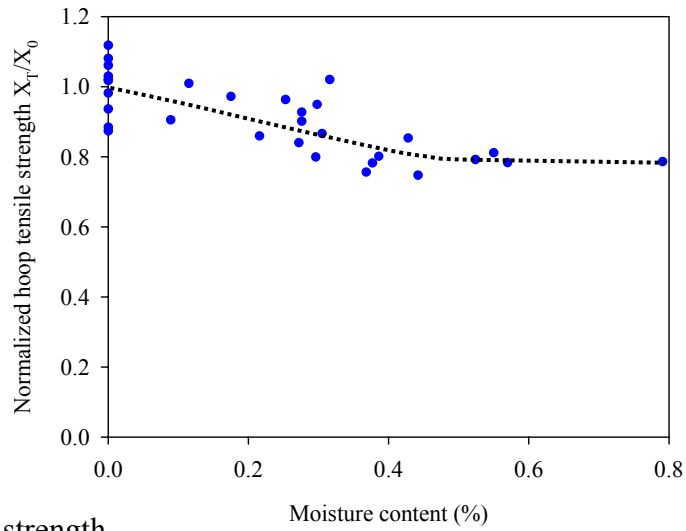


a) Variation of strength

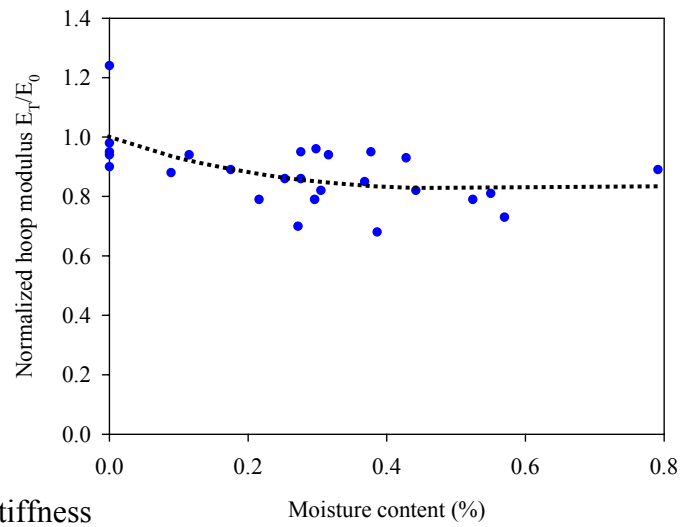


b) Variation of stiffness

Figure 59. Charts. Longitudinal tensile properties versus moisture content for Lancaster 12-inch tube.



a) Variation of strength



b) Variation of stiffness

Figure 60. Charts. Hoop tensile properties versus moisture content for Lancaster 12-inch FRP tube.

4.3.4.3.3 Aged properties for Hardcore 24-inch FRP tube

The longitudinal properties versus submergence time for this FRP shell are shown in figure 61.

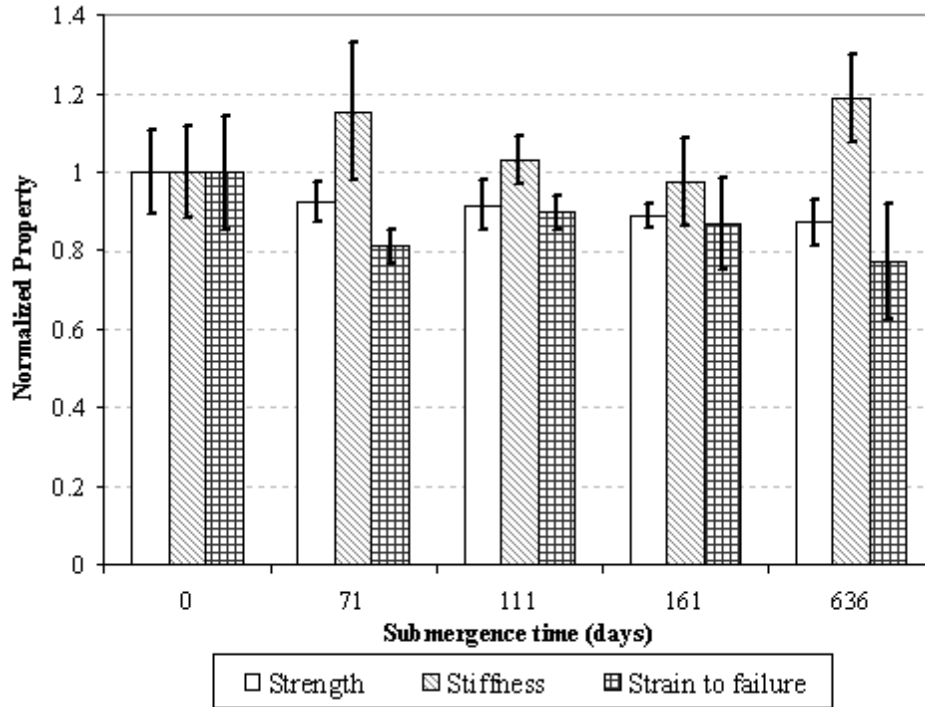
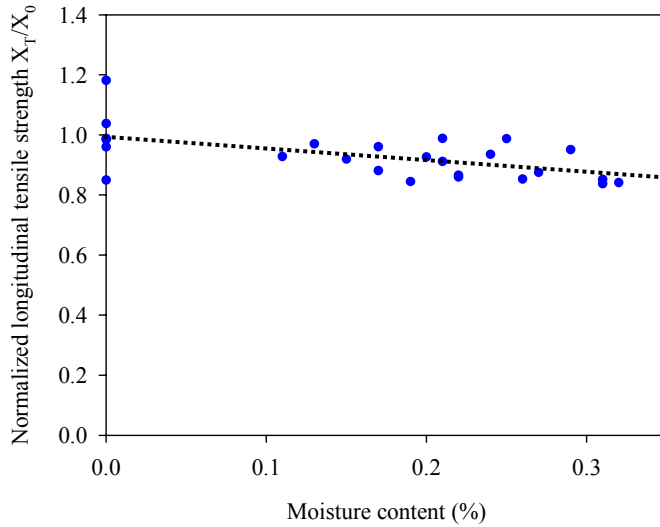


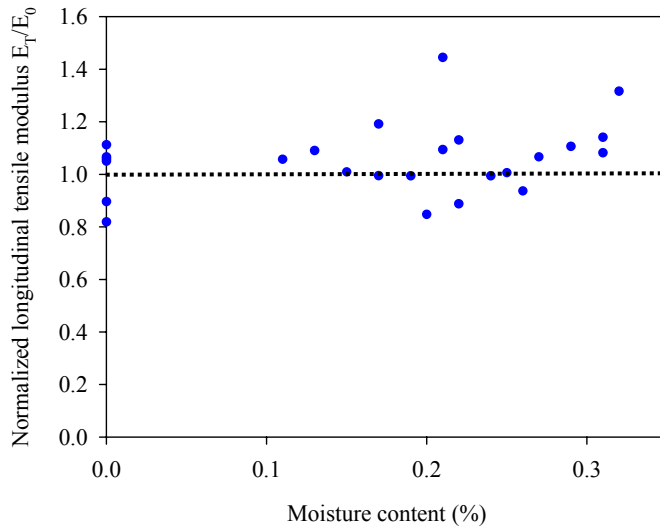
Figure 61. Graph. Longitudinal tensile properties versus submergence time for Hardcore 24-inch FRP tube.

Figure 61 shows that after approximately 636 days of submergence in fresh water at 22 °C (72 °F), the longitudinal tensile strength decreased about 13 percent. The strain to failure decreased by about 20 percent. The initial stiffness values (0 to 4,000 microstrains) did not show a clear trend with respect to the baseline values. The error bars shown indicate that the strain and stiffness values had considerable scatter.

The variation of the longitudinal tensile strength and stiffness versus percentage of moisture absorption are shown in figure 62. This figure shows a tensile strength loss of about 16 percent at the highest moisture content value of 0.33 percent. The initial stiffness values show considerable scatter, and no clear trend can be determined.



a) Variation of strength



b) Variation of stiffness

Figure 62. Charts. Longitudinal tensile properties versus moisture content for Hardcore 24-inch FRP tube.

4.3.4.3.4 Aged properties for Hardcore 12-inch FRP tube

The longitudinal and hoop tensile properties versus submergence time for this FRP shell are shown in figures 63 and 64, respectively.

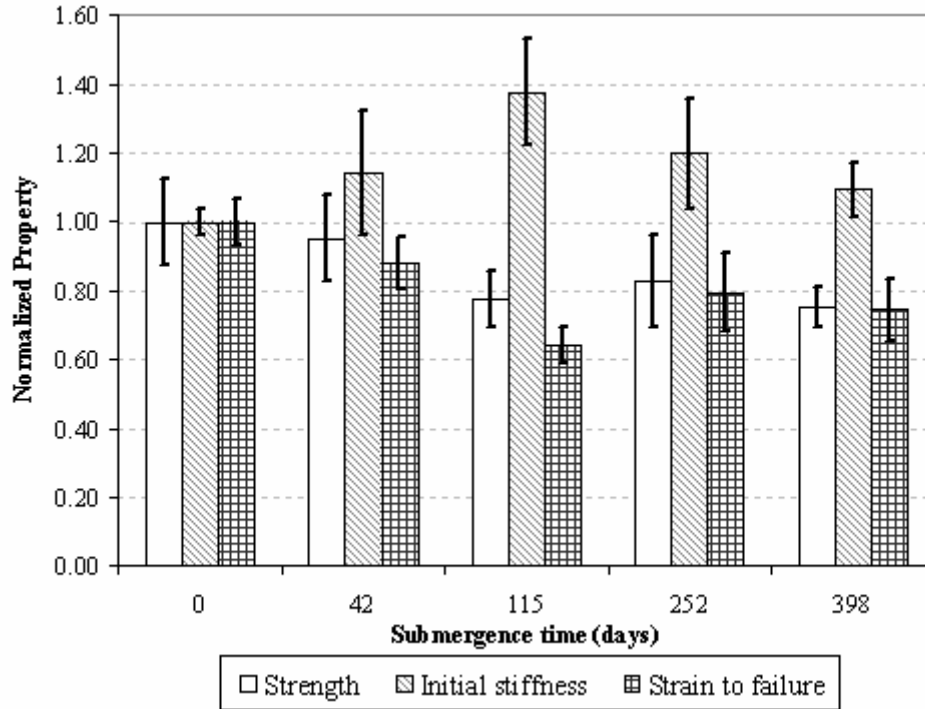


Figure 63. Graph. Longitudinal tensile properties versus submergence time for Hardcore 12-inch FRP tube.

Figure 63 shows that after approximately 398 days of submergence in fresh water at 22 °C (72 °F), the longitudinal tensile strength and strain to failure decreased by about 24 percent and 25 percent, respectively. The initial stiffness increased by about 10 percent.

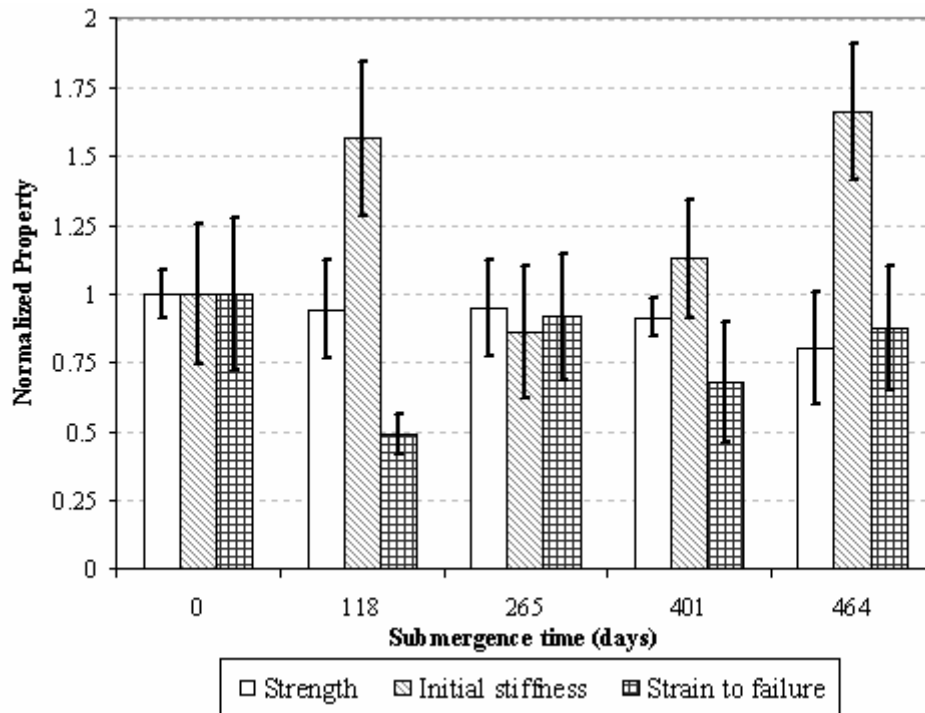
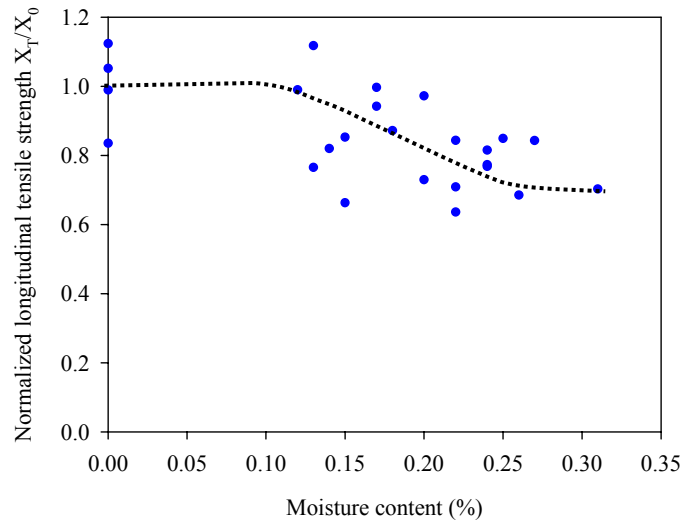


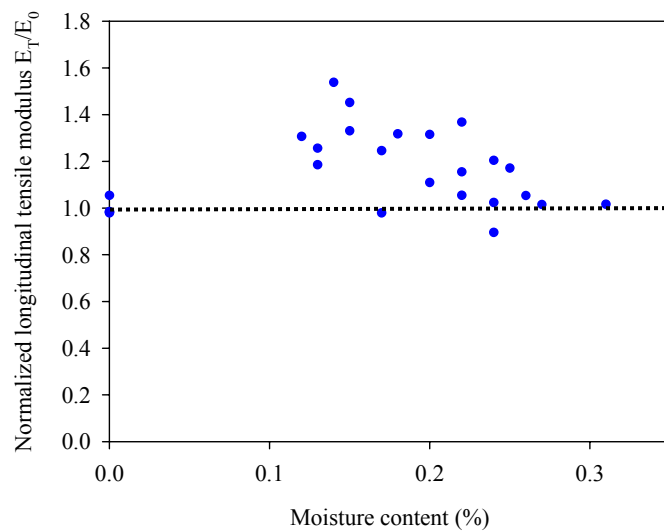
Figure 64. Graph. Hoop tensile properties versus submergence time for Hardcore 12-inch FRP tube.

Figure 64 shows that after approximately 464 days of submergence in fresh water at 22 °C (72 °F), the hoop tensile strength decreased by about 20 percent. The stiffness and strain-to-failure values showed very high scatter. This could be related to material variability. Another possible reason could be related to the infusion tubes used to inject the resin during manufacturing of the FRP tubes. These tubes were removed prior to hoop split disk testing; however, at these locations the FRP shell wall thickness increased and decreased sharply within a small distance. It is possible that high stress concentrations occurred at these locations and affected the results.

The variation of tensile strength and stiffness versus percentage of moisture absorption for the longitudinal and hoop directions are shown in figures 65 and 66, respectively.



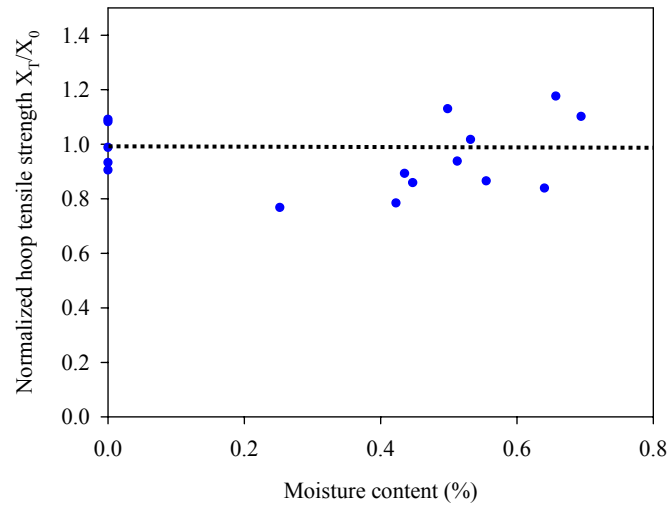
a) Variation of strength



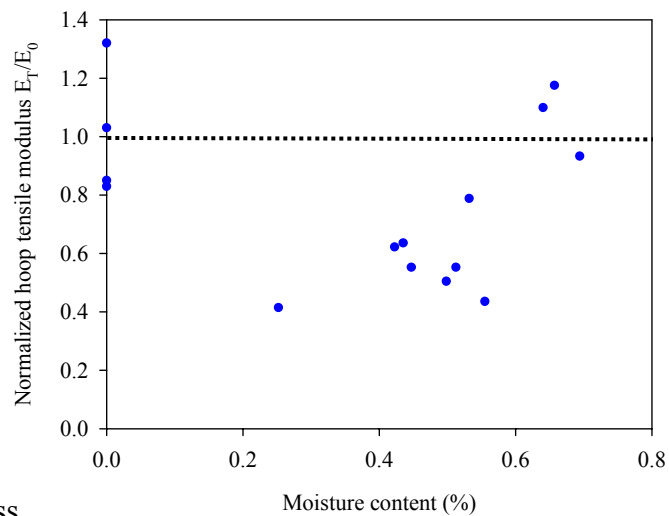
b) Variation of stiffness

Figure 65. Charts. Longitudinal tensile properties versus moisture content for Hardcore 12-inch FRP tube.

As shown in figure 65a, the longitudinal tensile strength decreases with increasing moisture content. The maximum tensile strength degradation was about 25 percent at a moisture content of about 0.25 percent. No clear trend was observed between longitudinal tensile modulus and moisture content.



a) Variation of strength



b) Variation of stiffness

Figure 66. Charts. Hoop tensile properties versus moisture content for Hardcore 12-inch FRP tube.

Figure 66 shows very high scatter for hoop tensile strength and stiffness, hence no clear relationship was observed with moisture content. As mentioned before, the high scatter in the hoop tensile properties for the 12-inch (0.31-m) Hardcore shell could be related to material variability, and the sharp variations of FRP shell wall thickness near the location of the resin infusion tubes may have created high stress concentrations and affected the results.

4.3.5 Freeze-Thaw Degradation of Saturated FRP Samples

Longitudinal tensile tests were performed on saturated coupon samples after 0, 100, 300, and 500 freeze-thaw cycles. The saturated coupons refer to specimens that were soaked in 22 °C (72 °F) water until they reached moisture content at saturation, that is, M_{∞} (see figures 47 through 50 for the time of soaking required to reach M_{∞}). Three or more samples were tested at each stage. The typical temperature cycle undergone by the specimens is shown in figure 44. The specimens were cycled between -17 °C (1.4 °F) and +6 °C (43 °F), and the duration of each cycle was about 2.4 hours. The test setup is described in section 4.3.2.4.

The results are presented in figures 67 through 70. These figures are normalized with respect to the properties obtained from samples submerged in 22 °C (72 °F) water at or near the saturation moisture content (M_{∞}).

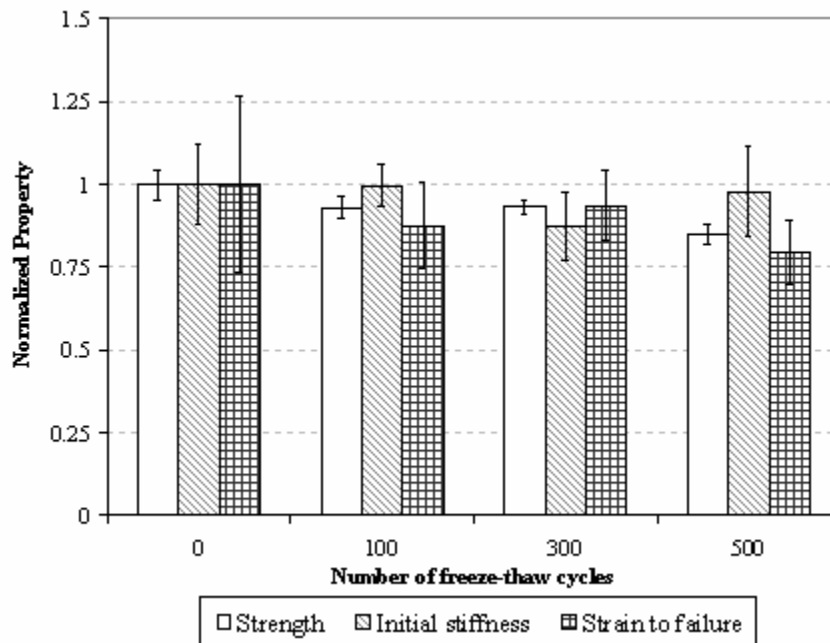


Figure 67. Graph. Influence of freeze-thaw cycling on the longitudinal tensile properties for the Lancaster 24-inch FRP tube.

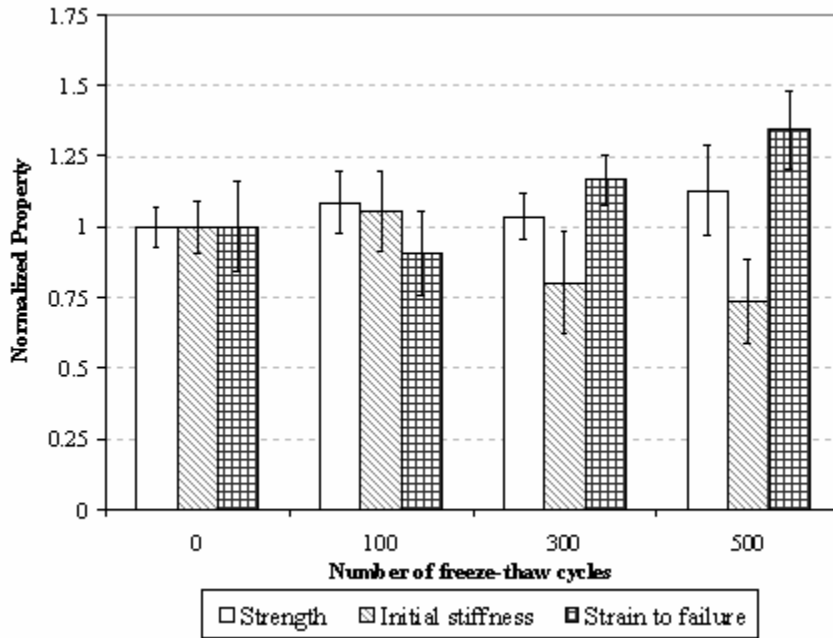


Figure 68. Graph. Influence of freeze-thaw cycling on the longitudinal tensile properties for the Lancaster 12-inch FRP tube.

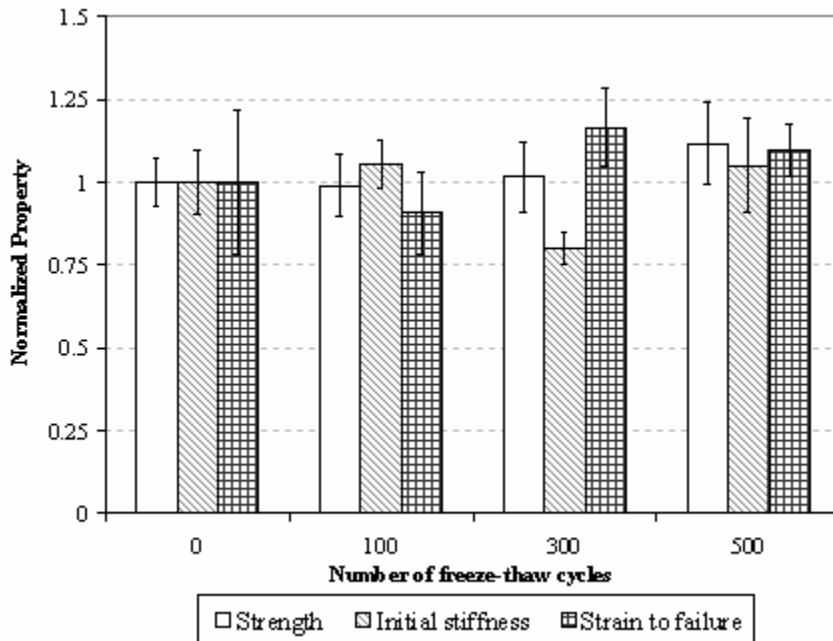


Figure 69. Graph. Influence of freeze-thaw cycling on the longitudinal tensile properties for the Hardcore 24-inch FRP tube.

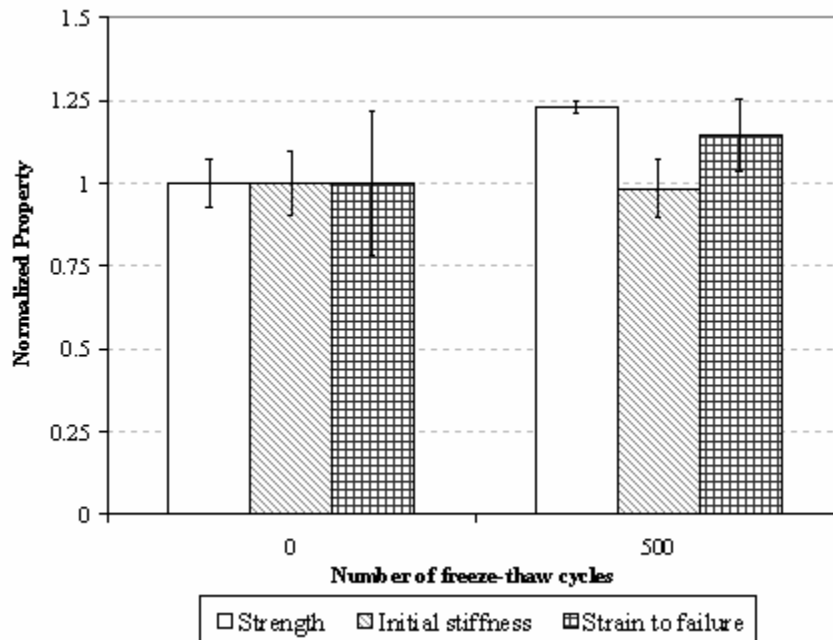
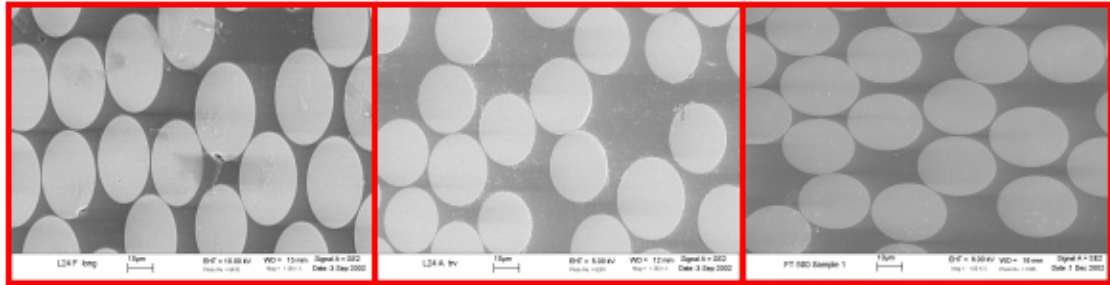


Figure 70. Graph. Influence of freeze-thaw cycling on the longitudinal tensile properties for the Hardcore 12-inch FRP tube.

The freeze-thaw data indicates little change in the longitudinal tensile properties of the FRP tubes except for the Lancaster 24-inch (0.61-m), where a strength decrease of about 20 percent was recorded after exposure to 500 freeze-thaw cycles.

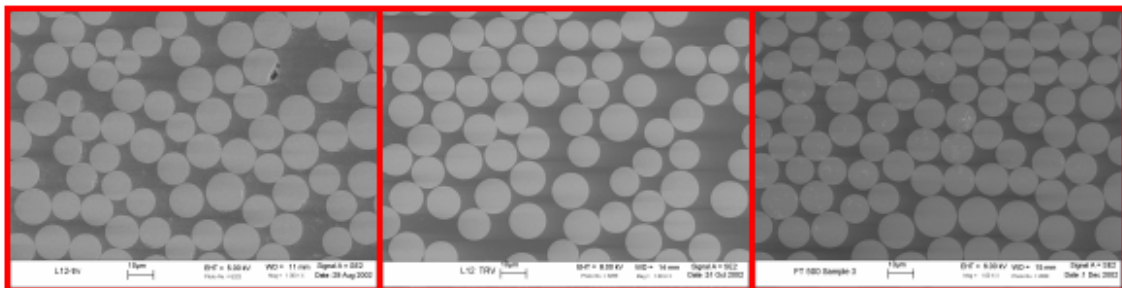
4.3.6 SEM Imaging

Scanning electron microscopy was used to investigate the damage mechanisms for the FRP composite tubes. The SEM images allowed examination of the state of the fibers and the surrounding matrix at different exposure conditions used in the experimental program. For each FRP tube type, SEM micrographs were obtained for the following conditions: as-received, at the end of moisture absorption in 22 °C (72 °F) water (i.e., saturation), and after freeze-thaw cycling. SEM images for the four types of FRP tubes investigated are shown in figures 71 through 74.



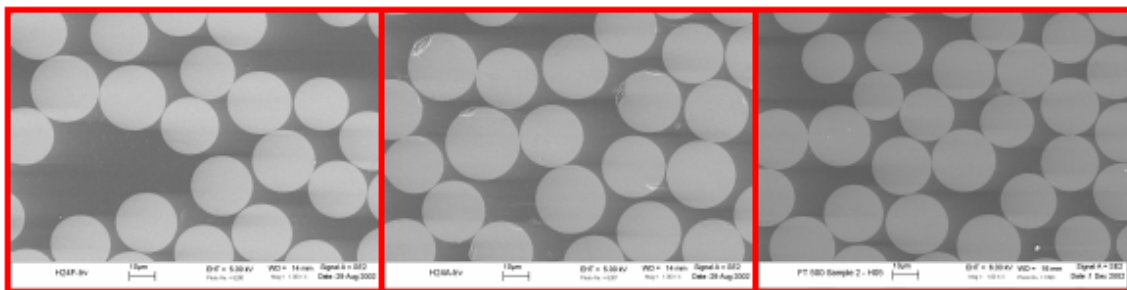
a) as-received condition b) at saturation moisture c) after 500 freeze-thaw cycles
 (Note: magnification is x1,000 for the three micrographs)

Figure 71. Photo. SEM images of Lancaster 24-inch FRP tube.



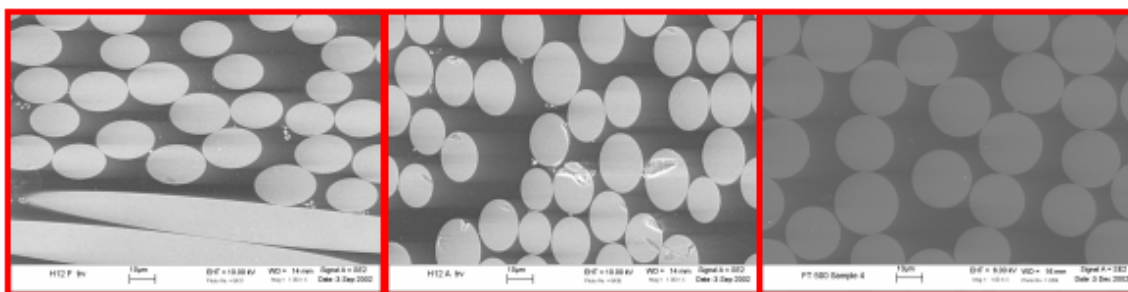
a) as-received condition b) at saturation moisture c) after 500 freeze-thaw cycles
 (Note: magnification is x1,000 for the three micrographs)

Figure 72. Photo. SEM images of Lancaster 12-inch FRP tube.



a) as-received condition b) at saturation moisture c) after 500 freeze-thaw cycles
 (Note: magnification is x1,000 for the three micrographs)

Figure 73. Photo. SEM images of Hardcore 24-inch FRP tube.



a) as-received condition b) at saturation moisture c) after 500 freeze-thaw cycles
 (Note: magnification is x1,000 for the three micrographs)

Figure 74. Photo. SEM images of Hardcore 12-inch FRP tube.

Some damage was noticed in the SEM images taken at the saturation moisture state. The signs of degradation included damage at the fiber and at the interface between the fiber and matrix.

4.4 LONG-TERM STRUCTURAL CAPACITY OF FRP COMPOSITE PILES

The durability experimental program described above was based on testing FRP coupons submerged in 22 °C (72 °F) water with their edges coated to approximate 1-D diffusion conditions. For a concrete-filled FRP pile, the diffusion will be predominantly in the radial direction. Furthermore, the boundary conditions on the inner and outer surfaces of the FRP shell of the pile will be different from the boundary conditions of the experimental program. A more realistic estimation of the FRP strength as a function of time can be modeled by calculating the average moisture content of the FRP shell using the approach described in Appendix B and in Pando, et al. (2001). This approach involves calculating the moisture content of the FRP shell of the pile versus time, using a radial moisture diffusion model and incorporating more appropriate boundary conditions. Once the relationship between the FRP shell moisture content and time is computed, one can calculate the FRP strength-versus-time relationships using the experimental data presented in section 4.3. Although relationships of FRP properties versus time are useful, for the purpose of estimating the long-term capacity we only need the residual values for the FRP mechanical properties (i.e., the estimated long-term FRP properties).

4.4.1 Long-Term Structural Capacity of Composite Pile

This section presents a simplified example, intended for illustrative purposes only, to demonstrate the importance of considering evaluation of moisture aging effects on the FRP strength and stiffness (especially for bending capacity). The long-term structural capacity of concrete-filled FRP piles can be estimated using the short-term models for axial and flexural structural behavior by Fam and Rizkalla (2001a and b, 2002), coupled with the long-term mechanical properties of the FRP tube after degradation has occurred. The long-term mechanical properties of the FRP tube can be estimated using experimental relationships between FRP properties and moisture content, such as those

presented earlier in this chapter. The moisture content used to estimate the long-term FRP properties should correspond to the long-term average moisture concentration expected in the field for the FRP tube in the pile. A procedure to estimate the long-term moisture content for a cylindrical FRP is described in Appendix B and in Pando, et al. (2002b).

As an example, the long-term axial capacity for the 12-inch (0.31-m) Lancaster pile is estimated. With the FRP dimensions and as-received properties presented in Section 4.3.3, and using the model of Fam and Rizkalla (2001a and b), we obtain the axial load-strain response curve shown as a solid line in figure 75. If we now assume a 25 percent and 40 percent long-term reduction for the FRP hoop stiffness and strength, respectively, we obtain the long-term load-strain curve shown as the dashed line in this same figure (note these degradation values are higher than the measured degradation levels in this study). This represents approximately a 5 percent ultimate (structural) axial capacity reduction.

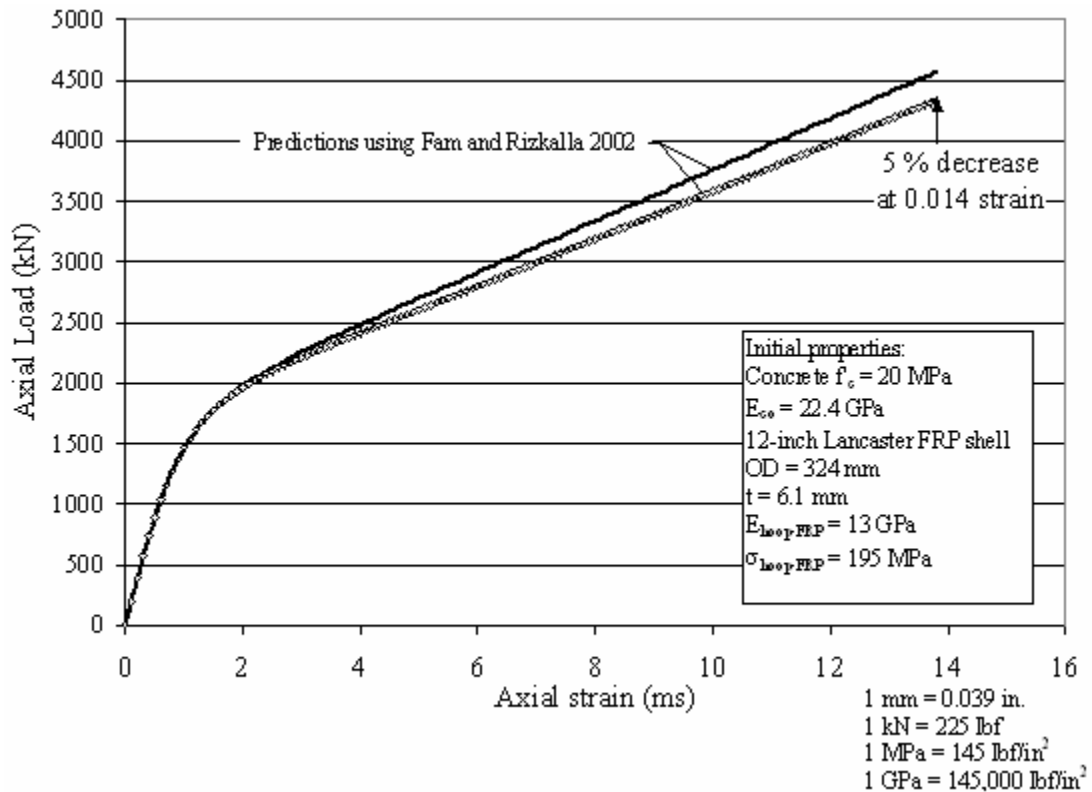


Figure 75. Graph. Estimated long-term axial capacity of the 12-inch Lancaster pile.

As shown in figure 75, the impact of degradation of the FRP mechanical properties on the long-term axial structural capacity of concrete-filled FRP composite piles is small due to the fact that the majority of the capacity contribution is from the concrete infill.

Similarly, the long-term flexural capacity (structural) for the same Lancaster pile can be predicted using the model proposed by Fam and Rizkalla (2002). The short-term moment-curvature response is shown as the solid line in figure 76. Assuming similar stiffness and strength reduction levels as before, but in the longitudinal direction, we

obtain the dashed moment-curvature line shown in figure 76. This represents a 24 percent reduction in the long-term structural flexural capacity.

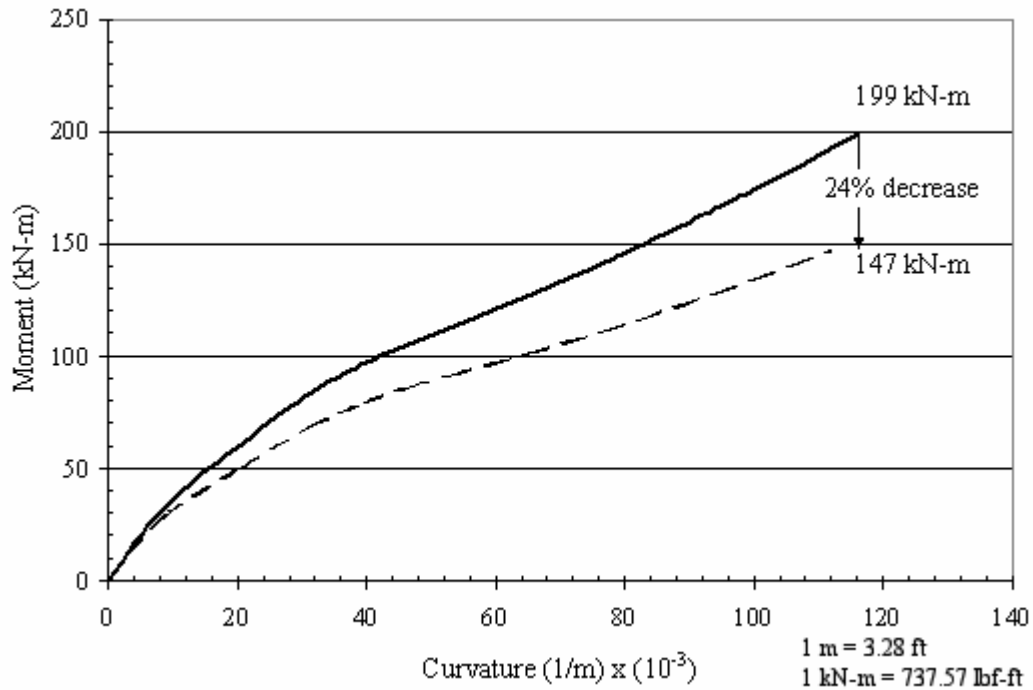


Figure 76. Graph. Estimated long-term flexural capacity of the 12-inch Lancaster pile.

Figure 76 shows that the impact of FRP degradation is more significant for the flexural capacity because the FRP shell provides most of the capacity contribution on the tension side of the pile in flexion.

4.4.2 Comments Related to the Axial Strain Levels in Piles

The structural ultimate limit state for axially loaded concrete-filled FRP columns or piles occurs at axial strain levels that exceed the normal range of ultimate strains typically used for normal unconfined concrete (e.g., 0.001 to 0.003). As shown in chapter 2, and as reported by Fam and Rizkalla (2002) and others, the presence of the FRP shell allows this type of structural element to undergo much larger axial strains (e.g., to about 0.009 to 0.013). It is important to compare these strain levels to the strain levels that can be allowed to develop in a pile before serviceability limits are exceeded.

The strain distribution along the pile depends on the soil conditions. A pile that develops all or most of its resistance from end bearing, such as piles with their tips founded on hard soil or rock, have almost a constant axial strain distribution with depth. For piles that develop their resistance from side friction, the strain decreases with depth at a rate dependent on the side friction distribution along the pile length. The maximum strain in a pile will occur within the portion of the pile above the ground surface. The maximum axial strains in an axially loaded pile will be influenced by the allowable pile settlement

determined from serviceability requirements. Typically the allowable settlement is between 25 and 50 mm (0.975 and 1.95 inches). For the case of an end-bearing pile with an allowable settlement of 37 mm (1.44 inches), the length of the pile would have to be less than 12 m (39 ft) to develop axial strains in the pile above 0.003. For piles carrying their load purely in side friction, and with an allowable settlement of 37 mm (1.44 inches), the length of the pile would have to be less than 24 m (79 ft) to start developing axial strains above 0.003. The pile lengths would have to be shorter if the allowable pile settlement is below 37 mm (1.44 inches). This simple example illustrates how the additional strength and ductility provided by the FRP shell may not be utilized in the field for piles with serviceability requirements, as described above. Thus, serviceability may control design of FRP piles in many practical applications.

4.5 SUMMARY

A laboratory testing program was completed to study the long-term performance of FRP composite pipe piles. This durability study, which addressed the FRP shells of Lancaster and Hardcore composite piles, included FRP shell characterization, determination of baseline mechanical properties, measurement of moisture absorption as a function of time and temperature, measurement of mechanical properties as a function of moisture absorption, and measurement of mechanical properties as a function of freeze-thaw cycles.

From the results of the durability study, the following conclusions and observations were made.

1. Moisture absorption has a small impact on the strength of some FRP composites, and a larger impact on others.
2. Curve fits using the Fickian and Langmuirian models were performed on the experimental moisture absorption data gathered for the different FRP shells evaluated in this study. The results indicate that Langmuirian diffusion, which has four curve-fitting parameters (D , M_{∞} , α , β), is better able to track the measured moisture absorption than the Fickian diffusion, which has two-curve fitting parameters (D , M_{∞}). This finding is particularly relevant for samples submerged at temperatures between 55 and 80 °C (131 and 176 °F).
3. The levels of strength degradation corresponding to steady state moisture contents reached after about 2.5 years of submergence were as follows:
 - Longitudinal tensile strength reductions on saturated FRP specimens were measured to be 0.5 , 7.1, 12.7, and 24.9 percent for the Lancaster 24-inch (0.61-m), Lancaster 12-inch (0.31-m), Hardcore 24-inch (0.61-m), and Hardcore 12-inch (0.31-m) samples, respectively.
 - Measured hoop tensile strength reductions due to moisture were 7.6, 17.3, and 19.6 percent for the Lancaster 24-inch (0.61-m), Lancaster 12-inch (0.31-m),

Hardcore 24-inch (0.61-m), and Hardcore 12-inch (0.31-m) samples, respectively.

4. Degradation of longitudinal mechanical properties for the 24-inch (0.61-m) Lancaster pile was not as significant as for the Hardcore pile because of the different fiber layups. The Lancaster pile was matrix dominated in the longitudinal direction because the fibers with closest alignment to the longitudinal axis were 35 degrees off alignment.
5. The impact of FRP degradation on the long-term structural capacity of the piles was investigated using models by Fam and Rizkalla (2001a and b, and 2002). This approach showed that, for a 12-inch (0.31-m) diameter FRP pile, the axial structural capacity will decrease about 5 percent if the FRP tube hoop properties degrade 25 percent and 40 percent in stiffness and strength, respectively. The small impact that the FRP degradation has on the axial pile capacity is due to the fact that majority of the capacity contribution is coming from the concrete infill. The impact on larger diameter piles is expected to be even smaller. For the flexural capacity of a 12-inch (0.31-m) pile, the results show that a 24 percent reduction in flexural capacity can be expected if the FRP tube longitudinal tensile properties degrade 25 percent and 40 percent in stiffness and strength, respectively. This result is as expected, because the concrete is weak in tension and the FRP tube provides the tensile reinforcement to the pile during bending.
6. Exposure to freeze-thaw cycles was found to have little effect on the longitudinal tensile properties of the saturated FRP tubes. This is based on longitudinal tensile tests on samples exposed to 100, 300, and 500 freeze-thaw cycles.

CHAPTER 5. FIELD LOAD TESTS AT THE ROUTE 40 BRIDGE

5.1 INTRODUCTION

In 2000, the Virginia Department of Transportation (VDOT) employed concrete-filled FRP composite piles for an entire bent of the new Route 40 Bridge over the Nottoway River in Sussex County, VA. As part of this project, a test pile program was performed at the bridge site to investigate and compare the driveability, axial load capacity, and lateral load response of a composite pile and a standard prestressed concrete pile. The same type of composite pile was used in the test pile program as was used in the bridge bent. This project is believed to be the first to use this type of composite pile in a long-term, load-bearing application such as a bridge. Previously, these piles have been primarily used in marine fendering projects, in light load applications, or for experimental research. A summary of the overall project and the main findings of the field load test program are presented in this chapter. Results from this project have also been published by Pando, et al. (2000), and Fam, et al. (2003).

5.2 DESCRIPTION OF THE BRIDGE

5.2.1 The Former Bridge

VDOT decided to replace the existing Route 40 Bridge (Structure No. 1006) over the Nottoway River in Sussex County, VA, at the location shown in figure 77. The old bridge, which consisted of a steel truss supported by concrete piers as shown in figure 78, suffered from excessive deterioration in both superstructure and substructure. Full-height vertical cracks existed in the concrete columns of the piers, as shown in figure 79(a). Spalling and cracking of the concrete bearing seats were observed, as shown in figure 79(b). Map cracking, up to 1.6 mm (1/16 inch) width, was also observed in the abutment bearing seats, as shown in figure 79(c). In addition to the deterioration of the substructure, excessive corrosion with large section losses was observed in the roller bearing devices of the truss supports. Additionally, the floor beams suffered from section losses up to 3.2 mm (1/8 inch) in both the web and bottom flanges. The bridge was functionally obsolete with a roadway clearance of only 7.3 m (24 ft) curb to curb, and was rated as scour critical.

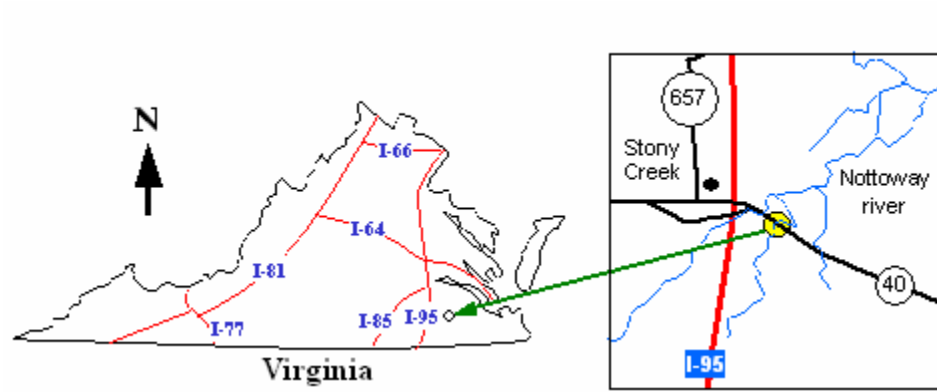
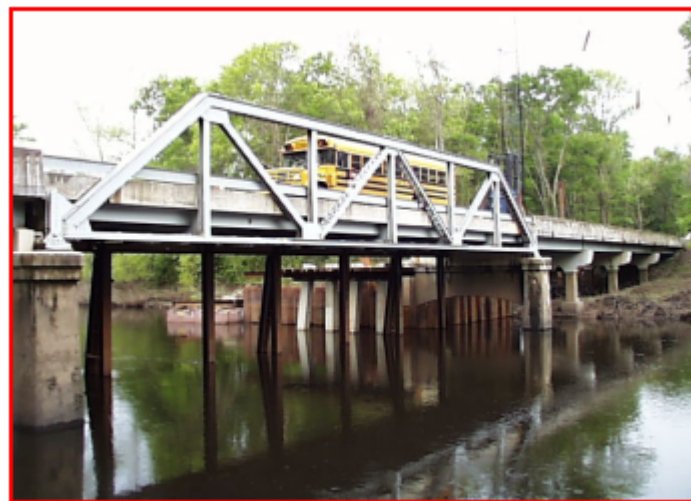
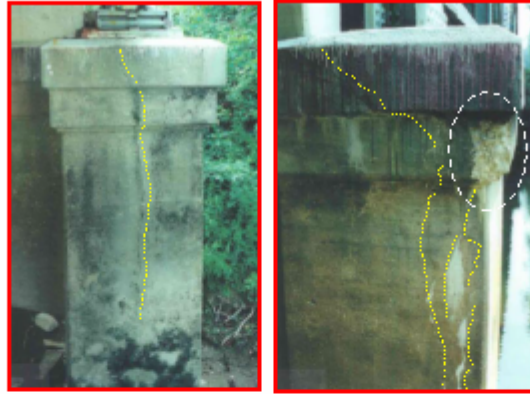


Figure 77. Map. Location map of the Route 40 Bridge project in Sussex County, VA (Fam, et al., 2003).



(Photo courtesy of VDOT)

Figure 78. Photo. Former Route 40 Bridge.



(a) Vertical cracks
In column (b) Spalling and cracking
of bearing seats



(c) Map cracking in beams

(Photos courtesy of VDOT)

Figure 79. Photos. Signs of deterioration of the former Route 40 Bridge (Fam, et al., 2003).

5.2.2 The New Bridge

The new bridge is 85.3 m (280 ft) long and 15.2 m (50 ft) wide, and consists of a five-span slab-type superstructure supported by four piers and two end abutments, as shown in figure 80. Each pier consists of a reinforced concrete beam-type elevated pile cap supported by ten piles. Based on the design requirements, VDOT specified a 508 mm (20-inch) prestressed solid square pile, as shown in figure 83. The design axial load of each pile was 667 kN (150 kips). As a part of the composite piles study sponsored by the Federal Highway Administration (FHWA), VDOT took the initiative to use an alternative composite pile system consisting of concrete-filled FRP tubes for the entire group of piles supporting Pier No. 2 (see figure 80). The objectives of the VDOT initiative were to examine the feasibility of using composite piles for bridge substructures, particularly to examine the driveability of the piles using conventional pile drivers, to assess performance under axial and lateral loading conditions using full-scale field tests, and to compare composite piles to conventional prestressed concrete piles. The following

section provides a brief description of both the prestressed concrete test pile and the precast composite test pile.

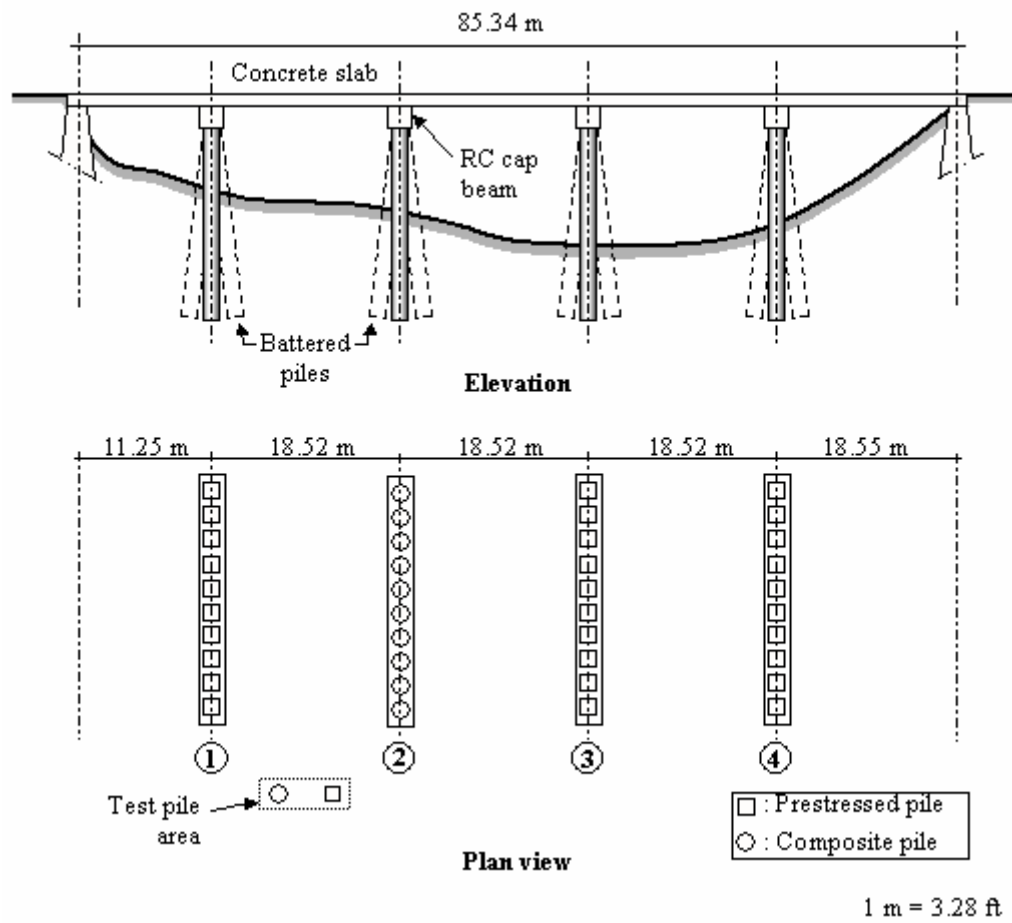


Figure 80. Illustration. Schematic of the new Route 40 Bridge.

5.3 DESCRIPTION OF TEST PILES

5.3.1 Composite Test Pile

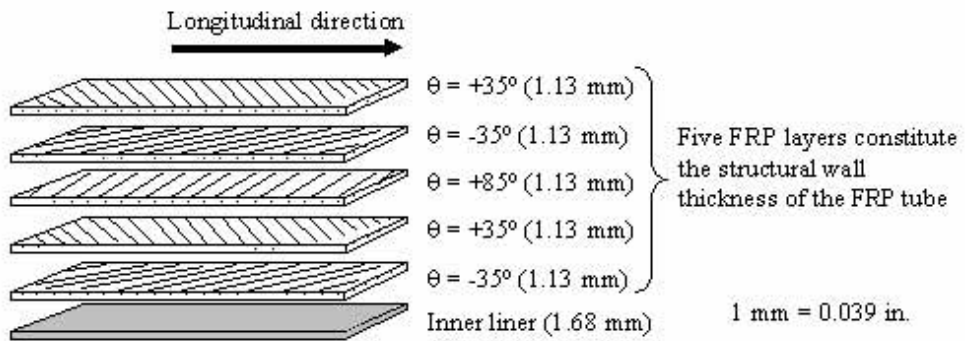
The composite test pile used for this project consists of a concrete-filled tubular FRP pile, in which the FRP tube serves as both a permanent lightweight noncorrosive formwork for the concrete and a reinforcement element. Figure 81(a) is a photograph of the composite piles installed at bridge bent No. 2. The FRP tube is composed of several layers of fibers embedded in a polymeric resin. The layers of fibers are oriented in several different directions with respect to the longitudinal axis of the tube in order to provide strength and stiffness in both the axial and circumferential directions. The circumferential stiffness and strength of the FRP tube provides confinement to the concrete core under axial stress. This confinement increases the strength and ductility of the pile. The axial strength of the FRP tube contributes to the flexural strength of the pile.

A 13.1 m (43 ft) long GFRP tube, type CP40, was fabricated using a filament-winding technique wherein E-glass continuous fiber rovings were impregnated with polyester resin and wound over a rotating steel mandrel, following a predetermined winding pattern. The average measured fiber volume fraction of the FRP tube was 51.2 percent. The FRP tube has an average outer diameter of 625 mm (24.6 inches) and a total wall thickness of 7.35 mm (0.289 inches). The tube has a 1.68-mm- (0.066-inch-) thick liner at the inner surface, which results in a net structural wall thickness of 5.67 mm (0.223 inches). The wall structure of the tube consists of five layers, each 1.13 mm (0.044 inches) thick. The two inner and outer layers contain fibers oriented at $\theta = \pm 35$ degrees, where θ is the inclination of the fibers with respect to the longitudinal axis of the tube. The middle layer, which is sandwiched between the inner and outer layers, contains fibers oriented at $\theta = 85$ degrees, which means that the middle fibers are oriented nearly circumferentially. The laminate structure of the FRP tube is shown in figure 81(b). The mechanical properties of the FRP tube are provided in table 27.

The FRP tube was filled with a concrete mix that includes an expansive additive to reduce the effect of shrinkage and thereby enhance the bond between the concrete and the FRP tube. The specified compressive strength of the concrete fill at 28 days is 41.4 MPa (6 ksi). Compressive strength tests carried out on concrete core samples from the composite test pile are shown in figure 82. The measured compressive strength is about 60 MPa. The measured modulus of elasticity is about 15 GPa, which is smaller than the typical values expected for normal concrete of the same compressive strength. The reason for the small modulus of elasticity value for the concrete in the composite pile was not investigated, but it could be related to the expansive additive.



a) Photograph of composite piles installed at Pier No. 2 of the Route 40 Bridge



b) FRP tube laminate structure of composite pile

Figure 81. Photo and Illustration. Concrete-filled tubular piles.

Table 27. Mechanical properties of FRP shell of composite pile.

Mechanical Property*	Longitudinal Axial Direction	Hoop Direction
Tensile strength	113 MPa	138 MPa
Tensile modulus**	15 GPa	22.1 GPa
Strain to failure	1–1.4%	1.25%

Notes: * From coupon tests (see chapter 4 for more details on mechanical properties of FRP shell)

** Elastic modulus for the strain range between 0 to 4,000 microstrains.

1 MPa = 145 lbf/inch²; 1 GPa = 145,000 lbf/inch²

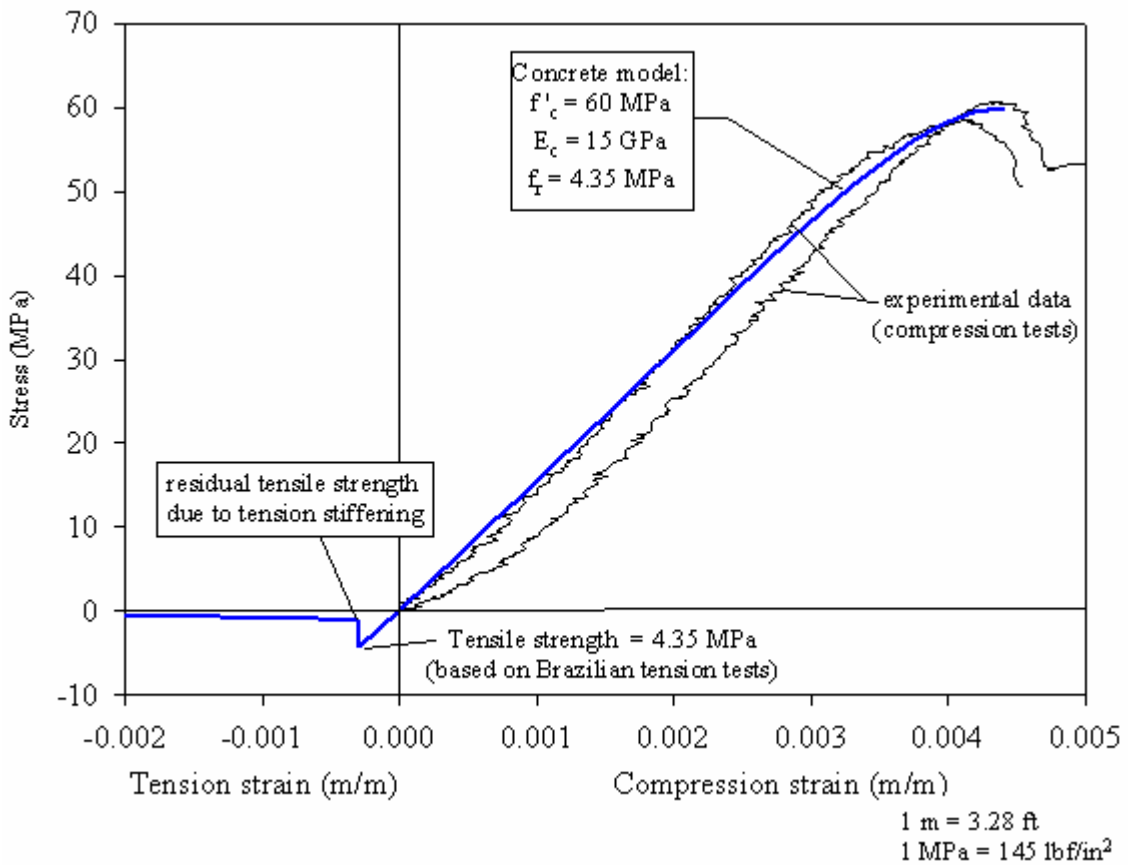


Figure 82. Graph. Stress-strain response of concrete used in the composite pile.

5.3.2 Prestressed Concrete Test Pile

The performance of the composite test pile was compared with that of a prestressed concrete test pile, which is the pile type commonly used in VDOT bridge projects. The prestressed concrete test pile is a 508-mm (20-inch) square pile with a length of about 13.1 m (43 ft). Figure 83 shows the pile details. The pile is prestressed using a total of fourteen, 12.7-mm (0.5-inch) diameter, 7-wire strands of 1861 MPa (270 ksi) ultimate strength, pretensioned to produce a prestress level of 5.6 MPa (0.809 ksi) in accordance with VDOT standards. The specified concrete compressive strength at 28 days is 40 MPa (5.8 ksi). The ties consist of No. 16M (No. 5) gage spiral wire, as shown in figure 83. Concrete test results indicated a 28-day compressive strength of about 43 MPa (6.2 ksi) for this pile.

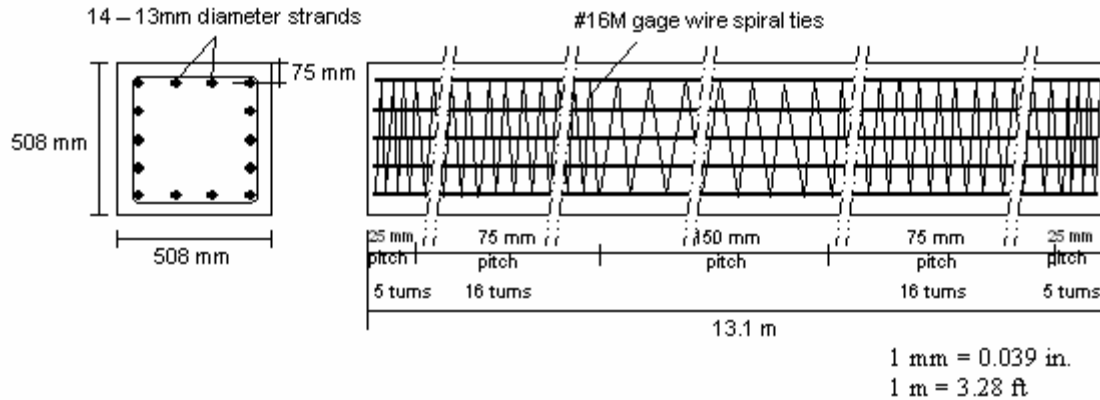


Figure 83. Illustration. Reinforcement details of prestressed concrete pile.

5.4 SOIL CONDITIONS AT THE TEST SITE

In general, the soil conditions in the vicinity of the test piles consist of about 7.9 m (25.9 ft) of loose to medium-dense silty sand with some gravel, underlain by very stiff to hard silty clay, as shown in figure 84. The clay was encountered to the maximum depth investigated, which was 15.7 m (51.5 ft). The ground water level was observed at a depth of about 8.1 m (26.6 ft).

The sand in the upper 4 m (13.1 ft) was brown, medium fine, with some fine gravel and traces of silt. Standard penetration resistance (SPT) blow counts (N-values) in the upper sand were five blows per 0.3 m (0.98 ft), which is indicative of a loose relative density. The sand below 4 m (13.1 ft) and extending to a depth of 7.9 m (25.9 ft) was brown to gray, fine-grained, silty with some gravel. SPT blow counts in the lower sand ranged from 17 to 25 blows per 0.3 m (0.98 ft), which corresponds to a medium density. Underlying the sand was green, very stiff to hard, silty clay, with SPT blow counts ranging from 41 to 88. The average SPT N-value below 10 m (32.8 ft) depth was 75 blows per 0.3 m (0.98 ft). The near-surface stratum of loose sand comprises the soil of most significance to the lateral response of the piles.

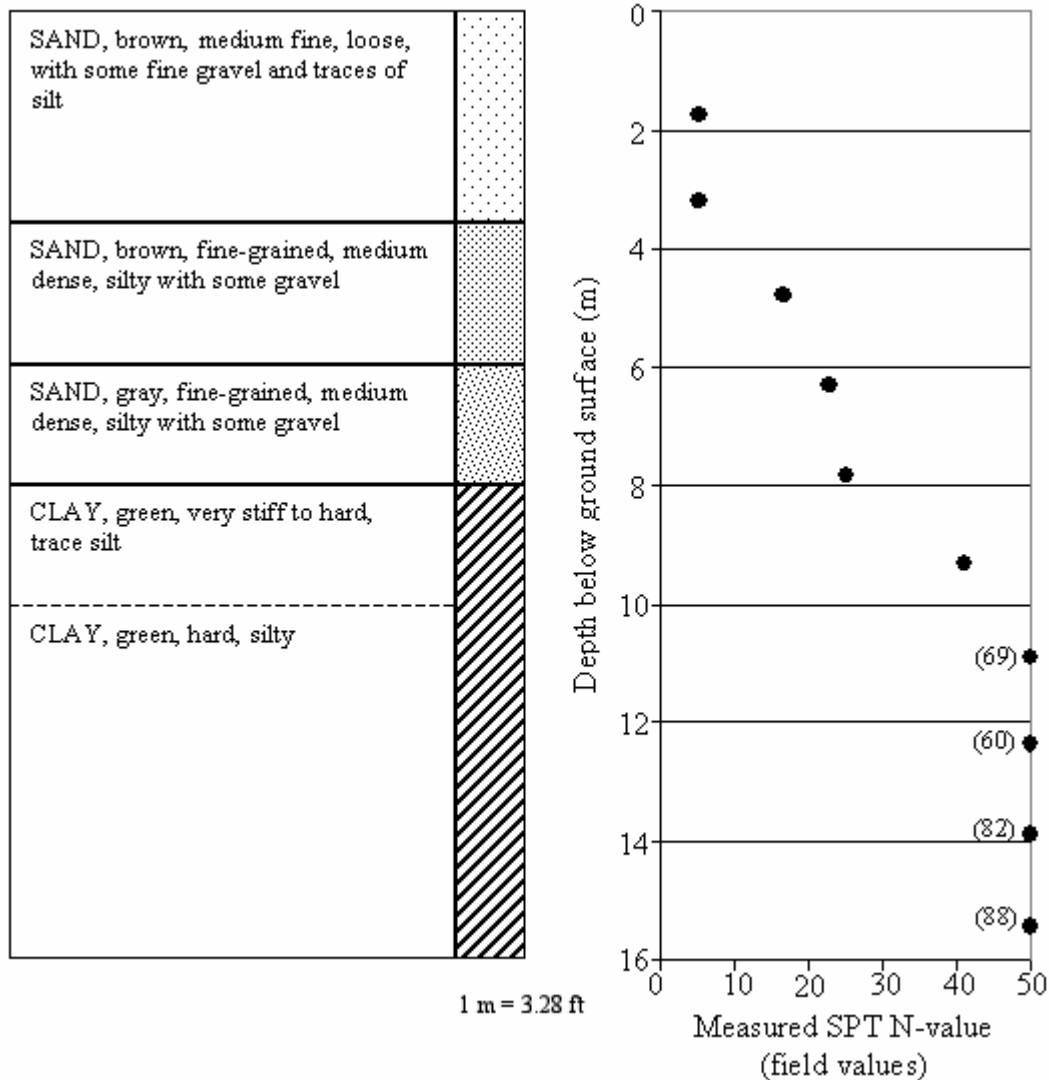


Figure 84. Illustration. Simplified soil stratigraphy near test pile area.

5.5 PILE FABRICATION AND INSTALLATION

5.5.1 Fabrication of the Piles

The prestressed concrete piles were fabricated at the precasting plant in accordance with VDOT standards, as shown in figure 85. After fabricating and curing, the piles were shipped to the bridge site. The FRP tubes for the composite piles were shipped to the precast plant and filled with concrete while held in an inclined position and supported by a steel beam along the full length of the tubes, as shown in figure 86(a and b). Wooden end plugs were used to seal both ends of the tube. The plugs were secured in position using metal straps connected to both the plug and the composite tube in radial directions, as shown in figure 86(b). Concrete was pumped into the upper end through a hole in the wooden plug. The concrete-filled composite tubes were handled using eight-point lifting devices along the length of the pile, as shown in figure 86(c).



Figure 85. Photo. Fabrication of prestressed concrete pile.



(a) Pumping concrete into the upper end



(b) Rear end showing wooden plugs



(c) Handling of the pile using 8-point supports

(Photos courtesy of Dr. E. Hoppe)

Figure 86. Photos. Fabrication of concrete-filled FRP Piles.

5.5.2 Pile Installation

Both the composite and prestressed test piles were driven using a hydraulic impact hammer, type ICE model 160S, which was also used to drive the production piles for the Route 40 Bridge. The ram weight is 71.2 kN (16,000 lbs), and the manufacturer's rated energy at the maximum stroke of 1.2 m (3.9 ft) is 85.4 kN-m (63,025 lbf-ft). A 190-mm- (7.5-inch-) thick plywood pile cushion was used during pile driving. Figure 87(a and b) shows the composite pile during and after driving, as well as the prestressed pile during driving.



a) Driving of composite pile

b) Driving of prestressed pile

Figure 87. Photos. Driving of test piles.

First, the composite pile was driven to a depth of about 8.5 m (27.9 ft), which was slightly above the originally planned embedment depth. The composite pile driving was stopped sooner than planned based on the driving monitoring information, which suggested that the 4,000 kN Statnamic device might not have been sufficient to test the pile if the pile were driven deeper. Next, the prestressed pile was driven to a 9.4 m (30.8 ft) depth. This depth produced the same pile tip elevation for both test piles. Figure 88 shows the driving records for both piles expressed in terms of number of blows per 0.25 m (0.82 ft) versus the depth of the pile tip below the driving template. At the end of driving, the blow count was 6 blows per 25 mm (1 inch) of pile penetration for the composite pile and 4 blows per 25 mm (1 inch) for the prestressed concrete pile.

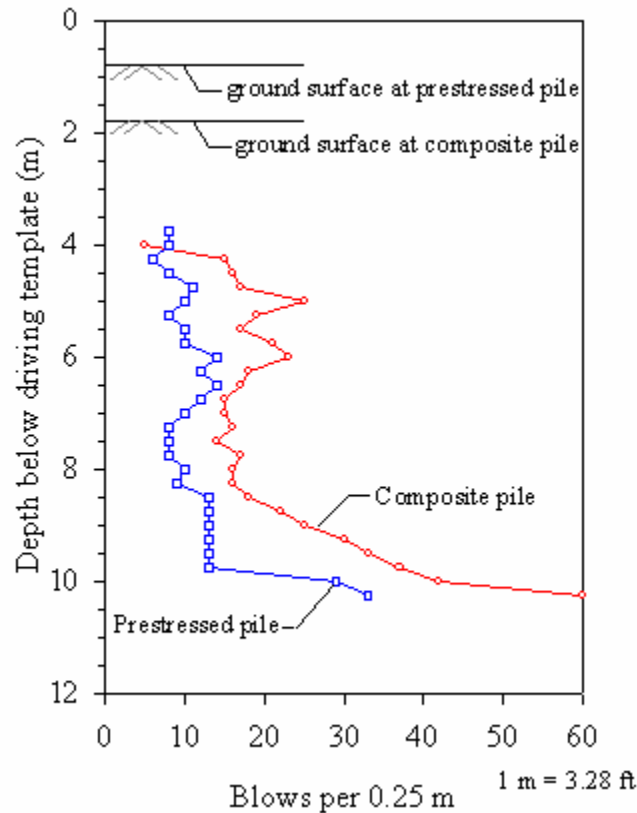


Figure 88. Graph. Driving records for test piles.

During pile driving, two sets of independent dynamic measurements were taken: Pile Driving Analyzer (PDA) measurements recorded by Federal Highway Administration (FHWA) personnel, and Foundation Pile Diagnostic System (FPDS) measurements. A summary of the most relevant dynamic testing results is presented herein, and a more detailed discussion can be found in Muchard, et al. (1999). Dynamic testing was accomplished by attaching strain transducers and accelerometers at about 2 diameters from the top of the piles in pairs spaced 180 degrees apart. To attach the transducers to the composite pile, small windows were cut out of the FRP shell, which allowed the instrumentation to be directly attached to the concrete infill. PDA records for both types of piles at the end of initial driving are shown in figure 89. Both pile types show similar dynamic behavior. The PDA records for both piles show two force peaks: the first at about 0 and the second at about L/c (where L is the pile length, and c the wave speed). This type of response is produced by the natural frequency of the hammer and driving train used. A velocity peak can also be seen at about $2L/c$. This peak is characteristic of reflected tensile waves from the toe. The recorded driving tensile stresses were relatively small. This is partly explained by the relatively heavy hammer, which generates larger compressive waves than the reflected tensile waves coming up from the toe. Table 28 provides some of the measurements obtained during pile driving. It can be seen that the wave speeds, maximum compressive stresses, and maximum tensile stresses are each similar in the different pile types. The measured stress levels are lower than the allowable stresses recommended for prestressed piles (Hannigan, et al., 1996). No standards are

currently available for allowable driving stresses of composite piles. Estimates of pile capacity from the dynamic strain and acceleration measurements were obtained using the Case method (Muchard, et al., 1999). Using a Case damping value of 0.4, Muchard, et al., (1999) estimated end-of-driving pile capacities of 3390 kN (762 kips) and 3160 kN (710 kips) for the composite and prestressed test piles, respectively.

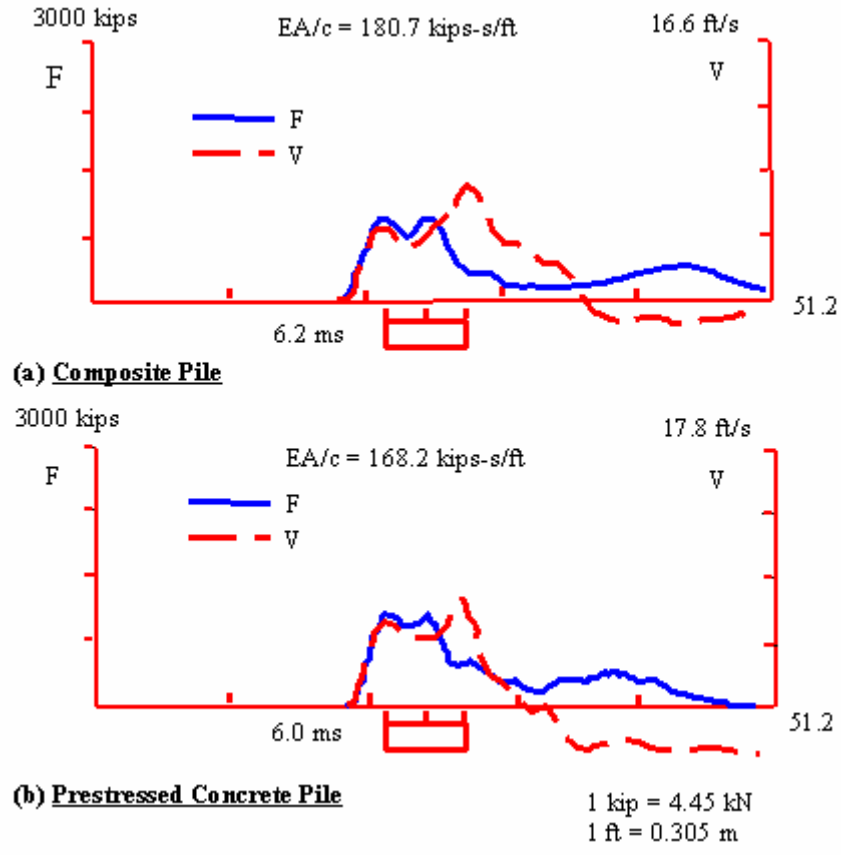


Figure 89. Graphs. End-of-driving PDA recordings.

Table 28. Pile-driving measurements for the prestressed and composite piles.

Measurement	Pile Type	
	Prestressed	Composite
Wave speed	3705 m/s	3612 m/s
Maximum compression stress measured during driving	17.6 MPa	19.2 MPa
Maximum tensile stress measured during driving	4.8 MPa	2.9 MPa
Allowable stresses	Tension < 7 MPa Comp. < 31 MPa	No standards available

1 m = 3.28 ft; 1 MPa = 145 lbf/inch²

Using the TNOWAVE wave equation software, Muchard, et al. (1999), performed signal-matching analyses on strain and acceleration data for selected blows near the end of each pile driving. The signal matching was performed using a two-layer soil model consisting of a 7.5 m (24.6 ft) sand layer overlaying stiff clay. The predicted capacities from signal-matching analyses are summarized in table 29.

Table 29. Summary of signal-matching analyses at end of driving (from Muchard, et al., 1999).

Pile Type	Signal-Matching Analyses Predicted Capacity		
	Total	Skin	End Bearing
Prestressed	3070 kN	1780 kN	1290 kN
Composite	3140 kN	1750 kN	1390 kN

1 kN = 225 lbf

The signal-matching analyses predictions suggest that about 57 percent of both pile capacities is due to skin friction contribution. When comparing the pile capacities described above, it is important to keep in mind the differences in end bearing and skin friction areas of the piles. Due to differences in cross section and embedment depths, the composite pile has a skin area 12.6 percent smaller, and a tip area 18.9 percent larger, than the prestressed pile.

5.6 STATNAMIC FIELD TESTING OF TEST PILES

Prior to installation of the production piles for the new Route 40 Bridge, the two test piles were subjected to axial and lateral loading using a Statnamic testing device. The Statnamic testing system is a patented system. This system applies the load to the pile by

combustion of fuel within a closed chamber, in which gas pressure builds and “launches” a heavy reaction mass upward (or laterally) at a very high acceleration close to 20 g’s. When the reaction mass is launched, an equal and opposite reaction force acts on the test pile. The Statnamic setup is such that the load is applied in a somewhat gradual manner, as opposed to an impact load like the one produced by a driving hammer. The applied force is a time-dependent load with a duration typically between 0.2 to 0.3 seconds. From the recorded Statnamic force, one can estimate the equivalent static load by subtracting the inertia and damping forces. This equivalent static force can be derived by using the Unloading Point Method (UPM) proposed by Middendrop, et al. (1992). The Statnamic test methodology and data reduction procedure have been described by Middendrop, et al. (1992), and Brown (1994).

The following sections provide a description of the instrumentation used for Statnamic testing, and a summary of the most relevant Statnamic test results carried out at the Route 40 Bridge. The main goal of this discussion is to provide some insight on the relative performance of the composite pile compared to a prestressed concrete pile. Detailed coverage and discussion of the Statnamic load test results carried out for this project are presented in Muchard, et al. (1999).

5.6.1 Instrumentation

Both the composite and the prestressed concrete test piles were instrumented with strain gages in the axial direction at three levels along the length of the piles. At each level, two strain gages were placed near the two opposite faces of the pile, as shown in figure 90. The strain gages were mounted on 914-mm- (36-inch-) long No. 13M steel bars, embedded in the concrete core. After completion of axial load testing, each test pile was also instrumented with a string of eight lateral motion sensors to measure the lateral displacement profile of the pile during lateral Statnamic load testing. The sensors were lowered inside a slope inclinometer casing embedded in the test piles. The locations of the lateral motion sensors are shown in figure 90. One embedded accelerometer was installed near the pile toe to measure the pile toe movement during Statnamic axial load tests.

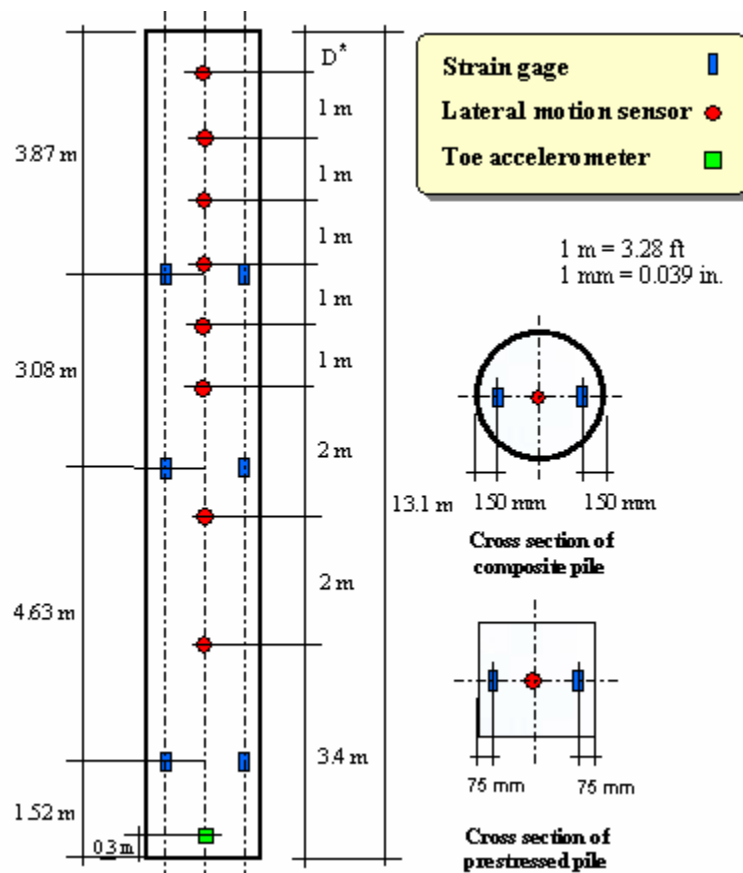


Figure 90. Illustration. Test Pile Instrumentation.

5.6.2 Axial Load Tests

Axial Statnamic load tests were carried out on both test piles seven days after pile driving. The axial load setup using the Statnamic testing system is shown in figure 91. During the Statnamic test, several measurements are taken, including the applied load, the pile head displacement, the toe accelerometer readings, and strains. Pile head displacement is measured using a laser beam device shown in figure 91. A detailed description of the Statnamic technique can be found in Brown (1994). Each test pile was subjected to three loading cycles with an increasing magnitude of applied load.

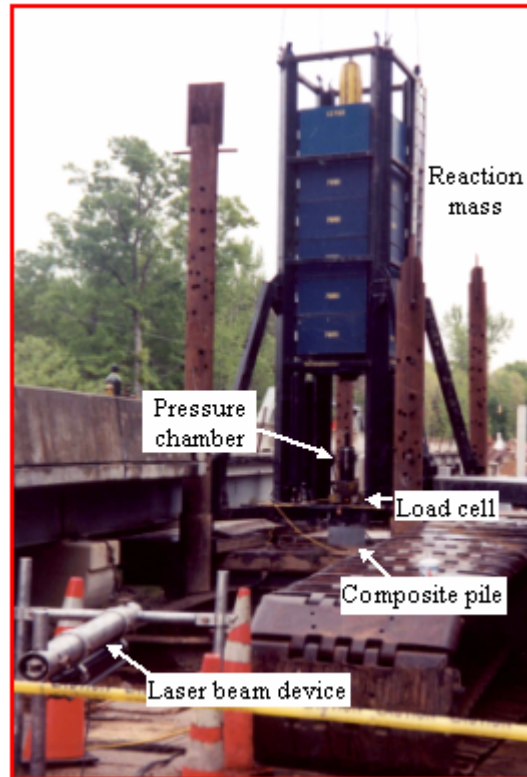


Figure 91. Photo. Axial load test using the Statnamic device.

The equivalent static load versus pile head axial displacement for the prestressed concrete and composite piles for the three cycles are shown in figure 92. In both piles, the behavior during the last cycle showed that the geotechnical capacity of the piles was fully mobilized, as evident from the rapid increase of the pile displacement near the end of the test. Davisson's failure criterion (Davisson 1972) was applied considering the failure envelope encompassed by all three load cycles. Based on this criterion, the composite pile has an ultimate load capacity of 4,359 kN (980 kips) at a head displacement of about 18 mm (0.70 inch). The Davisson criterion was not satisfied for the prestressed concrete pile. However, the maximum load applied was 4,190 kN (942 kips) at a displacement of about 13 mm (0.51 inch). Both piles exhibited similar axial capacities, even though their shaft areas and end areas are slightly different.

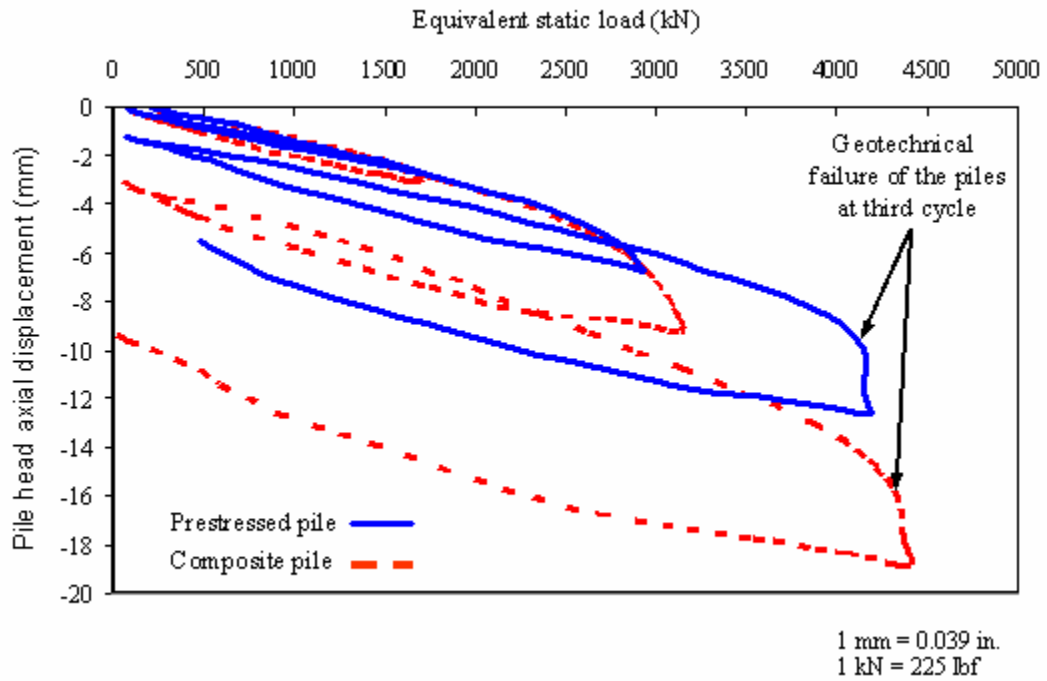


Figure 92. Graph. Pile head displacement versus equivalent axial static load.

Figure 93 shows the equivalent axial static load versus axial strain behavior of both the composite and prestressed piles based on the peak load and corresponding strain during each of the three load cycles. The axial strain is based on the average strain of the two uppermost strain gages (closest to the loading end), since they measured the maximum axial strain induced in the pile. Figure 93 shows that the behavior of the two piles was relatively similar, with the composite pile being slightly stiffer than the prestressed pile. The figure also shows that the design load of the piles, 667 kN (150 kips), is significantly lower than the ultimate load.

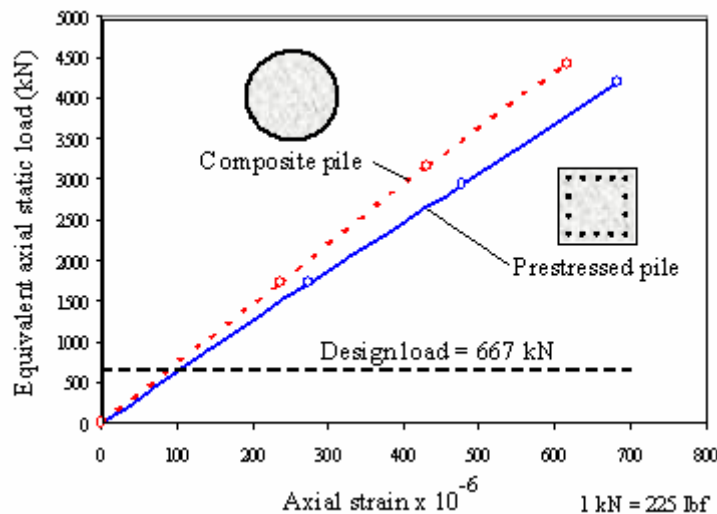


Figure 93. Graph. Axial load—axial strain behavior of test piles.

The variation of the axial strains along the length of both the prestressed and composite piles is shown in figure 94. It can be seen that the measured strains along the depth are similar in both piles. The figure also shows that the strain level is reduced with increasing depth; this is attributed to the gradual transfer of axial load from the pile to the soil through skin friction along the pile shaft.

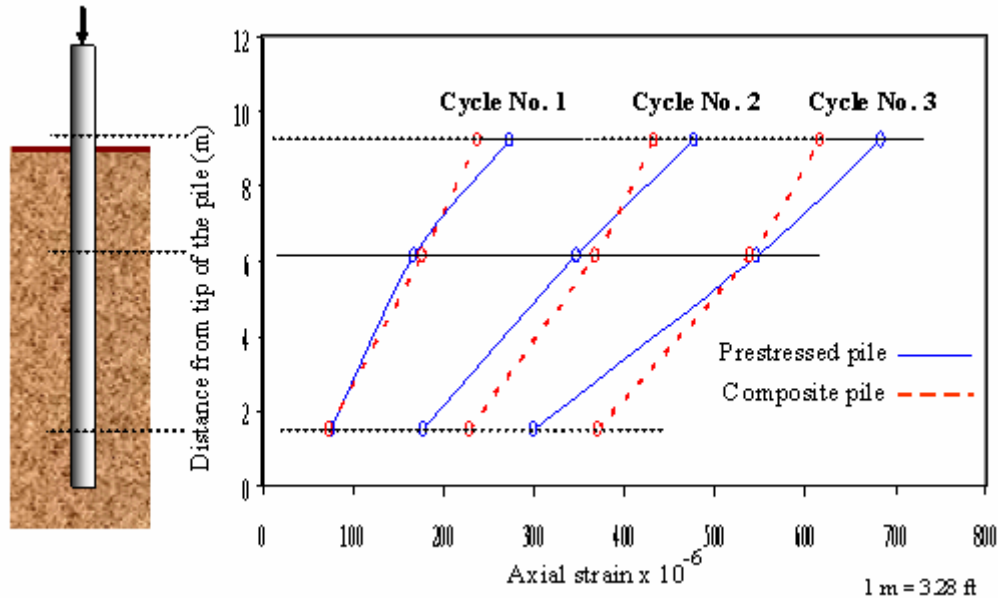


Figure 94. Illustration and Graph. Variation of axial strain along pile length for three Statnamic loads.

5.6.3 Lateral Load Tests

Following the axial load tests, lateral load tests were conducted on both the composite and prestressed piles using the Statnamic Testing System shown in figure 95. The loading system is similar to that used for the axial load test; however, the setup was placed horizontally in order to produce a lateral load. The thrust against the pile is transferred through a calibrated load cell and hemispherical bearing. During lateral Statnamic testing, several measurements are taken, including the applied load and the lateral displacement of the pile at different depths. The two test piles were subjected to four progressively increasing cycles of load, with measured peak forces ranging up to about 290 kN (65,250 lbf) for the composite pile and about 350 kN (78,750 lbf) for the prestressed concrete pile. The Statnamic device operated on a sled resting upon falsework, which supported the device so that the loading was applied at the same elevation for both piles. Based on the falsework elevation, the point of lateral load application was approximately 3 m (9.84 ft) and 2 m (6.56 ft) above the ground surface for the composite and prestressed pile, respectively. As noted earlier, the ground surface elevation at the prestressed concrete pile is about 1 m (3.28 ft) higher than at the composite pile.

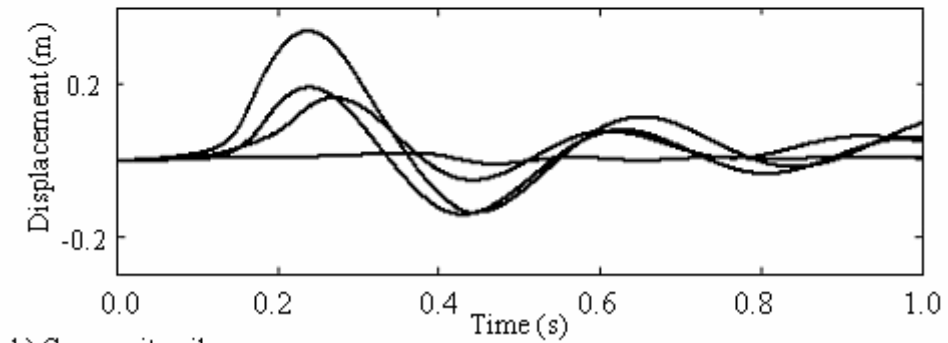
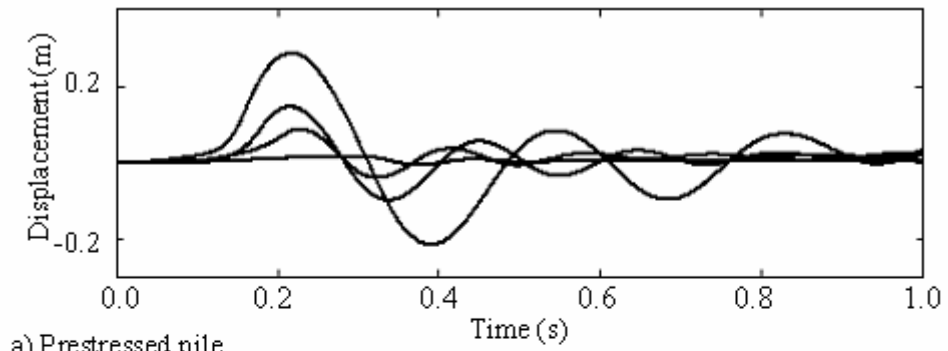


Figure 95. Photos. Lateral Statnamic setup at the Route 40 project.

The responses of the test piles were measured using multiple displacement transducers and subsurface accelerometers. Redundant measurements of displacement at the point of loading were made using both types of instruments. For subsurface displacements, eight down-hole lateral motion accelerometers were used to track the lateral movement profiles of the piles (see figure 90). The accelerometers were placed inside inclinometer casings at depths ranging from near the top of the pile to 8.8 m (28.9 ft) below the loading point. The time-dependent displacement at the location of each accelerometer was derived by double integration of the recorded acceleration versus time record. All of the data were monitored using a data acquisition system with a sampling rate of 5,000 samples per second for each channel. Data were recorded with a pretrigger of about 0.3 seconds prior to firing the Statnamic device and a duration after trigger of 1 to 2 seconds.

The plots in figure 96(a and b) are the displacement versus time records at the loading point for each of the four loads applied to the prestressed concrete pile and the composite pile, respectively. It can be seen that the period of oscillation increased with increasing displacement amplitude, indicating nonlinearity in the pile response. Compared to the prestressed concrete pile, the larger displacement amplitude (at a smaller maximum load) and lower frequency (longer period) of the composite pile indicates a less stiff lateral response.

The peak lateral displacements obtained from the string of subsurface lateral motion accelerometers provide the displaced shapes shown in figure 97 for each of the four cycles of Statnamic load applied to each pile. Both piles appeared to form a hinge at a depth of about 5 m (16.4 ft) below the point of loading. For the last two load cycles, the deflection profile along the depth of the piles was almost bilinear, with a sudden change in slope occurring at a depth of about 4.8 m (16 ft) measured from the loading point. This suggests that failure may have been initiated in both piles at the location of the sudden change in slope during the last two cycles.



[1 m = 3.28 ft]

Figure 96. Graphs. Displacement time histories at the loading point for both piles (Pando, et al., 2004).

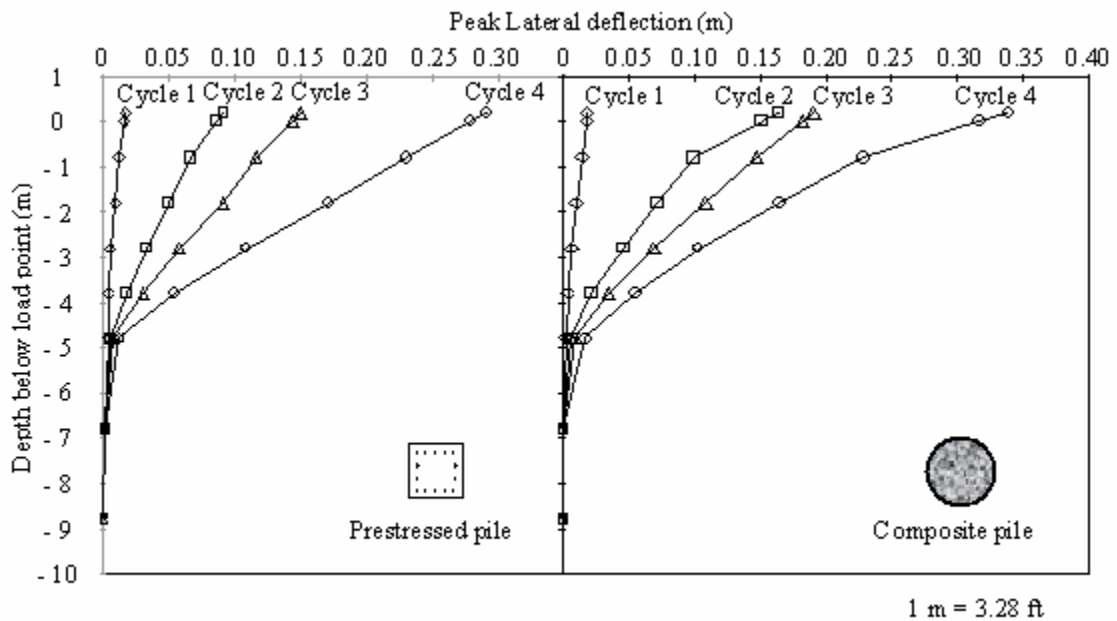


Figure 97. Graphs. Peak lateral displacement profiles for both test piles at different cycles of Statnamic load.

A simple, single-degree-of-freedom system model, as described by Brown (unpublished paper), can be used to derive the equivalent static pile response from the Statnamic lateral test measurements. Interpretation of the Route 40 lateral Statnamic data was originally presented by Muchard, et al. (1999). More recently, Pando, et al. (2004), reanalyzed the data incorporating the composite pile nonlinearity. A summary of the methodology for lateral Statnamic data reduction is presented below.

The single-degree-of-freedom model includes inertia of the pile rotating about a hinge point below the groundline, a viscous damping component, and a nonlinear static spring resistance.

$$F_{statnamic} = F_{inertia} + F_{damping} + F_{static} \quad (9)$$

where

$F_{statnamic}$ = measured force on the Statnamic load cell

$F_{inertia}$ = inertial resistance from effective mass of the foundation

$F_{damping}$ = effective viscous damping resistance

F_{static} = effective static soil resistance

The inertial resistance is approximated as that of a cylinder rotating about its base, with a diameter equal to that of the pile and a height taken as approximately 5.5 meters (18.0 ft). The height is based on the observed depth of about 5 m (16.4 ft) to a hinge, as shown in figure 97, plus the 0.5 m (1.6 ft) of pile that extends above the loading point. For a round pile of radius (r), height (h), and mass (m), the mass moment of inertia about the base (I_y), is

$$I_y = m \left(\frac{r^2}{4} + \frac{h^2}{3} \right) \quad (10)$$

and for a square pile of width b, I_y is

$$I_y = m \left(\frac{b^2}{12} + \frac{h^2}{3} \right) \quad (11)$$

The rotational acceleration of such a cylinder in relation to a displacement x at the loading point z (approximately 5 m (16.4 ft) above the base of the rotating cylinder in this case) would be \ddot{x}/z . Equating expressions for the inertial moment about the base,

$$(F_{inertia})_z = (I_y) \frac{\ddot{x}}{z} \quad (12)$$

Therefore,

$$F_{inertia} = (I_y) \frac{\ddot{x}}{z^2} = m_e \ddot{x} \quad (13)$$

where $m_e = I_y/z^2$.

The effective mass (m_e) may be thought of as a lumped mass, which if placed at the loading point z, would produce the same inertial reaction as the rotating cylinder. For the

tests at the Route 40 site, m_e is calculated to be 1.36 kN-s²/m (93.3 lbf-s²/ft) for the prestressed concrete pile and 1.6 kN-s²/m (109.8 lbf-s²/ft) for the composite pile. In order to include the effect of some accelerating mass from the soil surrounding the piles, this effective mass is increased slightly and is estimated as approximately 1.5 and 1.75 kN-s²/m (102.9 and 120.1 lbf-s²/ft) for the prestressed concrete and composite piles, respectively.

The damping resistance is represented by a viscous damper in which the force $F_{damping}$ is proportional to the velocity, \dot{x} , by a constant, c (which is in units of force-time/length). In order to relate this more meaningfully to a system damping parameter, the damping constant, D , is expressed as a percentage of the critical damping, c_c , by

$$D = \frac{c}{c_c} = \frac{c}{2\sqrt{km_e}} \quad (14)$$

where k is the static stiffness. Thus,

$$F_{damping} = c\dot{x} = D(2\sqrt{km_e})\dot{x} \quad (15)$$

The static resistance, F_{static} , is modeled as a function of displacement, x , using a spring with stiffness, k , that varies with each load level. The spring stiffness, k , represents the effect of the entire lateral soil reaction along the length of the pile. The soil response for lateral loading at large strains is known to be highly nonlinear. Pando, et al. (2004), took into account the nonlinear stiffness of the soil by using a linear stiffness for each load, but decreasing the value of k as the load magnitude increases.

The model uses equations 9, 13, and 15, and the parameters are m_e , D , and k . Because m_e was evaluated as described above for the test piles, the only unknown parameters are D and k . Values of D and k were obtained by fitting the model to the data shown in figure 96. The parameter values that produced the best fit with the data for the prestressed concrete pile model are: an effective mass, m_e , of 1.5 kN-s²/m (102.9 lbf-s²/ft) an effective damping ratio, D , ranging from 25 percent at small loads to 18 percent at the largest load; and a stiffness, k , that varies from 2,000 kN/m (137,200 lbf/ft) at small displacements (less than 20 mm (0.78 inch)) to 500 kN/m (34,300 lbf/ft) at the maximum displacement. The parameter values that produced the best fit for the composite pile model are an effective mass (m_e) of 1.75 kN-s²/m (120.1 lbf-s²/ft); an effective damping ratio (D) ranging from 25 percent at small loads to 18 percent at the largest load; and a stiffness (k) that varies from 2,000 kN/m (137,200 lbf/ft) at small displacements (less than 20 mm (0.78 inch)) to 360 kN/m (24,696 lbf/ft) at the maximum displacement. The lower stiffness of both piles at large amplitudes, and of the composite pile relative to the prestressed pile, are indicated by the lower frequencies of motion.

Using these parameter values, both the static soil resistance, F_{static} , and the total soil resistance, $F_{static} + F_{damping}$, can be calculated. The peak values of F_{static} and $F_{static} + F_{damping}$ versus displacement at the loading point for each cycle of Statnamic loading are plotted in figure 98. It can be seen that the resistance contributed by damping is not large. The figure also demonstrates that there is a pronounced change in the slope of the load versus deflection curve for the composite pile at a lateral load of about 50 kN (11,250 lbf),

indicating that first cracking of the composite pile may have occurred at this load. However, the composite pile exhibits a continuing capacity to sustain additional lateral load, albeit at substantially larger displacements. The prestressed concrete pile, on the other hand, exhibits a change in slope of its load versus deflection curve at a lateral load of about 125 kN (28,125 lbf), with comparatively little ability to sustain additional load beyond that point.

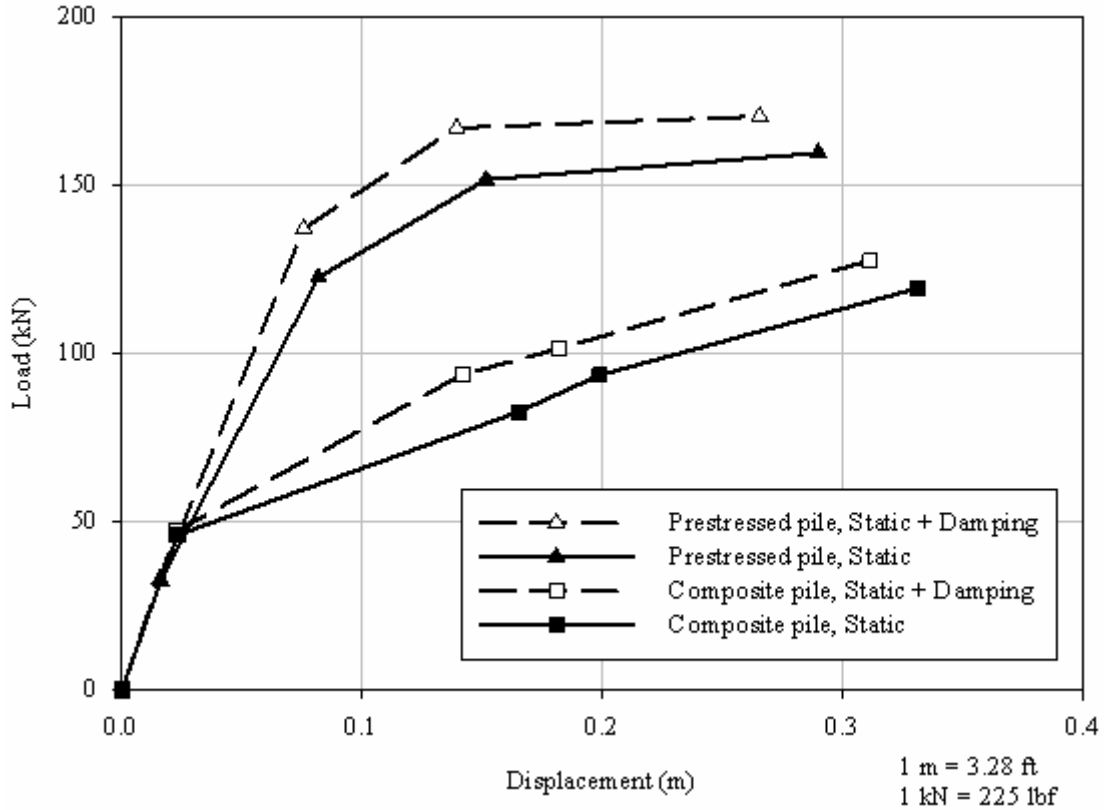


Figure 98. Graph. Calculated static and dynamic (static + damping) resistances for both test piles.

Pando, et al. (2004), performed p-y lateral pile analyses to predict the lateral load-deflection behavior of the Route 40 test piles. The analyses were carried out using the program LPILE (Reese, et al., 2000) and incorporated nonlinearity of both the soil resistance, P, and the pile flexural stiffness, EI.

The nonlinear flexural stiffness was obtained from the moment-curvature relationship derived for both piles. For the concrete-filled FRP tubes, the moment-curvature relationship was estimated using a sectional analysis as described by Mirmiran, et al. (2000), and Fam and Rizkalla (2002). This methodology assumes that sections normal to the neutral axis remain plane after bending, and that the FRP shell is perfectly bonded to the concrete interior (i.e., a linear strain distribution through the entire cross section). The method consists of discretizing the pile cross section into a series of strip elements so that the normal stresses can be integrated over the cross-sectional area. The discretization results in strip elements that include both FRP and concrete components. The stress integration is done by assigning the appropriate constitutive model for each material. The

FRP shell can be modeled accurately as linear elastic within the limiting tensile and compressive strains. The concrete can be modeled using relationships of the type shown in figure 82. This analysis methodology can be easily programmed and can be used to generate moment-curvature and interaction diagrams. This methodology was used by Fam (2000) to calculate the moment-curvature response of two concrete-filled FRP tubes of the same type as used at the Route 40 Bridge, except that the concrete strength was lower. The good agreement between the measured and calculated moment-curvature behavior for the two piles tested by Fam (2000) is shown in figure 99.

Using the procedure described above, the moment-curvature relationships were calculated for the composite piles used at the Route 40 Bridge project, and the results are shown in figure 99. It can be seen that the response is initially stiff until a moment of about 110 kN-m (80,850 lbf-ft) is reached, at which point the first cracking of the concrete occurs. Beyond this point, the composite pile can sustain additional moment, although the response is much less stiff than initially. Failure is predicted to occur at a bending moment of about 630 kN-m (463,050 lbf-ft), when the FRP shell ruptures in tension.

The moment-curvature behavior of the prestressed concrete piles was predicted analytically using equilibrium and strain compatibility. A modified Ramberg-Osgood function was used to model the stress-strain relationship of the prestressing steel strands. A generalized expression, given by Popovics, was used to model the nonlinear stress-strain relationship of concrete (Collins and Mitchell, 1997). The moment-curvature response based on the analysis of the prestressed concrete pile is shown in figure 99. The moment-curvature calculations were terminated when the compressive strain in the concrete reached 0.003.

It can be seen that the derived static load versus displacement curves from figure 98 have a similar nature to the moment-curvature response shown in figure 99, for both the prestressed concrete and composite piles. For the composite pile, the sudden change in stiffness at a lateral load of 48.9 kN (11 kips) reflects the cracking point. For the prestressed pile, the initial stiffness is high due to the prestressing effect, as well as the higher elastic modulus of steel.

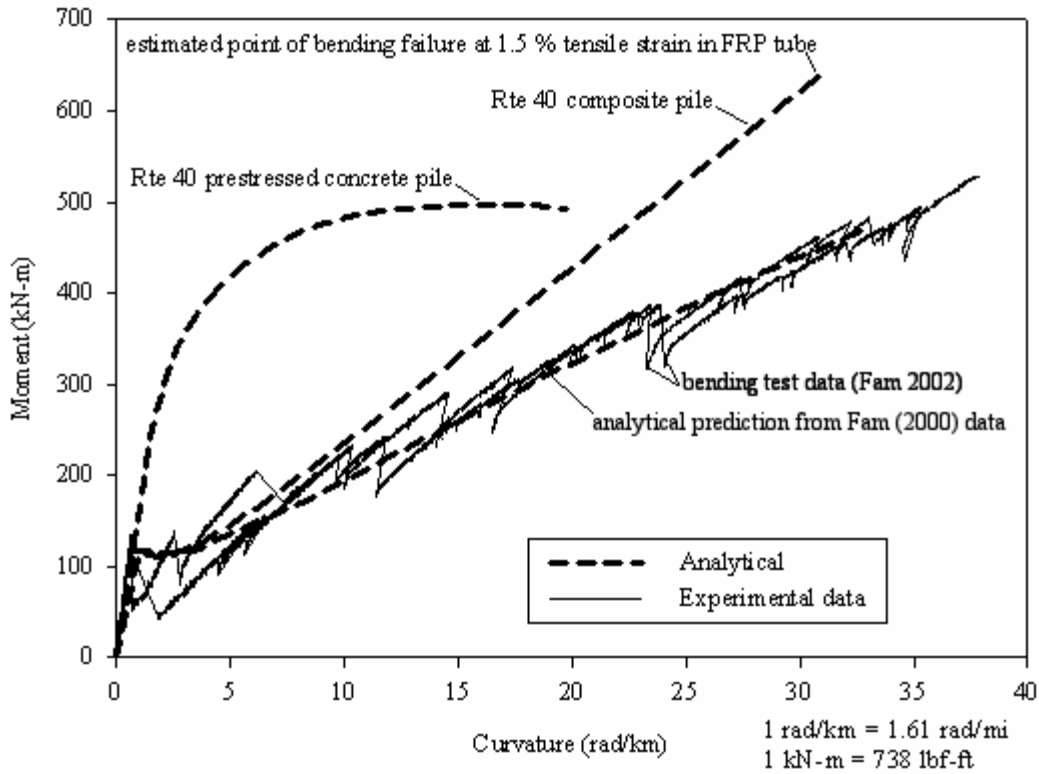


Figure 99. Graph. Moment-curvature responses for composite and prestressed concrete piles.

Using the moment-curvature relationships in figure 99 and the soil property values proposed in the standard Reese, et al. (1974), p-y formulation, the predicted lateral response for the test piles is shown in comparison to the measured response in figure 100. It can be seen that the calculated and measured responses for the composite pile are in good agreement. For the prestressed concrete pile, the calculated and measured stiffnesses are in good agreement initially, but the calculated minimum load is less than the measured maximum load.

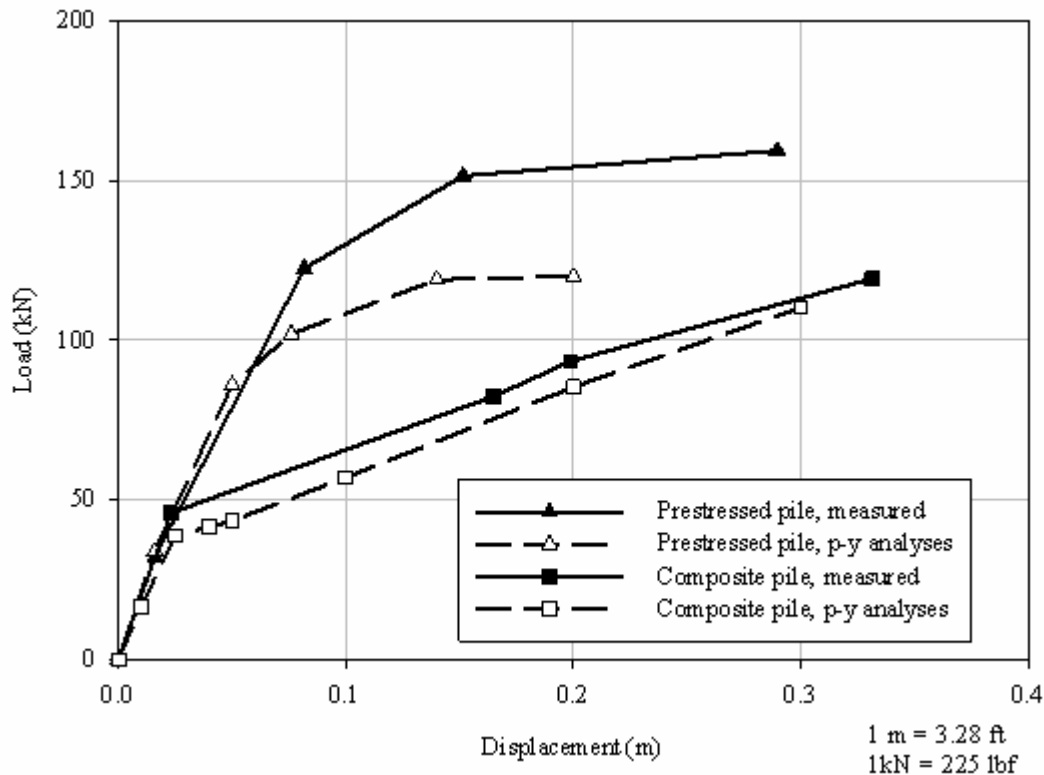


Figure 100. Graph. Computed and measured lateral load-displacement response for both test piles (Pando, et al., 2004).

5.7 COMPOSITE PILES IN THE NEW ROUTE 40 BRIDGE

Pier No. 2 (see figure 80) of the Route 40 Bridge consists of a reinforced concrete cap beam supported by 10 composite piles. The composite production piles are identical to the composite test pile in terms of size, laminate structure of the tube, and the methods of construction and driving. The installed composite piles of Pier No.2 are shown in figure 81(a).

5.7.1 Connection of Piles with Pile Cap Beam

After driving both the prestressed concrete and composite piles, and prior to casting the cap beams, special preparation of the pile heads was necessary to facilitate connecting the piles to the cap beams. Eight, 25-mm- (1-inch-) diameter holes were drilled through the top flat surface of each pile, using a regular rock drill. The holes were 460 mm (18 inches) deep, parallel to the longitudinal axis of the piles. In the prestressed concrete piles, the holes were equally spaced in a 330-by-330-mm (13-by-13-inch) square pattern. In the composite pile, the holes were equally spaced in a 447-mm (17.6-inch) diameter circular pattern as shown in figure 101. These arrangements allow for a 76 mm (3-inch) concrete cover for each hole. Eight, 1,219-mm (48-inch) long, No. 22M (No. 7) steel rebars were inserted in the holes and epoxy resin was used to secure the bars inside the concrete. Figure 101(a and b) shows the details of the pile head and the steel dowels in

both the prestressed concrete and composite piles. The formwork arrangement of the cap beams were placed such that the bottom surface of the cap beam is 152 mm (6 inches) below the upper surfaces of the piles to allow for embedment of the piles inside the cap beam. Figure 102(a) shows elevation views of Pier No. 2 through and in between the composite piles. Figure 102(b) shows the No. 22M (No. 7) steel bars, which are embedded 762 mm (30 inches) inside the cap beam. Figure 103 shows closeup views of Pier No. 2 and the connection between the composite pile and cap beam. A general view of the new completed bridge is shown in figure 104. The bridge was opened for traffic in the year 2000.

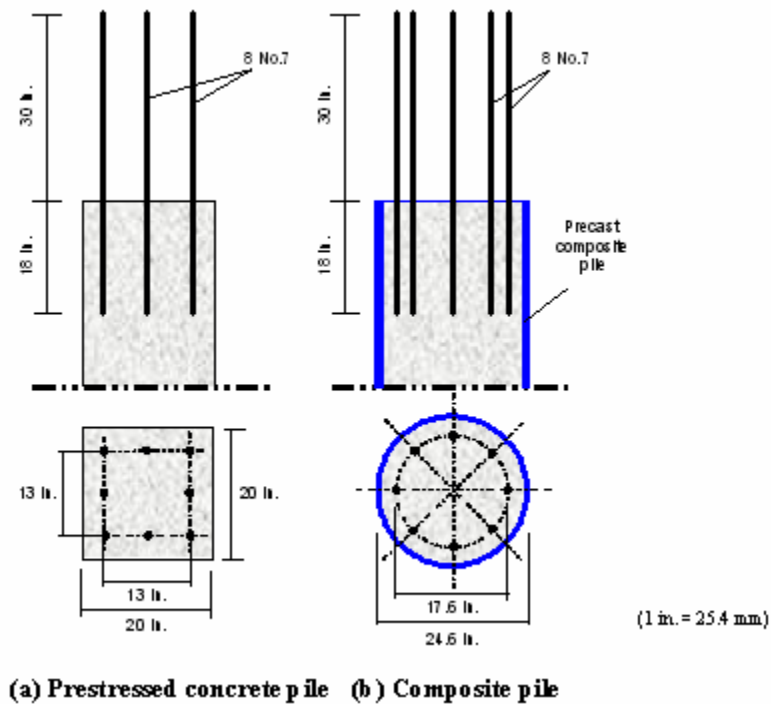


Figure 101. Illustration. Details of pile head showing the bars used to connect the pile to cap beam.

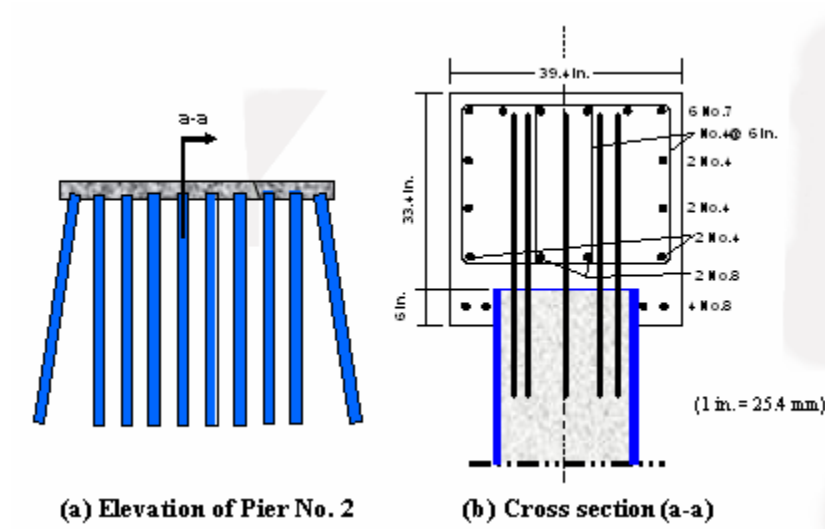


Figure 102. Illustration. Connection of composite piles to cap beam at Pier No. 2.



Figure 103. Photos. Pier No. 2 including the composite piles and reinforced concrete cap beam.



Figure 104. Photo. The new Route 40 Bridge over the Nottoway River in Virginia.

5.8 SUMMARY AND CONCLUSIONS

In 2000, VDOT replaced the old Route 40 Bridge (Structure No. 1006) over the Nottoway River. New precast composite piles, consisting of concrete-filled GFRP tubes, were used to support one of the cast-in-place reinforced concrete cap beams that directly support the superstructure. Prior to construction, full-scale field tests were undertaken to investigate the feasibility of construction, handling, and drivability, as well as the structural performance of the new composite piles in comparison to conventional prestressed concrete piles. Based on the testing, analysis, and construction experience, the following conclusions can be drawn.

1. Both the composite and prestressed concrete piles performed similarly during pile driving, as demonstrated by the driving records, PDA traces, measured wave speed generated by the driving hammer, and measured compressive and tensile stresses tests.
2. Both the composite and prestressed concrete piles performed similarly under the axial load tests. Full geotechnical capacity was mobilized in both cases before structural failure of the piles. The axial loads at failure were significantly higher than the design pile load.
3. Initially, the composite test pile exhibited a lateral stiffness similar to that of the prestressed concrete test pile up to a load of about 40 to 50 kN (9,000 to 11,250 lbf). This load level was found to correspond to first cracking of the composite pile. Beyond this load, the composite pile exhibited a much lower stiffness than the

prestressed concrete pile, but the composite pile did demonstrate a continuing ability to sustain lateral load with additional relatively large deformations.

4. The flexural strength of the 625-mm- (24.6-inch-) diameter composite pile with a 5.85-mm- (0.230-inch-) thick GFRP tube was calculated to be higher than the flexural strength of the 508-mm- (20-inch-) square concrete pile prestressed with fourteen, 12.7-mm (0.5-inch) strands, as shown in figure 99.
5. Calculations show the composite pile fails in bending by fracture of the GFRP tube on the tension side, while the prestressed concrete pile fails by yielding of the strands in tension, followed by crushing of the concrete in compression.
6. The lateral load field tests on both the composite and prestressed piles showed similar behavior to that obtained from laboratory flexural test and analysis.
7. The lateral load-versus-deflection response for the composite pile was predicted with good accuracy using conventional procedures typically used for prestressed concrete piles.
8. Similar pile-to-cap beam connections were used for the composite and prestressed concrete piles, including eight No. 7 steel dowels embedded 457 mm (18 inches) inside the piles from one end and extending 762 mm (30 inches) into the cap beam. The piles themselves were embedded 152 mm (6 inches) inside the cap beam.
9. Concrete-filled FRP tubes were successfully installed as piling for a bridge pier at the Route 40 Bridge. To date, no indications of unsatisfactory performance have been reported.

CHAPTER 6. FIELD LOAD TESTS AT THE ROUTE 351 BRIDGE

6.1 INTRODUCTION

This chapter summarizes the results and findings of field load tests carried out at the Route 351 Bridge project in Hampton, VA. The test pile program described here involved one prestressed concrete pile and two different types of composite piles that were subjected to axial and lateral load testing. One of the composite piles consisted of an FRP tube that was filled with concrete and reinforced with steel bars. The other composite pile was formed of polyethylene with steel reinforcing bars. In addition to the test pile program, two instrumented piles, consisting of a prestressed concrete pile and an FRP pile, have been installed in the bridge to study long-term performance and load-transfer behavior. The focus of this chapter is the test pile program, including descriptions of the test piles, subsurface conditions, pile driving, dynamic testing, static axial load testing, and static lateral load testing. The instrumented production piles and the long-term performance study are described in chapter 9. Results from the Route 351 tests also have been published by Pando et al. (2003).

6.2 DESCRIPTION OF THE BRIDGE

6.2.1 The Original Bridge

In 2001, VDOT started a bridge replacement project at the Route 351 Bridge crossing of the Hampton River in Hampton, VA. A general location map and an aerial view of the original bridge are shown in figures 105 and 106, respectively. Wide-angle photographic views of the original bridge are shown in figure 107. The original bridge, built in the early 1940s, was 228.45 m (749.5 ft) long and had a roadway 10.35 m (34 ft) wide. The rated capacity of the bridge was for 133.5-kN (15-ton) trucks. The bridge was composed of 16 equal spans supported on steel beams. The superstructure was supported by 15 piers and 2 end abutments. The foundations of the piers and abutments consisted of groups of timber piles with reinforced concrete pile cap beams.

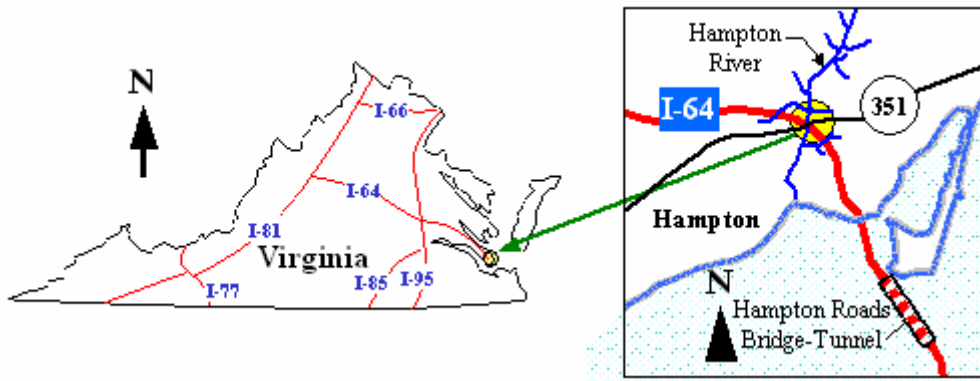
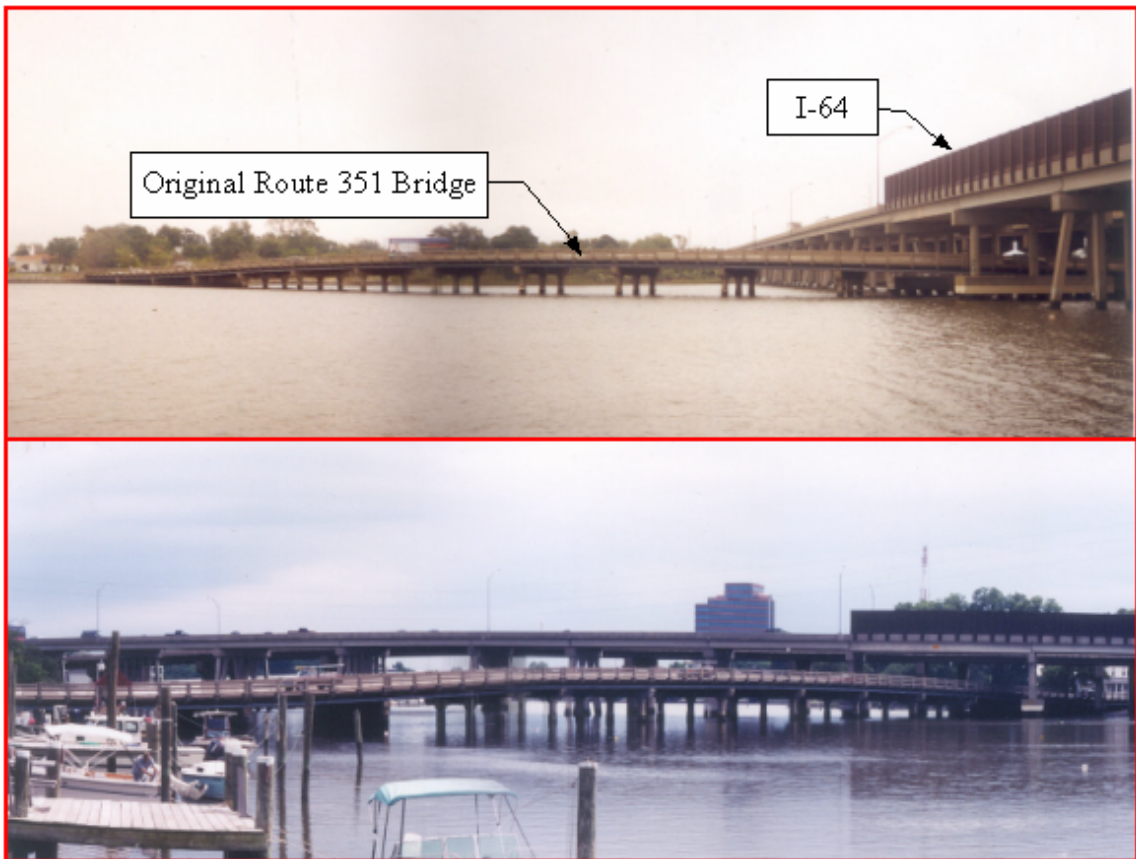


Figure 105. Map. Location map of the Route 351 Bridge in Hampton, VA.



Figure 106. Photo. Aerial view of the Route 351 Bridge in Hampton, VA.



(Photos taken from the north side)

Figure 107. Photos. Wide-angle views of the original Route 351 Bridge.

The bridge suffered from excessive deterioration in the superstructure and substructure, which led to the decision of replacement. Some signs of deterioration in the original bridge can be seen in figure 108.



(Photo taken from the south side)

Figure 108. Photo. Signs of deterioration of the original Route 351 Bridge.

6.2.2 The New Bridge

The new bridge is 228.5 m (749.7 ft) long and 12.8 m (42 ft) wide, and consists of a 13-span superstructure supported by 12 piers and 2 end abutments, as shown in figure 109. The bridge deck is supported on American Association of State Highway and Transportation Officials (AASHTO) Type II prestressed concrete beams for most of the bridge; however, on the first four spans on the west side of the bridge, the deck is supported on steel plate girders. The steel plate girders are used in the portion of the bridge underneath the Highway I-64 overpass. As shown in figure 109, this area corresponds to Piers 1, 2, and 3. These spans are longer than on the east side of the bridge and the orientation of the piers had to be aligned with Highway I-64 due to workspace limitations imposed by the I-64 overpass. The bridge piers, except for Pier 2 located under highway I-64, consist of an elevated reinforced concrete beam-type pile cap supported by a group of seven prestressed concrete piles. The bridge rated capacity is for MS18 loading and alternate military loading. Based on the design requirements, VDOT specified use of 610-mm (24-inch) prestressed solid square piles for the pier foundations. The design axial load for the piles in the piers is 890 kN (200 kips). The new bridge was completed and opened to traffic in 2003.

As part of this study, an instrumented FRP composite pile was installed at the center of the group of piles supporting Pier 11 (see figure 109), and an instrumented prestressed concrete pile was installed in the center of Pier 10. Through monitoring of these piles, the long-term performance and durability of the two pile types can be assessed and compared. The long-term study is described in chapter 9.

The following sections provide a brief description of both the conventional prestressed piles and the composite piles.

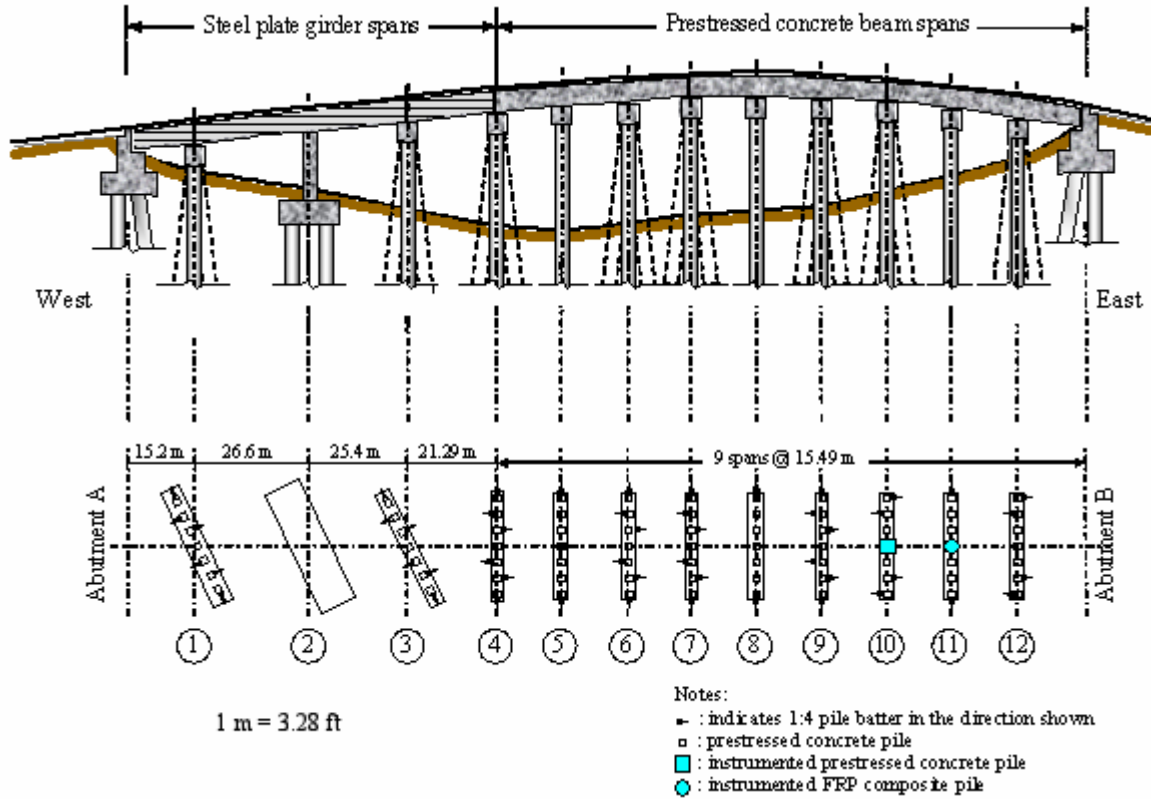


Figure 109. Illustration. Schematic of the new Route 351 Bridge.

6.3 DESCRIPTION OF TEST PILES

The three test piles, whose cross sections are shown in figure 110, are described in the following subsections.

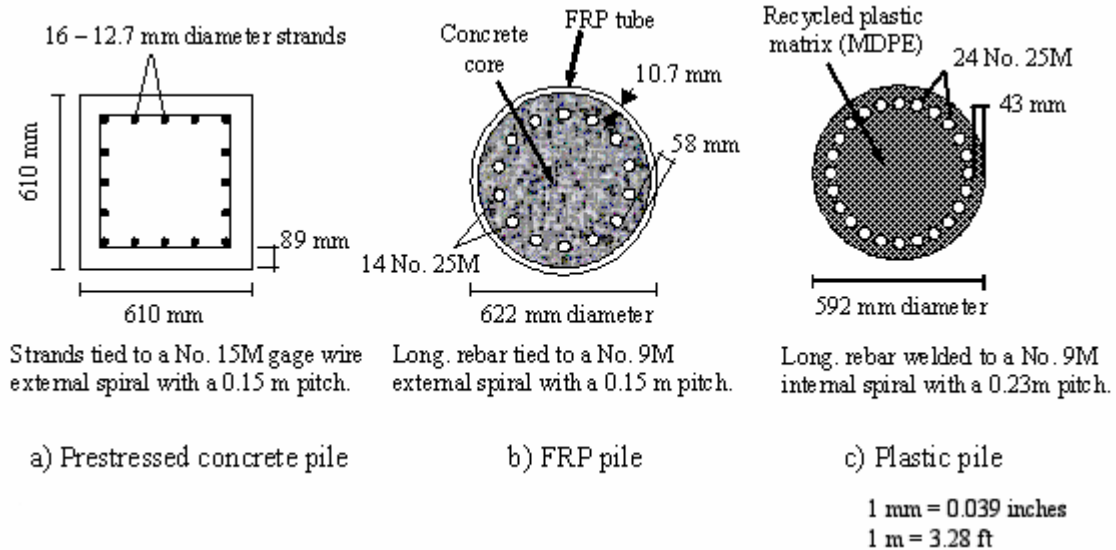


Figure 110. Illustration. Test pile cross section details.

6.3.1 Prestressed Concrete Test Pile

The prestressed concrete pile is a 610 mm (24 inch) square pile, 18 m (59.1 ft) long. The pile is prestressed with 16, 12.7 mm (0.5 inch)-diameter, 7-wire strands of 1.86 GPa (270 ksi) yield strength steel. The strands were strained to produce an effective prestress of 5.5 MPa (0.803 ksi) after losses. The spiral ties consist of No. 16M (No. 5) wire with a pitch of 150 mm (6 inches). The 28-day strength of the concrete was specified to be at least 35 MPa (5,080 psi), and the test results show that the strength of concrete was 55 MPa (7,980 psi) at the time of the load tests.

Figure 111(a) shows the stress-strain diagrams for the concrete and steel components of the prestressed concrete pile. The concrete stress-strain diagrams were obtained from laboratory tests, and the steel diagram shows the minimum yield strength specified for 1.86 GPa steel strands. Based on these stress-strain diagrams, the calculated axial stiffness, EA (where E is the Young's modulus and A is the cross-sectional area) of the pile is 8.2×10^6 kN (1.84×10^6 kips), as shown in figure 112. Figure 113 shows the moment-curvature and flexural stiffness diagrams calculated using the procedures described in Collins and Mitchell (1997).

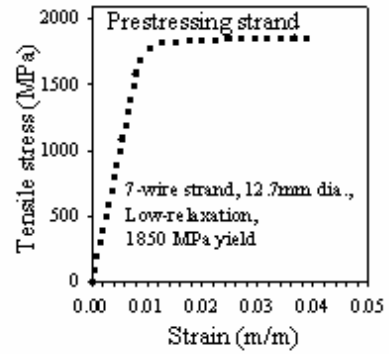
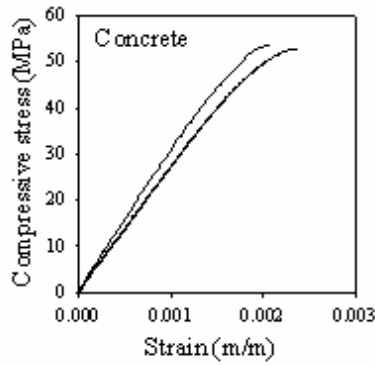
6.3.2 FRP Composite Test Pile

The FRP composite test pile consists of an 18.3-m (60-ft) long FRP tube filled with concrete and reinforced with steel bars prior to driving. The FRP tube consists of a tube with an outside diameter of 622 mm (24.3 inch) and a wall thickness of 10.7 mm (0.417

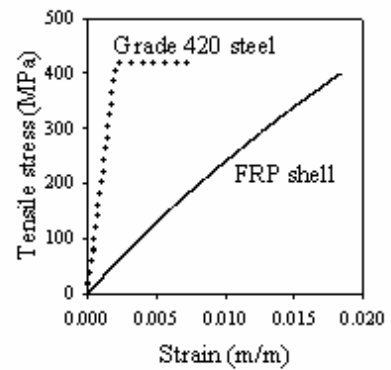
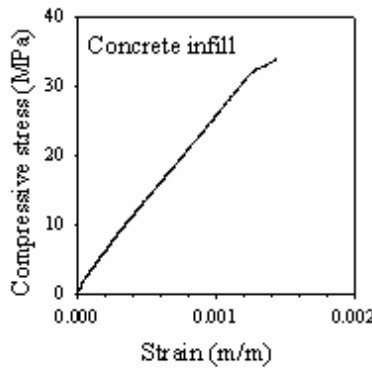
inch). The polymer used is Dow vinyl ester Derakane resin, and the fiber reinforcing consists of four plies of stitch-bonded glass fiber fabric. Each ply includes four layers of fibers oriented at 0, +45, -45, and 90 degrees with respect to the longitudinal axis of the tube. The average ply thickness is 1.93 mm (0.0753 inch). The minimum fiber volume fraction is 50 percent.

Prior to driving, the tube was filled with nonshrink concrete with 19 mm (0.75 inch) aggregate and Sika Viscocrete additive to produce a fluid, self-compacting concrete. The 7-day strength of the concrete was 27.4 MPa (3,970 psi), and the strength at the time of driving was about 34 MPa (4,930 psi). The pile is reinforced with 14 No. 25M steel bars, grade 420 (No. 8 steel bars, grade 60). The spiral ties consist of No. 10M (No.3) gage wire with a pitch of 150 mm (6 inches).

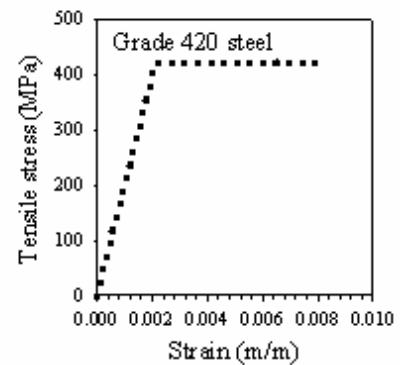
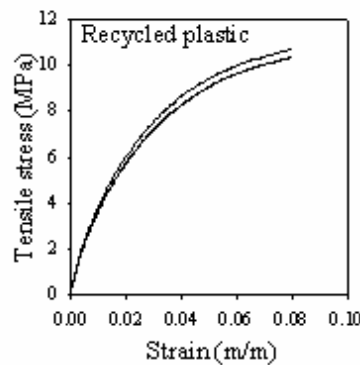
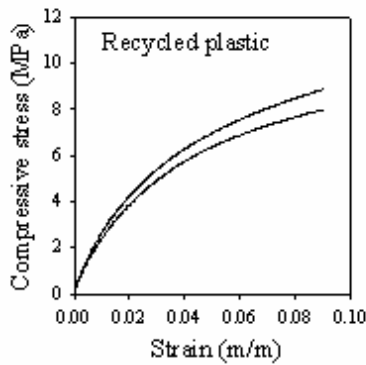
Figure 111(b) shows the stress-strain diagrams for the FRP, concrete, and steel components of the FRP pile. The FRP and concrete stress-strain diagrams were obtained from laboratory tests, and the steel diagram shows the minimum yield strength specified for Grade 420 steel. Based on these stress-strain diagrams, the calculated axial stiffness, EA, of the pile is 7.36×10^6 kN (1.65 x 10⁶ kips), as shown in figure 112. Figure 113 shows the moment-curvature and flexural stiffness diagrams calculated using the procedures described in Fam 2000.



a) Prestressed concrete pile



b) FRP pile



c) Plastic pile

1 m = 3.28 ft
1 MPa = 145 lbf/in²

Figure 111. Graphs. Test pile material properties.

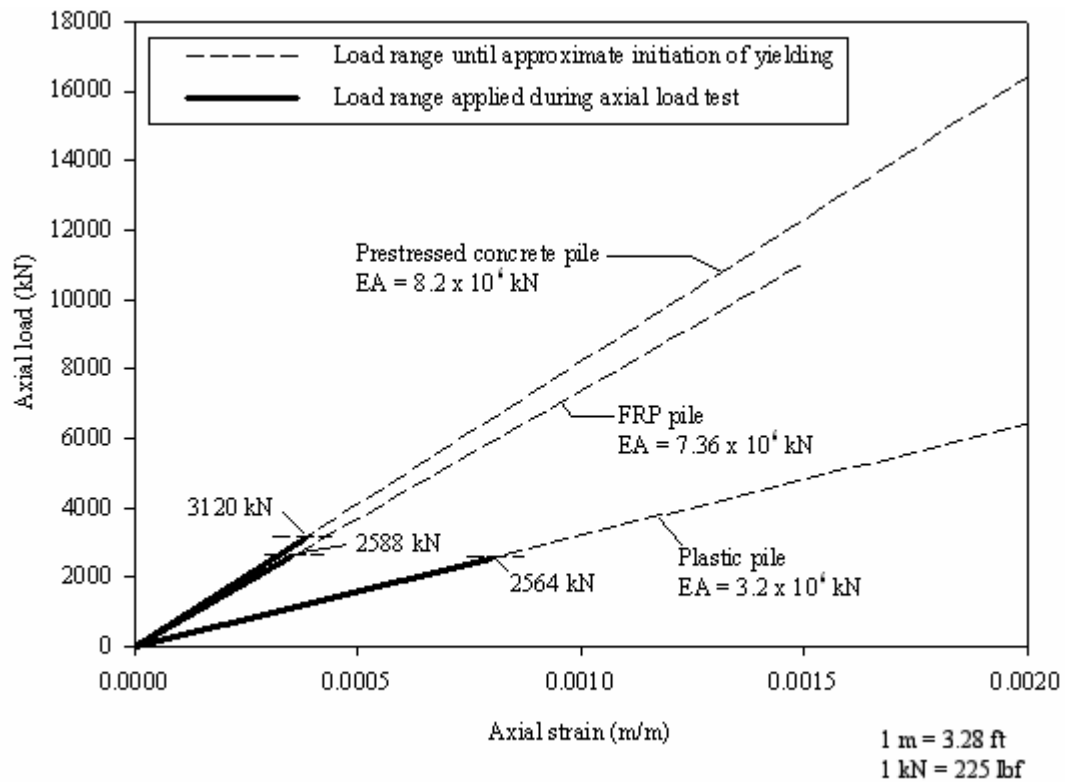


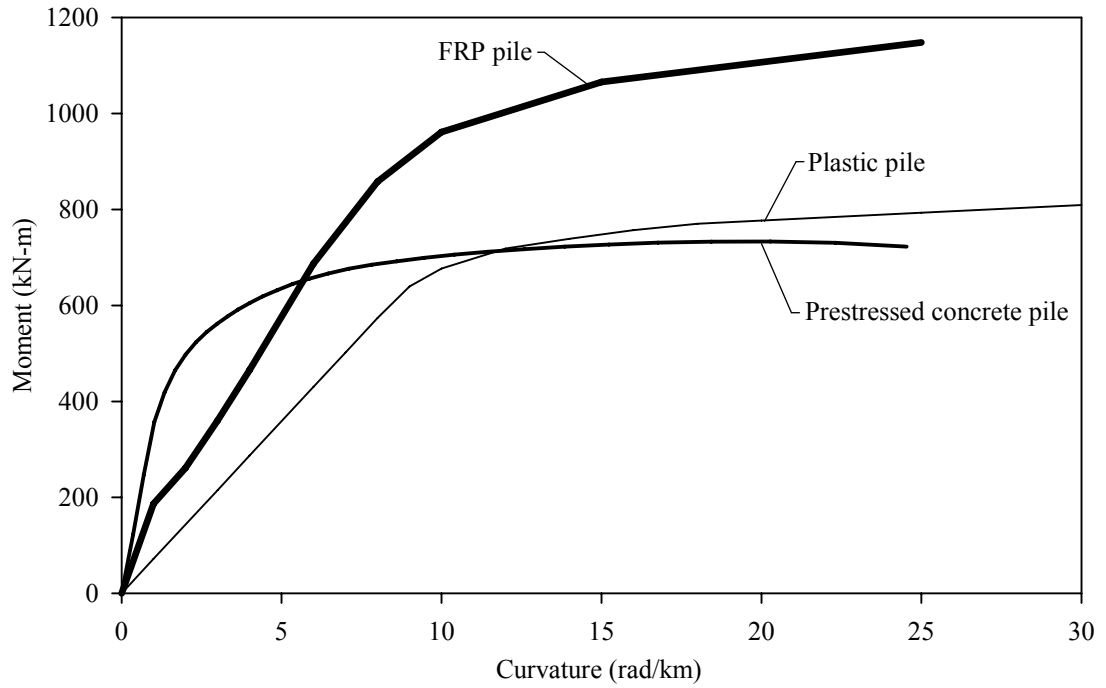
Figure 112. Graph. Axial load-axial strain behavior of test piles.

6.3.3 Polyethylene Composite Test Pile

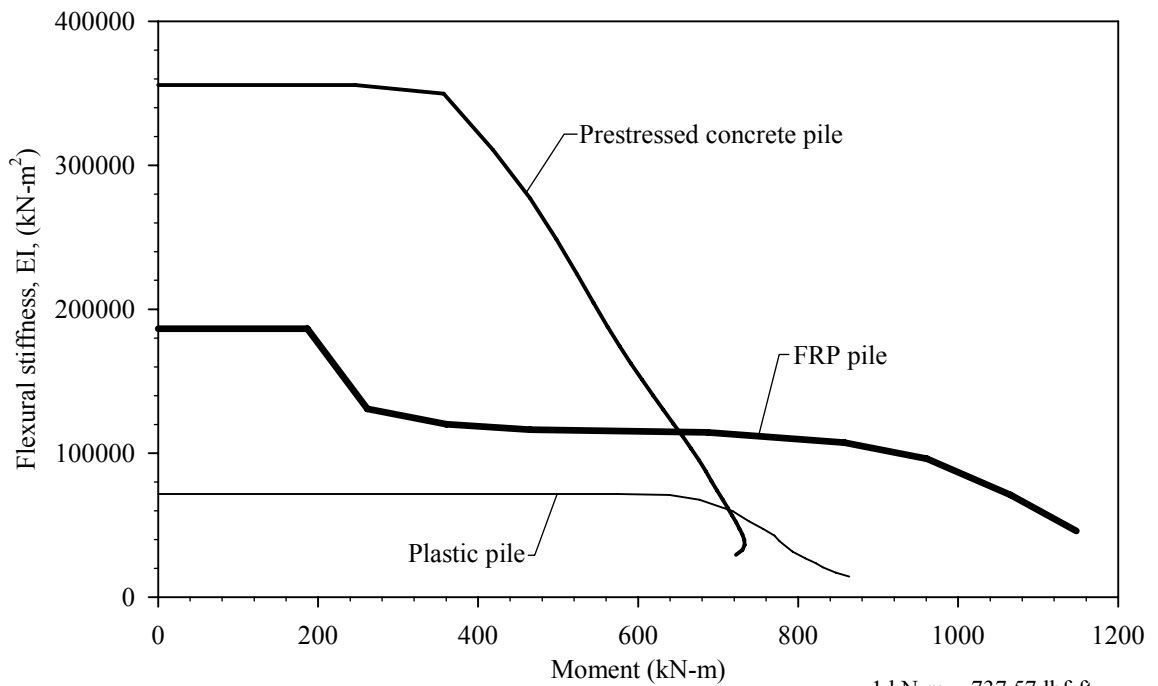
The polyethylene composite pile consists of a plastic matrix and a steel reinforcing cage. The plastic matrix is a proprietary mixture of recycled postconsumer and/or postindustrial polyethylene thermoplastics, with added colorants, UV inhibitors, and antioxidants. The final density of the plastic ranges from 7.1 to 9.4 kN/m³ (45 to 60 pcf). The Young's modulus of the plastic is specified by the manufacturer to be at least 275 MPa (40 ksi). The pile is reinforced with 24 No. 25M steel bars, grade 420 (No. 8 steel bars, grade 60). The spiral ties, which consist of No. 10M (No. 3) gage wire with a pitch of 230 mm (9 inches), were welded to the longitudinal bars. The pile is fabricated by forcing molten plastic into a mold under a 3.4 MPa (500 psi) pressure at 260 °C (500 °F). The plastic pile is 592 mm (23 inches) in diameter and 18.3 m (60 ft) long. A steel pipe with an outside diameter of 141 mm (5.5 inches) and a wall thickness of 6.35 mm (0.25 inches) was cast in the plastic pile to provide a place for installing an inclinometer casing after the pile was cast. The steel pipe was used because of concerns that standard inclinometer casings might not survive the high temperature and high pressure of the plastic molding process.

Figure 111(c) shows the stress-strain diagrams for the polyethylene and steel components of the polyethylene pile. The polyethylene stress-strain diagrams were obtained from laboratory tests, and the steel diagram shows the minimum yield strength specified for Grade 420 steel. Based on these stress-strain diagrams, the calculated axial stiffness, EA,

of the pile is 3.2×10^6 kN (720×10^6 poundforce), as shown in figure 112. Figure 113 shows the moment-curvature and flexural stiffness diagrams calculated using the same equilibrium and strain compatibility concepts used for the other two piles (Collins and Mitchell 1997, Fam 2000).



a) Moment—curvature



b) Flexural stiffness as a function of applied moment

1 kN-m = 737.57 lbf-ft
 1 rad/km = 0.621 rad/mile
 1 kN-m² = 2421 lbf-ft²

Figure 113. Graphs. Flexural characteristics for the three test piles.

6.4 SOIL CONDITIONS AT THE TEST SITE

The test pile program was conducted on a spit of land projecting into the Hampton River near the Route 351 crossing of the Hampton River in the Chesapeake Bay area of Virginia. The location of the test pile program is shown in figure 114.

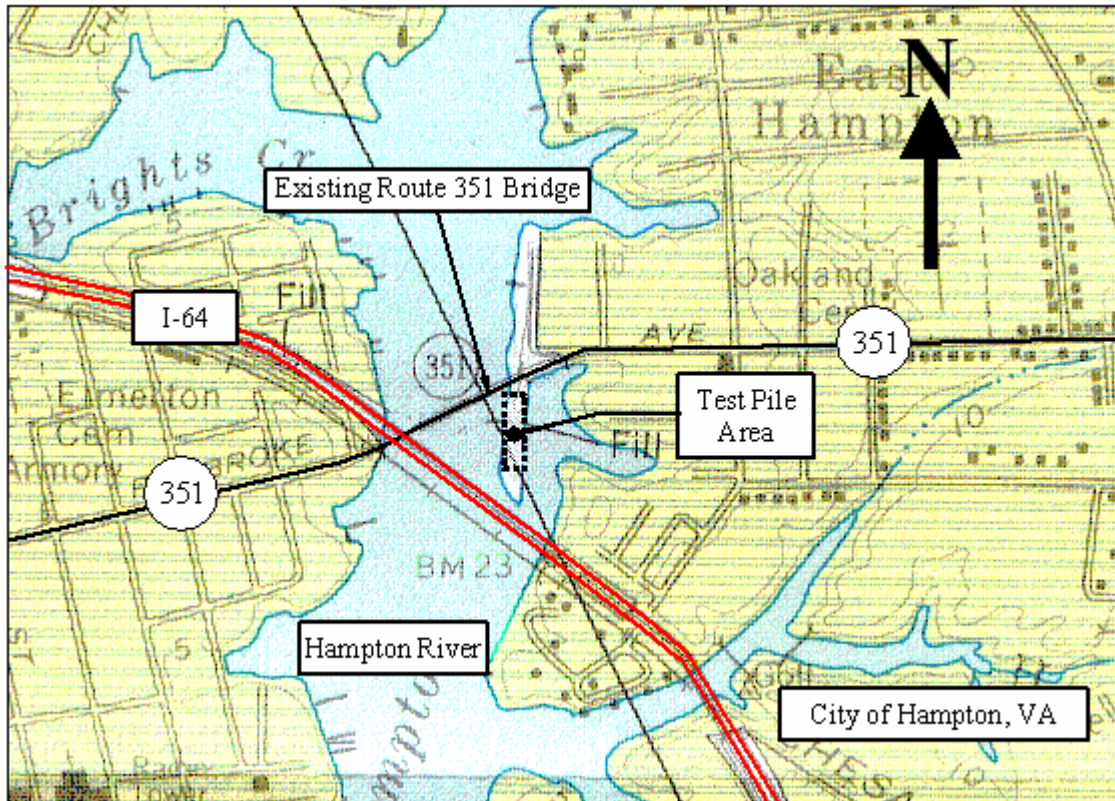


Figure 114. Map. Location of test pile site at the Route 351 Bridge.

6.4.1 Geology

The test site is located in the area of Chesapeake Bay that falls in the Coastal Plain geologic province of Virginia. The Chesapeake Bay is about 10,000 years old, and originated during the early Pleistocene epoch when the rising of the Atlantic Ocean sea level resulted in flooding and deposition of marine sediments. This flooding and deposition alternated with sea level lowering and erosion of older sedimentary deposits (Frye 1986, Meadors 1977). The numerous transgressions and regressions of the Atlantic Ocean created the present-day stratigraphy in this area (Martin, et al., 1987).

The east and west banks of the Hampton River consist of Tabb Formation deposits underlain by the Yorktown Formation (Johnson 1976, Frye 1986). The Tabb Formation deposits generally consist of nearshore marine clayey and silty sands with occasional gravels (Johnson 1976). The Yorktown Formation has experienced numerous cycles of erosion, desiccation, and deposition. Soils from this formation are generally silty sands containing varying amounts of minor shell fragments (Martin, et al., 1987, Johnson 1976).

6.4.2 Subsurface Conditions

The soil stratigraphy at the test site is shown in figure 115. The uppermost layer at the test pile site is silty fine sand fill, approximately 1.0 m (3 ft) thick. The fill is underlain by loose to medium dense silty fine sand to a depth of 13.0 m (42.5 ft). The silty fine sand is underlain by stiff sandy clay to a depth of 15.5 m (51 ft). Beneath the clay, medium dense to dense silty and clayey sand was encountered to the bottom of the borings at a depth of 30.6 m (100 ft). The ground water level, which is controlled by the adjacent Hampton River, is at 0.9 to 1.5 m (3 to 5 ft) below the ground surface.

The test site was investigated with two hollow stem auger borings, four cone penetrometer probes, and one dilatometer probe. The locations of the borings and probes are shown in relation to the test pile layout in figure 116. The borings were advanced using hollow-stem auger techniques, and standard penetration tests (SPT) were performed in the borings using a safety hammer. The field SPT N-values are shown in figure 115, together with descriptions of the materials encountered in the borings. Figure 115 also shows the tip resistance and the sleeve friction from the four cone penetrometer test (CPT) probes. Additional subsurface investigation information for the pile load test area is included in appendix C.

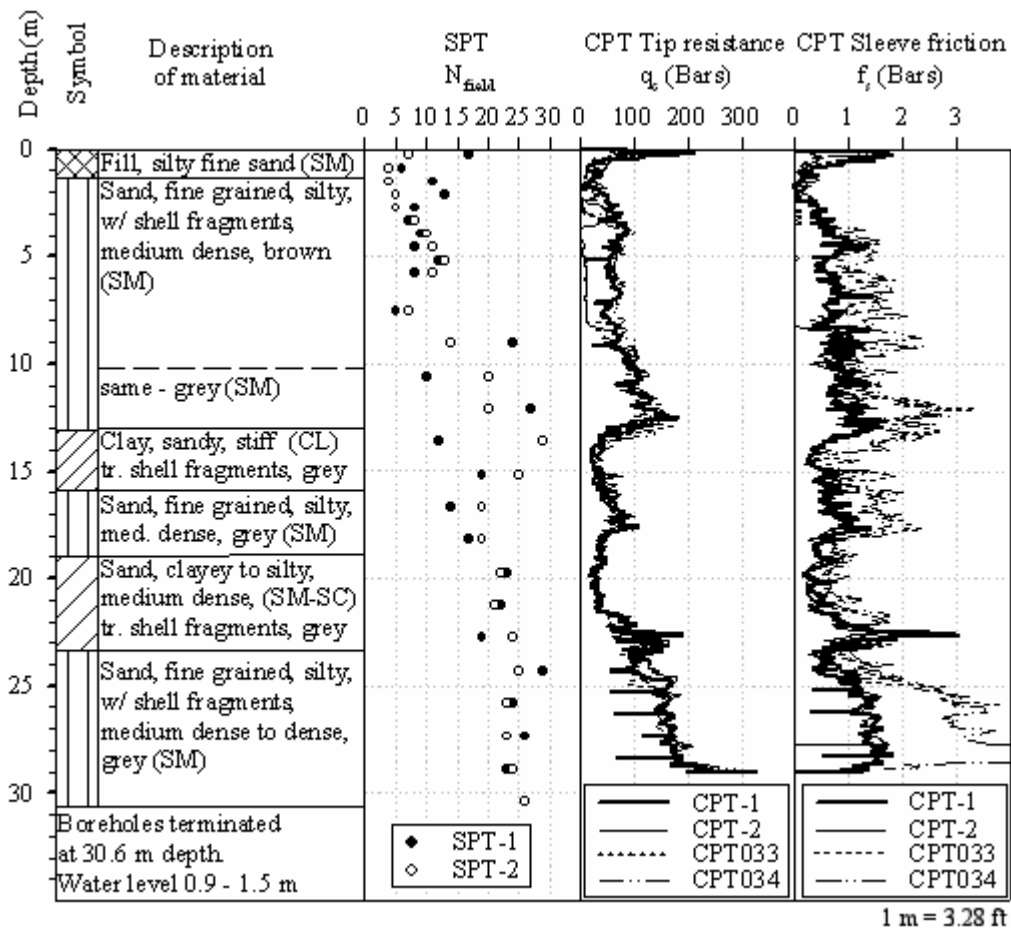


Figure 115. Charts. Simplified soil stratigraphy near test pile area.

6.4.3 Hampton River

The water from the Hampton River is salty or brackish. Water samples taken from the bridge site were tested at Virginia Tech. Anion tests showed concentrations of chloride, bromide, and sulfate of 11,720, 28.3, and 1,498 mg/L (1.56, 0.00376, and 0.199 oz/gal), respectively. Cation tests showed concentrations of sodium, potassium, magnesium, and calcium of 6,151, 226, 558, and 259 mg/L (0.818, 0.030, 0.0742, and 0.0344 oz/gal), respectively.

The water level of this river is tidal. The mean low and high water level are -0.4 m (-1.3 ft) and +0.5 m (1.6 ft) with respect to mean sea level, respectively. The extreme high water level event for this area was recorded in 1932 at +2.180 m (7 ft) above mean sea level.

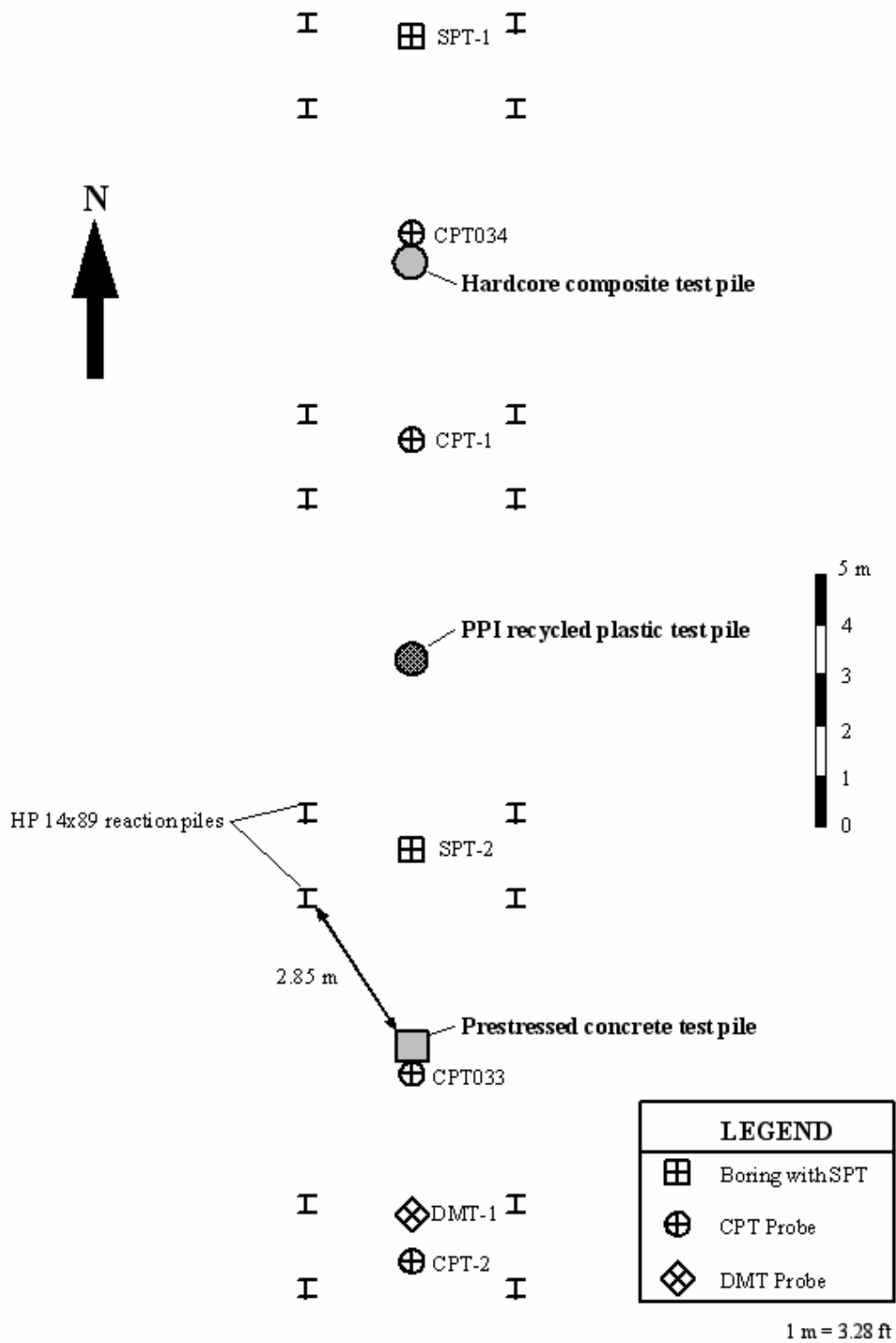


Figure 116. Illustration. Pile load test layout.

6.5 TEST PILE INSTRUMENTATION AND FABRICATION

6.5.1 Test Pile Instrumentation

All three test piles were instrumented with 16 sister bar strain gages located at 6 levels. A pair of gages was located at each level to provide gages on opposite sides of the pile. Two extra gages were installed at the uppermost and lowermost levels for redundancy. Each strain gage consisted of a No. 12M, grade 420 steel bar (No. 4 steel bar, grade 60), 0.9 m (2.9 ft) long, with four foil resistance strain gages that were precision mounted on each bar. The foil gages were mounted and wired to configure a full Wheatstone bridge that would cancel out any bending strains induced in the steel bar. For the polyethylene plastic pile, the foil gages and lead wires were made of materials capable of withstanding the high temperatures involved in manufacturing this pile. The sister bar strain gage survival rates, after pile manufacturing, driving, and restrike, were 50 percent, 56 percent, and 81 percent for the prestressed concrete, FRP, and plastic piles, respectively. An inclinometer casing was also installed in each test pile to permit better resolution of the deflected shapes during lateral load testing.

The as-built instrumentation layout for the prestressed concrete test pile is shown in figure 117.

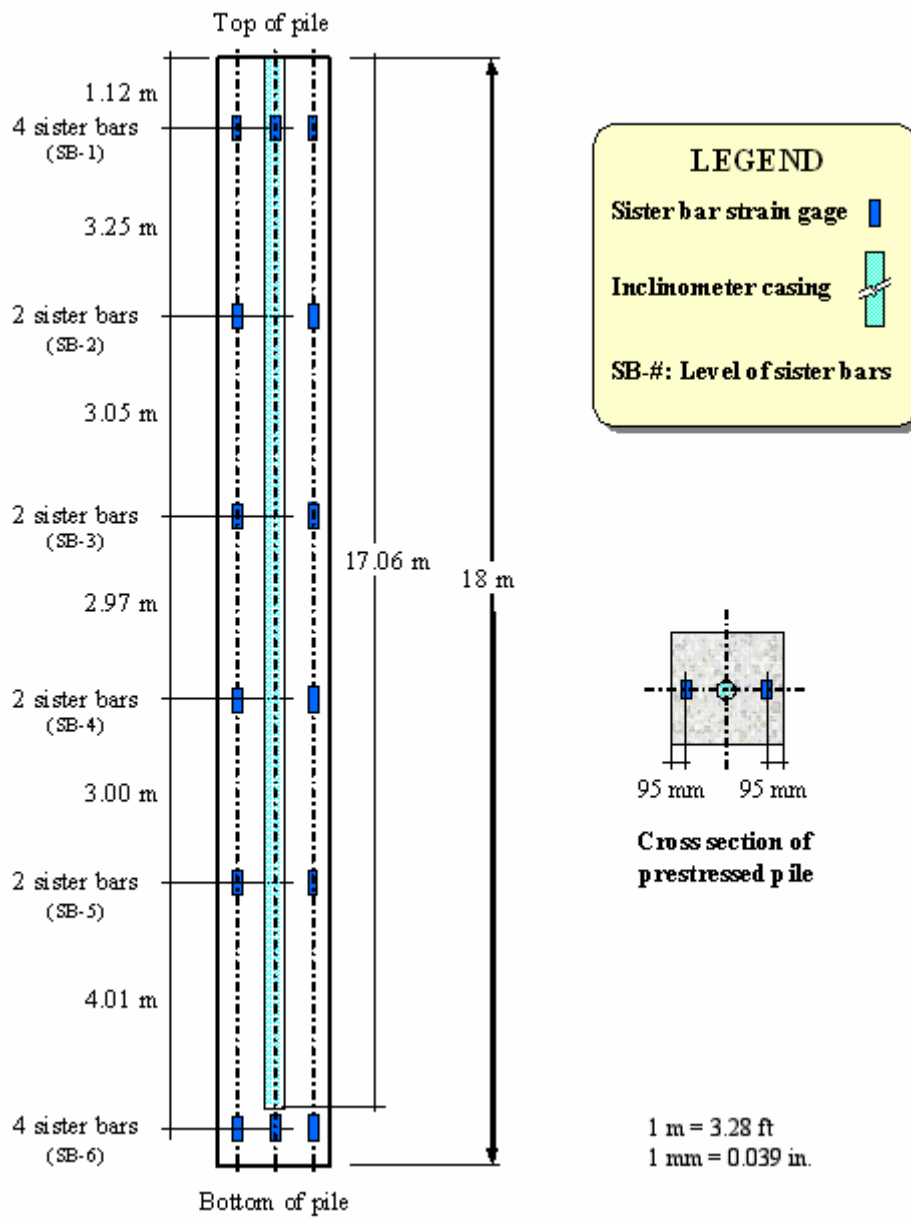
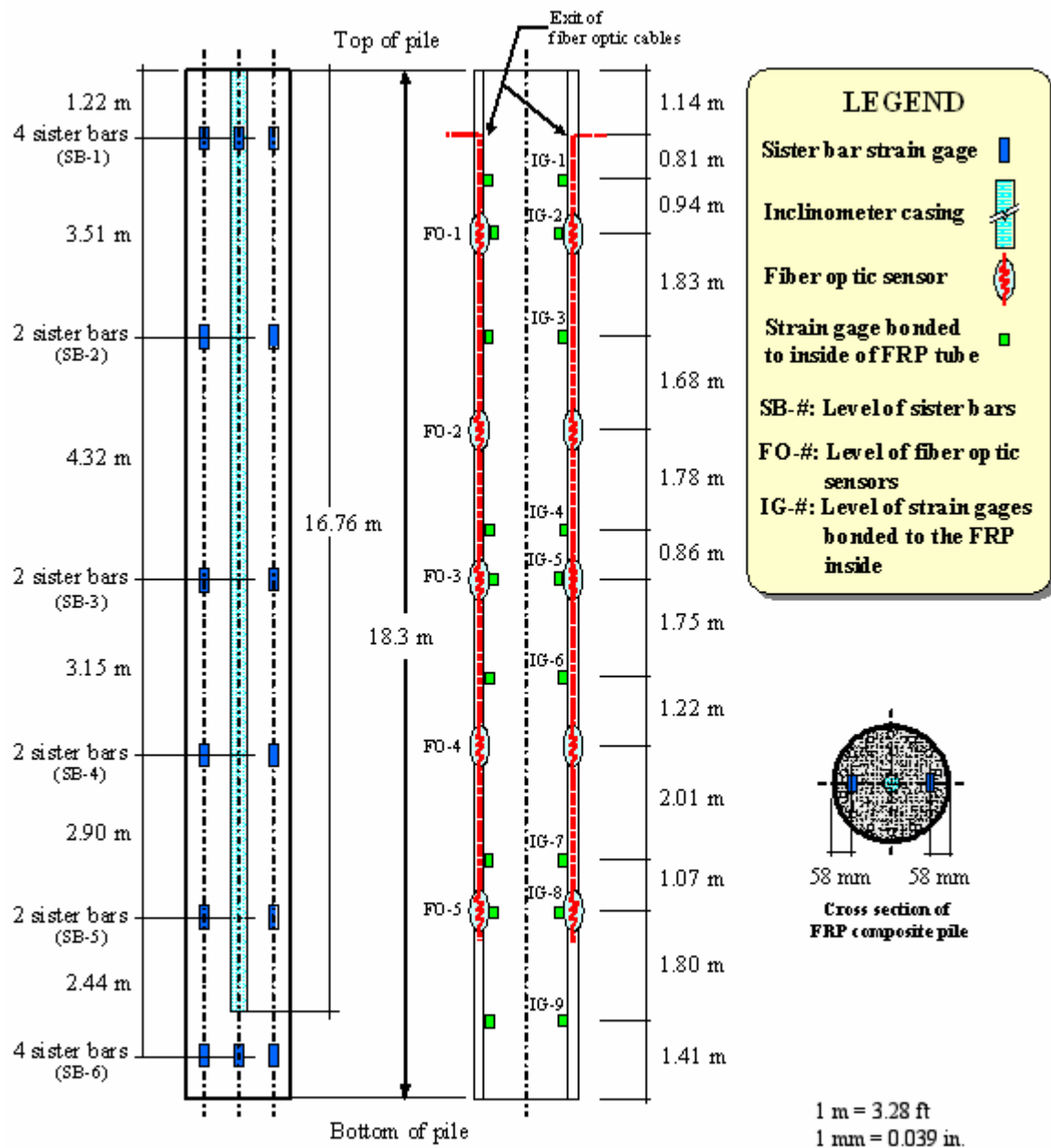


Figure 117. Illustration. Instrumentation layout for prestressed concrete test pile.

In addition to the 16 sister bar gages, the FRP test pile had the following instrumentation to monitor strains in the FRP tube:

- Eighteen foil gages bonded to the internal wall of the FRP tube. The foil gages were type CEA-13-500UW-350, temperature compensating, underwater, resistance strain gages. The gages were configured in a one-quarter active bridge. A protective coating system was used to cover these gages to protect them from possible moisture and chemical attack during filling of the tubes with concrete. The protective coating consisted of a Teflon film, overlain by a layer of polymer compound, overlain by aluminum foil, overlain by another layer of polymer compound, overlain by another layer of aluminum foil, with the edges sealed with a rubber coating.
- Fiber optic sensors embedded in the FRP tube. To make it possible to embed the sensors, the fiber optic cable and sensors were installed during the manufacturing of the FRP tubes. The installation, data collection, and interpretation of the fiber optic sensors were carried out by an FHWA contractor.

The as-built instrumentation layout for the FRP test pile is shown in figure 118. The instrumentation of the plastic composite pile was similar to that used for the prestressed concrete pile. The as-built instrumentation layout for the plastic composite test pile is shown in figure 119.



a) Instruments embedded in concrete infill

b) Instruments embedded or bonded to the FRP tube

Figure 118. Illustration. Instrumentation layout for FRP composite test pile.

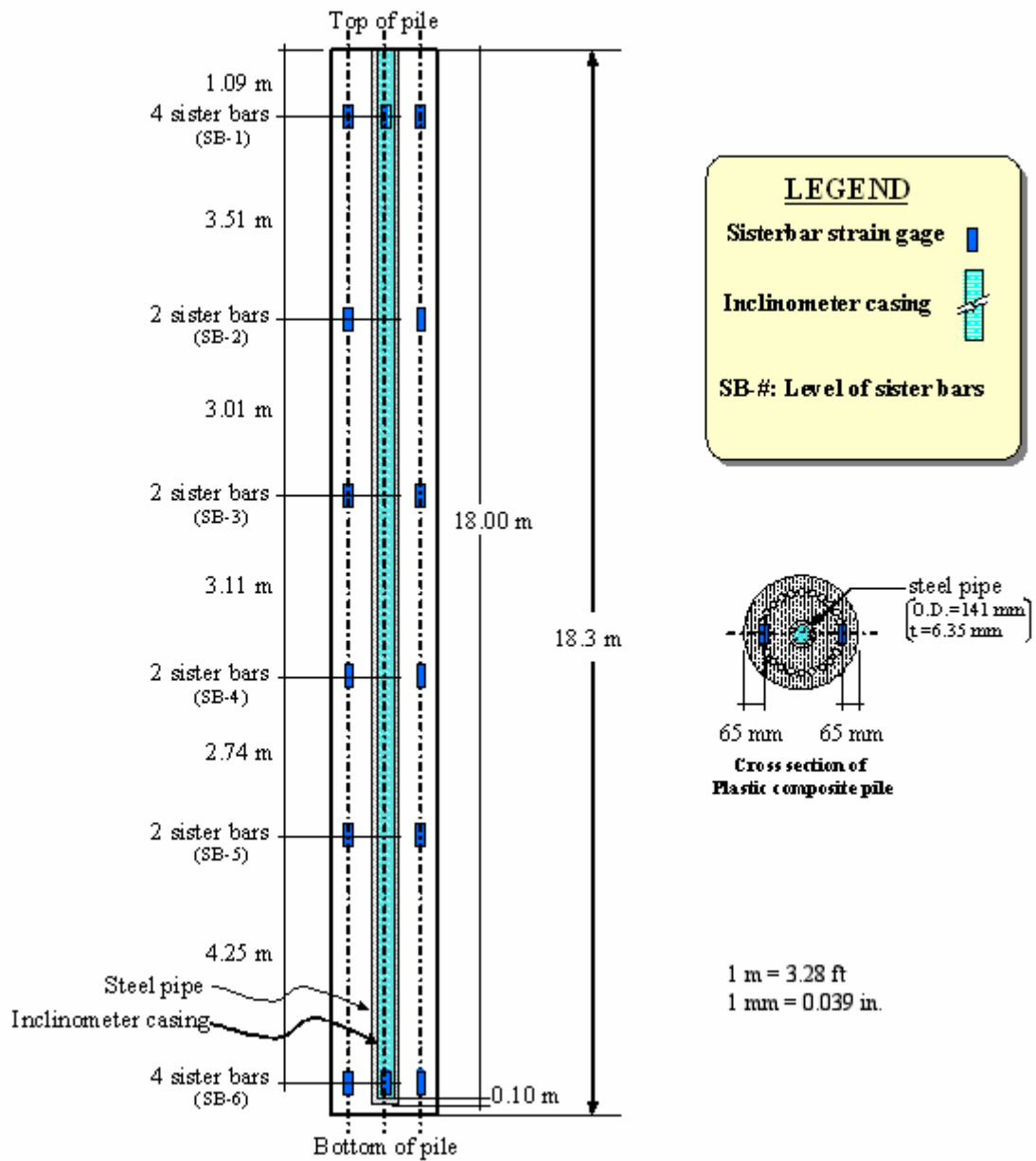


Figure 119. Illustration. Instrumentation layout for plastic composite test pile.

6.5.2 Fabrication of Prestressed Concrete Test Pile

On August 14, 2001, the prestressed concrete test pile was fabricated in general accordance with VDOT standards. Photos of test pile fabrication are shown in figure 120. After fabricating and curing, the piles were shipped to the bridge site.



Figure 120. Photos. Fabrication of prestressed concrete test pile.

6.5.3 Fabrication of FRP Composite Test Pile

In January 2002, two FRP tubes were shipped to a casting yard in Virginia Beach, VA. The two FRP tubes were 18.3 m (60 ft) and 21.3 m (70 ft) long for the test pile and production pile, respectively. The tubes are shown in figure 121(a). The instrumentation of the FRP piles was carried out prior to concrete pouring between January 24 and February 2, 2002. Figure 121(b) shows installation of the foil gages to the inside wall of the FRP tube.

Prior to concrete pouring, the steel rebar cage was inserted into the FRP tubes as shown in figure 121(c). The piles were then raised with a crane and secured in a vertical position with the aid of steel sheet piles and steel bracing as shown in figures 122(a) and (b). The bottoms of the FRP tubes were fitted into 76-mm (3-inch) grooves in a concrete slab. The bottoms of the FRP tubes were also bolted to the concrete slab by means of L-shaped angles, as shown in figure 122(c). An elephant trunk, shown in figure 122(d), was lowered into the pile with a hopper located at the top of the pile. The concrete was then poured through the hopper using a 2-cubic-yard (1.53-cubic-meter) bucket and a crane. Photos of the concrete pour are shown in figure 123. Concrete filling of the FRP composite piles took place on February 6, 2002.

After fabrication, the piles were left in a vertical position for 2 weeks. The piles were shipped to the bridge site on February 20, 2002.



(a) FRP tubes received at the precast plant



(b) Installation of foil gages on the inside of FRP tube



(c) Insertion of instrumented rebar cage into FRP tube

Figure 121. Photos. Fabrication of concrete-filled FRP piles.



(a) FRP tube with steel cage inside is placed vertically to prepare for concrete filling



(b) Bracing system used to secure FRP tube and steel cage in a vertical position



(c) The base of the FRP tubes is bolted to a concrete slab



(d) Hopper and elephant trunk used to pour concrete into the FRP composite piles

Figure 122. Photos. Setup used for concrete filling of FRP composite piles.



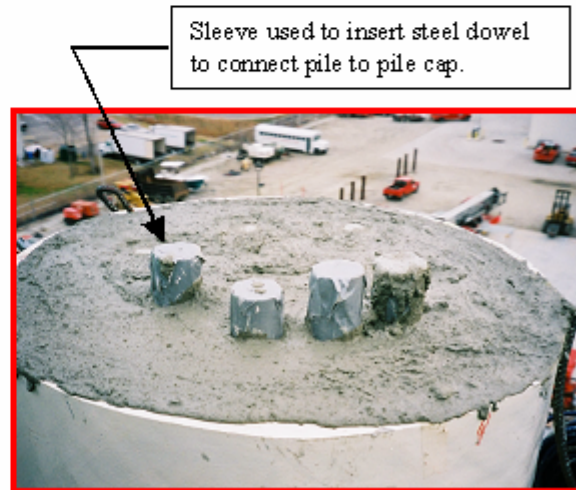
(a) Concrete is poured into bucket



(b) Bucket with concrete is positioned over the pile with crane



(c) Concrete pouring is controlled by operators located in the adjacent manhole lift



(d) Top of the production pile after concrete pour

Figure 123. Photos. Concrete filling of FRP composite piles.

6.5.4 Fabrication of Plastic Composite Test Pile

The polyethylene composite test pile was instrumented with special sister bar strain gages made of materials capable of withstanding the high temperatures and pressures involved in manufacturing of the pile. The instrumentation was installed between August 20 and August 22, 2001.

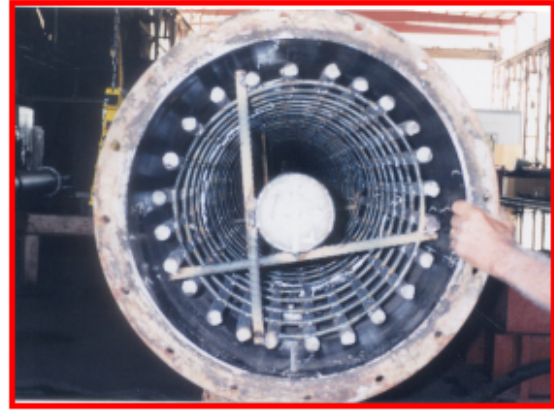
Photos of test pile fabrication are shown in figures 124 and 125. After fabricating, the pile was shipped to the bridge site.



Figure 124. Photos. Rebar cage of the plastic composite test pile.



a) Instrumented rebar cage is inserted into steel mold



b) View of bottom end of mold before closing (plastic injected from other end)



c) Mold submerged in cooling tank



d) Finished pile ready to be extruded from mold



e) Finished plastic test pile

Figure 125. Photos. Manufacturing process for the plastic composite test pile.

6.6 PILE INSTALLATION AND DYNAMIC TESTING

6.6.1 Pile Driving

The test piles were driven at the locations shown in figure 116. Prior to driving, all three piles were placed in pits approximately 1.0 m (3 ft) deep, thus removing the man-made fill materials. An ICE model 80S single-acting diesel hammer was used to drive the piles. The maximum rated energy of the hammer is 108.6 kN-m (80,000 ft-lbs). All piles were driven with 230-mm- (9-inch-) thick plywood pile cushions. After driving, the pile cushions were about 140 mm (5.5 inches) thick. The prestressed concrete, FRP, and plastic piles were driven to depths of 16.76, 17.22, and 17.27 m (55.0, 56.5, and 56.6 ft), respectively, below the original ground surface. The pile-driving records are shown in figure 126. Pile installation photos for the prestressed concrete, FRP, and plastic piles are shown in figures 127 through 129, respectively.

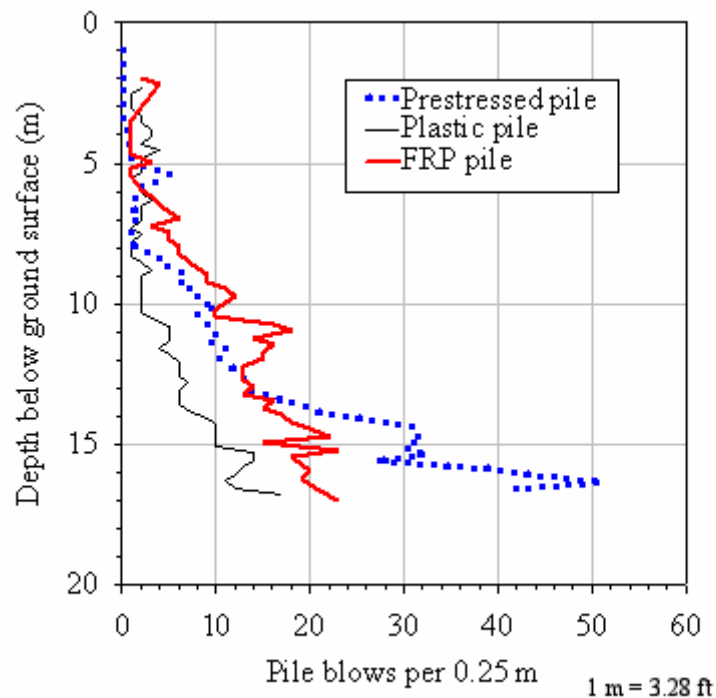


Figure 126. Graph. Driving records for test piles.



a) Driving of prestressed pile

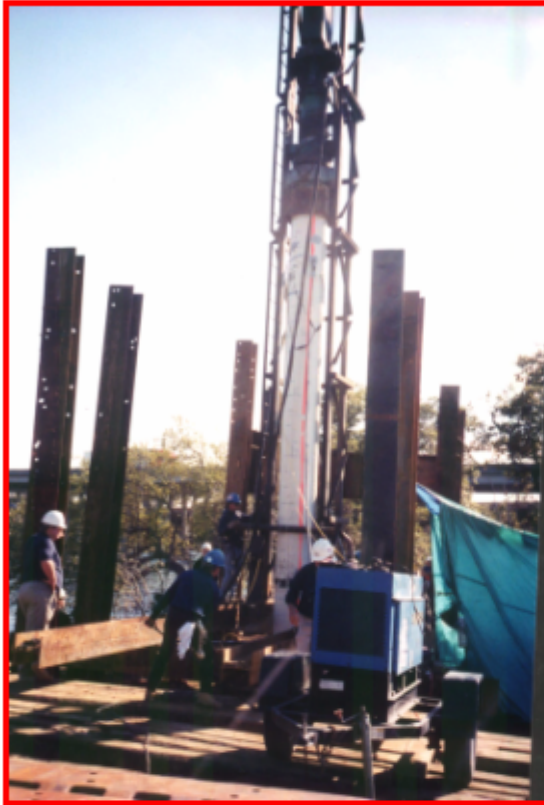


b) End of driving of prestressed pile showing driving cushion compressed



c) Restrike of prestressed pile

Figure 127. Photos. Installation of prestressed concrete test pile.



a) Driving of FRP pile



b) End of driving of FRP pile



c) End of driving of FRP pile showing driving cushion compressed

Figure 128. Photos. Installation of FRP composite test pile.



a) Driving of plastic pile



b) End of driving of plastic pile



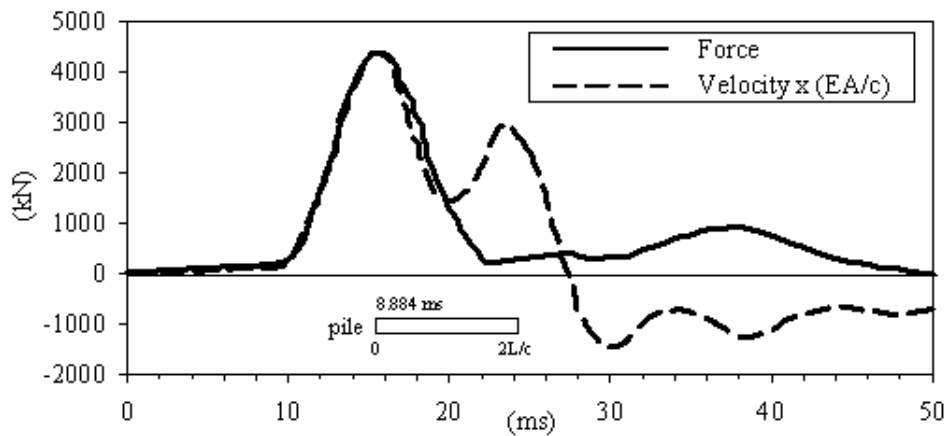
c) Restrike of plastic pile

Figure 129. Photos. Installation of plastic composite test pile.

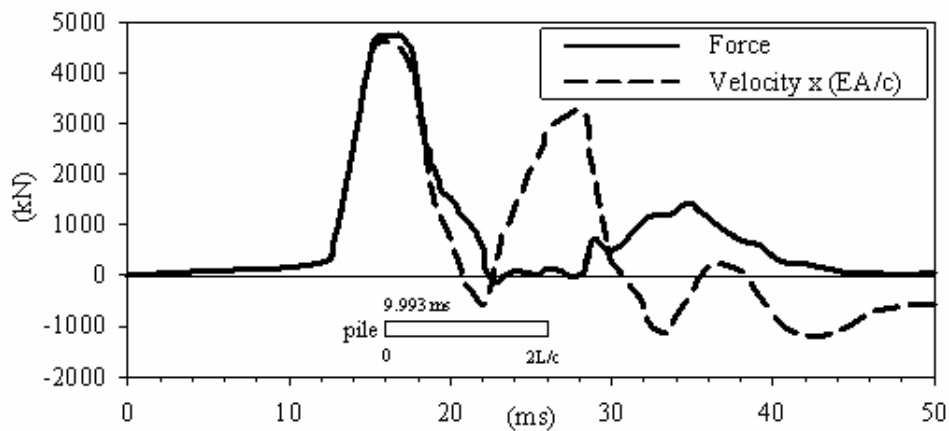
6.6.2 Dynamic Testing

Dynamic monitoring was performed using a Pile Driving Analyzer (PDA). Monitoring was performed during initial driving and during restrrike, which occurred 5 days after initial driving. Dynamic testing was accomplished by attaching strain transducers and accelerometers at about 2 diameters from the top of the piles in pairs spaced 180 degrees apart. To attach the transducers to the FRP composite pile, small windows were cut out of the FRP shell, which allowed the instrumentation to be directly attached to the concrete infill. For the plastic pile, the transducers were bolted to the recycled plastic.

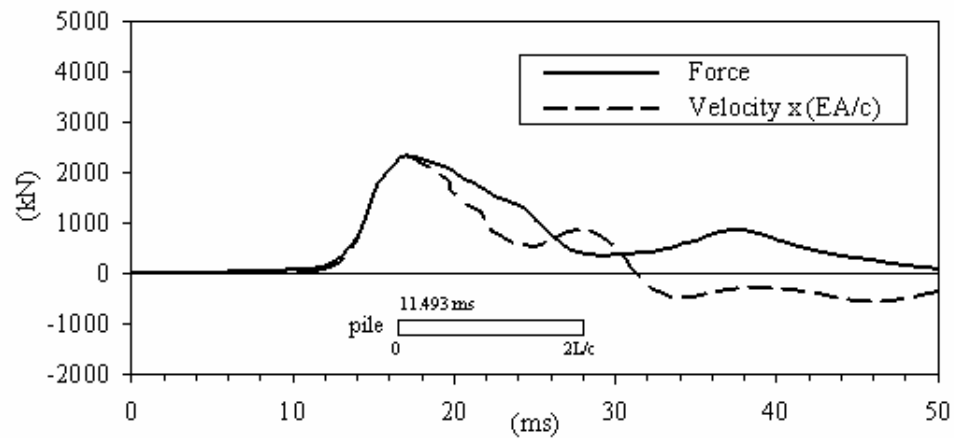
PDA records for the three types of piles at restrrike are shown in figure 130. The PDA records show a force peak at about time 0 (measured with respect to the horizontal bars that are shown in figure 130, which represent the wave travel time for two pile lengths for each pile). A velocity peak can also be seen at about $2L/c$ (where L is the pile length, and c the wave speed). This peak is characteristic of a reflected tensile wave from the toe. The prestressed concrete and FRP composite piles show similar dynamic behavior. A large separation was observed between the force and velocity traces, beginning at about L/c for both of these piles. For the plastic pile, a gradual separation between the force and velocity traces starts to occur shortly after 0. Spiro and Pais (2002a and b) encountered problems during interpretation of the dynamic data from the plastic test pile. The stress-strain nonlinearity of the plastic (to which the transducers were attached), the strain rate dependency of the elastic properties, and the presence of voids in the plastic were all considered by the authors as possible reasons for poor quality of the dynamic data for the plastic pile. The velocity peak at $2L/c$, which is due to tensile wave reflection at the toe, was not as pronounced for the plastic pile as for the other two piles.



(a) Prestressed concrete pile



(b) FRP composite pile



(c) Plastic composite pile

1 kN = 225 lbf

Figure 130. Graphs. PDA recordings during restrike.

Table 30 provides some of the measurements obtained during pile driving. It can be seen that the prestressed and FRP piles had similar wave speeds, and the wave speed recorded in the plastic pile was about 18 percent lower than the prestressed pile. The maximum compressive and tensile stresses were lower than the allowable stresses recommended for prestressed piles (Hannigan, et al., 1996). The highest driving stresses were recorded in the FRP composite pile; however, no standards are currently available for allowable driving stresses for composite piles.

Table 30. Summary of pile-driving measurements for the prestressed and composite piles (after Spiro and Pais 2002a and b).

Measurement	Pile Type		
	Prestressed	FRP	Plastic
Wave speed	3,800 m/s	3,782 m/s	3,100 m/s
Maximum compression stress measured during driving	11.0 MPa	16.2 MPa	9.9 MPa
Maximum tensile stress measured during driving	5.6 MPa	8.5 MPa	3.3 MPa
Allowable stresses	Comp. < 24.5 MPa Tension < 6.7 MPa	No standards available	No standards available

1 MPa = 145 lbf/inch²

Estimates of pile capacity from the dynamic strain and acceleration measurements were obtained using the Case method (Spiro and Pais 2002a and b). The strain and acceleration data from restrike were subjected to CAPWAP analyses (Spiro and Pais 2002a and b). Both the Case method and CAPWAP capacities are listed in table 31. For all three test piles, substantial increases in the Case method-derived capacity occurred between the end of initial driving and restrike 5 days later. According to the CAPWAP analyses, the prestressed concrete pile has the highest capacity at 1,960 kN (440 kips), and the FRP pile and the plastic pile have lower capacities equal to 96 percent and 77 percent, respectively, of the prestressed concrete pile capacity. The CAPWAP analyses also indicate that the shaft capacities, as percentages of the total capacities, are 46 percent, 43 percent, and 41 percent for the prestressed concrete, FRP, and plastic piles, respectively.

**Table 31. Summary of CASE and CAPWAP analyses results
(Spiro and Pais 2002a and b).**

Method	Capacity Component	Prestressed Concrete Pile	FRP Pile	Plastic Pile
Case ⁽¹⁾ (end-of-driving)	Total	200 kN	1,600 kN	520 kN
Case ⁽¹⁾ (restrike ⁽²⁾)	Total	1,800 kN	2,300 kN	1,300 kN
CAPWAP ⁽³⁾ (restrike ⁽²⁾)	Shaft	894 kN	815 kN	618 kN
	Toe	1,066 kN	1,069 kN	894 kN
	Total	1,960 kN	1,884 kN	1,512 kN

Notes: (1) Case method using a Case damping coefficient of 0.60.
(2) Restrike of piles performed 5 days after initial driving.
(3) CAPWAP equivalent damping coefficient = 0.35.

1 kN = 225 lbf

6.7 PILE INTEGRITY TESTING OF TEST PILES

Pile integrity tests (PIT) were performed on the test piles before and after pile installation. These tests consisted of applying a small impact load to the top of the pile with a hand-held hammer. The impact from the hammer generates a small downward compression wave (low strain) that travels along the pile with a wave speed, *c*. The PIT tests prior to installation were performed by tapping the piles while they were lying horizontally on the ground. Figure 131 shows selected photos of PIT tests before and after installation.

For a uniform pile, supported without any resistance to deformation and without any imperfections, voids, or damage, the compression wave will travel unchanged to the bottom of the pile and will be reflected upward as a tension wave. However, if the compression wave encounters a void or damage before reaching the bottom of the pile, a tension wave will be generated sooner than the reflection from the pile toe. Damage of the pile is assessed based on the velocity curve, which is investigated for wave reflections that may indicate change in pile properties due to defects. However, it is important to point out that reflections also occur due to soil resistance, particularly for piles with high shaft friction. For long piles with high shaft friction, the reflection from the toe may be very small. To help improve identification of the reflections, the records are amplified exponentially with time.



a) PIT on plastic pile after installation



b) PIT on FRP pile before installation



c) PIT on FRP pile after installation

Figure 131. Photos. PIT tests on test piles.

PIT results for the prestressed concrete test pile before and after driving are shown in figures 132 and 133, respectively. No discernable damage was noted based on comparison of the pre- and postdriving PIT soundings. The soil resistance in the pile after installation results in a smaller toe reflection, as shown in figure 133.

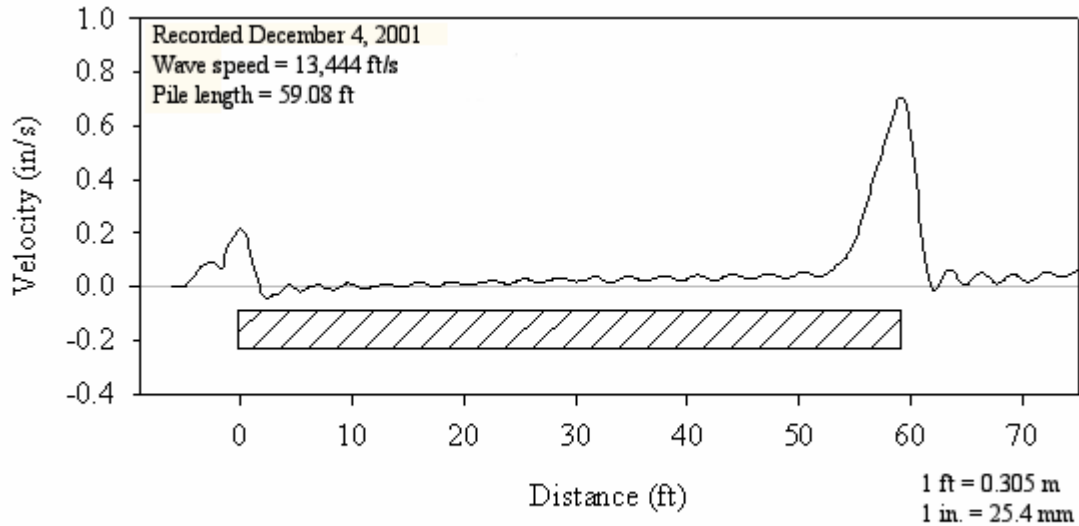


Figure 132. Graph. PIT sounding on the prestressed concrete test pile before installation.

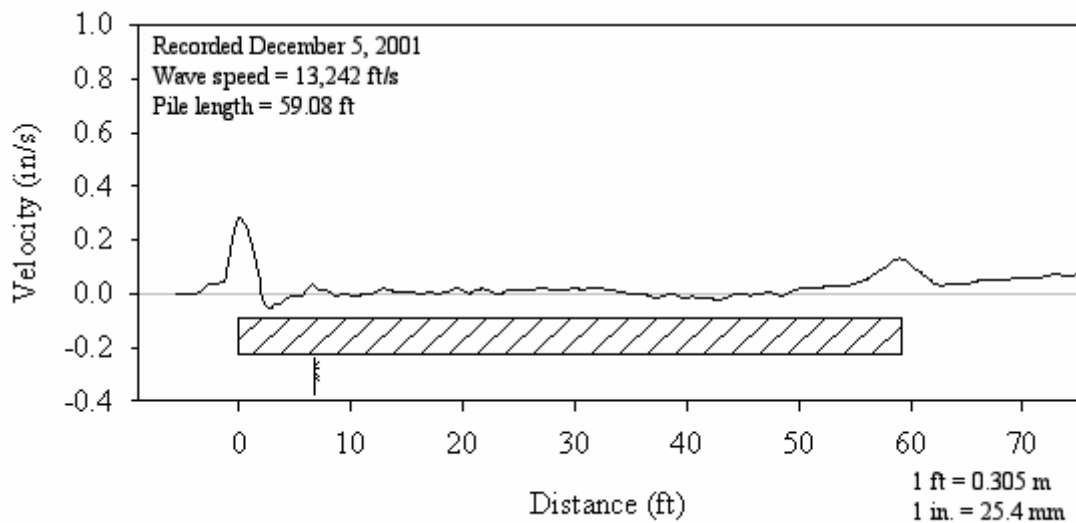


Figure 133. Graph. PIT sounding on the prestressed concrete test pile after installation.

PIT results for the FRP test pile are shown in figures 134 and 135. No significant difference between the pre- and postdrive PIT traces was observed for the FRP pile, and similar velocity changes were noted at about 17 and 35 ft (5.19 and 10.7 m) from the pile top. Toe reflection in the postdrive PIT is almost not discernible, probably due to high soil resistance. No discernable damage was noted based on comparison of the pre- and postdriving PIT soundings.

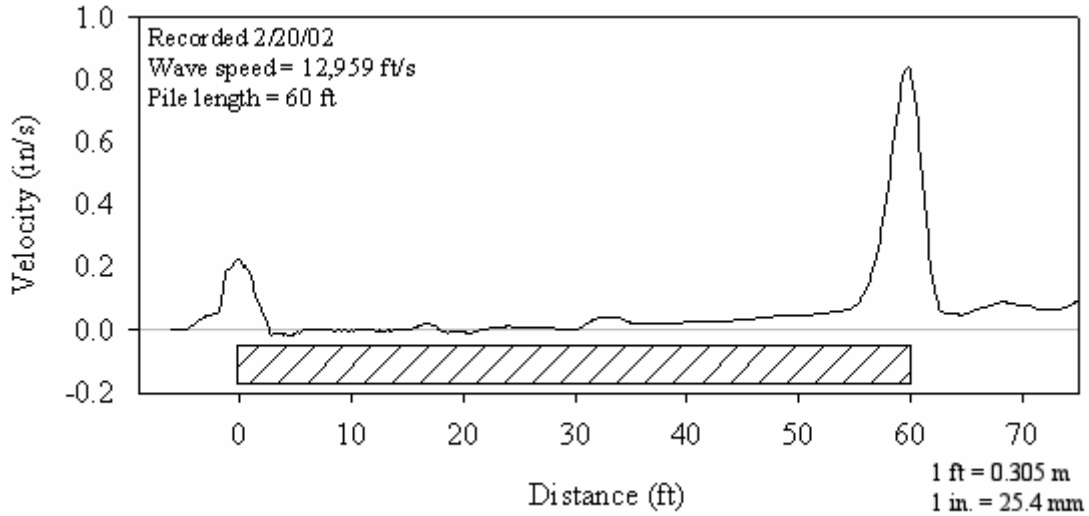


Figure 134. Graph. PIT sounding on the FRP composite test pile before installation.

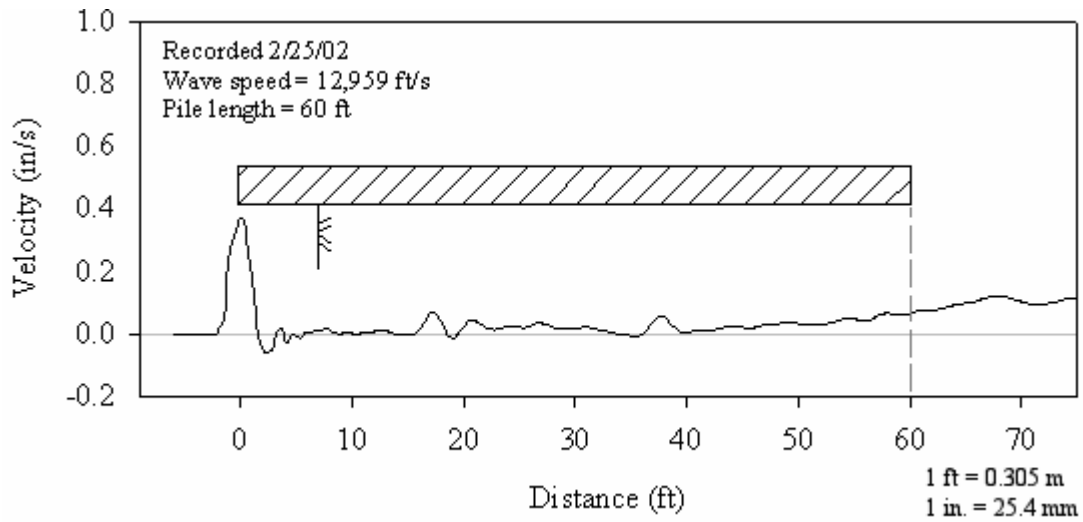


Figure 135. Graph. PIT sounding on the FRP composite test pile after installation.

PIT results for the plastic composite test pile are shown in figures 136 and 137.

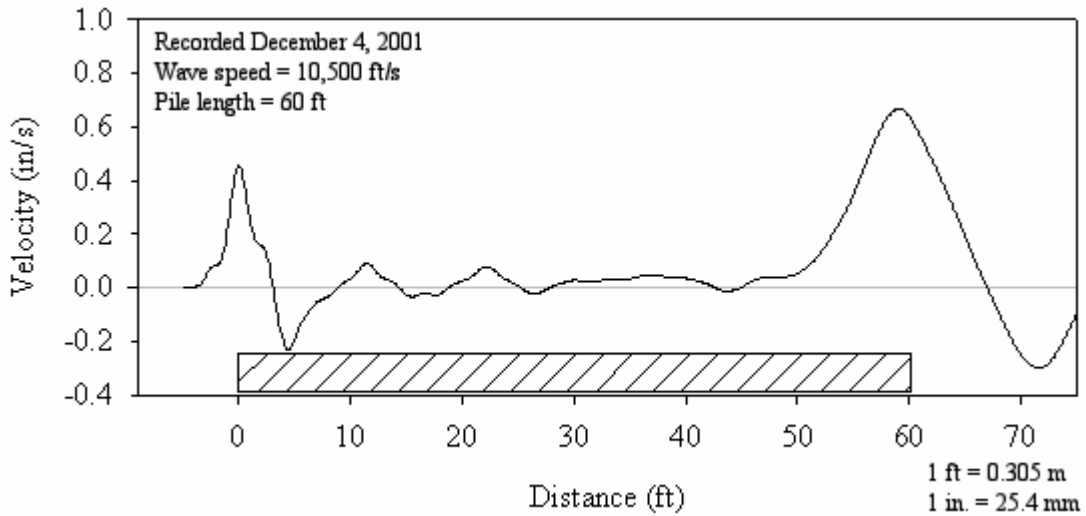


Figure 136. Graph. PIT sounding on the plastic composite test pile before installation.

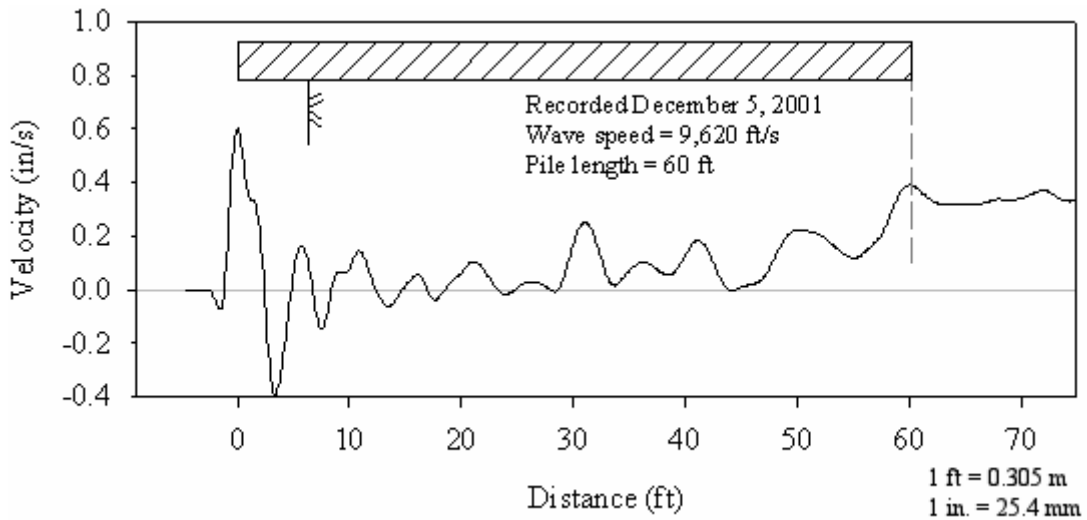


Figure 137. Graph. PIT sounding on the plastic composite test pile after installation.

Differences can be seen between the pre- and postdrive PIT traces from the plastic pile. Some of the new velocity peaks observed in the postdriving PIT may be due to soil resistance. However, these peaks may also be related to damage that may have occurred in the pile during pile driving. The observed differences in PIT records are not conclusive to indicate whether the pile was damaged during pile installation.

6.8 FIELD TESTING OF TEST PILES

The axial and lateral load test results for the three test piles are summarized in the following sections. Important date information for the Route 351 test pile program is summarized in table 32.

Table 32. Test dates for the test pile program at the Route 351 Bridge project.

Pile Type	Cross Section	Length (m)	Fabrication Date	Driving Date	Restrike Date	Axial Load Test Date	Lateral Load Test Date
Prestressed concrete	610 mm square	18	8/14/01	12/5/01	12/10/01	12/17/01	12/17/01
Plastic	592 mm circular	18.3	8/23/01	12/5/01	12/10/01	12/21/01	12/21/01
FRP	622 mm circular	18.3	2/6/02	2/21/02	2/26/02	3/4/02	3/5/02

1 mm = 0.039 inches; 1 m = 3.28 ft

6.8.1 Axial Load Tests

Static axial load tests were performed on the three test piles in accordance with ASTM D1143. The compressive test loads were applied by jacking against a steel frame anchored by eight, HP 14x89 reaction piles placed as shown in figure 116. The reaction system was designed for a maximum load of 4,448 kN (1,000 kips). The load was applied by three calibrated hydraulic jacks connected to a common manifold and pressure gage and operated by a single hydraulic pump. The load applied by this jacking system was measured using a 4,448 kN (1,000 kips) calibrated load cell. The deflections were monitored using dial gages, LVDTs (linear variable deformation transducers), and a wire and mirror system, with support provided by an isolated reference beam. Figure 138 show photos of the axial load test setup.

The axial load test was carried out by increasing the axial load using constant load increments of 89 kN (20 kips). After each load increment, the load was held constant for a time interval of 2.5 minutes. This type of loading sequence is called Quick Maintained-Load Test (Fellenius 1990) and is in general accordance with the Quick Load procedure included in ASTM D1143.

The data from the dial gages and wire and mirror system were collected by an FHWA contractor. The data from the LVDTs, sister bar strain gages, foil gages used in the FRP pile, and load were acquired using a MEGADAC[®] data acquisition system. FHWA operated the MEGADAC system.

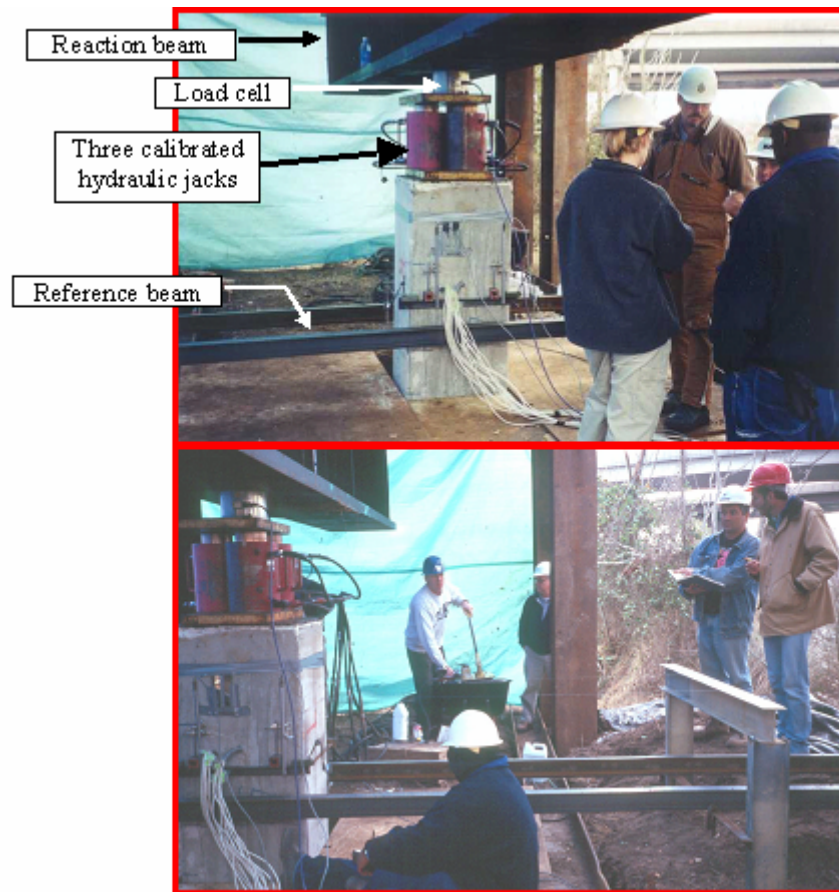


Figure 138. Photos. Axial load test of prestressed concrete pile.

Figure 139 shows the measured axial load versus pile head displacement diagrams for all three test piles. It can be seen in figure 139 that the prestressed concrete pile and the FRP pile exhibit stiffer initial response than the plastic pile.

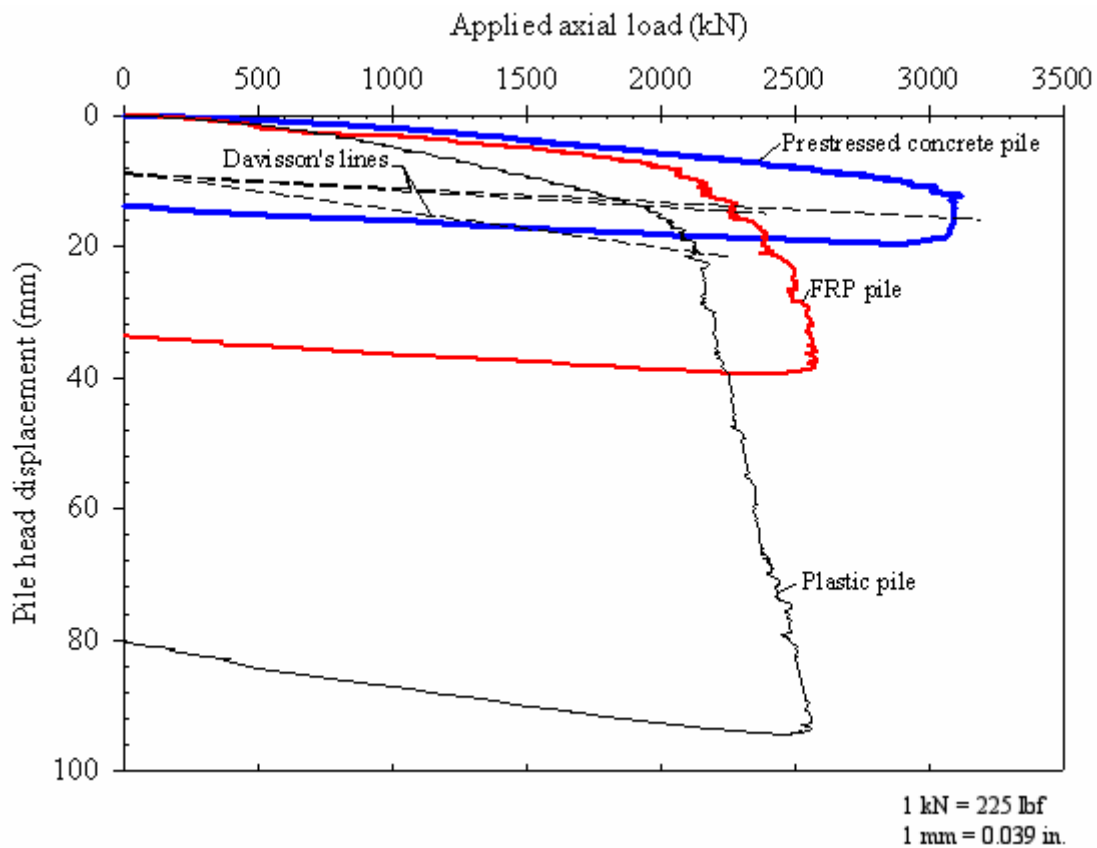


Figure 139. Graph. Axial load test results.

The pile capacities according to Davisson's criterion (Davisson 1972) are also shown in figure 139. The pile failure loads obtained using this criterion and other commonly used methods described by Fellenius (1990) are listed in table 33.

Based on Davisson's criterion, the prestressed concrete pile exhibited the highest capacity at 3,095 kN (696 kips), and the FRP pile and the plastic pile have lower capacities equal to 73 percent and 69 percent, respectively, of the prestressed concrete pile capacity.

Table 33. Comparison of failure loads for the three test piles.

Failure Criterion ⁽¹⁾	Prestressed Pile Failure Load (kN)	FRP Pile Failure Load (kN)	Plastic Pile Failure Load (kN)
De Beer's	3,095	2,070	2,040
Vander Veen's	3,180	2,600	2,250
Brinch-Hansen's (90% criterion)	3,080	2,113	2,163
Chin's	3,080	2,815	2,615
Brinch-Hansen's (80% criterion)	3,103	2,576	2,459
Davisson's	3,095	2,260	2,130

Note: (1) Description of failure criteria can be found in Fellenius (1990).

1 kN = 225 lbf

6.8.1.1 Residual stresses

The strain gages that were installed in the test piles permitted calculation of the residual strains and stresses locked in the pile after pile driving.

The residual strains were calculated by comparing the strain gage readings before and after pile installation. The residual load distributions along the piles were then obtained by multiplying the recorded residual strains by the respective pile axial stiffness (EA). The residual load distributions are shown in figure 140.

The average residual stresses acting along the pile shaft can be estimated by considering the vertical equilibrium of the different pile segments between the levels of sister bar strain gages. Using this procedure, the estimated residual stress distributions for the three test piles are shown in figure 141. The residual stresses for the prestressed concrete and FRP piles are estimated to range between ± 9 kPa (1.305 lbf/inch²). The estimated residual stresses for the plastic pile do not seem very realistic; nevertheless, their values ranged between +28 kPa (4.06 lbf/inch²) and -40 kPa (5.8 lbf/inch²).

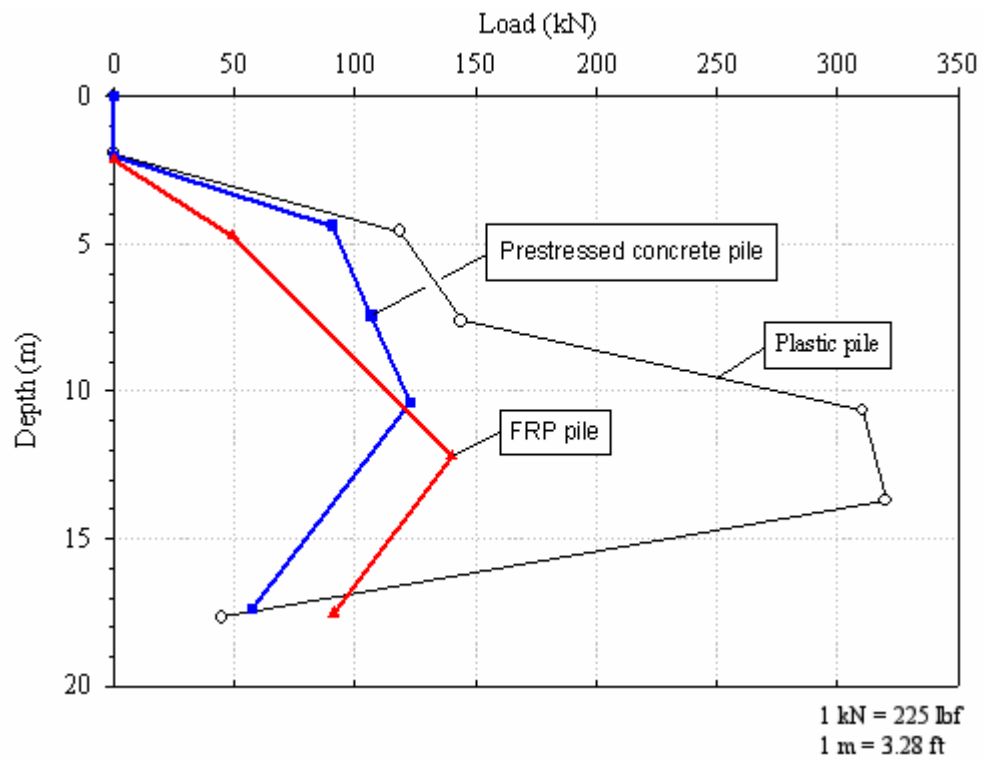


Figure 140. Graph. Distribution of residual loads.

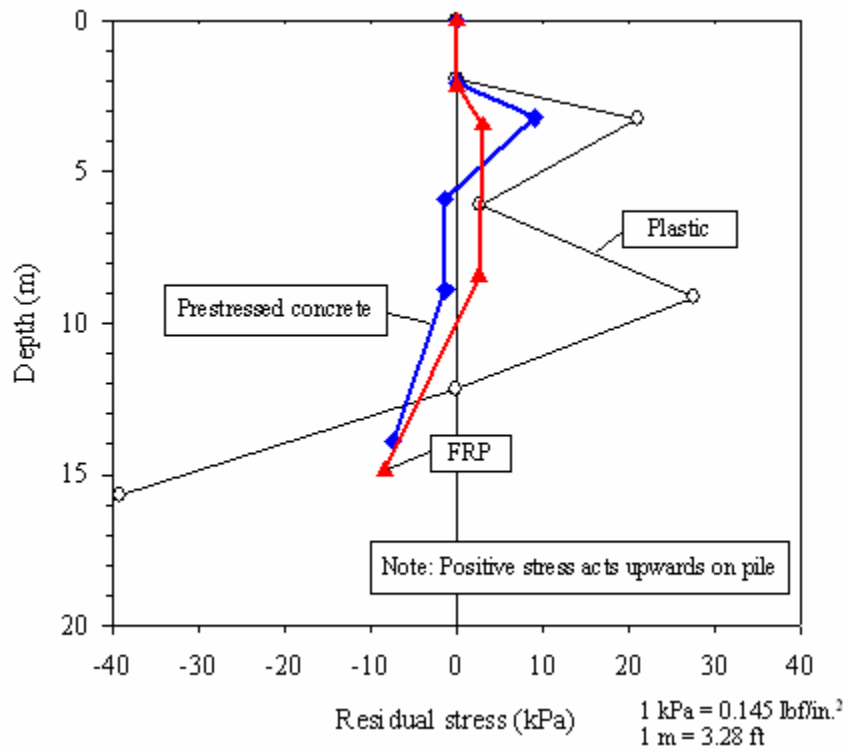


Figure 141. Graph. Distribution of residual stresses.

6.8.1.2 Load transfer

The three test piles have different embedded shaft areas and different toe areas. Consequently, it is informative to separate the shaft and end resistances, and to normalize these resistances by the shaft and toe areas. The strain gages that were installed in the test piles permitted calculations of load transfer from the piles to the ground. These calculations were performed with consideration of residual stresses after driving, using the procedures described in Fellenius (2002). The resulting load transfer diagrams are shown in figure 142. From these diagrams, the shaft and toe components of pile capacities can be determined at the Davisson failure loads, and these are listed in table 34. The shaft capacities, as percentages of the total capacities, are 78 percent, 65 percent, and 70 percent for the prestressed concrete, FRP, and plastic piles, respectively.

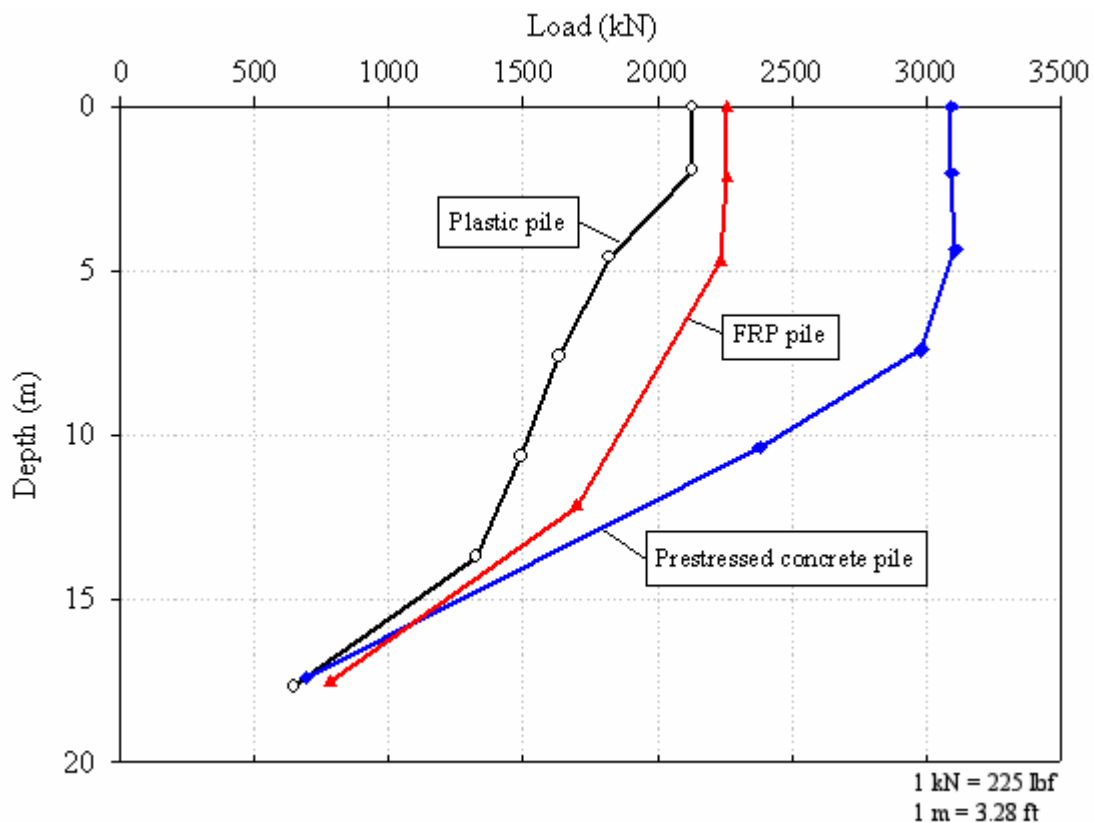


Figure 142. Graph. Load distribution for the three test piles at the Davisson failure loads.

Table 34. Load distributions from static load tests at the Davisson failure loads.

Capacity Component	Prestressed Concrete Pile		FRP Pile		Plastic Pile	
	Capacity (kN)	Days after EOID*	Capacity (kN)	Days after EOID	Capacity (kN)	Days after EOID
Shaft	2,406	12	1,480	11	1,487	16
Toe	689		780		643	
Total	3,095		2,260		2,130	

* EOID = the end of initial driving

1 kN = 225 lbf

Using the shaft and toe capacities from the static load tests, together with the embedded pile shaft areas and the pile end areas, the average unit shaft resistances (f_s) and the unit toe resistances (q_t) were determined for conditions at the Davisson failure loads. The resulting values are listed in table 35, which shows that the average unit shaft resistances decrease in order, from the prestressed concrete pile to the plastic pile to the FRP pile, and that the unit toe resistances increase in the same order from the prestressed concrete pile to the plastic pile to the FRP pile. The observed relationship between mobilized average shaft stress and toe stress for each of the three piles is shown in figure 143.

Table 35. Unit shaft and toe resistances from static axial load tests.

Pile Type	Average Unit Shaft Resistance, f_s (kPa)	Unit Toe Resistance, q_t (kPa)
Prestressed concrete pile	61.8	1,854
FRP pile	46.9	2,564
Plastic pile	48.9	2,339

Note: (1) Resistance values are for Davisson failure loads.

1 kPa = 0.145 lbf/inch²

There are notable differences between the results of the static load tests and the CAPWAP analyses on restrike hammer blows, as shown in table 31. The capacities from the static load tests are higher than the capacities from the CAPWAP analyses by 58 percent, 20 percent, and 41 percent for the prestressed concrete, FRP, and plastic piles, respectively. Strength gain during the 6 to 11 days that passed between restrike and the static load tests may be due to continued setup during this time period. This apparent strength gain versus elapsed time after end of initial driving (EOID) is illustrated in figure 144 by plotting the capacities determined using the Case method, CAPWAP analyses, and static load test results. It is also noted that the shaft capacities from the static load tests are much higher percentages of total capacity than are the shaft capacities from the CAPWAP analyses. Again, this may be due (at least in part) to changes in capacity distribution occurring during setup. It is also recognized that CAPWAP analyses and static load tests are different methods of determining pile capacity, and thus may produce different total capacities and different capacity distributions.

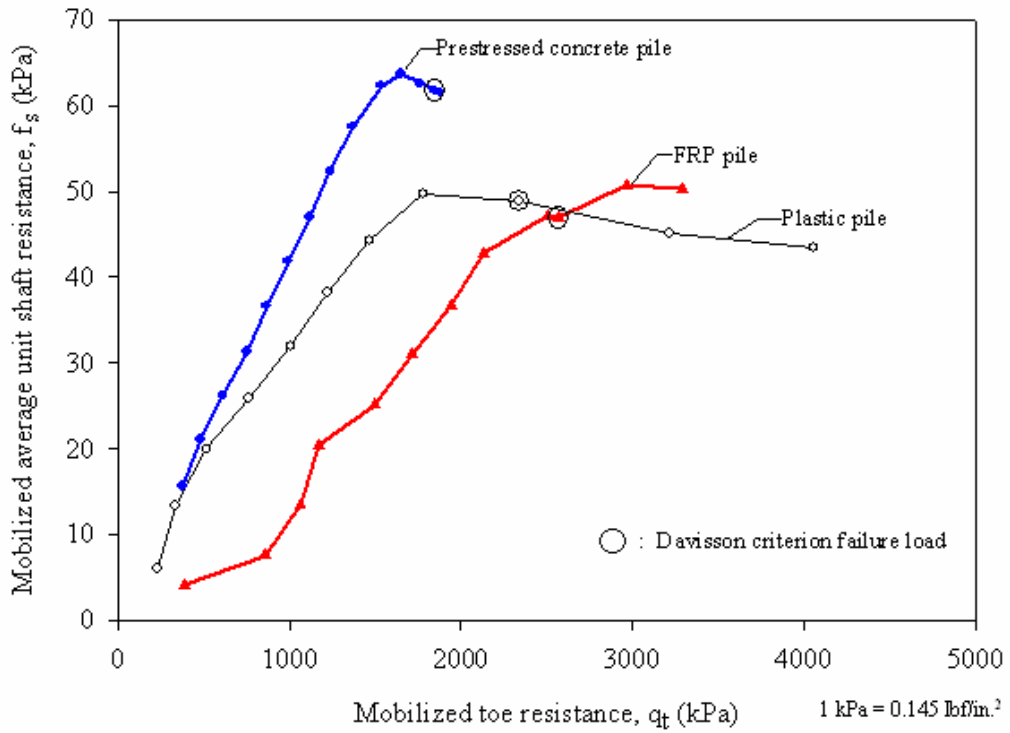


**Figure 143. Graph. Mobilized average unit shaft resistance—
toe resistance relationships for the three test piles.**

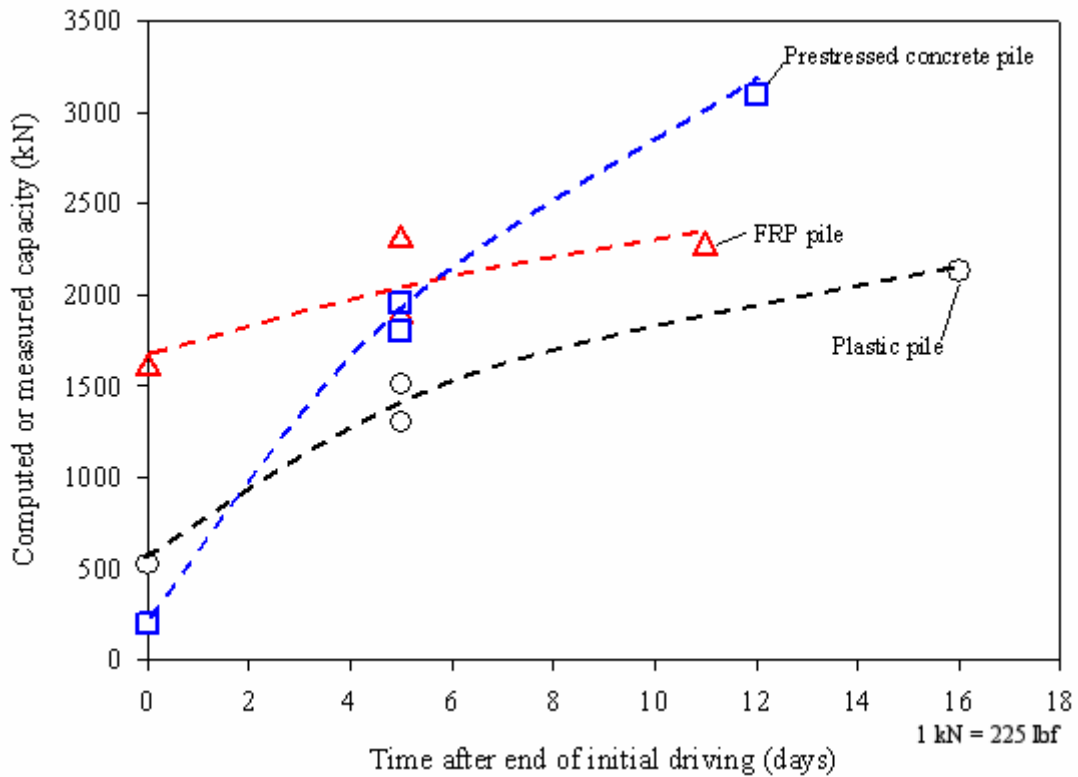


Figure 144. Graph. Apparent strength gain with time in the three test piles.

6.8.2 Lateral Load Tests

For each test pile, a static lateral load test was performed on the same day as, or the first day following, the static axial load test. The lateral load tests were performed in accordance with ASTM D3966, using the same reaction system as used for the axial load tests. A calibrated jack and a calibrated load cell were used. Displacements near the pile head were monitored with dial gages and LVDTs, with support provided by an isolated reference beam.

Deformed shapes of the piles at several different lateral load magnitudes were obtained from standard inclinometer probe surveys along the installed casings. These shapes are shown in figure 145, together with the elevations of the original ground surface, the bottom of the pits at the test pile locations, and the points of load application. The piles exhibit negligible lateral deformation below depths of 6, 3.3, and 3.5 m (19.7, 10.8, and 11.5 ft) below the bottom of the pits at the test pile locations for the prestressed concrete, FRP, and plastic piles, respectively.

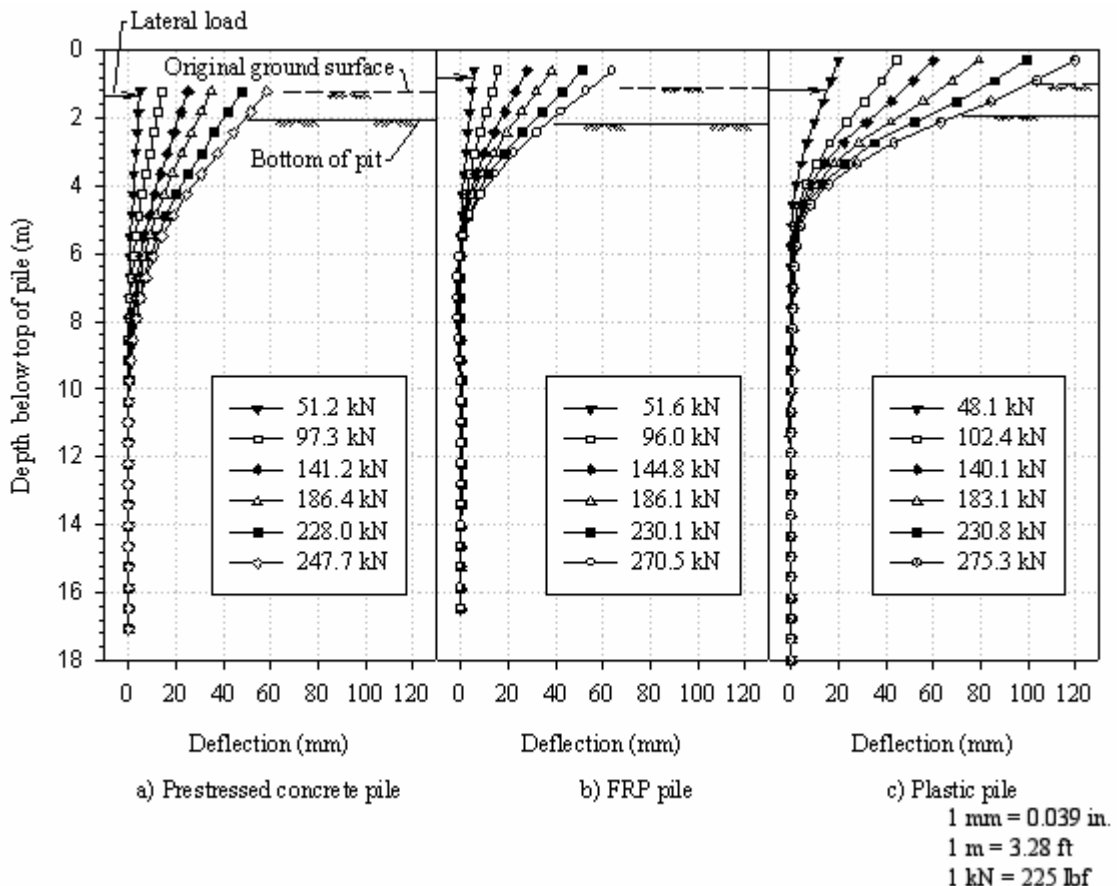


Figure 145. Graphs. Deformed shapes of piles at different lateral loads.

The measured load is plotted against pile deflection at the original ground surface in figure 146, which shows that the prestressed concrete pile and the FRP pile exhibited similar load-deflection response and that the plastic pile deformed the most. At a lateral

load of 200 kN (45 kips), the deflections were approximately 35, 33, and 70 mm (1.37, 1.29, and 2.73 inches) for the prestressed concrete, FRP, and plastic piles, respectively.

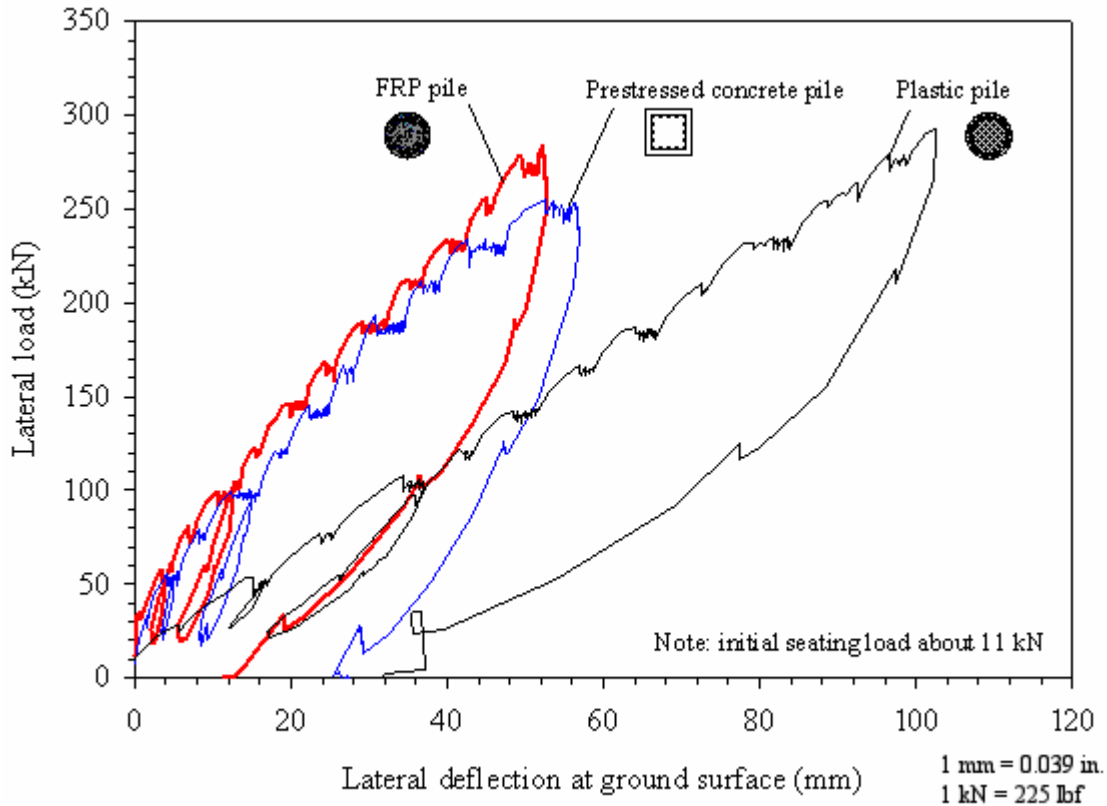


Figure 146. Graph. Measured lateral deflections at ground surface for the three test piles.

6.9 SUMMARY AND CONCLUSIONS

A test pile program was conducted to permit direct comparison of the axial and lateral load behavior of three test piles: (1) a conventional, 610-mm (23.8-inch) square, prestressed concrete pile; (2) a 622-mm (24.3-inch) diameter composite pile formed of an FRP shell and filled with concrete and steel reinforcing bars; and (3) a 592-mm (23.1-inch) diameter composite pile formed of a polyethylene plastic matrix with steel reinforcing bars. Laboratory tests were performed on the pile materials, and the axial and bending stiffnesses of the piles were calculated. The piles are all about 18 m (59.0 ft) long. The soils at the test site were investigated, and they consist primarily of medium-dense silty sand with a 2.5-m (8.20-ft) thick layer of stiff sandy clay located about 1 to 3.5 m (3.28 to 11.5 ft) above the pile toes. The field testing program included dynamic measurements with CAPWAP analyses, static axial load tests, and static lateral load tests.

The following conclusions can be drawn from the test program.

1. The axial stiffness (EA) of the prestressed concrete pile and the FRP pile are similar to each other and about 2.5 times the axial stiffness of the plastic pile.
2. Over a working range of bending moments, the flexural stiffness (EI) decreases in order from the prestressed concrete pile to the FRP pile to the plastic pile.
3. All three piles exhibited substantial setup after installation based on comparisons of Case method capacities at the end of initial driving and restrike 5 days later, as well as comparisons of CAPWAP analyses of restrike and static axial load tests several days after restrike.
4. Applying Davisson's failure criterion to the static axial load tests, the axial capacities were 3,090, 2,260, and 2,130 kN (695,250, 508,500, and 479,250 lbf) for the prestressed concrete pile, the FRP pile, and the plastic pile, respectively.
5. When evaluated at the Davisson failure load, the average unit shaft resistances are 61.8, 46.9, and 48.9 kPa (8.96, 6.80, and 7.09 lbf/inch²) for the prestressed concrete pile, the FRP pile, and the plastic pile, respectively, and the corresponding unit toe resistances are 1,854, 2,564, and 2,339 kPa (268.8, 371.8, and 339.2 lbf/inch²).
6. The prestressed concrete pile and the FRP pile exhibited similar load-deflection response in static lateral load tests. The plastic pile exhibited much larger deflections at the same lateral loads.

CHAPTER 7. ANALYSES OF THE AXIAL LOAD TESTS AT THE ROUTE 351 BRIDGE

7.1 INTRODUCTION

In this chapter, calculations using methods commonly employed in practice are presented for the pile axial load capacity, and for the load-deflection behavior, of the three test piles at the Route 351 Bridge project. The calculations are compared with the recorded pile capacities and the measured load-deflection responses. Background information for the methodologies used to perform the analyses is also presented and discussed in this chapter.

7.2 AXIAL PILE CAPACITY

7.2.1 Methods to Estimate Axial Load Capacity of Driven Piles in Sand

The axial capacity of driven piles in sand is possibly the area of greatest uncertainty in foundation design (Randolph, et al., 1994), and many methods are available for predicting pile capacity. Despite the extensive amount of research in this area, the appropriateness and accuracy of current design methods are often questioned (Randolph, et al., 1994, Olson 2002). In practice it is common to use factors of safety of two, three, or more, since measured pile capacities of driven piles have been found to differ from the calculated capacities by more than three times (Olson 2002). It is expected that these uncertainties will be applicable to driven composite piles. With this in mind, the predictions for the composite piles presented in this chapter are expected to show at best a level of accuracy similar to the predictions for conventional piles.

The predictions presented herein are based primarily on design methods commonly used by U.S. highway agencies, with the exception of a relatively new method proposed by Jardine and others at the Imperial College in England; that method seems to provide a rational approach for assessing axial load capacity of driven piles (Jardine and Chow 1996).

A sketch of the axially loaded pile problem is shown in figure 147. Generally, most methods estimate the ultimate pile capacity based on consideration of vertical equilibrium of the pile at the state of incipient bearing capacity failure (i.e., when the settlement of the pile increases rapidly with little further increase in load at the pile head). From figure 147, the ultimate axial capacity of a pile is given by the equation:

$$Q_T = Q_s + Q_b - W_p \quad (16)$$

where Q_T is the estimated ultimate axial capacity, Q_s is the ultimate shaft capacity resulting from the surrounding soil in side shear, Q_b is the total ultimate tip load at the base or tip of the pile (total indicates the weight of the displaced volume of soil is

included), and W_p is the weight of the pile. In practice, the term W_p is usually neglected since it is considered small compared to the accuracy of the prediction of Q_T .

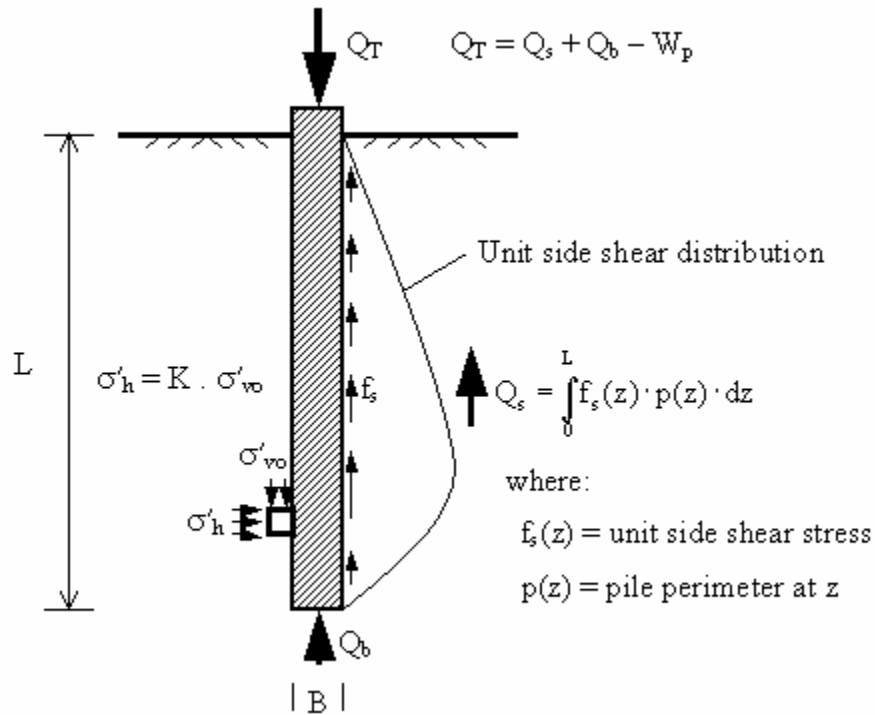


Figure 147. Illustration. Load transfer in an axially loaded pile.

The load capacity contributed by the shaft side shear (Q_s) is calculated by integrating the side shear stresses along the pile's embedded length:

$$Q_s = \int_0^L f_s(z) p(z) dz \quad (17)$$

where $f_s(z)$ is the shear stress between the pile and the soil at a depth z , $p(z)$ is the pile perimeter at depth z , and L is the embedment depth of the pile.

The expression used for the tip or end-bearing of the pile is usually of the form:

$$Q_b = A_b q_b \quad (18)$$

where A_b is the tip or end area of the pile, and q_b is the total ultimate end-bearing or tip stress.

The different pile capacity determination methods deal with ways of estimating the side friction (f_s) and the ultimate end-bearing stress (q_b). The following sections summarize the most common methods used in practice to estimate f_s and q_b for piles driven in sands.

7.2.1.1 Nordlund's method

Nordlund's method is often used by U.S. highway agencies and is advocated by the FHWA (Olson 2002). Nordlund's method is a semiempirical method based on a database of pile load tests (Nordlund 1963, 1979). The method accounts for differences in soil-pile interface for different piles. For the sake of brevity, only the most pertinent details of the method are presented. A complete description of this method can be found in Hannigan, et al. (1996).

According to the Nordlund's method, the shaft shear stress (f_s) of a uniform cross section of pile embedded at a length L can be estimated as follows (Hannigan, et al., 1996):

$$f_s = K_\delta C_F \sigma'_v(z) \sin(\delta) \quad (19)$$

where

K_δ = coefficient of lateral earth pressure

C_F = correction factor for K_δ when $\delta \neq \phi$

$\sigma'_v(z)$ = free-field effective overburden pressure at depth z

δ = interface friction angle between pile and soil

As pointed out by Olson (2002), the term $\sigma'_v(z)$ in equation 19 should, rigorously speaking, correspond to the effective vertical stress at depth z , right next to the pile shaft. Because this stress is unknown, it is common to use the free-field vertical stress that corresponds to the in situ value far away from the influence of the pile.

The expression proposed by Nordlund for the ultimate end-bearing stress (q_b) is as follows:

$$q_b = \alpha_T N'_q \sigma'_v(z = L) \quad (20)$$

where

α_T = dimensionless factor dependent on pile depth-width ratio

N'_q = bearing capacity factor (function of ϕ')

$\sigma'_v(z = L)$ = free-field effective overburden pressure at the pile tip ($z = L$)

Values for the coefficients K_δ , C_F , N'_q , and α_T , and for the interface friction angle δ , are typically read from design charts found in the technical literature, such as the FHWA manual for driven piles (Hannigan, et al., 1996).

7.2.1.2 API method

The American Petroleum Institute (API) provides design recommendations for axially loaded piles in the API RP 2A publication titled *Recommended Practice for Planning, Designing, and Constructing Fixed Offshore Platforms* (API 1993). Although this method is not as commonly used by highway agencies as is Nordlund's method, it is worth presenting here because the API recommendations are based on a large database of axial pile load tests that is continually evaluated and updated (Pelletier, et al., 1993). According to API (1993), the shaft shear for piles in sands can be estimated using:

$$f_s(z) = \sigma'_v(z) K \tan(\delta) \quad (21)$$

where

$\sigma'_v(z)$ = free-field effective overburden pressure at depth z

K = earth pressure coefficient

δ = interface friction angle between pile and soil (as per table 36)

API (1993) recommends using a value of 1.0 for the earth pressure coefficient (K) for full displacement piles, such as the piles tested in this project. Equation 21 implies that the shaft friction can increase indefinitely with depth (i.e., with increasing effective overburden pressure). However, API recommends using limiting values for f_s , as shown in table 36. In the absence of interface friction angle test data, API recommends using the values of soil-pile interface friction angles (δ) listed in table 36.

Table 36. API recommendations for side friction in siliceous soil (API 1993).

Density	Soil Description	Soil-Pile Interface Friction Angle, δ^2 (degrees)	Limiting Shaft Friction, f_s	
			(kips/ft ²)	(kPa)
Very loose	Sand	15	1.0	47.8
Loose	Sand-silt ³			
Medium	Silt			
Loose	Sand	20	1.4	67.0
Medium	Sand-silt			
Dense	Silt			
Medium	Sand	25	1.7	81.3
Dense	Sand-silt			
Dense	Sand	30	2.0	95.7
Very dense	Sand-silt			
Dense	Sand	35	2.4	114.8
Very dense	Sand-silt			

Notes: (1) These values provided by API are intended as guidelines only, and where detailed information is available other values may be justified.

(2) Suggested values are for steel pipe piles driven in cohesionless soils.

(3) Sand-silt is described as soils with significant fraction of both sand and silt.

API recommends using the following expression to estimate the ultimate end-bearing or tip resistance for piles driven in sands:

$$q_b = \sigma'_v(z = L) N_q \quad (22)$$

where

$\sigma'_v(z = L)$ = free-field effective overburden pressure at the pile tip ($z = L$)

N_q = bearing capacity factor (as per table 37)

Similarly to f_s , API recommends limiting the value of the tip resistance (q_b). The recommended values of N_q and limiting q_b are shown in table 37.

Table 37. API recommendations for tip resistance in siliceous soil (API 1993).

Density	Soil Description	N_q	Limiting Tip Resistance, q_b	
			(kips/ft ²)	(MPa)
Very loose	Sand	8	40	1.9
Loose	Sand-silt			
Medium	Silt			
Loose	Sand	12	60	2.9
Medium	Sand-silt			
Dense	Silt			
Medium	Sand	20	100	4.8
Dense	Sand-silt			
Dense	Sand	40	200	9.6
Very dense	Sand-silt			
Dense	Sand	50	250	12.0
Very dense	Sand-silt			

7.2.1.3 LCPC method

The Laboratoire Central des Ponts et Chaussees (LCPC) method estimates pile capacities based on CPT tip resistance (q_c) values (Bustamante and Gianeselli 1982). A detailed description of the method can be found in Lunne, et al., 1997.

The unit shaft resistance (f_s) is determined based on the pile type, installation method, and the value of the CPT tip resistance (q_c). The recommended pile shaft resistance is obtained by dividing the measured q_c by a friction coefficient (α_{LCPC}). A limiting shaft friction is recommended based on pile and soil type. The values of recommended friction coefficients, α_{LCPC} , and maximum limit of f_s for driven piles in sands are summarized in table 38.

Table 38. LCPC friction coefficient α_{LCPC} for driven piles in sands (Bustamante and Gianeselli 1982).

State of Sand	q_c (MPa)	Pile Category			
		Coefficient, α_{LCPC}		Maximum Limit of f_s (MPa)	
		Concrete	Steel	Concrete	Steel
Loose	≤ 5	60	120	0.035	0.035
Medium dense	5 to 12	100	200	0.08	0.08
Dense to very dense	> 12	150	200	0.12	0.12

1 MPa = 145 lbf/inch²

The LCPC method correlates the pile unit tip resistance (q_b) to an equivalent average cone resistance (q_{ca}) calculated using the q_c values within 1.5 pile diameters (or widths) below and above the pile tip elevation, as described by Lunne, et al. (1997). The LCPC pile tip resistance (q_b) is calculated by multiplying the equivalent average cone resistance (q_{ca}) by an end bearing coefficient (k_c). The recommended values for end-bearing factors for driven piles in sands are summarized in table 39.

Table 39. LCPC bearing capacity factors for driven piles in sands (Bustamante and Gianeselli 1982).

State of Sand	q_c (MPa)	Factor k_c
Loose	≤ 5	0.5
Medium dense	5 to 12	0.5
Dense to very dense	> 12	0.4

1 MPa = 145 lbf/inch²

7.2.1.4 Imperial College method

This method was developed at the Imperial College in London, England, by Jardine and his colleagues based on a series of investigations using instrumented field test piles (Jardine 1985, Bond 1989, Lehane 1992, Chow 1996). The instrumented piles were tubular closed and open-ended steel piles driven in sands for supporting offshore structures used in the oil industry.

The major findings of the Imperial College experiments, related to piles driven in sands, are summarized below (Jardine and Lehane 1993, Jardine and Chow 1996):

- The peak local shaft friction (f_s) is related to the local radial effective stress at failure (σ'_{rf}) by the following simple Mohr-Coulomb effective stress criterion:

$$f_s = \sigma'_{rf} \tan(\delta_f) \quad (23)$$

where

σ'_{rf} = the local radial effective stress at failure

$\delta_f = \delta_{cv}$ = failure or constant volume interface friction angle

- The radial effective stresses developed around the pile shaft after installation (σ'_{rc}) were found to depend strongly on the initial relative density of the sand (D_r) and the distance to the pile tip from the point where the radial stress is being evaluated. The following empirical expression, based on statistical analyses of over 60 datasets of radial stress, is recommended to estimate the local radial effective stress (σ'_{rc}) of close-ended piles:

$$\sigma'_{rc}(z) = 0.029 q_c \left(\frac{\sigma'_v(z)}{P_a} \right)^{0.13} \left(\frac{h}{R} \right)^{-0.38} \quad (24)$$

where

$\sigma'_{rc}(z)$ = local radial effective stress after installation

q_c = CPT tip resistance

z = depth below ground surface

L = pile embedded length

$h = L - z$ = distance to pile tip

$\sigma'_v(z)$ = free-field effective overburden pressure at depth z

P_a = atmospheric pressure (= 100 kPa)

R = pile radius

$h/R = 8$ for points close to the tip where $h < 8R$

- Jardine and Lehane (1993) found that the radial stresses could rise considerably (by about 50 percent) due to localized dilation at the pile-soil interface during axial compression loading of the pile. The radial stresses were found to reach a maximum near the mobilization of the peak shear stresses. The increase in radial effective stresses was found to vary in inverse proportion to the pile radius, and was found to be predicted reasonably well using the simple elastic cylindrical cavity expansion theory proposed by Boulon and Foray (1986).
- Constant volume or residual interface friction angles (δ_{cv}) were found to control the developed peak local shear stresses in pile tests. The values determined from laboratory interface shear tests were found to correlate well with their field test measurements. The interface friction angle was found to depend on sand grain size, shape, and mineral type. The pile material hardness and surface roughness were also found to influence δ . Jardine and coworkers pointed out that the level of radial effective stress may also influence δ , but they indicated that more research is needed to investigate this further.

The Imperial College (IC) method provides a simple, practical, and rational approach to predict pile capacity of piles driven in sands. A complete description of the IC method can be found in Jardine and Chow (1996), and a brief description is presented here. The basic steps involved in the IC method to estimate the shaft capacity of closed-ended driven piles in sands are:

1. Calculate the local radial effective stress around the pile after pile installation, σ'_{rc} using equation 24.
2. Calculate the increase in radial effective stresses ($\Delta\sigma'_{rd}$) due to dilation during pile loading. Jardine and Chow (1996) recommend using the following expression based on cylindrical cavity expansion theory:

$$\Delta\sigma'_{rd} = 2G \frac{\delta h}{R} \quad (25)$$

where

G = operational shear modulus of sand (see note below)

δh = average radial displacement (see note below)

R = pile radius

Notes:

G : Since the shear stiffness of sands is nonlinear, pressure dependent, and anisotropic, the method recommends using reliable and appropriate measurements of the shear modulus. If these measurements are not available, the following expression (after Chow 1996) is recommended:

$$G = \frac{q_c}{[A + B\eta - C\eta^2]}$$

and,

$$\eta = \frac{q_c}{\sqrt{P_a \sigma'_v}} \quad (26)$$

where

q_c = CPT tip resistance

$A = 0.0203$

$B = 0.00125$

$C = 1.216 \times 10^{-6}$

σ'_v = free-field effective overburden pressure

P_a = atmospheric pressure (100 kPa)

δh : The term $\delta h/R$, in equation 25, comes from cylindrical cavity expansion theory, and corresponds to the cavity strain. The term δh refers to radial sand dilation, and can be estimated as being equal to the average

peak-to-trough height obtained from surface roughness measurements of the pile (Chow 1996). The average peak-to-trough height (R_i) is equal to twice the centerline average roughness parameter (R_{cla}). R_{cla} is a surface roughness parameter commonly used by material scientists, and it is defined as the average distance of peaks and troughs to the surface profile centerline taken over an 8-mm (0.312-inch) gage length.

3. Select the interface friction angle (δ) based on laboratory interface shear tests. Alternatively, δ can be estimated using published correlations, preferably if developed considering pile material characteristics (roughness and hardness) and sand characteristics (shape, D_{50} , mineralogy).

Calculate the local radial effective stress at failure, as follows:

$$\begin{aligned}\sigma'_{rf} &= \sigma'_{rc} + \Delta\sigma'_{rd} \quad (\text{for compression loading}) \\ \sigma'_{rf} &= 0.8\sigma'_{rc} + \Delta\sigma'_{rd} \quad (\text{for tension loading})\end{aligned}\tag{27}$$

where

σ'_{rc} from step 1 using equation 24

$\Delta\sigma'_{rd}$ from step 2 using equation 25

4. Calculate the local shear stresses using equation 23.
5. Determine the shaft capacity by integrating the local shear stresses (obtained in step 4) along the embedded shaft length.

The IC method defines the tip resistance as the total utilizable tip resistance at a pile head displacement equal to 10 percent of the pile diameter. The recommended pile base resistance for closed-ended, driven piles in sand is related to the CPT tip resistance (q_c) averaged near the pile tip, according to the following empirical equation:

$$q_b = \bar{q}_c \left[1 - 0.5 \log_{10} \left(\frac{D}{D_{CPT}} \right) \right] \geq 0.13\bar{q}_c\tag{28}$$

where

q bar subscript c = the CPT tip resistance averaged over 1.5 pile diameters above and below the pile tip

D = the pile diameter

D_{CPT} = 0.036 m = the CPT diameter

The equation shown above is based on IC pile load test data that showed that the measured profiles of pile tip resistance (q_b) fell close to the CPT q_c traces. The ratio q_b/q_c was found to be less than unity and to decrease with pile diameter (Jardine and Chow

1996). Equation 28 tends to zero at $D = 3.6$ m (11.8 ft); therefore, a lower bound value of $q_b = 0.13 \cdot \bar{q}_c$ is recommended for $D > 2$ m (6.56 ft).

7.2.2 Predicted Axial Capacities

Predictions for the three piles tested at the Route 351 Bridge project were made using the four methods described in section 7.2.1. The predictions presented in the following sections were based on the geotechnical investigation results presented in chapter 6 and the interpreted average CPT and SPT design profiles, shown in figure 148. The predictions for each pile type included the specific information for each pile capacity prediction method. Pile-specific information included cross-sectional shape and dimensions, embedment depths, surface roughness, and interface friction values.

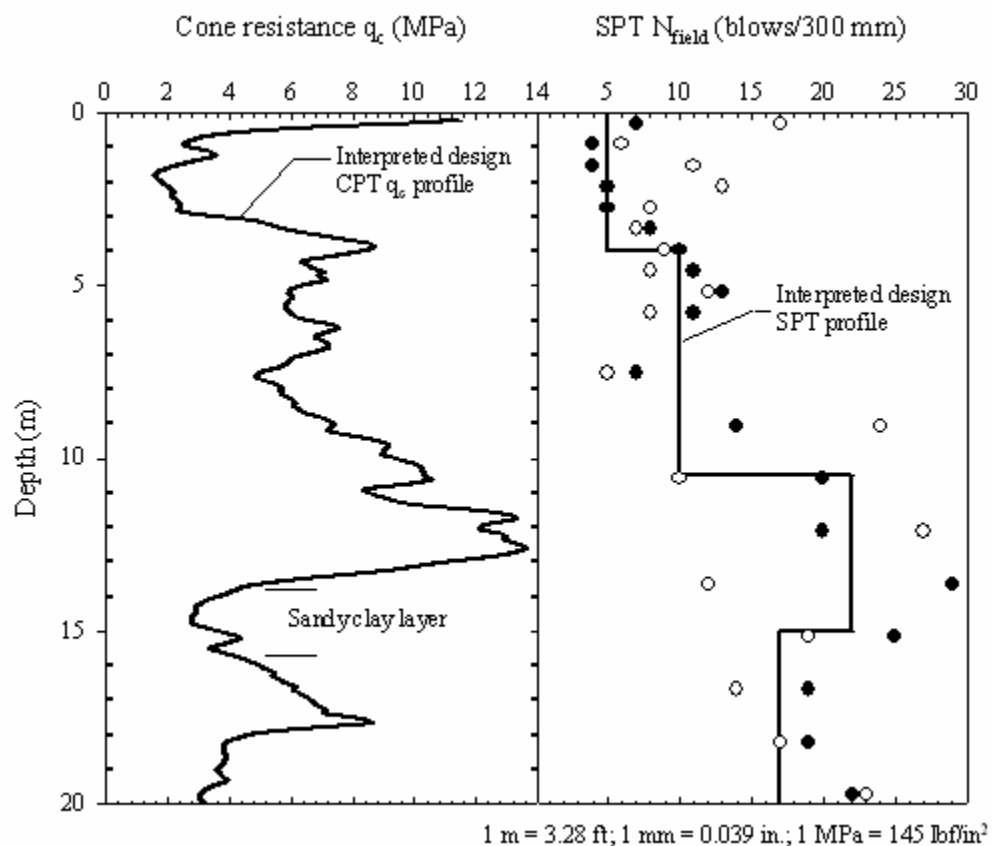


Figure 148. Graphs. Interpreted average CPT and SPT design profiles for Route 351 test site.

7.2.2.1 Nordlund's method predictions

Two sets of axial capacity predictions were made using Nordlund's method. One set of predictions was carried out using the recommended values of δ read directly from the Nordlund's design charts. The curve for concrete was used for the prestressed concrete

pile, and the curve for steel was used for the composite piles. The second set of Nordlund method predictions used the constant volume interface friction angles (δ_{cv}) obtained in this research, as presented in chapter 3. The two sets of axial pile capacity predictions using Nordlund's method were compared to the measured pile capacities evaluated from the load test results using the Davisson's failure criterion; these predictions are depicted in figures 149 and 150.

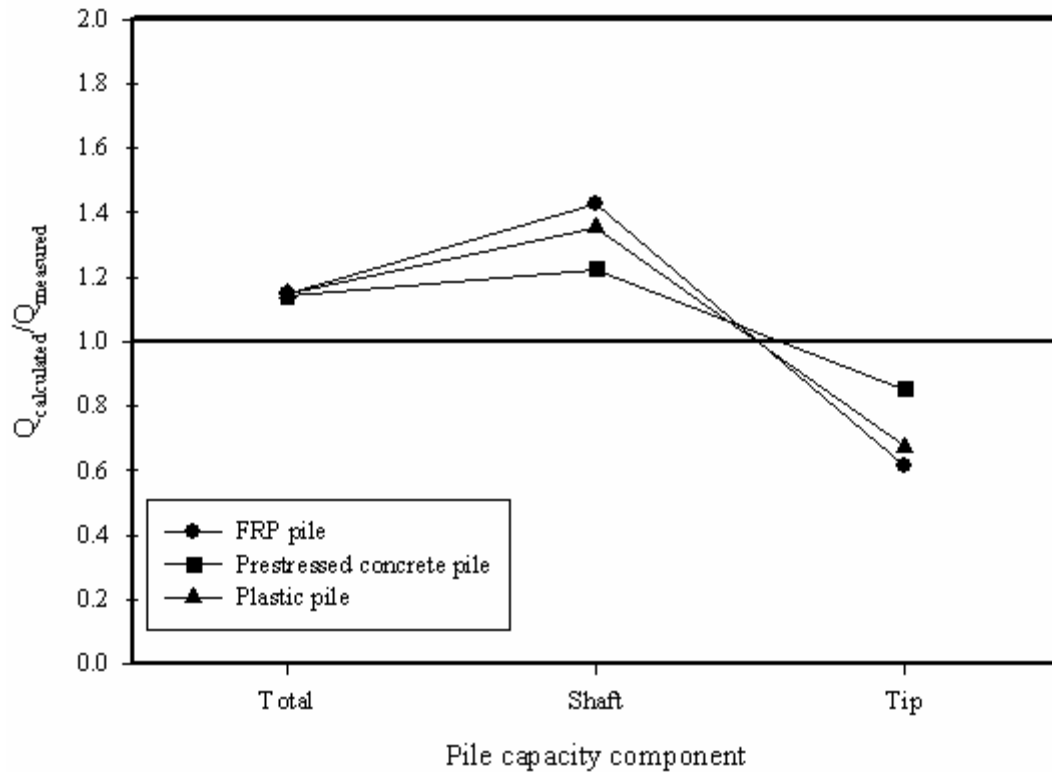


Figure 149. Graph. Accuracy of Nordlund's method predictions using δ values from Nordlund's charts.

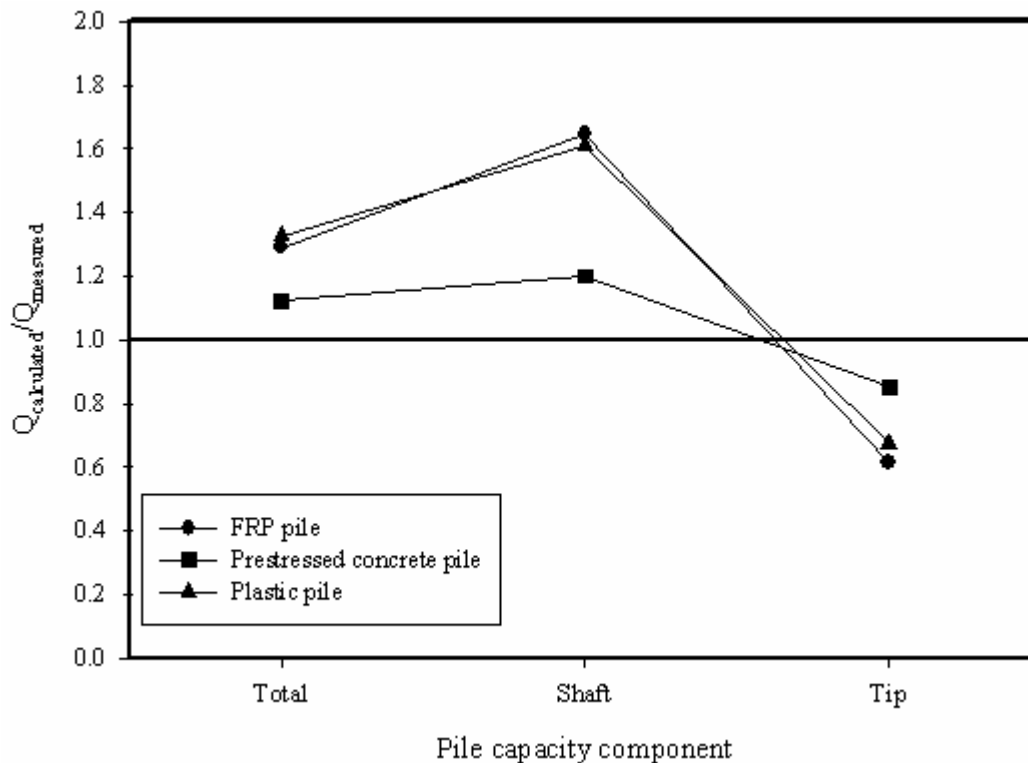


Figure 150. Graph. Accuracy of Nordlund's method predictions using δ values from interface shear tests.

Figures 149 and 150 show that the tip capacities (Q_b) were underpredicted by about 35 percent for the composite piles and 15 percent for the prestressed concrete pile. The shaft capacities were overpredicted in both sets of predictions. The shaft capacities predicted using Nordlund's recommended interface friction angles, using the steel curve for the composite piles, were 35 to 43 percent higher than those measured for the composite piles and 23 percent higher for the prestressed concrete pile. The shaft capacities calculated using the δ values from interface shear tests were about 65 percent higher for the composite piles and 20 percent higher for the prestressed concrete pile. The average coefficient of lateral earth pressure (K_δ) from Nordlund's method was about 1.67. This value of K_δ may be over predicting the effective radial normal stresses acting at the pile-soil interface, thereby producing higher shaft capacities than measured. To match the shaft capacities from the pile load tests, the coefficient of lateral earth pressure (K_δ) would have to be around 1.0 for the composite piles and about 1.4 for the prestressed concrete pile, when using the δ values from the interface shear tests.

7.2.2.2 API method predictions

Two sets of axial capacity predictions were made using the API (1993) method. One set of predictions was carried out using API's recommended value of δ from table 36. The second set of API method predictions used the constant volume interface friction angles

(δ_{cv}) from the interface shear tests presented in chapter 3. Comparisons of the two API predictions and the measured pile capacities are shown in figures 151 and 152.

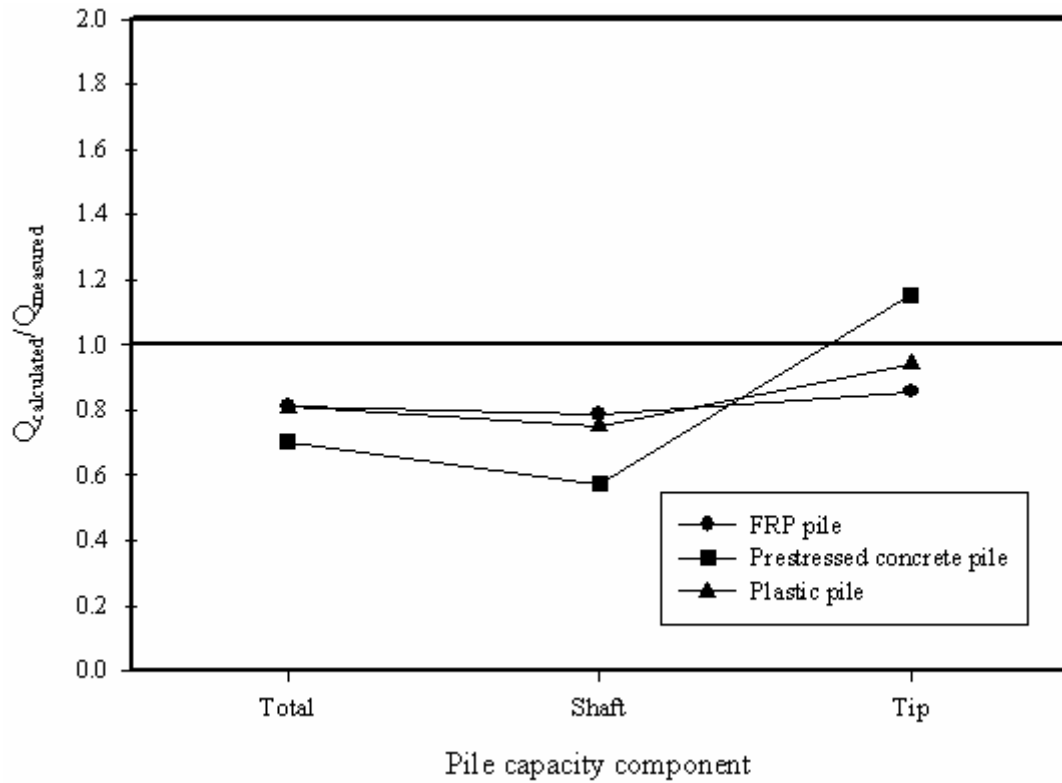


Figure 151. Graph. Accuracy of API method predictions using δ values from table 36.

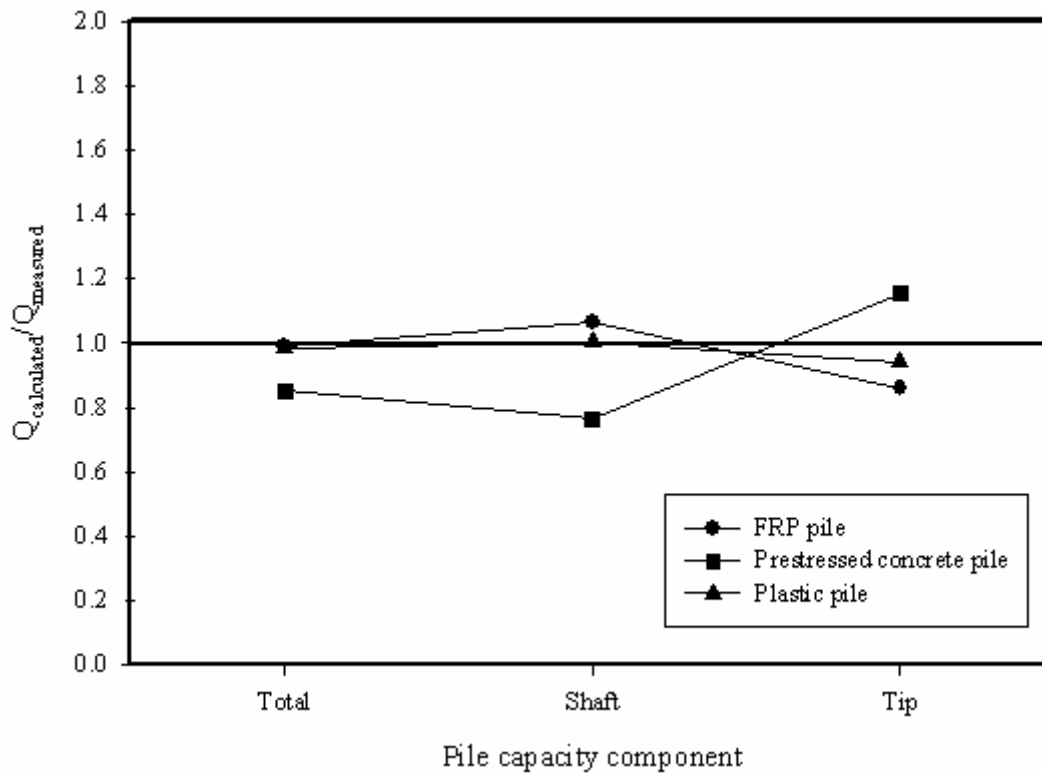


Figure 152. Graph. Accuracy of API method predictions using δ values from interface shear tests.

The tip capacities (Q_b) predicted for the three piles, using the API method, were within ± 15 percent of the measured values based on the Davisson failure criterion. The shaft capacities estimated using the API recommended interface friction angles, which are for steel pipe piles, were about 23 percent lower than measured for the composite piles and 43 percent lower for the prestressed concrete pile. The shaft capacities estimated using the δ values from the interface shear tests were between 0.3 and 6 percent higher for the composite piles and 23.5 percent lower for the prestressed concrete pile. The average coefficient of lateral earth pressure (K) from the API method is 1.0. This value of K , coupled with the δ values from the interface shear tests, resulted in very reasonable predictions of the pile shaft capacities for the composite piles.

7.2.2.3 LCPC method predictions

Axial capacity predictions using the LCPC method (Bustamante and Ganeselli 1982) were based on the average obtained from applying the method to the CPT tip resistance (q_c) data available at the test site, except that probe CPT-2 was excluded because it produced anomalous data in the depth range of 3 to 8 m (9.84 to 26.2 ft). For each pile type, two LCPC capacity calculations were performed: one assumes the particular pile under consideration is a steel pile, and the other assumes the pile is a concrete pile. Comparisons of the measured pile capacities and the LCPC predictions using the steel and concrete pile assumptions are shown in figures 153 and 154, respectively.

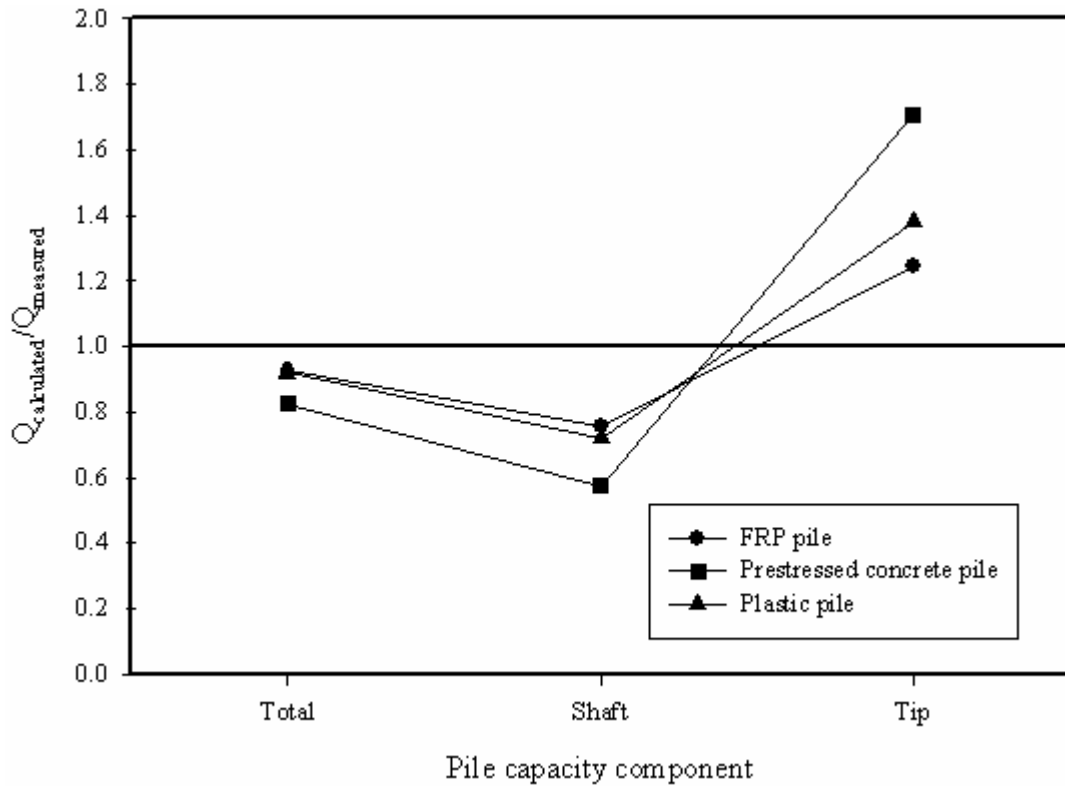


Figure 153. Graph. Accuracy of LCPC method predictions using steel pile assumption.

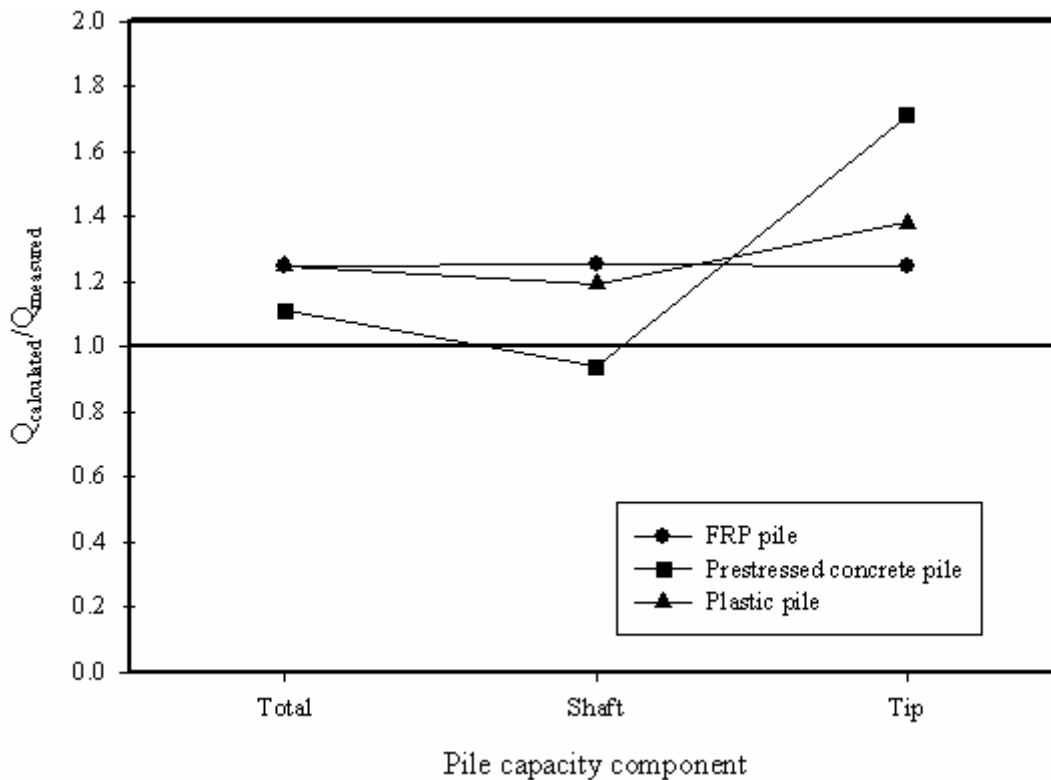


Figure 154. Graph. Accuracy of LCPC method predictions using concrete pile assumption.

The tip capacities (Q_b) estimated using the LCPC method over predicted the test results by 25 and 38 percent for the composite piles and by 71 percent for the prestressed concrete pile. The shaft capacities estimated using the LCPC steel pile approach were 24 and 28 percent lower than those measured for the composite piles and 43 percent lower for the prestressed concrete pile. The shaft capacities estimated using LCPC concrete pile approach were 19 and 25 percent higher than those measured for the composite piles and 6 percent lower for the prestressed concrete pile.

7.2.2.4 Imperial College method predictions

The IC method (Jardine and Chow 1996) was used to predict the axial capacities of the three test piles using the average interpreted design CPT tip resistance (q_c) profile shown in figure 148, and the interface friction angle and surface roughness data presented in chapter 3. Comparisons of the measured pile capacities and the IC method predictions are shown in figure 155.

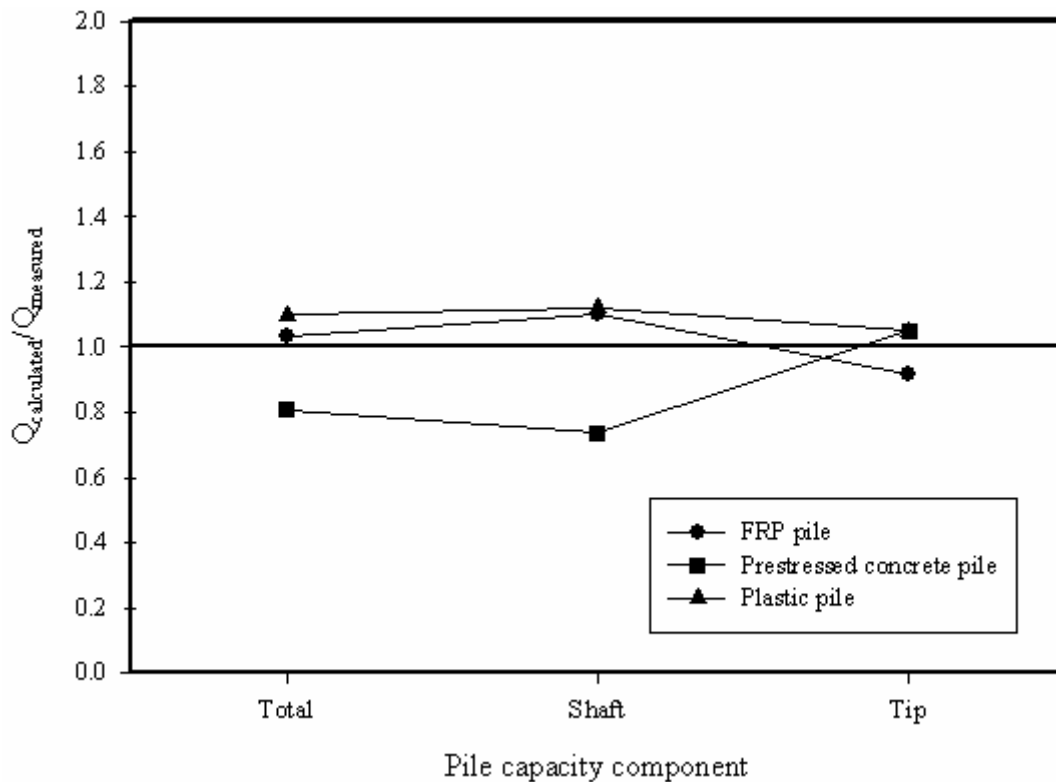


Figure 155. Graph. Accuracy of IC method predictions using δ values from interface shear tests.

The predicted tip capacities (Q_b) using the IC method were 8 percent below those measured for the FRP composite pile, 5 percent above those measured for the plastic composite pile, and 5 percent above those measured for the prestressed concrete pile. The shaft capacities estimated using the IC approach were 10 and 12 percent higher than those measured for the composite piles, and 26 percent lower for the prestressed concrete pile. The level of agreement between measured and calculated capacities is quite good for all cases except the total and shaft capacities of the prestressed concrete pile.

7.2.3 Summary of Axial Pile Capacity Predictions

The predicted axial pile capacities presented in the preceding sections are summarized in table 40.

Table 40. Predicted axial capacities for the test piles at Route 351.

Pile	Prediction Method	Total Capacity		Shaft Capacity		Toe Capacity	
		Q _c (kN)	Q _c /Q _m	Q _c (kN)	Q _c /Q _m	Q _c (kN)	Q _c /Q _m
PSC	Nordlund (w/ IST δ's)	3,480	1.12	2,890	1.2	590	0.85
	Nordlund (Concrete)	3,530	1.14	2,950	1.23	590	0.85
	API (w/ recommended δ's)	2,180	0.7	1,380	0.57	800	1.16
	API (w/ IST δ's)	2,640	0.85	1,840	0.76	800	1.16
	LCPC—Steel	2,560	0.83	1,380	0.57	1180	1.71
	LCPC—Concrete	3,440	1.11	2,260	0.94	1180	1.71
	Imperial College	2,500	0.81	1,770	0.74	720	1.05
FRP	Nordlund (w/ IST δ's)	2,920	1.29	2,440	1.65	480	0.62
	Nordlund (Steel)	2,600	1.15	2,120	1.43	480	0.62
	API (w/ recommended δ's)	1,830	0.81	1,160	0.79	670	0.86
	API (w/ IST δ's)	2,240	0.99	1,570	1.06	670	0.86
	LCPC—Steel	2,090	0.93	1,120	0.76	970	1.25
	LCPC—Concrete	2,820	1.25	1,850	1.25	970	1.25
	Imperial College	2,340	1.04	1,630	1.1	710	0.92
Plastic	Nordlund (w/ IST δ's)	2,830	1.33	2,400	1.61	430	0.68
	Nordlund (Steel)	2,450	1.15	2,010	1.35	430	0.68
	API (w/ recommended δ's)	1,720	0.81	1,120	0.75	610	0.94
	API (w/ IST δ's)	2,100	0.99	1,490	1	610	0.94
	LCPC—Steel	1,960	0.92	1,070	0.72	890	1.38
	LCPC—Concrete	2,660	1.25	1,770	1.19	890	1.38
	Imperial College	2,340	1.1	1,670	1.12	670	1.05

Notes: IST δ's refers to interface friction angles from interface shear tests. Q_c = calculated value (shown with three significant digits), Q_m = measured value corresponding to Davisson's failure criterion. Q_c/Q_m = the ratio of calculated to measured. Conversion factor: 1 kN = 225 lbf.

The various methods used to predict axial pile capacity led to ratios of calculated-to-measured pile capacities (Q_c/Q_m) ranging from 0.70 to 1.14 for the prestressed concrete pile, and from 0.81 to 1.33 for the composite piles. If only the predictions from the IC method and the API method using the δ-values from the interface shear tests are considered, the Q_c/Q_m ratios ranged from 0.81 to 0.85 for the prestressed concrete pile and from 0.99 to 1.10 for the composite piles. In other words, these two methods underpredict the capacity of the prestressed concrete pile by about 20 percent, and overpredict the capacities for the composite piles by about 10 percent. In routine deep-foundation design practice, factors of safety as low as 1.5 are sometimes used, but typically they are 2.0 or higher. Even a lower bound factor of safety of 1.5 would ensure that the ultimate geotechnical capacity of the composite piles is not exceeded, but it may not be high enough to ensure acceptable deformations of the foundation system.

In summary, it can be seen from the prediction results that the level of accuracy of the predictions is comparable for all three types of piles. In terms of axial pile capacity predictions, the results presented in this chapter seem to indicate that conventional static analysis methods are applicable to composite piles. However, additional case histories would be needed to corroborate and extend this conclusion to other composite pile types and to different soil conditions.

7.3 LOAD-SETTLEMENT BEHAVIOR, AXIALLY LOADED SINGLE PILES

7.3.1 Introduction

The settlement of a single pile in soil under compressive axial loading is a function of several factors, such as:

- Soil stratigraphy and characteristics (stiffness, density, compressibility, nonlinearity).
- Pile shape and dimensions.
- Pile stiffness.
- Pile-soil interaction characteristics.

Several methods are reported in the literature for computation of load-settlement behavior of a single pile under axial compression loading. The methods are typically divided in the following main categories:

- Elastic methods.
- Load-transfer (T-Z) methods.
- Modified hyperbolic methods.
- Numerical techniques (including finite element and finite difference methods).

A good overview of the different techniques available can be found in Poulos (1989). For this study we focus mainly on the load-transfer (T-Z) methodology, which is commonly used by FHWA and U.S. State transportation agencies. This methodology has recently become more accessible to U.S. highway agencies with the release of the FB-Pier program, which uses this technique for settlement calculations of single and pile groups (Hoit, et al., 2000). The development of this program was sponsored by FHWA and is distributed freely to U.S. transportation agencies. Other commonly used programs that employ the T-Z methodology to analyze settlement of axially loaded single piles include A-Pile (Ensoft 1998) and CAXPILE (Dawkins 1982).

A brief overview of the load-transfer T-Z methodology is provided in the following section.

7.3.2 Background, Load-Transfer Method for Pile Settlement Predictions

The load-transfer (T-Z) method is probably the most widely used technique to study the problem of single axially loaded piles, and is particularly useful when the soil behavior is clearly nonlinear and/or when the soil surrounding the pile is stratified. This method involves modeling the pile as a series of elements supported by discrete nonlinear springs, which represent the resistance of the soil in skin friction (T-Z springs), and a nonlinear spring at the pile tip representing the end-bearing (Q_b -Z) spring. The soil springs are nonlinear representations of the soil reaction, T (or Q_b for the pile tip), versus displacement (Z) as shown schematically in figure 156. Assuming the T-Z and Q_b -Z curves are available, the axial load-settlement response can be obtained with the aid of a computer program such as FB-Pier.

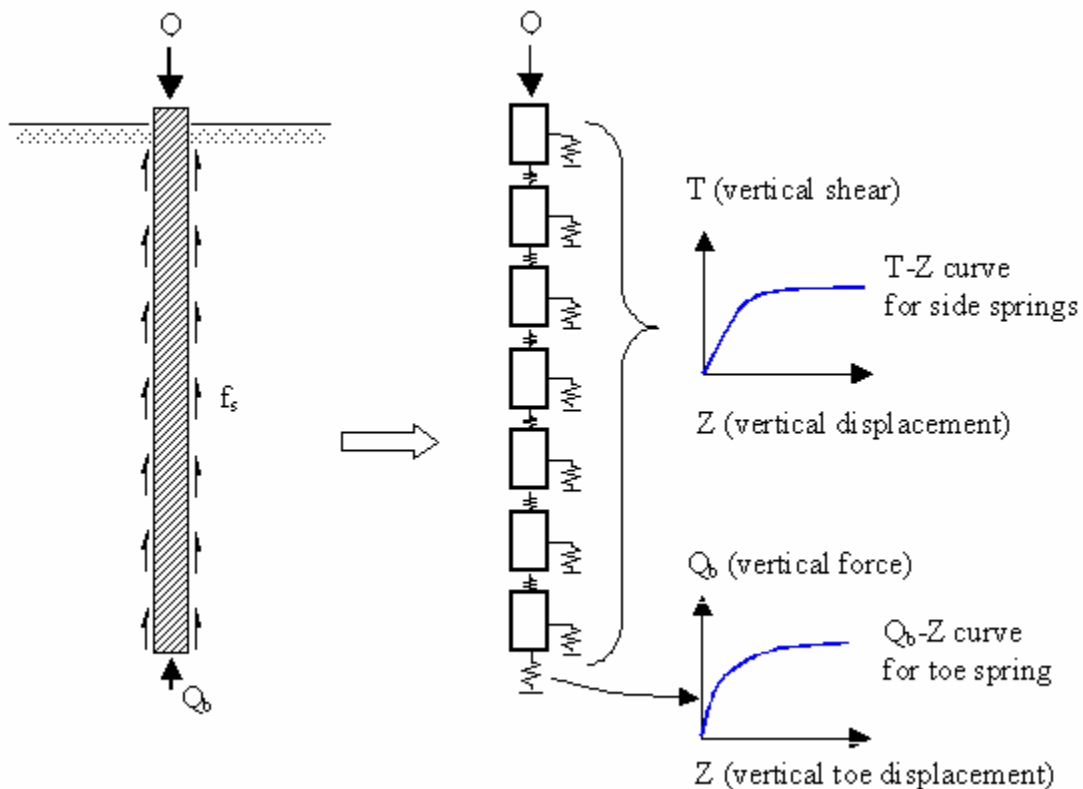


Figure 156. Illustration. Idealized model used in T-Z load-transfer analyses.

Adequate T-Z and Q_b -Z curves are essential in this method to obtain reliable settlement and load transfer calculations for axially loaded single piles. Such load-transfer curves were originally obtained empirically; one example is the work of Coyle and Sulaiman (1967), who published empirical T-Z curves based on model and full-scale pile load tests in sand. Building on this work, and based on additional empirical results, general recommendations for estimating T-Z and Q_b -Z curves for driven piles in sands have been proposed by Vijayvergiya (1977) and API (1993). Load-transfer curves can also be constructed satisfactorily using a theoretical approach related to the shear stiffness of the soil surrounding the pile (Poulos 2001). Several methodologies to develop theoretically

based load transfer curves have been proposed (e.g., Kraft, et al., 1981, Chow (1986), McVay, et al., 1989, and Randolph 1994).

Section 7.3.3 presents settlement predictions for the test piles using empirical load-transfer curves (API 1993, Vijayvergiya 1977), while section 7.3.4 presents prediction results using new theoretical load-transfer curves.

7.3.3 Predictions Using Empirical Load-Transfer Curves

7.3.3.1 Predictions using load-transfer curves recommended by API (1993)

7.3.3.1.1 Load-transfer curves recommended by API (1993)

In the absence of more precise information, API (1993) recommends the use of the following T-Z curve expression for noncarbonate sands:

$$\begin{aligned}
 f_s &= f_{s,\max} \frac{z}{z_c} && (\text{for } z \leq z_c) \\
 f_s &= f_{s,\max} && (\text{for } z > z_c)
 \end{aligned}
 \tag{29}$$

where

f_s = the unit side shear stress mobilized along a pile segment at movement, z

$f_{s,\max}$ = the maximum unit side shear stress

z = movement of pile segment

z_c = movement required to mobilize $f_{s,\max}$ (0.1 inches for sands)

In the absence of more definitive criteria, API (1993) recommends using the pile tip load versus tip settlement curve shown in figure 157.

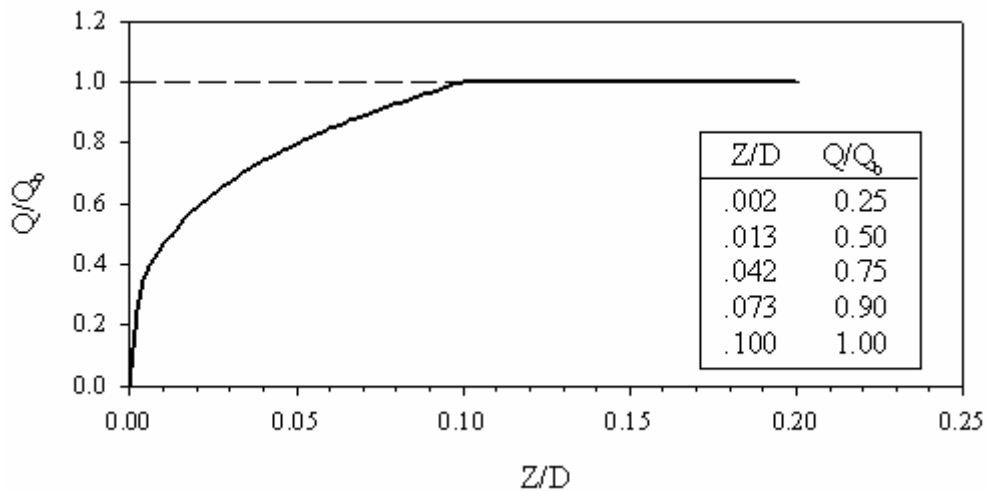


Figure 157. Graph. Pile tip load—pile tip displacement curve (Q-Z) (API 1993).

In figure 157, Q is the mobilized end-bearing capacity at an axial tip displacement z , and Q_b is the ultimate end-bearing load (computed using q_b from equation 22 times the pile tip area). As shown in figure 157, Q_b is mobilized at a pile tip displacement equal to 10 percent of the pile diameter, D .

7.3.3.1.2 Maximum shaft shear stress distributions recommended by API (1993)

As described previously in section 7.2.1.2, API recommends using maximum shear stresses for the pile shaft that increase linearly with depth until they reach a prescribed limiting value. Graphical representations of the maximum shaft shear stresses for the three test piles, as recommended by API (1993), are shown in figure 158. In section 7.2.3 it was indicated that better pile capacity estimates were obtained using the API method with δ values from interface shear tests. Despite this finding, the shear stresses shown in figure 158 correspond to the δ values recommended by API (1993). This was done to be able to assess the pile settlement predictions using the original method without major modifications.

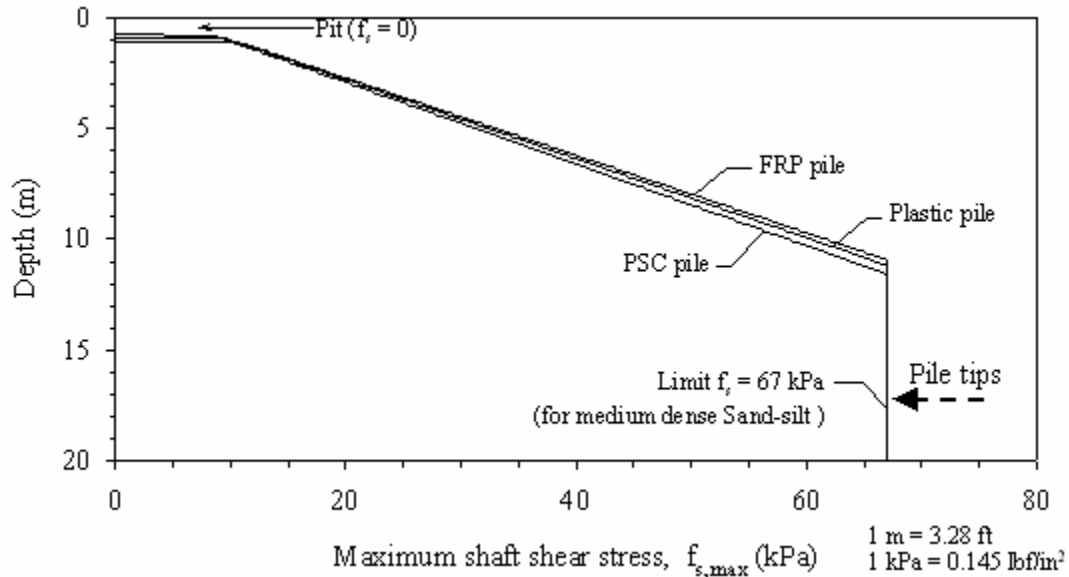


Figure 158. Graph. Maximum shear stress distribution along pile shaft, according to API (1993).

7.3.3.1.3 Prediction for the prestressed concrete test pile

The load-settlement responses predicted for the concrete test pile, using the API (1993) T-Z and Q_b -Z curves, are shown in figure 159. The curve showing a lower predicted capacity is based on the API load-transfer curves using a limiting shear stress. The second prediction was made using the API curves but without a limiting shaft shear stress.

Figure 159 shows that the predicted settlement curves have relatively good agreement in the initial portion of the load settlement curve. However, they both underpredict the

measured pile capacity. This is consistent with the axial pile capacity predictions presented in section 7.2.2.2, where the predicted API pile capacity (using the API recommended δ values) was shown to be about 30 percent lower than measured. The predicted load-settlement curve using no limiting f_s shows a slightly better agreement with the field measurements, but also underpredicts the pile capacity by about 18 percent. The extent of this underprediction is due to the low shaft capacity estimated using the API (1993) method, which (as indicated in section 7.2.2.2), was 43 percent lower than measured.

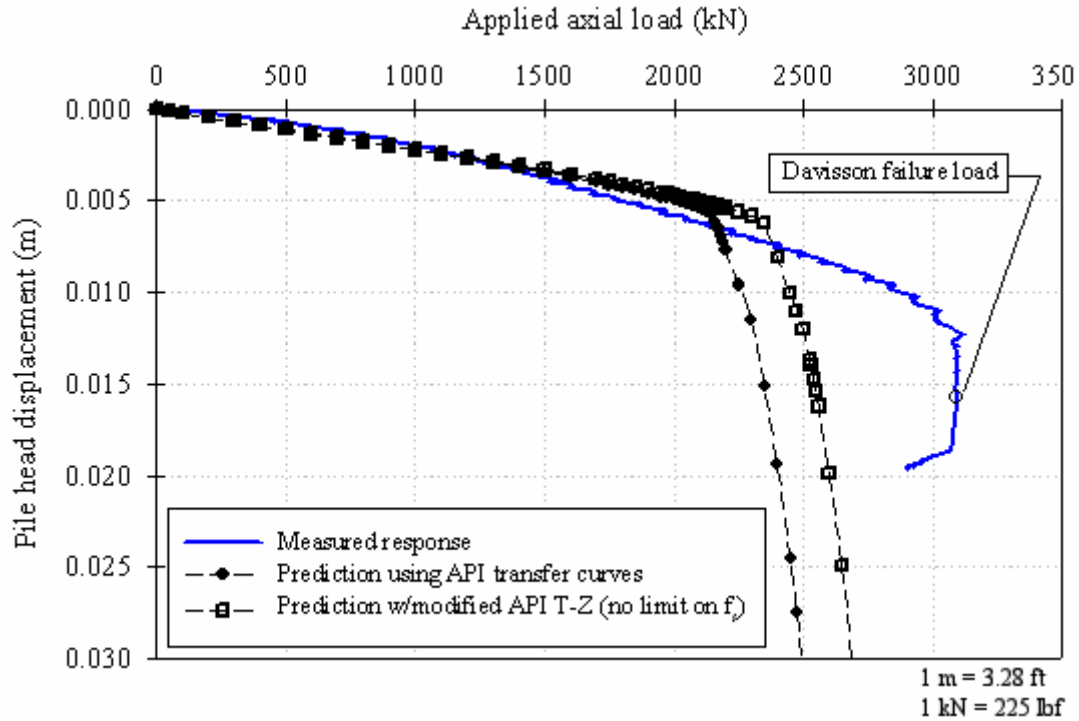


Figure 159. Graph. Settlement predictions for the prestressed concrete pile using API (1993).

7.3.3.1.4 Prediction for the FRP test pile

The predicted load-settlement curves for the FRP test pile, using the API (1993) load-transfer curves with and without a limiting shaft shear stress, are shown in figure 160.

Figure 160 shows a good agreement for the initial portions of the predicted settlement curves and the measured load-settlement curve. However, similar to the prestressed concrete pile predictions, the API prediction using an f_s cutoff underpredicts the pile capacity, and the onset of large settlements occurs at lower load than observed in the field measurements. The prediction with no f_s cutoff shows a much better correspondence with the field measurements, but also shows the onset of large settlements occurring at a load slightly below that measured in the field.

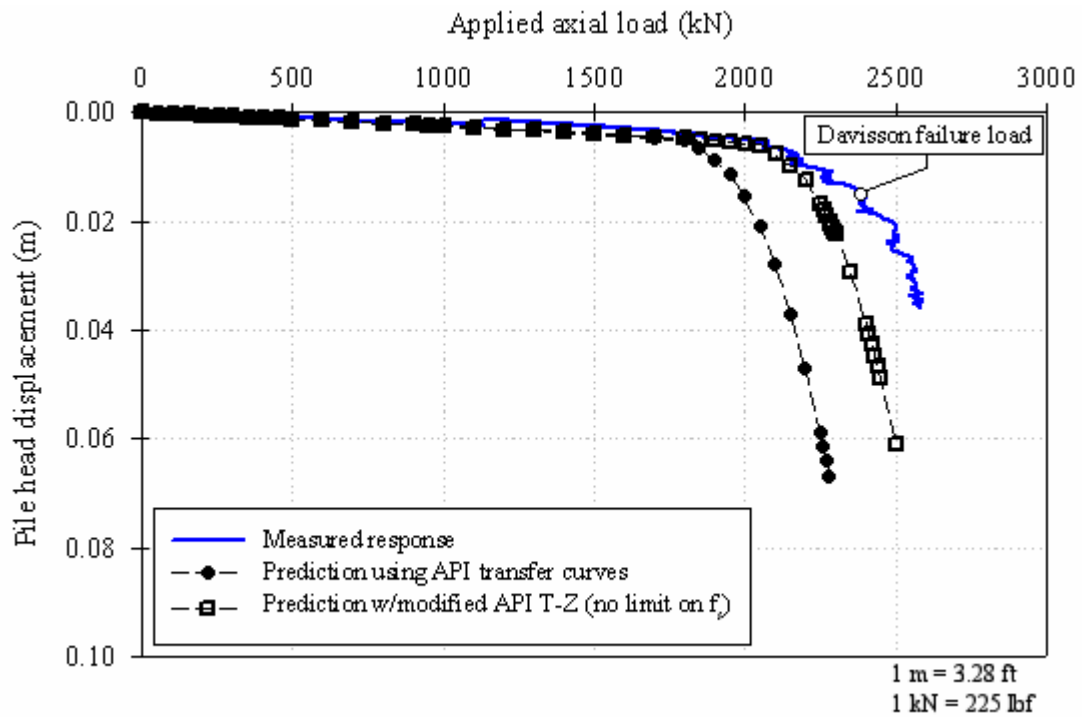


Figure 160. Graph. Settlement predictions for the FRP pile using API (1993).

7.3.3.1.5 Prediction for plastic test pile

The predicted load-settlement curves for the plastic test pile, using the API (1993) load-transfer curves with and without a limiting shaft shear stress, are shown in figure 161. Figure 161 shows that the predicted load-settlement curve, using the API (1993) method with a limiting f_s , agrees well with the initial portion of the field measurements, but large settlements start to occur sooner than observed at about 1,700 kN (382,000 lbf). On the other hand, the API prediction using no f_s cutoff shows very good agreement in both the initial and final portions of the settlement curve from the pile load test.

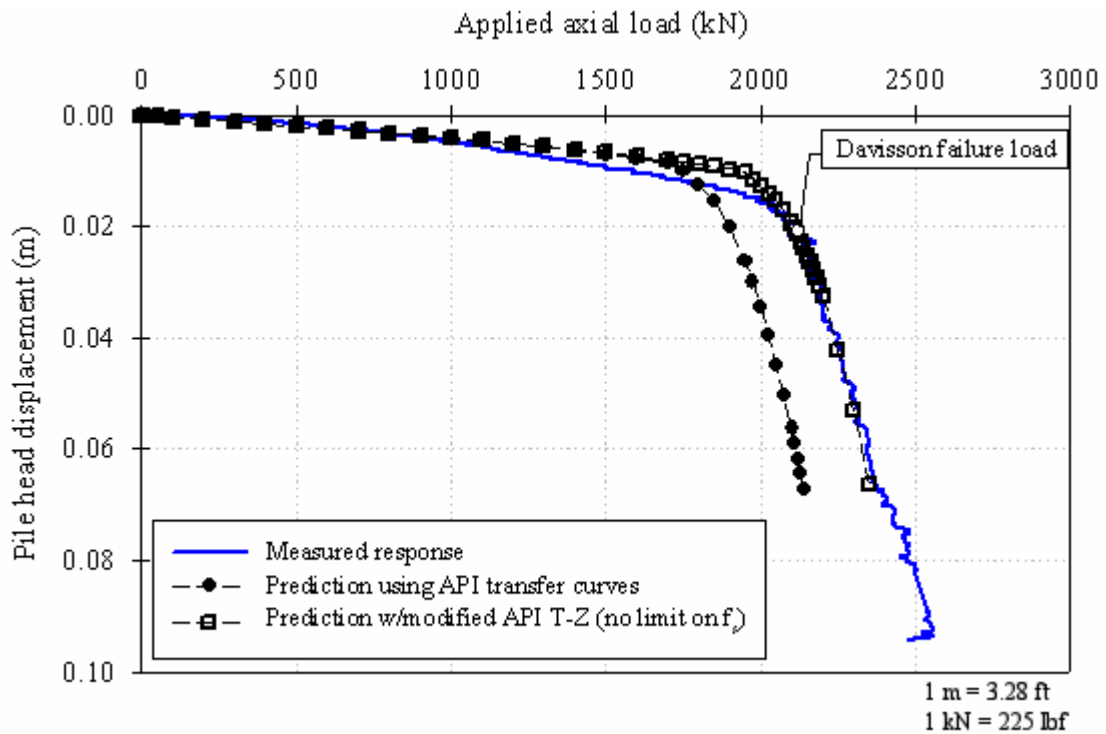


Figure 161. Graph. Settlement predictions for the plastic pile using API (1993).

7.3.3.2 Predictions using Vijayvergiya (1977) load-transfer curves

7.3.3.2.1 Load-transfer curves recommended by Vijayvergiya (1977)

Vijayvergiya (1977) recommends the following load-transfer expression of mobilized unit side shear (f_s) as a function of shaft movement (Z):

$$\begin{aligned}
 f_s &= f_{s, \max} \left(2 \sqrt{\frac{z}{z_c} - \frac{z}{z_c}} \right) \quad (\text{for } z \leq z_c) \\
 f_s &= f_{s, \max} \quad (\text{for } z > z_c)
 \end{aligned}
 \tag{30}$$

where

f_s = the unit side shear stress mobilized along a pile segment at movement, z

$f_{s, \max}$ = the maximum unit side shear stress

z = movement of pile segment

z_c = movement required to mobilize $f_{s, \max}$ (0.3 inches for sands)

The normalized T-Z curve obtained from equation 30 is shown in figure 162. For comparison purposes, the API (1993) T-Z curve is also shown in this figure.

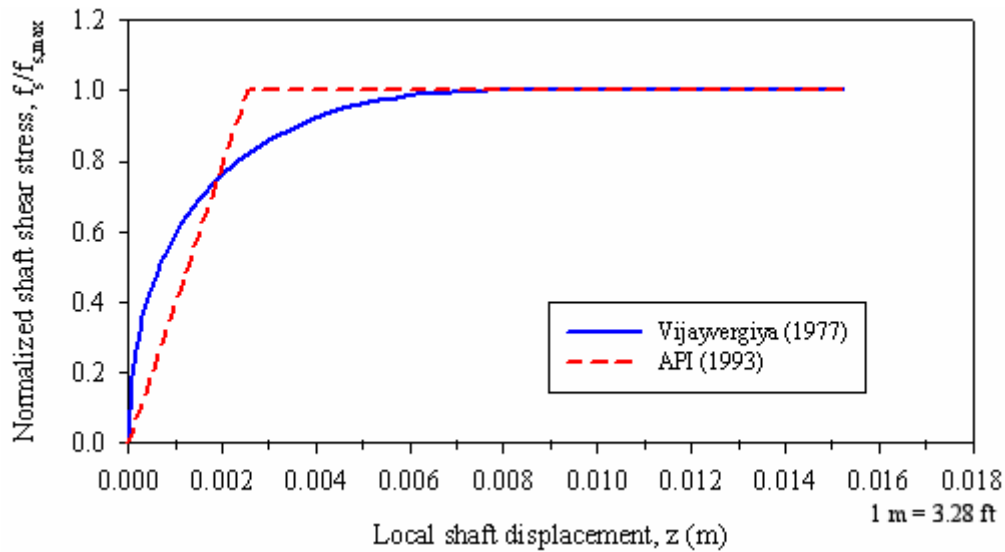


Figure 162. Graph. Normalized T-Z curves according to API (1993) and Vijayvergiya (1977).

Similarly, the following expression for pile tip load versus tip settlement for piles in sands is proposed by Vijayvergiya (1977):

$$\begin{aligned}
 q &= \left(\frac{z}{z_c} \right)^{\frac{1}{3}} q_{\max} \quad (\text{for } z \leq z_c) \\
 q &= q_{\max} \quad (\text{for } z > z_c)
 \end{aligned}
 \tag{31}$$

where

q = the pile tip resistance mobilized at displacement z

q_{\max} = the maximum tip resistance (end bearing)

z = movement of pile segment

z_c = movement required to mobilize q_{\max} (0.25 inch for sands)

The normalized Q-Z curve proposed by Vijayvergiya (1977) is shown in figure 163. For comparison purposes, the corresponding API (1993) curve for a 24-inch diameter pile is also shown.

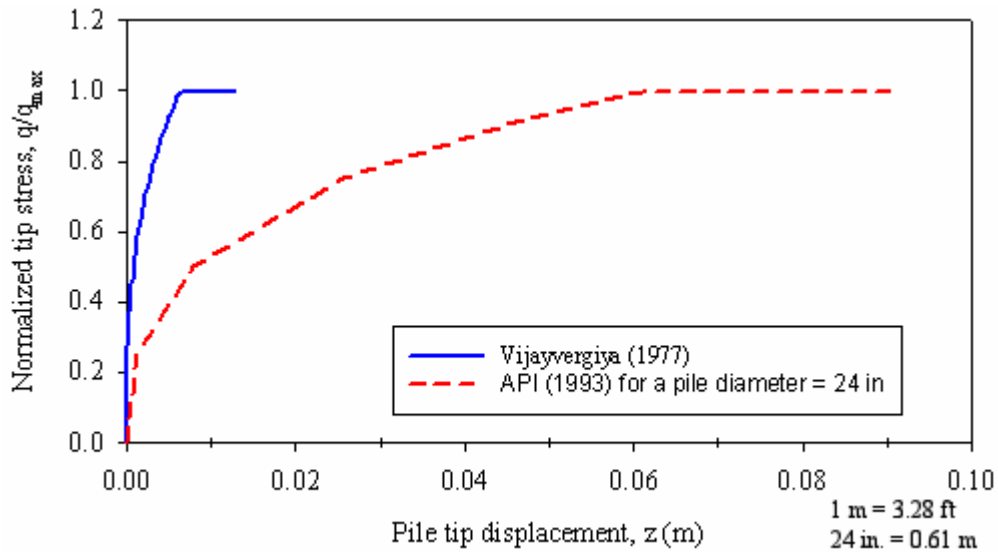


Figure 163. Graph. Normalized Q-Z curves according to Vijayvergiya (1977) and API (1993).

It is clear from figure 163 that the Q-Z curve proposed by Vijayvergiya mobilizes the full end-bearing capacity at much smaller displacement than the API curve. Vijayvergiya (1977) estimates that about 6.35 mm (0.25 inches) of tip displacement are required to mobilize the ultimate pile end-bearing capacity, while API (1993) estimates that a pile tip displacement equal to 10 percent of the pile diameter is required.

7.3.3.2.2 Maximum shaft shear stress distributions

Vijayvergiya (1977) recommended using an expression similar to API (1993) to estimate the maximum shear stresses along the pile (see equation 21). The author indicated that the coefficient of lateral earth pressures (K) can be as high as 1.25 for driven piles in medium-dense to dense sand.

The predictions presented in the following subsections are based on shaft shear stresses calculated using equation 21, with the δ values from the interface shear tests presented in chapter 3, and K values of 1.0 and 1.25. The shear stress distributions used are shown in figure 164. No limiting value of shear stress was used, although it should be pointed out that Vijayvergiya (1977) does mention the existence of a limiting value in the 1971 version of the API guidelines.

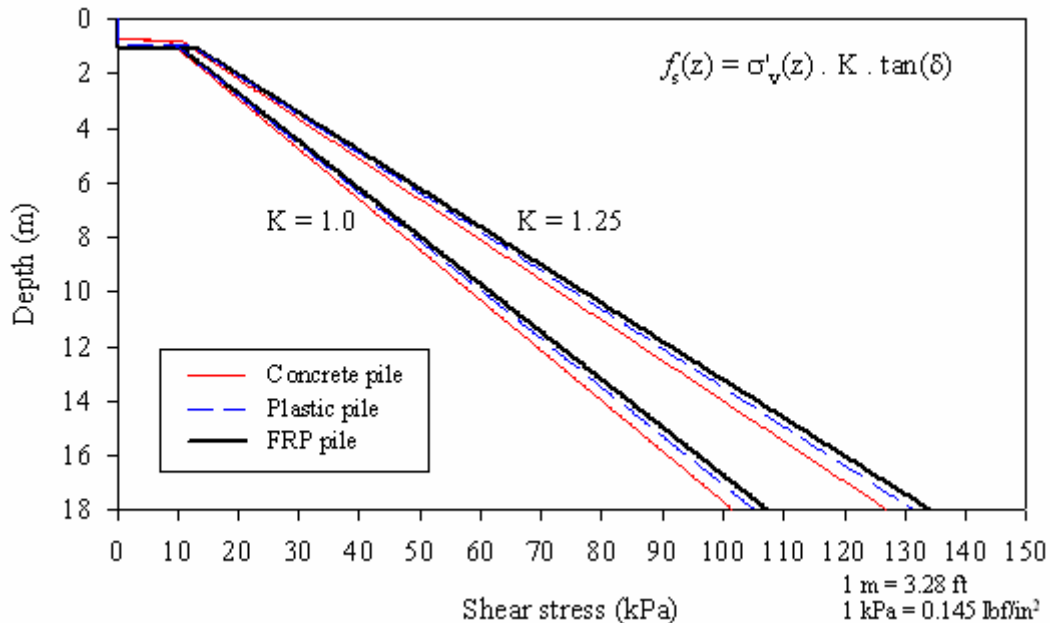


Figure 164. Graph. Maximum shear stress distributions used in predictions using Vijayvergiya (1977).

7.3.3.2.3 Tip resistances

Vijayvergiya (1977) recommends estimating the tip resistance for piles driven in sands as the product of a bearing capacity factor (N_q) and the free-field effective overburden stress at the base of the pile (σ'_v).

The values recommended by API (1993) were used in the predictions presented in the following sections.

7.3.3.2.4 Prediction for the prestressed concrete test pile

The predicted load-settlement curves for the prestressed concrete test pile, using the recommendations proposed by Vijayvergiya (1977) for load-transfer curves, are shown in figure 165.

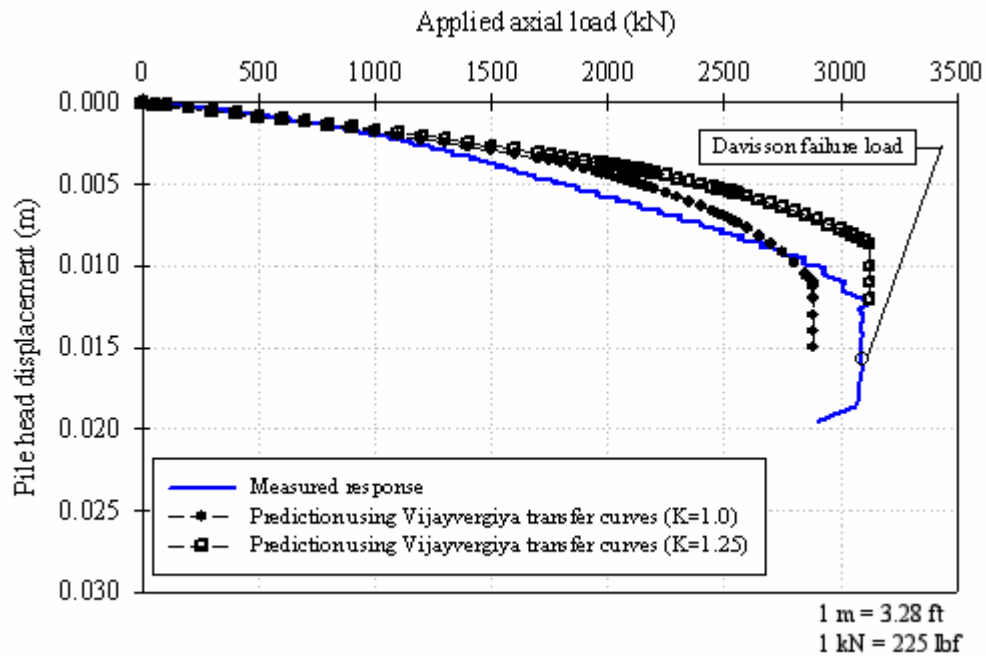


Figure 165. Graph. Settlement predictions for the concrete pile using Vijayvergiya (1977).

Figure 165 shows that the predicted load-settlement curve, using Vijayvergiya's (1977) recommendations, agrees well with the initial portion of the field measurements, but shows a stiffer response for loads higher than 1,000 kN (225,000 lbf). The ultimate pile capacities, predicted using coefficients of lateral earth pressures (K) of 1.0 and 1.25, were about 2,885 and 3,125 kN (649,125 and 703,125 lbf), respectively. These capacities, as percentages of the pile capacity measured in the field, are about 93 percent and 101 percent for K equal to 1.0 and 1.25, respectively.

7.3.3.2.5 Prediction for the FRP test pile

The predicted load-settlement curve for the FRP test pile, using the Vijayvergiya (1977) load-transfer curves with a coefficient of lateral earth pressure (K) equal to 1.0, is shown in figure 166.

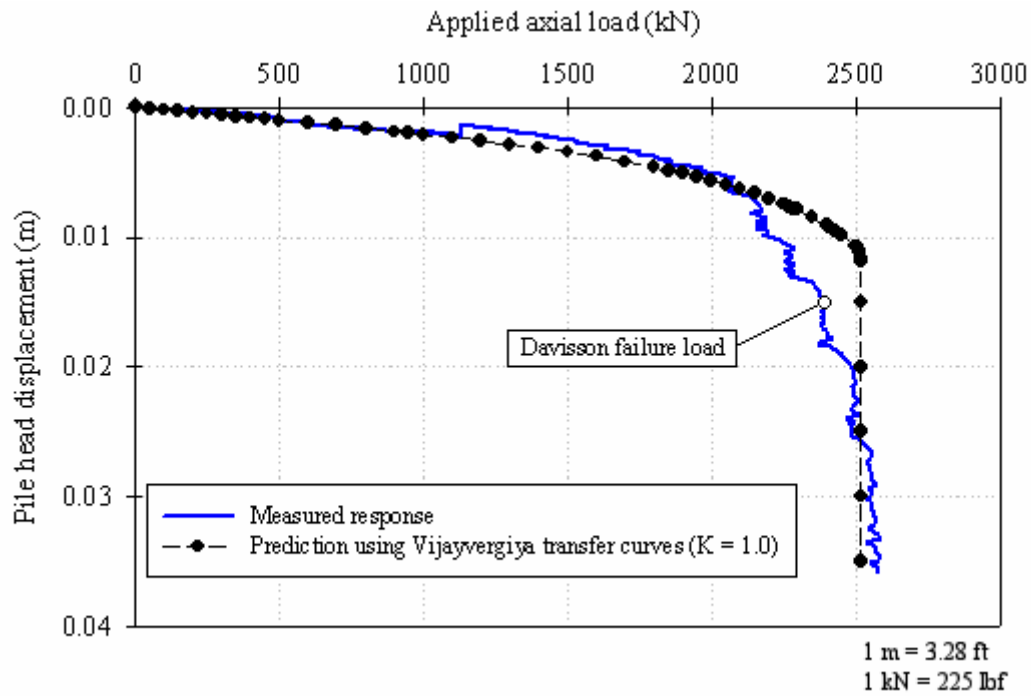


Figure 166. Graph. Settlement predictions for the FRP pile using Vijayvergiya (1977).

Figure 166 shows that the predicted load-settlement curve, using Vijayvergiya’s (1977) method with a lateral earth pressure coefficient (K) equal to 1.0, agrees reasonably well with the field measurements.

7.3.3.2.6 Prediction for the plastic test pile

The predicted load-settlement curve for the FRP test pile, using the Vijayvergiya (1977) load transfer curves and with a lateral earth pressure coefficient (K) equal to 1.0, is shown in figure 167.

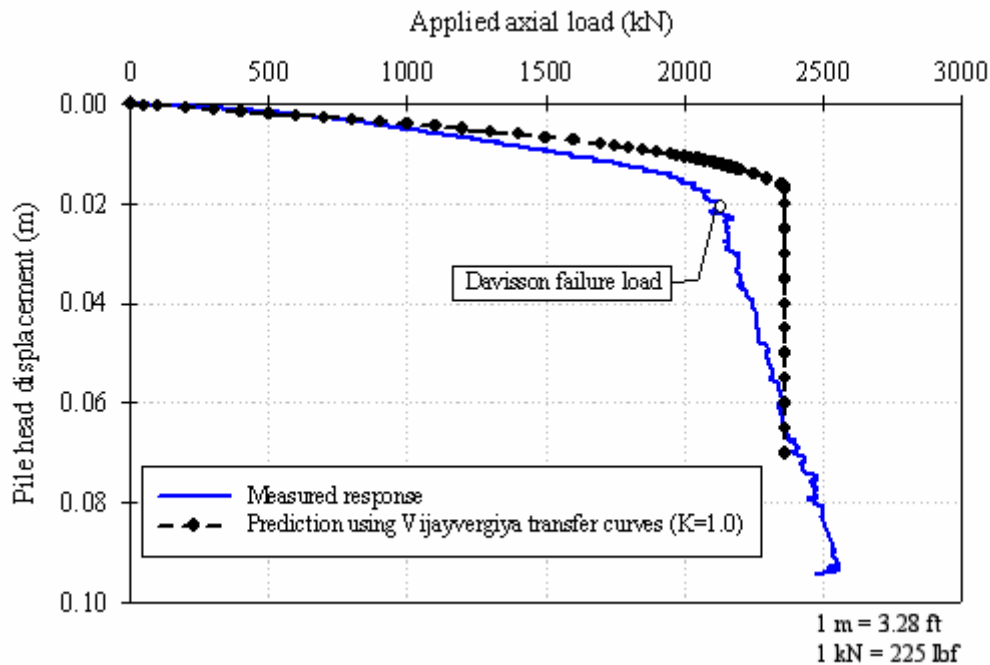


Figure 167. Graph. Settlement predictions for the plastic pile using Vijayvergiya (1977).

Figure 167 shows that the predicted load-settlement curve, using Vijayvergiya's (1977) recommendations and with a lateral earth pressure coefficient (K) equal to 1.0, is stiffer than observed in the field.

7.3.3.3 Comments on the predictions obtained using empirical load-transfer curves

The exactness of load-settlement behavior predicted using the load-transfer (T-Z) method depends to a great extent on the accuracy of the predicted ultimate shaft and tip capacities (e.g., as presented in section 7.2.2 for the API method), and on the displacement characteristics (e.g. stiffness, linear or nonlinear, displacement required for full-strength mobilization) chosen to model the soil-pile interface and the soil-pile tip during load transfer. For example, the results for the prestressed concrete pile, presented in the previous section and calculated using the API method, showed a significant underprediction of the pile capacity. This result is related to the low ultimate shaft resistance predicted compared to the actual ultimate shaft capacity recorded in the field. The prediction using Vijayvergiya's (1977) recommendations, with a coefficient of lateral earth pressure (K) equal to 1.25, was reasonably good. The predictions for the composite piles were more accurate because the calculated ultimate shaft and tip capacities were much closer to the actual values measured.

7.3.4 Predictions Using Theoretical Load-Transfer Curves

The following sections present the background and describe the methodology used in this research to develop theoretically based load-transfer curves. Most of the work in this area is based on the pioneering work by Kraft, et al. (1981).

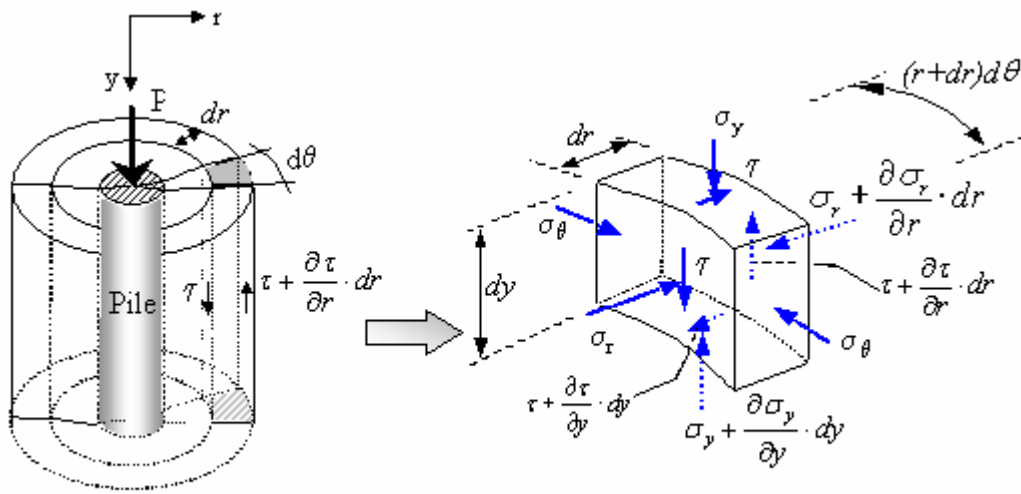
7.3.4.1 Theoretical load-transfer curves for a linear elastic soil

The soil deformation around a pile shaft can be idealized as concentric cylinders in shear (Frank 1974, Randolph and Wroth 1978). This idealization assumes the soil displacement due to the pile loads is predominantly vertical, and that radial displacements are negligible. Studies by Frank (1974) and Baguelin, et al. (1975), have shown that the concentric cylinder approach is a good approximation of the deformation patterns obtained using more rigorous analyses such as the finite element method.

Randolph and Wroth (1978) derived an expression for pile settlement in a linear elastic soil based on the concentric cylinder assumption. The author's derivation starts by first considering the vertical equilibrium of the annular-shaped soil element (ring of soil between two concentric cylinders) shown in figure 168:

$$\left(\tau + \frac{\partial \tau}{\partial r} dr \right) (r + dr) d\theta dy - \tau r d\theta dy + \left(\sigma_y + \frac{\partial \sigma_y}{\partial y} dy \right) \left(r + \frac{dr}{2} \right) d\theta dr - \sigma_y \left(r + \frac{dr}{2} \right) d\theta dr = 0 \quad (32)$$

where the term definitions are shown in figure 168. The vertical stress (σ_y) shown in this figure refers to net change in vertical stress due to the axial load (P) applied to the pile.



a) Concentric cylinders around loaded pile b) Stresses in soil element

Figure 168. Illustrations. Concentric cylinder model for settlement analysis of axially loaded piles (adapted from Randolph and Wroth 1978).

Simplifying and neglecting second-order terms, equation 32 reduces to:

$$\frac{\partial(\tau r)}{\partial r} + r \frac{\partial \sigma_y}{\partial y} = 0 \quad (33)$$

However, according to Randolph and Wroth (1978), the rate of change of vertical stress with respect to depth is much less than the rate of change of shear stress with respect to radial distance during axial loading of a pile. Therefore the second term of equation 33 can be neglected, and the equilibrium equation shown above can be approximated as:

$$\frac{\partial(\tau r)}{\partial r} \approx 0 \quad (34)$$

Integrating this last expression, we obtain:

$$\int_{r_o}^r d(\tau r) = 0 \Rightarrow [\tau(r)r - \tau(r_o)r_o] = 0$$

$$\tau(r) = \frac{\tau(r_o)r_o}{r} = \frac{\tau_o r_o}{r} \quad (35)$$

where

$\tau(r)$ = shear stress acting at a radial distance (r) from the centerline of the pile

$\tau_o = \tau(r_o)$ = shear stress at the pile/soil interface (i.e., at a radial distance r_o)

r_o = pile radius (or equivalent radius for noncircular piles)

Equation 35 indicates that the shear stresses in the vicinity of the pile are inversely proportional to the radial distance to the pile.

The concentric cylinder model assumes that simple shear conditions prevail. This model also assumes that the radial displacements are negligible compared to the vertical displacements of the soil. Therefore the shear strain (γ) can be approximated as:

$$\gamma = \frac{\partial u}{\partial z} + \frac{\partial w}{\partial r} \approx \frac{dw}{dr} \quad (36)$$

where

u = radial displacement (neglected)

w = vertical displacement

For linear elastic soils, the shear strain is related to the shear stress as follows:

$$\gamma(r) = \frac{dw}{dr} = \frac{\tau(r)}{G(r)} \quad (37)$$

By substituting equation 35 into equation 37, we obtain:

$$\gamma(r) = \frac{dw}{dr} = \frac{\tau_o r_o}{rG(r)}$$

$$dw = \frac{\tau_o r_o}{G(r)} \frac{dr}{r} \quad (38)$$

The settlement of the pile shaft (w_s) as originally proposed by Randolph and Wroth (1978), is obtained by integrating equation 38 and assuming a linear elastic soil with no radial variation of G (i.e., $G(r) = G$), as follows:

$$w_s = \tau_o r_o \int_{r_o}^{r_m} \frac{dr}{Gr} = \frac{\tau_o r_o}{G} \ln \left(\frac{r_m}{r_o} \right) \quad (39)$$

where r_m is the radial distance at which shear stresses in the soil become negligible

Randolph and Wroth (1978) suggested estimating r_m using the following empirical expression:

$$r_m = 2.5 l \rho (1 - \nu) \quad (40)$$

where

l = pile embedment depth

ρ = factor of vertical homogeneity of soil stiffness = $G(\text{at pile middepth})/G(\text{at pile tip})$

ν = Poisson's ratio of the soil.

Equation 39 results in an equivalent linear T-Z load-transfer curve, as shown in figure 169. The stiffness or slope of this T-Z curve is:

$$K_s = \frac{G}{r_o \ln \left(\frac{r_m}{r_o} \right)} \quad (41)$$

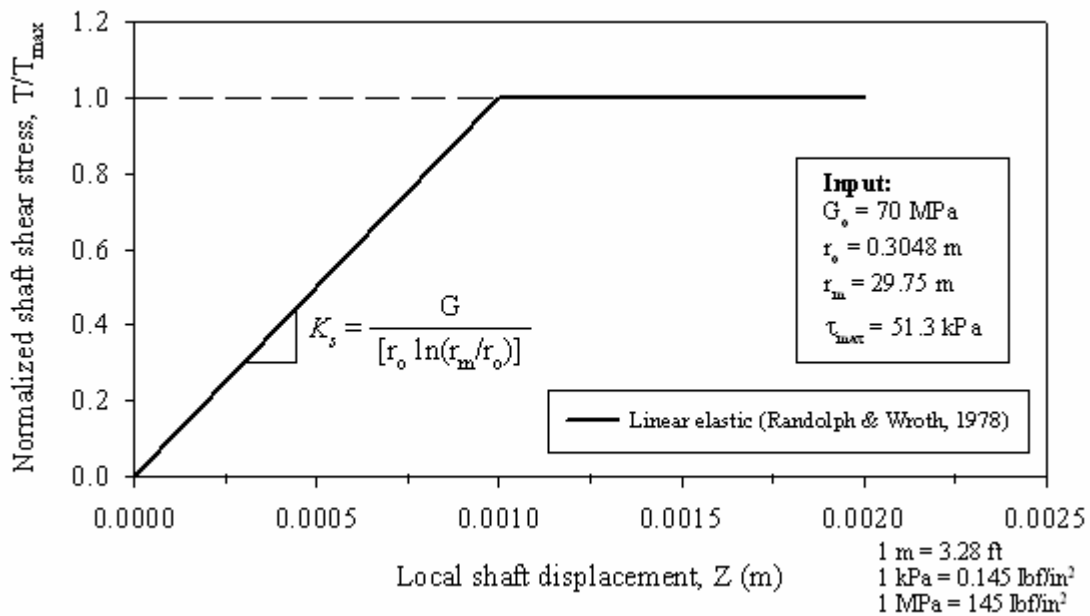


Figure 169. Graph. Linear T-Z curve obtained using Randolph and Wroth (1978).

The value selected for r_m has a large influence on the resulting pile settlement. A recent study by Guo and Randolph (1999) used finite element and fast Lagrangian analysis of continua (FLAC) analyses to determine the value of r_m more precisely. As a first approximation, equation 40 provides reasonable values for r_m (Randolph and Wroth 1978).

The load-transfer curve for the pile tip can be approximated using Boussinesq's solution for a rigid footing resting on an elastic half-space (Poulos and Davis 1990):

$$Z_{base} = \frac{Q_b(1-\nu^2)}{2E_s r_o} \quad (42)$$

where

Q_b = the pile tip load

E_s, ν = elastic modulus and Poisson's ratio of soil beneath pile tip

r_o = pile radius

Equation 42 can be expressed in terms of the shear modulus by substituting $E_s = 2G(1+\nu)$ as follows:

$$Z_{base} = \frac{Q_b(1-\nu)}{4Gr_o} \quad (43)$$

The resulting Q_b -Z load transfer curve is shown in figure 170.

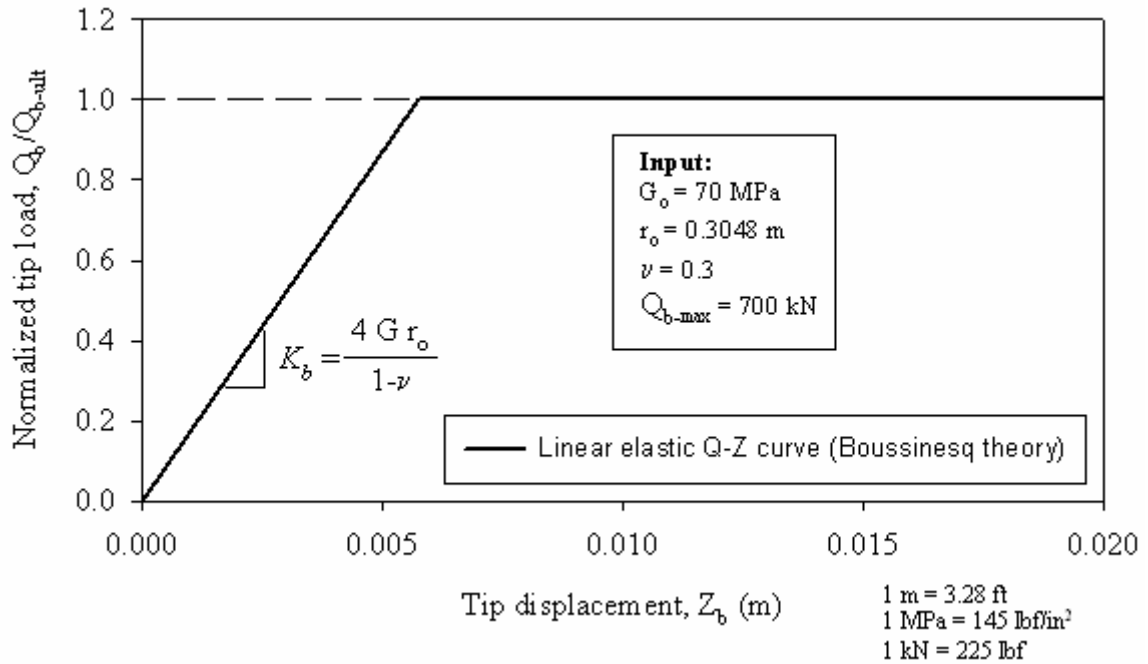


Figure 170. Graph. Linear Q_b - Z curve obtained using Boussinesq's theory.

The slope of the linear Q_b - Z corresponds to the stiffness coefficient of the pile tip spring, and is given by:

$$K_{base} = \frac{4Gr_o}{1-\nu} \quad (44)$$

In the preceding derivations it was assumed that the soil is linear and elastic, with the parameters G and ν constant with both strain level and with radial distance from the pile. However, most soils exhibit stress-strain behavior that is highly nonlinear and their stiffness can decay rapidly with strains (Atkinson 2000). If settlement predictions are made using the linear elastic load-transfer curves shown above, the appropriate elastic properties should be used. Poulos (2001) recommends using a secant shear modulus corresponding to the load range applied to the pile. For the tip of a pile in sand, Poulos (2001) recommends increasing the shear modulus to account for soil densification below the pile tip due to driving. Successful application of a linear theory to a nonlinear problem requires judicious selection of elastic property values.

Nonlinear load-transfer curves that include soil nonlinearity are derived in the following subsections.

7.3.4.2 Theoretical load-transfer curves for a nonlinear soil

7.3.4.2.1 Initial shear modulus

As shown in section 7.3.4.1, the shear stiffness of the soil deposit is a key property required in calculations of pile settlements. Sands typically only behave as linear elastic at very small shear strains of less than about 10 microstrains ($\gamma \leq 10^{-3}$ percent). The shear modulus in this range of very small shear strains is often referred to as the initial maximum or elastic shear modulus. Here it will be referred to as the initial shear modulus (G_0). To perform nonlinear pile settlement analyses, the initial shear modulus profile along the length of the pile must be estimated.

Elastic theory relates G_0 to the shear wave speed (V_s) as follows:

$$G_0 = \rho V_s^2 \quad (45)$$

where ρ is the soil mass density

Therefore, the initial shear modulus could be obtained from in situ measurements of the shear wave speed, such as from seismic CPT soundings. If seismic tests are not available, as is the case for the Route 351 site, G_0 can be estimated using empirical correlations with in situ CPT tests (Lunne, et al., 1997).

Several equations have been proposed to estimate G_0 from CPT q_c ; some of the most important ones are:

- Baldi, et al. (1989), from calibration chamber tests on uncemented, quartzitic sands:

$$\left(\frac{G_0}{q_c} \right)_{Average} = 1615 \left(\frac{q_c}{\sqrt{\sigma'_{vo}}} \right)^{-0.764} \quad (46)$$

where σ'_{vo} is the in situ effective overburden pressure at the depth of q_c , and the units of G_0 , q_c , and σ'_{vo} are in kPa.

- Rix and Stokoe (1991) from calibration chamber tests on uncemented, quartzitic sands:

$$\left(\frac{G_0}{q_c} \right)_{Average} = 1634 \left(\frac{q_c}{\sqrt{\sigma'_{vo}}} \right)^{-0.75} \quad (47)$$

where σ'_{vo} is the in situ effective overburden pressure at the depth of q_c , and where G_o , q_c , and σ'_{vo} are in kPa.

- Equation 48, originally proposed by Chow (1996). Equation 48 is based on a reinterpretation of the calibration chamber tests run by Baldi, et al. (1989):

$$G = \frac{q_c}{[A + B\eta - C\eta^2]}$$

and

$$\eta = \frac{q_c}{\sqrt{P_a \sigma'_v}} \quad (48)$$

where

q_c = CPT tip resistance

$A = 0.0203$

$B = 0.00125$

$C = 1.216 \times 10^{-6}$

σ'_v = free-field effective overburden pressure

P_a = atmospheric pressure (100 kPa)

7.3.4.2.2 Modeling soil nonlinearity using hyperbolic models

Hyperbolic stress-strain models have been found to adequately represent the nonlinear behavior of most soils (Kondner 1963, Kondner and Zelasko 1963, Duncan and Chang 1970). Use of hyperbolic functions to model nonlinear load-transfer functions for piles has been proposed by several researchers (e.g., Kraft, et al., 1981, Chow 1986, McVay, et al., 1989). The hyperbolic form of the shear stress-shear strain relationship is given by:

$$\tau = \frac{\gamma}{\frac{1}{G_o} + \frac{\gamma}{\tau_{ult}}} \quad (49)$$

where

γ = shear strain

G_o = initial tangent shear modulus

τ_{ult} = shear stress value that the hyperbola tends asymptotically (not to be confused with τ_{max})

τ = shear stress value corresponding to strain, γ

Duncan and Chang (1970) related the asymptotic value, τ_{ult} , to the maximum shear stress, τ_{max} , by:

$$\tau_{max} = R_f \tau_{ult} \quad (50)$$

where R_f is the failure ratio, and is typically a value less than or equal to one; for values of R_f less than 1.0 the failure stress (τ_{\max}) is reached at a finite shear strain; for R_f equal to 1.0, the failure stress would be reached asymptotically at a shear strain of infinity.

By substituting equation 50 and $\tau = G_{\text{sec}}\gamma$ into equation 49, we obtain the following expression for the secant shear modulus:

$$G_{\text{sec}} = G_o \left(1 - \frac{\tau R_f}{\tau_{\max}} \right) \quad (51)$$

If we include the radial variation of the shear stress (τ) obtained earlier using the concentric cylinder assumption (i.e., by substituting equation 35 into equation 51), we obtain:

$$G_{\text{sec}} = G_o \left(1 - \frac{\frac{\tau_o r_o}{r} R_f}{\tau_{\max}} \right) \quad (52)$$

Substituting the secant modulus G_{sec} from equation 52 into equation 38, and evaluating the integral from radial distances r_o to r_m , we obtain the following nonlinear load-transfer (T-Z) relationship:

$$w_s = \frac{\tau_o r_o}{G_o} \ln \left(\frac{\frac{r_m}{r_o} - \frac{\tau_o R_f}{\tau_{\max}}}{1 - \frac{\tau_o R_f}{\tau_{\max}}} \right) \quad (53)$$

Equation 53 results in the T-Z load-transfer curve shown in figure 171. For comparison, the linear T-Z curve derived earlier is also shown. It can be seen that the initial stiffness or slope of the nonlinear T-Z curve is the same as the linear curve (equation 41). The equation shown above becomes the linear elastic T-Z curve of equation 39 when $R_f = 0$.

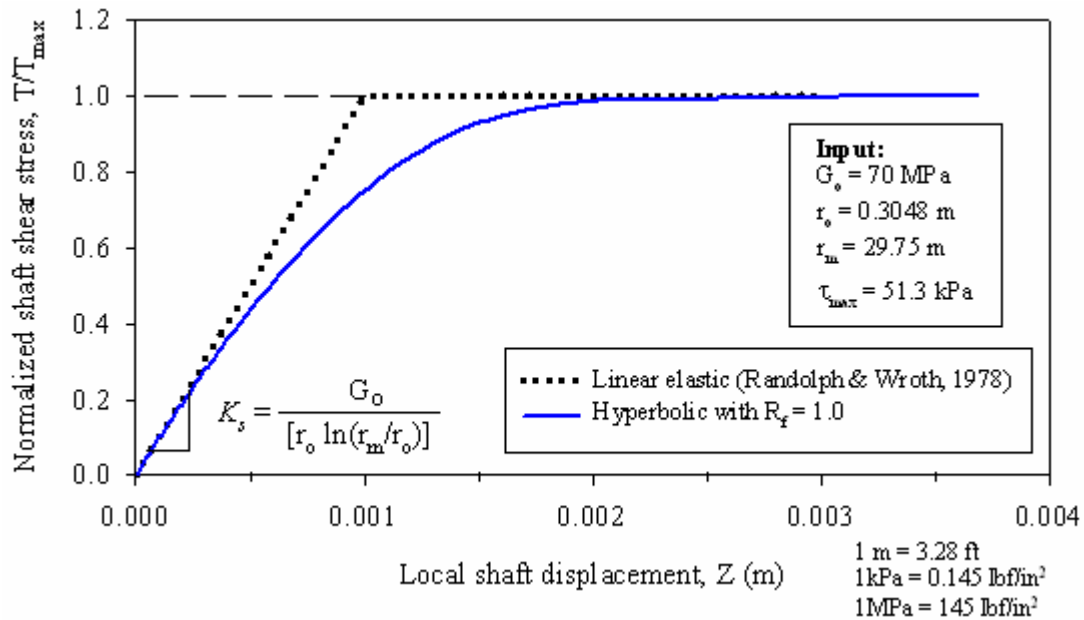


Figure 171. Graph. Hyperbolic T-Z curve.

For the hyperbolic model, the relationship between the normalized secant shear modulus (G_{sec}/G_o) and the normalized shear stress (τ/τ_{max}) plots as a straight line with slope $-R_f$, as shown in figure 172 (as given from equation 51). Fahey and Carter (1993) and Fahey, et al. (1994), showed that the hyperbolic model appropriately represented the shear modulus degradation observed in cyclic test data, but found that for monotonic tests on both normally consolidated and overconsolidated sands, the shear modulus degraded at a much faster rate than suggested by the hyperbolic model. Randolph (1994) also pointed this out, and indicated that in practice, real soils often show a more rapid decay of the secant shear modulus with shear stress. This rapid reduction in G_{sec} is observed when the very low strain initial shear modulus, obtained from dynamic tests, is used as initial reference (Randolph 1994, Atkinson 2000). The value of the initial shear modulus measured using conventional laboratory tests is smaller than the “true” initial shear modulus at very small strains measured using dynamic measurements (Atkinson 2000). The stiffness measured using conventional laboratory tests is lower because it is affected by factors such as the quality of the soil sample, small disturbances during sample setup in the test apparatus, seating of loading platen, and small misalignments of loading ram (Atkinson 2000). The conventional hyperbolic model may be more appropriate to capture the soil nonlinearity when the initial modulus used is from conventional laboratory tests. However, for initial soil modulus based on dynamic test measurements, the modified hyperbolic model such as the one proposed by Fahey and Carter (1993) may be more suitable (Randolph 1994).

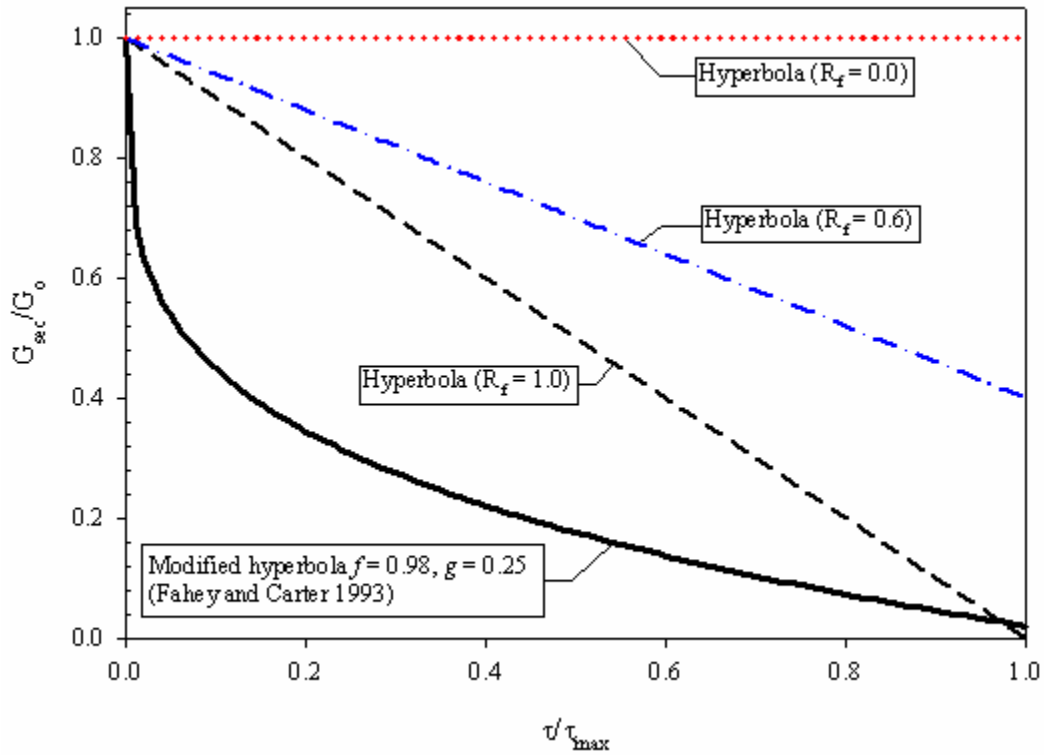


Figure 172. Graph. Variation of secant shear modulus for different hyperbolic-type models.

To allow for a faster degradation of the secant shear modulus degradation, with respect to the “true” initial very low strain shear modulus, Fahey and Carter (1993) proposed using the following modified form of the hyperbolic expression:

$$\frac{G_{sec}}{G_o} = 1 - f \left(\frac{\tau}{\tau_{max}} \right)^g \quad (54)$$

where

G_o = initial shear modulus (for shear strains below 10^{-5})

G_{sec} = secant shear modulus

τ = current shear stress

τ_{max} = maximum shear stress

f, g = empirical curve fitting parameters

Equation 54 becomes the standard hyperbolic model for $f = R_f$ and $g = 1$. Fahey and Carter (1993) found that the values of f of 0.98 and g of 0.25 gave a good fit for normally consolidated Toyoura sand. Toyoura sand is the Japanese standard sand, and it consists of a subangular fine sand with a mean particle size (D_{50}) of 0.17 mm (Ishihara 1996). This sand has characteristics similar to the in situ sand at the Route 351 project. The nonlinear

T-Z curve, corresponding to the Fahey and Carter (1993) modified hyperbolic G_{sec} curve, can be easily derived using the same procedure as before. This expression is as follows:

$$w_s = \frac{\tau_o r_o}{G_o g} \ln \left(\frac{\left(\frac{r_m}{r_o} \right)^g - f \left(\frac{\tau_o}{\tau_{max}} \right)^g}{1 - f \left(\frac{\tau_o}{\tau_{max}} \right)^g} \right) \quad (55)$$

Equation 55 becomes equation 53 (which corresponds to the conventional hyperbolic curve) when $f=R_f$ and $g=1$. The T-Z curve obtained using equation 55, and $f=0.98$ and $g=0.25$, is shown in figure 173. As shown in figure 173, the initial stiffness (K_s) of this T-Z curve is the same as the other two (since K_s depends only on G_o , r_o , and r_m), but this curve degrades at a much faster rate than the one based on the conventional hyperbolic equation.

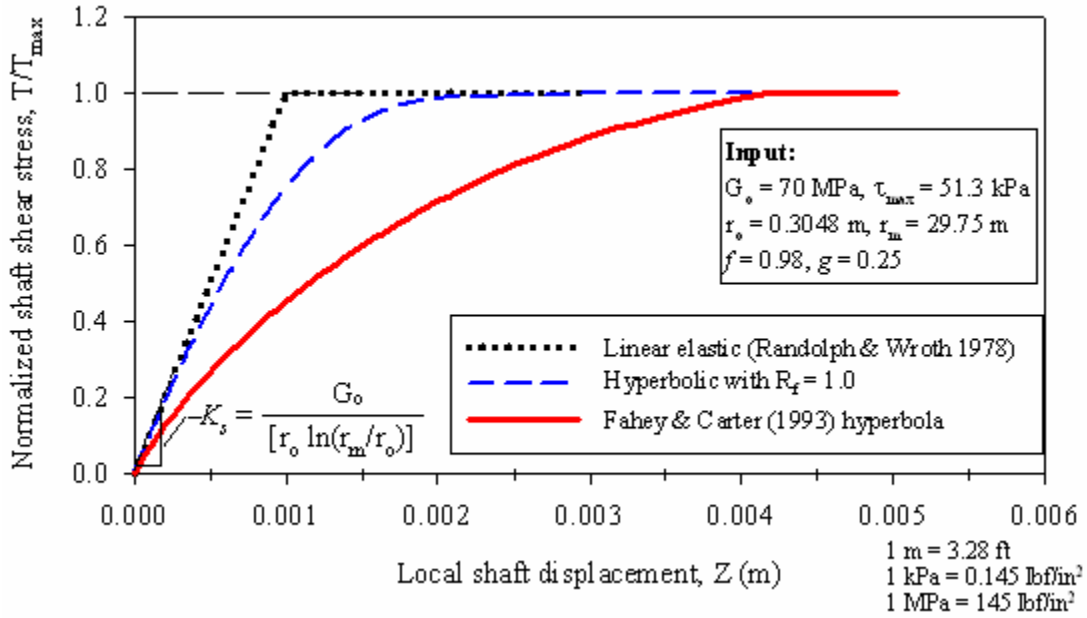


Figure 173. Graph. Theoretically derived T-Z curve using concentric cylinders and the modified hyperbola from Fahey and Carter (1993).

So far we have only dealt with the side shear load-transfer curves (T-Z curves). Because the nature of the shear strain distribution below a pile tip is more complex, it is not as straightforward to model soil nonlinearity for Q-Z curves as it was for the T-Z curves. An initial approximation consists of assuming a hyperbolic variation of the stiffness coefficient of the pile tip spring such as proposed by Chow (1986):

$$K_{secant}^{base} = K_o^{base} \left[1 - f \left(\frac{Q_b}{Q_{b-max}} \right)^g \right] \quad (56)$$

where K_o^{base} is equal to K_{base} from equation 44 (linear elastic soil case)

The expression for the load-transfer curve is:

$$Z_{base} = \frac{Q_b}{K_o^{base} \left[1 - f \left(\frac{Q_b}{Q_{b-max}} \right)^g \right]} \quad (57)$$

The Q_b - Z load-transfer curve obtained using equation 57 is shown in figure 174. For comparison purposes the linear elastic and conventional hyperbola curves are also shown.

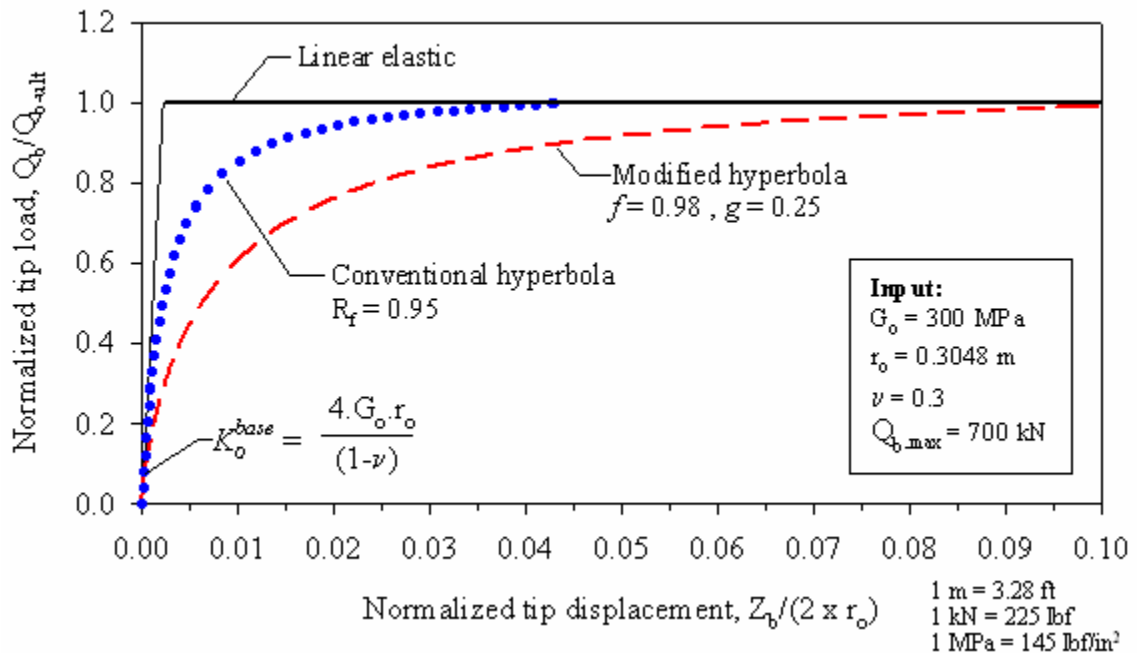


Figure 174. Graph. Theoretically derived Q-Z curve using Boussinesq's theory and the modified hyperbola from Fahey and Carter (1993).

As shown in figure 174, the ultimate tip resistance is developed at tip displacements of about 0.22 percent, 4.4 percent, and 10 percent, for the load-transfer curves based on the linear elastic, conventional hyperbolic ($R_f = 0.95$), and modified hyperbolic ($f = 0.98$, $g = 0.25$) models, respectively. The very small peak tip displacement in the linear elastic load-transfer curve is related to the use of the very low strain initial shear modulus. As mentioned earlier, use of a secant modulus is recommended to obtain more realistic displacements when using a linear elastic theory.

7.3.4.3 Input parameters using modified hyperbola theoretical load-transfer curves

To analyze the piles tested at the Route 351 Bridge project site using the modified hyperbolic load-transfer curves derived above, adequate values for the initial shear modulus (for shaft and base), and the maximum loads for the load-transfer curves (i.e., the maximum shear stress for the shaft T-Z, and maximum end-bearing pressure for the pile tip Q-Z) must be selected. The following subsections describe this selection process in detail.

7.3.4.3.1 Hyperbola parameters

Based on the characteristics of the sands encountered at the test site, modified hyperbola parameters of $f = 0.98$ and $g = 0.25$ were used.

7.3.4.3.2 Initial shear modulus

The profiles of initial shear modulus obtained using the equations 26, 46, and 47 shown above, and the design CPT profile for the Route 351 test site (figure 148), are shown in figure 175.

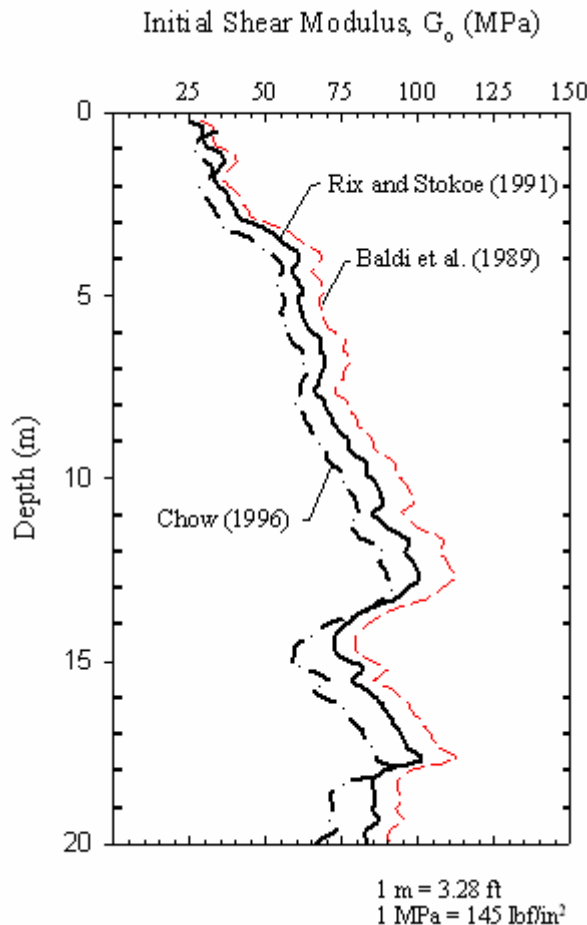


Figure 175. Graph. Route 351 initial shear modulus profile from CPT correlations.

Both the magnitude and distribution (radially and with depth) are important. Poulos (2001) distinguished the following different values of the shear modulus required for settlement calculations of single piles:

- The value of G_o in the vicinity of the pile shaft (this value will strongly influence the settlement of the pile).
- The value of G_o immediately below the pile tip.

Pile installation will greatly affect the shear modulus values in a zone near the pile (Poulos 1988). For driven piles in sands, the stiffness may actually be higher than the in situ value of the soil mass prior to pile installation (Randolph 1994). During pile installation the increase of radial stresses and associated densification will tend to increase the soil shear modulus; however, a competing effect which tends to reduce the shear modulus is the induced shear strains. The effects of pile installation on the magnitude and distribution of G_o are difficult to quantify. If the installation effects are known, Kraft, et al. (1981), and Randolph (1994) have presented procedures that can be used to include the radial variation of shear modulus in the theoretical load-transfer curves. However, both considered the installation effects less important than the nonlinear effects and generally minor compared to the uncertainties involved in the estimated soil properties. Therefore, the analyses presented in the following sections are based on the G_o profile presented in figure 175 with one exception: for the pile tip the G_o value selected was based on an average of the in situ G_o values measured immediately below the pile tip, multiplied by a factor of 4. This factor of 4 is used to account for sand densification below the pile tip. Poulos (2001) recommends increasing the in situ stiffness immediately below the tip of driven piles in sands by a factor between 3 and 5.

7.3.4.3.3 Maximum shear stresses

The maximum shear stresses are estimated using equation 21, using the interface friction angles obtained from interface friction tests. The coefficient of horizontal earth pressure (K) is assumed to range between 1.0 and 1.25. The range selected for K is consistent with the values recommended in the literature for displacement piles driven in sands (Bowles 1996, Poulos 2001).

7.3.4.3.4 Ultimate tip resistance

The theoretical Q_b - Z curves require as input, in addition to the initial shear modulus and the Poisson's ratio for the soil, the ultimate tip resistance, Q_{b-max} . For the predictions presented in the following sections, the Q_{b-max} values were selected from the Imperial College method estimates presented earlier (table 40). Q_{b-max} values from other prediction methods could have been used, but the IC method had the closest toe capacity predictions.

7.3.4.4 Prediction for the concrete test pile

The predicted load-settlement curves for the prestressed concrete test pile, using the proposed theoretically derived load-transfer curves, are shown in figure 176.

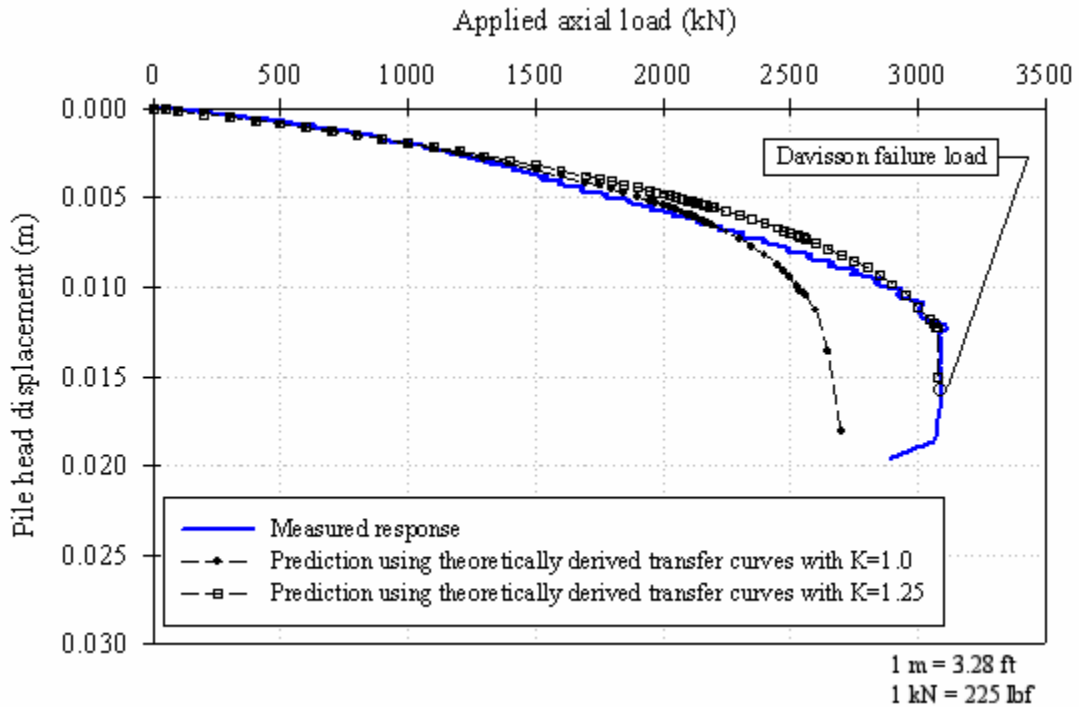


Figure 176. Graph. Settlement predictions for the concrete pile using theoretically derived transfer curves.

Using the maximum shear stresses calculated with a coefficient of horizontal earth pressures (K) of 1.25, the predicted load curve is in reasonably good agreement with the measured response. The analysis with $K = 1.25$ predicts the initial slope of the load-settlement curve and ultimate pile capacity quite well, but shows a slightly stiffer response for loads between 1,500 and 2,900 kN (337,500 and 652,500 lbf).

7.3.4.5 Prediction for the FRP test pile

Using the proposed theoretically derived load-transfer curves, and a value for K of 1.0, the load-settlement curve for the FRP test pile was predicted, as shown in figure 177.

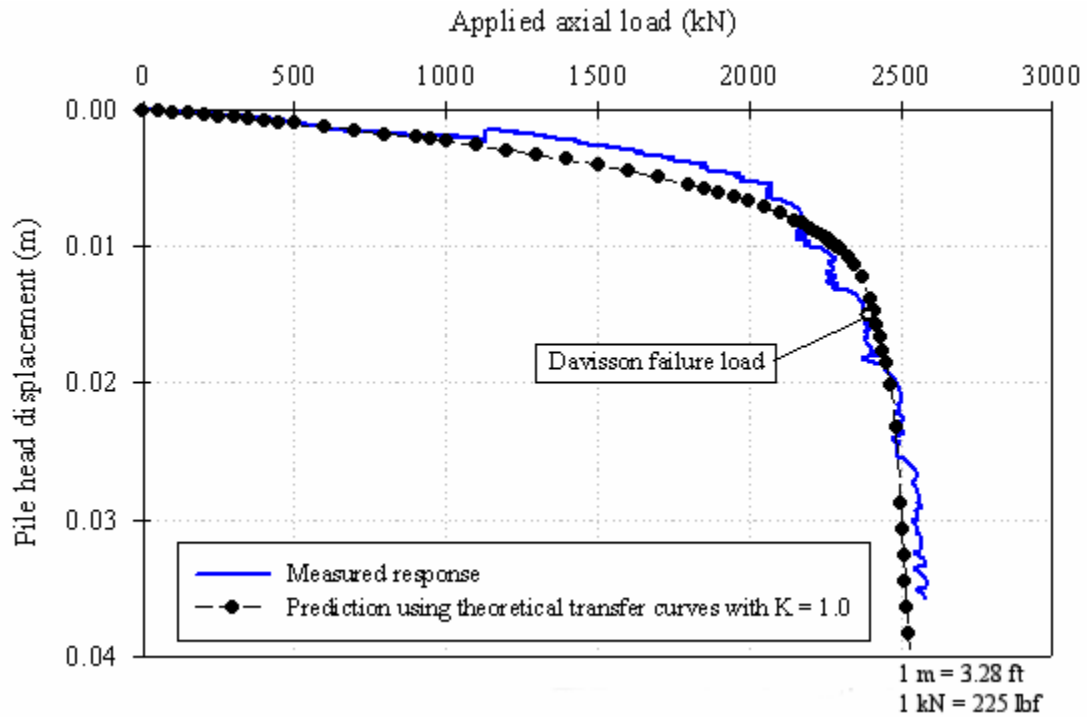


Figure 177. Graph. Settlement prediction for the FRP pile using theoretically derived transfer curves.

Figure 177 shows a good agreement between the predicted load-settlement curve and the measured response.

7.3.4.6 Prediction for the plastic test pile

The predicted load-settlement curves for the plastic test pile, using the proposed theoretically derived load-transfer curves, are shown in figure 178.

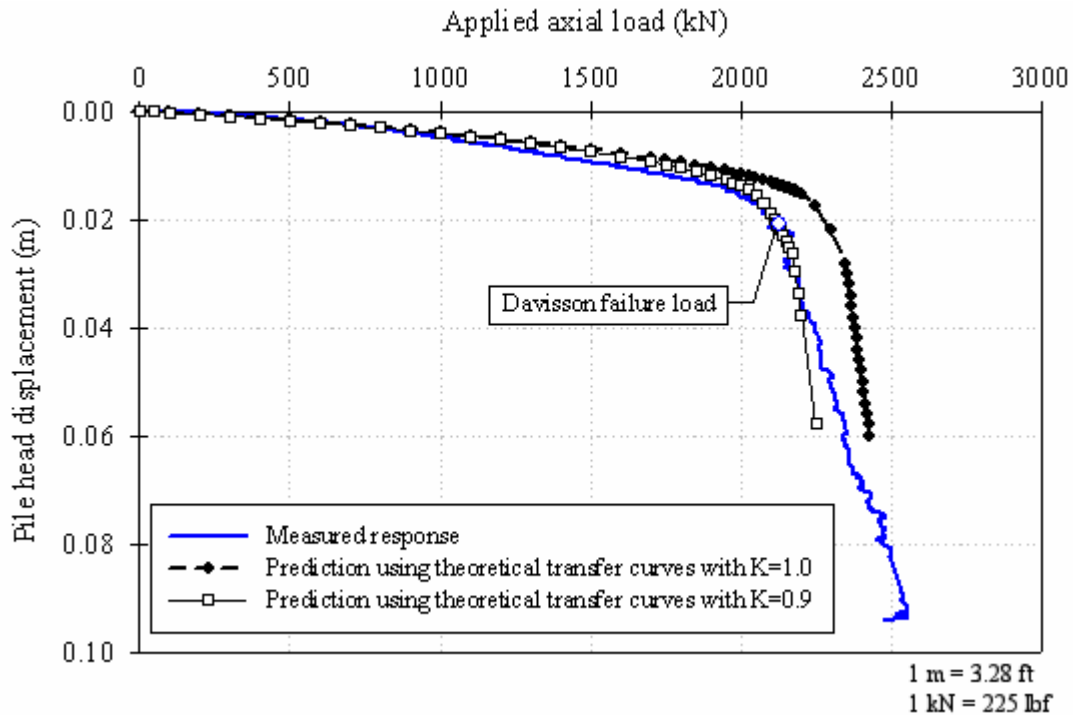


Figure 178. Graph. Settlement predictions for the plastic pile using theoretically derived transfer curves.

Using the maximum shear stresses calculated with values of the coefficient of horizontal earth pressures (K) of 0.90 and 1.00, the predicted load curves are, up to an applied axial load of approximately 2,250 kN (506,250 lbf), in reasonably good agreement with the measured response. The analysis with $K = 0.9$ predicts well the load at which the steep change of slope occurs. However, neither of the analyses captures the slope of the second portion of the curve.

7.3.4.7 Comments on the predictions using theoretical load-transfer curves

The predictions obtained using the theoretically derived load-transfer curves were in very good agreement with the measured field behavior. The best agreements were found for values of the coefficient of horizontal earth pressures (K) of 1.25, 1.0, and 0.9 for the prestressed concrete, FRP, and plastic piles, respectively. These differences in the K coefficient values are contrary to the expected outcome. The expected outcome was to have similar K values for the three test piles since they were installed in similar soil conditions, and all are full-displacement piles with similar cross sectional dimensions. It is possible that this result is again related to the δ values measured in the laboratory not being representative of field conditions, perhaps due to the small displacements (only 0.5 inches (12.7 mm)) used in the lab.

7.3.5 Residual Stresses

The analyses presented in this chapter did not include the effects of residual stresses, although their importance in obtaining more accurate predictions is recognized. Based on the small level of residual stresses measured in the field (see chapter 6), the effects of residual stresses were not considered. The impact of not incorporating residual stress effects would likely affect stiffness in the pile response rather than ultimate capacity.

7.4 CONCLUSIONS

The axial capacities of the three test piles were predicted using static analysis methods commonly employed in practice. The methods employed were the Nordlund method, the API method, the LCPC method, and the IC method. The various methods used to predict axial pile capacity yielded ratios of calculated to measured pile capacities ranging from 0.70 to 1.14 for the prestressed concrete pile, and from 0.81 to 1.33 for the composite piles. It was found that the level of accuracy of the predictions was comparable for all three test piles.

The prediction results seem to indicate that conventional static analysis methods are applicable to composite piles. However, it is the author's opinion that additional case histories are needed to corroborate and extend this conclusion to other composite pile types and to different soil conditions.

The load-settlement behavior was predicted using T-Z analyses. Several of these analyses were carried out to determine the adequacy of this method to analyze axially loaded composite pile types such as those studied in this research project. The analyses were completed using empirical load-transfer curves available in the literature (e.g., API 1993, Vijayvergiya 1977) and theoretically derived load-transfer curves.

The predictions using the empirical load transfer curves showed reasonable agreement with the field measurements for the composite piles. The predictions for the prestressed concrete pile showed less agreement, and tended to underestimate the measured pile capacity. This result could be related to the value of the interface friction angle used. The calculations were based on the interface friction angle measured in the lab, which may be inadequate to represent the field conditions experience by the pile (e.g., in the field the pile interface experienced much larger relative displacements compared to the 0.5 inches (12.7 mm) used in the laboratory).

The predictions obtained using the theoretically derived load-transfer curves were in very good agreement with the measured field behavior. However, the values of the coefficient of horizontal earth pressures (K) that resulted in the best matches with field behavior were 1.25, 1.0, and 0.9 for the prestressed concrete, FRP, and plastic piles, respectively. The differences in the K coefficient values are contrary to the expected outcome. The expected outcome was to have similar K values for the three test piles since they were installed in similar soil conditions, and all are full-displacement piles with similar cross sectional dimensions. It is possible that this result is again related to the δ values

measured in the laboratory not being representative of field conditions, perhaps due to the small displacements (only 0.5 inches (12.7 mm)) used in the lab.

The prediction results seem to indicate that conventional T-Z analyses are applicable to composite piles. However, it is believed that additional case histories are needed to corroborate and extend this conclusion to other composite pile types and to different soil conditions.

CHAPTER 8. ANALYSES OF THE LATERAL LOAD TESTS AT THE ROUTE 351 BRIDGE

8.1 INTRODUCTION

An important objective of this research is to determine whether accurate analyses of the lateral load-deflection behavior of composite piles can be performed using the same procedures typically used for prestressed concrete piles and other conventional pile types. If they can, this would remove one of the impediments to using composite piles by verifying that established procedures can be employed for design to resist lateral loads, at least for the type of composite piles studied in this research.

This chapter describes the procedure used for analyzing the lateral load tests of the three test piles at the Route 351 Bridge project. The results of the analyses are compared to the measured responses presented in chapter 6. A brief overview of the laterally loaded pile problem and a description of the methodology used in lateral pile analyses also are presented in this chapter.

8.2 GOVERNING DIFFERENTIAL EQUATION FOR THE LATERALLY LOADED PILE PROBLEM

A laterally loaded single pile presents a soil-structure interaction problem. The soil reaction is dependent on the pile movement, and the pile movement is dependent on the soil reaction. The solution must satisfy a nonlinear differential equation as well as equilibrium and compatibility conditions. The solution usually requires several iterations.

Elastic beam relationships that are used commonly in analysis of laterally loaded piles are summarized in table 41. These quantities are obtained from differentiating deflection y with respect to the distance along the pile (x).

Table 41. Relationships commonly used for elastic piles in flexion.

Variable	Formula	Units
Distance along the length of the pile (measured from pile head)	X	[L]
Distance to neutral axis within pile cross section	Z	[L]
Deflection	Y	[L]
Slope or rotation of pile section	$\phi = \frac{dy}{dx}$	[Dimensionless]
Curvature	$\kappa = \frac{d^2y}{dx^2}$	[Radians/L]
Bending moment	$M = E_p I_p \frac{d^2y}{dx^2} = E_p I_p \kappa$	[F x L]
Shear force	$V = E_p I_p \frac{d^3y}{dx^3}$	[F]
Axial load	Q	[F]
Soil reaction (or load intensity)	$p = E_p I_p \frac{d^4y}{dx^4}$	[F/L]

Notes: $E_p I_p$ = flexural stiffness of pile, where E_p = elastic modulus of pile material, and I_p = moment of inertia of pile cross section with respect to the neutral axis.

Figure 179 shows a loaded pile and typical profiles of net soil reaction, deflection, slope, and moment.

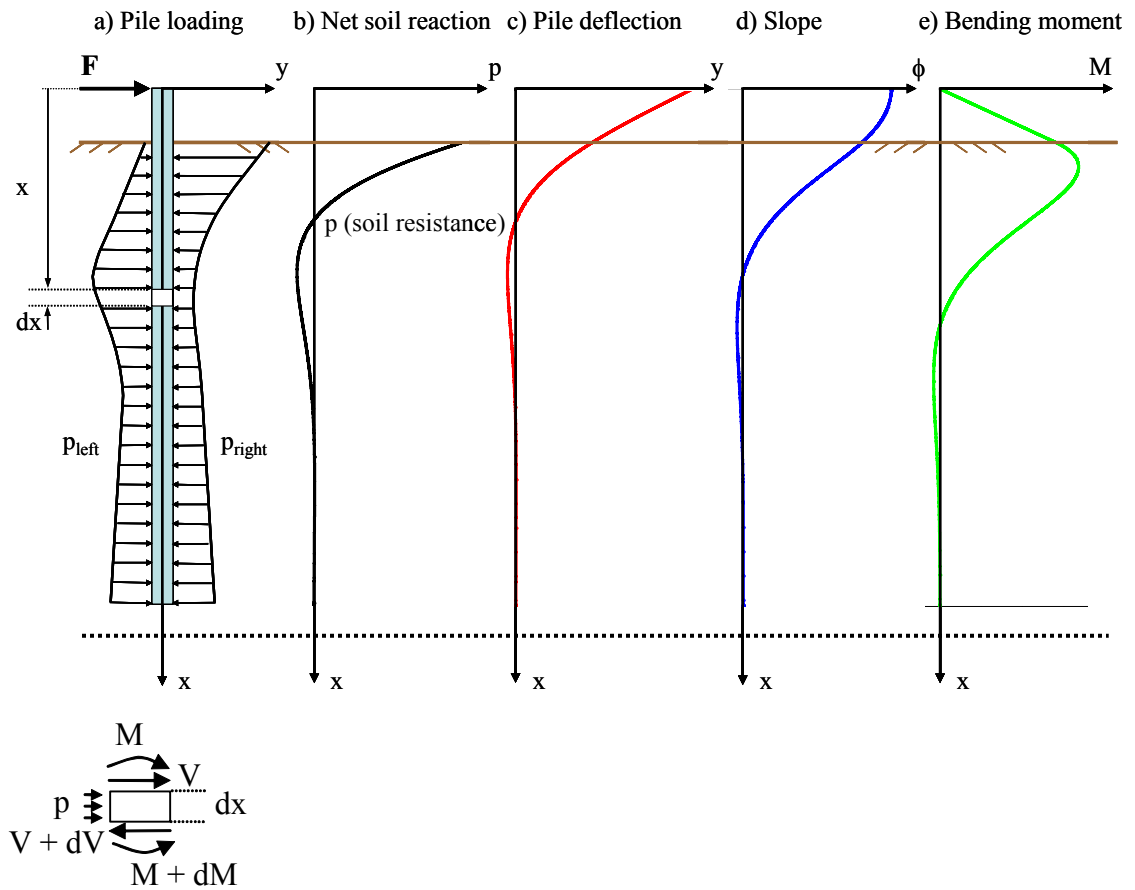


Figure 179. Illustration. Laterally loaded pile problem.

The governing differential equation for the problem of a laterally loaded pile was derived by Hetenyi (1946). The differential equation can be obtained by considering moment equilibrium of the infinitesimal element of length (dx) as shown in figure 179.

$$\sum M = (M + dM) - M - Vdx + Qdy - (pdx) \frac{dx}{2} = 0 \quad (58)$$

Neglecting quadratic terms, and differentiating twice with respect to x , we obtain:

$$\frac{d^2 M}{dx^2} + Q \frac{d^2 y}{dx^2} - \frac{dV}{dx} = 0 \quad (59)$$

The term involving the axial load, Q , can be ignored for the test piles investigated in this research since the vertical load present during testing was mainly from self-weight and can be considered negligible. The magnitude of the bending moment acting at a given

section of a pile can be calculated by integrating the normal stresses, $\sigma(z)$, acting within the cross section of area, A , as follows:

$$M = \int_A \sigma(z) z dA \quad (60)$$

If we assume that plane sections of the pile remain plane after loading, we can calculate the strains across the pile cross section if we know the rotation of the section, $\phi = dy/dx$, and the position of the neutral axis. For a given rotation, ϕ , we have the following:

$$\begin{aligned} u(x, y) &= \phi z = \frac{dy}{dx} z \\ \varepsilon(z) &= \frac{du}{dx} = \frac{d^2 y}{dx^2} z = \kappa z \\ \sigma(z) &= E_p \varepsilon(z) = E_p \kappa z \end{aligned} \quad (61)$$

where

$u(x, z)$ = is the displacement in the x-direction across the pile cross section

$\varepsilon(z)$ = strains in the x-direction across the pile cross section

z = distance to the neutral plane

Substituting the expression for $\sigma(z)$ from equation 61 into equation 60, we obtain:

$$M = \int_A (E_p \kappa z) z dA \quad (62)$$

If the pile material is linear elastic with a constant Young modulus, E_p , we would have:

$$M = E_p \kappa \int_A z^2 dA = E_p I_p \kappa = E_p I_p \frac{d^2 y}{dx^2} \quad (63)$$

Substituting equation 63 into equation 59 and ignoring the axial load term, Q , we obtain:

$$E_p I_p \frac{d^4 y}{dx^4} - \frac{dV}{dx} = 0 \quad (64)$$

From consideration of the horizontal force equilibrium of the infinitesimal element of the pile shown in figure 179, we obtain:

$$\begin{aligned} \sum F_H &= p(x) dx - dV = 0 \\ \text{or, } \frac{dV}{dx} &= p(x) \end{aligned} \quad (65)$$

Substituting equation 65 into equation 59, we obtain the following governing differential equation, which is commonly used to analyze piles under lateral loads:

$$E_p I_p \frac{d^4 y}{dx^4} - p(x) = 0 \quad (66)$$

The variable, $p(x)$, in equation 66 corresponds to the resultant soil resistance force per unit length of pile that occurs when the unit length of pile is displaced a lateral distance, y , into the soil. A crucial point for solution of the differential equation shown above is adequate representation of the soil reaction, p . If the soil reaction, p , has a linear relationship with lateral pile deflection, y , the equation has a closed-form solution. However, the relationship between the soil reaction (p) and the pile deflection (y) is nonlinear and also varies along the pile depth. In practice, it is common to solve this differential equation (equation 66) using numerical methods such as the finite difference method, and by modeling the soil reaction using nonlinear p - y curves. The analyses presented in this chapter were carried out using this approach. The p - y method used to model the soil reaction is discussed in section 8.3.

8.2.1 Assumptions and Limitations of the Governing Differential Equation

Implicit in the derivation of equation 66 is the fact that the pile is made of a homogeneous, isotropic, linear elastic material with the same modulus of elasticity in tension and compression. Hence, the flexural stiffness of the pile, $E_p I_p$, is assumed to remain constant during bending. As shown in chapter 6, this assumption is not valid for the piles tested in this research. The nonlinearity of the elastic properties of the piles can be dealt with during the numerical solution of the differential equation by means of successive iterations to account for the nonlinear properties of the structural materials of the pile (Reese and Van Impe 2001).

Another important assumption used in the derivation of equation 66 is that shear strains (or deformations) are small; that is, normals are assumed to remain normal to the neutral axis. This is a common assumption in classical beam theory or Bernoulli-Euler theory. The Mindlin beam theory, on the other hand, assumes normals to the neutral axis remain straight and undeformed, but not necessarily perpendicular to the neutral axis (Holzer, 2001). If we denote with ϕ the angle of rotation of the normal, we have the following for both beam theories:

$$\text{Bernoulli-Euler theory: } \phi = dy/dx$$

$$\text{Mindlin theory: } \phi = dy/dx + \gamma$$

If the shear strain, γ , is zero, the two theories are equal. The Mindlin theory assumes the shear strain is constant over the cross section, that is, independent of z . In reality, the shear strain (or stress) varies over the cross section; γ varies parabolically over a rectangular cross section made of a uniform material. The effect of shear deformations on beam deflections has been studied by Stippes, et al. (1961). They found that the total tip

deflection of a cantilever beam with uniformly distributed load and rectangular cross section is as follows:

$$\Delta = \frac{pL^4}{8EI} \left[1 + \frac{E}{2G} \left(\frac{D}{L} \right)^2 \right] \quad (67)$$

where the additional deflection due to shear deformations is given by the second term in the brackets.

The effect of shear deformations increases with increasing E/G ratios and decreasing slenderness ratios (L/D). For the piles tested at the Route 351 Bridge, the slenderness ratio (L/D) is about 15 (considering only the length of the pile where lateral deflections are significant), and the E/2G ratio is estimated to be about 1.3 for the prestressed concrete and FRP piles, and about 5 for the plastic pile. Therefore, the error associated with neglecting shear deformations is estimated to be less than 0.6 percent for the prestressed concrete and FRP piles, and less than 2.2 percent for the plastic pile. However, Han (1997) pointed out the importance of considering shear deformations when studying laterally loaded FRP composite piles. This is believed to be especially important when dealing with thin-walled or hollow FRP beams. Han (1997) reported values of E/2G between 4 and 15 for typical FRP composites materials (with no concrete infill). These E/2G ratios would result in deflection errors between 1.8 percent to 6.7 percent for a slenderness ratio of 15.

8.3 METHODOLOGY USED TO ANALYZE THE LATERALLY LOADED TEST PILES

The p-y method is widely used for design of laterally loaded piles. This method replaces the soil reaction with a series of independent nonlinear springs. The p-y curves represent the nonlinear behavior of the soil by relating the soil reaction and pile deflection at points along the pile length. A review of the p-y method is presented in sections 8.3.1 and 8.3.2.

8.3.1 P-y Curves

8.3.1.1 Introduction

The prediction of the soil resistance at any point along the pile as a function of pile deflection is perhaps one of the most critical factors in solving the problem of a laterally loaded pile. The distribution of stresses against a cylindrical pile before installation is shown in figure 180(a). At a given depth, the stresses will be uniform and normal to the pile wall (assuming the pile is installed vertically and without inducing bending) (Reese and Van Impe 2001). After the pile is subjected to lateral loading, the pile will deflect and the soil stresses acting on the pile would have a distribution similar to that shown in figure 180(b). It is important to point out that some of the stresses will not be perpendicular to the pile wall due to development of shear stresses at the interface

between the pile and the soil. The net soil reaction, $p(x)$, is obtained by integrating the stresses around the pile cross section. The units of $p(x)$ are force per unit length.

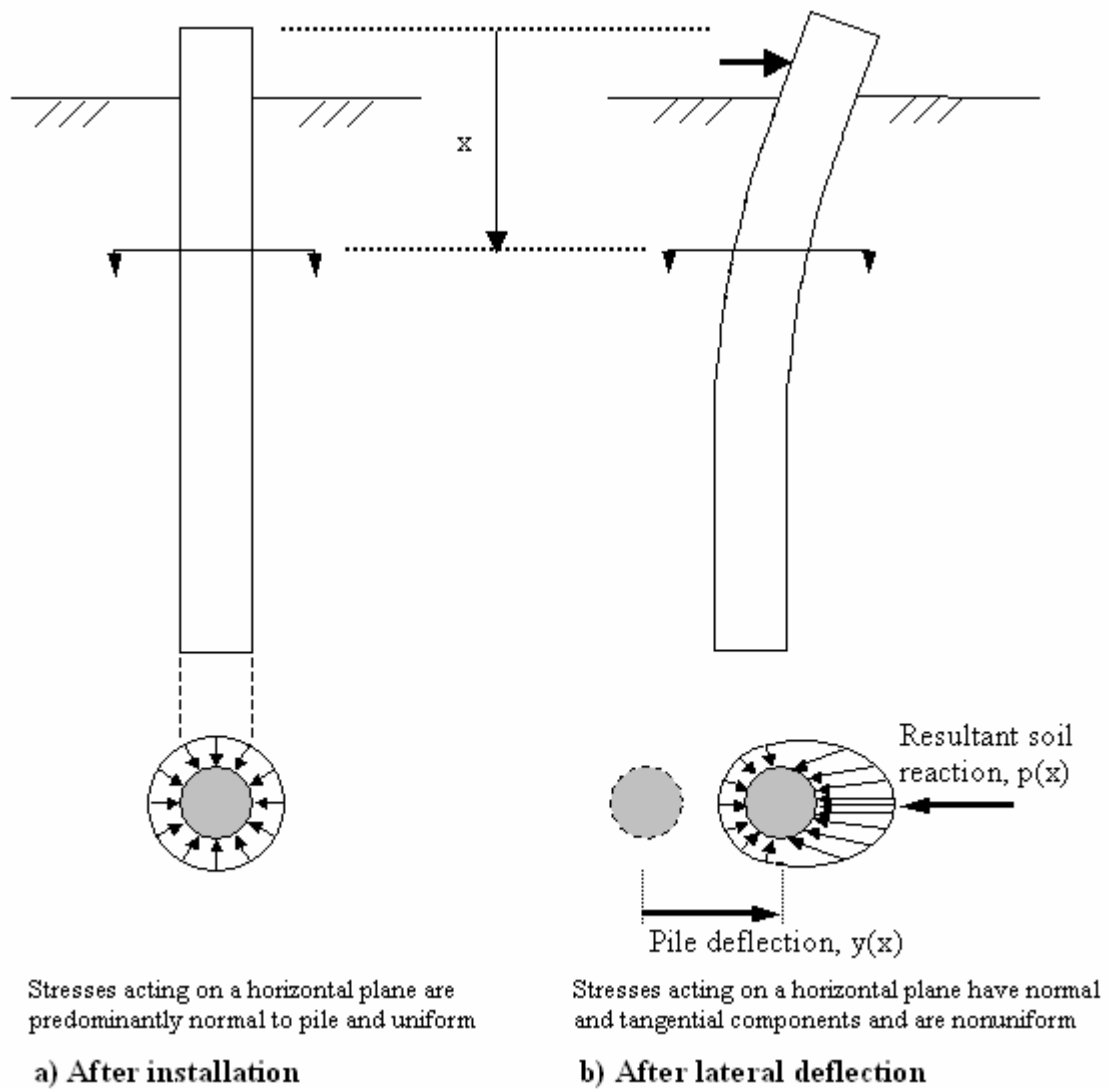


Figure 180. Illustration. Distribution of stresses against a pile before and after lateral loading (adapted from Reese and Van Impe 2001).

In general, p - y curves are nonlinear and they are a function of depth, soil type, and pile dimensions and properties. A typical p - y curve is shown in figure 181. Important elements of the p - y curve include the initial slope, E_{py-max} , and the ultimate soil resistance value, P_{ult} . At any point of the p - y curve the soil reaction, p , is related to the pile deflection, y , through the p - y modulus, E_{py} (Reese and Van Impe 2001). The p - y modulus is also known as the reaction modulus and it has units of force/length². Reese and Van Impe (2001) propose using the nomenclature given above instead of the modulus of subgrade reaction, which was originally developed to describe settlement of footings and relates the footing pressure (units of force/length²) to the footing settlement (units of length). These authors also point out that, although the subgrade modulus and E_{py} are

related to the values of the Young modulus of the soil, E_s , they are not only a function of the soil, but rather a result of the soil-structure interaction process between the soil and the footing and pile, respectively.

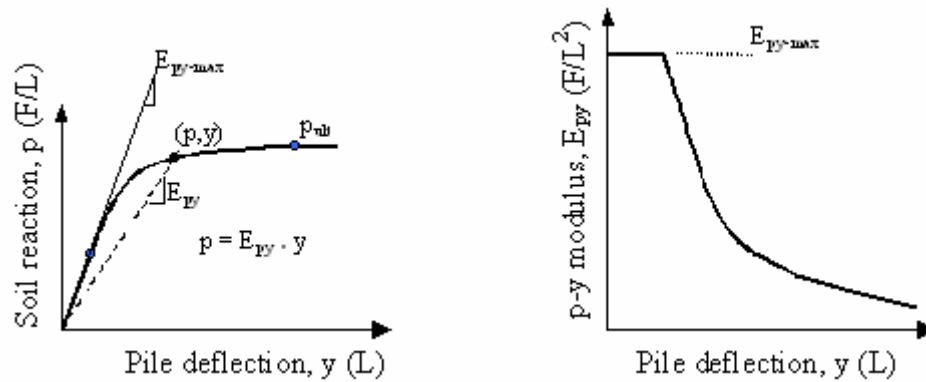


Figure 181. Graphs. Typical p-y curve and resulting p-y modulus (Reese and Van Impe 2001).

Ideally p-y curves should be generated from full-scale lateral load tests on instrumented test piles. In the absence of experimentally derived p-y curves, it is possible to use empirical p-y formulations that have been proposed in the literature for different types of soils. Table 42 lists the sources for some of the p-y expressions commonly used in practice.

Table 42. Recommended criteria for p-y curves in different soils (adapted from Reese, et al., 1997).

Soil Type and Condition	Reference
Soft clay below the water table	Matlock (1970)
Stiff clay below the water table	Reese, et al. (1975)
Stiff clay above the water table	Welch and Reese (1972), Reese and Welch (1975)
Sands	Reese, et al. (1974)
Sands	API (1993)
Soils with cohesion and friction	Evans and Duncan (1982)
Weak rock	Reese (1997)
Strong rock	Nyman (1980)

The p-y curves are not defined solely by soil characteristics (Ashour and Norris 2000). In addition to the properties of the soil surrounding the pile, the p-y curves are influenced by several other factors, such as: pile cross-sectional shape and dimensions, interface friction angle between soil and pile, pile bending stiffness, and pile head conditions (Ashour and Norris 2000, Reese and Van Impe 2001). Ashour and Norris (2000) used the strain wedge model to study analytically the influence of some of these factors on p-y curves. They found that for uniform sand deposits, a stiffer pile results in stiffer p-y curves. They also found that if two piles have the same width, but one has a circular cross section and the other has a square cross section, the resulting p-y curves will be different. The square pile in sand showed a soil-pile resistance higher than the circular pile. The findings from Ashour and Norris are based on analytical studies, and to the best of our knowledge no full-scale experiments have been reported to confirm their findings. Reese and Van Impe (2001) also pointed out the influence of the shape of the pile cross section on the soil resistance, p, as illustrated in figure 182.

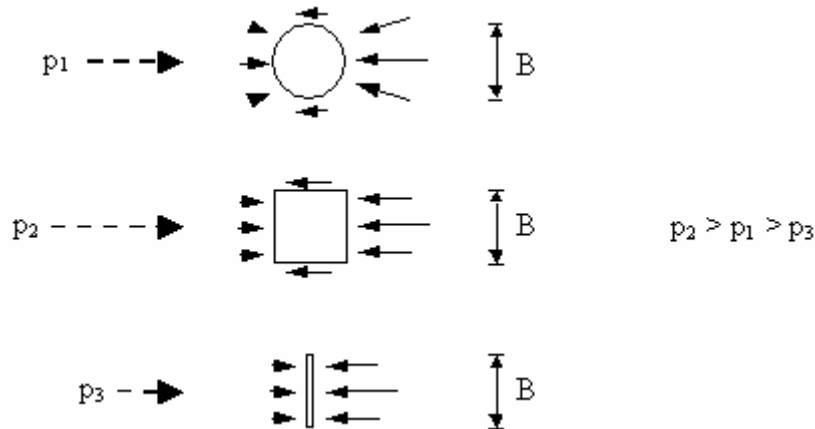


Figure 182. Illustration. Schematic showing the influence of shape of cross section of pile on the soil reaction p (adapted from Reese and Van Impe 2001).

The majority of the methods listed in table 42 consider only the influence of the soil properties and the pile width. If other factors such as pile shape and surface texture must be considered, p-y curves should be obtained experimentally based on full-scale tests.

The p-y analyses carried out in this research used published recommendations for p-y curves. The recommendations by Reese, et al. (1974), were used for the sandy soils at the test site. A brief description of these recommendations is provided below.

8.3.1.2 P-y curves for sands based on recommendations by Reese, et al., 1974

The typical shape of a p-y curve for sands, as recommended by Reese, et al., 1974, is shown in figure 183.

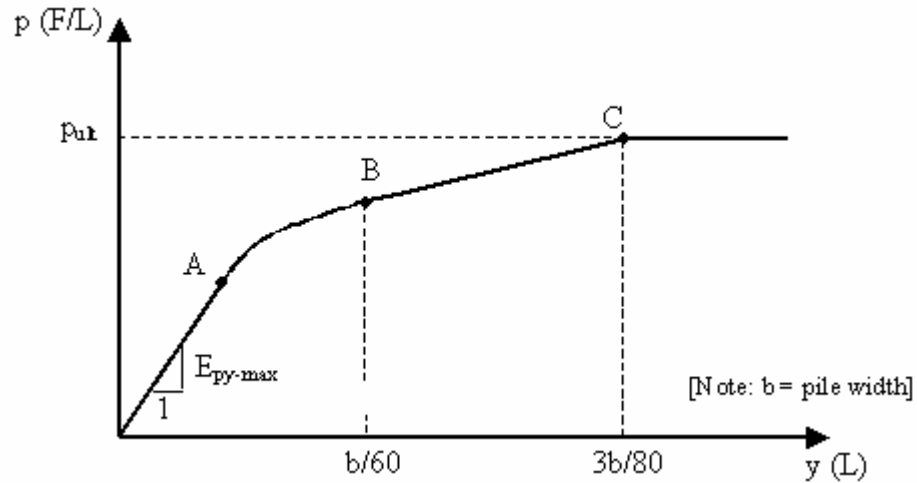


Figure 183. Graph. Elements of a characteristic p-y curve for sand based on recommendations by Reese, et al. (1974).

As shown in figure 183, the main elements that define the p-y curves for sands recommended by Reese, et al. (1974), are:

- Initial p-y modulus, E_{py-max} , that defines the initial portion of the curve up to point A.
- Ultimate soil resistance, p_{ult} , which defines the curve at point C and beyond.
- Transition zone between points A and C.

The coordinates of point C are $y = 3b/80$, and $p = p_{ult}$, where b is the pile width. The transition zone consists of two parts: a parabolic section between points A and B, and a straight line portion between points B and C. The coordinates of point B are defined as:

$$y_B = b/60$$

$$p_B = \frac{B_s}{A_s} p_{ult} \quad (68)$$

where A_s and B_s are coefficients obtained from charts provided by Reese, et al., 1974

The equation of the parabola is obtained knowing that it passes through point B and that it must be tangent to the straight line between points B and C. The coordinates of point A are obtained by finding the intersection point of the initial straight portion, with slope E_{py-max} , and the parabola.

The LPILE 4.0M program includes this type of p-y curve as a default p-y curve for sands. The p-y curves are generated automatically by the program. The user needs to specify the

initial slope of the curve (E_{py-max}) and the soil properties of the sand (effective unit weight and friction angle) to define the ultimate soil resistance (p_{ult}).

Reese, et al. (1974), recommend using a variation of E_{py-max} that increases linearly with depth, according to:

$$E_{py-max} = k x \quad (69)$$

where

k = a constant giving the variation of E_{py-max} with depth

x = depth below ground surface

Typical k values for loose and medium-dense sands below the water table are 5.4 and 16.3 MN/m³ (34,403 and 103,847 lbf/ft³), respectively (Reese, et al., 1974).

Before presenting the analyses results, a brief description of the p-y method of analysis is presented in the following section.

8.3.2 P-y Method of Analysis

The p-y method of analysis of laterally loaded piles is analogous to the T-Z method described in chapter 7 to analyze the axially loaded piles. In essence, the method consists of dividing the pile into a series of increments of equal length. The governing differential equation (equation 66) is solved using the finite difference technique. The soil is idealized as a series of independent nonlinear springs whose characteristics are represented by the p-y curves described in the previous section. The idealization used in the p-y method is shown in figure 184.

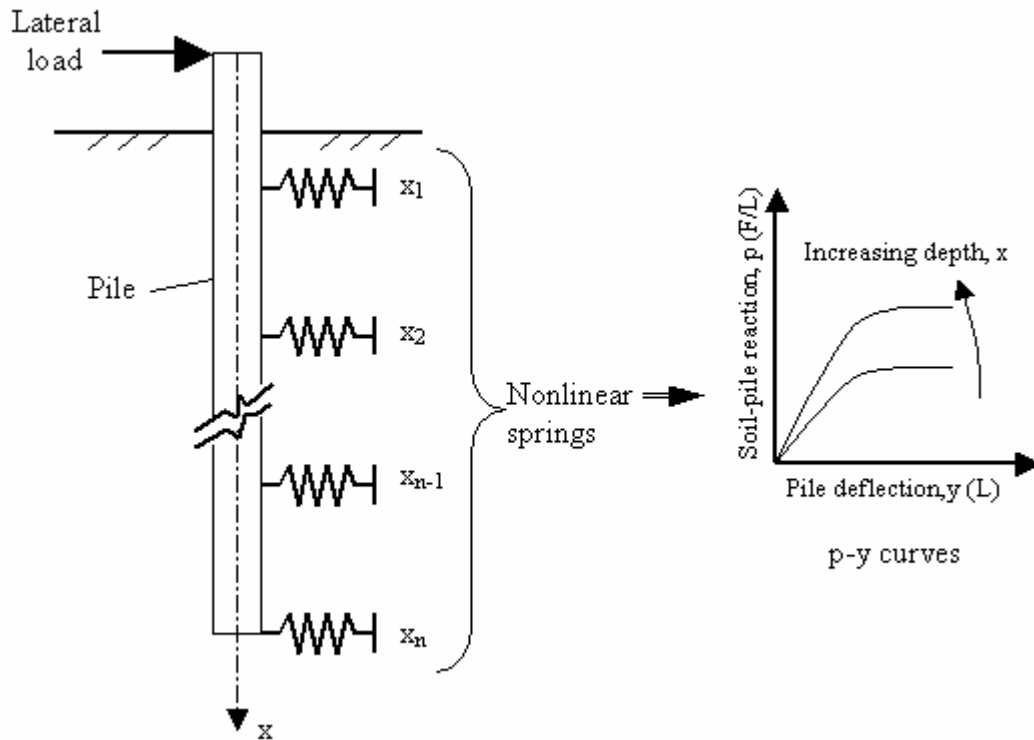


Figure 184. Illustration. Schematic showing p-y model used for analysis of laterally loaded piles.

The remainder of this chapter will deal with lateral load analyses carried out for the test piles at the Route 351 project.

8.4 NUMERICAL ANALYSES RESULTS

The analyses performed in this research used the p-y method and the computer program LPILE Plus 4.0M (2000). This program employs a finite difference formulation to solve the differential equation presented in the previous section, with nonlinear p-y curves to model the soil. LPILE Plus 4.0M allows computation of the pile response with user-specified nonlinear pile flexural stiffness, $E_p I_p$.

The program contains default p-y curves that can be used for different types of soils. As an alternative, the program also allows the user to input p-y curves developed using other formulations. For the analyses carried out in this research, the piles were discretized into 300 elements—the maximum number of increments allowed in the LPILE 4.0M program.

8.4.1 General Input Information

8.4.1.1 Pile information

Table 43 summarizes the pile properties used in the analyses. The nonlinear flexural stiffness relationships presented in chapter 6 were used for the three test piles.

Table 43. Properties of test piles.

Property	Prestressed Concrete Pile	FRP Pile	Plastic Pile
Width/diameter (m)	0.610	0.622	0.592
Perimeter (m)	2.44	1.95	1.86
Area (m ²)	0.372	0.304	0.275
Length (m)	18.0	18.3	18.3
Initial $E_p I_p$ (kN-m ²)	335,610	186,510	71,705
$E_p I_p$ versus M	See figure 113(b)	See figure 113(b)	See figure 113(b)

Notes: $E_p I_p$ = flexural stiffness of pile, M = bending moment.

1 m = 3.28 ft

1 kN-m² = 2,421 lbf-ft²

8.4.1.2 Upper soil stratigraphy information for p-y analyses

The soil stratigraphy near the top of the pile is the most important when studying laterally loaded piles (Duncan, et al., 1994). Typically, the significant lateral deflections of piles occur within the upper 8 to 10 diameters. The upper soil stratigraphy of the test pile site was found to be somewhat different at the north and south ends of the site.

Figure 185 shows representative in situ test information for the upper 10.0 m (32 ft) of stratigraphy at the northern end of the test pile site. The uppermost layer at the northern end of the test pile site is silty fine sand fill approximately 1.0 m (3.2 ft) thick. The fill is underlain by loose to medium-dense, silty fine sand to a depth of 13.0 m (42.6 ft).

The stratigraphy of the upper 10.0 m (32 ft) at the south end of the test pile site is shown in figure 186. The stratigraphy at the south end consists of 0.5 m (1.6 ft) of silty sand fill, which overlies a medium-stiff sandy, silty, clay layer that extends to about 1.8 m (5.9 ft) depth, which overlies loose to medium-dense silty sand. The extent of the clay layer was determined primarily based on the visual classification of the retrieved split spoon samples from boring SPT-2. The presence of the clay layer was confirmed indirectly via interpretation of the CPT and the flat dilatometer (DMT) test information available for the south end of the test site.

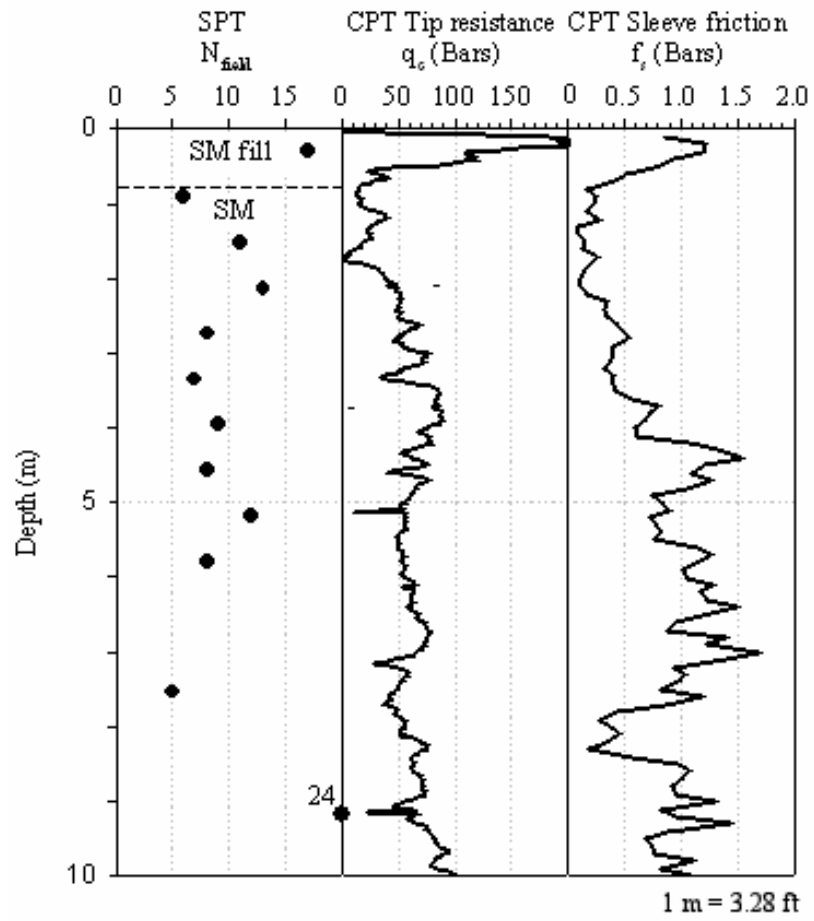


Figure 185. Graphs. In situ test data for the upper soils at the northern end of the test pile site.

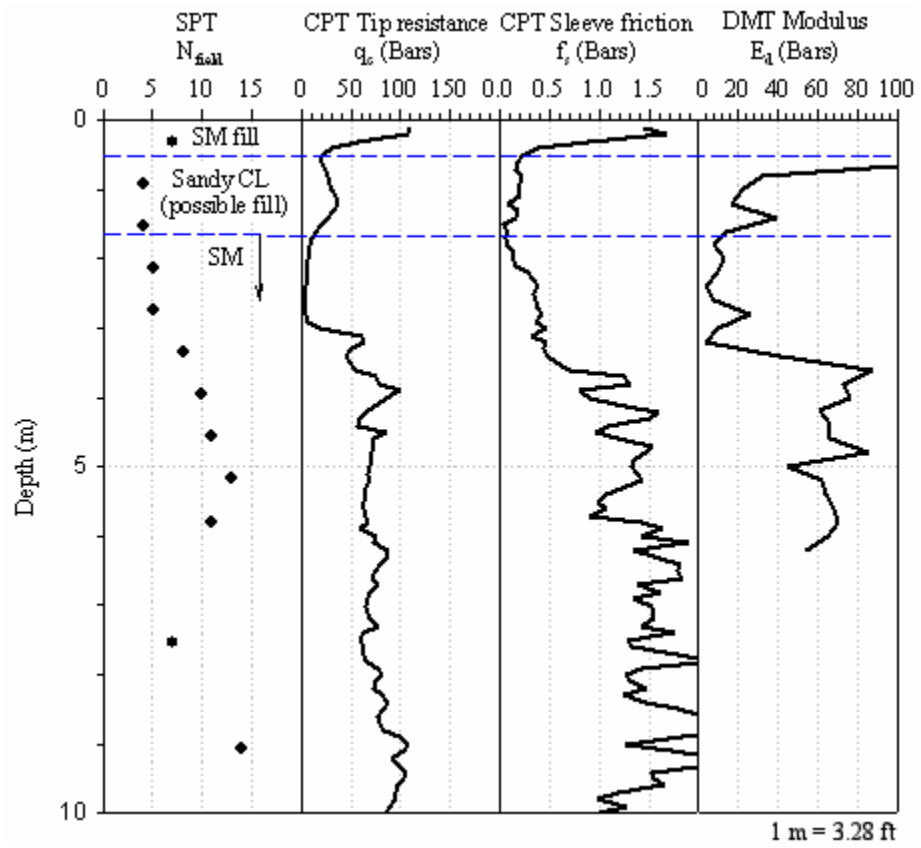


Figure 186. Graphs. In situ test data for the upper soils at the southern end of the test pile site.

8.4.2 P-y Analyses Results

A series of p-y analyses were carried out using the default p-y curves embedded in the LPILE program for different types of soils. As shown in section 8.4.1.2, the predominant type of soil at the test site consisted of silty sands. The default p-y curves recommended by Reese, et al. (1974), were selected to model these soils.

The uppermost soil layer at the test site consists of manmade fills, with an average thickness of about 1 m and 1.8 m (3.3 ft and 5.9 ft) at the north and south ends of the test site, respectively. Since all three test piles were installed in pits approximately 1.0 m (3.3 ft) deep, the majority of the fill materials were considered to be removed. Therefore, the p-y analyses were carried out using a soil model consisting of predominantly silty sands. However, it is recognized that the clayey fill layer present in the southern end extends about 0.9 m (2.9 ft) beyond the pit bottom of the prestressed concrete pile. This remnant fill was not specifically incorporated in the LPILE model for the test pile in the south side; instead, it was assumed to be part of the underlying silty sand deposit. This approximation was considered reasonable given the sandy and silty nature, and the thickness, of the low plastic clay fill layer. The results of the p-y analyses for the three test piles are summarized in the following sections.

8.4.2.1 Analyses for the prestressed concrete test pile

The prestressed concrete pile is located at the southern end of the test pile site. The surface stratigraphy for this pile is shown in figure 186. The pit excavated for this pile is 0.79 m (2.6 ft) deep. The original ground surface and the point of load application are 1.24 m and 1.34 m (4 ft and 4.4 ft) below the top of the pile, respectively.

The LPILE analyses were carried out using a two-layer model consisting of a layer of loose to medium-dense sand approximately 10 m (32.8 ft) thick, underlain by medium to dense sand. The LPILE model was constructed to take into account the 0.79 m- (2.5 ft-) deep pit excavated before installation of this pile. As mentioned earlier, the silty sands were modeled using the p-y curves recommended for sands by Reese, et al. (1974). The main input information required to define these curves is the initial p-y modulus and the friction angle of the sand. The initial p-y modulus for sands can be adequately modeled as increasing linearly with depth (Reese, et al., 1974). The rate of increase of the p-y modulus was selected based on trial-and-error until a best fit was obtained between the LPILE results and the field measurements. The p-y parameters that provided the best match are summarized in table 44. The initial p-y modulus values used in the analyses are shown in figure 187.

**Table 44. Parameters used to define default p-y curves
in LPILE for the prestressed concrete pile.**

Parameter	Loose Sand	Medium-Dense Sand
Default p-y curve	Reese, et al., 1974	Reese, et al., 1974
γ' , Submerged unit weight (kN/m ³)	10	11
c, Cohesion (kPa)	0	0
ϕ , Friction angle (degrees)	33	35
E_{py-max} , Initial modulus of p-y curve	See figure 187	See figure 187

1 kN/m³ = 6.36 lbf/ft³

1 kPa = 0.145 lbf/inch²

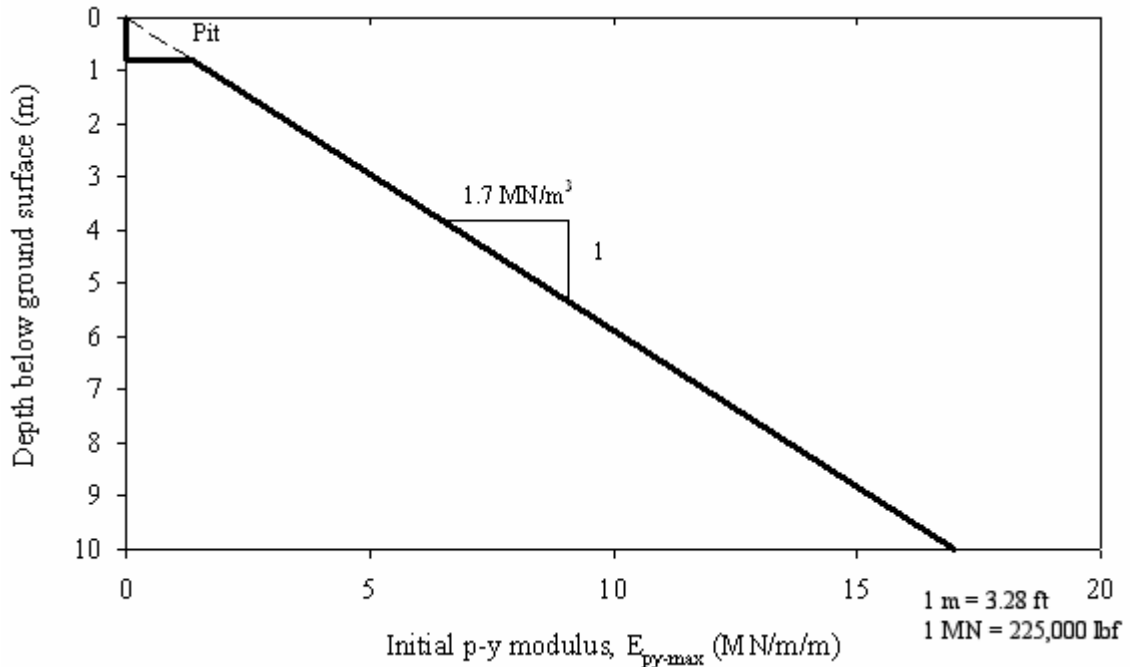


Figure 187. Graph. Initial p-y modulus profile used to define p-y default curves for LPILE analyses on the prestressed concrete pile.

The predicted deflected pile shapes are compared to the measured shapes in figures 188 through 190.

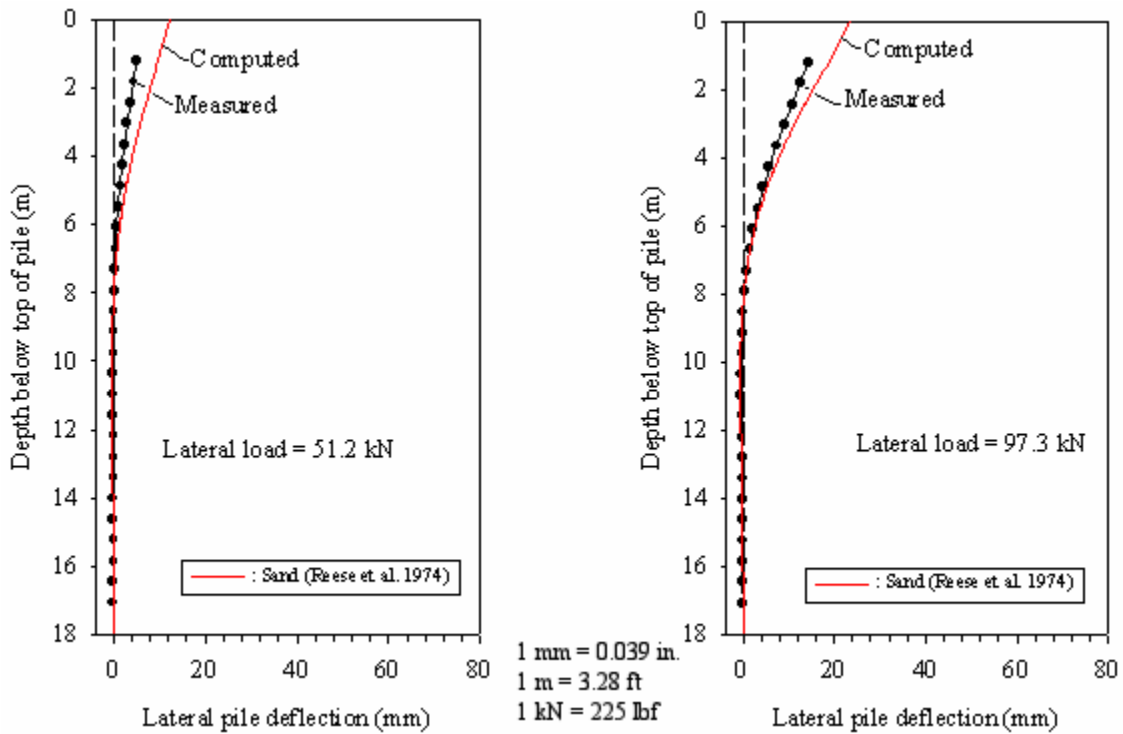


Figure 188. Graphs. Predicted versus measured lateral displacement profile for prestressed concrete pile (low lateral loads).

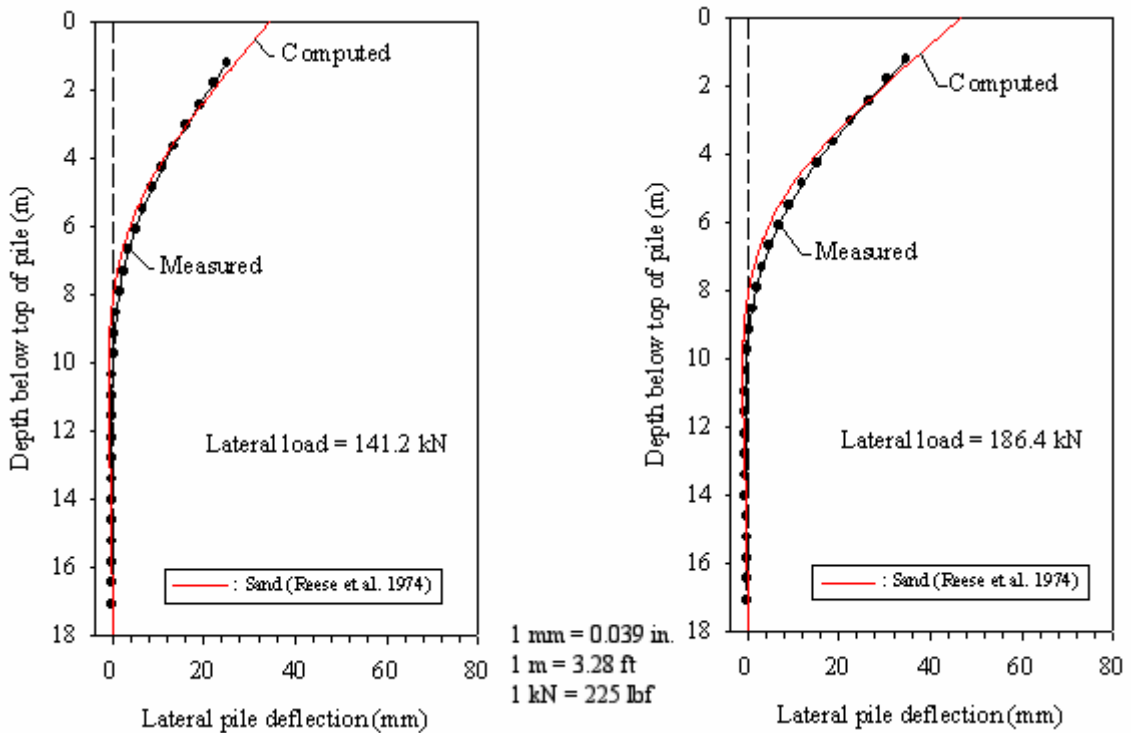


Figure 189. Graphs. Predicted versus measured lateral displacement profile for prestressed concrete pile (medium lateral loads).

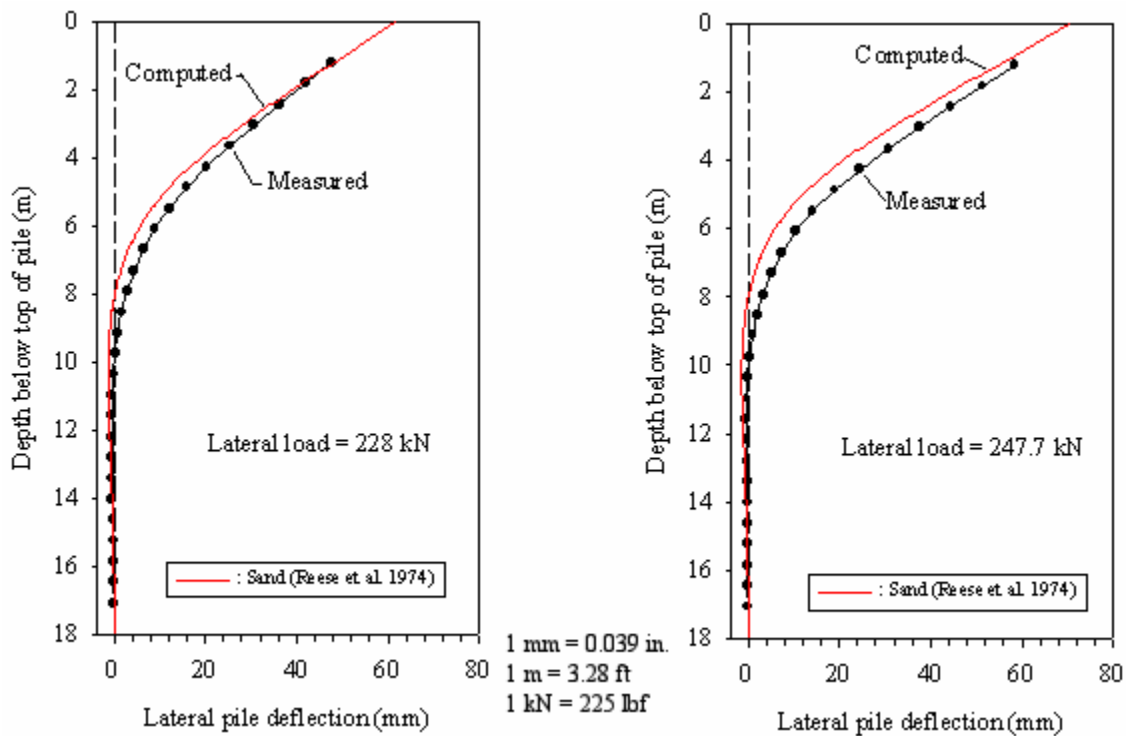


Figure 190. Graphs. Predicted versus measured lateral displacement profile for prestressed concrete pile (high lateral loads).

Figures 188–190 show that the deflected shapes of the pile are predicted reasonably well using the p - y modulus (E_{py-max}) values from figure 187 and the p - y curve equations recommended by Reese, et al., (1974). However, the predictions overestimate the lateral deflections for the two first loads of 51.2 and 97.3 kN (11,520 and 21,893 poundforce), and slightly underpredict the lateral deflections for the higher load levels. This could be related to the characteristics of the Reese, et al., (1974) p - y curves that may be on the “soft” side at low load levels and “stiff” at high load levels. As illustrated in figure 183, the Reese, et al., (1974) curves use a parabola and a straight section to connect the P_{ult} with the initial p - y modulus line. Since there are several possible ways to connect these two states, it is conceivable that other shapes of transition zone will result in different prediction results. A transition zone shape that is stiffer at low load levels and softer at high load levels may be better suited to capture the behavior of the soils encountered at this site. However, the approach was to use the default p - y model that would produce the best level of prediction possible.

Using the LPILE soil model described above, the pile lateral deflections and head rotations at ground surface were calculated. The results are shown in figures 191 and 192.

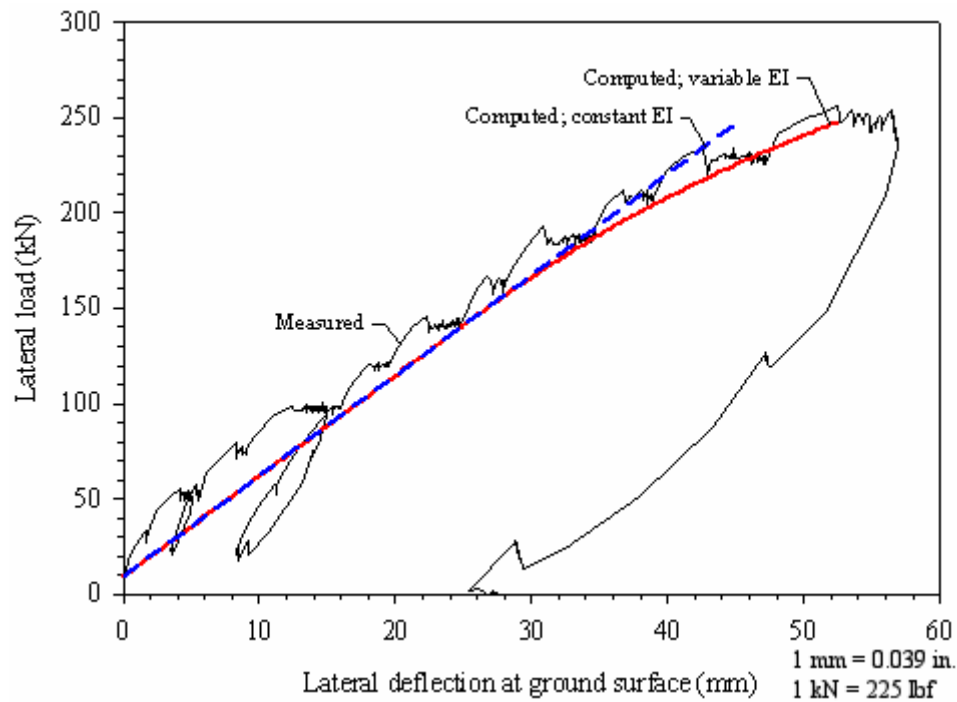


Figure 191. Graph. Calculated load-deflection curve for the prestressed concrete pile.

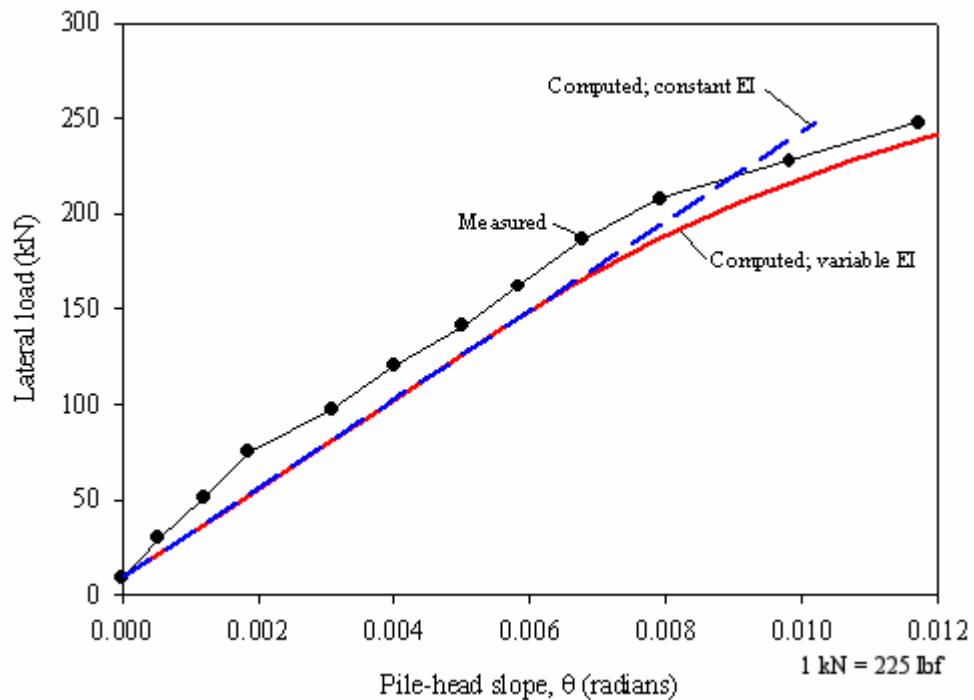


Figure 192. Graph. Calculated load-slope curve for the prestressed concrete pile.

The predicted values of lateral deflection and pile head rotation at the ground surface show reasonably good agreement with the field measurements. These figures also show

the predicted values if the flexural stiffness of the pile is modeled as being constant, that is, independent of the level of applied moment. The predicted deflections using constant pile flexural stiffness are approximately 7 percent lower than measured at the pile under large lateral loads (> 200 kN (45,000 lbf)), and the agreement is closer at lower lateral loads. This finding is reasonable since the flexural stiffness of the prestressed pile is approximately constant up to a moment of about 400 kN-m (295,028 lbf-ft) (see figure 113(b), chapter 6). Beyond this moment, the flexural stiffness of this pile decreases almost linearly with increasing applied moment. A similar behavior was observed for the head rotations.

8.4.2.2 Analyses for the FRP pile

The FRP pile is located at the northern end of the test pile site. The stratigraphy information for this pile is shown in figure 185. The pit excavated for this pile is 1.06 m (3.5 ft) deep. The original ground surface and the point of load application are 1.09 m (3.6 ft) and 0.79 m (2.6 ft) below the top of the pile, respectively.

For this pile, the LPILE model used in the analyses was constructed using two layers: an upper layer of loose to medium-dense sand, and a lower layer of medium to dense sand. The p-y parameters that provided the best match are summarized in table 45. Both sand layers were modeled using the p-y curves of the type recommended by Reese, et al. (1974).

Table 45. Parameters used to define default p-y curves in LPILE for the FRP pile.

Parameter	Loose Sand	Medium Dense Sand
Default p-y curve	Reese, et al., 1974	Reese, et al., 1974
γ' , Submerged unit weight (kN/m ³)	10	11
C, Cohesion (kPa)	0	0
ϕ , Friction angle (degrees)	33	35
E_{py-max} , Initial modulus of p-y curve	See figure 193	See figure 193

1 kN/m³ = 6.36 lbf/ft³

1 kPa = 0.145 lbf/inch²

The initial p-y modulus values that provided the best fit with the field measurements are shown in figure 193. The predicted deflected pile shapes are compared to the measured shapes in figures 194 through 196.

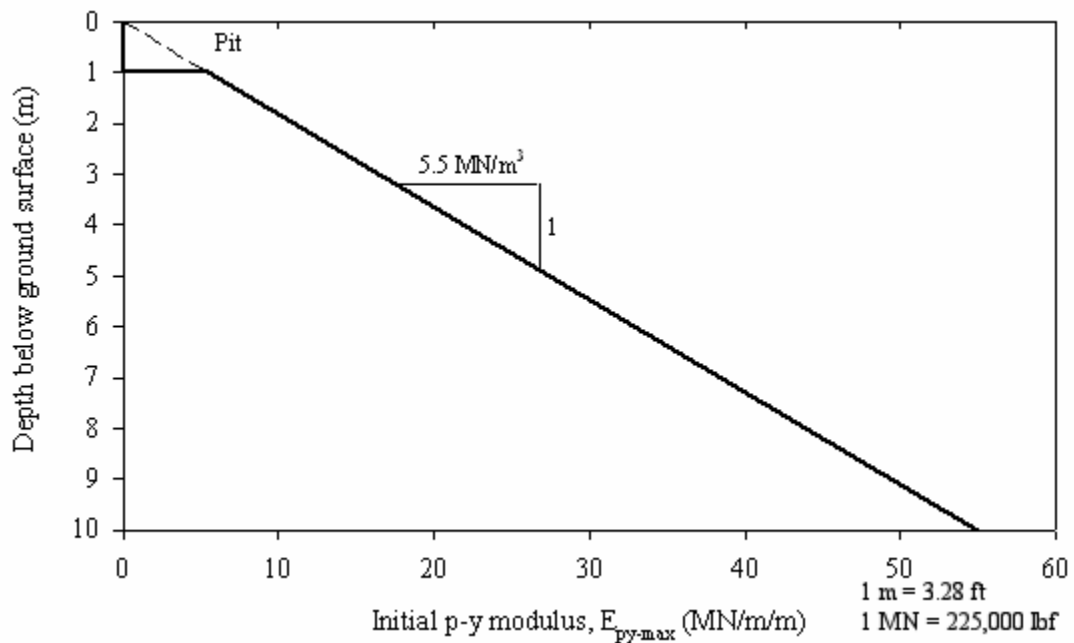


Figure 193. Graph. Initial p-y modulus profile used to define default p-y curves for LPILE analyses on the FRP pile.

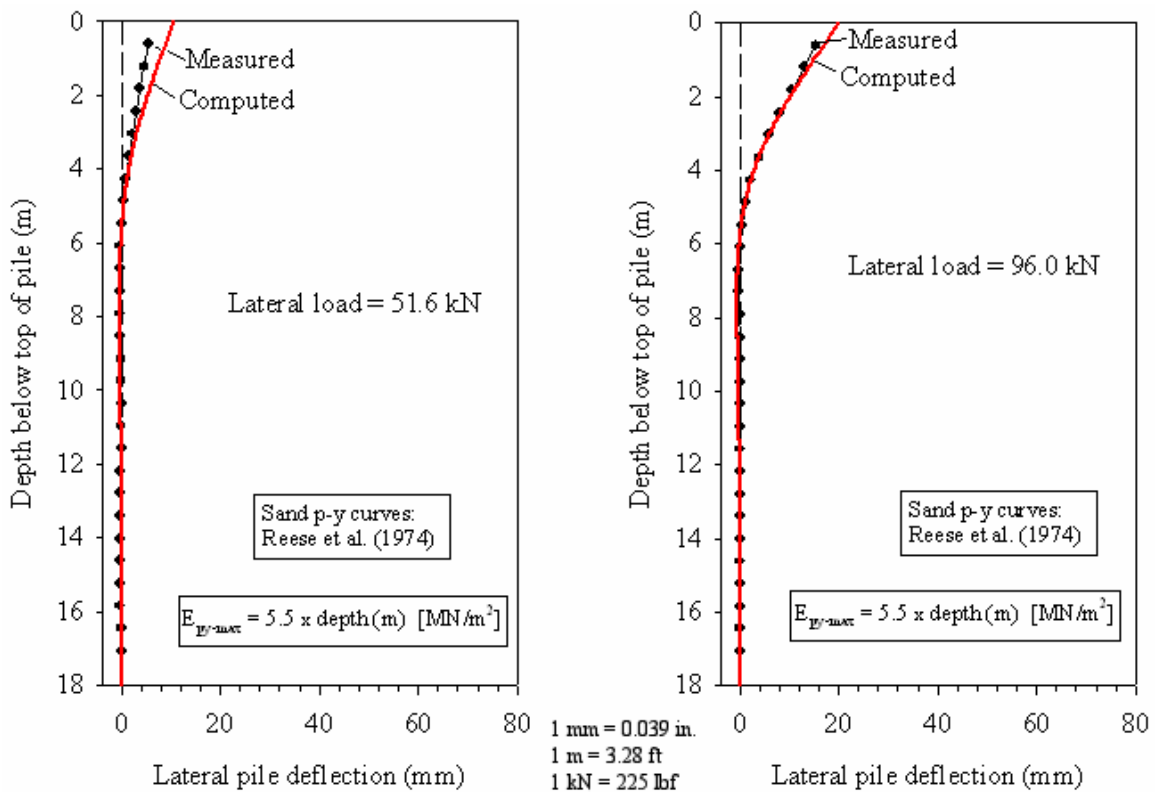


Figure 194. Graphs. Predicted versus measured lateral displacement profile for FRP pile (low lateral loads).

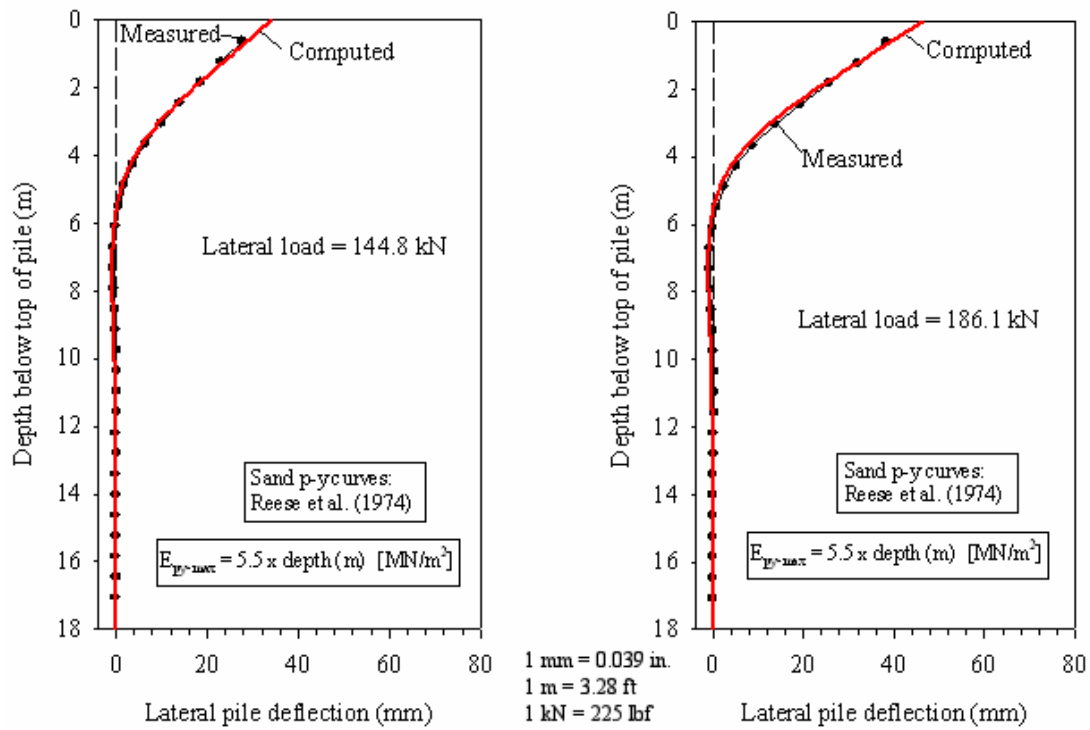


Figure 195. Graphs. Predicted versus measured lateral displacement profile for FRP pile (medium lateral loads).

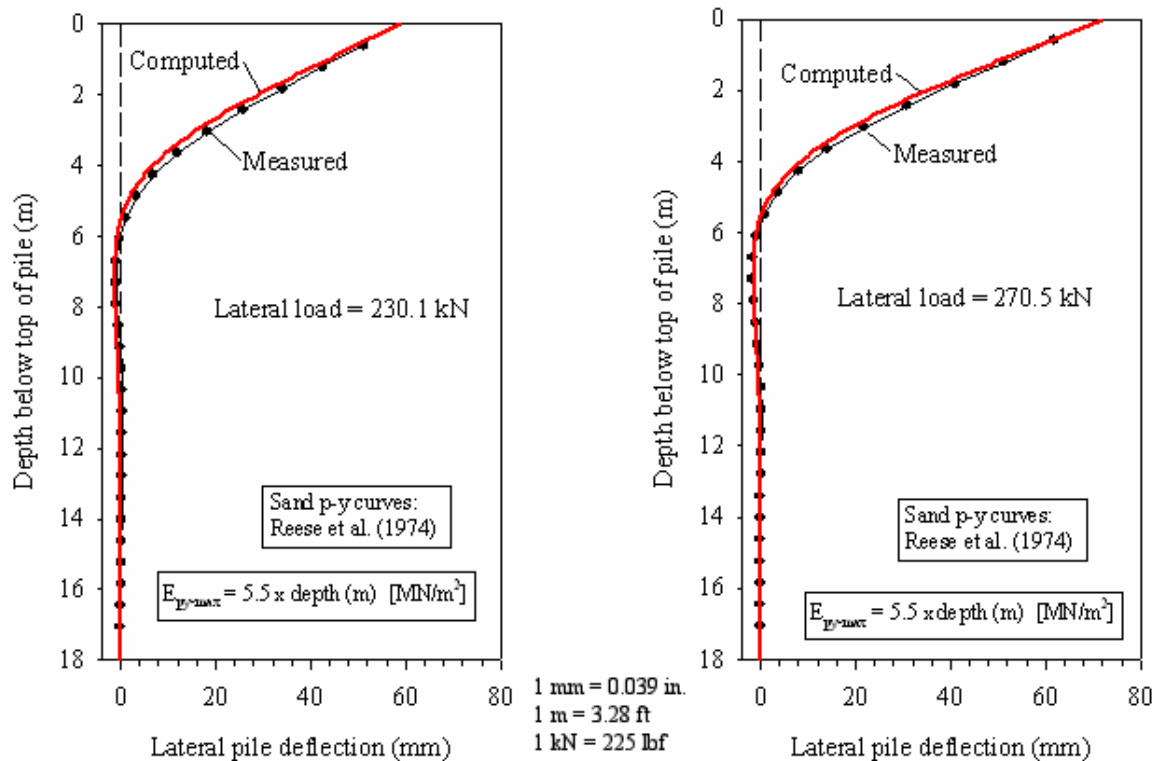


Figure 196. Graphs. Predicted versus measured lateral displacement profile for FRP pile (high lateral loads).

These figures show that the pile deflections are predicted reasonably well using the p-y curves recommended by Reese, et al. (1974), for sands and the p-y modulus (E_{py-max}) values from figure 194. For the first lateral load of 51.6 kN (11,610 lbf), the prediction overestimates the lateral deflections. This could be related to the p-y curve shape characteristics, as for the prestressed concrete pile.

Using the p-y curves given above to model the soil, lateral deflections and pile head rotations were computed for the FRP pile at the ground surface. The results are shown in figures 197 and 198.

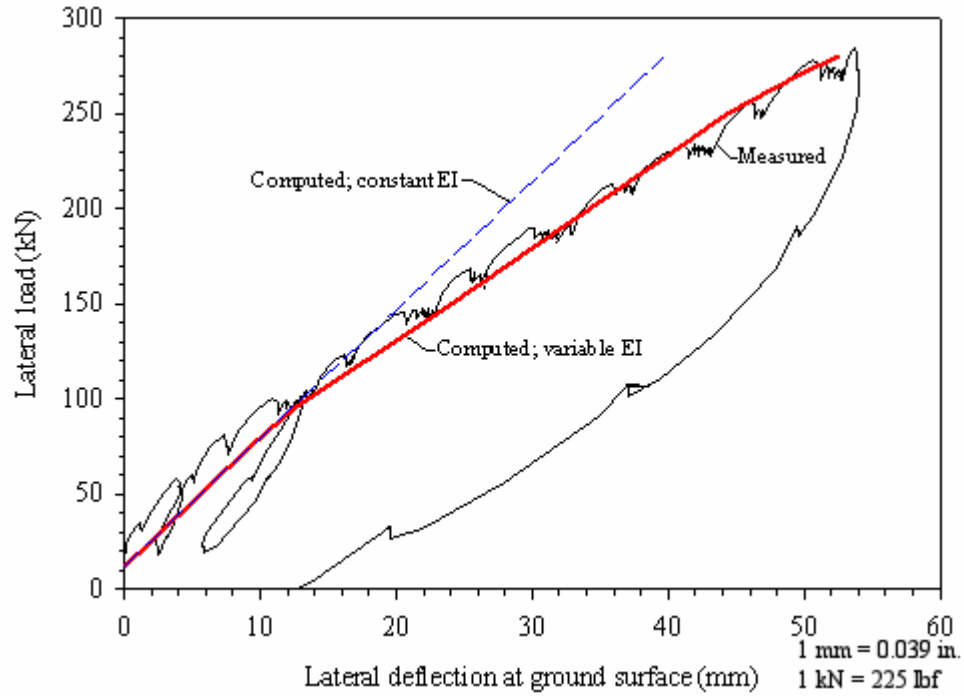


Figure 197. Graph. Calculated load-deflection curve for the FRP pile.

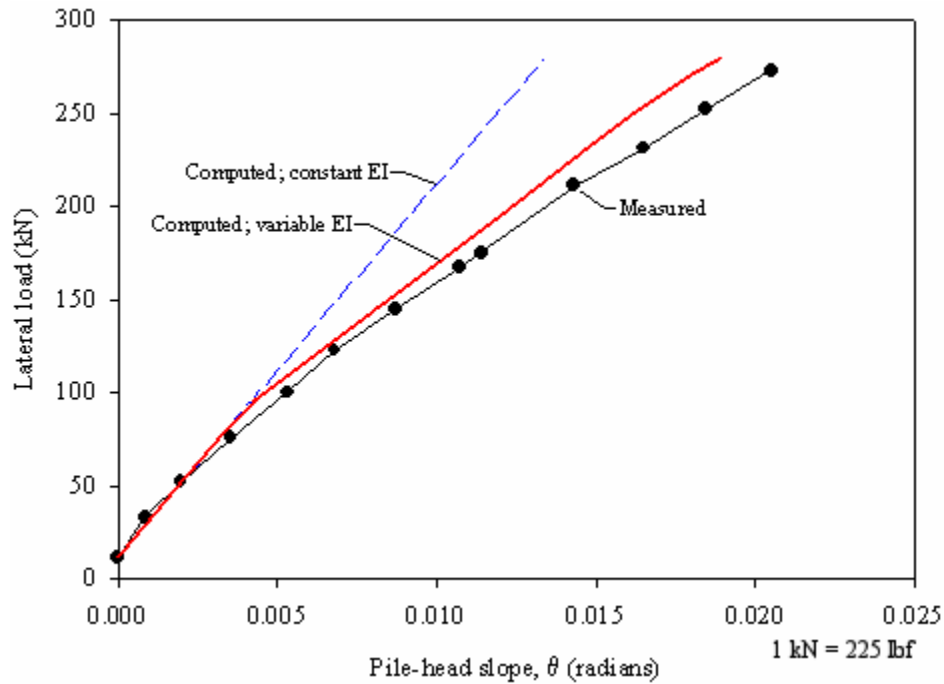


Figure 198. Graph. Calculated load-slope curve for the FRP pile.

The predicted values of lateral deflection and pile head rotation at the ground surface show good agreement with the field measurements. These figures also show the calculated values assuming that the flexural stiffness of the pile is constant, that is, independent of the level of applied moment. The predicted deflections using constant pile flexural stiffness are approximately 30 percent lower than measured under large lateral loads (> 150 kN (33,750 lbf)), and the agreement is closer at lower lateral loads. This finding is reasonable since the flexural stiffness of the FRP pile is approximately constant up to a moment of about 200 kN-m (147,514 lbf-ft) (as shown in figure 113(b), chapter 6). Beyond this moment, the flexural stiffness of this pile decreases with increasing applied moment. A similar behavior was observed for the pile head rotations.

8.4.2.3 Analyses for the plastic pile

The plastic pile is located at the center of the test pile site. The extent of the surficial fill at this location was not determined, but is expected to be similar to the conditions found at the south and north ends of the site. The pit excavated for this pile is 0.91 m (3 ft) deep. The original ground surface and the point of load application are 1.02 m and 1.21 m (3.3 ft and 4 ft) below the top of the pile, respectively.

For this pile, like the other piles, the two-layer LPILE model consisted of a layer of loose sand extending 10 m (32.8 ft) deep and an underlying layer of medium to dense sand. The p-y parameters that provided the best match are summarized in table 46. Both sand layers were modeled using the p-y curve types recommended by Reese, et al. (1974).

Table 46. Parameters used to define default p-y curves in LPILE for the plastic pile.

Parameter	Loose Sand	Medium Dense Sand
Default p-y curve	Reese, et al., 1974	Reese, et al., 1974
γ' , Submerged unit weight (kN/m ³)	10	11
c, Cohesion (kPa)	0	0
ϕ , Friction angle (degrees)	33	35
E_{py-max} , Initial modulus of p-y curve	See figure 199	See figure 199

1 kN/m³ = 6.36 lbf/ft³

1 kPa = 0.145 lbf/inch²

The profile of initial p-y modulus with the depth that provided the best match is shown in figure 199. The predicted deflected pile shapes are compared to the measured shapes in figures 200 through 202.

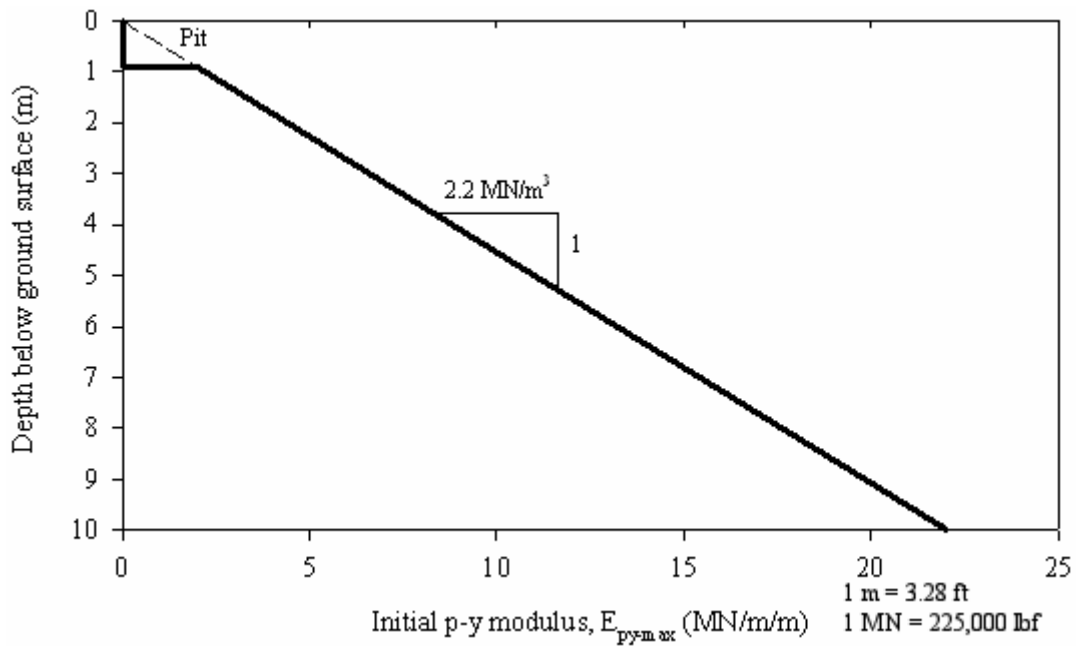


Figure 199. Graph. Initial p-y modulus profile used to define default p-y curves for LPILE analyses on the plastic pile.

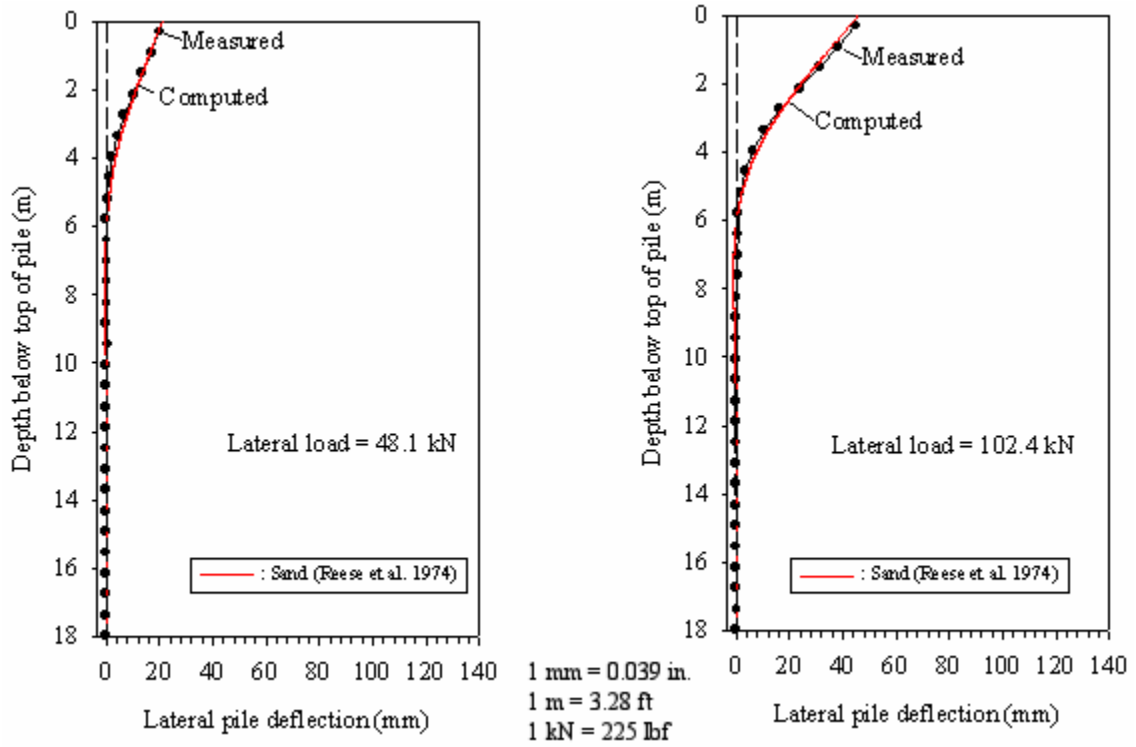


Figure 200. Graphs. Predicted versus measured lateral displacement profile for plastic pile (low lateral loads).

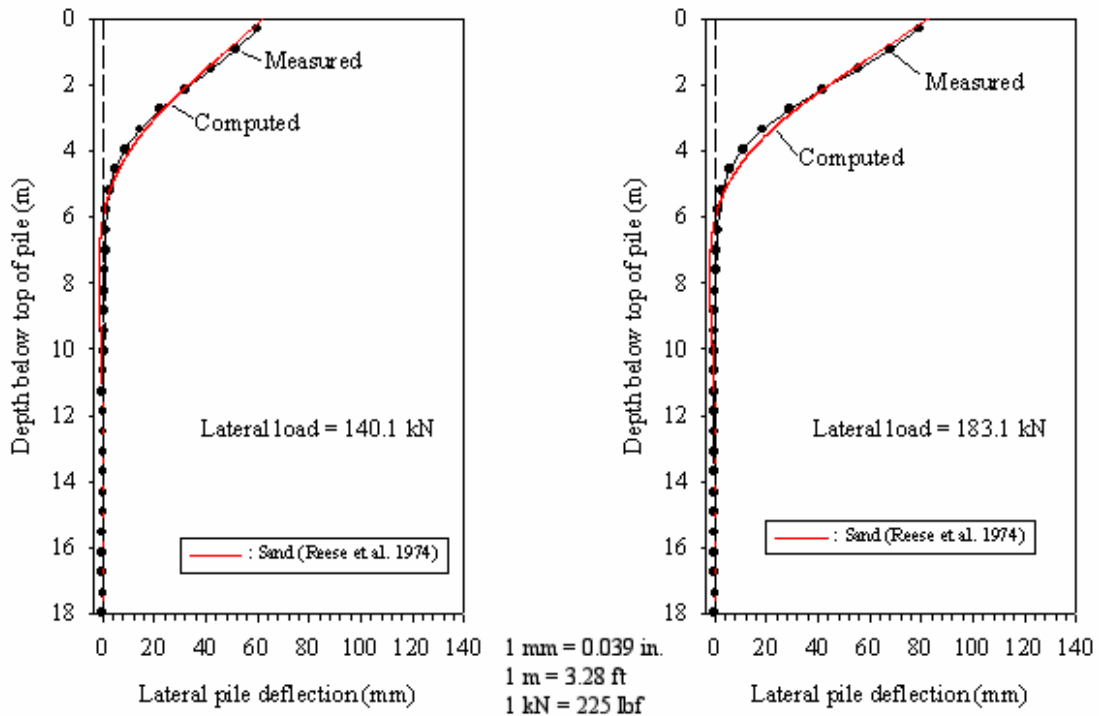


Figure 201. Graphs. Predicted versus measured lateral displacement profile for plastic pile (medium lateral loads).

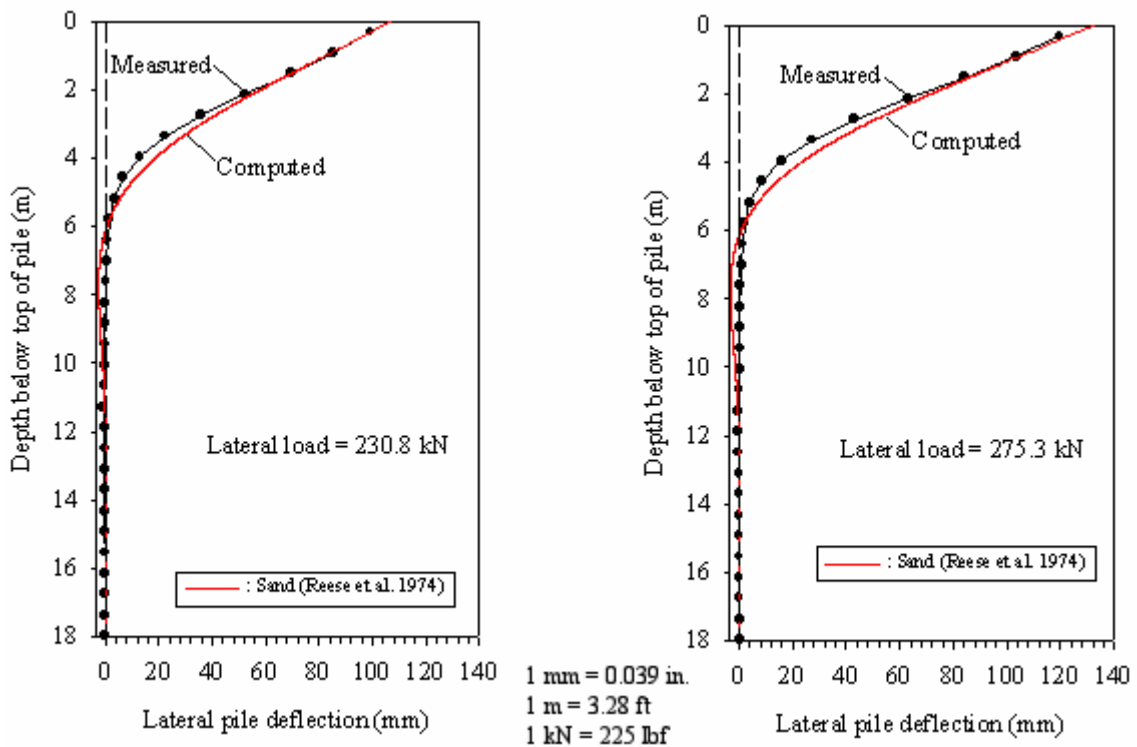


Figure 202. Graphs. Predicted versus measured lateral displacement profile for plastic pile (high lateral loads).

Figures 200–202 show that the pile deflections are predicted reasonably well using the p-y curves recommended by Reese, et al. (1974), for sands and the p-y modulus (E_{py-max}) values from figure 199. The level of agreement between the calculations and measurements was similar for the different load levels, suggesting that the Reese, et al., (1974) p-y curves adequately capture the response measured in the field.

Using the LPILE soil model described above, pile lateral deflections and head rotations at the ground surface were computed. The results are shown in figures 203 and 204.

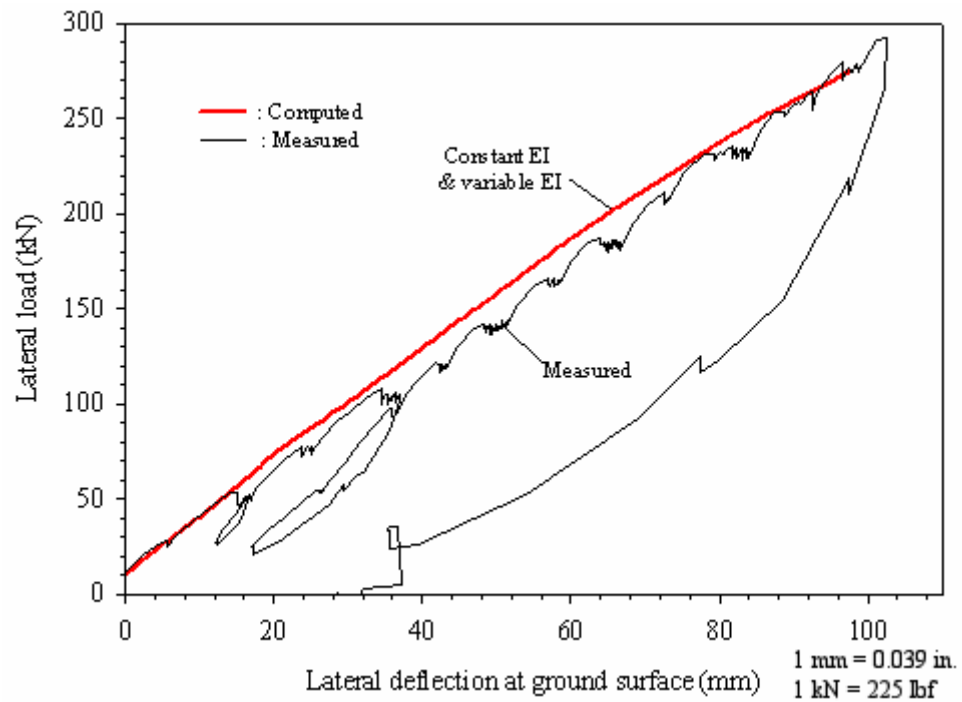


Figure 203. Graph. Calculated load-deflection curve for the plastic pile.

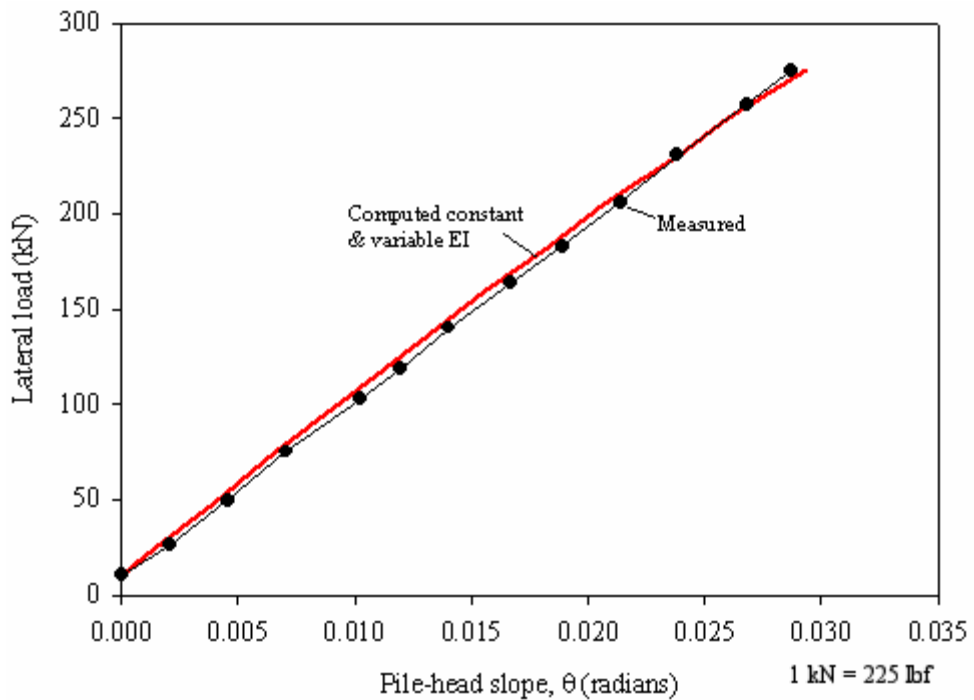


Figure 204. Graph. Calculated load-slope curve for the plastic pile.

The calculated values of lateral deflection and pile head rotation at the ground surface show good agreement with the field measurements. For this pile, the predicted values using variable and constant flexural stiffness of the pile are the same. This finding is reasonable because the flexural stiffness of the plastic pile is primarily the result of contributions from the steel rebar cage. Therefore, as shown in figure 113(b) (chapter 6), the flexural stiffness for this pile is approximately constant up to a moment of about 650 kN-m (479,421 lbf-ft). This moment was not exceeded during field load testing.

8.4.3 Comparison of the Initial p-y Modulus Curves for the Three Test Piles

The initial p-y modulus for the three test piles was assumed to increase linearly with depth. This assumption was considered reasonable for sand deposits such as those encountered at the test site. The rate of modulus increase with depth was selected to provide the best match between the analytical predictions and the field measurements. Using this approach, we obtained rates of modulus increase with depth of 1.7, 5.5, and 2.2 MN/m³ (10,831, 35,041, and 14,016 lbf/ft³) for the prestressed, FRP, and plastic piles, respectively. These variations are not in agreement with the trend expected based on the results of the axial load tests, for which the average unit shaft capacities were 61.8, 46.9, and 48.9 kPa (8.96, 6.80, and 7.09 (lbf/inch²)) for the prestressed concrete pile, the FRP pile, and the plastic pile, respectively.

The differences in the backcalculated rate of increase of the initial p-y modulus with depth can be due to several factors, such as:

- Differences in soil stratigraphy at the location of each test pile. For example, a thin clay layer was encountered at the southern end of the test pile area near the prestressed concrete test pile. This layer was found to extend about 0.9 m (2.9 ft) below the pit at the prestressed concrete pile location.
- Differences in pile properties such as cross-sectional shape, pile width, pile stiffness, surface roughness, and interface friction.

Although the methodology based on double derivation of the bending moment versus depth curves (Reese and Van Impe 2001) is more appropriate for detailed backcalculation of p-y curves, even this method would not have produced p-y curves in accordance with expectations based on the pile characteristics. It seems most likely that the differences in p-y curves are due largely to differences in subsurface conditions.

8.5 LIMITATIONS OF P-Y ANALYSES

The p-y method was selected to analyze the lateral load tests carried out at the Route 351 Bridge. This methodology was selected because it is commonly employed in practice. For this research project, it was desirable to verify whether established procedures, such as the p-y method, could be employed to analyze composite piles. Despite the popularity of this method, it has limitations as described below:

- The soil is idealized as a series of independent nonlinear springs represented by p-y curves. Therefore, the continuous nature of the soil is not explicitly modeled.
- The results are very sensitive to the p-y curves used. The selection of adequate p-y curves is the most crucial problem when using this methodology to analyze laterally loaded piles (Reese and Van Impe 2001).
- Selecting appropriate p-y modulus and p-y curves is a difficult task. While the selection of values of the initial p-y modulus (E_{py-max}) is related to the soil modulus, it is also related to the interaction between the pile and the soil. Reese and Van Impe (2001) point out that p-y curves and modulus are influenced by several pile-related factors, such as:
 - Pile type and flexural stiffness.
 - Type of loading (monotonic or cyclic).
 - Pile geometry.
 - Pile cap conditions.
 - Pile installation conditions.

8.6 SUMMARY

Numerous p-y analyses were carried out to determine the adequacy of this method to analyze laterally loaded composite pile types such as the ones studied in this research project.

A derivation of the governing differential equation for the laterally loaded pile problem was presented, and possible limitations in composite piles analysis were discussed.

The importance of considering shear deformations in lateral pile analyses was discussed. The impact of shear deformations increases with increasing E/G ratios, and decreases with increasing slenderness ratios (L/D). For the test piles assessed in this project, the error associated with neglecting shear deformations is estimated to be less than 2.5 percent.

The importance of including the nonlinearity of the flexural stiffness was discussed and illustrated with the analyses results.

The results of the p-y analyses using published p-y curves that are embedded in the LPILE 4.0M computer program showed reasonably good agreement with the field measurements.

The initial modulus of the p-y curves was found to increase with depth at the highest rate for the FRP pile, at an intermediate rate for the plastic pile, and at the lowest rate for the prestressed concrete pile.

CHAPTER 9. LONG-TERM MONITORING AT THE ROUTE 351 BRIDGE

9.1 INTRODUCTION

An important reason that composite piles have not gained wide acceptance in civil engineering practice is the lack of a long-term track record of performance. To help fill this void, a long-term monitoring program was implemented at the Route 351 Bridge project. The initial plan was to compare the performance of three adjacent bridge piers, each supported by different pile types. Coordination and logistical difficulties, however, prevented implementation of the initial plan. Consequently, the original long-term monitoring program was reduced to monitoring two instrumented piles installed at the center of two adjacent piers.

The instrumented production piles will be monitored for several years. This reduced program is not ideal, particularly because the bent where the FRP composite pile is located will have two types of piles, each with a different stiffness, and this may affect load distribution among the piles in the pier. In addition, the pile arrangements in the two piers are not the same. The pier with the FRP pile has five central piles installed vertically, and the two outer piles are installed with 4-to-1 batter in the direction perpendicular to the bridge axis. The pier with the instrumented prestressed concrete pile has three central piles installed vertically, and the two outer piles on each end of the pier are installed at 4-to-1 batter oriented in the direction of the bridge axis. Despite these shortcomings, this monitoring program is expected to provide some insight on the long-term durability and performance of the FRP composite pile. This chapter describes the instrumented production piles; the instrumentation used; the soil conditions at the locations of the instrumented piles; the installation information including driving records, PDA, CAPWAP, and PIT tests; and the monitoring data gathered to date.

9.2 INSTRUMENTED PRODUCTION PILES

Long-term instrumentation was installed in a Hardcore FRP composite pile and a prestressed concrete pile, and the piles were installed as the center piles of Piers 11 and 10, respectively. Figure 205 shows the locations of the instrumented production piles.

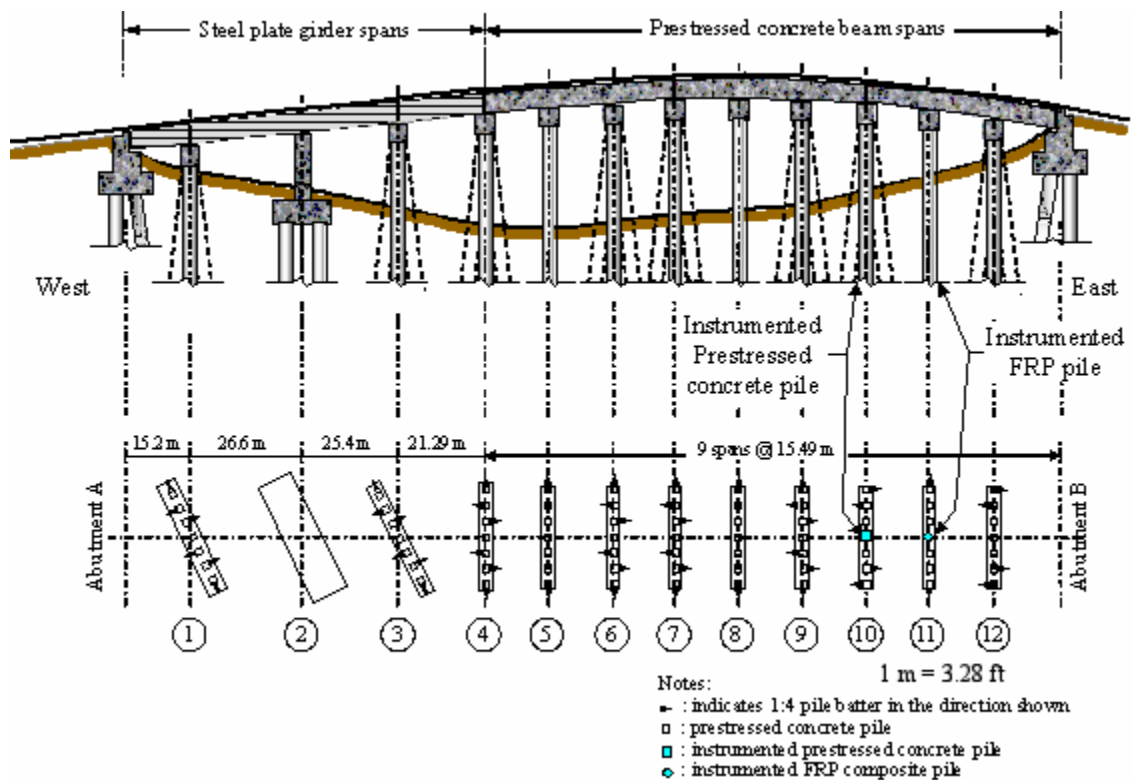


Figure 205. Illustration. Location of instrumented production piles at the Route 351 Bridge.

9.2.1 Prestressed Concrete Production Pile

The instrumented prestressed concrete production pile has characteristics similar to the test pile described in chapter 6. However, the production pile is longer, with a length of 22 m (72.2 ft). The 28-day strength of the concrete used in this pile is 61 MPa (8,845 lbf/inch²).

The prestressed concrete pile was instrumented with eighteen vibrating-wire sister bar strain gages located at seven levels, as shown in figure 206. These gages will be used to assess the load transfer from pile to soil.

As shown in figure 206, a pair of gages was located at each level to provide gages on opposite sides of the pile. Two extra gages were installed at the uppermost and lowermost levels for redundancy. The gages are Geokon Model 4911 rebar strain meter gages. These gages consist of two lengths of No. 12M, grade 420 steel bar (No. 4 steel bar, grade 60) welded onto each end of a miniature vibrating-wire strain gage element. The entire assemblage is 1.3 m (4.3 ft) long. The instrumentation for the prestressed concrete production pile was installed on November 6, 2001. The pile was cast on November 7, 2001. The vibrating-wire sister bar strain gage survival rate, after pile manufacturing, driving, and restrike, was 100 percent.

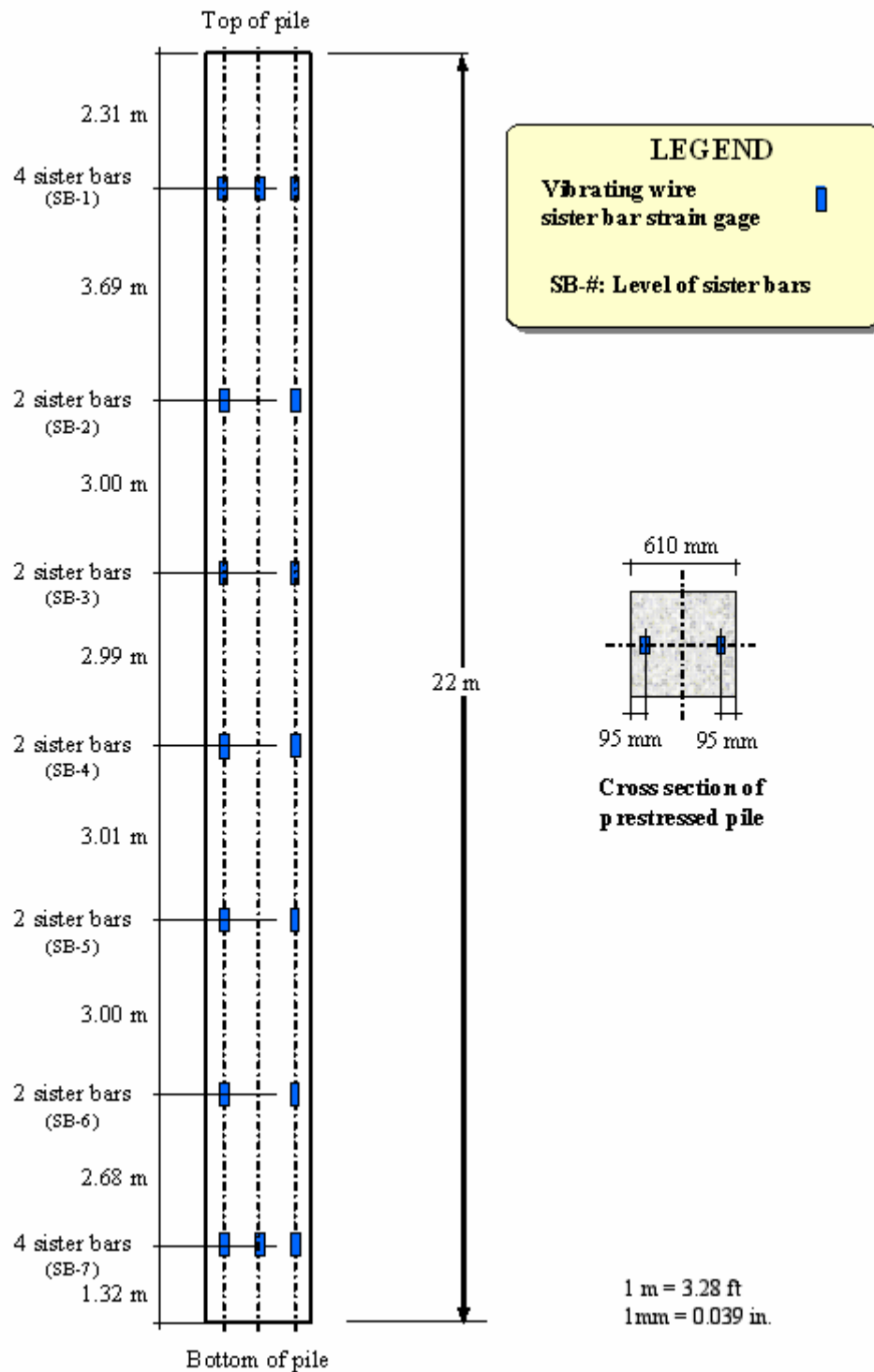


Figure 206. Illustration. Load transfer instrumentation layout for prestressed concrete production pile.

9.2.2 FRP Composite Production Pile

The instrumented FRP composite production pile has the same characteristics as the FRP composite test pile described in chapter 6, but the length of this pile is 21.2 m (69.6 ft). Similar to the prestressed concrete pile, the FRP composite production pile was instrumented with 18 vibrating-wire sister bar strain gages located at 7 levels, as shown in figure 207. These gages will be used to assess the load transfer from pile to soil.

The FRP pile was also instrumented with gages installed to study the performance and durability of the FRP tube. The following durability instrumentation was installed to monitor strains in the FRP tube:

- Two foil gages at each of six levels, labeled IG-1 through IG-6, as shown in figure 207, for a total of twelve gages bonded to the internal wall of the FRP tube. The foil gages are type CEA-13-500UW-350, temperature compensating, underwater, resistance strain gages. The gages are configured in a one-quarter active bridge. A coating system was used to cover these gages and protect them from possible moisture and chemical attack during filling of the tubes with concrete. The protective coating consisted of a Teflon film, overlain by a layer of polymer compound, overlain by aluminum foil, overlain by another layer of polymer compound, overlain by aluminum foil, with the edges sealed with a rubber coating.
- Four vibrating-wire strain gages were installed on the outside surface of the FRP pile at the locations shown in figure 208. These gages are Geokon Model VK4100 vibrating-wire strain gages. These gages have a 50 mm- (2 inch-) gage length. The gages were installed by epoxy bonding their mounting tabs to the pile exterior. In addition to providing strain data, these gages can measure temperature since they come with a thermistor incorporated.

The vibrating-wire sister bars and the internal foil resistance strain gages for the FRP composite production pile were installed between January 24 and February 1, 2002. The concrete was poured for this pile on February 6, 2002. The vibrating-wire sister bar strain gage survival rate, after pile manufacturing, driving, and restrrike, was 100 percent. The survival rate of the internal foil gages was 30 percent. The majority of the internal foil gages started to drift after the concrete was poured. This could be due to moisture from the concrete. The external vibrating-wire strain gages were installed after pile installation on November 7, 2002. As of December 30, 2002, all external gages were functioning.

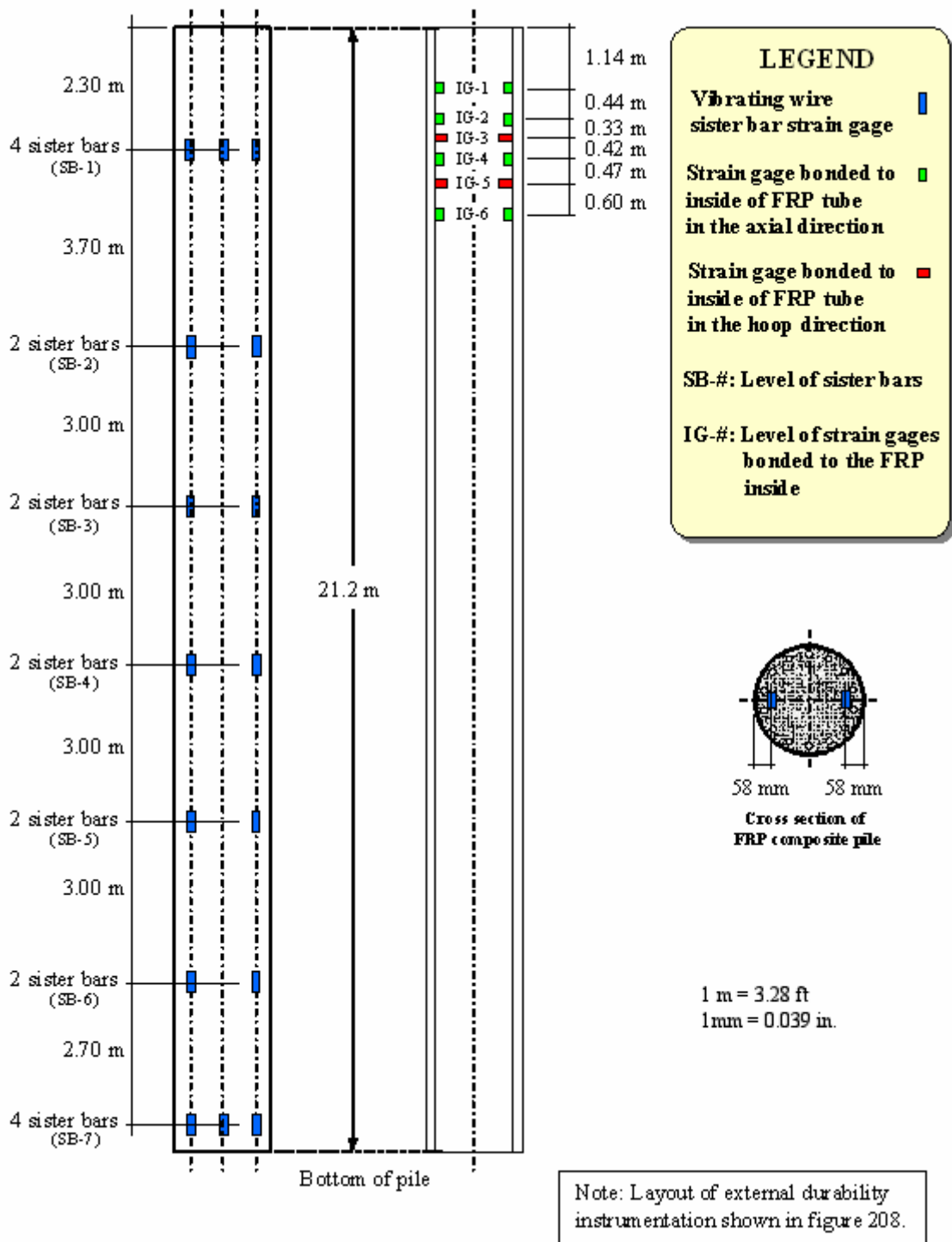


Figure 207. Illustration. Instrumentation layout for FRP composite production pile.

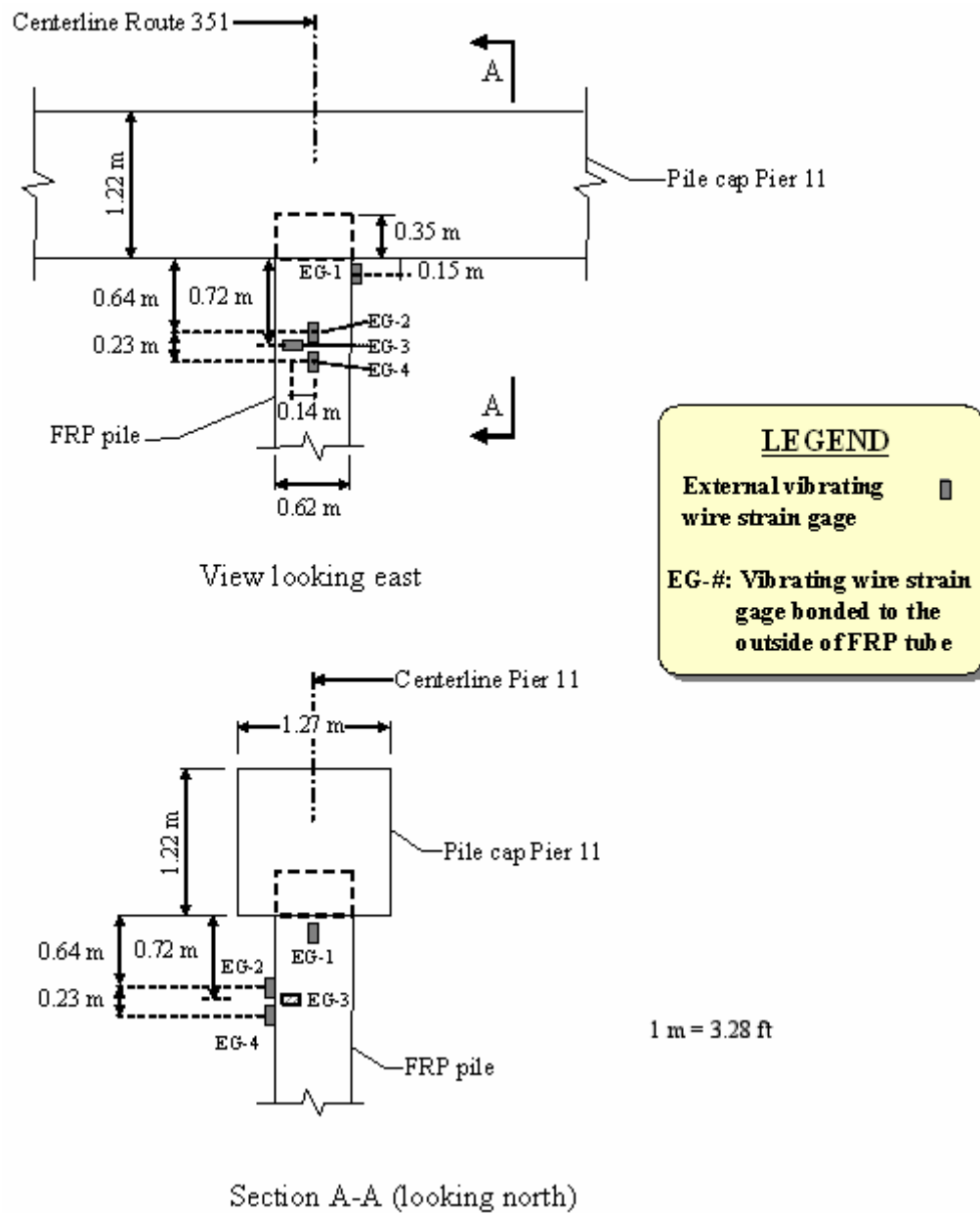


Figure 208. Illustration. Layout of external durability instrumentation used in the FRP composite production pile.

9.3 SOIL CONDITIONS AT THE INSTRUMENTED PRODUCTION PILES

VDOT investigated the soil conditions along the bridge alignment. The general soil stratigraphy found along the Route 351 Bridge alignment is shown in figure 209. The uppermost layer of river sediments consists of very soft to soft silty clay of varying thicknesses. The soft river sediments are underlain by loose to medium-dense, silty fine sand extending to variable depths depending on the location along the alignment. In general, the silty fine sand was found to increase in density with increasing depth, becoming dense to very dense at a depth of about 30 m (98.4 ft).

The specific soil conditions found at Piers 10 and 11 are shown in figures 210 and 211, respectively. As shown, a sandy, silty, clay interbed was found at Piers 10 and 11, between elevations -18.7 and -20 m (61.3 and 65.6 ft), and -11.6 to -20 m (38.0 and 65.6 ft), respectively. For reference, the elevations of the installed piles are also shown in these figures.

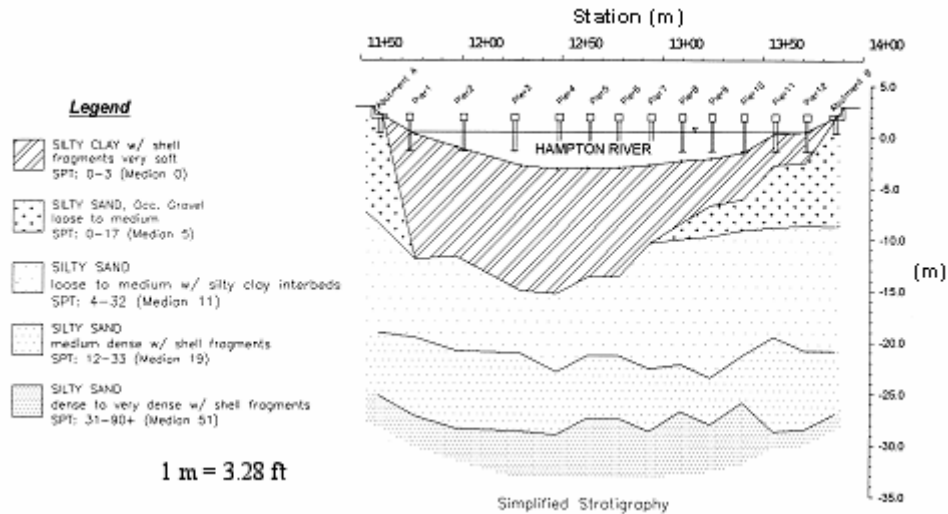


Figure 209. Graph. Simplified stratigraphy along the Route 351 Bridge alignment.

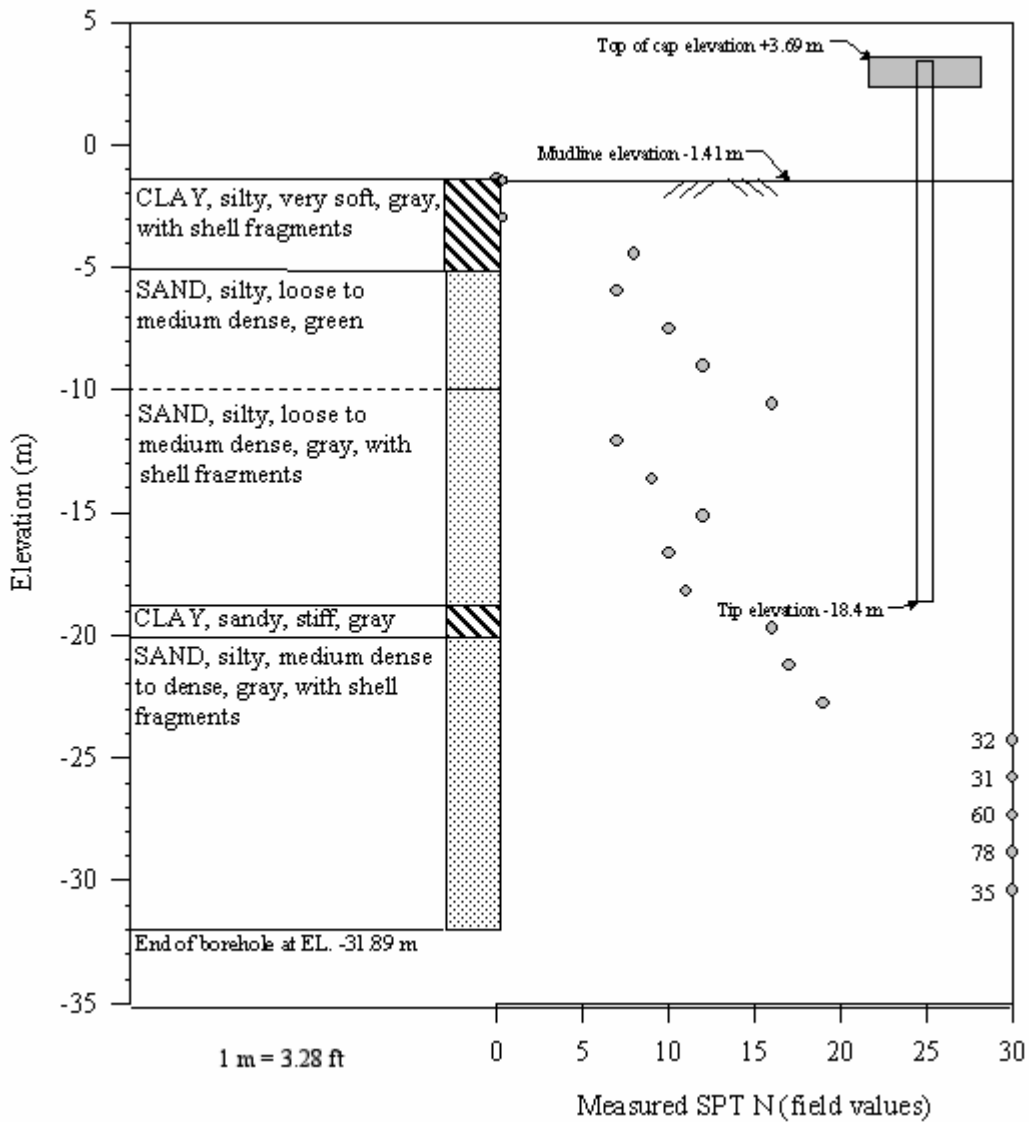


Figure 210. Graph. Simplified stratigraphy in the vicinity of the instrumented prestressed concrete pile installed at Pier 10.

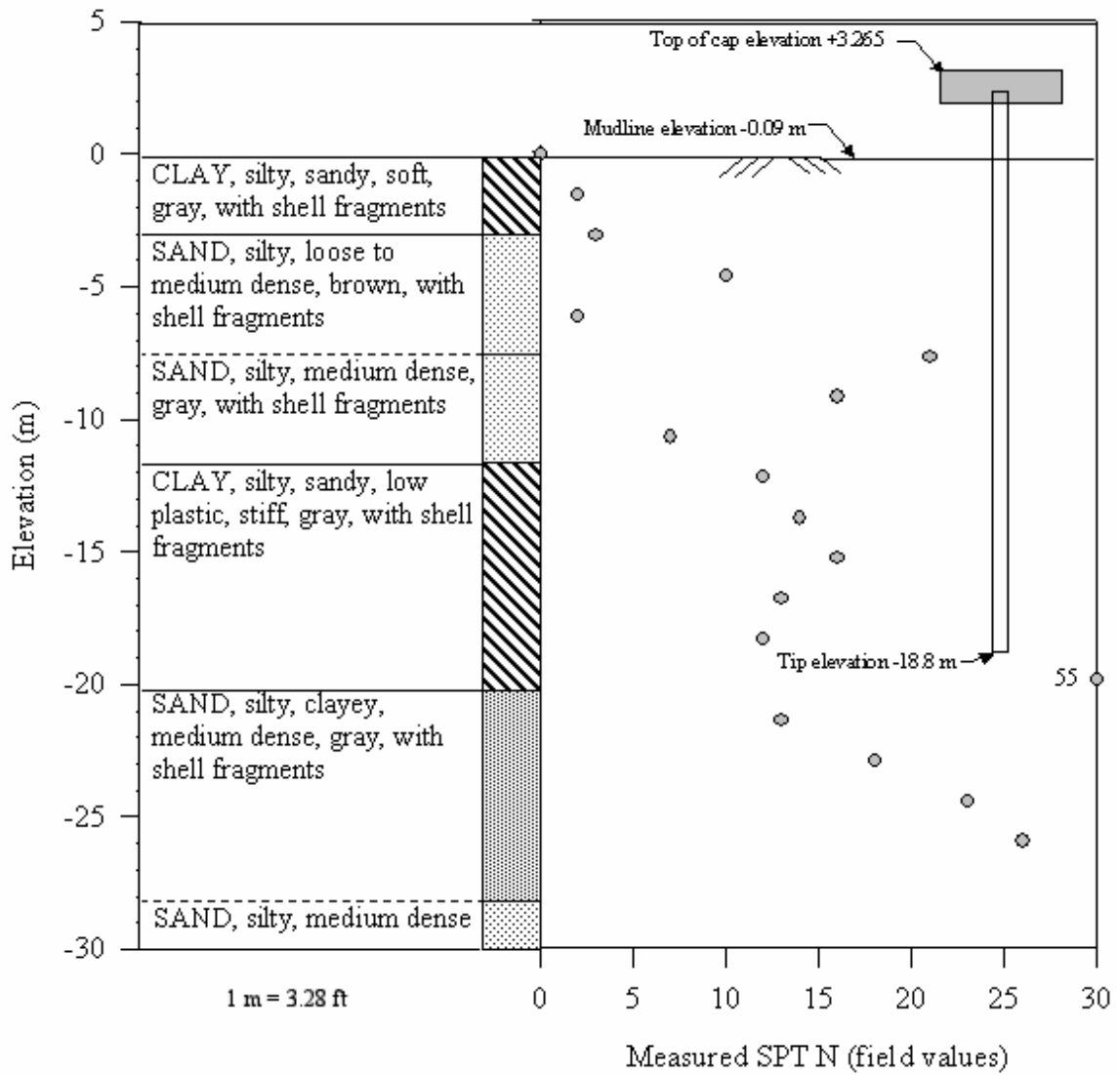


Figure 211. Graph. Simplified stratigraphy in the vicinity of the instrumented FRP composite pile installed at Pier 11.

9.4 PILE INSTALLATION AND DYNAMIC TESTING

9.4.1 Pile Driving

The instrumented production piles were driven with an ICE model 80S single-acting diesel hammer. The maximum rated energy of the hammer is 108.6 kN-m (80,000 ft-lbs). Both instrumented production piles were driven with 230 mm- (9 inch-) thick plywood pile cushions. The pile-driving records are shown in figure 212. The prestressed concrete pile and FRP pile were driven on June 13 and June 14, 2002, respectively.

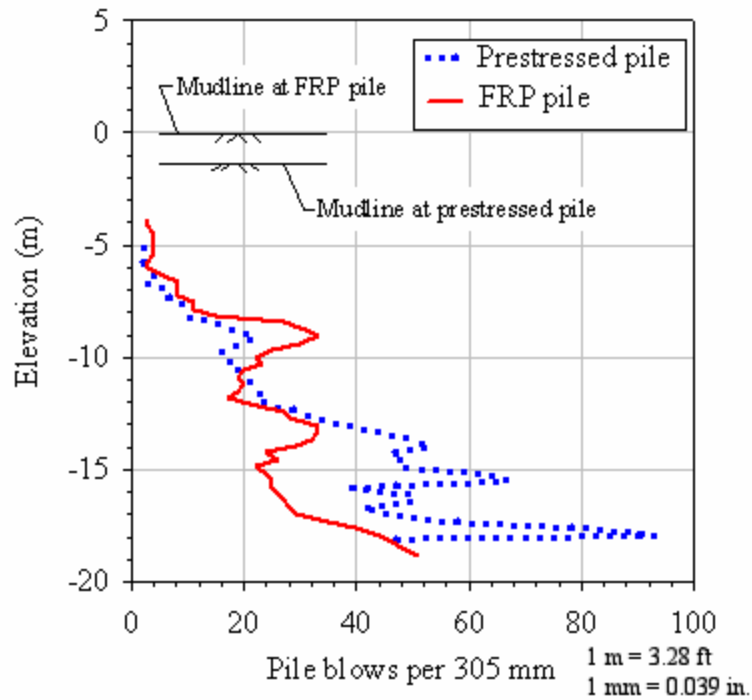
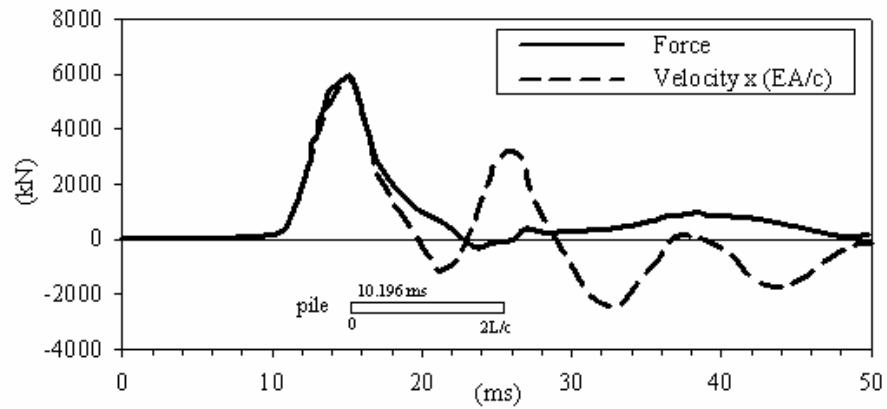


Figure 212. Graph. Driving records for instrumented production piles.

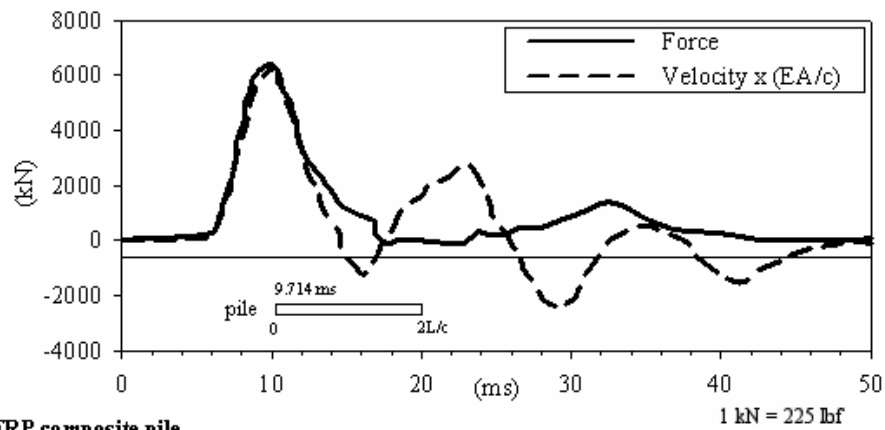
9.4.2 Dynamic Testing

Dynamic monitoring was performed using a Pile Driving Analyzer (PDA). The PDA monitoring and data processing were performed by an FHWA contractor. Monitoring was performed during both the initial driving and during restrike. Restrike occurred on June 18, 2002, which represents a setup period of 4 and 5 days after initial driving for the FRP composite pile and prestressed concrete pile, respectively. PDA records for the two instrumented production piles at restrike are shown in figure 213. The PDA records show a force peak at about time 0, measured with respect to the horizontal bars in figure 213 that represent the wave travel time for two pile lengths for each pile. The prestressed concrete and FRP composite piles show similar dynamic behavior. Both piles show a large increase in the velocity record and corresponding low force at about $2L/c$ (where L is pile length, and c is wave speed). This type of PDA record shape is characteristic of piles with a small toe resistance. Very little separation between the force and velocity traces appears between time 0 and about $0.5L/c$. This corresponds to the zone of zero to minimal shaft resistance; that is, the portion of the pile above the ground surface and the portion through the very soft river sediments where shaft resistance is small.

Table 47 provides some of the measurements obtained during pile driving. It can be seen that the wave speed (c) and impedance values (EA/c) recorded in the FRP composite pile were about 5.3 percent and 6.1 percent lower, respectively, than the prestressed pile. The maximum compressive and tensile stresses in the prestressed concrete pile were lower than the allowable stresses recommended for prestressed piles (Hannigan, et al., 1996). The highest driving stresses were recorded in the FRP composite pile; however, no standards are currently available for allowable driving stresses of FRP composite piles.



(a) Prestressed concrete pile



(b) FRP composite pile

Figure 213. Graph. PDA recordings during restrike (Spiro and Pais 2002b).

Table 47. Summary of pile-driving measurements for the prestressed and FRP production piles (after Spiro and Pais 2002b).

Measurement	Pile Type	
	Prestressed	FRP
Wave speed (c)	4054 m/s	3840 m/s
Impedance (EA/c)	3589 kN/m/s	3370 kN/m/s
Maximum compression stress measured during driving	11.7 MPa	13 MPa
Maximum tensile stress measured during driving	7 MPa	8.8 MPa
Allowable stresses	Comp. < 24.3 MPa Tension < 7 MPa	No standards available

1 m = 3.28 ft
 1 kN/m = 68.6 lbf/ft
 1 MPa = 145 lbf/inch²

Estimates of pile capacity from the dynamic strain and acceleration measurements were obtained using the Case method and CAPWAP analyses (Spiro and Pais 2002b). Both the Case method and CAPWAP capacities are listed in table 48. The FRP composite production pile showed an increase in the Case method capacity of about 125 percent between the end of initial driving and restrike 4 days later. According to the CAPWAP analyses, the prestressed concrete and FRP composite piles have capacities of 1,980 and 2,046 kN (445 and 460 kips), respectively. These CAPWAP capacities are over two times larger than the axial design load of 890 kN (200 kips) for the piles in the piers. The CAPWAP analyses also indicate that the shaft capacities, as percentages of the total capacities, are 82 percent and 71 percent for the prestressed concrete and FRP piles, respectively. These high shaft capacity percentage values agree with the observations made earlier regarding the shape of the PDA records being characteristic of piles with low toe resistance.

Table 48. Summary of CASE and CAPWAP analyses results (Spiro and Pais 2002b).

Method	Capacity Component	Prestressed Concrete Pile	FRP Pile
Case ⁽¹⁾ (End-of-Driving)	Total	Not available ⁽²⁾	890 kN
Case ⁽¹⁾ (Restrike ⁽³⁾)	Total	2091 kN	2002 kN
CAPWAP (Restrike ⁽³⁾)	Shaft	1624 kN	1459 kN
	Toe	356 kN	587 kN
	Total	1980 kN	2046 kN

Notes: (1) Case method using a Case damping coefficient of 0.60. 1 kN = 225 lbf, or 0.225 kip
 (2) Not available due to signal acquisition problems.
 (3) Restrike of piles performed 4 and 5 days after initial driving, for the FRP and prestressed concrete piles.

9.5 PILE INTEGRITY TESTING OF TEST PILES

Pile integrity tests (PIT) were performed on the instrumented production piles before and after pile installation. These tests were carried out using the same procedure used for the test piles described in chapter 6.

PIT results for the prestressed concrete production pile installed at Pier 10, performed before and after pile driving, are shown in figures 214 and 215, respectively. No discernable damage was noted based on comparison of the pre- and postdriving PIT soundings. The soil resistance in the pile after installation results in a smaller toe reflection, as shown in figure 215.

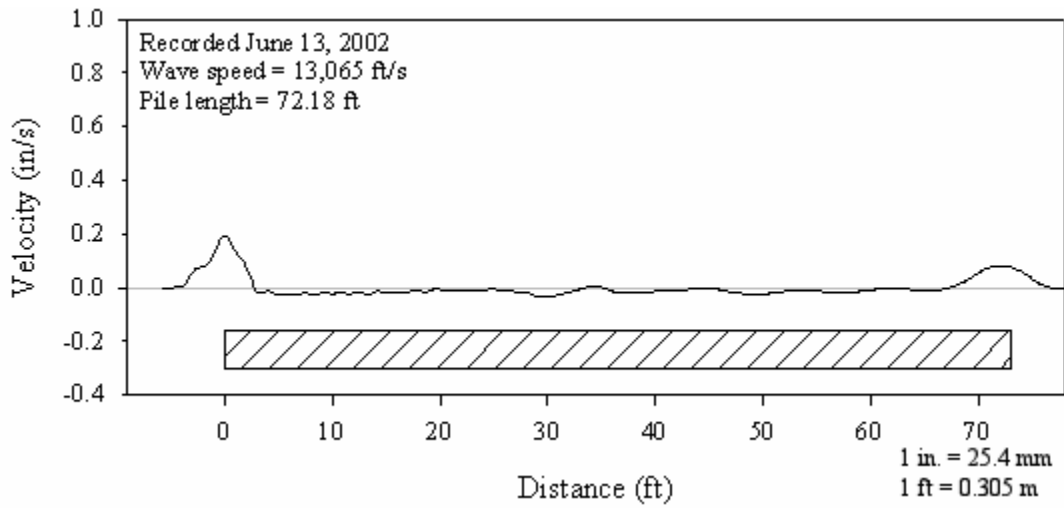


Figure 214. Graph. PIT sounding on the prestressed concrete production pile before installation.

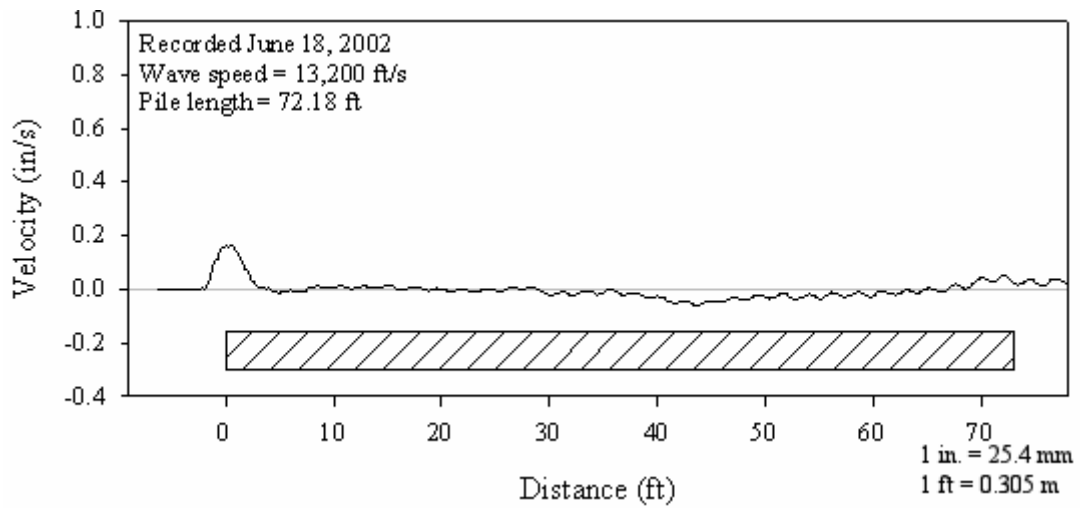


Figure 215. Graph. PIT sounding on the prestressed concrete production pile after installation and restrike.

PIT results for the FRP composite pile installed at Pier 11 are shown in figures 216 and 217. No significant difference between the pre- and postdrive PIT traces was observed for the FRP pile. Toe reflection in the postdrive PIT is almost not discernible, probably due to high soil resistance. No discernable damage could be detected based on comparison of the pre- and postdriving PIT soundings.

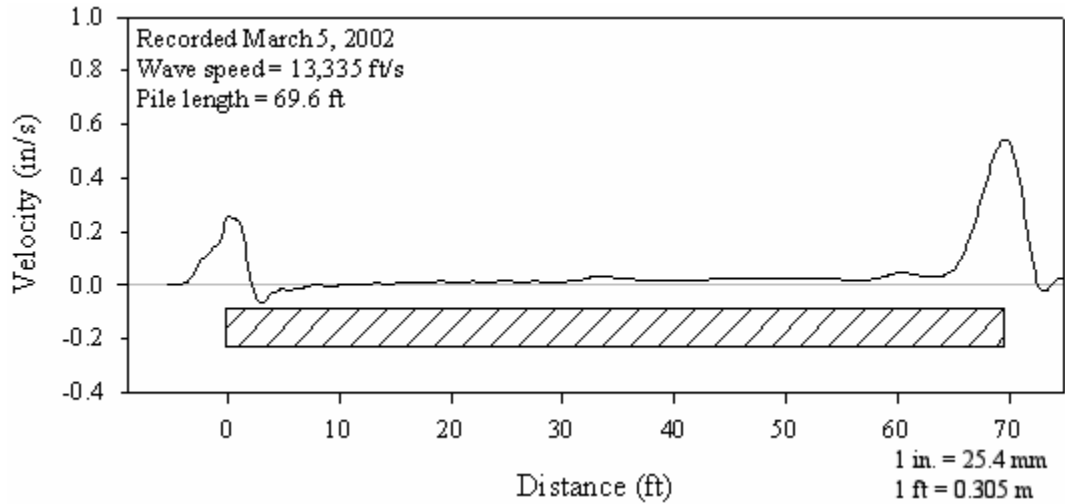


Figure 216. Graph. PIT sounding on the FRP composite production pile before installation.

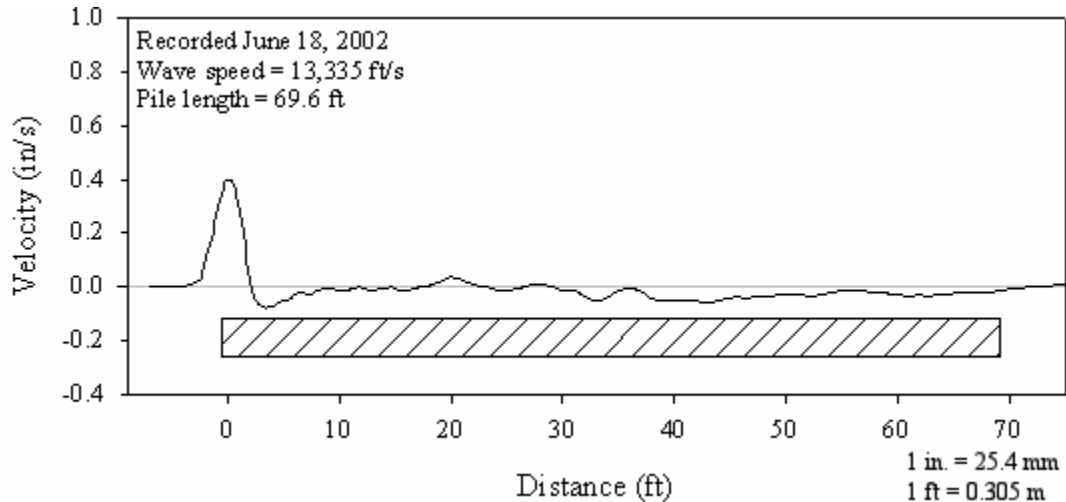


Figure 217. Graph. PIT sounding on the FRP composite production pile before installation.

9.6 MONITORING DATA GATHERED TO DATE

Important date information for these two piles is summarized in table 49.

Table 49. Test dates for the instrumented production pile program at the Route 351 Bridge.

Pile Type	Cross Section	Length (m)	Fabrication Date	Driving Date	Restrike Date
Prestressed concrete	610 mm square	22	11/7/01	6/13/02	6/18/02
FRP	622 mm circular	21.2	2/6/02	6/14/02	6/18/02

1 mm = 0.039 inch
1 m = 3.28 ft

Due to delays in the construction schedule of the bridge, only a few readings have been made on the instrumented production piles. The instrumentation for the prestressed and FRP composite piles have been read on the dates shown in tables 50 and 51, respectively. On December 30, 2002, the estimated loads acting on the prestressed concrete and FRP composite piles were 24.1 percent and 30.9 percent of the axial design load, respectively.

Table 50. Monitoring dates for prestressed concrete pile at the Route 351 Bridge.

Date	Description of Pile Loading Condition	Estimated Load on Pile
6/18/02	After pile installation and restrike	0 kN
11/7/02	Pile cap and girders from east span installed	110 kN
12/30/02	Pile cap and girders from adjacent spans installed. Deck slab for east span in place	227 kN

1 kN = 225 lbf

Table 51. Monitoring dates for FRP composite pile at the Route 351 Bridge.

Date	Description of Pile Loading Condition	Estimated Load on Pile
6/18/02	After pile installation and restrike	0 kN
11/7/02	Pile cap and girders from east and west spans installed	155 kN
12/30/02	Pile cap, girders, and deck slab from adjacent spans in place	290 kN

1 kN = 225 lbf

The loads acting on each pile were estimated based on the information reported in the bridge design drawings. The weight of the pile cap is based on unit weight for the reinforced concrete of 23.6 kN/m^3 (150 lbf/ft^3) and the pile cap dimensions of 1.22 by

1.27 by 12.5 m (4.00 by 4.17 by 41.0 ft). The load from the AASHTO Type II girders (7 girders per each span) is calculated based on a span length of 15.5 m (50.8 ft) and a girder weight per unit length of about 5.6 kN/m (384 lbf/ft) (Nilson 1987). The load due to the reinforced concrete bridge deck is based on a slab thickness of 0.2 m (0.656 ft) and a deck width of 12.8 m (42.0 ft). As a first approximation, the loads acting on the pile were estimated by dividing the total pier load by the number of piles in the pier.

A photo of the bridge taken on December 30, 2002, is shown in figure 218. This photo shows that Piers 7 through 12 have been installed and the bridge deck has been poured up to Pier 10. The photo also shows the formwork for the deck between Piers 9 and 10.

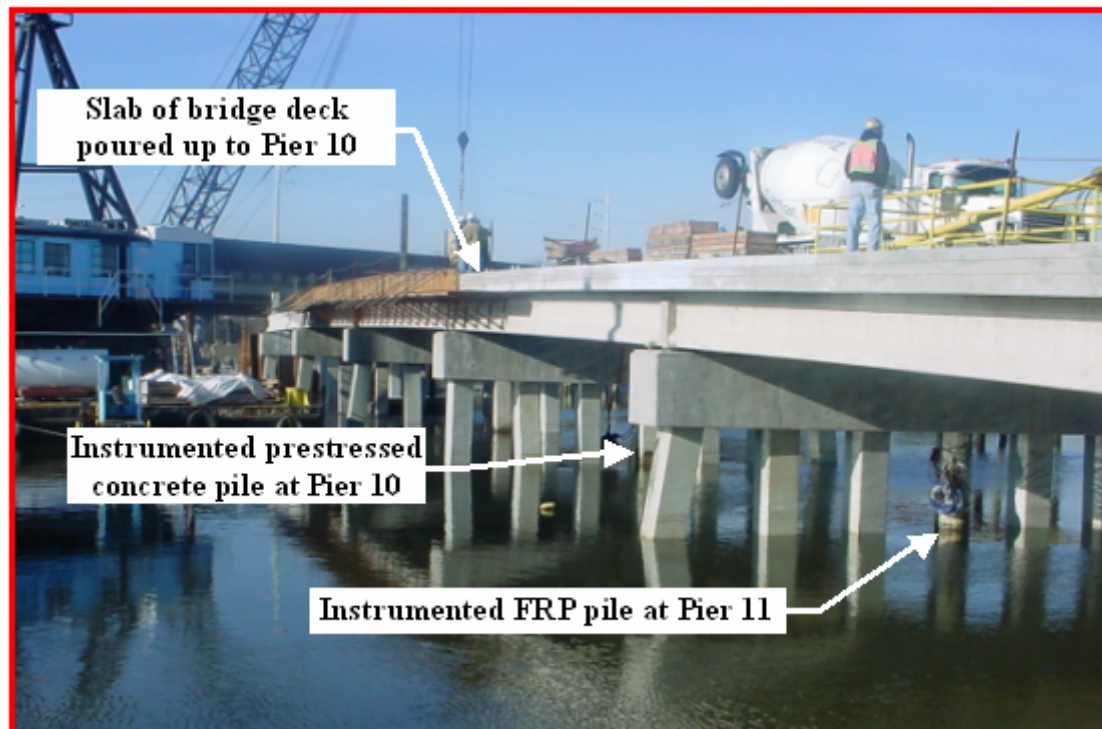


Figure 218. Photo. Route 351 Bridge under construction on December 30, 2002.

The load distributions estimated for the prestressed concrete and FRP composite piles are shown in figures 219 and 220, respectively. These load distributions were estimated by multiplying the average strain at each level of vibrating-wire sister bars by the values of axial stiffness (EA) of each pile (as reported in chapter 6). The load distributions were calculated considering the residual stresses after driving using the procedure described by Fellenius (2002).

Long-term monitoring and data collection responsibility are being transferred to VDOT and the Virginia Transportation Research Council (VTRC).

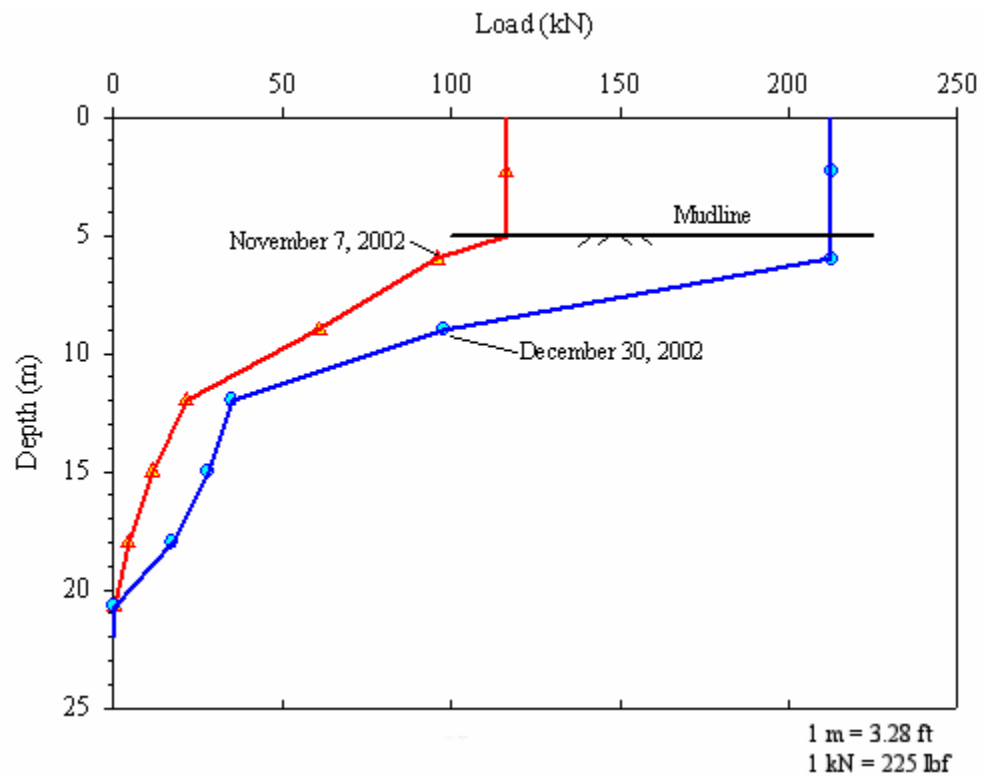


Figure 219. Graph. Load distributions on November 7, 2002, and December 30, 2002, for the prestressed concrete production pile at Pier 10.

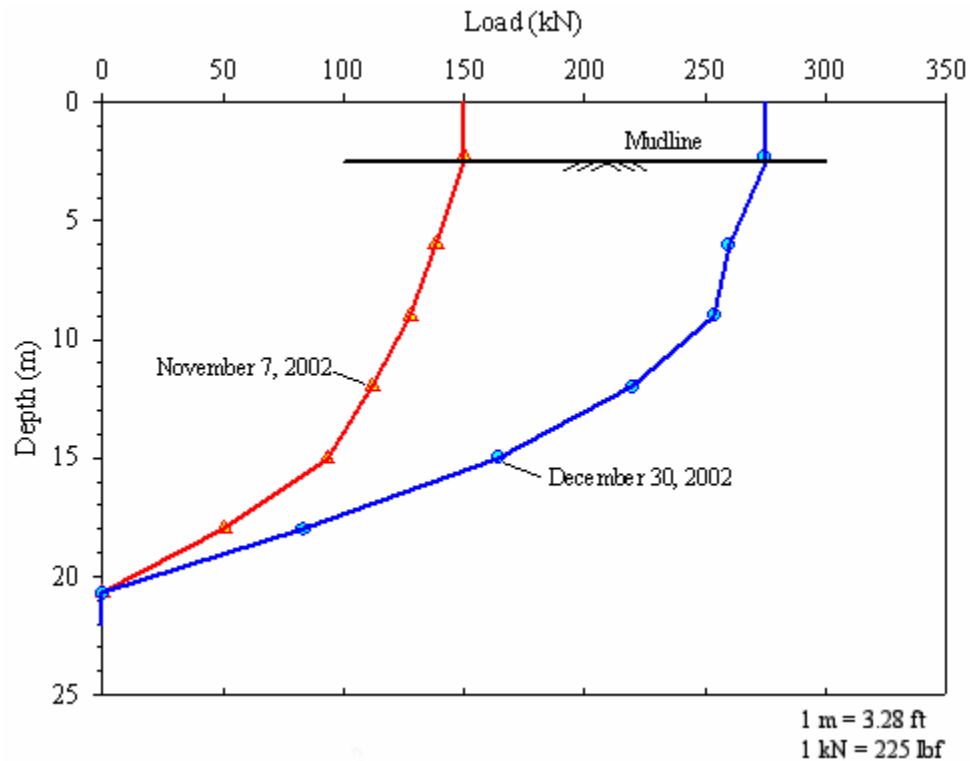


Figure 220. Graph. Load distributions on November 7, 2002, and December 30, 2002, for the FRP composite production pile at Pier 11.

9.7 SUMMARY

A monitoring program has been implemented at the Route 351 Bridge project to compare the long-term performance, load-transfer, and durability characteristics of an FRP composite pile and a standard prestressed concrete pile. The two production piles selected for monitoring were installed at the centers of Piers 10 and 11. The piles consist of (1) a conventional, 610-mm (23.8-inch) square, prestressed concrete pile installed at Pier 10, and (2) a 622-mm (24.3-inch) diameter composite pile formed of an FRP shell and filled with concrete and steel reinforcing bars installed at Pier 11. The instrumented production piles are about 22 m (72 ft) long.

Load-transfer instrumentation, consisting of 18 vibrating-wire sister bars, was installed at 7 levels in both piles. Durability instrumentation, consisting of resistance foil gages and vibrating-wire gages, was installed on the FRP composite pile to monitor the inside and outside of the FRP tube, respectively.

The soils at the production pile locations were investigated by VDOT, and consisted of very soft to soft silty clay underlain by loose to medium-dense silty sand. A sandy, silty, clay interbed was found at Pier 10 between elevations -18.7 and -20 m (61.3 and 65.6 ft), and at Pier 11 between elevations -11.6 to -20 m (38.0 and 65.6 ft).

The field testing of the instrumented production piles included PDA, CAPWAP, and PIT tests. The following conclusions can be drawn from this test program.

1. The FRP composite pile and prestressed concrete pile performed similarly during pile driving, as demonstrated by the driving records, PDA traces, measured wave speed generated by the driving hammer, and measured compressive and tensile stresses.
2. Using the Case method, instrumented production piles showed similar estimated pile capacities on pile restrike blows.
3. CAPWAP analyses at pile restrike showed similar estimated pile capacities and high shaft capacity components. The shaft capacities were estimated as being 82 percent and 71 percent of the total capacity for the prestressed concrete and FRP composite piles, respectively. Based on the CAPWAP analyses, the pile capacities were estimated to be more than twice the axial design load (890 kN (200,250 lbf)) of the pier piles.
4. No discernable damage was detected in the piles after installation, based on PIT testing performed on the piles before and after pile driving.
5. Monitoring data of the piles is limited to date. On December 30, 2002, the loads acting on the piles were estimated as 215 and 275 kN (48,375 and 61,875 lbf) for the prestressed concrete pile and FRP composite pile, respectively.

Durability instrumentation was installed on the FRP composite pile to monitor the inside and outside strains of the FRP tube. The durability instrumentation had to be installed after the construction activities near Pier 11 were completed. In addition to providing the strain data for the FRP shells, the durability strain gages will also provide records of temperature because vibrating-wire strain gages incorporate thermocouples to provide information necessary for reducing the strain gage data. The strain and temperature data will be used to interpret the performance of the FRP shells, as follows: knowledge of the exposure time and temperature can be used to estimate the FRP properties of modulus and strength from the laboratory durability study described in chapter 4; knowledge of the strain in the production piles can be combined with the modulus to give the stress in the FRP shell; and comparing the stress with the strength of the FRP shell indicates how close the shell is to failure.

CHAPTER 10. COST INFORMATION FOR COMPOSITE PILES

10.1 INTRODUCTION

Composite materials have attractive features such as high resistance to corrosion, high strength-to-weight ratios, and the ability to be used in infrastructure projects with little or no maintenance requirements (Meiarashi, et al., 2002). Recent studies have found that the lower weight of bridge decks made of FRP composite materials results in greater cost effectiveness due to shorter construction time and decreased cost of the bridge superstructure (Ehlen 1999). The economical competitiveness of composite piles needs to be assessed. To help provide data for such assessments, this chapter provides cost information for the composite piles and prestressed concrete piles used in this research project.

10.2 COST INFORMATION FOR THE ROUTE 40 BRIDGE PROJECT

The cost per unit length of the concrete-filled FRP composite piles used at the Route 40 Bridge project was \$312/m (\$95/ft). This unit cost includes the materials (GFRP tube and concrete infill), the manufacturing costs (including FRP tube and concrete casting), and shipping to the job site. The cost of driving the composite piles was \$66/m (\$20/ft). This results in a total cost of \$378/m (\$115/ft) for the installed composite pile. On the other hand, the total cost of the installed 508-mm (20-inch) square prestressed concrete pile was \$213/m (\$65/ft). Therefore, the initial cost comparison indicates about 77 percent higher unit cost for the composite pile. No instrumentation was installed in these piles.

No significant time differences were observed in the installation time required for these two types of piles. The unit weights of the two piles were similar due to the concrete infill; therefore, the high strength-to-weight ratio of the composite material was not utilized. The composite piles were not easy to lift or handle, and required special arrangements and equipment. For example, the slickness of the FRP pile's outer surface made it difficult to use conventional slings to lift the piles with the crane. In addition, the number of pick-up points had to be increased due to the lower cracking moment of these piles compared to the prestressed concrete pile. The difficulties encountered by the contractor in handling these piles also may have been associated with lack of experience in dealing with these piles. However, such problems are expected to occur in other projects until the use of composite piles becomes more common.

10.3 COST INFORMATION FOR THE ROUTE 351 BRIDGE PROJECT

The cost information for the three types of piles tested at the Route 351 Bridge project is provided below. These test piles were heavily instrumented, and the costs provided below do not include the instrumentation or its installation. However, pile fabrication and handling costs may have been increased due to the presence of the instrumentation.

10.3.1 Hardcore FRP Composite Pile

The cost for the 24-inch FRP tubes was \$165/m (\$50/ft). This cost is freight-on-board (FOB) at the Hardcore plant in New Castle, DE. The cost associated with steel reinforcement, concrete infill, and transportation was about \$541/m (\$165/ft). The resulting total unit cost for the pile delivered on site is \$705/m (\$215/ft). The cost of installation of the test piles at this project was about \$82/m (\$25/ft). Therefore, the initial cost of the installed FRP composite pile is \$787/m (\$240/ft).

10.3.2 Plastic Pile

The ordinary unit cost for this type of pile FOB at the Plastic Piling, Inc., (PPI) plant in Rialto, CA is \$410/m (\$125/ft). The cost for shipment of this test pile from Rialto, CA, to Hampton, VA, was \$209/m (\$64/ft). The resulting total unit cost for the pile delivered on site was \$619/m (\$189/ft). The cost of installation for the test piles at this project was about \$82/m (\$25/ft). Therefore, the initial cost of the installed PPI composite pile was \$701/m (\$214/ft).

10.3.3 Prestressed Concrete Pile

The total cost of the installed 610-mm (24-inch) square prestressed concrete pile was about \$180/m (\$55/ft).

10.3.4 Summary of the Route 351 Bridge Cost Information

The initial cost information given above indicates that the unit costs for the PPI plastic composite pile and the Hardcore composite pile are 289 percent and 337 percent higher than for the prestressed concrete pile, respectively.

No significant installation time differences were observed during handling and installation of the composite piles compared to the prestressed concrete pile. The handling and lifting of the FRP composite piles was the most difficult due to the slickness of the outer surface of the FRP shell. Special arrangements were required to handle this pile, including using steel anchors to keep the lifting slings from sliding and rolling. The location and number of pickup points for handling this pile had to be modified with respect to conventional practice due to the lower cracking moment of these piles compared to the prestressed concrete piles. These kinds of complications were not encountered during the handling and installation of the plastic composite pile.

10.4 SUMMARY

The initial costs of the composite piles studied in this project were higher than the initial unit costs for prestressed concrete piles. The initial unit costs of the installed composite piles at the Route 40 Bridge were about 77 percent higher than the unit costs for the prestressed concrete piles. The initial unit costs for the composite piles installed at the

Route 351 Bridge were higher than the cost of the prestressed concrete piles by about 289 percent and 337 percent for the plastic and FRP piles, respectively.

The cost effectiveness of the composite piles is expected to improve with economies of scale as production volume increases. The low maintenance requirements of these composite piles also increase their cost effectiveness. Life cycle cost analyses should consider the pile lifespan, the annualized maintenance costs, and the replacement costs of composite piles compared to prestressed concrete piles. The number of years of use that should be factored into the life cycle cost analyses may not be related only to the lifespan of the piles, but may also be governed by the actual lifespan of the bridge superstructure, which may be related to deterioration or increased traffic demands. A life cycle cost analysis was not performed for this study due to lack of maintenance cost and frequency information.

CHAPTER 11. SUMMARY AND CONCLUSIONS

11.1 INTRODUCTION

This study investigated the potential use of composite piles for load-bearing applications, specifically bridge substructures. The term “composite piles” refers to alternative pile foundations composed of FRPs, recycled plastics, or hybrid materials that are placed in the ground to support axial and/or lateral loads. Conventional piles are made of steel, concrete, and timber; these materials have limited service life and high maintenance costs when used in harsh marine environments (Lampo, et al., 1998). Degradation problems of conventional piles include chloride attack on concrete, steel corrosion, and marine borer attack on timber piles. It has been estimated that repair and replacement of piling systems costs the United States more than \$1 billion annually (Lampo, et al., 1997). High repair and replacement costs drive the need to investigate the feasibility of using FRP composite materials for pile foundations (Lampo, et al., 1998; Iskander and Hassan 1998). FRP composite materials are considered an attractive alternative for marine and other harsh environments because they are resistant to the degradation mechanisms mentioned above.

Composite piles have been available in the North American market since the mid 1980s, but their use to date has been limited mainly to marine fender piles, load-bearing piles for light structures, and experimental test piles (Iskander, et al., 2001). Composite piles have not yet gained wide acceptance in the civil engineering industry, primarily due to the lack of a long track record of performance. However, FRP composite piles may have a longer life cycle and improved durability in harsh marine environments, which presents the potential for substantially reduced costs.

To confidently assess the feasibility of using composite piles for load-bearing structures, information and performance data were gathered in critical areas of structural behavior and performance; long-term durability; and geotechnical behavior, including driveability and soil-pile load-transfer interactions. The overall objective of this research project was to evaluate the feasibility of using composite piles in bridge substructures. Table 52 presents the four detailed objectives of the project and indicates how each objective was met.

Table 52. Detailed project objectives.

Objective	Evidence of Objective Completion
Evaluation of the long-term durability of concrete-filled FRP composite pipe piles.	An experimental study was designed and implemented to investigate the degradation of the mechanical properties of glass FRP composites used to fabricate composite piles. The study investigated the effects of moisture absorption and exposure to freeze-thaw cycles.
Performance of laboratory tests to evaluate the soil-pile interface behavior of concrete-filled FRP composite piles and compare them with tests carried out on conventional prestressed concrete piles.	Interface shear tests were carried out on four FRP composite piles, one plastic pile, and two conventional piles.
Design and performance of a test pile program to evaluate the driveability, axial and lateral behavior, and capacity of concrete-filled FRP composite piles compared to conventional prestressed concrete piles.	Full-scale test pile programs were performed at two bridge sites in Virginia. Field data were gathered, analyzed, and disseminated to contribute to the current state of knowledge of composite piles.
Design and performance of a production pile testing and monitoring program in a real bridge project to compare long-term performance, load-transfer capability, and durability of concrete-filled FRP composite piles and conventional prestressed concrete piles.	A long-term monitoring program was designed and implemented at the Route 351 Bridge. The program consisted of instrumenting two production piles of the bridge: a concrete-filled FRP pile and a conventional prestressed concrete pile. The long-term monitoring of the instrumented piles will provide useful information to compare the performance of these two pile types. The long-term monitoring will be carried out by VDOT.

The remainder of this chapter provides summaries of the projects’ activities and conclusions. The chapter concludes with a discussion of the practical implications of this research, and recommendations for future research.

11.2 SUMMARY OF ACTIVITIES AND CONCLUSIONS

This section summarizes the activities and conclusions for the literature review, the interface laboratory study, the durability study of concrete-filled FRP tubular piles, the field tests at the Route 40 and Route 351 Bridge projects, the analytical studies on axial and lateral behavior, the long-term monitoring program, and the composite pile cost information.

11.2.1 Literature Review

A literature review was performed to: (1) identify suitable composite pile candidates to be used in high load-bearing projects such as bridge substructures, (2) identify the research needs, and (3) help design the work plan for this research project.

11.2.2 Interface Study

The following laboratory activities were performed for the interface study:

- Selection of sand specimens for interface testing.
- Soil characterization tests to determine grain size distribution, minimum/maximum density, and specific gravity testing.
- Direct shear tests on Density and Model sands to determine internal friction angles.
- Selection of pile surface specimens for interface testing.
- Surface topography characterization and surface hardness determination of seven pile surfaces. The seven pile surfaces included four FRP composites (commercially available from two FRP composite pile manufacturers), one recycled plastic pile, and two conventional pile materials (a prestressed concrete pile and a steel sheet pile).
- Design and construction of a modified top half shear box to permit testing of curved pile surfaces obtained from the FRP composite tubes.
- Interface shear tests for the seven piles and two sand types to determine the interface behavior and interface friction angles of these interfaces.

Interface shear tests were performed on 14 types of soil-pile interfaces. Tests were carried out for two types of sands: Density sand ($D_{50} = 0.5$ mm (0.0195 inch), subrounded to rounded particle shape) and Model sand ($D_{50} = 0.18$ mm (0.00702 inch), subangular to angular particle shape). Seven pile surfaces were tested: Lancaster FRP composite (curved), Hardcore FRP composite (curved), Hardcore FRP composite plate (flat), Hardcore FRP composite plate with bonded sand treatment (flat), PPI recycled plastic coupon (flat), prestressed concrete pile coupon (flat), and a steel sheet pile coupon (flat).

The peak and residual interface friction angles for the 14 sand-to-pile interfaces tested are summarized in tables 10 through 12 (chapter 3).

From the results of the interface study, the following conclusions and observations were made:

1. The interface friction angle values obtained for the Density sand tested against the Lancaster FRP composite pile were much lower than the values obtained for the other

pile surfaces. The peak and residual interface friction angles obtained for the Lancaster FRP composite pile were 19.7° and 16.6° , respectively. In contrast, the interface friction angle values obtained for the Density sand tested against the other pile surface types ranged from 27.6° to 33° , and from 24.9° to 27.8° , for the peak and residual conditions, respectively.

2. The Lancaster FRP composite pile was found to have the largest average mean line spacing (S_m) and the second-lowest maximum peak-to-valley height (R_t) as reported in table 8 (chapter 3). These values make this pile surface the smoothest of all seven surfaces tested.
3. In general, the subangular to angular Model sand gives slightly higher interface friction angles than the subrounded to rounded Density sand. However, for the Lancaster FRP composite pile, the interface friction angles obtained with the Model sand are much higher than the Density sand values.
4. In general, the interface friction angles, both peak and residual, were found to increase with increasing relative asperity height (R_t/D_{50}).
5. In general, the interface friction angles, both peak and residual, were found to increase with decreasing relative spacing (S_m/D_{50}), which is reasonable over the range of S_m/D_{50} tested.
6. Linear regression analyses between the interface friction coefficients and the variables R_t/D_{50} , S_m/D_{50} , and HV showed moderate fit strengths (where R_t and S_m are surface roughness parameters and HV is the Vickers hardness number). The regression analyses suggest other factors besides R_t/D_{50} , S_m/D_{50} , and HV also have important influences on the values of interface friction coefficient.
7. The bonded sand surface treatment used for the Hardcore FRP plate was successful in increasing the interface friction angle values.

11.2.3 Durability Study

A laboratory testing program was completed to study the long-term performance of FRP composite pipe piles. This durability study addresses the FRP shells of the Lancaster and Hardcore composite piles, and included FRP shell characterization, determination of baseline mechanical properties, measurement of moisture absorption as a function of time and temperature, measurement of mechanical properties as a function of moisture absorption, and measurement of mechanical properties as a function of freeze-thaw cycles.

From the results of the durability study, the following conclusions and observations were made:

1. The experimental program revealed strength and stiffness degradation due to moisture absorption at room temperature of up to 25 percent for the E-glass composites tested. These levels of degradation correspond to steady-state moisture contents reached after about 2.5 years of submergence.
2. Degradation of longitudinal mechanical properties of the 24-inch (0.61-m) Lancaster pile was not as significant as for the Hardcore pile because of the different fiber lay-ups. The Lancaster pile was matrix dominated in the longitudinal direction, since the fibers with closest alignment to the longitudinal axis were 35 degrees off alignment.
3. For the composite piles with fiber-dominated composite, the levels of degradation of mechanical properties were similar in hoop and axial directions.
4. The impact of FRP degradation on the long-term structural capacity of the piles was investigated using models recommended by Fam and Rizkalla (2001a and b, and 2002). This approach showed that, for a 12-inch (0.305-m) diameter FRP pile, the axial structural capacity will decrease about 5 percent if the FRP tube hoop properties degrade 25 percent and 40 percent in stiffness and strength, respectively. The small impact FRP degradation on the axial pile capacity is due to the fact that the majority of the capacity contribution comes from the concrete infill. The impact on larger diameter piles is even smaller. A similar analysis was carried out for the flexural capacity of a 12-inch (0.305-m) pile. The results show that a 24 percent reduction in flexural capacity can be expected if the FRP tube longitudinal tensile properties degrade 25 percent and 40 percent in stiffness and strength, respectively.
5. Exposure to freeze-thaw cycles was found to have little effect on the longitudinal tensile properties of the saturated FRP tubes. This conclusion is based on longitudinal tensile tests of samples exposed to 100, 300, and 500 freeze-thaw cycles.

11.2.4 Field Tests at the Route 40 Bridge

In 2000, VDOT replaced the old Route 40 Bridge (Structure No. 1006) over the Nottoway River. New precast composite piles, consisting of concrete-filled GFRP tubes, were used to support one of the cast-in-place reinforced concrete cap beams that directly support the superstructure. Before construction, full-scale field tests were undertaken to investigate the feasibility of construction, handling, and driveability, as well as the structural performance of the new composite piles in comparison to conventional prestressed concrete piles.

Based on the testing, analysis, and construction experience at the Route 40 Bridge, the following conclusions and observations were made.

1. Both the composite and prestressed concrete piles performed similarly in the axial load tests. Full geotechnical capacity was mobilized in both cases without structural failure of the piles. The axial loads at geotechnical capacity were significantly higher than the design pile load.

2. Initially, the composite test pile exhibited a lateral stiffness similar to that of the prestressed concrete test pile up to a load of about 40 to 50 kN (9,000 to 11,250 lbf). This load level was found to correspond to first cracking of the composite pile. Beyond this load, the composite pile exhibited a much lower stiffness than the prestressed concrete pile, but the composite pile did demonstrate a continuing ability to sustain lateral load with additional relatively large deformations.
3. The flexural strength of the 625-mm (24.6-inch) diameter composite pile with a 5.85-mm (0.230-inch) thick GFRP tube was calculated to be higher than the flexural strength of the 508-mm (20-inch) square concrete pile prestressed with fourteen, 12.7-mm (0.5-inch) strands, as shown in figure 99 (chapter 5).
4. Calculations show that the composite pile fails in bending by fracture of the GFRP tube on the tension side, while the prestressed concrete pile fails by yielding of the strands in tension, followed by crushing of the concrete in compression.
5. The lateral load field tests on both the composite and prestressed piles showed similar behavior to that obtained from laboratory flexural tests and analysis.
6. The lateral load-versus-deflection response for the composite pile was predicted with good accuracy using conventional procedures typically used for prestressed concrete piles.
7. Similar pile-to-cap beam connections were used for the composite and prestressed concrete piles, including eight No.7 steel dowels embedded 457 mm (18 inches) inside the piles from one end and extending 762 mm (30 inches) into the cap beam. The piles themselves were embedded 152 mm (6 inches) inside the cap beam.
8. Concrete-filled FRP tubes were successfully installed as piling for a bridge pier at the Route 40 Bridge. To date, no indications of unsatisfactory performance have been reported.

11.2.5 Field Tests at the Route 351 Bridge

A test pile program was conducted to permit direct comparison of the axial and lateral load behavior of three test piles: (1) a conventional, 610-mm (23.8 inch) square prestressed concrete pile; (2) a 622-mm (24.3-inch) diameter composite pile formed of an FRP shell and filled with concrete and steel reinforcing bars; and (3) a 592-mm (23.1-inch) diameter composite pile formed of a polyethylene plastic matrix with steel reinforcing bars. Laboratory tests were performed on the pile materials, and the axial and bending stiffnesses of the piles were calculated. The piles are all about 18 m (59.0 ft) long. The soil at the test site consists primarily of medium-dense silty sand with a layer of stiff sandy clay located about 1 to 3.5 m (3.28 to 11.5 ft) above the pile toes. The field testing program included dynamic measurements with CAPWAP analyses, static axial load tests, and static lateral load tests.

Based on the testing, analysis, and construction experience, the following conclusions and observations were made.

1. The axial stiffness (EA) of the prestressed concrete pile and the FRP pile are similar to each other and about 2.5 times the axial stiffness of the plastic pile.
2. Over a working range of bending moments, the flexural stiffness (EI) decreases in order from the prestressed concrete pile to the FRP pile to the plastic pile.
3. All three piles exhibited substantial setup after installation based on comparisons of Case method capacities at the end of initial driving and restrrike 5 days later, as well as comparisons of CAPWAP analyses of restrrike and static axial load tests several days after restrrike.
4. Applying Davisson's failure criterion to the static axial load tests, the axial capacities were 3,090, 2,260, and 2,130 kN (695,250, 508,500, and 479,250 lbf) for the prestressed concrete pile, the FRP pile, and the plastic pile, respectively.
5. When evaluated at the Davisson failure load, the average unit shaft resistances are 61.8, 46.9, and 48.9 kPa (8.96, 6.80, and 7.09 lbf/inch²) for the prestressed concrete pile, the FRP pile, and the plastic pile, respectively, and the corresponding unit toe resistances are 1,854, 2,564, and 2,339 kPa (268.8, 371.8, and 339.2 lbf/inch²).
6. The prestressed concrete pile exhibited a geotechnical capacity slightly above the midpoint between the capacities calculated using the LCPC methods for core penetrometer testing of steel and concrete piles of the same geometry as the test pile. The FRP and the plastic piles exhibited geotechnical capacities much closer to the LCPC-derived calculations for steel piles than for concrete piles of the same geometries as the test piles.

11.2.6 Axial Analyses

The axial capacities of the three test piles were predicted using static analysis methods commonly employed in practice. The methods employed were the Nordlund method, the API method, the LCPC method, and the IC method. The various methods used to predict axial pile capacity yielded ratios of calculated to measured pile capacities ranging from 0.70 to 1.14 for the prestressed concrete pile, and from 0.81 to 1.33 for the composite piles. It was found that the level of accuracy of the predictions was comparable for all three test piles.

The prediction results seem to indicate that conventional static analysis methods are applicable to composite piles. However, it is the author's opinion that additional case histories are needed to corroborate and extend this conclusion to other composite pile types and to different soil conditions.

The load-settlement behavior was predicted using T-Z analyses. Several analyses were carried out to determine the adequacy of this method to analyze axially loaded composite pile types such as those studied in this research project. The analyses were completed using empirical load-transfer curves available in the literature (e.g., API 1993, Vijayvergiya 1977) and using theoretically derived load-transfer curves.

The predictions using the empirical load-transfer curves showed reasonable agreement with the field measurements for the composite piles. The predictions for the prestressed concrete pile showed less agreement, and tended to underestimate the measured pile capacity. This result could be related to the value of the interface friction angle used. The calculations were based on the interface friction angle measured in the lab, which may be inadequate to represent the field conditions experienced by the pile (e.g., in the field the pile interface experienced much larger relative displacements compared to the 0.5 inches (12.7 mm) used in the laboratory).

The predictions obtained using the theoretically derived load-transfer curves were in very good agreement with the measured field behavior. However, the values of the coefficient of horizontal earth pressures (K) that resulted in the best matches with field behavior were 1.25, 1.0, and 0.9 for the prestressed concrete, FRP, and plastic piles, respectively. The differences in the K coefficient values are contrary to the expected outcome. The expected outcome was to have similar K values for the three test piles since they were installed in similar soil conditions, and all are full-displacement piles with similar cross-sectional dimensions. It is possible that this result is again related to the δ values measured in the laboratory not being representative of field conditions, perhaps due to the small displacements (only 0.5 inches (12.7 mm)) used in the lab.

The prediction results seem to indicate that conventional T-Z analyses are applicable to composite piles. However, it is believed that additional case histories are needed to corroborate and extend this conclusion to other composite pile types and to different soil conditions.

11.2.7 Lateral Analyses

Numerous p-y analyses were carried out to determine the adequacy of this method to analyze laterally loaded composite piles, such as the ones studied in this research project.

A derivation of the governing differential equation for the laterally loaded pile problem was presented, and possible limitations in analyzing composite piles were analyzed and discussed.

The importance of considering shear deformations in lateral pile analyses was discussed. The impact of shear deformations increases with increasing E/G ratios, and decreases with increasing slenderness ratios (L/D). For the test piles assessed in this project, the error associated with neglecting shear deformations is estimated to be less than 2.5 percent.

The importance of including nonlinearity of the flexural stiffness was discussed and illustrated with analyses results.

The results of the p-y analyses using published p-y curves that are embedded in the LPILE 4.0M computer program showed reasonably good agreement with the field measurements.

The initial modulus of the p-y curves was found to increase with depth at the highest rate for the FRP pile, at an intermediate rate for the plastic pile, and at the lowest rate for the prestressed concrete pile. This outcome is not as expected, and the reason for the difference in initial modulus values is not known.

Although the analysis results seem to indicate that conventional p-y analyses are applicable to composite piles, additional case histories are needed to determine what factors govern the appropriate value of the initial p-y modulus for different pile types in various soils.

11.2.8 Long-Term Monitoring

A monitoring program has been implemented at the Route 351 Bridge project to compare the long-term performance, load-transfer, and durability characteristics of an FRP composite pile and a standard prestressed concrete pile. The two production piles selected for monitoring were installed at the centers of Piers 10 and 11.

The field testing of the instrumented production piles included PDA, CAPWAP, and PIT tests. The following conclusions can be drawn from this test program.

1. The FRP composite pile and prestressed concrete pile performed similarly during pile driving, as demonstrated by the driving records, PDA traces, measured wave speed generated by the driving hammer, and measured compressive and tensile stresses.
2. Using the Case method, both instrumented production piles showed similar estimated pile capacities on pile restrike blows.
3. CAPWAP analyses at pile restrike showed similar estimated pile capacities and high shaft capacity components. The shaft capacities were estimated as being 82 percent and 71 percent of the total capacity for the prestressed concrete and FRP composite piles, respectively. Based on the CAPWAP analyses, the pile capacities were estimated to be more than twice the axial design load of 890 kN (200,250 lbf).
4. No discernable damage was detected in the piles after installation, based on PIT testing performed on the piles before and after pile driving.

Load-transfer instrumentation was installed in both piles. Durability instrumentation was installed on the FRP composite pile to monitor the inside and outside strains of the FRP tube. Monitoring data on the piles is limited to date; therefore, no conclusions can be

drawn at this time regarding the long-term performance of concrete-filled FRP composite piles.

11.2.9 Cost Information for Composite Piles

Composite materials have attractive features such as high resistance to corrosion, high strength-to-weight ratios, and the ability to be used in infrastructure projects with little or no maintenance requirements (Meiarashi, et al., 2002). Recent studies have found that the lower weight of bridge decks made of FRP composite materials results in greater cost effectiveness due to shorter construction time and decreased cost of the bridge superstructure (Ehlen 1999). The economical competitiveness of composite piles needs to be assessed. To help provide data for such assessments, cost information for the composite piles and prestressed concrete piles used in this research project was compiled and presented.

The initial costs of the composite piles studied in this project were found to be higher than the initial unit costs for prestressed concrete piles. The initial unit costs of the installed composite piles at the Route 40 Bridge were about 77 percent higher than the unit costs for the prestressed concrete piles. The initial unit costs for the composite piles installed at the Route 351 Bridge were higher than costs of the prestressed concrete piles by, for the plastic piles, about 289 percent and, for the FRP piles, about 337 percent.

The cost effectiveness of composite piles is expected to improve with economies of scale as production volume increases. The low maintenance requirements of these composite piles also increase their cost effectiveness. Life cycle cost analyses should consider the pile lifespan, the annualized maintenance costs, and the replacement costs of composite piles compared to prestressed concrete piles. The number of years of use that should be factored into the life cycle cost analyses may not be related only to the lifespan of the piles but may also be governed by the actual lifespan of the bridge superstructure, which depends on the rate of superstructure deterioration and changing traffic demands. Life cycle cost analyses were not performed for this study due to lack of maintenance cost and frequency information.

11.3 RECOMMENDATIONS FOR FUTURE WORK

Based on the findings from this investigation, the following recommendations are made for future work on composite piles.

11.3.1 Geotechnical Studies

Additional full-scale field load test programs are recommended to extend the conclusions of this study to other composite piles and soil types. Well-documented field loading tests of composite piles are scarce, and this lack of reliable data may be one reason that composite piles are not in widespread use for load-bearing applications. Therefore, it is important to increase the database of instrumented load tests of composite piles.

Finite element analyses are recommended to model the field tests of the test piles. This type of analysis takes into account the continuous nature of the soil deposits, as opposed to the T-Z and p-y approaches used in this study. Comparison of the results from the different analysis approaches would be useful.

Laboratory studies involving lateral load tests on model or small-diameter piles installed in uniform and controlled soil conditions may be useful to study the influence that pile characteristics and flexural stiffness have on p-y curves.

Pile damage should be assessed after pile driving by excavating the piles. Visual inspections of the retrieved piles will permit assessment of changes in the pile surface due to scratching and scraping of the outer surface. The conclusions drawn from the laboratory interface study regarding the influence of surface roughness and hardness characteristics on interface friction behavior at relatively small displacements may not be applicable to real piles that may experience severe surface wear during pile installation.

11.3.2 Durability Studies

Studies of small-diameter concrete-filled FRP piles may be useful to examine the durability of axial and flexural structural capacity. Smaller diameter tubes could allow a larger number of tests at a reasonable cost and within a reasonable time frame. A larger number of tests would permit interpreting the data scatter associated with inherent variability of the material properties.

A durability study that includes piles exposed to salt water and other aqueous solutions representing groundwater conditions in industrial sites is recommended.

Other recommended studies include assessment of degradation due to UV radiation and exposure to high temperatures, resistance to fire, and corrosion of the steel cage in PPI piles.

11.3.3 Structural Tests

Test involving compression, bending, and combined axial and bending loading are recommended to determine the full interaction diagrams of composite piles. To date, limited data is available for the combined loading condition.

The influence of temperature on structural behavior should be determined, and the effects that differences in coefficients of thermal expansion of the different pile constituents have on pile performance also require study. For example, in concrete-filled FRP piles, the coefficient of thermal expansion of the FRP tube will be a function of factors such as fiber and resin type, number of fiber layers, fiber lay-up, fiber volume fraction, etc. If the resulting thermal coefficient of the FRP tube is significantly different from that of the concrete core, it is conceivable that the two materials would debond.

Resistance to fire exposure should be investigated. Although the majority of the pile length is embedded in the ground or submerged in water, there is usually a portion of the pile that is exposed. Although the probability of exposure to fire is low, fire resistance properties could be important in locations where the piles form part of priority bridge structures that have to survive more severe conditions.

Additional recommended studies include tests to assess the behavior under cyclic loading of composite piles, studies of creep under axial compression, and the influence of rate of loading on the pile structural behavior.

11.3.4 Cost Analyses

It is recommended that detailed life cycle cost analyses be performed for different composite pile types and conventional piles.

APPENDIX A. INTERFACE TEST RESULTS

This appendix contains the results of all the interface tests performed for the interface study described in chapter 3.

Table 53. Organization of the figures in appendix A.

Pile/Material	Density Sand ⁽¹⁾	Model Sand ⁽²⁾
Lancaster composite FRP shell (CP40)	Figure 221	Figure 228
Hardcore composite FRP shell (24-4)	Figure 222	Figure 229
Hardcore FRP plate—untreated surface	Figure 223	Figure 230
Hardcore FRP plate—treated surface	Figure 224	Figure 231
PPI plastic pile	Figure 225	Figure 232
Prestressed concrete pile	Figure 226	Figure 233
Steel sheet pile	Figure 227	Figure 234

Notes: (1) See table 10, chapter 3, for a summary of interface shear test results on Density sand.
 (2) See table 11, chapter 3, for a summary of interface shear test results on Model sand.

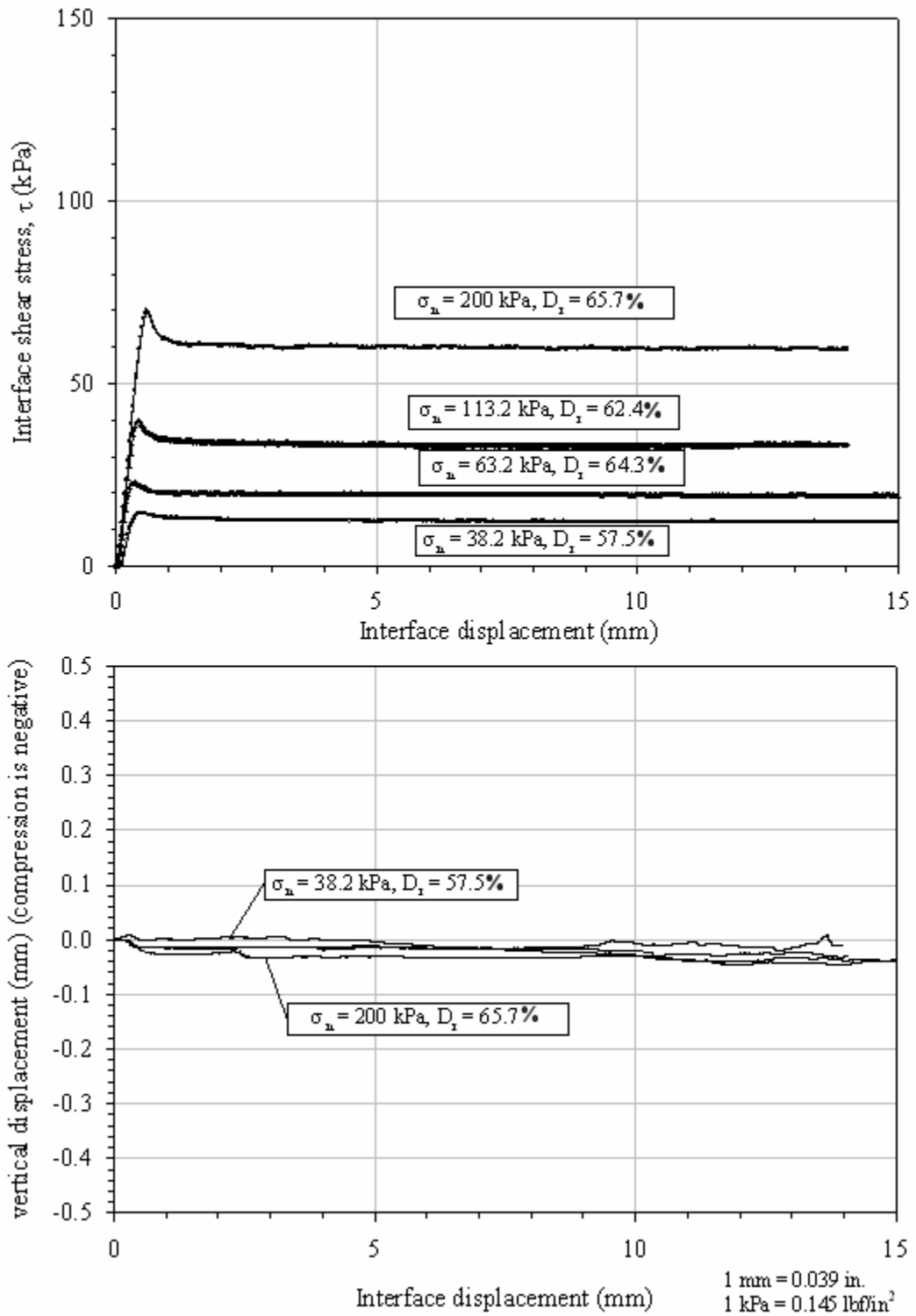


Figure 221. Graphs. Interface shear test results, Density sand-to-Lancaster FRP shell interface.

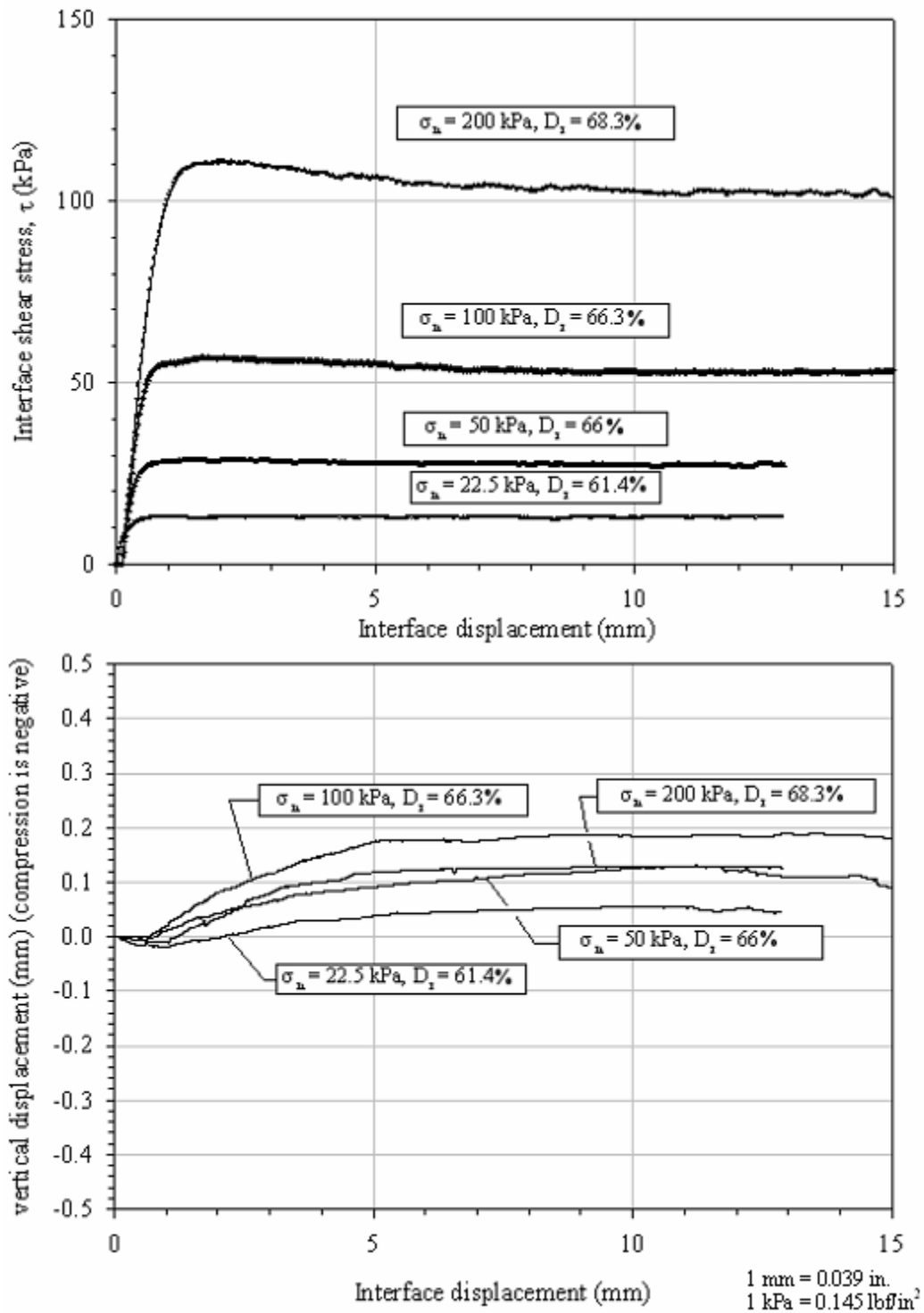


Figure 222. Graphs. Interface shear test results, Density sand-to-Hardcore FRP shell interface.

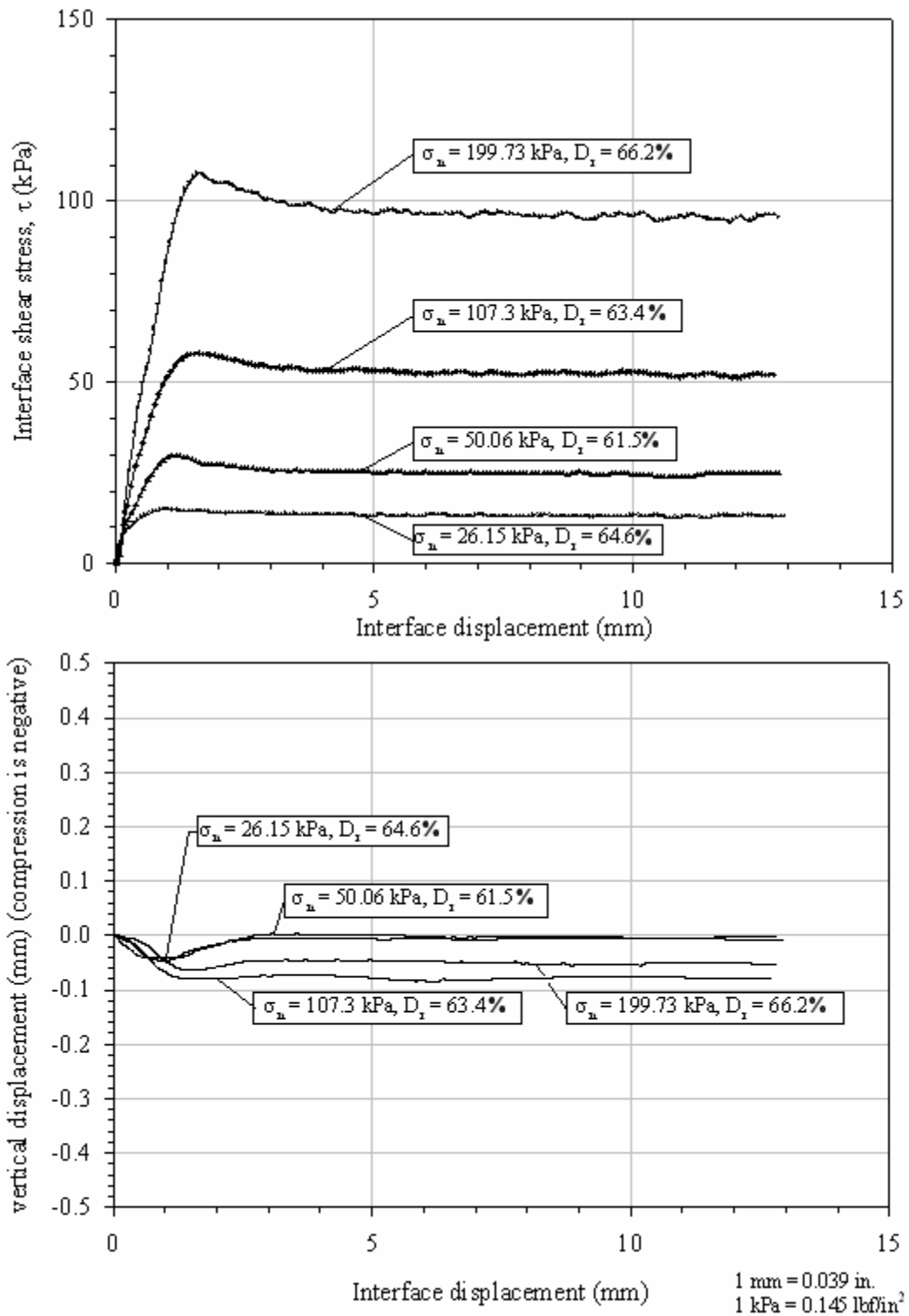


Figure 223. Graphs. Interface shear test results, Density sand-to-Hardcore FRP plate (untreated) interface.

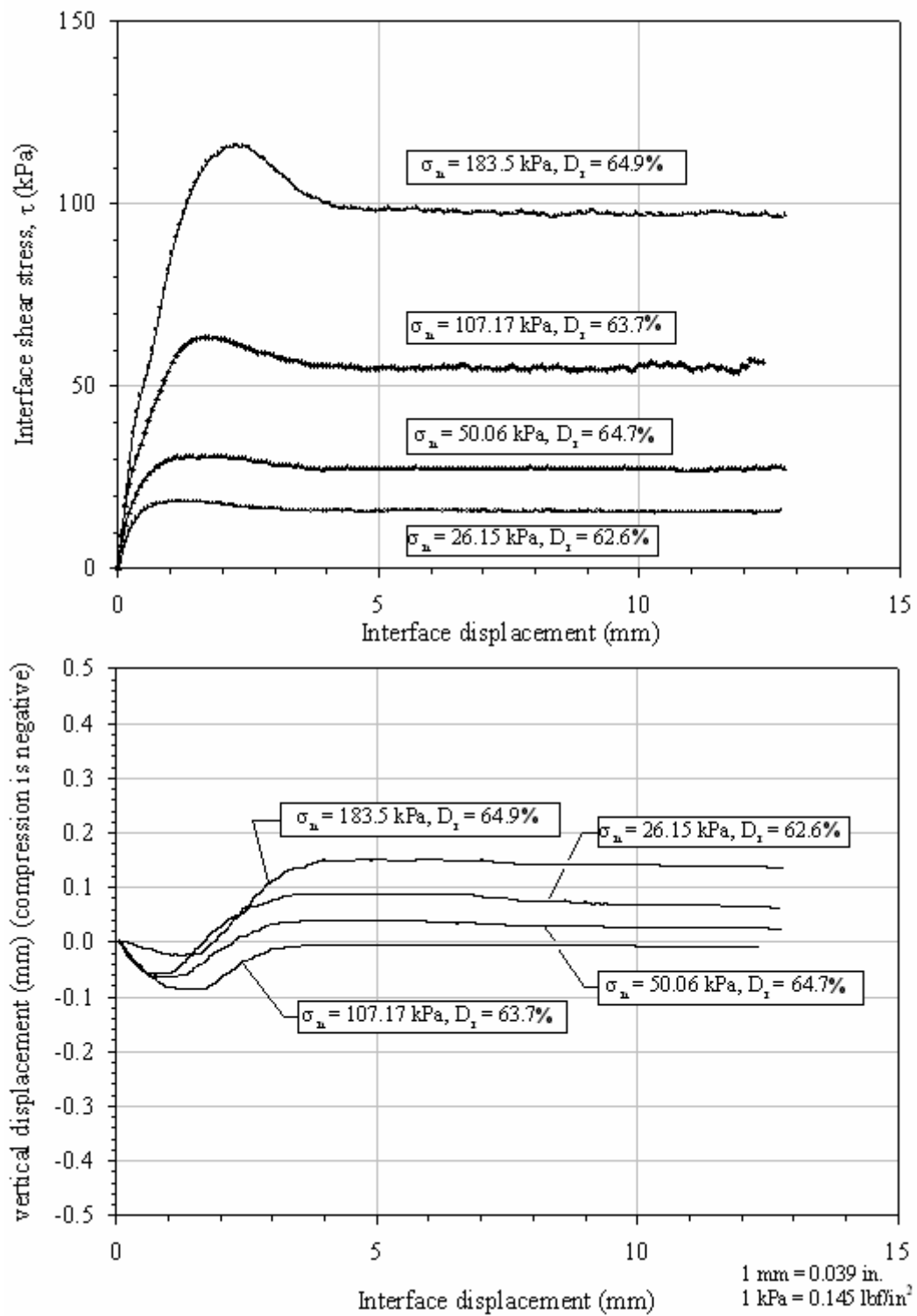


Figure 224. Graphs. Interface shear test results, Density sand-to-treated Hardcore FRP plate interface.

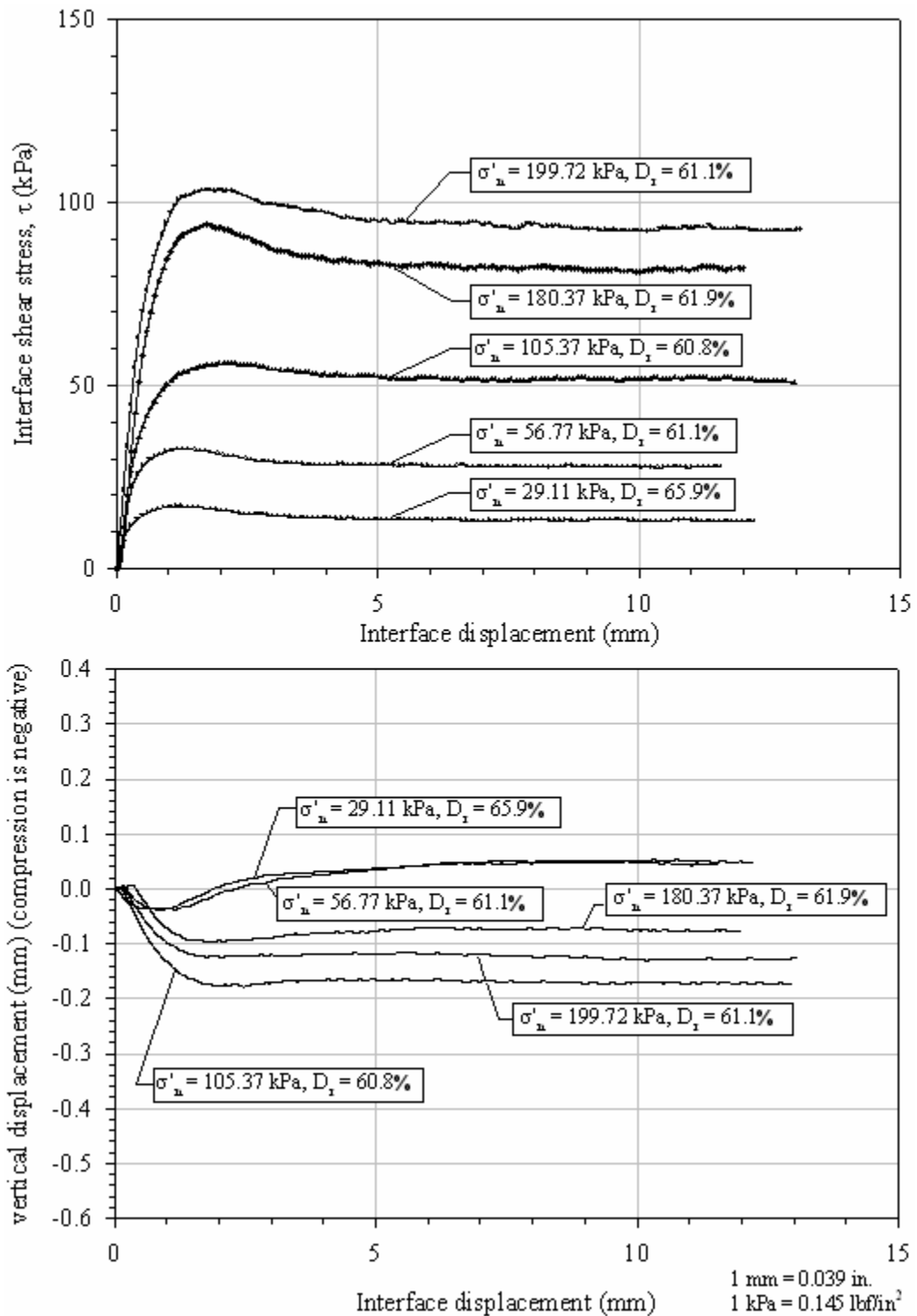


Figure 225. Graphs. Interface shear test results, Density sand-to-plastic interface.

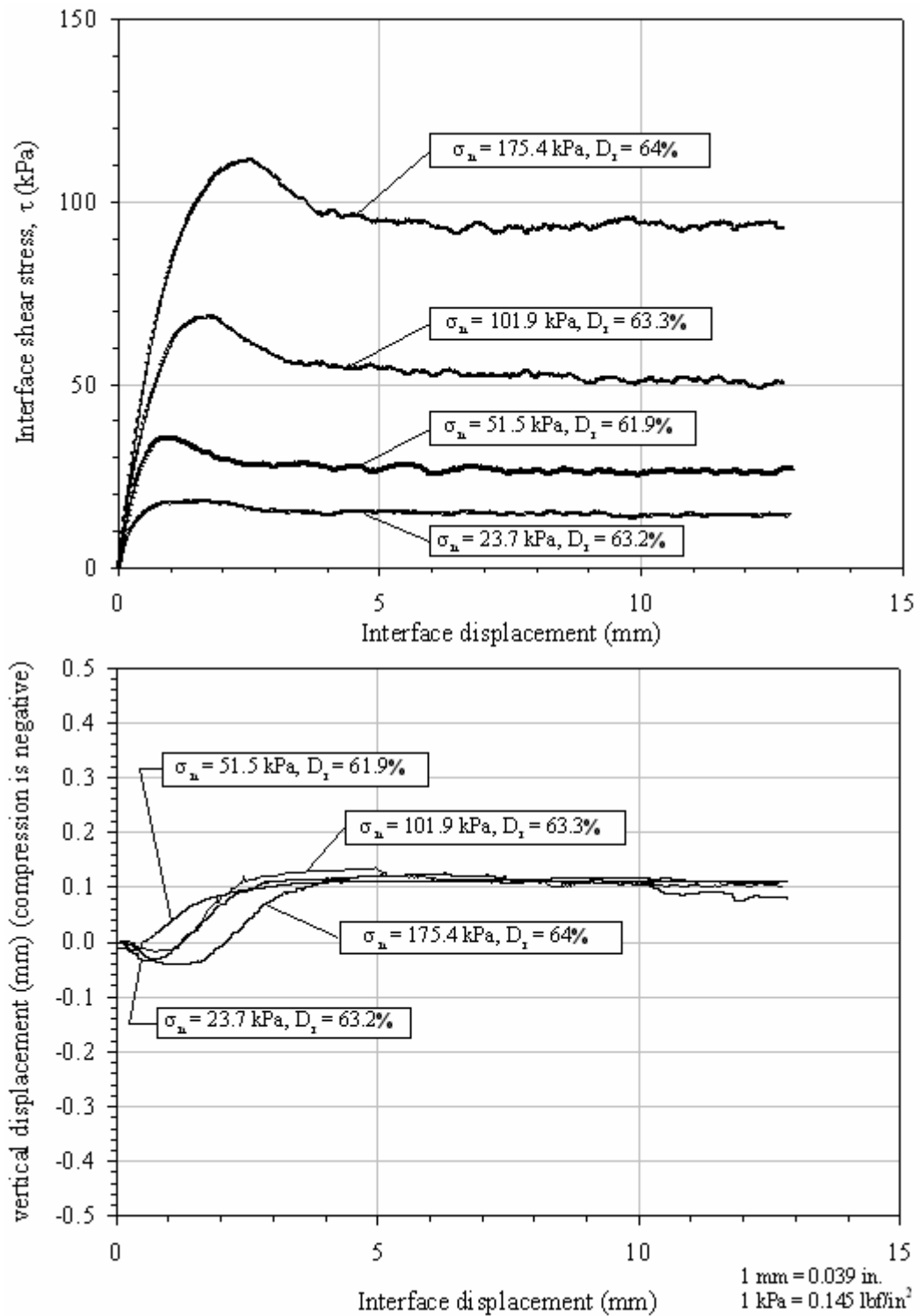


Figure 226. Graphs. Interface shear test results, Density sand-to-concrete interface.

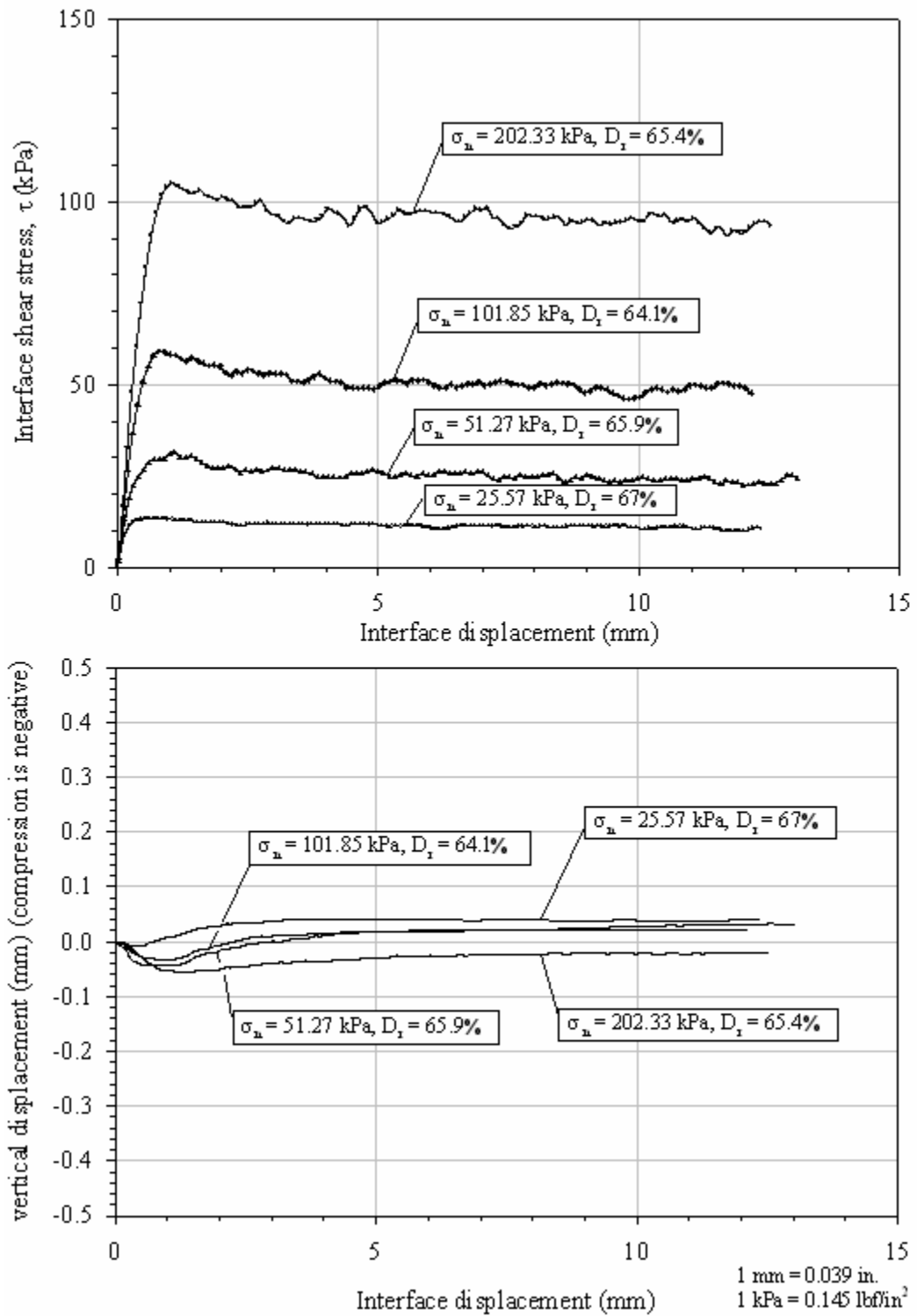


Figure 227. Graphs. Interface shear test results, Density sand-to-steel interface.

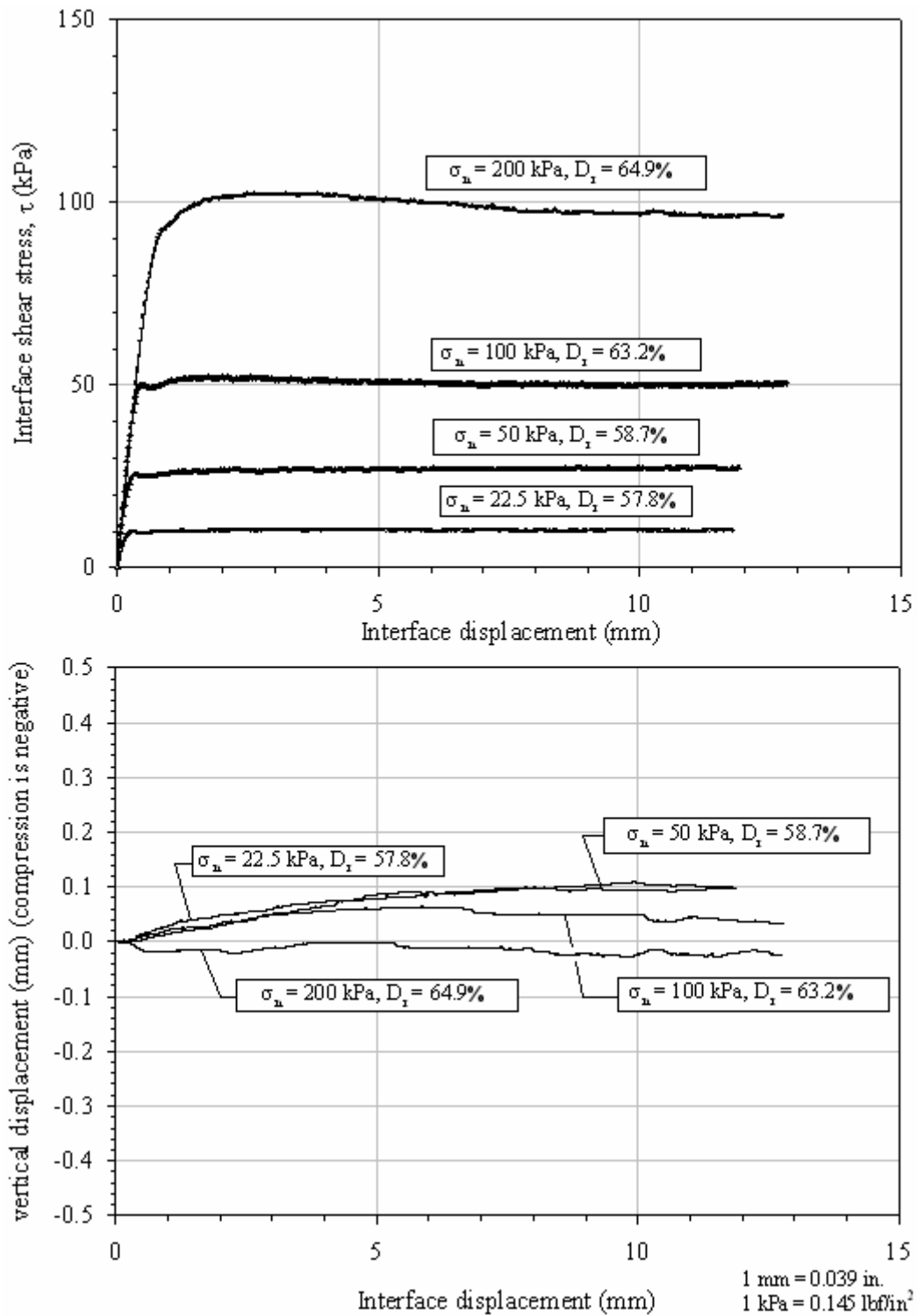


Figure 228. Graphs. Interface shear test results, Model sand-to-Lancaster FRP shell interface.

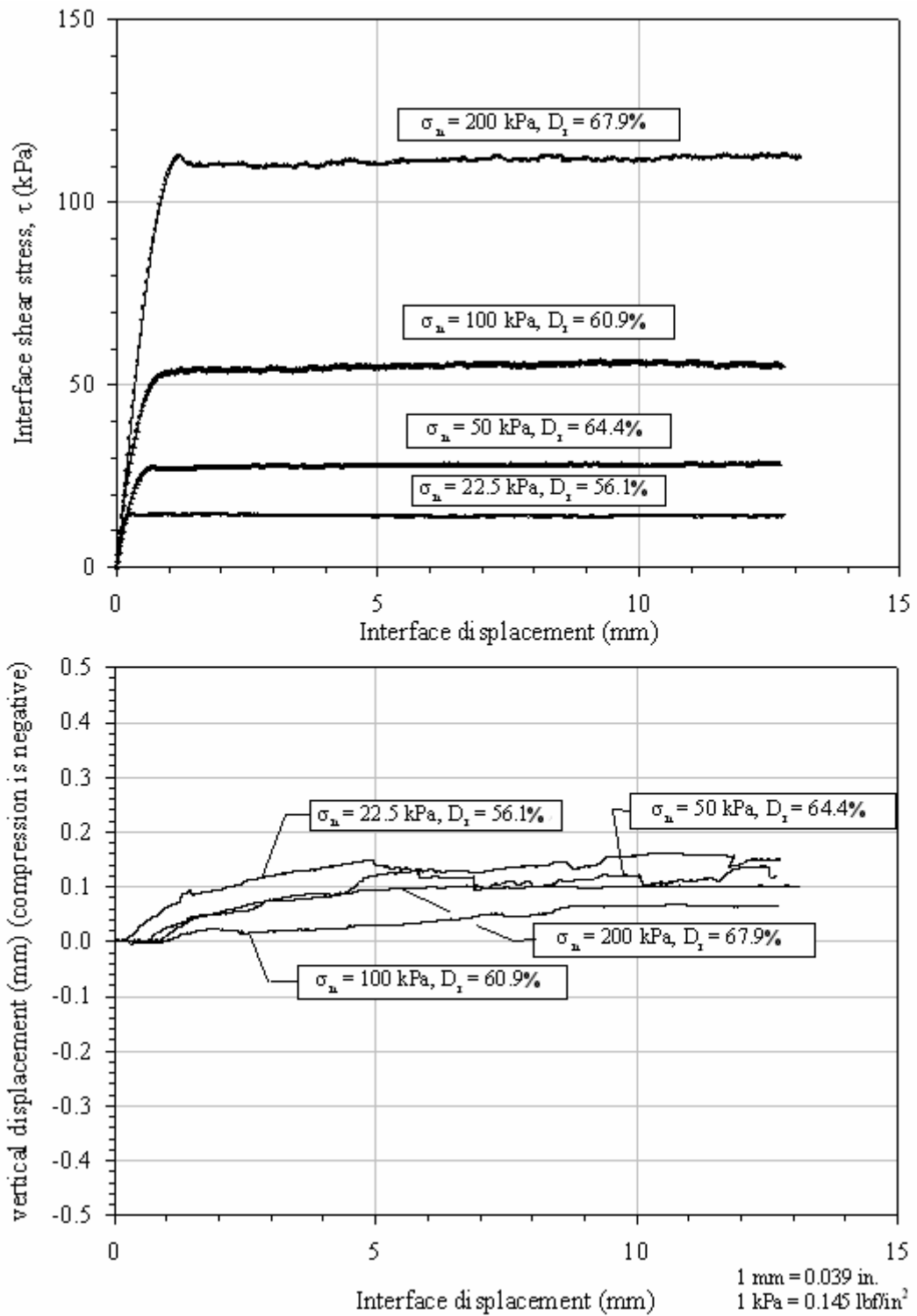


Figure 229. Graphs. Interface shear test results, Model sand-to-Hardcore FRP shell interface.

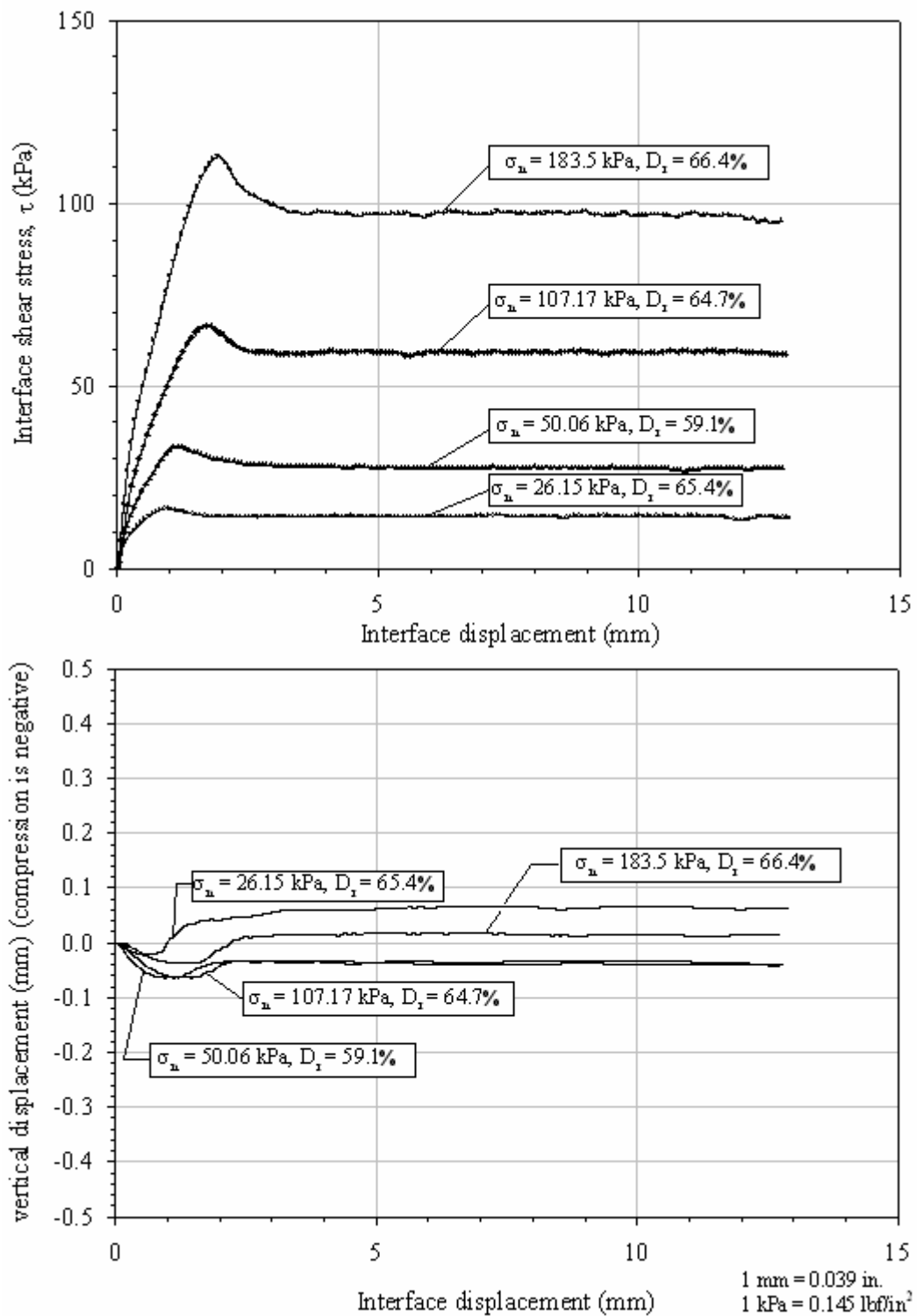


Figure 230. Graphs. Interface shear test results, Model sand-to-Hardcore FRP plate (untreated) interface.

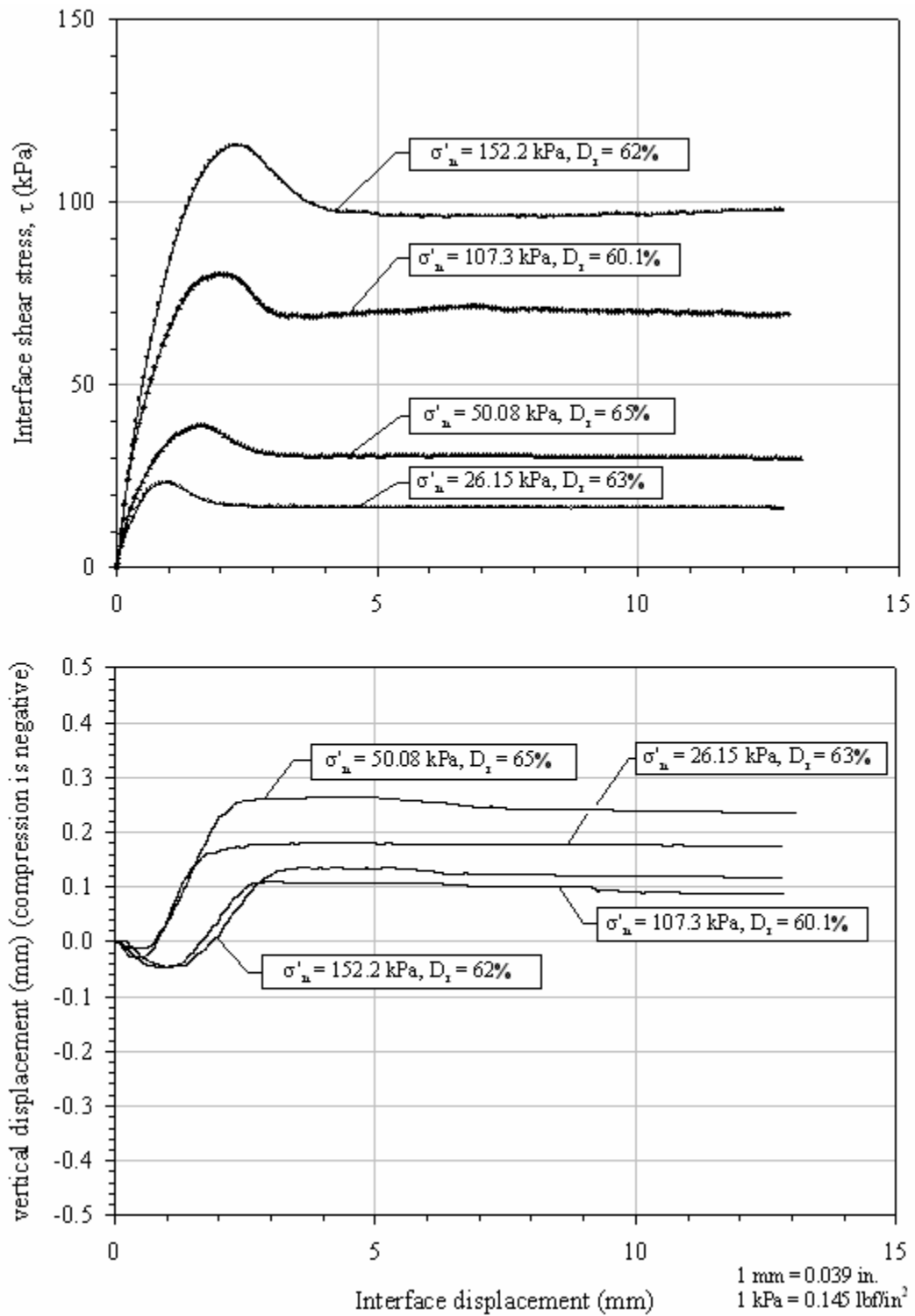


Figure 231. Graphs. Interface shear test results, Model sand-to-treated Hardcore FRP plate interface.

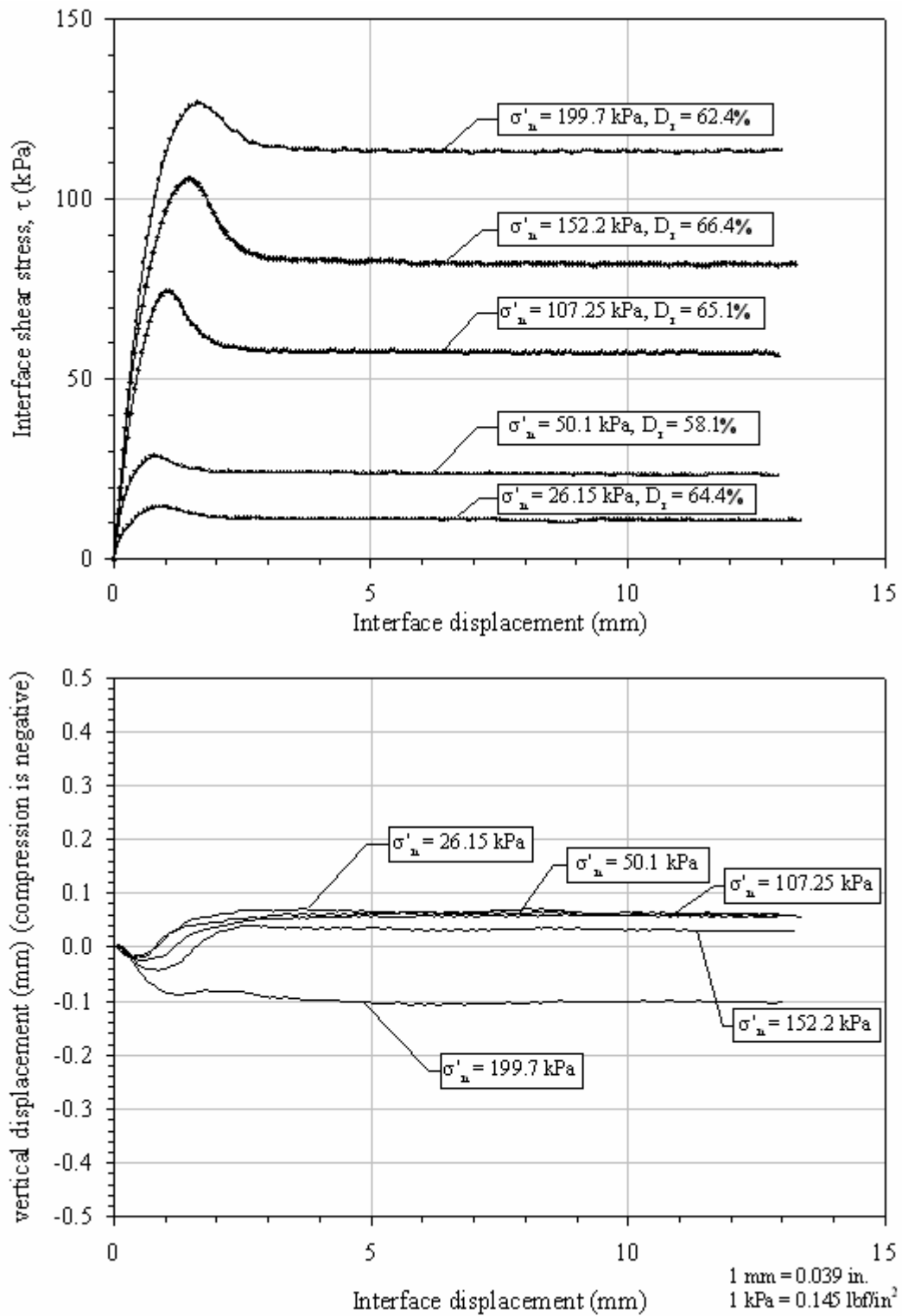


Figure 232. Graphs. Interface shear test results, Model sand-to-plastic interface.

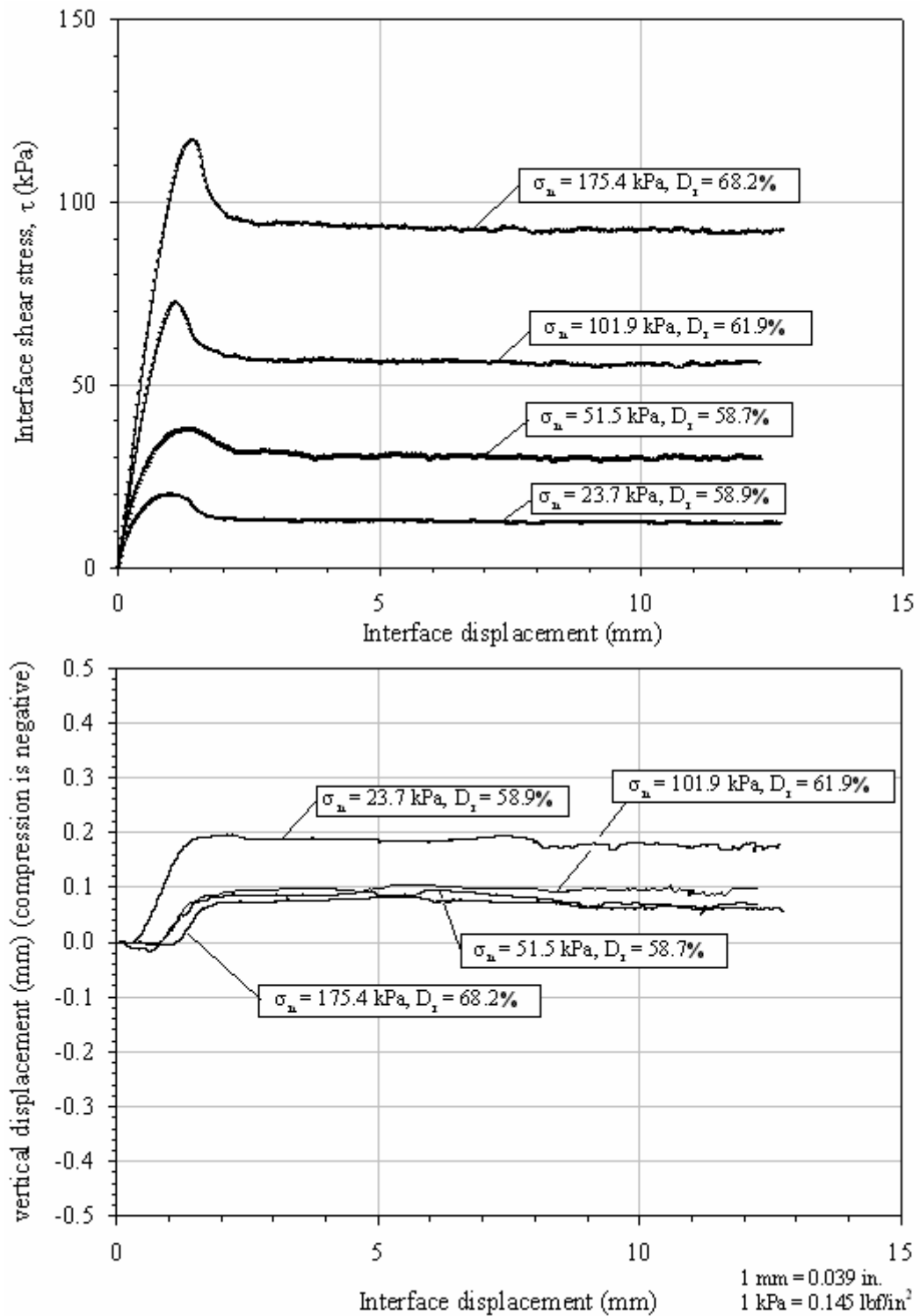


Figure 233. Graphs. Interface shear test results, Model sand-to-concrete interface.

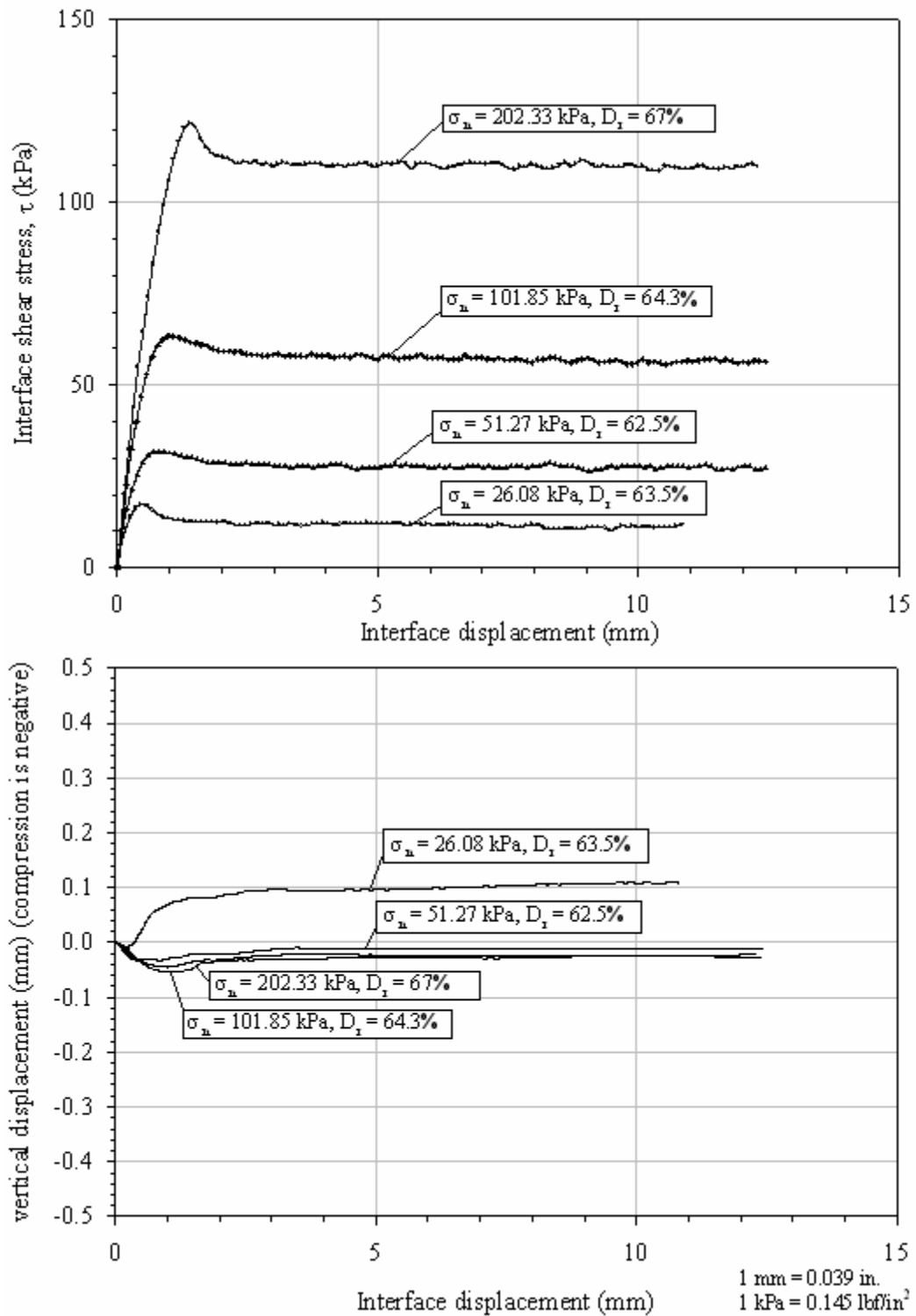


Figure 234. Graphs. Interface shear test results, Model sand-to-steel interface.

APPENDIX B. MOISTURE DIFFUSION INTO A CYLINDRICAL FRP COMPOSITE

The procedure for calculating moisture diffusion into the FRP of a composite pile is presented in this appendix. The diffusion is assumed to be Fickian, and based on the geometry of the FRP pile, it is further assumed to be predominantly in the radial direction. For these conditions, the governing partial differential equation for the moisture concentration is given by

$$\frac{\partial^2 C}{\partial r^2} + \frac{1}{r} \frac{\partial C}{\partial r} = \frac{1}{D_r} \frac{\partial C}{\partial t} \quad (70)$$

where C is the moisture concentration (also $C = M(t)$) and D_r is the diffusivity for radial diffusion.

If we assume the FRP shell is initially dry, the initial condition for the moisture concentration is given by

$$C(r,0) = 0 \quad (71)$$

The last requirement for the solution of the diffusion problem is that of the boundary conditions on the inner and outer radii of the FRP shell. As a first approximation, we specify that these concentrations are constant; that is,

$$\begin{aligned} C(r_i, t) &= C_i \\ C(r_o, t) &= C_o \end{aligned} \quad (72)$$

where r_i and r_o are the inner and outer radii, respectively, and C_i and C_o are the corresponding concentrations.

To solve equation 70 subject to the initial condition given by equation 71 and the boundary conditions in equation 72, the separation-of-variables technique can be used. This technique requires homogeneous boundary conditions rather than inhomogeneous conditions. Therefore, a solution of the following form is sought:

$$C(r,t) = c(r,t) + \tilde{C}(r) \quad (73)$$

where $\tilde{C}(r)$ satisfies the time-independent form as follows:

$$\frac{d^2 \tilde{C}}{dr^2} + \frac{1}{r} \frac{d\tilde{C}}{dr} = 0 \quad (74)$$

with boundary conditions given by

$$\begin{aligned}\tilde{C}(r_i) &= C_i \\ \tilde{C}(r_o) &= C_o\end{aligned}\tag{75}$$

This solution is given by

$$\tilde{C}(r) = \frac{(C_o - C_i)}{\ln \frac{r_o}{r_i}} \ln \frac{r}{r_i} + C_i\tag{76}$$

By combining equation 76 with equations 70 through 72, we find that $c(r,t)$ is the solution of equation 70 with boundary conditions given by

$$\begin{aligned}c(r_i, t) &= 0 \\ c(r_o, t) &= 0\end{aligned}\tag{77}$$

and an initial condition given by

$$\begin{aligned}c(r, 0) &= -\tilde{C}(r) \\ &= -\left[\frac{(C_o - C_i)}{\ln \frac{r_o}{r_i}} \ln \frac{r}{r_i} + C_i \right]\end{aligned}\tag{78}$$

Problems of this type have been studied in detail by a number of researchers. In particular, using the results of Necati Özişik (1989), the solution is given by

$$C(r, t) = \tilde{C}(r) + \sum_{m=1}^{\infty} e^{-D_r \beta_m^2 t} K_0(\beta_m, t) \int_{r_i}^{r_o} K_0(\beta_m, r) \tilde{C}(r) dr\tag{79}$$

where

$$K_0(\beta_m, r) = \frac{\pi \beta_m J_0(\beta_m r_o) Y_0(\beta_m r_o)}{\sqrt{2} \sqrt{1 - \frac{J_0^2(\beta_m r_o)}{J_0^2(\beta_m r_i)}}} \left[\frac{J_0(\beta_m r)}{J_0(\beta_m r_o)} - \frac{Y_0(\beta_m r)}{Y_0(\beta_m r_o)} \right]\tag{80}$$

and β_m represents the positive root of the transcendental

$$\frac{J_0(\beta r_i)}{J_0(\beta r_o)} - \frac{Y_0(\beta r_i)}{Y_0(\beta r_o)} = 0 \quad (81)$$

where J_0 and Y_0 are Bessel functions of the first and second kind (order zero), respectively.

The moisture content for the FRP shell can be bound by two extreme cases that should bound the FRP moisture absorption behavior. In the first case, we assume that the composite is saturated on the outer radius due to its immersion in water, and that it remains completely moisture-free on the inner surface. The corresponding boundary conditions are given by

$$\begin{aligned} C(r_i, t) &= 0 \\ C(r_o, t) &= M_\infty \end{aligned} \quad (82)$$

where M_∞ is the saturation concentration from the experimental data in chapter 4. Assuming that $C(r_i, t) = 0$ should give the lowest values for the moisture content in the pile, and hence the highest FRP strength (since the strength is reduced by an increase of moisture).

In the second case, we assume that the FRP shell is saturated on both the inner and outer radii. The corresponding boundary conditions are given by

$$\begin{aligned} C(r_i, t) &= M_\infty \\ C(r_o, t) &= M_\infty \end{aligned} \quad (83)$$

This case should give us the highest values for the moisture content in the FRP shell of the pile, and hence the lowest FRP strength.

The procedure described above provides a means to estimate the bounds for the moisture content distribution within the FRP shell of a composite pile. To do so, the values of M_∞ and diffusivity (D_r) must be known. For the piles studied in this project, these values can be taken from tables 23-26.

The results of this approach for the Lancaster 24-inch FRP shell are shown in figures 235 and 236. These figures correspond to the predicted moisture concentration profiles for the two boundary condition cases described above. The value of D used corresponds to 22 °C (72 °F) temperature.

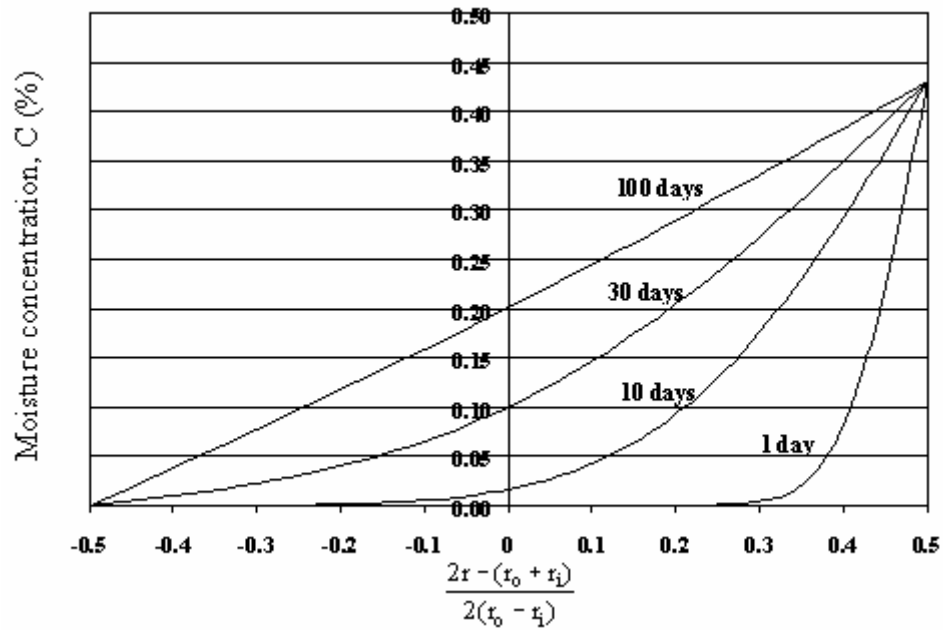


Figure 235. Graph. FRP moisture concentration profile, inner radius dry, outer radius saturated.

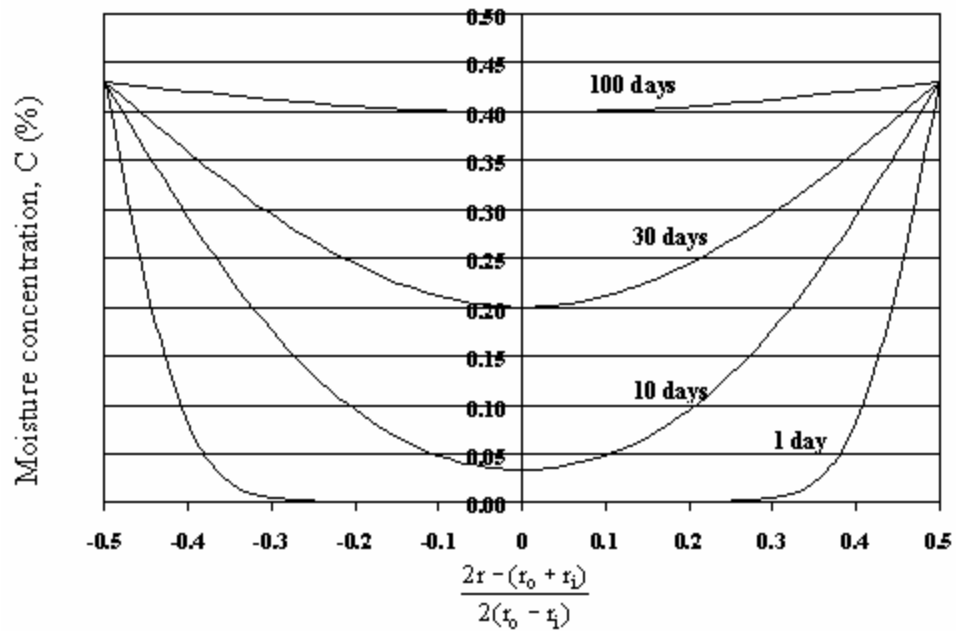


Figure 236. Graph. FRP moisture concentration profile, inner and outer radii saturated.

APPENDIX C. STRUCTURAL TESTS RESULTS FROM COMPOSITE PILE CUTOFF SECTIONS FROM THE ROUTE 40 BRIDGE PROJECT

This appendix contains results from structural tests carried out on cutoff Lancaster composite pile samples obtained for the Route 40 bridge project. The structural tests include:

- C.1. Pushout tests to assess the bond strength between the concrete core and the inner surface of the FRP tubes.
- C.2. A creep bending test carried out on an 18-ft (5.49-m) long pile piece.

The results are summarized in the following pages.

C.1 PUSHOUT TEST RESULTS

Pushout tests were performed to investigate the strength of the bond between the concrete and the FRP shell of Lancaster composite piles. The pushout test specimens were prepared by cutting slices from composite pile cutoff sections from the Route 40 Bridge project. The pushout specimens had a nominal diameter of 0.6 m (24 inches), and ranged from 75 mm to 150 mm (3 to 6 inches) in length.

Some of these tests were performed by VTRC, and some were performed by Virginia Tech (VT). Each institution used a different test setup. The VTRC tests were performed by setting the test specimens on a block with a carefully fabricated hole that permits the block to support the FRP shell but allows the concrete core to pass through the hole. The load was applied at a rate of 3,000 lbs/min (1,362 kg/min). The VTRC test setup is shown in figure 237.



Figure 237. Photo. VTRC pushout test setup.

The tests at VT were performed by bonding the outside of the FRP shell to a slightly larger steel pipe section, supporting the steel pipe section, and pushing the concrete core so it begins to move out of the FRP shell. Tests were carried out at a displacement rate of 0.002 inches/min (0.0508 mm/min). The VT test setup for the pushout tests is shown in figure 238. The test results are summarized in table 54.



Figure 238. Photo. VT pushout test setup.

Table 54. Summary of pushout test results.

	VTRC ⁽¹⁾	VT ⁽²⁾	Total
Number of tests	13	6	19
Average peak bond strength (psi)	29.95	14.1	24.9
Standard deviation (psi)	9.75	20.1	15.3

Notes: (1) Load controlled test at 3,000 lb/min (1,362 kg/min).

1 psi = 6.89 kPa

(2) Displacement controlled tests. Bond strengths were corrected for voids in the bond area.

As shown in table 54, regardless of the test setup, the bond strength values obtained are fairly low, with an overall bond strength average of 170 kPa (24.9 psi). Test results also show a wide scatter of bond strength values. This wide variability of results could be related to factors such as the presence of voids between the concrete core and the interior of the FRP shell; possible damage to bond during cutting, shipping, and handling; temperature effects (expansion and contraction); and scale or size effects. Smaller bond strengths were obtained using the VT test setup compared to the VTRC test results. The bond strength magnitude differences are likely related to inherent differences in the test setup and load application procedure, as well as possible additional specimen disturbance of the VT specimens during the extra shipping and handling required to move the specimens from VTRC to VT.

C.2 CREEP BENDING TEST

A four-point creep bending test setup was designed and built to perform a creep test on an 18-ft (5.49-m) long section of 24-inch (0.61-m) diameter Lancaster composite pile. This pile was left over from VDOT's Route 40 Bridge project, where Lancaster composite piles were used for one bent. The test facility was built at VT's Kentland Farms, approximately 16 km (10 miles) west of Blacksburg, VA.

A photograph of the creep bending test setup is shown in figure 239. As shown in this photo, two dead weights of about 32 kN (7.2 kips) are hung at the middle thirds of the beam. These loads induce a maximum moment of about 58 kN-m (43 kip-ft). This moment is not a large percentage of the expected ultimate moment, but it is a moment that can be applied economically.

The centerline deflection curve obtained from the test is shown in figure 240.



1 kip = 4.45 kN

Figure 239. Photo. Creep bending test setup.

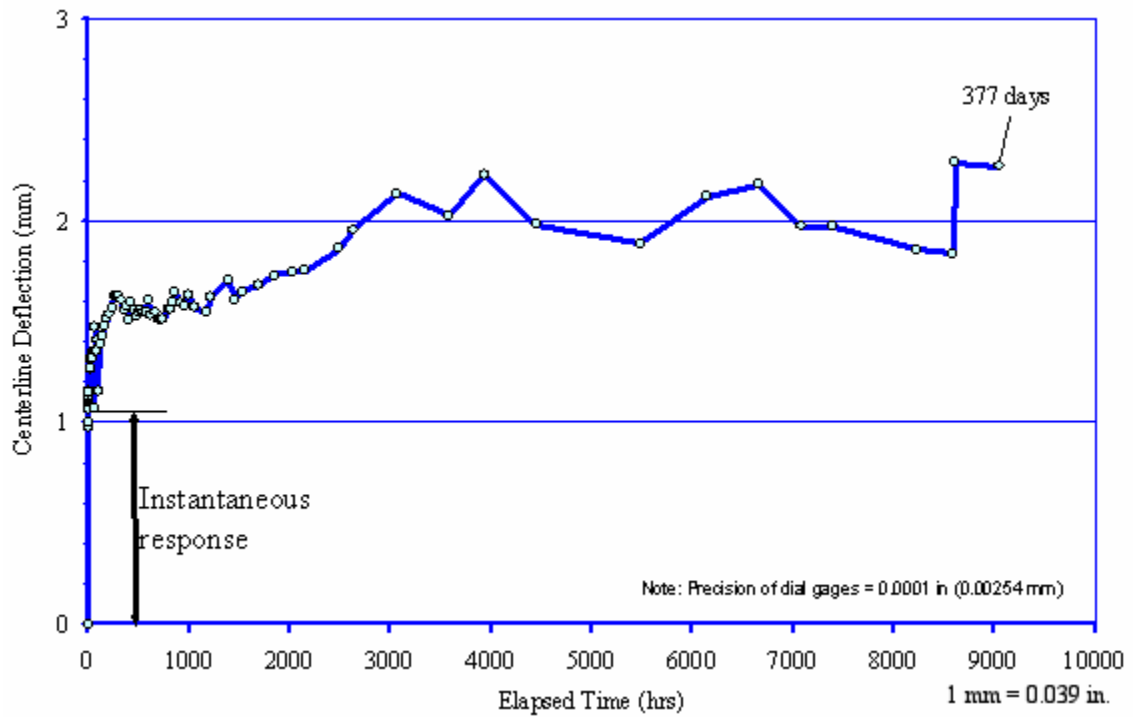


Figure 240. Graph. Creep deflection test results.

APPENDIX D. GEOTECHNICAL FIELD INVESTIGATIONS AT THE ROUTE 351 BRIDGE TEST SITE

This appendix contains the results of geotechnical field investigations completed at the test site of the Route 351 Bridge project.

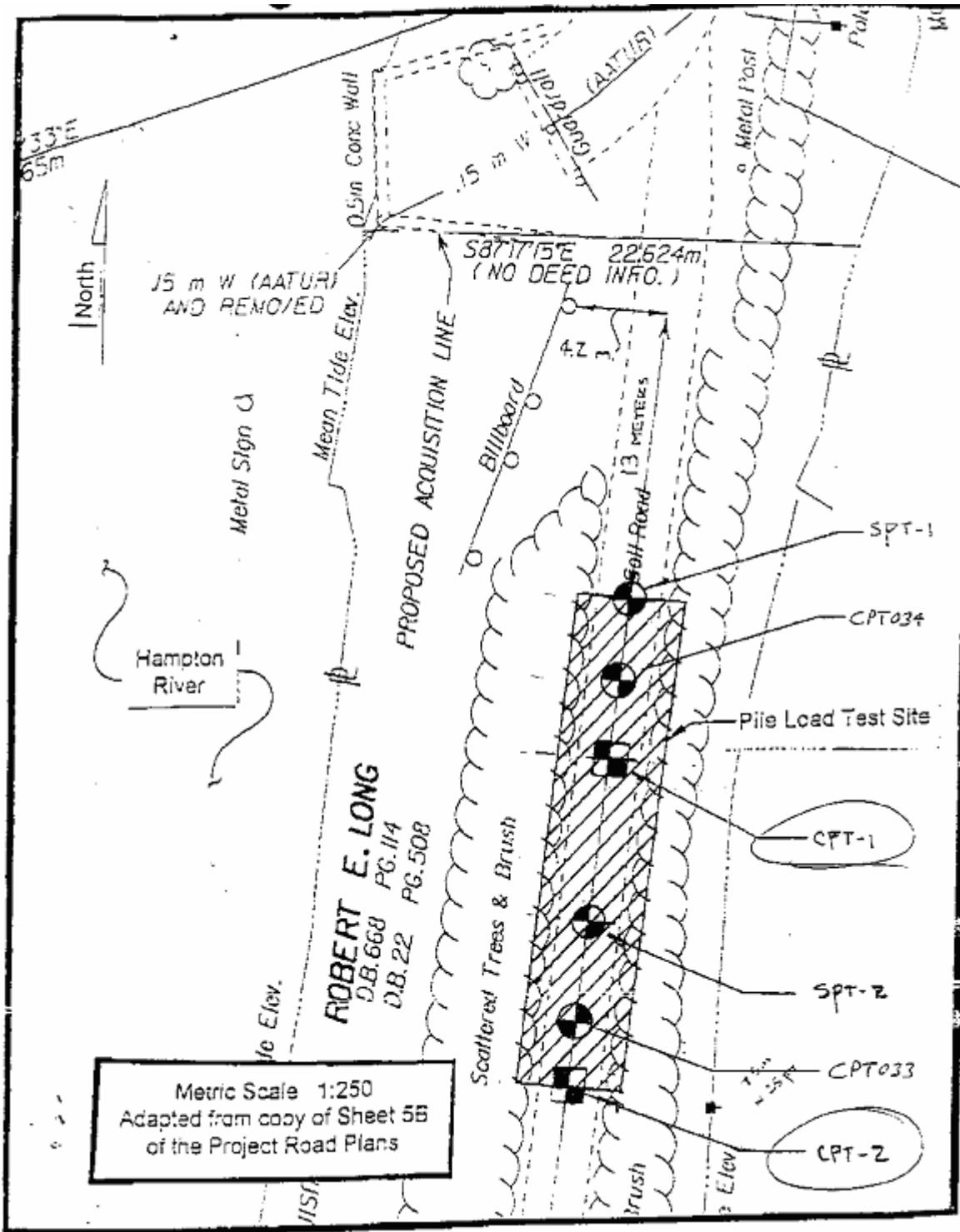
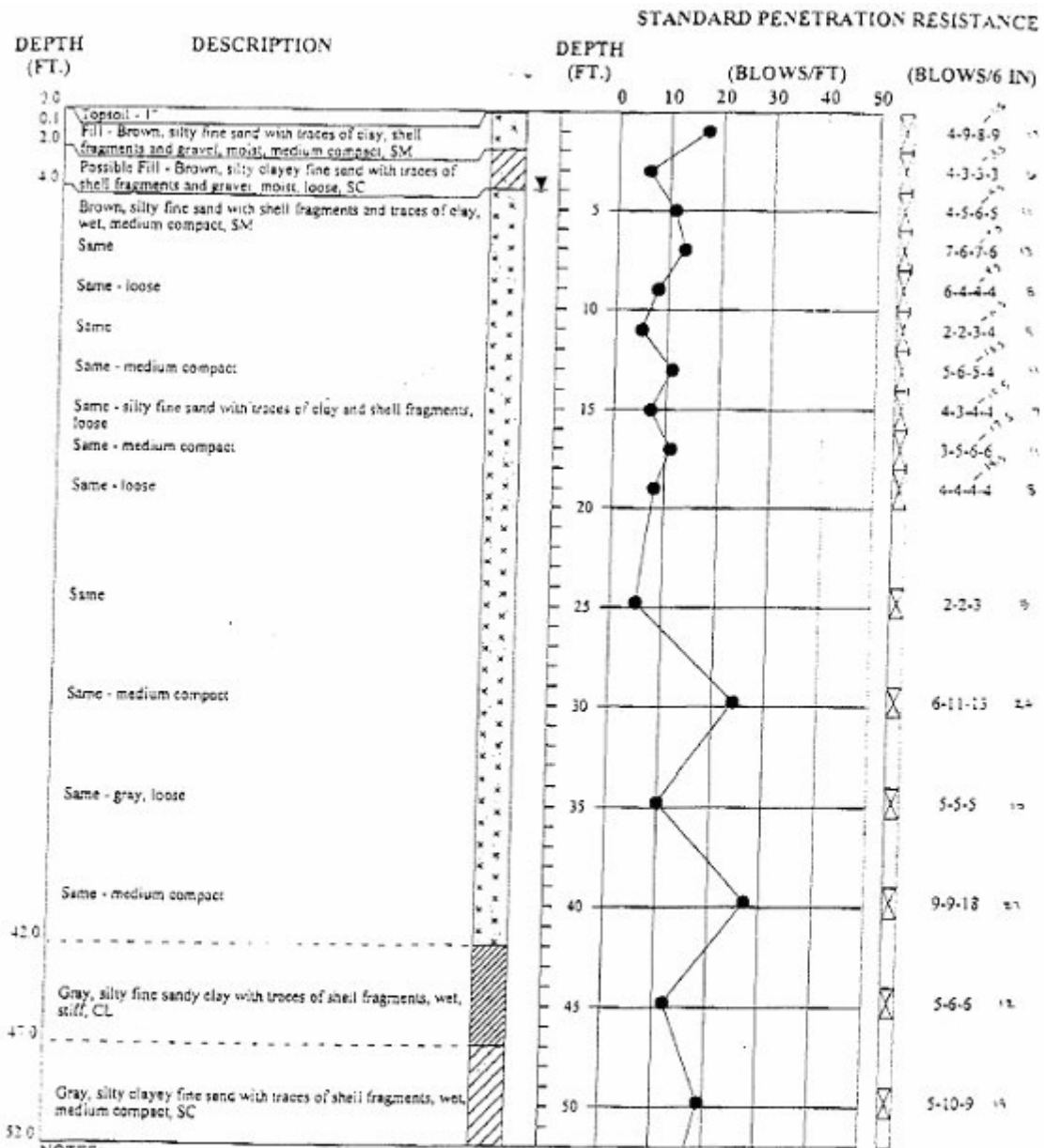


Figure 241. Map. Location of field tests.



NOTES:

- Gradual Stratum Change
- - - Approximate Stratum Change
- Penetration Resistance (N - value)
- ⊗ Standard Penetration Test
- ▬ Undisturbed Sample
- ⊕ Groundwater Level at Time of Boring
- ⊗ Stabilized Groundwater Level Reading

TEST BORING RECORD	
BORING NUMBER	B-1
DATE DRILLED	June 4, 2001
PROJECT NUMBER	01-2315
PROJECT	Route 351 (Pembroke Ave.)
LOCATION	Hampton, Virginia
McCALLUM TESTING LABORATORIES, INC.	

Figure 242. Chart. Boring B-1 (SPT-1).

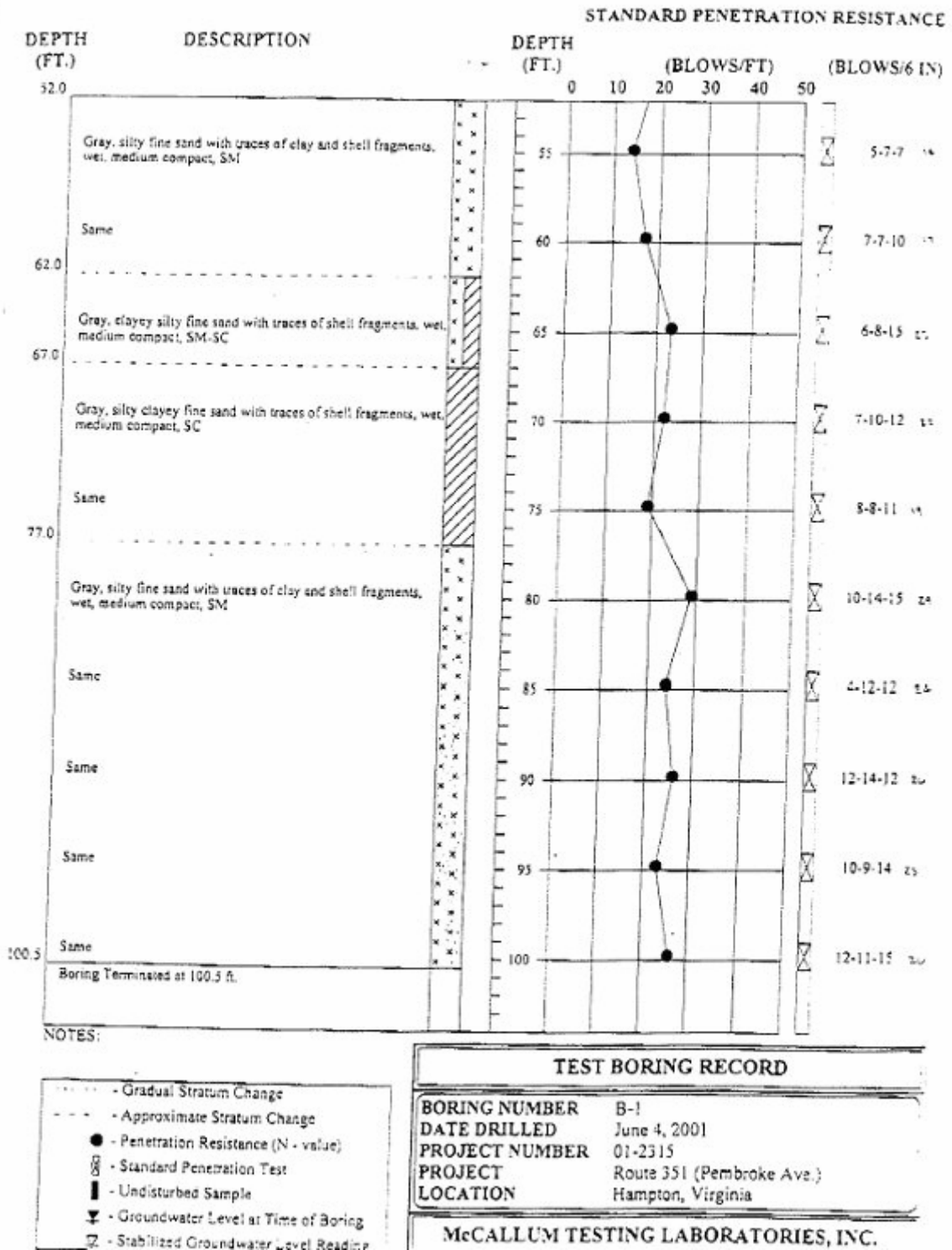


Figure 242. Chart. Boring B-1 (SPT-1)—Continued

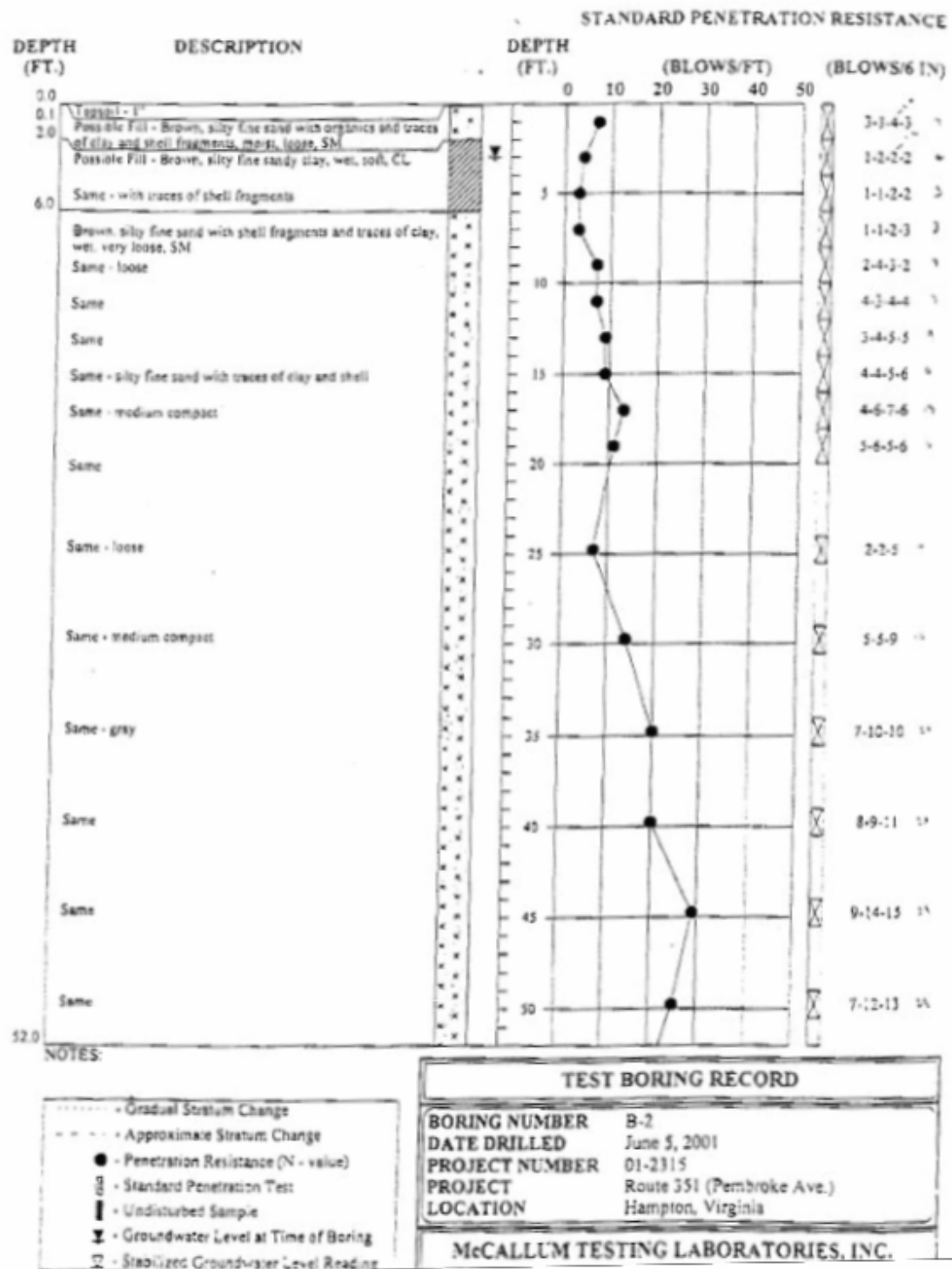


Figure 243. Chart. Boring B-2 (SPT-2).

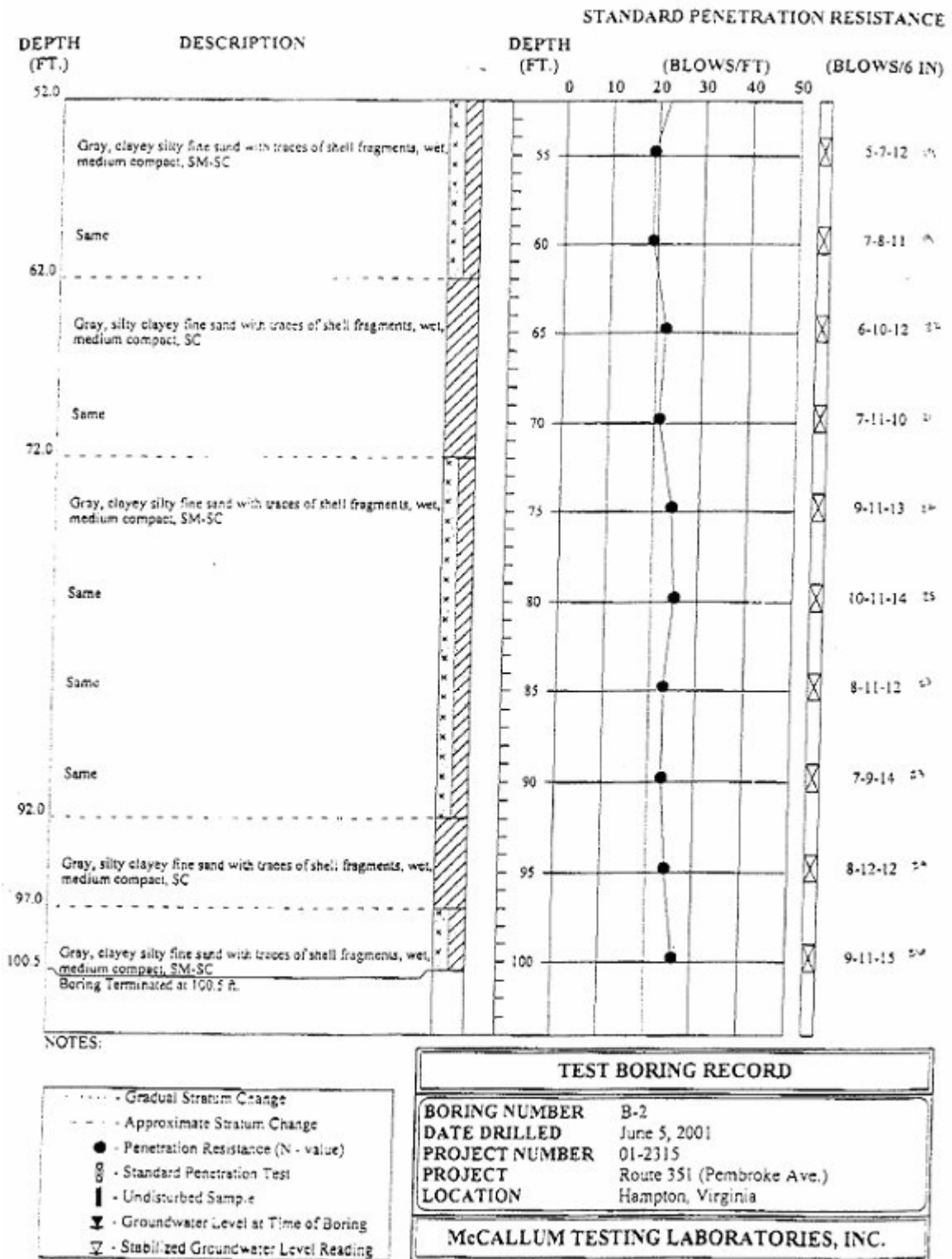


Figure 243. Chart. Boring B-2 (SPT-2)—Continued

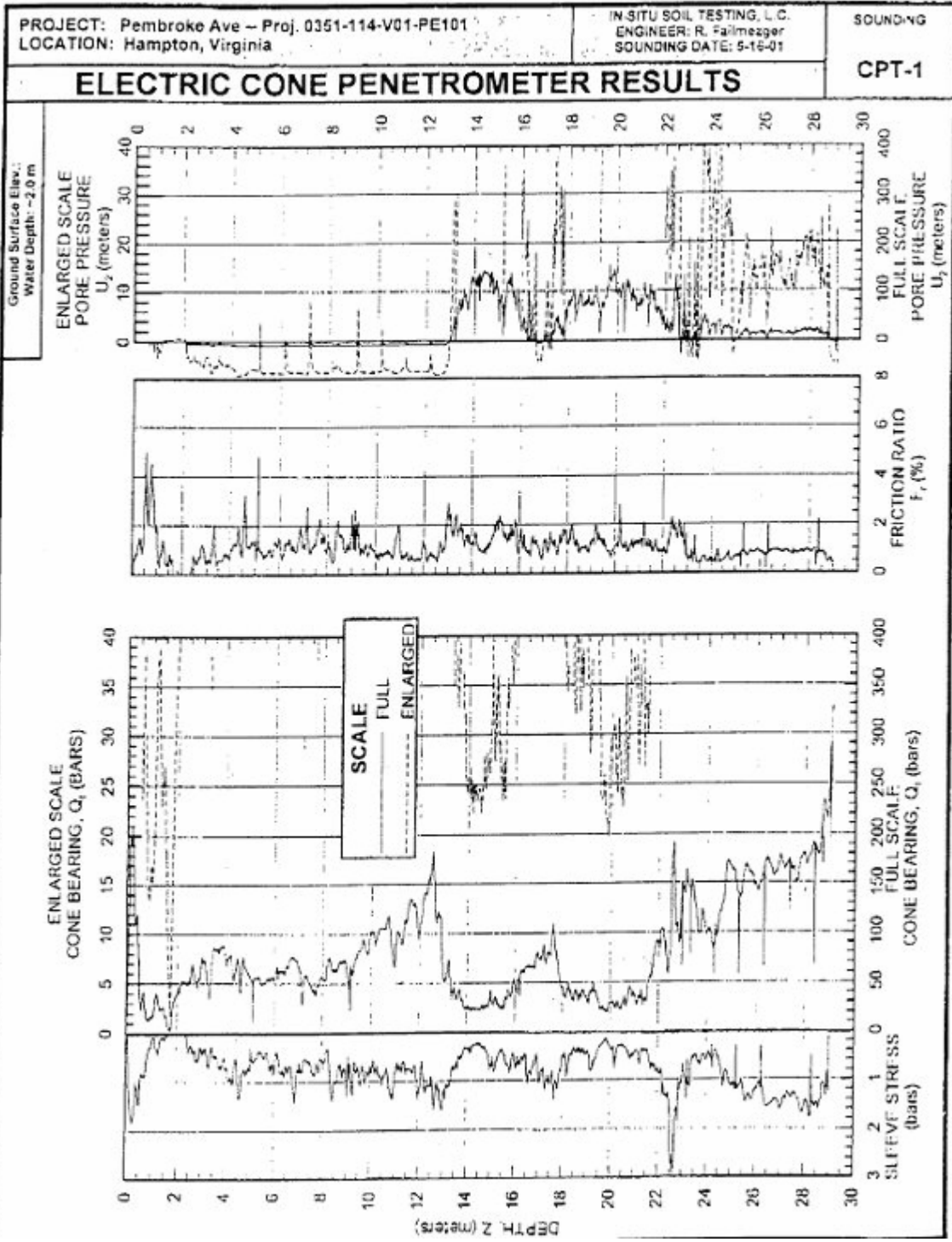


Figure 244. Chart. CPT-1.

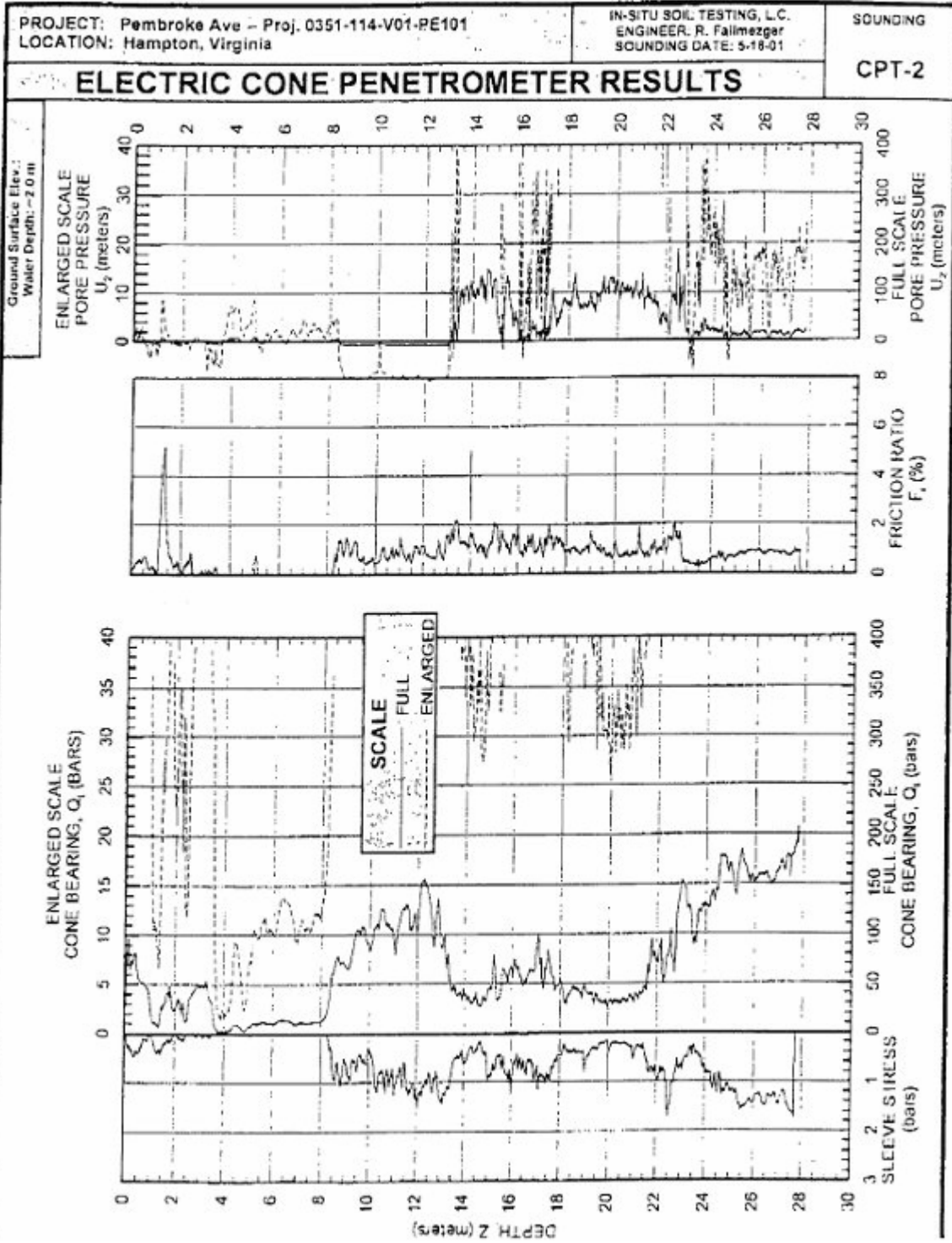


Figure 245. Chart. CPT-2.

CONE PENETROMETER TEST LOG



PROJECT #: 0351-114-V01-C501

CPT033

LOCATION: Hampton_Roads

PAGE 1 OF 4

STATE NORTHING: 0

NORTHING: 0

STATE EASTING: 1

EASTING: 1

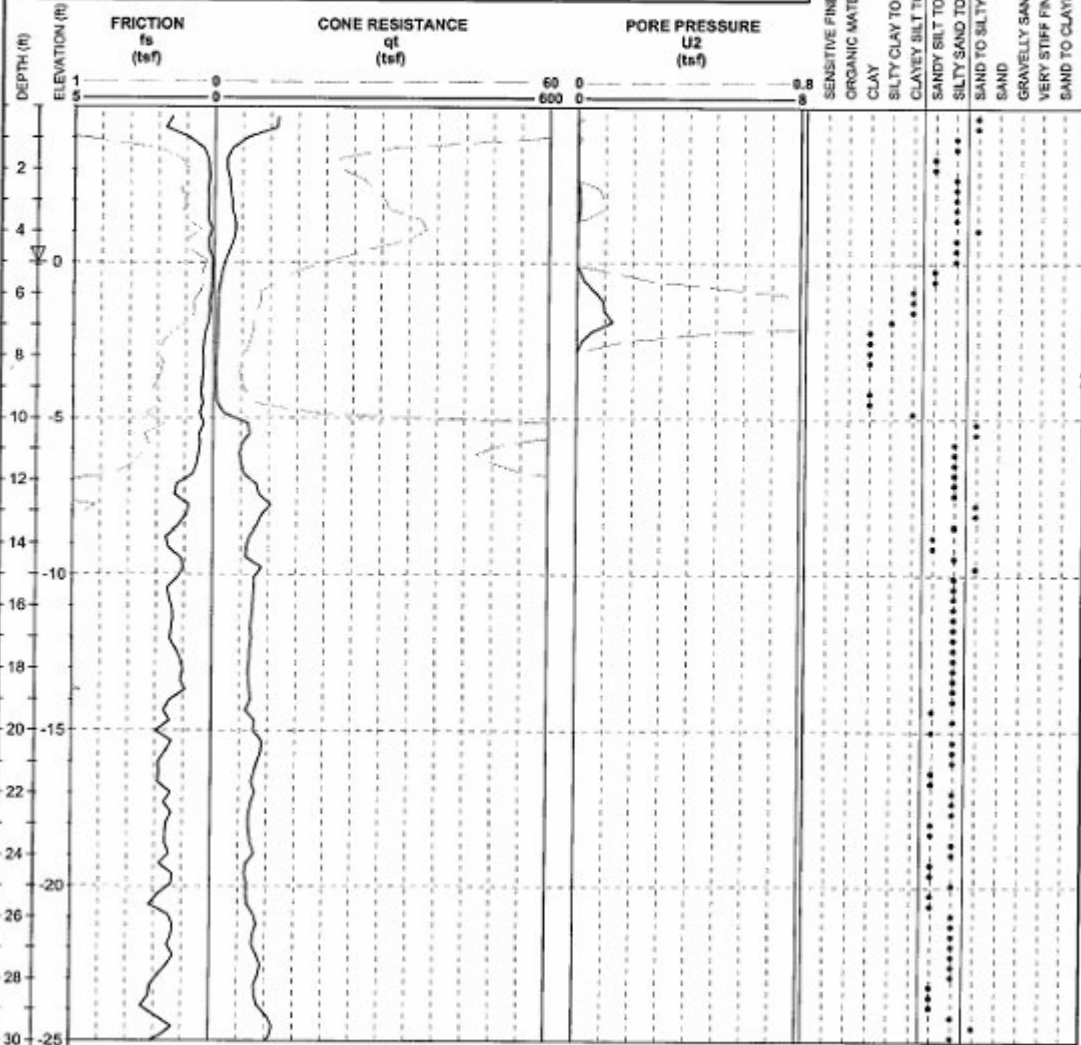
SURFACE ELEVATION: 5.0 ft

BENCHMARK LOCATION: None

DRILLER: VDOT
 CONE TYPE: Subtraction
 CONE SIZE: 10_sq_cm
 CONE ID No.: 771TC

DATE(S) DRILLED:
 8/16/2001 - 8/16/2001
 GROUNDWATER: 5 ft depth
 LOGGER: CBW

SOIL BEHAVIOR TYPE *



VDOT_CPTU-00001 8/16/2001 8/16/2001

REMARKS:
 Virginia_Tech_Pile_Tests

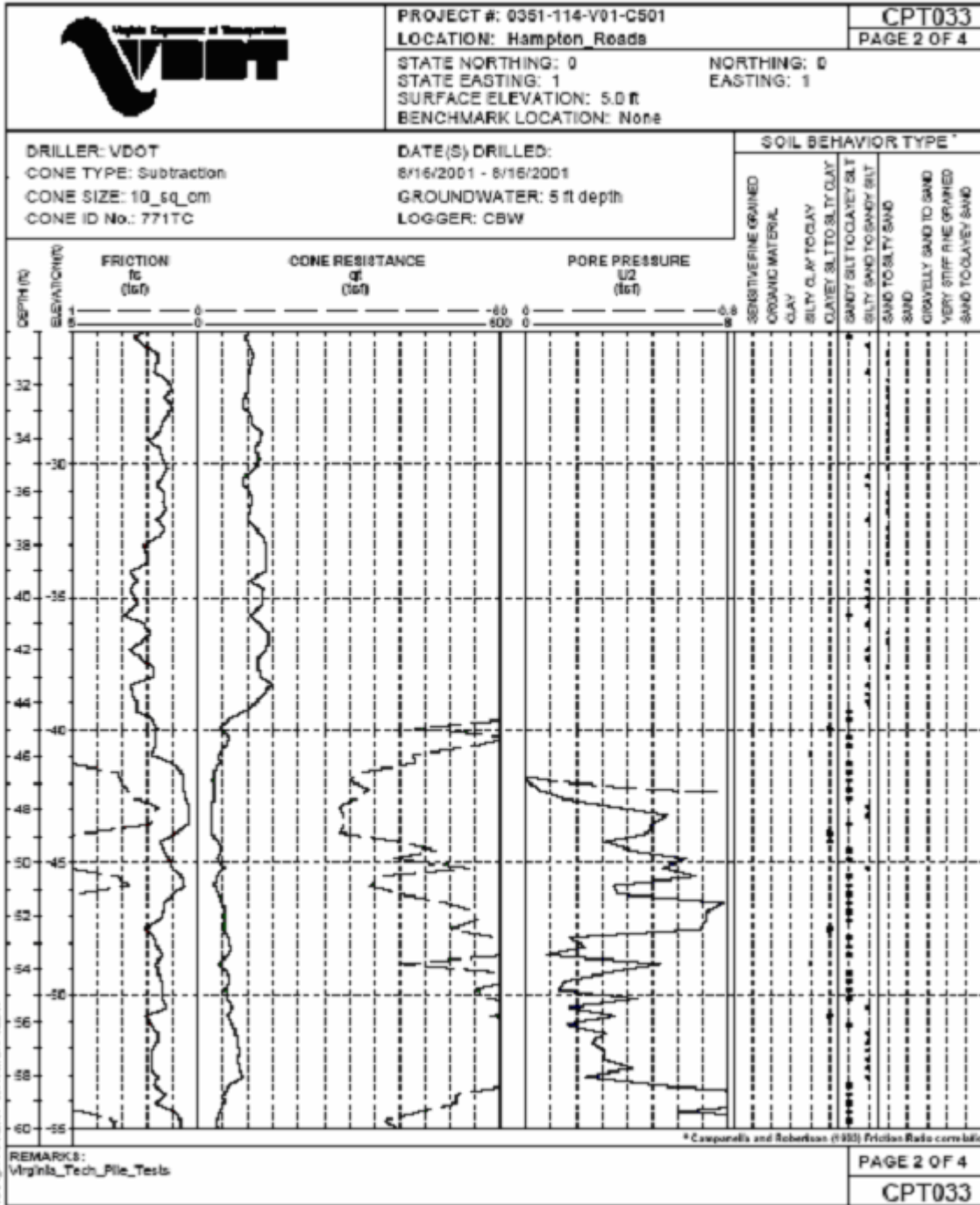
* Campanella and Robertson (1983) Friction Ratio correlation

PAGE 1 OF 4

CPT033

Figure 246. Chart. CPT033.

CONE PENETROMETER TEST LOG



REMARKS:
Virginia_Tech_Pile_Tests

Figure 246. Chart. CPT033—Continued

CONE PENETROMETER TEST LOG



PROJECT #: 0351-114-V01-C501

CPT033

LOCATION: Hampton Roads

PAGE 3 OF 4

STATE NORTHING: 0

NORTHING: 0

STATE EASTING: 1

EASTING: 1

SURFACE ELEVATION: 5.0 ft

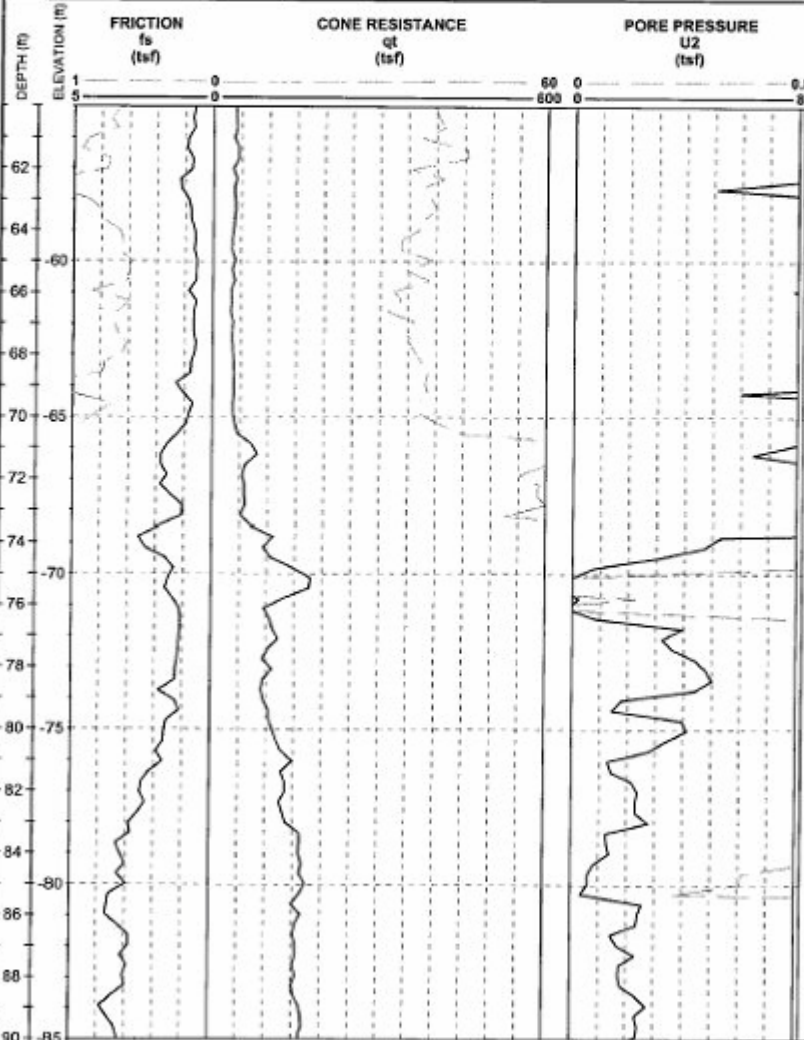
BENCHMARK LOCATION: None

DRILLER: VDOT
 CONE TYPE: Subtraction
 CONE SIZE: 10_sq_cm
 CONE ID No.: 771TC

DATE(S) DRILLED:
 8/16/2001 - 8/16/2001
 GROUNDWATER: 5 ft depth
 LOGGER: CBW

SOIL BEHAVIOR TYPE*

- SENSITIVE FINE GRAINED ORGANIC MATERIAL
- CLAY
- SILTY CLAY TO CLAY
- CLAYEY SILT TO SILTY CLAY
- SANDY SILT TO CLAYEY SILT
- SILTY SAND TO SANDY SILT
- SAND TO SILTY SAND
- SAND
- GRAVELLY SAND TO SAND
- VERY STIFF FINE GRAINED SAND TO CLAYEY SAND



VDOT_CPTU_062001_GINT033.GPJ 8/22/01

REMARKS:
 Virginia_Tech_Pile_Tests

* Campanella and Robertson (1983) Friction Ratio correlation

PAGE 3 OF 4

CPT033

Figure 246. Chart. CPT033—Continued

CONE PENETROMETER TEST LOG



PROJECT #: 0351-114-V01-C501

CPT034

LOCATION: Hampton Roads

PAGE 1 OF 3

STATE NORTHING: 0

NORTHING: 0

STATE EASTING: 1

EASTING: 1

SURFACE ELEVATION: 5.0 ft

BENCHMARK LOCATION: None

DRILLER: VDOT

DATE(S) DRILLED:

CONE TYPE: Subtraction

8/19/2001 - 8/16/2001

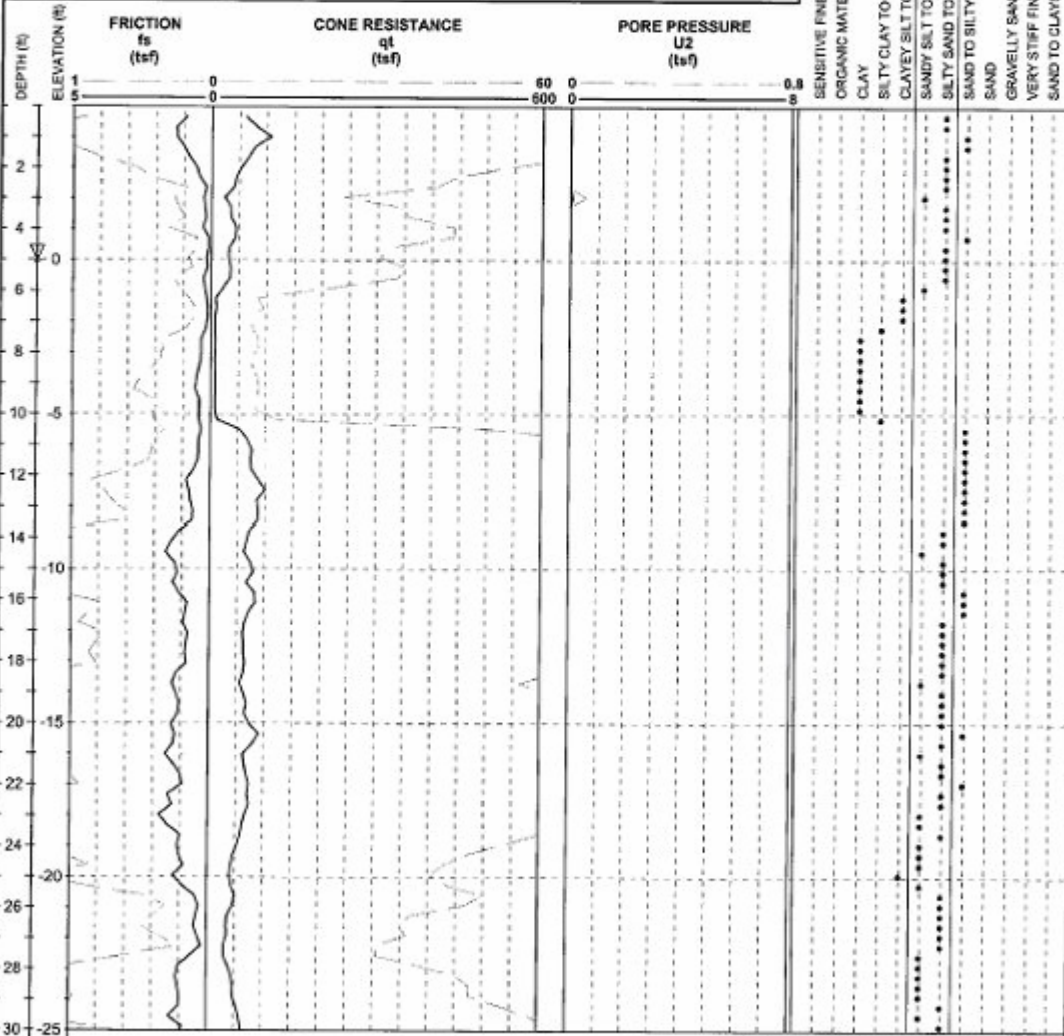
CONE SIZE: 10_sq_cm

GROUNDWATER: 5 ft depth

CONE ID No.: 771TC

LOGGER: CBW

SOIL BEHAVIOR TYPE*



VDOT CPTU-02001 GNT034.GPJ 8/22/01

REMARKS:
Virginia_Tech_Pile_Tests

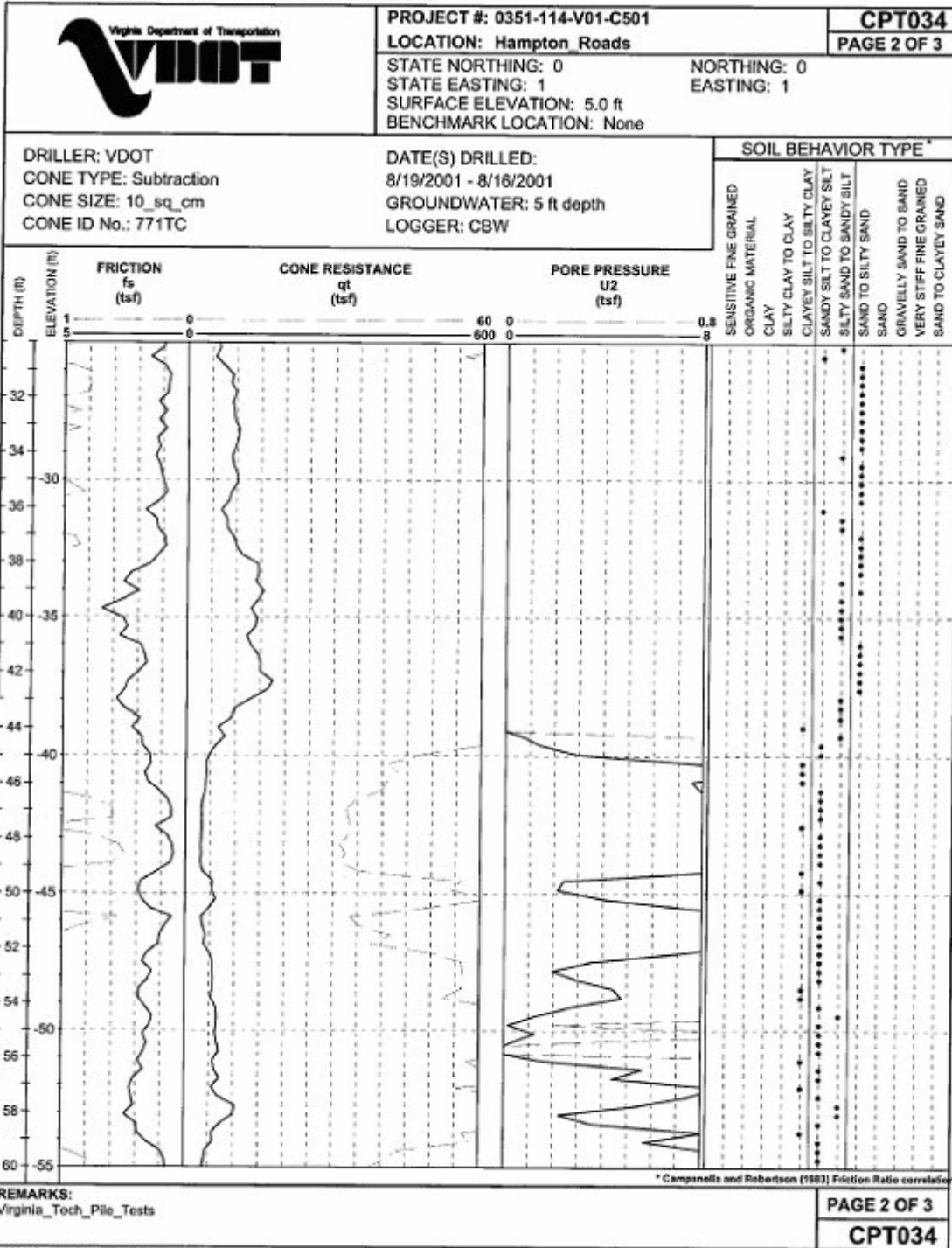
* Campanella and Robertson (1983) Friction Ratio correlation

PAGE 1 OF 3

CPT034

Figure 247. Chart. CPT034.

CONE PENETROMETER TEST LOG



VDOT_CPT034_082001_CPT034.GPJ 8/23/01
 © 2001, Commonwealth of Virginia

Figure 247. Chart. CPT034—Continued

CONE PENETROMETER TEST LOG

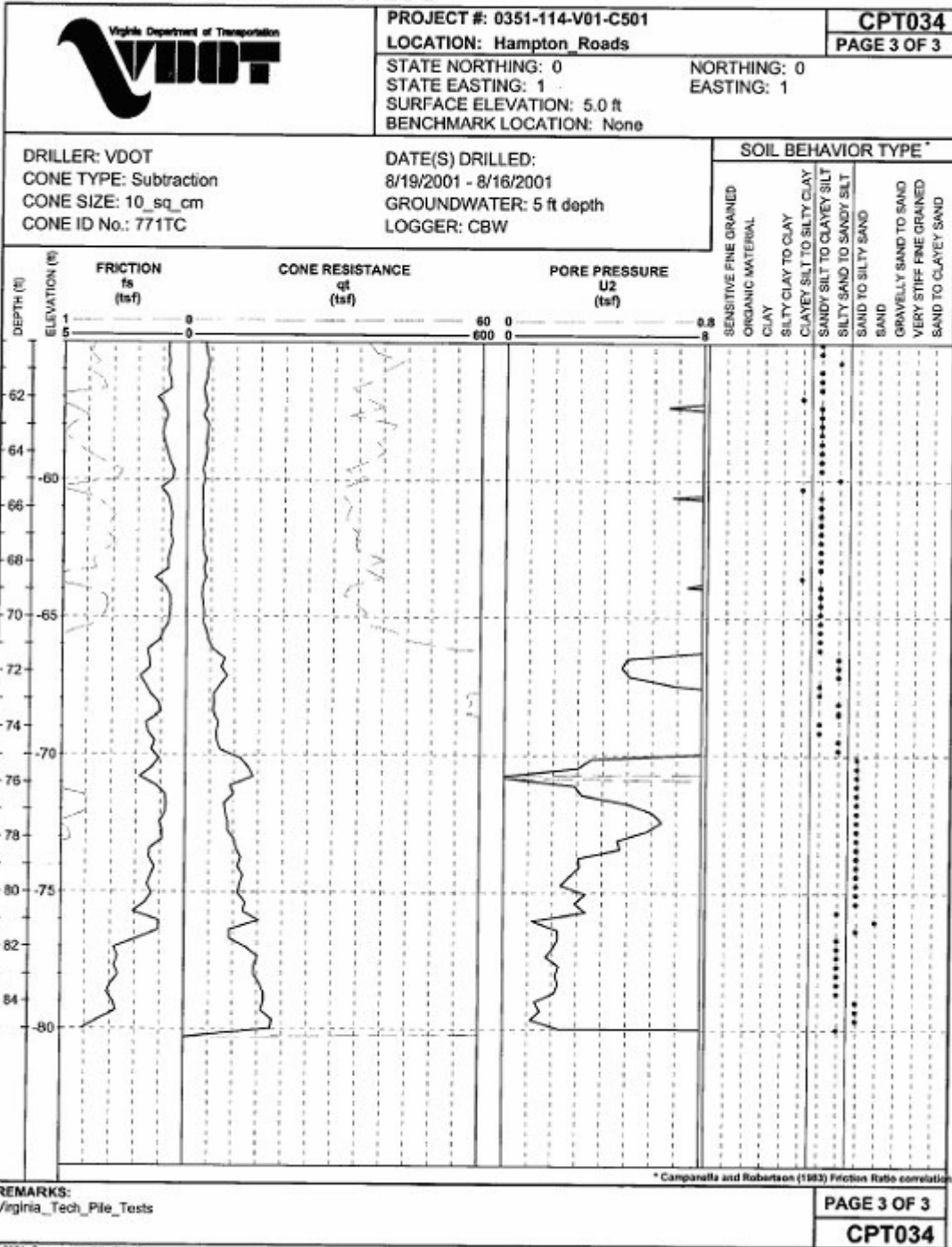


Figure 247. Chart. CPT034—Continued

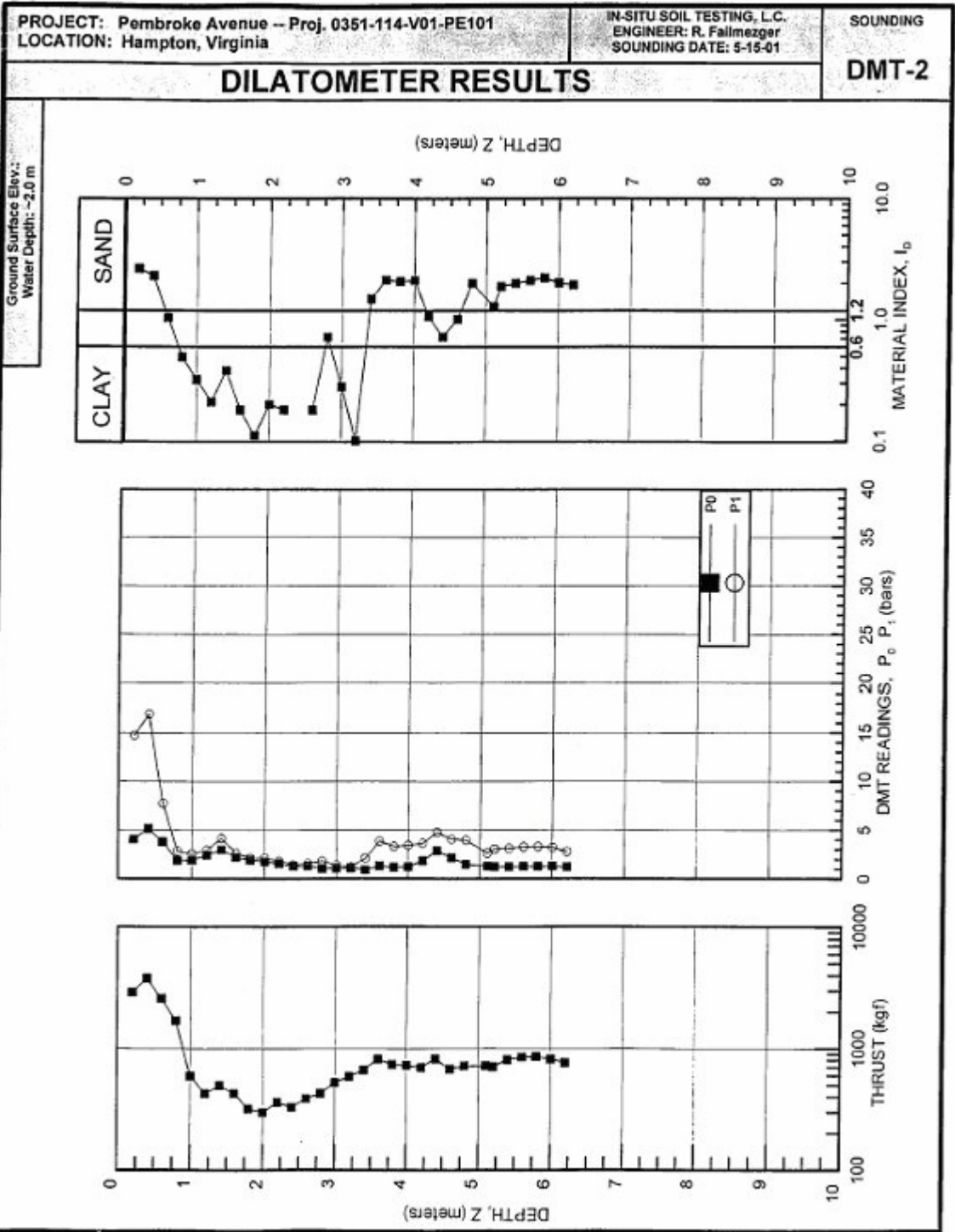


Figure 248. Chart. DMT.

REFERENCES

- American Society for Testing and Materials (ASTM). “Standard method of testing piles under axial compressive load.” *Annual Book of ASTM Standards*, D1143-81, 1994.
- American Society for Testing and Materials (ASTM). “Standard method of testing piles under lateral loads.” *Annual Book of ASTM Standards*, D3966-90, 1995.
- American Society for Testing and Materials (ASTM). “Standard test method for determining the coefficient of soil and geosynthetic or geosynthetic and geosynthetic friction by the direct shear method.” *Annual Book of ASTM Standards*, D5321-97, 1997.
- American Society for Testing and Materials (ASTM). “Standard test method for direct shear test of soils under consolidated drained conditions.” *Annual Book of ASTM Standards*, D3080-98, 1998.
- American Society for Testing and Materials (ASTM). “Standard test method for microindentation hardness of materials.” *Annual Book of ASTM Standards*, E384-99, 1999.
- American Society for Testing and Materials (ASTM). “Standard test method for determining the compressive properties of polymer matrix composite laminates using a combined loading compression test fixture.” *Annual Book of ASTM Standards*, D6641M-01e1, 2001.
- American Society for Testing and Materials (ASTM). “Standard test method for ignition loss of cured reinforced resins.” *Annual Book of ASTM Standards*, D2584-02, 2002.
- API. “Recommended practice for planning, designing and constructing fixed offshore platforms—Working stress design.” 20th Edition, American Petroleum Institute, Washington, DC, 1993.
- Asaro, R.J. “Three point bend test of plastic pilings hybrid HDPE/LDPE steel pile.” *Testing Report for Plastic Piling, Inc.*, 2000.
- Ashford, S.A., and W. Jakrapiyanun. “Drivability of Glass FRP Composite Piling.” *Journal of Composites for Construction*, 5(1), 2001, pp. 58–60.
- Ashour, M., and G. Norris. “Modeling lateral soil-pile response based on soil-pile interaction.” *Journal of Geotechnical and Geoenvironmental Engineering*, 126(5), 2000, pp. 420–428.

- Atkinson, J.H. "Non-linear soil stiffness in routine design." *Geotechnique*, 50(5), 2000, pp. 487–508.
- Baguelin, F., et al. "La capacité portante des pieux." *Annales Institut Technique du Bâtiment et des Travaux Publics*, France, No. 330, SF116, 1975, pp. 1–22.
- Baguelin, F., and R. Frank. "Theoretical studies of piles using the finite element method." Institution of Civil Engineers (ICE). *Numerical Methods in Offshore Piling*, London, 1983, pp. 83–91.
- Baldi, G., R. Bellotti, V.N. Ghionna, M. Jamiolkowski, and D.F.C. Lo Presti. "Modulus of sands from CPTs and DMTs." *Proceedings, 12th International Conference on Soil Mechanics Foundations*, Rio de Janeiro, Brazil, I, 1989, pp. 165–170.
- Ballinger, C. "Composites poised to make inroads as highway structural materials." *The Journal: Roads and Bridges*, April 1994, pp. 40–44.
- Bank, L.C. "Flexural and shear moduli of full-section fiber reinforced plastic (FRP) pultruded beams." *Journal of Testing and Evaluation*, 17(1), 1989, pp. 40–45.
- Becque, J., A.K. Patnaik, and S. Rizkalla. "Analytical models for concrete confined with FRP tubes." *Journal of Composites for Construction*, 7(1), 2003, pp. 31–38.
- Bond, A.J. "Behaviour of displacement piles in over-consolidated clays." PhD Thesis, University of London, London, UK, 1989.
- Boulon, M., and P. Foray. "Physical and numerical simulation of lateral shaft friction along offshore piles in sand." *Proceedings, 3rd International Conference on Numerical Methods in Offshore Piling*, Nantes, France, 1986, pp. 127–147.
- Bowles, J.E. *Foundation Analysis and Design*, 5th edition, McGraw-Hill, New York, NY, 1996.
- Brown, D.A. "An experiment with Statnamic lateral loading of a drilled shaft." GSP No. 88, Austin, Texas, 1999, pp. 309–318.
- Brown, D.A. "Evaluation of static capacity of deep foundations from Statnamic testing." *Geotechnical Testing Journal*, 17(4), 1994, pp. 403–414.
- Brown, D.A., S.A. Hidden, and S. Zhang. "Determination of P-Y curves using inclinometer data." *Geotechnical Testing Journal*, 17(2), 1994, pp. 150–158.
- Brown, D.A. (Unpublished paper). "Rapid lateral load testing of deep foundations."
- Bustamante, M., and L. Ganeselli. "Pile bearing capacity prediction by means of static penetrometer CPT." *Proceedings, 2nd European Symposium on Penetration Testing*, Amsterdam, The Netherlands, II, 1982, pp. 493–500.

- Chin, J.W., T. Nguyen, and K. Aouadi. "Effects of environmental exposure on fiber-reinforced plastic (FRP) materials used in construction." *Composites Technology & Research*, 19(4), 1997, pp. 205–213.
- Chin, S.T., and H.G. Poulos. "A T-Z approach for cyclic axial loading analysis of single piles." *Computers and Geotechnics*, 12, 1991, pp. 289–320.
- Chow, F.C. "Investigations into the behaviour of displacement piles for offshore foundations." PhD thesis, Imperial College of Science, Technology, and Medicine, University of London, London, UK, 1996.
- Chow, Y.K. "Analysis of vertically loaded pile groups." *International Journal for Numerical and Analytical Methods in Geomechanics*, 10, 1986, pp. 59–72.
- Chow, F.C., R.J. Jardine, J.F. Nauroy, and F. Bruzy. "Time-related increases in the shaft capacities of driven piles in sand." *Géotechnique*, 47(2), 1997, pp. 353–361.
- Coch, N.K. "Geology of the Bennis Church, Smithfield, Windsor and Cuckatuck Quadrangle, Virginia." Report of Investigations 17, Virginia Division of Mineral Resources, Department of Conservation and Economic Development, Charlottesville, VA, 1968.
- Coch, N.K. "Geology of the Newport News South and Bowers Hill Quadrangles, Virginia." Report of Investigations 28, Virginia Division of Mineral Resources, Department of Conservation and Economic Development, Charlottesville, VA, 1971.
- Collins, M.P., and D. Mitchell. *Prestressed concrete structures*. Response Publications, Toronto, Canada, 1997.
- Coyle, H.M., and L.C. Reese. "Load transfer for axially loaded piles in clay." *Journal of the Soil Mechanics and Foundation Division*, ASCE, 92(SM2), 1966, pp. 1–26.
- Coyle, H.M., and I.H. Sulaiman. "Skin friction for steel piles in sand." *Journal of the Soil Mechanics and Foundation Division*, ASCE, 93(SM6), 1967 pp. 261–278.
- Daniel, I.M., and O. Ishai. *Engineering mechanics of composite materials*. Oxford University Press, New York, 1994.
- Davis, D., and D. Hoy, "Fender piling." *Military Engineer*, 88(579), 1996, pp. 45–46.
- Davisson, M.T. "High capacity piles." *Proceedings, Soil Mechanics Lecture Series on Innovations in Foundation Construction*, ASCE, Chicago, 1972, pp. 81–112.
- Dawkins, W.P. "User's guide: Computer program for soil-structure interaction analysis of axially loaded pile (CAXPILE)." *Rep. K84-4*, U.S. Army Corps of Engineers, Waterways Experiment Station, Vicksburg, MS, 1982.

- dos Reis, H.L.M., and R.B. Goldman. "Thin-walled laminated composite cylindrical tubes: Part II-bending analysis." *Journal of Composites Technology & Research*, 9(2), 1987, pp. 53–57.
- Dove, J.E., J.D. Frost, J. Han, and R.C. Bachus. "The influence of geomembrane surface roughness on interface strength." *Proceedings, Geosynthetics '97*, Long Beach, CA, 1997, pp. 863–876.
- Dove, J.E., and J.D. Frost. "Peak interface friction behavior of smooth geomembrane-particle interfaces." *Journal of Geotechnical Engineering, ASCE*, 125(7), 1999, pp. 544–555.
- Dove, J.E., and J.C. Harpring. "Geometric and spatial parameters for analysis of geomembrane/soil interface behavior." *Proceedings, Geosynthetics '99*, International Fabrics Association International, Boston, MA, I, 1999, pp. 575–588.
- Dove, J.E., and J.B. Jarrett. "Behavior of dilative sand interfaces in a geotribology framework." *Journal of Geotechnical and Geoenvironmental Engineering, ASCE*, 128(1), 2002, pp. 25–37.
- Dudek, T.J. "Young's and shear moduli of unidirectional composites by a resonant beam method." *Journal of Composite Materials*, 4, 1970, pp. 232–241.
- Duncan, J.M., P. Byrne, K.S. Wong, P. Mabry. "Strength, stress-strain and bulk modulus parameters for finite element analyses of stresses and movements in soil masses." *Rep. VCB/GT/80-01*, Department of Civil Engineering, University of California, Berkeley, CA, 1980.
- Duncan, J.M., and C-Y. Chang. "Nonlinear analysis of stress and strain in soils." *Journal of Soil Mechanics Foundations Division, ASCE*, 96(SM5), 1970, pp. 1629–1653.
- Duncan, J.M., L.T. Evans, and P.S. Ooi. "Lateral load analysis of single piles and drilled shafts." *Journal of Geotechnical Engineering, ASCE*, 120(6), 1994, pp. 1018–1033.
- Ehlen, M.A. "Life-cycle costs of fiber-reinforced-polymer bridge decks." *Journal of Material and Civil Engineering*, 11(4), 1999, pp. 224–230.
- El Naggar, M.H. "Interpretation of lateral Statnamic load test results." *Geotechnical Testing Journal*, 21(3), 1998, pp. 169–179.
- Elghazouli, A.Y., M.K. Chryssanthopoulos, and A. Spagnoli. "Experimental response of glass-reinforced plastic cylinders under axial compression." *Marine Structures*, 11(1998), 1998, pp. 347–371.
- El-Tawil, S., and G. Deierlein. "Strength and ductility of concrete encased composite columns." *Journal of Structural Engineering*, 125(9), 1999, pp. 1009–1019.

- Ensoft. *APILE Plus Version 3.0—A program for the analysis of the axial capacity of driven piles*. Ensoft, Inc., Austin, TX, 1998.
- Eustis Engineering Co., Inc. “Dynamic pile testing, Port of New Orleans, Composite Marine Pilings, Nashville Avenue “C” Wharf, New Orleans, LA.” *Report for Seaward International, Inc.*, Metairie, LA, 1996.
- Evans, L.T., and J.M. Duncan. “Simplified analysis of laterally loaded piles.” *UCB/GT/82-04*, University of California, Berkeley, CA, 1982.
- Fahey, M., and J.P. Carter. “A finite element study of the pressuremeter test in sand using a non-linear elastic-plastic model.” *Canadian Geotechnical Journal*, 30(2), 1993 pp. 348–362.
- Fahey, M., R.K. Robertson, and A.A. Soliman. “Towards a rational method of predicting settlement of spread footings on sand.” *Geotechnical Special Publication No. 40*, ASCE, I, 1994, pp. 598–611.
- Fam, A. “Concrete-filled fiber-reinforced polymer tubes for axial and flexural structural members.” PhD Dissertation, University of Manitoba, Canada, 2000.
- Fam, A.Z., and S.H. Rizkalla. “Concrete-filled FRP tubes for flexural and axial compression.” *Proceedings, 3rd International Conference on Advanced Composite Materials in Bridges and Structures*, Ottawa, Canada, 2000, pp. 315–322.
- Fam, A.Z., and S.H. Rizkalla. “Behavior of axially loaded concrete-filled circular fiber-reinforced polymer tubes.” *ACI Structural Journal*, 98(3), 2001a, pp. 280–289.
- Fam, A.Z., and S.H. Rizkalla. “Confinement model for axially loaded concrete confined by FRP tubes.” *ACI Structural Journal*, 98(4), 2001b, pp. 251–461.
- Fam, A.Z., and S.H. Rizkalla. “Flexural behavior of concrete-filled fiber-reinforced polymer circular tubes.” *Journal of Composites for Construction, ASCE*, 6(2), 2002, pp. 123–132.
- Fam, A.Z., D. Schnerch, and S.H. Rizkalla. “Moisture Effect on Durability of Concrete-Filled GFRP Tubular Piles.” NCSU-CFL Report No. 02-04, North Carolina State University, 2002.
- Fam, A.Z., M.A. Pando, G. Filz, and S.H. Rizkalla. “Precast Piles for Route 40 Bridge in Virginia Using Concrete Filled FRP Tubes,” *PCI Journal*, Precast/Prestressed Concrete Institute, 48(3), May–June 2003, pp. 32–45.
- Fardis, M.N., and H. Khalili. “Concrete encased in fiberglass plastic.” *ACI Proceedings*, 78, Document JL78-38, 1981, pp. 440–446.

- Fellenius, B.H. "Guidelines for interpretation and analysis of the static loading test." *Report, Deep Foundation Institute*, 1990.
- Fellenius, B.H. "From strain measurements to load in an instrumented pile." *Geotechnical News*, March 2003, pp. 35–38.
- Fellenius, B.H. "Determining the true distributions of load in instrumented piles." 2002.
- Fleming, W.G.K. "A new method for single pile settlement prediction and analysis." *Geotechnique*, 42(3), 1992, pp. 411–425.
- Frank, R. "Etude théorique du comportement des pieux sous charge verticales: Introduction de la dilatance." Dr-Ing thesis, Université Pierre et Marie Curie, France, 1974.
- Frost, J.D., and J. Han. "Behavior of interfaces between fiber-reinforced polymers and sands." *Journal of Geotechnical and Geoenvironmental Engineering*, ASCE, 125(8), 1999, pp. 633–640.
- Frye, K. *Roadside Geology of Virginia*. Mountain Press Publishing Company, VA, 1986.
- Garcia, K., M.D. Hayes, N. Verghese, and J.J. Lesko. "The effects of cycling moisture aging on glass/vinyl ester composite system." *Proceedings, 3rd International Conference on Progress in Durability Analysis of Composite Systems*, 1998, pp. 173–179.
- Goble, G.G., F. Rausche, and G. Likins. "Discussion on evaluation of static capacity of deep foundations from Statnamic testing." *Geotechnical Testing Journal*, 18(4), 1995, pp. 493–498.
- Gómez, J.E., G.M. Filz, and R.M. Ebeling. "Development of an improved numerical model for concrete-to-soil interfaces in soil-structure interaction analyses." *Rep. ITL-99-1*, U.S. Army Engineer Research and Development Center, Vicksburg, MS, 2000.
- Guo, W.D., and M.F. Randolph. "An efficient approach for settlement prediction of pile groups." *Geotechnique*, 49(2), 1999, pp. 161–179.
- Gurtin, M.E., and C. Yatomi. (1979). "On a model for two phase diffusion in composite materials." *Journal of Composite Materials*, 13, 1979, pp. 126–130.
- Han, J. "An experimental and analytical study of the behavior of fiber-reinforced polymer piles and pile-sand interactions." PhD dissertation, Georgia Tech, Atlanta, GA, 1997.
- Han, J. and J. Frost. "An experimental and analytical study of the behavior of fiber-reinforced polymer piles and pile-sand interactions." *NSF Research Report*, Arlington, VA, 1997.

- Han, J., J.D. Frost, and V.L. Brown. "Design of fiber-reinforced polymer composite piles under vertical and lateral loads." *TRB 2003 Annual Meeting*, CD-ROM, 2003, 21 pp.
- Hannigan, P.J., G.G. Goble, G. Thendeau, G.E. Likins, and F. Rausche, F. "Design and construction of driven piles." *Rep. No. FHWA-HI-96-033*, FHWA, Washington, DC, 1996.
- Hardcore Composites. 2001. <http://www.hardcorecomposites.com>.
- Harmon, T.G., P.L. Gould, E. Wang, and S. Ramakrishnan. "Behavior of confined concrete under cyclic loading." *Proceedings, Composites in Infrastructure; 2nd International Conference*, Tucson, AZ, pp. 398–410.
- Heinz, R. "Plastic piling." *Civil Engineering* (April), 1993, pp. 63–65.
- Helmers, M.J., J.M. Duncan, and G.M. Filz. "Use of ultimate load theories for design of drilled shaft sound wall foundations." The Charles E. Via, Jr. Department of Civil Engineering, Virginia Tech, Blacksburg, VA, 1997.
- Hetyenyi, M. *Beams on elastic foundation*. University of Michigan Press, Ann Arbor, MI, 1946.
- Hoit, M., C. Hays, M. McVay, and M. William, M. "FB-Pier v. 2.0." Florida Bridge Software Institute, 2000. <http://bsi-web.ce.ufl.edu>.
- Holzer, S.M. "Finite element analysis of structure." Course notes for CE5414, Virginia Tech, Blacksburg, VA, 2001.
- Horeczko, G. "Marine application of recycled plastics." *Proceedings, Structures Congress XIII, Restructuring: America and Beyond*, ASCE, Boston, MA, I, 1995, pp. 934–938.
- Hoy, D. "Study of recycled plastic fender piles." *TM-2158-SHR*, Naval Facilities Engineering Service Center, Port Hueneme, CA, 1995.
- Hoy, D., G. Warren, and D. Davis. "Environmentally acceptable piling for use in Navy pier fender systems." *Proceedings, 4th Materials Engineering Conference*, Washington, DC, 1996, pp. 1189–1198.
- Hryciw, R.D., and Irsyam, M. "Behavior of sand particles around rigid ribbed inclusions during shear." *Soils and Foundations*, 33(3), 1993, pp. 1–13.
- Irsyam, M., and R.D. Hryciw. "Friction and passive resistance in soil reinforced by plane ribbed inclusions." *Géotechnique*, 41(4), 1991, pp. 485–498.
- Ishihara, K. *Soil behaviour in earthquake geotechnics*, Clarendon Press, Oxford, UK, 1996.

- Iskander, M., and M. Hassan. "State of the practice review in FRP composite piling." *Journal of Composites for Construction, ASCE*, 2(3), 1998, pp. 116–120.
- Iskander, M., and M. Hassan. "Accelerated degradation of recycled plastic piling in aggressive soils." *Journal of Composites for Construction, ASCE*, 5(3), 2001, pp. 179–187.
- Iskander, M.G., S. Hanna, and A. Stachudsla. "Driveability of FRP Composite Piling," *Journal of Geotechnical and Geoenvironmental Engineering*, 127(2), 2001, pp. 169–176.
- Iskander, M., A. Mohamed, and S. Sadek. "Compressive strength of foamed polymer piling." *Proceedings, TRB 2003 Annual Meeting*, CD-ROM, 2003, 25 p.
- Iskander, M.G., and A. Stachula. "FRP composite polymer piling: An alternative to timber piling for water-front applications." *Geotechnical News*, 4, December 1999, pp. 27–29.
- Iskander, M.G., and A. Stachula. "Wave equation analyses of Fiber-Reinforced Polymer Composite Piling." *Journal of Composites for Construction, ASCE*, 6(2), 2002, pp. 88–96.
- ISO. "Geometrical product specification (GPS)-surface texture: profile method-terms, definitions, and surface texture parameters." ISO Standard 4287, International Organization for Standardization, Geneva, Switzerland, 1997.
- Iyer, S. "Fiber reinforced polymer (FRP) tubes for pile/column applications." *The Indian Concrete Journal*, 75(1), 2001, pp. 65–70.
- Iyer, S.L., S. Ramabhadran, and B.S. Vulcan. "Field testing and evaluating carbon prestressed pile." *Proceedings, 4th Materials Engineering Conference*, Washington, DC, 1996, pp. 386–393.
- Jardine, R.J. "Investigations of pile-soil behaviour with special reference to the foundations of offshore structures." PhD dissertation, Imperial College of Science, Technology and Medicine, University of London, London, UK, 1985.
- Jardine, R.J., and F.C. Chow. "New design methods for offshore piles." *Report MTD 96/103*, Marine Technology Directorate Report, London, UK, 1996.
- Jardine, R.J., and B.M. Lehane. "Research into the behaviour of offshore piles: Field experiments in sand and clay." *Report OTH 93-401*, Health and Safety Executive, London, UK, 1993.
- Johnson, G.H. "Geology of the Yorktown, Poquoson West, and Poquoson East Quadrangles, Virginia." Report of Investigations 30, Virginia Division of Mineral Resources, Department of Conservation and Economic Development, Charlottesville, VA, 1972.

- Johnson, G.H. "Geology of the Mulberry Island, Newport News North, and Hampton Quadrangles, Virginia." Report of Investigations 41, Virginia Division of Mineral Resources, Department of Conservation and Economic Development, Charlottesville, VA, 1976.
- Johnson, M.L. "Characterization of geotechnical surfaces via stylus profilometry." MSc Thesis, Georgia Tech, Atlanta, GA, 2000.
- Kanatharana, J., and L-W. Lu. "Strength and ductility of concrete columns reinforced by FRP tubes." *Proceedings, Composites in Infrastructure; 2nd International Conference*, Tucson, AZ, pp. 320–384.
- Karbahari, V.M. "Response of fiber reinforced polymer confined concrete exposed to freeze and freeze-thaw regimes." *Journal of Composites for Construction*, 6(1), 2002, pp. 35–40.
- Karbahari, V.M., and D.A. Eckel. "Strengthening of concrete column stubs through resin infused composite wraps." *Journal of Thermoplastic Composite Materials*, 6(2), 1993, pp. 92–107.
- Karbahari, V.M., K. Murphy, and S. Zhang. "Effect of concrete based alkali solutions on short-term durability of E-glass/vinylester composites." *Journal of Composite Materials*, 36(17), 2002, pp. 2101–2121.
- Kishida, H., and M. Uesugi. "Tests of the interface between sand and steel in the simple shear apparatus." *Géotechnique*, 37(1), 1987, pp. 45–52.
- Knowles, R.B., and R. Park. "Axial load design for concrete filled steel tubes." *Journal of the Structural Division*, ASCE, 96(ST10), 1970, pp. 2125–2153.
- Kondner, R.L. "Hyperbolic stress-strain response: Cohesive soils." *Journal of the Soil Mechanics and Foundations Division*, ASCE, 89(SM1), 1963, pp. 115–143.
- Kondner, R.L., and J.S. Zelasko. "A hyperbolic stress-strain formulation for sands." *Proceedings, 2nd Pan-American Conference on Soil Mechanics and Foundations Engineering*, Sao Paulo, Brazil, I, 1963, pp. 289–324.
- Kozera, D.W. "Dynamic pile testing services, fiberglass/concrete composite piling." Lancaster Composite, Inc., Lancaster, PA, 1996.
- Kozera, D.W. "Pile installation and load test report, Hardcore Test Program, New Castle, DE." *Report DWK#97059*, Baltimore, MD, 1997.
- Kraft, L.M. "Performance of axially loaded pipe piles in sand." *Journal of Geotechnical Engineering*, ASCE, 117(2), 1991, pp. 272–296.
- Kraft, L.M., R.P. Ray, and T. Kagawa. "Theoretical T-Z curves." *Journal of Geotechnical Engineering*, ASCE, 107(11), 1981, pp. 1543–1561.

- Lampo, R. "Federal interest gives recycled plastic lumber a leg up." *ASTM Standardization News*, 1996, pp. 26–31.
- Lampo, R., A. Maher, J.P. Busel, and R. Odello. "Design and development of FRP composite piling systems." *Proceedings, International Composites Expo 1997*, Nashville, TN, 16-C.
- Lampo, R., T. Nosker, D. Barno, J. Busel, A. Maher, P. Dutta, and R. Odello. "Development and demonstration of FRP composite fender, loadbearing, and sheet piling systems." *USACERL TR-98/123*, U.S. Army Corps of Engineers (CERL), 1998.
- Lampo, R.G. "Recycled plastics as engineered materials." *Proceedings, Structures Congress XIII*, Boston, MA, 1995, pp. 815–818.
- Lancaster Composite. "Technical manual." 1999. <http://www.lancastercomposite.com>.
- Lehane, B.M. "Experimental investigations of pile behavior using instrumented field piles." PhD Thesis, University of London, London, UK, 1992.
- Lehane, B.M., R.J. Jardine, A.J. Bond, and R. Frank. "Mechanisms of shaft friction in sand from instrumented pile tests." *Journal of Geotechnical Engineering*, ASCE, 119(1), 1993, pp. 19–35.
- Lindsay, K. "Composite piling market heats up." *Composite Design & Application*, SPI-Composite Institute, 1996, pp. 12–13.
- LPILE Plus 4.0M. "A program for the analysis of piles and drilled shafts under lateral loads." By L. Reese, S.T. Wang, J.A. Arrellaga, and J. Hendrix, ENSOFT, Inc., Houston, TX, 2000.
- Lunne, T., P.K. Robertson, and J.J.M. Powell. *Cone penetration testing in geotechnical practice*. Blackie Academic and Professional, New York, 1997.
- Maher, M.H., N. Gucunski, Y.S. Chae, and R. Lampo. "Composite fender and sheet piles in marine front systems." *Proceedings, Composites in Infrastructure*, Tucson, AZ, 1996, pp. 665–675.
- Mander, J.B., M.J.N. Priestly, and R. Park. "Theoretical stress-strain model for confined concrete." *Journal of Structural Engineering*, ASCE, 114(8), 1988, pp. 1804–1826.
- March, F.A., and M.T. Colturi. "Market advancement for composite marine piling and timber." *Proceedings, Ports '98*, Long Beach, CA, 1998, pp. 824–829.
- Martin, R.E., J.J. Seli, G.W. Powell, and M. Bertoulin. "Concrete pile design in Tidewater Virginia." *Journal of Geotechnical Engineering*, ASCE, 113(6), 1987, pp. 568–585.

- Matlock, H. "Correlations for design of laterally loaded piles in soft clay." *Proceedings, Offshore Technology Conference*, Houston, TX, I, 1970, pp. 557–594.
- McBagonluri, F., K. Garcia, M. Hayes, N. Verghese, and J.J. Lesko. "Characterization of fatigue and combined environment on durability performance of glass/vinyl ester composite for infrastructure applications." *International Journal of Fatigue*, 22(1), 2000, pp. 53–64.
- McVay, M.C., F.C. Townsend, D.G. Bloomquist, M.O. O'Brien, and J.A. Caliendo. "Numerical analysis of vertically loaded pile groups." *Proceedings, Foundation Engineering Congress: Current Principles and Practices*, Evanston, IL, 1989, pp. 675–690.
- Meadors, G.S., Jr. "The geology and construction techniques of the second Hampton Roads crossing, Norfolk, Virginia." *Proceedings, 28th Annual Highway Geology Symposium*, Rapid City, SD, 1977, pp. 61–82.
- Meiarashi, S., I. Nishizaki, and T. Kishima. "Life-cycle cost of all-composite suspension bridge." *Journal of Composites for Construction*, 6(4), 2002, pp. 206–214.
- Middendrop, P., P. Berminghammer, and B. Kuiper. "Statnamic load testing of foundation piles," *Proceedings, 4th International Conference of Applications of Stress-wave Theory to Piles*, The Hague, The Netherlands, 1992, pp. 581–588.
- Mirmiran, A. "FRP-encased concrete piles—Phase III." *Rep. No. FDOT-WPI 0510700*, Florida DOT, January 1999.
- Mirmiran, A., and M. Shahawy. "A new concrete-filled hollow FRP composite column." *Composites Part B: Engineering*, Elsevier, 27B(3-4), 1996, pp. 263–268.
- Mirmiran, A., and M. Shahawy. "Behavior of concrete columns confined by fiber composites." *Journal of Structural Engineering*, ASCE, 123(5), 1997, pp. 583–590.
- Mirmiran, A., and M. Shahawy. "Comparison of over- and under-reinforced concrete-filled FRP tubes." *Proceedings, 13th ASCE Engineering Mechanics Division Conference*, Baltimore, MD, 1999.
- Mirmiran, A., M. Shahawy, and M. Samaan. "Strength and ductility of hybrid FRP-concrete beam-columns." *Journal of Structural Engineering*, 125(10), 1999, pp. 1085–1093.
- Mirmiran, A., M. Shahawy, and T. Beitleman. "Slenderness limit for hybrid FRP-concrete columns." *Journal of Composites for Construction*, 5(1), 2001, pp. 26–34.
- Mirmiran, A., M. Shahawy, C. El Khoury, and W. Naguib. "Large beam-column tests on concrete-filled composite tubes." *ACI Structural Journal*, 97(2), 2000, pp. 268–276.

- Mirmiran, A., Y. Shao, and M. Shahawy. "Analysis and field tests on the performance of composite tubes under pile driving impact." *Composite Structures*, 55, 2002, pp. 127–135.
- Miura, N. "Point resistance of piles in sand." *Proceedings, 11th International Conference on Soil Mechanics and Foundation Engineering*, San Francisco, CA, III, 1985, pp. 1445–1448.
- Miyauchi, K., S. Nishibayashi, and S. Inoue. "Estimation of strengthening effects with carbon fiber sheet for concrete columns." *Proceedings, 3rd International Symposium, Non-Metallic (FRP) Reinforcement for Concrete Structures*, I, 1997, pp. 217–224.
- Mokwa, R.L., J.M. Duncan, and M.J. Helmers. "Deflections and bending moments in drilled shaft sound wall foundations under working load conditions." The Charles E. Via, Jr. Department of Civil Engineering, Virginia Tech, Blacksburg, VA, 1997.
- Moran, D.A., and C.P. Pantelides. "Variable strain ductility ratio for fiber-reinforced polymer-confined concrete." *Journal of Composites for Construction*, 6(4), 2002a, pp. 224–232.
- Moran, D.A., and C.P. Pantelides. "Stress-strain model for fiber-reinforced polymer-confined concrete." *Journal of Composites for Construction*, 6(4), 2002b, pp. 233–240.
- Mosher, R.L. "Load transfer criteria for numerical analysis of axially loaded piles in sand." U.S. Army Engineering Waterways Experimental Station, Automatic Data Processing Center, Vicksburg, MS, 1984.
- Muchard, M.K., A.G. Mullins, and D.T. Robertson. "Pile load test program—Route 40 over the Nottoway River." *AFT Report No. 195011*, Applied Foundation Testing, Inc., Green Cove Springs, FL, 1999.
- Murchison, J.M., and M.W. O'Neill. "Evaluation of p-y relationships in cohesionless soils." *Proceedings, Symposium of Analysis and Design of Pile Foundations*, ASCE, San Francisco, CA, 1984, pp. 174–191.
- Naguib, W., and A. Mirmiran. "Time-dependent behavior of fiber-reinforced polymer-confined concrete columns under axial loads." *ACI Structural Journal*, 99(2), 2002, pp. 142–148.
- Navayogarah, N., and S. Chandra. "Analysis of axially loaded long piles." *Indian Geotechnical Journal*, 15(4), 1985, pp. 231–245.
- Necati Özişik, M. *Boundary value problems of heat conduction*. Dover Publications, New York, 1989.

- Nilson, A.H. *Design of prestressed concrete*, 2nd edition. John Wiley and Sons, Inc., 1987.
- Nishizaki, I., and S. Meiarashi. "Long-term deterioration of GFRP in water and moist environment." *Journal of Composites for Construction*, ASCE, 6(1), 2002, pp. 21–27.
- Nordlund, R.L. "Point bearing and shaft friction of piles in sand." *Proceedings, 5th Annual Fundamentals of Deep Foundation Design*, Missouri-Rolla, MO, 1979.
- Nordlund, R.L. "Bearing capacity of piles in cohesionless soils." *Journal of Soil Mechanics and Foundations Division*, ASCE, SM3, 1963, pp. 1–35.
- Nyman, K.J. "Field load tests of interpreted drilled shafts in coral limestone." M.S. Thesis, University of Texas at Austin, 1980, 181 pp.
- Oaks, R.Q., Jr., and N.K. Coch. "Post-miocene stratigraphy and morphology, South-Eastern Virginia." *Bulletin 82*, Virginia Division of Mineral Resources, Department of Conservation and Economic Development, Charlottesville, VA, 1973.
- Olson, R.E. "Axial load capacity of driven piles." *Proceedings, 50th Annual Geotechnical Engineering Conference*, St. Paul, MN, 2002, pp. 161–178.
- O'Neill, M.W. "Side resistance in piles and drilled shafts." *Journal of Geotechnical and Geoenvironmental Engineering*, ASCE, 127(1), 2001, pp. 3–16.
- Ooi, P., J. Duncan, K.B. Rojiani, and R. Barker. "Engineering manual for driven piles." *NCHRP Report No. 343*, TRB, Washington, DC, II, 1991, pp. 54–114.
- O'Rourke, T.D., S.J. Druschel, and A.N. Netravali. "Shear strength characteristics of sand-polymer interfaces." *Journal of Geotechnical Engineering*, ASCE, 116(3), 1990, pp. 451–469.
- Ortigao, J.A.R. "FRP applications in geotechnical engineering." *Proceedings, 4th Materials Engineering Conference*, Washington, DC, 1996, pp. 535–544.
- Pando, M., G. Filz, J. Dove, and E. Hoppe. "Interface shear tests on FRP composite piles." *Proceedings, ASCE International Deep Foundations Congress*, Orlando, FL, II, 2002a, pp. 1486–1500.
- Pando, M., G. Filz, C. Ealy, and E. Hoppe. "Axial and lateral load performance of two composite piles and one prestressed concrete pile." *Proceedings, TRB 2003 Annual Meeting*, CD-ROM, 2003, 20 pp.
- Pando, M., G. Filz, E. Hoppe, C. Ealy, and M. Muchard. "Performance of a composite pile in a full scale Statnamic load testing program." *Proceedings, 53rd Canadian Geotechnical Conference*, Montreal, Canada, I, 2000, pp. 909–916.

- Pando, M., J.J. Lesko, and S. Case. "Preliminary Development of a Durability Model for concrete-filled FRP piles." *Proceedings, 46th International Society for the Advancement of Material and Process Engineering (SAMPE) Conference*, Long Beach, CA, 2001, pp. 1597–1611.
- Pando, M., J.J. Lesko, A. Fam, and S. Rizkalla. "Durability of Concrete-filled Tubular FRP Piles." *Proceedings, 3rd International Conference on Composites in Infrastructure (ICCI) Conference*, San Francisco, CA, CD-ROM, 2002b, 12 pp.
- Pando, M.A., D.A. Brown, and G. Filz. "Performance of a laterally loaded composite pile at the Nottoway River Bridge," *ASCE Geotechnical Special Publications*, issue 126; *Proceedings of Geo-Trans 2004 (Geotechnical Engineering for Transportation Projects)*, Los Angeles, CA, I, 2004, 10 pp.
- PCI Committee Report. "Recommended practice for design, manufacture, and installation of prestressed concrete piling." *PCI Journal*, 38(2), 1999, pp. 14–41.
- Pelletier, J.H., J.D. Murff, and A.G. Young. "Historical development and assessment of the current API design methods for axially loaded piles." *Proceedings, 25th Offshore Technology Conference*, Houston, TX, 1993, pp. 253–282.
- Phair, M. "Composite piles gaining ground." *ENR*, 238(1), 17, 1997.
- Phifer, S., and J.J. Lesko. "Moisture absorption and strength characterization of hygrothermally aged neat and clay filled vinyl ester and pultruded vinyl ester e-glass laminates." *Proceedings, CDCC 2002*, Montreal, Canada, 12 pp.
- Phifer, S.P. "Hygrothermal evaluation of pultruded polymer composite laminates—Experimentation, analysis, and prediction." PhD dissertation, Department of Engineering Science and Mechanics, Virginia Tech, Blacksburg, VA, 2003.
- Phifer, S.P., K.N.E. Verghese, J. Haramis, and J.J. Lesko. "Temperature-moisture-mechanical response of vinyl ester resin and pultruded vinyl ester/e-glass laminated composites." *Proceedings, 3rd International Conference on Advanced Composite Materials in Bridges and Structures*, Ottawa, Canada, 2000, pp. 29–36.
- Pianka, R. "Composite fender piling." *The Military Engineer*, 90(594), 1998, pp. 45–46.
- Plastic Pilings, Inc. 2001. <http://www.plasticpilings.com>.
- Polyzois, D., S. Ibrahim, and J.G. Raftoyiannis. "Performance of fiber-reinforced plastic tapered poles under lateral loading." *Journal of Composite Materials*, 33(10), 1999, pp. 941–960.
- Poskitt, T.J. "Discussion on 'A new method for single pile settlement prediction and analysis' by Fleming (1992) *Geotechnique* 42(3)." *Geotechnique*, 43(4), 1993, pp. 615–619.

- Poulos, H.G. "Modified calculation of pile group settlement interaction." *Journal of Geotechnical Engineering*, ASCE, 114(6), 1988, pp. 697–705.
- Poulos, H.G. "Pile behaviour—theory and application." *Geotechnique*, 39(3), 1989, pp. 365–415.
- Poulos, H.G. "Pile foundations." In *Geotechnical and Geoenvironmental Engineering Handbook*, Edited R.K. Rowe, Kluwer Academic Press, 2001.
- Poulos, H.G. "Settlement of single piles in nonhomogeneous soil." *Journal of Geotechnical Engineering*, ASCE, 105(5), 1979, pp. 365–415.
- Poulos, H.G., and E.H. Davis. *Pile foundation analysis and design*. Wiley and Sons, New York, 1990.
- PPI. "Compression of 16-inch steel rebar cage core plastic piling." *Plastic Piling, Inc. Newsletter*, 8(5), 2002.
- Prian, L., and A. Barkatt. "Degradation mechanism of fiber-reinforced plastics and its implications to prediction of long-term behavior." *Journal of Materials Science*, 34(16), 1999, pp. 3977–3989.
- Randolph, M.F. "Design methods for pile groups and pile drafts." *Proceedings, XIII ICSMFE*, New Delhi, India, 1994, pp. 61–82.
- Randolph, M.F., and C.P. Wroth. "Analysis of deformation of vertically loaded piles." *Journal of Geotechnical Engineering*, ASCE, 104(2), 1978, pp. 1465–1488.
- Randolph, M.F., J. Dolwin, and R. Beck. "Design of driven piles in sand." *Geotechnique*, 44(3), 1994, pp. 427–448.
- Reddy, E.S., D.N. Chapman, and V.V.R.N. Sastry. "Direct shear interface test for shaft capacity of sand." *Geotechnical Testing Journal*, ASTM, 23(2), 2000, pp. 199–205.
- Reese, L., S.T. Wang, J.A. Arrellaga, and J. Hendrix. *A program for the analysis of piles and drilled shafts under lateral loads*. ENSOFT, Inc., Houston, TX, 2000.
- Reese, L.C. "Analysis of laterally loaded piles in weak rock." *Journal of Geotechnical and Geoenvironmental Engineering*, ASCE, 123(11), 1997, pp. 1010–1017.
- Reese, L.C. "Handbook on Design of Piles and Drilled Shafts Under Lateral Load." *Report FHWA-IP-84-1*, Federal Highway Administration, Washington, DC, 1984.
- Reese, L.C., and R.C. Welch. "Lateral loading of deep foundations in stiff clay." *Journal of Geotechnical Engineering*, ASCE, 101(GT7), 1975, pp. 633–649.
- Reese, L.C., and W.F. Van Impe. *Single piles and pile groups under lateral loading*. A. A. Balkema, Brookfield, VT, 2001.

- Reese, L.C., W.M. Isenhower, and S.T. Wang. "Lateral capacity of caissons." *Proceedings, Conference on Excellence in Geotechnical Engineering*, Harrisburg, PA, 1997, 24 pp.
- Reese, L.C., W.R. Cox, and F.D. Koop. "Analysis of laterally loaded piles in sand." *Proceedings, VI Annual Offshore Technology Conference*, Houston, TX, II(OTC 2080), 1974, pp. 473–485.
- Reese, L.C., W.R. Cox, and F.D. Koop. "Field testing and analysis of laterally loaded piles in stiff clay." *Proceedings, VII Annual Offshore Technology Conference*, Houston, TX, II(OTC 2312), 1975, pp. 672–690.
- Richwien, W., and Z. Wang. "Displacement of a pile under axial load." *Geotechnique*, 49(4), 1999, pp. 537–541.
- Rix, G.J., and K.H. Stokoe. "Correlation of initial tangent modulus and cone resistance." *Proceedings, International Symposium on Calibration Chamber Testing*, Potsdam, NY, 1991, pp. 351–362.
- Robertson, P.K., M.P. Davies, and R.G. Campanella. "SPT-CPT design of laterally loaded driven piles using the flat dilatometer." *Geotechnical Testing Journal*, 12(1), 1989, pp. 30–38.
- Roeder, C.W., B. Cameron, and C.B. Brown. "Composite action in concrete filled tubes." *Journal of Structural Engineering*, 125(5), 1999, pp. 477–484.
- Rollins, K.M., N.P. Miller, and D. Hemenway. "Evaluation of pile capacity prediction methods based on cone penetration testing using results from I-15 load tests." *Transportation Research Record*, 1675, 1999, pp. 41–50.
- Rosselli, F. "Three-point bending of composite piles." *Report No. 95-001*, University of Delaware Center for Composite Materials, 1996, Wilmington, DE.
- Saafi, M., H.A. Toutanji, and Z. Li. "Behavior of concrete columns confined with fiber reinforced polymer tubes." *ACI Materials Journal*, 96(4), 1999, pp. 500–509.
- Salgado, R., and M.F. Randolph. "Analysis of cavity expansion in sand." *International Journal of Geomechanics*, 1(2), 2001. pp. 175–192.
- Samaan, M., A. Mirmiran, and M. Shahawy. "Modeling of concrete confined by fiber composites." *Journal of Structural Engineering*, ASCE, 124(9), 1998, pp. 1025–1031.
- Schultheisz, C.R., W.G. McDonough, S. Kondagunta, C.L. Schutte, K.S. Macturk, M. McAuliffe, and D.L. Hunston. "Effect of moisture on e-glass/epoxy interfacial and fiber strengths." *Composite Materials: Testing and Design*, ASTM, STP 1242, 1997. pp. 257–286.

- Scott, D.W., M.E. Pace, T.S. Poole, and F.A. Tavarez. "Composite materials piles soil-structure interaction—Task A: Review of past and present research and state of practice." *Interim Report*, U.S. Army Corps of Engineers, Waterways Experiment Station, Vicksburg, MS, 1998.
- Seaward International. 2001. <http://www.seaward.com/SEAPILE.html>.
- Sen, R., M. Issa, P. Wadsack, and M. Shahawy. "Driving stresses in fiberglass pretensioned piles." *ACI Structural Journal*, 90(6), 1993, pp. 666–674.
- Shahawy, M., A. Mirmiran, and M. Samaan. "Hybrid columns of FRP and concrete." *Proceedings, 4th Materials Engineering Conference*, Washington, DC, 1996, pp. 73–82.
- Shao, Y., and S. Kouadio. (2002). "Durability of fiberglass composite sheet piles in water." *Journal of Composites for Construction*, 6(4), 2002, pp. 280–287.
- Shehata, I. A., L.A.V. Carneiro, and L.C.D. Shehata. "Strength of short concrete columns confined with CFRP sheets." *Materials and Structures*, 35, 2002, pp. 50–58.
- Shen, C.-H., and G.S. Springer. "Moisture absorption and desorption of composite materials." *Journal of Composite Materials*, 10, 1976, pp. 2–20.
- Simonini, P. "Analysis of behavior of sands surrounding pile tips." *Journal of Geotechnical Engineering*, ASCE, 122(11), 1996, pp. 897–905.
- Simons, H.A. "A theoretical study of pile driving," PhD dissertation, Cambridge University, Cambridge, UK, 1985.
- Smith, E.A.L. "Impact and longitudinal wave transmission." *Transactions of the American Society of Mechanical Engineers*, 77, 1955, pp. 963–972.
- Smith, E.A.L. "Pile-driving analysis by the wave equation." *Journal of the Soil Mechanics and Foundations Division*, ASCE, 86(EM 4), 1960, pp. 35–61.
- Spiro, B.R., and M.A. Pais. "Dynamic pile evaluation and pile load test results—Piers 10, 11, and 12 Pembroke Avenue Bridge Replacement, Hampton, VA." *GSI Project No. 21-3-126*, Geotechnical Specialties, Inc., Norfolk, VA, June 2002.
- Spiro, B.R., and M.A. Pais. "Dynamic pile evaluation and pile load test results—Test Piles TP#1, TP#2, and TP#3 at Spit Area, Pembroke Avenue Bridge Replacement, Hampton, VA." *GSI Project No. 21-3-126*, Geotechnical Specialties, Inc., Norfolk, VA, 2 vols., March and July, 2002.
- Spolestra, M.R., and G. Monti. "FRP-confined concrete model." *Journal of Composites for Construction*, 3(3), 1999, pp. 143–150.

- Springer, G.S. "Effects of temperature and moisture on sheet molding compounds." *Journal of Reinforced Plastics and Composites*, 2, 1983, pp. 70–89.
- Springer, G.S., et al. "Environmental effects on GFRP polyester and vinyl ester composites." *Journal of Composite Materials*, 14, 1980, pp. 213–223.
- Stapleman, J. "Pile on the abuse." *Composites Technology*, September/October 1997, 3 pp.
- Stippes, M.C., G. Wempner, M. Stern, and R. Beckett. *An introduction to the mechanics of deformable bodies*. Merrill Books, 1961.
- Stokes, F. "Axial compression test on 15.25" PPI pile." *Test Report for Plastic Piling, Inc.*, Lehigh University, Lehigh, PA, 2002.
- Taylor, R.B. "Composite recycled plastic marine piling and timber: An alternate to traditional wood products for marine use." *Proceedings, Ports '95*, Tampa, FL, 1995, pp. 711–722.
- Tetra Tech EM, Inc. "Plastic pier piling evaluation report." *Tetra Tech EM Report*, 1999.
- Toutanji, H.A. "Stress-strain characteristic of concrete columns externally confined with advanced fiber composite sheets." *ACI Materials Journal*, 96(3), 1999, pp. 397–404.
- Toutanji, H.A., and M. Saafi. "Stress-strain behavior of concrete columns confined with hybrid composite materials." *Materials and Structures*, 35, 2001, pp. 338–347.
- Uesugi, M., H. Kishida, and Y. Tsubakihara. "Behavior of sand particles in sand-stell friction." *Soils and Foundations*, 28(10), 1988, pp. 107–118.
- Van Impe, W.F. "Deformations of deep foundations." *Proceedings, 10th European Conference on Soil Mechanics and Foundation Engineering*, Florence, Italy, III, 1991, pp. 1031–1062.
- Vecchio, F. and M. Collins. "Modified compression field theory for reinforced concrete elements subject to shear." *ACI Journal*, 83(2), 1986, pp. 219–231.
- Verghese, K.N.E., et al. "Freeze-thaw durability of polymer matrix composites in infrastructure." *Proceedings, International Conference on Progress in Durability Analysis of Composite Systems*, Brussels, Belgium, 1999, pp. 457–464.
- Vijayvergiya, V.N. "Load-movement characteristics of piles." *Proceedings, Ports '77: 4th Annual Symposium of the Waterway, Port, Coastal, and Ocean Division*, Long Beach, CA, 1977, pp. 269–284.
- Warren, G. "Limited flexural tests of plastic composite pile configurations." *Test report for Plastic Piling, Inc.*, 1996.

- Weaver, T.J., K.M. Rollins, and K.T. Peterson. "Lateral Static load testing and analysis of a pile group." *Proceedings, Geotechnical Earthquake Engineering and Soil Dynamics III*, Seattle, WA, 1998, pp. 1319–1330.
- Welch, R.C., and L.C. Reese. "Laterally loaded behavior of drilled shafts." *Research Report 3-5-65-89*, Center for Highway Research, University of Texas, Austin, TX, 1972.
- Woo, S.M., and C.H. Juang. "Analysis of pile test results." *Developments in Deep Foundations and Ground Improvement Schemes*, 1994, pp. 69–88.
- Wu, H.-C. "Confinement efficiency of FRP wrapping on concrete." *Proceedings, 1999 ASME International Mechanical Engineering Congress and Exposition*, Nashville, TN, pp. 231–235.
- Yoshimi, Y., and T. Kishidi. "A ring torsion apparatus for evaluating friction between soil and metal surfaces." *Geotechnical Testing Journal*, ASTM, 4, 1982, pp. 145–152.